# HYDRODYNAMIC AND SEDIMENT TRANSPORT ANALYSES FOR CONOWINGO POND

**Exelon Generation Company, LLC**
300 Exelon Way
Kennett Square, Pennsylvania

**June, 2017**

# HYDRODYNAMIC AND SEDIMENT TRANSPORT ANALYSES FOR CONOWINGO POND

Prepared for:

Exelon Generation Company, LLC
300 Exelon Way
Kennett Square, Pennsylvania

Prepared by:

HDR
1 International Boulevard
10th Floor, Suite 1000
Mahwah, New Jersey

June, 2017

# AUTHORSHIP AND ACKNOWLEDGEMENTS

The primary authors of this report are Mark Velleux and James Hallden (HDR). Other contributors include Ruta Rugabandana, Carmen Santos, Badri Yadav, James Glassley, Tobin Lilly, James Wands, and James Fitzpatrick (HDR). Analyses of relationships between moisture content and wet bulk density for Conowingo Pond sediments and review comments were provided courtesy of Dr. Marjorie Zeff (AECOM). HEC-RAS simulations results used as inputs to the Conowingo Pond model were provided courtesy of Dr. Martin Teal and John Viducich (WEST Consultants). HSPF simulation results were provided courtesy of Gopal Bhatt (Chesapeake Bay Program). Bathymetric survey data, other site information, and review comments were provided courtesy of Gary Lemay, Tim Sullivan, and Tom Sullivan (Gomez and Sullivan). Water level and meteorological data for Conowingo Pond were provided courtesy of Exelon.

The authors gratefully acknowledge review comments from Dr. Steve Scott (University of Mississippi) and Dr. Peter Wilcock (Utah State University).

# TABLE OF CONTENTS

# LIST OF FIGURES

# LIST OF TABLES

# 1. INTRODUCTION

This report was developed as part of the Lower Susquehanna River Integrated Sediment and Nutrient Monitoring Program. The project includes development and application of a coupled suite of hydrodynamic, sediment transport, and nutrient transport models for Conowingo Pond (Pond). The coupled suite of models is termed the Conowingo Pond Mass Balance Model (CPMBM). The Pond is formed by Conowingo Dam, which is the last impoundment in a sequence of three hydropower facilities on the Susquehanna River before it reaches Chesapeake Bay (Bay). CPMBM hydrodynamic and sediment transport simulations were developed to evaluate conditions in the Pond (e.g., sediment bed elevation changes in response to flow events) and to drive nutrient transport simulations to evaluate nutrient loads and reactivity. The intent of these simulations is to generate load estimates and system responses to inform development of the Phase 6 HSPF (Hydrologic Simulation Program FORTRAN) watershed model that the U.S. Environmental Protection Agency (USEPA) Chesapeake Bay Program (CBP) will use in the 2017 mid-point assessment called for as part of the 2010 Total Maximum Daily Load (TMDL) assessment for the Bay.

The ECOM (Estuarine, Coastal, and Ocean Model) framework and its integrated SEDZLJS (SEDiment dynamics by Ziegler, Lick, Jones, and Sandford) sediment transport module, were used to develop the hydrodynamic and sediment transport components of the CPMBM suite of models. ECOM has a long history of development and application and has been used to support regulatory decision-making. The hydrodynamic and sediment transport model generates flow, temperature, sediment concentration, and erosion and deposition flux information that will be used by the nutrient transport model.

Model parameters (e.g., bottom roughness, sediment grain size distributions, particle diameters, etc.) were assigned or calibrated based on field measurements and other site information. Suspended solids and temperature inputs from the Susquehanna River watershed were derived from other models, including the USEPA HSPF watershed model (Phase 6, Beta 2; P6B2) and HEC-RAS simulations for Lakes Clarke and Aldred (WEST, 2016), the two impounded reservoirs immediately upstream of Conowingo Pond. Simulations were performed to estimate spatial patterns of erosion and deposition over time as well as estimate concentrations of suspended sediments transported out of Conowingo Pond over time. Hydrodynamic and sediment transport model results were compared to site data to evaluate model performance. Comparisons include water surface elevations over time, water temperatures at different points in the reservoir, suspended sediment concentrations over time, and spatial patterns of sediment bed elevation changes over time. In the descriptions sections of this report, the term “simulated” is used to represent quantities calculated by the numerical model and the term “measured” is used to represent quantities measured in the field or laboratory.

# 2. HYDRODYNAMIC AND SEDIMENT TRANSPORT MODEL THEORY

A three-dimensional (3-D) hydrodynamic model for Conowingo Pond was constructed using the ECOM framework (HQI, 2010). ECOM is the hydrodynamic module of the framework and SEDZLJS (Jones and Lick, 2001; James et al. 2010; USEPA, 2014; USEPA, 2016) is its integrated sediment transport module. When used with its sediment transport module, it is also known as ECOMSED or ECOM-SEDZLJS. For simplicity, the acronym ECOM is used hereafter to describe the model and its hydrodynamic and sediment transport modules. A general overview of model governing equations follows.

ECOM has been successfully applied to rivers, lakes, estuaries, coastal and ocean areas worldwide. Its predictive capabilities have been assessed through extensive comparisons with data to demonstrate that the model represents the predominant physics of different water bodies in a realistic manner. These applications include: Delaware River, Delaware Bay, and adjacent continental shelf (Galperin and Mellor, 1990a,b,c), South Atlantic Bight (Blumberg and Mellor, 1983), Hudson-Raritan estuary (Oey et al., 1985a,b), Gulf of Mexico (Blumberg and Mellor, 1985), Chesapeake Bay (Blumberg and Goodrich 1990), Massachusetts Bay (Blumberg et al., 1993), St. Andrew Bay (Blumberg and Kim, 2000), New York Harbor and Bight (Blumberg et al., 1999), Onondaga Lake (Ahsan and Blumberg, 1999), Lake Michigan (Schwab et al., 1999), Lake Pontchartrain (Signell and List, 1997), Lower Fox River (HQI, 2000; Baird, 2000a; Baird, 2000b) Green Bay (HQI, 1999g; HQI, 2001), Lake Ontario (HQI, 2005 and 2008), and the Lower Passaic River (USEPA, 2014; USEPA, 2016).

ECOM uses a conformal curvilinear coordinate system with variable grid resolution. Fine spatial (horizontal) resolution can be achieved by using a smaller model grid size in areas of special interest or concern. In the vertical direction, the model uses a transformed σ-coordinate system, which allows it to follow changes in bottom topography and surface elevation and to resolve associated vertical velocity profiles. The model solves coupled three-dimensional advection-diffusion equations for water mass, momentum, heat, and salinity and employs a two-equation turbulent-closure scheme (Blumberg and Mellor, 1987; Galerpin et al., 1988; Mellor and Yamada, 1982) to provide realistic representation of vertical mixing processes. ECOM can be used as a stand-alone hydrodynamic model or in conjunction with its integrated sediment transport model to simulate erosion, deposition, and transport of cohesive and non-cohesive sediments.

## 2.1. HYDRODYNAMICS

Currents (and tides) move water (fluid) and transport sediments in the water column and sediment bed. Water movement is also influenced by meteorological conditions, temperature, and salinity differences. As water flows, it is subject to frictional resistance

(drag) along boundaries (surfaces) of all material it passes. The balance between gravity and drag forces along the flow path determines the velocity and flow depth. The force that flowing water exerts on the sediment bed is described in terms of the shear stress. The hydrodynamic module in ECOM is used to simulate water velocities, water surface elevations (depths), and shear stresses.

The governing equations for hydrodynamics are:

***Conservation of Mass (Continuity): Fluid***

$$\frac{\partial U}{\partial x}+\frac{\partial V}{\partial y}+\frac{\partial W}{\partial z}=0 \tag{2-1}$$

***Conservation of Momentum: Fluid***

$$\frac{\partial U}{\partial t}+U\frac{\partial U}{\partial x}+V\frac{\partial U}{\partial y}+W\frac{\partial U}{\partial z}-fV=-\frac{1}{\rho_0}\frac{\partial P}{\partial x}+\frac{\partial}{\partial z}\left(K_M\frac{\partial U}{\partial z}\right)+F_x \tag{2-2}$$

$$\frac{\partial V}{\partial t}+V\frac{\partial V}{\partial x}+V\frac{\partial V}{\partial y}+W\frac{\partial V}{\partial z}-fU=-\frac{1}{\rho_0}\frac{\partial P}{\partial y}+\frac{\partial}{\partial z}\left(K_M\frac{\partial V}{\partial z}\right)+F_y \tag{2-3}$$

$$\rho g=-\frac{\partial P}{\partial z} \tag{2-4}$$

***Conservation of Mass (Continuity): Temperature***

$$\frac{\partial T}{\partial t}+U\frac{\partial T}{\partial x}+V\frac{\partial T}{\partial y}+W\frac{\partial T}{\partial z}=\frac{\partial}{\partial z}\left(K_H\frac{\partial T}{\partial z}\right)+F_T \tag{2-5}$$

***Conservation of Mass (Continuity): Salinity***

$$\frac{\partial S}{\partial t}+U\frac{\partial S}{\partial x}+V\frac{\partial S}{\partial y}+W\frac{\partial S}{\partial z}=\frac{\partial}{\partial z}\left(K_H\frac{\partial S}{\partial z}\right)+F_S \tag{2-6}$$

where:

*U, V, W* = mean (Reynolds-average) velocities in the x-, y-, and z-directions, respectively [L $T^{-1}$]

$T$ = temperature [$\theta$] [1]

$S$ = salinity [dimensionless] (e.g., parts per thousand)

$\rho_0$ = reference density of water [M $L^{-3}$]

$\rho$ = local density of water [M $L^{-3}$]

$g$ = gravitational acceleration [L $T^{-2}$]

$f$ = Coriolis parameter [$T^{-1}$];

$P$ = pressure [M $L^{-1}$ $T^{-2}$]

$K_M$ = vertical eddy viscosity for fluid [$L^2$ $T^{-1}$]

$K_H$ = vertical eddy diffusivity for temperature and salinity [$L^2$ $T^{-1}$]

$F_x$, $F_y$ = horizontal diffusion of momentum in the x- and y-directions, respectively [$L^2$ $T^{-1}$]

$F_T$, $F_S$ = horizontal diffusion of temperature and salinity, respectively [$\theta$ $T^{-1}$, $T^{-1}$]

Horizontal diffusion terms represent small (sub-grid) scale processes not directly resolved by the model grid and are expressed in a form analogous to molecular diffusion:

$$F_x = \frac{\partial}{\partial x}\left(2A_M \frac{\partial U}{\partial x}\right) + \frac{\partial}{\partial y}\left[A_M\left(\frac{\partial U}{\partial y} + \frac{\partial V}{\partial x}\right)\right] \quad (2\text{-}7)$$

$$F_y = \frac{\partial}{\partial y}\left(2A_M \frac{\partial V}{\partial y}\right) + \frac{\partial}{\partial x}\left[A_M\left(\frac{\partial U}{\partial y} + \frac{\partial V}{\partial x}\right)\right] \quad (2\text{-}8)$$

$$F_T = \frac{\partial}{\partial x}\left(A_H \frac{\partial T}{\partial x}\right) + \frac{\partial}{\partial y}\left[A_H\left(\frac{\partial T}{\partial y}\right)\right] \quad (2\text{-}9)$$

$$F_S = \frac{\partial}{\partial x}\left(A_H \frac{\partial S}{\partial x}\right) + \frac{\partial}{\partial y}\left[A_H\left(\frac{\partial S}{\partial y}\right)\right] \quad (2\text{-}10)$$

where:

$A_M$ = horizontal eddy viscosity [$L^2$ $T^{-1}$]

$A_H$ = horizontal eddy diffusivity [$L^2$ $T^{-1}$]

[1] The symbol θ is used to represent fundamental units of temperature in the LTMθ system (see Dingman, 2002). θ indicates degree and $\theta^{-1}$ indicates degree$^{-1}$.

In developing these equations, two simplifying assumptions were made: (1) the weight of the fluid identically balances the pressure (hydrostatic pressure assumption); and (2) density differences are negligible unless those differences are multiplied by the gravitational acceleration (Boussinesq approximation). As implemented in the model, these equations are transformed into a terrain-following, sigma (σ)-level coordinate system in the vertical direction and an orthogonal, curvilinear coordinate system in the horizontal direction as described by HQI (2010).

The governing equations contain Reynolds stress and flux terms that account for turbulent diffusion of momentum as expressed by eddy viscosity. The turbulence closure approach of Mellor and Yamada (1982) is used to solve these equations. Turbulent mixing terms ($K_M$) in the governing equations also occur in relationships between velocity gradients (∂U/∂z and ∂V/∂z) and shear stresses at the air-water and sediment-water interfaces (boundaries conditions). Shear stress at the sediment-water interface depends on a drag coefficient that relates surface roughness to velocity gradients at the bottom of the water column. Drag coefficients are determined using a logarithmic velocity profile to describe how velocities change near a boundary using the following relationship:

$$C_D = \left[ \frac{1}{\kappa} \ln\left( \frac{z}{z_0} \right) \right]^{-2} \qquad (2\text{-}11)$$

where:

$C_D$ = coefficient of drag [dimensionless]

$\kappa$ = von Karman constant = 0.4 [dimensionless]

$z$ = height above the sediment bed [L]

$z_0$ = hydrodynamic roughness height of the sediment bed [L]

The height above the sediment bed ($z$) used in the logarithmic velocity profile is termed the matching height. Operationally, the matching height is equal to one half the thickness of the bottom layer of water in the model. When five, equally-spaced sigma-layers (i.e., vertical layers in the water column) are used in the model, each water column layer is one fifth (20%) of the water depth and the matching height is one tenth (10%) of the water depth. As water depth increases, hydrodynamic drag on the water column will decrease to a minimum value ($C_{D,min}$). Operationally, the minimum drag coefficient is in the range of 0.0025 to 0.003 and is used as a floor function (i.e., $C_D$ can never be less than $C_{D,min}$). If the drag coefficient value calculated using Equation (2-11) is less than $C_{D,min}$, $C_D$ is set to the minimum value. In practical terms, the drag coefficient will be at its minimum value when water depth is greater than approximately 98 feet (30 meters) when $C_{D,min}$ = 0.0025 and $z_0$ = 0.001 meters. For the model application to Conowingo Pond detailed in this report, water depths are less than 98 feet (30 meters) for the minimum drag threshold.

Using this approach, the primary model calibration parameters for hydrodynamics are hydrodynamic roughness height, $z_0$, and minimum coefficient of drag ($C_{D,min}$). Principal outputs of the hydrodynamic model are water depths (water surface elevations), water velocities in the x, y, and z directions, and total hydrodynamic shear stresses at the sediment-water interface. The total hydrodynamic shear stress exerted on the bed depends on the coefficient of drag and flow velocity:

$$\tau_b = \rho_w C_D u^2 \quad (2\text{-}12)$$

where:

$\tau_b$ = total (hydrodynamic) bed shear stress [M $L^{-1}$ $T^{-2}$]

$\rho_w$ = density of water [M $L^{-3}$]

$C_D$ = coefficient of drag [dimensionless]

$u$ = flow velocity (U in x- direction, V in y-direction) [L $T^{-1}$]

Further descriptions of shear stress are provided in the description of the sediment transport model and Appendix A.

## 2.2. SEDIMENT TRANSPORT

In the water column, particles are transported by advection (movement with currents) and can be exchanged between the sediment bed and water column by erosion and deposition. Particles may be transported as suspended load (fully entrained in the water column) or as bedload (in contact with the bed). Sediment behavior can be classified across a continuum from cohesive to non-cohesive. Cohesive sediments are typically described in terms of aggregate properties (i.e., properties of the sediment as a whole) because of the tendency of individual sediment grains to aggregate and flocculate in the water column and exhibit erosional resistance in the sediment bed. Non-cohesive sediments are described in terms of the properties of individual grains because the individual grains comprising the sediment mixture do not flocculate in the water column and do not exhibit erosional resistance beyond that attributable to individual grains.

### 2.2.1. Shear Stress Partitioning and Surface Drag

The shear stress at the sediment–water interface generated by water flowing over the bed surface is a primary determinant of the extent to which materials settling out of the water column are deposited on the bed or are eroded from it and whether particles in motion are transported as suspended load or bed load. Near the bed, vertical velocity gradients exist because water velocities decrease and typically diminish to zero at the sediment-water

interface. Vertical velocity gradients generate shear stresses that act on the bed. Very close to the bed, at scales that typically ranged from a few particle diameters to the length of bedforms (e.g., ripples and dunes), the total (hydrodynamic) bed shear stress can be separated (partitioned) into two components: (1) surface drag, and (2) form drag. The relationship between total shear stress and its components is:

$$\tau_b = \tau_g + \tau_f \quad (2\text{-}13)$$

where:

$\tau_b$ = total (hydrodynamic) bed shear stress [M $L^{-1}$ $T^{-2}$]

$\tau_g$ = surface drag ("grain") shear stress [M $L^{-1}$ $T^{-2}$]

$\tau_f$ = form drag shear stress [M $L^{-1}$ $T^{-2}$]

Surface drag acts to initiate particle movement off the bed surface, through the bottom boundary layer, and into the main body of the flow. The surface drag component of total bed shear stress is often termed "grain" shear stress or "skin friction". The form drag component to total bed shear stress depends on the critical shear stress for sediment erosion and the diameter of particles comprising the sediment bed following the methods described by van Rijn (1993). A more detailed description of the process used to separate total hydrodynamic shear stress into surface drag and form drag components is presented in Appendix A.

### 2.2.2. Erosion

Erosion is the process by which particles at rest in the sediment bed are set into motion. Sediments may erode in a cohesive or non-cohesive manner as a function of clay content and grain size (i.e., weighted average diameter) of particles comprising the bed. Threshold clay content and average grain size values are specified as model inputs. Rates at which sediments erode vary widely because sediment characteristics vary by location and also with depth in the sediment bed. Erosion rates for cohesive sediments are highly variable and generally must be determined from site-specific flume studies. Rates for non-cohesive sediment vary with composition (i.e., grain size distribution) and can be estimated from tabulated results of laboratory flume studies. SEDZLJS (Jones and Lick, 2001; Scott et. al. 2010; USEPA, 2014; USEPA, 2016) allows use of erosion rate measurements performed using the SEDFLUME device. SEDFLUME measurements for various sediments are illustrated by McNeil et al. (1996), Jepsen et al. (1997, 2000), Roberts et al. (1998, 2003), and the U.S. Army Corps of Engineers sediment transport study of Conowingo Pond (USACE, 2014).

In the SEDZLJS framework, erosion rates at known shear stress levels and depths in the sediment bed are tabulated based on SEDFLUME measurements. These erosion rates apply

to the overall matrix of particles comprising the bed. Erosion rates at shear stresses and depths between measured values are estimated by interpolating between pairs of measured values as follows:

$$E(\tau_g) = \left(\frac{\tau_{m+1} - \tau_g}{\tau_{m+1} - \tau_m}\right) E_m + \left(\frac{\tau_g - \tau_m}{\tau_{m+1} - \tau_m}\right) E_{m+1} \quad (2\text{-}14)$$

$$\ln[E(D)] = \left(\frac{{D_0}^n - D}{{D_0}^n}\right) \ln[E^n] + \left(\frac{D}{{D_0}^n}\right) \ln[E^{n+1}] \quad (2\text{-}15)$$

where:

$E(\tau_g)$ = erosion at a grain shear stress equal to $\tau_g$ [L $T^{-1}$]

$\tau_g$ = grain shear stress [M $L^{-1}$ $T^{-2}$]

$\tau_{m+1}$ = measured grain shear stress greater than $\tau_g$ [M $L^{-1}$ $T^{-2}$]

$\tau_m$ = measured grain shear stress less than $\tau_g$ [M $L^{-1}$ $T^{-2}$]

$E_m$ = measured erosion at a measured grain shear stress $\tau_m$ [L $T^{-1}$]

$E_{m+1}$ = measured erosion at a measured grain shear stress $\tau_{m+1}$ [L $T^{-1}$]

$E(D)$ = erosion rate at a depth in the sediment bed equal to $D$ [L $T^{-1}$]

$D$ = depth in the sediment bed within sediment layer $n$ [L]

$D_0^n$ = initial thickness of sediment layer $n$ prior to erosion [L]

$E^n$ = measured erosion at the top of sediment layer $n$ [L $T^{-1}$]

$E^{n+1}$ = measured erosion at the top of sediment layer $n+1$ (i.e., measured rate at the bottom of sediment layer $n$) [L $T^{-1}$]

Equations (2-14) and (2-15) are used to express erosion rate variation as a function of both shear stress and depth in the sediment bed. SEDFLUME measurements are typically used to characterize erosion rates for sediments that erode in cohesive or non-cohesive fashion.

Erosion occurs when grain shear stress at the sediment surface exceeds the critical shear stress for erosion (i.e. the incipient motion threshold), $\tau_{ce}$. In the SEDZLJS framework, $\tau_{ce}$ values represent the aggregate behavior of the overall matrix of particles comprising the bed and are determined from SEDFLUME measurements or other physical properties (e.g., clay content and plasticity). Sediments behave in a cohesive manner and erode in an aggregate manner when the average diameter of particles comprising the bed is less than a size threshold (e.g., 200 μm) or when the clay content of the bed is less than a clay content threshold (e.g., 10% clay). Sediments behave in a non-cohesive manner and may be subject

to grain-by-grain erosion when the overall matrix of particles within the surface layer of the bed exceeds the size threshold and the clay content is below the clay content threshold.

The critical shear stress for erosion of each particle type simulated is specified as a model input and can be estimated from grain size using the Shields (1936) curve as described in standard references (see Julien, 1998). Formulae by van Rijn (1984a), Soulsby (1997), or Guo (2002) provide approximations to the Shields curve. The formula of Guo (2002) is:

$$\tau_{ce} = \left(G_p - 1\right)\rho_w g d_p \left( \frac{0.23}{d_*} + 0.054\left[1 - \exp\left( -\frac{d_*^{0.85}}{23} \right)\right]\right) \quad (2\text{-}16)$$

$$d_* = d_p \left[ \frac{\left(G_p - 1\right)g}{\nu^2} \right]^{-1/3} \quad (2\text{-}17)$$

where:

$\tau_{ce}$ = critical shear stress for erosion [M $L^{-1}$ $T^{-2}$]

$G_p$ = sediment particle specific gravity ≈ 2.65 [dimensionless]

$\rho_w$ = fluid density ≈ 1000 kg/$m^3$ (≈ 1025 kg/$m^3$ for seawater) [M $L^{-3}$]

$g$ = gravitational acceleration = 9.81 m/$s^2$ [L $T^{-2}$]

$d_p$ = sediment particle diameter [L]

$d_*$ = dimensionless particle diameter [dimensionless]

$\nu$ = kinematic viscosity [$L^2$ $T^{-1}$]

Equation (2-16) is applicable when particles are transported as discrete grains. When interpreting SEDFLUME measurements, the onset of erosion is operationally defined as the shear stress at which erosion occurs at a rate of $10^{-4}$ cm/s.

### 2.2.3. Bedload and Suspended Load Transport

Two distinct modes of sediment transport occur: (i) bedload, and (ii) suspended load. During bedload transport, particles move by rolling, sliding, or saltation in a thin layer in contact with the bed surface. During suspended transport, particles are fully entrained in the water column and do not have contact with the bed. Finer particles are not typically transported as bedload because they are readily entrained into the water column in full suspension. Larger particles are transported as bedload, suspended load, or a combination of the two.

When shear stresses acting on the bed surface are less than the critical shear stress for erosion ($\tau_{ce}$), sediment particles on the bed surface will be stationary. When shear stresses on the bed exceed the critical shear stress for erosion ($\tau_{ce}$) but are less than the critical shear stress for suspension ($\tau_{cs}$), sediment particles will be transported as bedload. When shear stresses on the bed exceed the critical shear stress for suspension, some or all of the sediment in motion will be entrained and transported as suspended load. The fraction of sediments transported as bedload or suspended load are determined as (van Rijn, 1993; van Rijn, 1984b; Jones and Lick, 2001; James et al. 2010):

$$f_{BL} = \begin{cases} 0 & for \quad \tau_g \le \tau_{ce} \\ 1 - f_{SL} & for \quad \tau_g > \tau_{cs} \end{cases} \tag{2-18}$$

$$f_{SL} = \begin{cases} 0 & for \quad \tau_g \le \tau_{cs} \\ \dfrac{\ln\left(u_* / w_s\right) - \ln\left(\sqrt{\tau_{cs}/\rho_w}/w_s\right)}{\ln(4) - \ln\left(\sqrt{\tau_{cs}/\rho_w}/w_s\right)} & for \quad \tau_g > \tau_{cs} \quad and \quad u_*/w_s < 4 \\ 1 & for \quad \tau_g > \tau_{cs} \quad and \quad u_*/w_s \ge 4 \end{cases} \tag{2-19}$$

$$\tau_{cs} = \begin{cases} \rho_w \left( \dfrac{4 w_s}{d_*} \right)^2 & for \quad d_p \le 400\,\mu m \\ \rho_w \left(0.4 w_s\right)^2 & for \quad d_p > 400\,\mu m \end{cases} \tag{2-20}$$

where:

$f_{BL}$ = fraction of sediment transported as bedload [dimensionless]

$f_{SL}$ = fraction of sediment transported as suspended load [dimensionless]

$\tau_g$ = surface drag (grain) component of total shear stress

$\tau_{ce}$ = critical shear stress for erosion [M $L^{-1}$ $T^{-2}$]

$\tau_{cs}$ = critical shear stress for suspension [M $L^{-1}$ $T^{-2}$]

$u_{*g}$ = surface drag (grain) component of total shear velocity [L $T^{-1}$]

$w_s$ = particle settling velocity [L $T^{-1}$]

$\rho_w$ = fluid density ≈ 1000 kg/$m^3$ (≈ 1025 kg/$m^3$ for seawater) [M $L^{-3}$]

$d_*$ = dimensionless particle diameter [dimensionless]

$d_p$ = sediment particle diameter [L]

Equations (2-18) through (2-20) are used for each particle type in combination with the particle grain size distribution to express the erosion flux of sediment by grain size that is transported by bedload and suspended load as a function of grain shear stress. For fine particles that are readily carried in full suspension rather than as bedload (e.g., discrete clay particles), $\tau_{cs}$ would be set equal to the value of $\tau_{ce}$ for that particle type.

### 2.2.4. Settling and Deposition

Sediment particles in the water column move downward (i.e., settle) under the force of gravity and may be deposited on the bed surface depending on shear stress conditions. The effective settling velocity of a particle is a function of its settling characteristics under quiescent conditions and its probability of deposition (i.e., likelihood that a particle will come to rest on the bed surface). Cohesive and non-cohesive particle types have different settling and deposition characteristics. Descriptions of cohesive sediment behavior are presented by HQI (2010), and other references (e.g., van Rijn, 1993; Winterwerp and van Kesteren, 2004).

The effective settling velocity of a particle is computed as:

$$w_{se} = w_{sq} P_{dep} \tag{2-21}$$

where:

$w_{se}$ = effective settling velocity [L T$^{-1}$]
$w_{sq}$ = quiescent settling velocity [L T$^{-1}$]
$P_{dep}$ = probability of deposition [dimensionless]

For natural, non-flocculating particles, quiescent settling velocities can be determined using the formula of Cheng (1997):

$$w_{sq} = \frac{\nu}{d_p}\left[\left(25 + 1.2 d_*^{\,2}\right)^{0.5} - 5\right]^{-1.5} \tag{2-22}$$

where:

$w_{sq}$ = quiescent settling velocity [L T$^{-1}$]
$\nu$ = kinematic viscosity of water [L$^2$ T$^{-1}$]
$d_p$ = sediment particle diameter [L]
$d_*$ = dimensionless particle diameter [dimensionless]

Alternatively, the settling velocity of particles, including floc-forming particle types, can be determined from field studies.

As a result of turbulence and other factors, not all particles settling through a column of flowing water necessarily reach the sediment-water interface or are incorporated into the bed. The effective settling velocity of a particle is described as a reduction in the quiescent settling velocity by a probability of deposition. Probability of deposition varies with particle size and shear stress near the sediment bed. As particle size decreases or shear stress increases, the probability of deposition decreases. In the SEDZLJS framework, the probability of deposition for particles with diameters greater than a user-defined limit (e.g., 200 micrometers [μm]) is described as a function of grain shear stress and critical shear stress for deposition using the approach described by Gessler (1965; 1967; 1971):

$$P_{dep} = P = \frac{1}{\sqrt{2\pi}} \int_{-\infty}^{Y} e^{-0.5x^2} dx \qquad (2\text{-}23)$$

$$Y = \frac{1}{\sigma}\left( \frac{\tau_{cd}}{\tau_g} - 1 \right) \qquad (2\text{-}24)$$

where:

$P_{dep}$ = probability of deposition [dimensionless]

$P$ = probability integral for the Gaussian distribution [dimensionless]

$\sigma$ = experimentally determined constant = 0.57

$\tau_g$ = surface (grain) component of total shear stress [M $L^{-1}$ $T^{-2}$]

$\tau_{cd}$ = critical shear stress for deposition [M $L^{-1}$ $T^{-2}$]

Similarly, the probability of deposition for particles with diameters less than the user-defined limit, which are presumptively cohesive in nature, is described as a function of grain shear stress and critical shear stress for deposition using the approach described by Krone (1962):

$$P_{dep} = P = \begin{cases} \left( 1 - \frac{\tau_g}{\tau_{cd}} \right) & for\ \tau_g < \tau_{cd} \\ 0 & for\ \tau_g \geq \tau_{cd} \end{cases} \qquad (2\text{-}25)$$

where:

$P_{dep}$ = probability of deposition [dimensionless]

$\tau_g$ = surface (grain) component of total shear stress [M $L^{-1}$ $T^{-2}$]

$\tau_{cd}$ = critical shear stress for deposition [M $L^{-1}$ $T^{-2}$]

Based on the approach of Gessler (1965; 1967; 1971), the critical shear stress for deposition is the point at which 50% of particles of a specified type will deposit to the bed (with the other 50% remaining in transport). In the SEDZLJS framework, the critical shear stress for deposition is assumed to equal the critical shear stress for suspension, $\tau_{cd}$ equals $\tau_{cs}$. Thus, when the shear stress acting on particles is less than $\tau_{cs}$, particles will settle out of the water column and enter the bedload layer according to the probability of deposition, with particles then depositing to the bed when the shear stress acting on those particles is less than their critical shear stress for erosion, $\tau_{cs}$. Similarly, based on the approach of Krone (1962), $\tau_{cd}$ equals $\tau_{cs}$ and, if those particles are not transported as bedload, $\tau_{cs}$ equals $\tau_{ce}$.

# 3. MODEL APPLICATION FOR CONOWINGO POND

The ECOM framework and its sediment transport module were applied to Conowingo Pond (the Pond) as part of CPMBM development. The Pond, formed by Conowingo Dam, is the farthest downstream impoundment in a sequence of three hydropower facility impoundments on the Susquehanna River before it reaches Chesapeake Bay (Bay). In upstream to downstream order, the impoundments are Lake Clarke, which is formed by Safe Harbor Dam, Lake Aldred, which is formed by Holtwood Dam, and Conowingo Pond, which is formed by Conowingo Dam. Three-dimensional numerical simulations were performed to evaluate hydrodynamic and sediment transport in the Pond and were also used to drive nutrient transport simulations to evaluate nutrient loads and reactivity. Short-term simulations were performed for the period 2008-2014 and provide the basis for model parameterization and calibration. Long-term simulations for the period 1997-2014 were also performed and provided additional information to refine initial conditions for the erosion resistance of the sediment bed. These simulation periods were selected based on the needs of USEPA modeling efforts for the 2017 mid-point assessment and the ability to define initial bed elevations at the start of each period.[2] Long-term simulation results were subsequently provided to the USEPA CBP to support mid-point assessment efforts.

The hydrodynamic and sediment transport components of the CPMBM were used to estimate:

- Suspended sediment concentrations and loads exported from the Pond;
- Spatial patterns of net sediment accumulation over time;
- Water temperatures to demonstrate model performance and facilitate nutrient transport simulation development.

With the exception of their initial bathymetric conditions, short-term and long-term simulations used the same parameterizations and yielded very similar results for the 2008-2014 timeframe. To place this model application and its results into context, it is important to note that system response is driven by factors that include:

- Inflows at Holtwood. This is the largest source of flow to Conowingo Pond. These inflows have not been measured previously and are influenced by hydropower operations upstream of Conowingo Pond (i.e., Safe Harbor and Holtwood). These inflows were estimated from water surface elevation changes (indicating changes in storage) and flows at Conowingo; and

[2] The U.S. Geological Survey (USGS) collected bathymetric data in Lake Clarke, Lake Aldred, and Conowingo Pond during August-October 1996. Data for the Pond were used to define initial conditions for simulations starting in January, 1997.

- Upstream suspended sediment loads and grain size distributions at Holtwood. This is the largest source of sediment to Conowingo Pond. These incoming loads have not been measured previously and are likely to be influenced by ambient sediment transport processes and hydropower operations in upstream impoundments (Lakes Clarke and Aldred) over time. These loads were estimated from other models. During early iterations of model development, loads from HSPF simulations were evaluated (e.g., P6B2 loads). As model development progressed, HEC-RAS simulations by WEST (2016) were the source of this loading information. Model results subsequently transmitted to USEPA were based on HEC-RAS loads at Holtwood.

## 3.1. SITE DESCRIPTION

### 3.1.1. Physical Setting

The site description that follows is derived primarily from licensing documents Exelon submitted to the Federal Energy Regulatory Commission (FERC) (Exelon, 2012a,b) and the Lower Susquehanna River Watershed Assessment (LSRWA) report prepared by the U.S. Army Corps of Engineers, Baltimore District (USACE), and the Maryland Department of the Environment (MDE) (USACE, 2014).

The Conowingo Dam and hydroelectric facility are located in the State of Maryland on the Susquehanna River at River Mile 10 (Figure 1). The impoundment formed by Conowingo Dam includes areas in both Pennsylvania and Maryland. The upstream limit of the study area is Holtwood Dam. Upstream of Holtwood the watershed has an area of 26,740 square miles ($mi^2$) and drains portions of New York, Pennsylvania, and Maryland. The downstream study limit is Conowingo Dam. At Conowingo, the watershed has a drainage area of 27,100 $mi^2$, indicating a mainstem river difference of 360 $mi^2$ from the upstream and downstream study boundary. Between Holtwood and Conowingo, the site receives flow and other inputs from other small tributaries and ungaged areas. Muddy Creek, which drains an area of approximately 133 $mi^2$, and Broad Creek, which drains an area of approximately 41 $mi^2$, are the two largest of these local tributaries. Ungaged areas account for approximately 186 $mi^2$ of the Pond's local drainage area. The area of interest is approximately 15 miles long, including the main reservoir and the Holtwood Dam tailrace area. The Muddy Run Pumped Storage Facility (MRPSF) is located along the east bank (left bank, facing downstream) of the reservoir approximately two miles downstream of Holtwood Dam. The Peach Bottom Atomic Power Station (PBAPS) is located along the west bank (right bank, facing downstream) approximately seven miles upstream of Conowingo Dam.

Conowingo Dam was completed in 1928, has a maximum height of approximately 94 feet (28.6 meters), and a length of 4,648 feet (1,417 meters). It is comprised of four sections from east (left bank, facing downstream) to west (right bank): a 1,190-foot (362.7 meter) long non-

overflow section with an elevation of 115.7 feet (35.3 meters) (NGVD29[3]); an ogee shaped spillway, the major portion of which is 2,250 feet (685.8 meters) long with a crest elevation of 86.7 feet (26.4 m) (NGVD29), and the minor portion of which is 135 feet (41.1 meters) long with a crest elevation of 99.2 feet (30.2 meters) (NGVD29); an intake-powerhouse, which is 946 feet (288.3 m) long; and a 127-foot (38.7 meter) long abutment. U.S. Highway Route No. 1 traverses the top of the dam.

At flows less than 86,000 cubic feet per second (cfs) (2,435 cubic meters per second [cms]), all flow normally passes through the intake-powerhouse. Flows in excess of 86,000 cfs (2,435 cms) are spilled. Flows over the spillway are controlled by 50 crest gates and two regulating gates. Each crest gate is 22.5 feet (6.9 meters) high by 38 feet (11.6 meters) wide and has a discharge capacity of approximately 16,000 cfs (453 cms) at a reservoir pool elevation of 109.2 feet (33.3 meters) (NGVD29). Each regulating gate is 10 feet (3 meters) high by 38 feet (11.6 meters) wide and has a discharge capacity of approximately 4,000 cfs (113.3) at a pool elevation of 109.2 feet (33.3 meters) (NGVD29). Flow passes through the intake-powerhouse until it reaches a threshold of approximately 400,000 to 500,000 cfs (11,330 to 14,158 cms), after which all river flow is spilled.

The normal full pool water surface elevation of the reservoir is 109.2 feet (33.3 meters) (NGVD29). At full pool, water depths average 27.3 feet (± 13.2 feet) (8.31 meters ± 4.0 meters) and range from approximately six feet (1.83 meters) to 72.3 feet (21.72 meters) near Conowingo Dam. These depths reflect conditions as estimated from analysis of sediment bed elevation surveys of the reservoir conducted over the period 2008 – 2015 and supplemented with additional elevation data for the Holtwood Dam and Muddy Run tailrace areas. The dam has a total impoundment design volume of approximately 310,000 acre-feet at normal full pond (Exelon, 2012b). Cross-channel and longitudinal water depth variations reflect remnant channels and terraces/bars of the river prior to impoundment in addition to sediment bed changes over time. The Conowingo Project License (Exelon, 2012b) allows for the Pond to fluctuate between elevation 101.2 (30.8 meters) and 110.2 feet (33.6 meters) (NGVD29), though in practice the pond is normally maintained between elevation 104.2 and 109.2 feet (31.8 and 33.3 meters) (NGVD29). The Pond also maintains a weekend minimum elevation of 107.2 feet (32.7 meters) (NGVD29) or greater during the summer recreation season (weekends from Memorial Day to Labor Day).

### 3.1.2. Hydrological Setting

Conowingo Pond is the downstream-most of a sequence of three impoundments along the Susquehanna River near its confluence with Chesapeake Bay. Flow through this reservoir reflects natural flow variation with additional modulation due to hydropower operations. A graphical summary of daily flow statistics computed from values reported at the U.S.

[3] Some other reports have presented elevations using the local Project datum, referred to as "Conowingo Datum". Conowingo datum elevations are 0.7 feet lower than NGVD29 elevations, such that elevation 108.5 ft Conowingo Datum equals elevation 109.2 ft NGVD29.

Geological Survey (USGS) gage for the Susquehanna River at Conowingo (Station 01578310) for the period October 1, 1967 through December 15, 2015 is presented in Figure 2. The average river flow for this period is 40,853 cfs (1,157 cms). The 10th percentile flow is 6,010 cfs (170 cms) and the 90th percentile flow is 84,700 cfs (2,398 cms). The 86,000 cfs (2,435 cms) threshold flow at which crest gates are opened and spill over the dam begins exceeds the 90th percentile flow. The maximum daily flow for the full period of record (1967 – 2015) is 1,120,000 cfs (31,715 cms) and occurred in 1972 during Hurricane Agnes. Another flow event of note occurred in 2011 during Tropical Storm Lee, during which a maximum daily flow of 709,000 cfs (20,077 cms) occurred. These flow data were acquired from the USGS National Water Information System (http://waterdata.usgs.gov/usa/nwis/uv?01578310).

Although detailed records exist for Conowingo, the USGS has not measured flow at Holtwood. Similarly, flow at Safe Harbor has not been measured. The nearest upstream flow monitoring station along the Susquehanna River is at Marietta, PA (Station 01576000), which is upstream of both the Holtwood and Safe Harbor Dams.

Water surface elevations generally vary over a narrow range and are reported at three locations within Conowingo Pond: (1) MRPSF (Muddy Run) tailrace; (2) PBAPS (Peach Bottom) cooling water intake canal; and Conowingo Dam headworks. At the MRPSF, water surface elevations were reported on an hourly basis and were available in electronic form for the period May 2004 through December 2014. Based on 85,729 measurements, water surface elevations at Muddy Run tailrace averaged 109.34 feet (33.33 meters) (NGVD29), with a standard deviation of ±1.71 feet (±0.52 meters). At PBAPS, water surface elevations were reported on an approximately two-minute basis and were available in electronic form for the period July 2007 through July 2015. Prior to calculating statistics, the raw dataset of nearly 1.9 million observations was averaged into hourly intervals. The datum for PBAPS water surface elevation measurements was not reported. Those measurements were assumed to be reported in the local datum for Conowingo Pond and were converted to NGVD29. Based on 69,428 hourly intervals, water surface elevations at Peach Bottom averaged 108.12 feet (32.74 meters) (NGVD29), with a standard deviation of ±0.87 feet (±0.26 meters). At Conowingo, water surface elevations were reported on a 30-minute basis and were available in electronic form for the period January 2004 through December 2015. Based on 210,526 measurements, water surface elevations at Conowingo averaged 108.05 feet (32.93 meters) (NGVD29), with a standard deviation of ±0.86 feet (±0.26 meters). Elevation data were acquired from Exelon, courtesy of operators at MRPSF, PBAPS, and Conowingo Dam.

### 3.1.3. Hydrothermal and Meteorological Setting

The ultimate use of the suite of models comprising the CPMBM is to simulate nutrient transport and export from Conowingo Pond. Water (and sediment) temperatures affect reaction rates of organic material and nutrient cycling. The hydrodynamic model simulates

water temperatures for subsequent use by the nutrient model and includes the salient features of the Pond's hydrothermal and meteorological setting. The largest thermal inputs to the Pond are temperature inputs from the watershed, solar radiation and associated meteorological factors, and the thermal load from cooling water used by Peach Bottom. Watershed thermal loads at Holtwood, Muddy Creek and Broad Creek were defined from flows and the heat content inflows as estimated from numerical models (e.g., HSPF).

Solar radiation and related heat flux inputs were defined from a range of sources with a cascading priority. The lowest priority was solar radiation calculated from relationships based on the latitude and longitude of the site (Ahsan and Blumberg, 1999). A higher priority was given to regional solar radiation reported at National Aeronautics and Space Administration (NASA) Aerosol Robotic Network (AERONET) monitoring stations and meteorological data reported at National Climatic Data Center (NCDC) stations. Data from NCDC stations were wind speed and direction, cloud cover, atmospheric pressure, air temperature, and relative humidity (calculated from air temperature and dew point temperature). NCDC stations used for this intermediate priority include New Castle County Airport (Delaware), Lancaster Airport (Pennsylvania), Aberdeen Proving Grounds, and Buoy 44057 near the Susquehanna River mouth. The highest priority was given to local solar radiation and meteorological data reported at Muddy Run and Peach Bottom. Those data were collected during 2010-2013 as part of hydrothermal studies for Peach Bottom as summarized by Normandeau and ERM (2014). Data for Peach Bottom also included detailed descriptions of flows and net temperature rises associated with service water and cooling water discharges and their variation with the number of cooling towers in operation over time (Normandeau and ERM, 2014). The following summary of thermal inputs from PBAPS was derived from the Normandeau and ERM (2014) report.

PBAPS is located approximately 7 miles upstream of Conowingo Dam and withdraws water from the Pond for cooling and service needs through an outer intake structure. There are six circulating water pumps that supply cooling water and six additional service water pumps that supply water for process and equipment needs. Each circulating water pump has a capacity of 250,000 gallons per minute (gpm) (557 cfs; 15.8 cms). Each service water pump has a capacity of 14,000 gpm (31.2 cfs; 0.88 cms). Heated water is discharged to a basin leading to a 4,700-foot (1,433-meter) long canal that terminates downstream of PBAPS at a submerged jet discharge structure. The design temperature rise of the system is 22 degrees Fahrenheit (°F) (12.2 degrees Celsius [°C]) for cooling water and 10.7 °F (5.9 °C) for service water. During operation, temperature rises are generally less than design values because of heat loss along the discharge canal and also become smaller as a function of the number of cooling towers in operation. Prior to 2011, no cooling towers were in operation and the average temperature rise was 19 °F (10.6 °C). In 2011, one cooling tower was typically in operation with an average temperature rise of 17.4 °F (9.7 °C). During 2012, two towers were in operation and the average temperature rise was 15.2 °F (9.7 °C). Starting in 2013 and to the present, three towers are in operation and the average temperature rise was 13.9 °F (7.7 °C).

In addition to Peach Bottom hydrothermal studies, ambient water temperatures and other water quality parameters were measured as part of surveys completed between April and October, 2010. Temperatures were reported for 19 stations along five transects throughout the reservoir as shown in Figure 3 (adapted from Normandeau and GSE, 2011).

### 3.1.4. Sediment Transport Setting

#### 3.1.4.1. Sediment Loadings

A solids budget for Conowingo Pond cannot be directly defined from field measurements alone and in isolation of upstream reservoirs because sediment (and flow) inputs to the Pond were not measured. Prior to 2015, suspended sediment concentration (SSC) was periodically measured at Conowingo, but not at Holtwood or tributaries to the Pond.[4] Over the period 1996-2014, the USGS measured instantaneous SSC and flow 410 times at Conowingo.[5] Measured concentrations at Conowingo range from 1 to 3,680 milligrams per liter (mg/L), with an average of 61.7 mg/L and standard deviation of ±265 mg/L. The geometric mean SSC is 15.3 mg/L and is relevant given the three order of magnitude range of measured values. Instantaneous flows measured at the times SSC samples were collected range from 565 to 623,000 cfs (16 to 17,640 cms), with an average of 91,400 cfs (2,588 cms), a standard deviation of ±103,122 cfs (±2,920 cms), and a geometric mean of 46,244 cfs (1,309 cms). From these measurements, instantaneous estimates of suspended sediment loads leaving Conowingo Pond range from approximately 23 tons/day to 5.93 million tons/day (21 metric tons [MT] per day [MT/day] to 5.38 million MT/day, and average 64,200 tons/day (58,200 MT/day), with a standard deviation of ±419,000 tons/day (±380,000 MT/day), and a geometric mean of 1,909 tons/day (1,732 MT/day). Measured SSC, associated instantaneous flows, and loads calculated as the product of flow and concentration are presented in Table 1.

The wide range and variability of estimated sediment loads at Conowingo, as evidenced by the vary large standard deviation of SSC values, are a reflection of significant skew in the underlying distributions of instantaneous SSC and flow measurements as well as the general trend of increasing SSC with increasing flow. A graphical presentation of the relationship between measured SSC and flow, and corresponding loads (calculated as the product of flow and concentration) is presented in Figure 4. SSC and flow measurements exist for the USGS station at Marietta, but that station is upstream of both Safe Harbor and Holtwood Dams. Consequently, sediment inflows to Conowingo Pond can only be

[4] Continuous turbidity measurement at Holtwood began in April 2015. Additionally, SSC samples have been collected periodically at Holtwood and Conowingo Pond tributaries since 2015 when mainstem flows exceed 100,000 cfs.

[5] The SSC record also includes a value reported as "V 7" (collected September 2, 2009) and another of 2 mg/L reported at what appears to be an erroneous instantaneous flow of 2.5 cfs and a daily flow of 19,400 cfs (collected December 4, 2014). Both values were excluded from analysis.

estimated from numerical models (e.g., HSPF or HEC-RAS) or other assumptions regarding SSC and flow at Holtwood. As previously noted, the model results transmitted to USEPA were based on HEC-RAS loads at Holtwood (WEST, 2016).

### 3.1.4.2. Bed Elevation Differences and Net Accumulation

#### *Description of Bathymetric Surveys*

Over the past 21 years, a number of bathymetric surveys of Conowingo Pond have been completed. Survey years for which records could be acquired are 1996, 2008, 2011, 2013, 2014, and 2015.[6] The portion of the Pond for which interpolations were performed and sediment bed elevation differences could be estimated is roughly the area from Muddy Creek to Conowingo Dam. All data were acquired from Gomez and Sullivan Engineers (Gomez and Sullivan). The 1996 and 2008 surveys were conducted by the USGS (1997a, 2009). The remaining surveys were conducted by Gomez and Sullivan. Surveys differ in terms of numbers and locations of targeted transit lines ("transects"), positioning along individual transects, and data density. Locations of transect lines for each survey are presented in Figure 5. A summary of survey characteristics is presented in Table 2.

The 1996 survey included 4,138 measurements, with 23 transects oriented across the channel that were approximately (but not always) bank to bank and with an average spacing of approximately 2,400 feet (720 meters) between transects. The upstream limit of the 1996 survey was approximately 6,900 feet (2,100 meters) downstream of Muddy Creek and the downstream limit was 1,000-1,600 feet (300-500 meters) upstream of Conowingo Dam. This survey provided the least spatial coverage of all the surveys evaluated.

The 2008 survey included 513,363 raw measurements (comparable to 51,337 soundings at a reporting frequency of 1 Hz), with 26 transects oriented across the channel and an average spacing of 2,300 feet (707 meters) between transects. The upstream limit of the survey was Muddy Creek and the downstream limit was 1,700-1,800 feet (520-550 meters) upstream of Conowingo Dam. Although locations and alignments differ, the 2008 survey includes transects at many of the approximate locations surveyed in 1996, with additional coverage of the upstream portion of the survey area near Muddy Creek. The 2008 survey included two diagonal survey lines that were used for QA/QC purposes.

The 2011, 2013, 2014, and 2015 surveys were consistent in design and included approximately 83,000 to 89,400 measurements, with 59 cross-channel transects plus an additional five (5) longitudinal transects running the length of the main reservoir. The upstream limit of these four surveys was Muddy Creek and the downstream limit was Conowingo Dam. Measurements for each survey were collected at a frequency of 10-30 measurements per second and averaged by the instrumentation to a reporting frequency of

[6] Bathymetric data were collected in 2016 but were not compiled at the time this report was prepared.

one measurement per second. The average spacing between the 59 cross-channel transects was 1,025 feet (314 meters). Although the exact locations of individual measurements comprising each transect vary, these recent surveys included transects at the approximate locations of transects comprising the 2008 and 1996 surveys. The 2011, 2013, 2014, and 2015 surveys provide the most extensive coverage of the pond.

The accuracy of bathymetric surveys is affected by measurement errors attributable to instrumentation accuracy and environmental conditions. In general, instrumentation error is proportional to water depth. Environmental conditions include horizontal positioning and vertical error caused by the roll, pitch, yaw, surge, sway, and heave of the survey vessel. Bathymetric surveying technology has also changed significantly over the timeframe of these surveys. As a result, each survey has different measurement errors.

During the 1996 survey, an electronic and paper recording fathometer were used with survey vessel position determined using a global positioning system (GPS). Data were recorded to provide 150 – 200 soundings along each transect. Fathometer accuracy was checked against physical measurements (e.g., a bar check). As noted by the USGS (1997a), differences between fathometer readings and physical measurements were within the ±1-foot (±30 cm) limit of vertical accuracy for the instrument and environmental conditions that occurred during the survey. Horizontal accuracy limits for the 1996 survey were not reported. However, GPS-guided surveys conducted before May, 2000 would be expected to have less horizontal accuracy because GPS employed a feature called Selective Availability (see http://www.gps.gov/systems/gps/performance/accuracy/) that degraded civilian accuracy on a global basis.

During the 2008 survey, a Navisound echo sounder was used with vessel positioning determined using a differential GPS (DGPS) system and with an additional unit used for quality assurance purposes (USGS, 2009). Relative to each other, readings from the two DGPS units differed by 5 – 10 feet (1.5 – 3.0 meters), providing an estimate of horizontal positioning accuracy. The vertical accuracy of the survey was estimated to be ±0.5 feet (±15 cm) (USGS, 2009).

The 2011, 2013, 2014, and 2015 surveys were conducted using a Sontek RiverSurveyor M9 Acoustic Doppler Current Profiler (ADCP) with a stated accuracy of ±1% of the water depth (Exelon, 2012c). For a maximum water depth of approximately 70 feet (21 meters), the maximum vertical error of the ADCP would be ±0.7 feet (±21 cm). For an average water depth of 27 feet (8.3 meters), the vertical error would be ±0.27 feet (±8.3 cm). A real time kinematic (RTK) GPS was used to determine vessel position. Five of the 59 cross-channel transects were surveyed with the GPS unit in differential mode so that the horizontal survey accuracy was approximately ±1.6 feet (49 cm). The remaining 52 cross-channel transects and all five longitudinal transects were surveyed with the GPS unit in RTK mode so that the horizontal survey accuracy was approximately ±0.28 feet (±8.5 cm) when the survey vessel was at a maximum distance of 5 miles (8,000 meters) from the base station. Comparisons of

bed elevation measurements at points where cross-channel and longitudinal transects intersect indicate that the overall vertical measurement accuracy of Gomez and Sullivan surveys, accounting for instrumentation error and environmental conditions, is approximately ±0.20 feet (±6 cm) (Exelon, 2012c).

### *Spatial Interpolation of Bathymetric Surveys*

The bathymetric surveys provide bed elevation measurements at individual points. As a rough approximation based on the types of sounding equipment used for surveys, each individual point would be representative of a 1 – 3 square foot ($ft^2$) (0.1 – 0.28 $m^2$) area of the bed. To estimate elevations for areas between survey points, measurements need to be spatially interpolated to provide estimates over the entire bed surface area. The spatial interpolation process is also used to extrapolate elevations for areas beyond survey limits. Such extrapolation is needed for unsurveyed areas such as those between the last transect measured and Conowingo Dam, from the start and end points of each transect to the shoreline, and around islands or other obstructions not traversed by the survey vessel. In the description that follows, interpolation between survey points and extrapolation beyond survey points are collectively termed "interpolation" for simplicity.

Bed elevation measurements were interpolated using the Ordinary Kriging method in the GeoStatistical Analyst Extension for ArcGIS 10.3 (ESRI, 2014) to generate a continuous set of elevation estimates over the entire surface of the Pond for each survey year. Kriging was used for interpolation because it yielded lower estimates of root mean square (RMS) error than other methods such as inverse distance weighting (IDW). Interpolations were performed for each survey year using grid-snapped and raw data because measurement locations vary for each survey. As part of the "grid-snapping" process, data were adjusted (e.g., averaged) before interpolation to achieve more consistent data densities and alignment along transect lines and to standardize locations between each survey year. Raw data were not adjusted prior to interpolation.

Given different numbers and locations of transects for different surveys, interpolations were also performed to compare results for two cases: (1) using data for all points of measurement; and (2) limiting data to the locations of the 26 transects traversed during the USGS 2008 survey. Kriging calculations for both cases were performed with the nugget effect set to zero so that the interpolated elevation at each point of measurement exactly equaled the reported value at that point. The RMS error of interpolated elevations ranged from ±0.67 – ±1.30 feet (±20 – ±40 cm) and provides an estimate of one component of the overall uncertainty in interpolation results. The largest RMS error was associated with the interpolation of the 1996 survey.

Differences in sediment bed elevations over time were estimated by subtracting interpolations for successive survey years (e.g., 2014 minus 2011; 2011 minus 2008, etc.) and then summarizing differences for each cell in the model grid. For reference, a description

of the model grid is presented in Section 3.2 ("Model Grid"). A summary of estimated bed elevation differences for successive surveys is presented in Table 3. These survey-to-survey bed elevation difference estimates do not account for the effects of measurement error or other interpolation errors.

In general, interpolated elevations for the 1996 survey are likely to be more uncertain than those for other years because of large differences in data density (i.e., less than 5% of the measurements spread along the fewest number of transects with the largest average distance between transects and the greatest area of extrapolation beyond survey bounds). As previously noted, the 1996 survey began approximately 6,900 feet (2,100 meters) downstream of where other surveys began and (similar to the 2008 survey) ended approximately 1,000 – 1,600 feet (300 – 500 meters) upstream of Conowingo Dam. As a result, interpolated bed elevations for the 1996 survey include more areas where gradients calculated by the kriging algorithm were extrapolated from the nearest measurements to estimate elevations along the upstream, downstream, and shoreline boundaries of the interpolation area. Similarly, interpolated bed elevations for the 2008 survey include a region of extrapolation near Conowingo Dam. Thus, survey-to-survey differences calculated using interpolated bed elevations for 1996 are more uncertain, and can lead to potentially erroneous conclusions about bed elevation differences over time, than for comparisons using other survey years.

Differences in data density (i.e., locations and numbers of bathymetric measurements for each survey) affect interpolations and introduce "noise" that affects interpretation of bed elevation differences. This is illustrated by comparing alternative interpolations prepared from subsets of data from the same survey. In this example, "grid-snapped" data were used to construct alternative interpolations for the 2011 and 2015 bathymetric surveys. The first alternative interpolation was constructed using data for all 59 cross-channel transects in the survey. The second alternative was constructed only using data from a subset of 26 transects. Because data for the 26 transects common to both interpolations are identical, this test provides an estimate of the additional error that occurs when calculating elevation differences between interpolations constructed with roughly half the data density. For alternatives constructed using only 2011 data, the unweighted average difference was 0.81 feet (25 cm) and the area-weighted average difference was 0.57 feet (17 cm).[7] For alternatives constructed using only 2015 data, the unweighted average bed elevation difference was 0.80 feet (24 cm) and the area-weighted average difference was 0.60 feet (18 cm). In contrast, the average difference between interpolations for 2015 and 2011 as calculated using grid-snapped data for all transects (i.e., 59 cross channel and 5 longitudinal) was nearly zero, with an unweighted average difference of 0.006 feet (0.18 cm) and an area-weighted average difference of 0.02 feet (0.60 cm). Consequently, based on

[7] Unweighted differences represent an arithmetic average of differences for individual model grid cells in the surveyed portion of the Pond, independent of the surface area of each cell. Weighted differences represent an arithmetic average of area-weighted differences for individual model grid cells in the surveyed portion of the Pond.

data density differences between earlier surveys and more recent ones, there may be 0.60 – 0.80 feet (18 – 24 cm) of additional uncertainty above and beyond interpolation RMS errors that arises when calculating differences between survey years.

These comparisons demonstrate that data density differences alter interpolation outcomes such that the overall error and uncertainty for any one year may be similar to, or larger than, bed elevation differences between survey years. Thus, inferences drawn between survey years at any spatial scale may be more a reflection of a combination of measurement error, interpolation uncertainties, and unconstrained extrapolation rather than demonstrable differences in sediment accumulation or loss from the bed over time. Conclusions regarding elevation differences over time should include consideration of measurement error, data density differences, and the range of interpolation errors. This is particularly important for comparisons that rely on interpolation of the 1996 survey because of its low data density. Further discussion of these factors and other aspects of uncertainties are presented in Section 5 ("Discussion and Interpretation of Results").

#### 3.1.4.3. Sediment Bed Physical Property Characterization

Sediment collected from locations throughout the Pond during sampling events in 1990 (USGS, 1992), 1996 (USGS, 1997b), 2000 (SRBC, 2006), 2012 (USACE, 2014), and 2015 (AECOM, 2016) were used to characterize sediment bed properties. The primary properties of interest were wet bulk density and grain size distribution, including coal content. In 1990, 22 surficial bed material grab samples were collected. Sediment grain size and moisture content were measured. Moisture content was converted to wet bulk density using relationships detailed by AECOM (2016) and under the assumption that particle density was 165.4 pounds/ft$^3$ (pcf) (2.65 g/cm$^3$). In 1996, 27 surficial bed material grab samples were measured for water content and a subset of 10 of those samples were also analyzed for grain size. Water content for the 1996 samples was also converted to wet bulk density using relationships detailed by AECOM (2016) and under the assumption that particle density was 165.4 pcf (2.65 g/cm$^3$). Surface grab samples for the 1991 and 1996 sampling efforts were assumed to represent the 0 to 6 inch (0 to 15 cm) interval of the bed.

In 2000, sediment cores were collected from 21 locations in Conowingo Pond and analyses were performed on 83 core slices from a variety of surface and subsurface intervals to a depth of 13 feet (397 cm) below the sediment-water interface. Analyses were performed on 4 inch (10 cm) core slices and included moisture content on a wet basis, grain size, and coal content. As part of the SRBC (2006) study, moisture content was converted to wet bulk density under the assumption that particle density was 169.8 pcf (2.72 g/cm$^3$). SRBC samples still included coal, which was separated from samples as part of subsequent processing. In 2012, eight sediment cores were collected and wet bulk density and grain size were reported for 51 intervals at varying depths into the bed ranging from the bed surface to a depth of 14 inches (36 cm). Wet bulk density values were determined from moisture content on a dry basis assuming a particle density of 165.4 pcf (2.65 g/cm$^3$).

However, grain size samples were sieved to remove particles larger than 850 μm.[8] USACE (2014) noted that field crews were not able to collect sediments at depths below 14 inches (36 cm) and concluded that sediments at greater depths were highly consolidated and likely to be more erosion resistant. In 2015, cores were collected from 10 locations and analyses were performed on 160 slices from surface and subsurface intervals to a depth of 10 feet (305 cm) below the sediment-water interface. Moisture content and wet bulk density were measured for all 160 core slices. Grain size was reported for 156 core slices.

Discrete bed property values were spatially interpolated using the ordinary kriging method to generate spatially-continuous estimates for wet bulk density and grain size components. Data from all five sampling events were included in interpolations. Raw grain size data were rescaled to account for the presence of coal in Pond sediments. For samples where coal content was not explicitly measured, the fraction of coal present was assumed to equal the approximate value (excluding visible layers) of 10% as reported by SRBC (2006). Grain size components were summarized as clay (< 4 μm), silt (4 – 62 μm), sand (62 – 2,000 μm), gravel (> 2,000 μm), and coal. Prior to interpolation, data were linearly interpolated in the vertical to align slices from different cores to a common layering scheme with depth into the bed. Separate spatial interpolations were then performed for each bed layer. Ten (10) depth layers were used as follows:

- Layer 1: 0 to 0.16 feet (0 to 5 cm)
- Layer 2: 0.16 to 0.33 feet (5 to 10 cm)
- Layer 3: 0.33 to 0.49 feet (10 to 15 cm)
- Layer 4: 0.49 to 0.66 feet (15 to 20 cm)
- Layer 5: 0.66 to 0.82 feet (20 to 25 cm)
- Layer 6: 0.82 to 0.98 feet (25 to 30 cm)
- Layer 7: 0.98 to 1.64 feet (30 to 50 cm)
- Layer 8: 1.64 to 3.28 feet (50 to 100 cm)
- Layer 9: 3.28 to 6.56 feet (100 to 200 cm)
- Layer 10: 6.56 to 9.84 feet (200 to 300 cm)

This layering approach was selected as a reflection of near surface bed property variations inferred from USACE (2014) cores and variations deeper in the bed as inferred from SRBC (2006) and AECOM (2016) cores. Cokriging with bed elevations was chosen as the method for interpolation because it yielded results with lower estimates of RMS error in comparison to other methods such as IDW. Although uncertainties in interpolations are large as a consequence of relatively large variations in bed properties and distances between points, cokriging captured spatial variations better than block averaging or nearest neighbor (e.g., thiessen polygon) types of methods.

[8] In several instances, USACE (2014) reported D90 sediment size values in excess of 850 μm. Consequently, it is not clear if all samples were sieved in the same manner.

### 3.1.4.4. Sediment Bed Erosion Characterization

As described by the USACE (2014), erosion characteristics of sediments from Conowingo Pond were estimated from cores using the SEDFLUME device. The cores collected were relatively short. Five out of the eight cores were 7.9 inches (20 cm) or smaller. The average depth of penetration for the cores was just 9.2 inches (23.4 cm), with a maximum of 14.2 inches (36 cm) and a minimum of only 6.9 inches (17.5 cm). Erosion characteristics estimated were critical shear stresses for erosion ($\tau_{ce}$) and erosion rate parameters. Critical shear stress values defining the onset of erosion as reported by USACE (2014) ranged from 0.004 to 0.033 pounds per square foot [psf] (2 to 16 dynes/cm$^2$, 0.2 to 1.6 Pascals [Pa]). Erosion rates across the range of applied shear stresses were variable. Critical shear stresses and erosion rates were not correlated to each other or other physical properties of the cores, such as depth below the surface, bulk density, or grain size components. A general trend of increasing critical shear stress for erosion with depth in cores appears to reflect the methodology by which applied shear stresses are varied during tests (e.g. lower shear stresses were applied near the core surface and were gradually increased as cores eroded). As a broad generalization, across all depth intervals and all shear stresses at which tests were performed for all eight cores, erosion rates spanned a range of roughly 0.236 to 2.36 feet/hour (0.002 to 0.02 cm/s) (Figure 6).

Substantial uncertainty exists with critical shear stress and erosion rate values estimated by the SEDFLUME study. USACE (2014) sediment transport simulations and those subsequently described in this report show that (grain) shear stresses generated as water moves through the Pond during flow events can be quite large. They are often in the range of 0.1 to 0.2 psf (50 to 100 dynes/cm$^2$, 5 to 10 Pa) in the lower reservoir and can be much larger in upstream areas. It is unlikely that sediments could accumulate and persist in locations routinely subjected to such high shear stresses if they were as easy to erode as implied by SEDFLUME results. Given the very large forces that can act on the bed, the USACE (2014) had to augment SEDFLUME-based erosion parameter estimates with literature values, particularly for sediments more than one foot below the sediment-water interface. In effect, given the physical inconsistency of easily eroded sediments in locations with routinely high shear stresses, the critical shear stress for erosion was varied as a calibration parameter following a general trend of increasing critical shear stress with distance upstream of Conowingo Dam (see Section 6 of USACE, 2014).

As an alternative to characterizing erosion properties based solely on SEDFLUME study estimates, a site-specific relationship between the clay content and plasticity index of Conowingo sediments was used to provide initial estimates of the critical shear stress for erosion. Jacobs et al. (2011) investigated physical properties that contribute to cohesion and found that the critical shear stress for erosion was related to sediment plasticity index:

$$\tau_{ce} = 1.61(PI)^{0.80} \quad (3\text{-}1)$$

where:

$\tau_{ce}$ = critical shear stress for erosion (dynes/cm$^2$) [M L$^{-1}$ T$^{-2}$]

*PI* = plasticity index (%) = LL – PL

*LL* = liquid limit (%)

*PL* = plasticity limit (%)

The PI, LL, and PL, terms in Equation (3-1) are geotechnical properties known as Atterberg Limits and express how soils and sediments change from granular to plastic to liquid behaviors as water content increases. Atterberg Limits were reported for 108 of the 160 core slices analyzed by AECOM (2016) and used to calculate PI. Using these data, site-specific relationships between the PI and other measurements were explored. Although properties such as wet bulk density or depth below the sediment-water interface were not correlated, the clay content of Conowingo sediment samples (as a percentage) was correlated with PI (Figure 7) and regression yielded the following relationship:

$$PI = 3.7023\mathrm{e}^{0.0727(\%\mathrm{Clay})} \quad (3\text{-}2)$$

where:

%Clay = clay content of the sediment bed (mass basis) (%)

As defined by substituting Equation (3-2) into Equation (3-1), the relationship between clay content and the critical shear stress for erosion was used in the sediment transport model to dynamically calculate the erosion resistance of sediment layers that deposit to the bed during a simulation. Thus, the erosion resistance of sediment layers that accumulate on the bed can vary with the clay content of those materials in certain conditions. The SEDZLJS framework can simulate erosion for sediments considered to be cohesive and non-cohesive. The relationship defined by Equations (3-1) and (3-2) is used to assign the critical shear stress for erosion for deposited sediment layers that are considered to be cohesive. The sediment transport model was parameterized so that sediments would be treated as cohesive in most situations. Similar to the process described by USACE (2014), erosion resistance of sediments comprising the bed at the start of the simulation (which is termed the "parent bed") was assigned as part of model calibration. Erosion thresholds for the parent bed at the start of the simulation were calibrated so that computed bed elevation changes over the course of the simulation were in rough agreement with spatial and temporal pattern and pond-wide average bed elevation change determined from interpolated bathymetric survey results. Similar to the calibration described by USACE (2014), there was a general trend of increasing critical shear stress with distance upstream of Conowingo Dam.

## 3.2. MODEL GRID

Model calculations for all simulations were performed using a spatially-variable network of segments (i.e., "grid cells"). The collection of grid cells representing the study area is termed the model grid. An overview of the CPMBM grid is presented in Figure 8. Grid cell sizes and alignment were selected to minimize computational requirements while capturing depth variations that reflect remnant channels and bed features that define the morphological characteristics of the physical setting. There are 305 cells in the model grid. Cells are approximately 2,300 feet (700 m) long by 1,100 feet (345 m) wide. The grid has 5 vertical "sigma" layers in the water column, with each water layer representing 20% of the depth in each cell.

The hydraulics of Conowingo Dam were represented by spatially and temporally varying withdrawals from different sigma layers. There are 11 grid cells along the face of the dam, numbered from right to left (facing the dam from upstream) as Cells 36, 3 – 36, 13, with Cells 36, 5 – 36, 6 representing the power-intake and Cells 36, 7 – 36, 11 representing crest gates. Power-intake withdrawals occur from water column layers 3 – 5. Crest gate spill withdrawals occur from water column layers 1 – 2. Each of the five cells representing the gated portion of the dam was assumed to contain 10 crest gates. For simplicity, it was assumed that gates open and close in the same sequence. Anytime flows are large enough for spill to occur, withdrawals begin from Cell 36, 7 (gates 1-10) and move across the face of the dam in sequence to Cell 36, 11 (gates 41-50) with each conceptual gate opening one at a time as determined by the overall flow being spilled.

At the start of simulations, the grid includes 10 sediment bed layers. The number of bed layers and their thicknesses in any model grid cell can change over time based on the flux of sediment deposited to or eroded from the bed at each time step during a simulation. The thickness of erodible sediment throughout the Pond is unknown. Because 15 sediment core samples collected from the pond were from depth intervals of ~10 feet or more, the overall thickness (sum for all bed layers) of sediment in each grid cell at the start of simulations was set to a depth of approximately 10 feet (300 cm).

## 3.3. MODEL SET-UP AND CALIBRATION

Model set-up and calibration was performed for a seven-year period, from January 1, 2008 through December 31, 2014 ("short-term" simulation period). This timeframe was selected because it includes several flow events of interest (e.g., Tropical Storm Lee in September 2011) and also includes: detailed water surface elevation measurements at three locations across the Pond, suspended sediment concentration measurements at Conowingo, grain size and other bed property characterization (e.g., bulk density) for sediment cores collected within the Pond, water temperatures and supporting meteorological measurements (e.g., solar radiation), and detailed sediment bed elevation surveys for several years. Additional simulations were also performed for an 18-year period, from January 1, 1997 through

December 31, 2014 ("long-term" simulation period). With the exception of initial conditions, short-term and long-term simulations were based on the same parameterizations and yielded very similar results for the 2008-2014 timeframe. Long-term simulation results were subsequently provided to the USEPA CBP to support mid-point assessment efforts.

Within the surveyed potion of the reservoir (Muddy Creek to Conowingo Dam), starting water depths for short-term simulations reflect conditions estimated from bed elevation surveys over the period 2008 – 2015. For long-term simulations, starting water depths in the reservoir reflect conditions interpolated from the 1996 bed elevation survey. Upstream of the surveyed portion of the reservoir (Holtwood Dam to Muddy Creek), initial water depths for both simulations were based on bed elevation data for the Holtwood Dam and Muddy Run tailrace areas, which were surveyed in 2006 and 2010, respectively.

### 3.3.1. Hydrodynamic and Hydrothermal Model

The hydrodynamic model is driven by the balance between inflows specified at Holtwood and other tributaries and outflows at Conowingo. Differences between inflows and outflows control water surface elevation in the Pond. Flow resistance influences the time of travel and attenuation of waves as they pass through the Pond. The hydrothermal model is driven by the balance between the heat content of inflows specified at Holtwood and other tributaries, the net temperature rise at Peach Bottom, ambient heating and cooling by solar radiation and meteorological factors, and outflows at Conowingo.

#### 3.3.1.1. Estimation of Inflows

Outflows at Conowingo Dam and water surface elevations throughout the Pond are measured. Inflows from Muddy Creek and Broad Creek were estimated from the USEPA HSPF watershed model (Phase 6, Beta 2). The time series of inflows at Holtwood was estimated from this information according to the following equation:

$$Q_H = Q_C - \left(Q_M + Q_B\right) + \frac{\Delta E_C A}{\Delta t} \qquad (3\text{-}3)$$

where:

$Q_H$ = estimated flow at Holtwood [$L^3$ $T^{-1}$]

$Q_C$ = measured flow at Conowingo [$L^3$ $T^{-1}$]

$Q_M$ = HSPF estimate of flow from Muddy Creek [$L^3$ $T^{-1}$]

$Q_B$ = HSPF estimate of flow from Broad Creek [$L^3$ $T^{-1}$]

$\Delta E$ = Hourly difference in water surface elevations at Conowingo [L]

$A$ = Surface area of Conowingo Pond = 8,953 acres ($3.62 \times 10^7$ m$^2$) [L$^2$]

$\Delta t$ = time interval = 1 hour (3,600 seconds) [T]

Calculations were performed to generate an hourly time series of flows at Holtwood. Before October 2007, the USGS published daily flows at Conowingo.[9] Those daily flows were linearly interpolated to generate an hourly time series. After October 2007, the USGS published 15-minute flows at Conowingo. Those flows were averaged to generate an hourly time series. Water surface elevation measurements reported on a 30-minute basis at Conowingo were available beginning in January, 2004. These data were averaged to an hourly interval. A low-pass filter (Lanczos algorithm) with a 168-hour bandwidth was used to generate the time series of hourly values used in Equation (3-3). The low-pass filter was applied to help better account for the cyclical nature of hydropower operations and reduce high-frequency fluctuations that appear to be the results of surface waves and other localized transients at Conowingo. Use of a 168-hour bandwidth was guided by graphical comparison of residual noise in filtered elevations for a range of bandwidths (e.g., 2-, 4-, 8-, 24-, 48-, 96-, 168-hour, etc.). Before the availability of measurements in January 2004, the difference in water surface elevations was assumed to be zero (i.e., $\Delta E = 0$). It should be noted that any flow from the ungaged portion of the watershed draining to Conowingo Pond is implicitly included in the flow assigned at Holtwood.

#### 3.3.1.2. Flow Resistance Calibration

Given that water depths in Conowingo Pond are less than the approximately 30 meter (98 feet) limit before the minimum coefficient of friction ($C_{D,min}$) affects simulations, the primary model calibration variable was the hydrodynamic roughness height of the sediment bed ($z_0$). As part of calibration, a series of exploratory simulations were performed to evaluate model response as $z_0$ values were incrementally varied from a low of 0.0004 m (0.4 mm) to a high of 0.002 m (2 mm). For reference, this range of $z_0$ values corresponds to Manning $n$ values that range from 0.026 to 0.031. In all simulations, values of $C_{D,min}$ was set to 0.0025. Based this evaluation, $z_0$ was set to a value of 0.001 meters (1 mm) for all subsequent simulations, corresponding to Manning $n$ values that range from 0.027 to 0.028 for the range of water depths that occur in the Pond.

#### 3.3.1.3. Hydrothermal Model Set-up

The hydrothermal model was set up and operated using site-specific data and was not calibrated to adjust parameter values. Heat inputs at Holtwood and from other tributaries

[9] Instantaneous flows have been reported at the Conowingo gage at a 15-minute interval since February, 1988. However, the USGS accuracy notes indicate that daily discharges calculated from these instantaneous data may differ from published daily values by 1 to 5 percent. To simplify model development, daily flows were used prior to October 1, 2007 to ensure consistency with published flows.

were calculated from HSPF flows and temperatures. Environmental heating and cooling parameters (e.g., wind speed, wind direction, solar radiation, etc.) were specified based on site-specific measurements and augmented with regional values as described in Section 3.1.3 ("Hydrothermal and Meteorological Setting"). The intake and release of service and cooling water for PBAPS was represented as a series of loop diffusers, with one intake-discharge pair for each of the six service water and six cooling water pumps. The operating cycle and corresponding temperature rise of discharges was specified as described by Normandeau and ERM (2014).

#### 3.3.1.4. Hydrodynamic and Hydrothermal Simulation Results

Hydrodynamic model results were evaluated by comparing measured and simulated water surface elevations over time. For simplicity and convenience of presentation, results presented in the main body of this report are from the long-term simulation. Comparisons of simulated and measured water levels for the 2008-2014 portion of the long-term simulation are presented in Figures 9-15. The full set of long-term model results for the period 1997-2014 is presented in Appendix B. Short-term simulation water surface elevation results are presented in Appendix C. For consistency across years, results are presented with a y-axis range large enough to present the high water surface elevation conditions that occur during Tropical Storm Lee in 2011, which is the largest event that occurred during the simulation periods. With one exception, the model closely follows the trends and magnitudes of measured values at Muddy Run, Peach Bottom, and Conowingo Dam. The exception is a transient elevation decrease of approximately 3-6 feet (1-2 meters) at Conowingo that occurs in the model during Tropical Storm Lee (see Figures 12 and 19). Discussion of this model behavior is presented in Section 5 ("Discussion and Interpretation of Results"). Probability distributions of differences between pairs of simulated and measured water surface elevations for the 2008-2014 portion of the long-term simulation are presented in Figures 16-22. The median difference between simulated and measured hourly water levels averaged +0.043 feet (+0.013 meters) and ranged from -0.69 feet (-0.21 meters) to +0.52 feet (+0.16 meters).

Hydrothermal model results were evaluated by comparing measured and simulated water temperatures over time at monitoring locations used in the PBAPS thermal study in 2010. Comparisons of simulated and measured temperatures at 19 stations throughout the Pond for the year 2010 of the long-term simulation are presented in Figures 23-27. Short-term simulation temperature results are presented in Appendix D. The model closely follows the trend and magnitudes of measured values. Probability distributions of differences between pairs of simulated and measured water temperatures are presented in Figures 28-32. Across all monitoring stations and depths, the median difference between simulated and measured temperatures averaged -0.2 °F (-0.1 °C) and ranged from -6.2 °F (-3.4 °C) to +5.9 °F (+3.3 °C).

### 3.3.2. Sediment Transport Model

The sediment transport model includes five size classes of particles: clay, silt, sand, gravel, and coal. As detailed in Section 3.3.2.2 ("Sediment Transport Parameterization and Calibration"), coal was assumed to have a physical diameter in the range of 0.5 – 1 mm with a particle density of 1.5 g/cm$^3$ (93.6 pcf) and was represented in the model as a particle with an equivalent diameter of approximately 0.35 mm (350 μm) and a particle density of 2.65 g/cm$^3$ (165.4 pcf). The model simulates the movement of sediments to and from the bed and their transport from the Pond as driven by sediment loads, their grain size distributions, applied shear stresses, and the corresponding balance between deposition and erosion fluxes. The hydrodynamic and sediment transport models are dynamically coupled. Applied shear stresses are determined from water levels and velocities as calculated by the hydrodynamic model and are influenced by changes in bed elevations as determined by the sediment transport model.

#### 3.3.2.1. Estimation of Sediment Loads

Sediment loads at Holtwood, Muddy Creek, and Broad Creek, were determined from flow and suspended sediment concentration estimates for each of the five state variables in the model. Sediment concentrations at Holtwood were obtained from the HEC-RAS sediment rating curve for 1997-2007 and HEC-RAS simulations for 2008-2014 (WEST, 2016). The model internally calculates load as the product of flow specified at the model boundary, calculated from flow at Conowingo using Equation (3-3), and the specified concentration time series for each particle type. Although HEC-RAS rating curve closely approximates simulated concentrations at Holtwood for 2008-2014, there is some loss of precision (i.e., concentrations for each size class are binned by flow ranges such that loads from the rating curve are not identical to the mass from the HEC-RAS simulation). To maximize coupling between models (and minimize differences), WEST's HEC-RAS simulations results were used for 2008-2014 in favor of the rating curve. Sediment concentrations at Muddy Creek and Broad Creek were obtained from HSPF (P6B2) for all years. HSPF and HEC-RAS provided estimates of sediment concentrations for three of the five state variables used in the sediment transport model: sand, silt, and clay. Concentrations of gravel and coal were assumed to be zero.

Alternative simulations in which sediment loads at Holtwood were obtained only from HSPF (P6B2) were also performed. Because of substantial differences in the simulated mix of particles (i.e., HSPF P6B2 loads are predominately clay-sized while WEST's HEC-RAS loads are primarily silt-sized) and the large difference in settling speeds for clay and silt, it was not feasible to construct a model driven by HSPF loads at Holtwood and still match the sediment bed elevation changes over time given the expected settling velocity of clay-sized particles. This is further discussed in Section 5 ("Discussion and Interpretation of Results"). Ultimately, all model results transmitted to USEPA were based loads at

Holtwood as estimated from the HEC-RAS sediment rating curve for 1997-2007 and HEC-RAS simulations for 2008-2014 (WEST, 2016).

Sediment concentrations at Holtwood estimated by HSPF and HEC-RAS (WEST, 2016) were often lower than measured SSC at Conowingo during non-event, quiescent conditions. During such non-event periods, the sediment load passing Conowingo Dam is very small in comparison to loads during high flow event periods. However, initial simulations performed using these boundary loads indicated that simulated SSC would be systematically low at times (e.g., simulated SSC at Conowingo Dam would be 1 mg/L or less, generally during summer months). Given this situation, a minimum sediment concentration of 10 mg/L was assumed to occur and whenever estimated SSC (sum of all particle sizes) at Holtwood was less than this floor, the concentration of the clay size class was increased so that SSC was equal to 10 mg/L. Sediment loads to the Pond for 1997-2014 as estimated with this floor concentration are presented in Figures 33-50.

Sediment loads at Holtwood show rapid fluctuations starting in October 2007 (see Figure 43). As described in Section 3.3.1.1 ("Estimation of Inflows"), inflows at Holtwood were calculated from flow at Conowingo and water surface elevations using Equation (3-3). Before October 2007, the flow record for Conowingo is comprised of daily flows that were linearly interpolated to hourly intervals. In October 2007, 15-minute flow measurements at Conowingo were used and averaged to hourly intervals. Those 15-minute flows show rapid fluctuations. Flow modulation at Conowingo, combined with fluctuating water surface elevations in the Pond, contribute to flow and load modulation at Holtwood.

#### 3.3.2.2. Sediment Transport Parameterization and Calibration

The effective particle diameter ($d_p$), settling velocity ($v_s$), critical shear stress for suspension ($\tau_{cs}$), and critical shear stress for erosion ($\tau_{ce}$) for each of the five sediment types simulated were assigned based on site-specific information and equations presented in Section 2. Effective diameters and settling velocities for particles were estimated from site-specific values for Conowingo Pond presented by Sanford et al. (2016). Dimensionless diameters and critical shear stress values for each particle type were then determined based on effective diameter using Equations (2-16), (2-17), and (2-20). In the model, the critical shear stress for deposition ($\tau_{cd}$) is set equal to the critical shear stress for suspension. For the clay, silt, sand, and gravel size classes, the particle density was assumed to be 2.65 g/cm$^3$ (165.4 pcf). For coal, the physical particle diameter was assumed to be in the range of 0.5 – 1 mm and average particle density 1.5 g/cm$^3$ (93.6 pcf) as reported by SRBC (2006). Based on this density difference, the coal size class was parameterized with an equivalent diameter of approximately 0.35 mm (350 μm) at a particle density of 2.65 g/cm$^3$. The equivalent diameter approach was used for coal particles because the sediment transport model assumes all size classes have a particle density of 2.65 g/cm$^3$ (165.4 pcf). A particle with a diameter of 0.35 mm and a density 2.65 g/cm$^3$ has the same dimensionless diameter ($d_*$) as

a particle with a diameter of approximately 0.5 mm and a density of 1.5 g/cm$^3$. Parameters for each size class are summarized in Table 4.

Grain size distributions and wet bulk densities were parameterized based on zonal summaries of spatial interpolations in each grid cell for each of the ten layers comprising the sediment bed. Bed properties vary from cell to cell and layer to layer. A summary of interpolated bed properties for each grid cell and bed layer in the model is presented in Attachment 1 (available in electronic format only). Erosion threshold for sediments in each bed layer of each grid cell was first estimated using the site-specific relationship between clay content, plasticity, and the critical shear stress for erosion. Although typically larger than estimates that the USACE (2014) inferred from SEDFLUME results, erosion thresholds estimated from clay and plasticity were still found to be unreasonably low and resulted in bed elevation changes that were inconsistent with interpolated elevation differences between bathymetric surveys over time.[10] In many locations, estimated critical shear stresses for the onset of erosion were generally less than grain shear stresses that occur during even moderate flow conditions; such easily erodible sediments are unlikely to exist in locations where shear stresses routinely exceed their critical shear stress for erosion. Subsequently, erosion thresholds for initial bed layers at the start of simulations were adjusted during sediment transport model calibration. Interpolated bed elevation differences between bathymetric surveys, maximum shear stresses exerted during high flow events, and nutrient flux considerations, were used as constraints to guide assignment of erosion thresholds. A summary of initial erosion thresholds for each grid cell and bed layer in the model is also presented in Attachment 1. Erosion thresholds for bed layers that deposited during simulations were calculated by the model based on clay content (representing plasticity) as indicated by Equations (3-1) and (3-2).

Whenever grain shear stress acting on the bed exceed the critical shear stress for erosion, cohesive sediments were assumed to erode at a rate of 0.236 feet/hour (0.002 cm/s), based on consideration of net bed elevation changes over time and spatial patterns of nutrient concentrations that occurred during subsequent nutrient transport simulations. This cohesive sediment erosion rate is near the lower end of values estimated using the SEDFLUME device. Similarly, non-cohesive sediments were assumed to erode at a rate of 1.18 feet/hour (0.01 cm/s). This non-cohesive erosion rate is also within the range of USACE (2014) SEDFLUME measurements. In nearly all cases during simulations sediment behave in a cohesive manner.

[10] Grain shear stresses acting on the sediment bed are expected to regularly exceed 20-50 dynes/cm$^2$ in large portions of the Pond during even modest events such as Spring freshets. See Figure 70: thick deposits of easily eroded sediment could not persist under such recurring high shear stress conditions.

#### 3.3.2.3. Sediment Transport Model Results

Sediment transport model results were evaluated by comparing measured and simulated SSC values at Conowingo as well as patterns and magnitudes of sediment bed elevation changes over time. Results comparing simulated and measured SSC for the 2008-2014 portion of the long-term simulation are presented in Figures 51-57. The full set of long-term simulation results for the period 1997-2014 is presented in Appendix E. Short-term simulation results are presented in Appendix F. For consistency across years, results are presented on a logarithmic scale with range large enough to show the minimum and maximum values that occurred during the simulation. Model results closely follow the trend and magnitudes of measured SSC values over time.

Comparisons of simulated and measured concentrations and loads at Conowingo and the 1:1 line of perfect agreement (with a slope of 1.0) are presented in Figures 58-59. Model results are shown as ranges (minimum to maximum) within a ±8 hour interval centered on sample collection times to account for differences attributable to the timing of flow and sediment inputs and transport processes in the Pond. Linear regressions were performed to characterize the correspondence between model results and field measurements. Using values for all flow ranges, the slope of the regression between simulated and measured concentrations was 0.88 and was 0.89 for load. Measured loads represent the product of measured concentration and the associated instantaneous flow value. Likewise, simulated loads represent the product of the simulated instantaneous concentration for the nearest point in time of output (reported every two hours) and the corresponding simulated flow. Based on this comparison, model results are approximately 11% lower than measured values across all sample collection times and flows. The range of model results often straddle the 1:1 line of perfect agreement, demonstrating that model results are in good correspondence with field values, including when flows are greater than 100,000 cfs (2,832 cms).

Cumulative and annual net bed elevation changes for the 2008-2014 portion of the long-term simulation are presented in Figures 60-66. The full set of long-term results for the period 1997-2014 is presented in Appendix G. Short-term results are presented in Appendix H. Two panels are shown on each of these figures. The panel on the left shows the cumulative change in bed elevation since the simulation start (e.g., 1997 for long-term and 2008 for short-term) and the right panel shows model results for the year specified.

Model results were also compared to net bed elevation differences between interpolated bathymetric surveys. Long-term simulation results were compared to differences between the 2008 survey and surveys for 2011, 2013, and 2014 as presented in Figures 67-69. The full set of long-term model comparisons for 13 combinations of paired survey years is presented in Appendix I. Similarly, the full set of short-term model comparisons for 10 combinations of paired survey years is presented in Appendix J. Two panels are also shown on each of these figures, with the left panel showing bed elevation differences estimated from

interpolated bathymetric surveys and the right showing model results for the corresponding timeframe.

Excluding 2011, the simulated average rate of net sediment accumulation over the 2008-2014 period in the long-term model was approximately 0.026 feet/year (0.8 cm/year). During 2011, there was more erosion than deposition in the long-term model and the average net bed elevation change was -0.11 feet (-3.43 cm). Including 2011, the average net sediment accumulation rate was approximately 0.006 feet/year (0.18 cm/year). Over the entire 1997-2014 period (inclusive of 2011), the net sediment accumulation rate was approximately 0.02 feet/year (0.6 cm/year) in the long-term model. Short-term model results are generally similar to long-term model results with the exception that there was an average net bed elevation change of -0.28 feet (-8.69 cm) during 2011. Net sediment accumulation rates in the short-term model averaged 0.024 feet/year (0.74 cm/year) when 2011 is excluded but was -0.02 feet/year (-0.61 cm/year) when 2011 is included.

Net sediment accumulation rates estimated from differences in interpolated bathymetric survey measurements are presented in Table 3. Based on differences between the 2008 and 2014 surveys, there was a bed elevation change of 0.004 feet (0.13 cm) over that seven-year period, corresponding to an average net sediment accumulation rate of 0.001 feet/year (0.02 cm/year) and a range of -0.03 to 0.038 feet/year (-0.80 to 1.11 cm/year). Thus, the differences between interpolated bed elevation surveys over time indicate that net bed elevation changes were near zero (i.e., no net change in bed elevation) and that long-term and short-term model results are well within the range of sedimentation rates estimated from bathymetric survey.

Absolute comparisons of cell-by-cell differences between simulated bed elevation changes and interpolated bathymetric surveys are more uncertain and difficult to assess. This is particularly true for comparisons involving the 1996 survey. Relative to interpolations for the 2008-2014 surveys, model results are generally within approximately 0.1 feet (3 cm) of pond-wide average bed elevation differences between surveys and also show some of the cell-by-cell pattern of elevation increases (deposition) and decreases (erosion). Relative to comparisons to the 1996 survey, model results generally appear to be more consistently depositional (i.e., more areas with some deposition) but with smaller pond-wide average bed elevation increases than inferred from interpolated surveys. However, differences between interpolations for the 1996 and more recent surveys show exceedingly large cell-by-cell elevation changes where increases (+) and decreases (-) between adjacent cells often exceed ~10 feet (300 cm) and are even larger in some locations. Such very large inferred differences occur near Muddy Creek, along riverbanks, and the more routinely depositional area along the left downstream bank near Conowingo Dam. These locations (i.e., near Muddy Creek, along banks, near Conowingo Dam) are areas where interpolated bed elevations are expected to have their greatest uncertainty. Consequently, the large inferred differences between surveys may reflect a combination of measurement uncertainty

(horizontal and vertical positioning errors) and other "noise" in the spatial interpolation that is attributable to the low data density of the 1996 survey.

The factor that drives erosion and net sediment accumulation in the model is the shear stress exerted on the bed surface. The maximum total shear stress and grain shear stress (i.e., the portion of the total shear stress that acts on particles within the bed) that occurred in the simulation during 2011 are presented in Figure 70. The year 2011 was used for this summary because the largest shear stresses over the course of the simulation occur during Tropical Storm Lee. Shear stresses vary across the bed surface and generally decrease with distance along the reservoir as it becomes deeper and wider. However, with the exception of a region of lower grain shear stresses along the left downstream bank near Conowingo Dam, shear stresses elsewhere remain relatively high, with maximum values in the range of 0.1 – 0.17 psf (50 – 80 dynes/cm$^2$, 5 – 8 Pa).

# 4. MANAGEMENT SCENARIOS

The hydrodynamic and sediment transport model was used to simulate management scenarios (also termed production runs) to explore a range of alternative sediment inputs and corresponding export from Conowingo Pond. Management scenarios were simulated as a "second cycle" of the model, with flows and other conditions from the first cycle of the model used to drive the next cycle for a range of different sediment input conditions.

## 4.1. MANAGEMENT SCENARIO SET-UP

Management scenarios were simulated as a second cycle of the model. Ending conditions in the long-term simulation (i.e., ending sediment bed elevations, ending water depths, ending sediment bed composition, etc.) were used as initial conditions for an additional 18-year simulation. For each scenario, flows and other forcing functions from the long-term simulation (the first cycle of the model) were repeated to drive the second model cycle with an alternative set of sediment inputs. The specific details of these production runs were worked out in consultation with the USEPA CBP.

Boundary conditions for sediment concentrations (and therefore loads) to Conowingo differed for each scenario as follows:

- **Scenario 0:** sediment loads to Conowingo Pond equal to existing loads (apply a scale factor of 1.0 to sediment inputs).
- **Scenario 1:** sediment loads to Conowingo Pond reduced by 35% relative to existing loads (apply a scale factor of 0.65 to sediment inputs).
- **Scenario 2:** sediment loads to Conowingo Pond reduced by 10.5% relative to existing loads (apply a scale factor of 0.895 to sediment inputs).
- **Scenario 3:** sediment loads to Conowingo Pond increased by 14% relative to existing loads (apply a scale factor of 1.14 to sediment inputs).

For each of these scenarios, sediment inputs at Holtwood, Muddy Creek, and Broad Creek were multiplied by the specified scale factor. These scale factors were applied "across the board" such that all particle size classes and all sources were adjusted in the same manner.

## 4.2. MANAGEMENT SCENARIO RESULTS

Summaries of annual sediment inputs (i.e., the sum of sediment loads entering from Holtwood, Muddy Creek, and Broad Creek) and simulated export over Conowingo Dam by hydrologic year for each management scenario are presented in Table 5 (metric units) and Table 6 (English units). Cumulative sediment influx, export, net bed elevation change, and net sediment accumulation rates over the 18-year duration of each scenario and the long-term simulation are summarized in Table 7. The maximum total shear stress and grain

shear stress that occurred in the management scenarios during hydrologic year 2011 are presented in Figures 71-74.

As expected based on its governing equations, the model responds linearly to changes in loads. Under the 35% load reduction in Scenario 1, the load exported from Conowingo Pond is reduced by approximately 35%. Responses for Scenarios 2 and 3 are also in proportion to changes in loads (i.e., -10.5% and +14%). The largest relative difference between scenarios occurs during hydrologic year 2011 when the Tropical Storm Lee high flow event occurs. Although grain shear stresses exerted on the bed during this second cycle of Tropical Storm Lee differ between scenarios by a small degree (and also differ from long-term model results), those differences do not materially alter the overall trend and magnitude of net sediment accumulation in the model. All scenarios show continued net sediment accumulation within the Pond, with simulations that have smaller loads accumulating less sediment than cases with larger inputs.

# 5. DISCUSSION AND INTERPRETATION OF RESULTS

The CPMBM model provides a spatially detailed representation of hydrodynamic and sediment transport processes within Conowingo Pond and advances the state of the science by providing the most extensive assessment of the Pond that has been completed to date. It builds on prior work by the USACE (2014) and adds a three-dimensional representation of flow. The spatially and temporally varying hydraulics of Conowingo Dam are incorporated into the model. Flow varies across the width of the dam and water is withdrawn from different vertical layers in response to changing operations and crest gate openings over time. The approach used to estimate upstream flows implicitly accounts for the influence of upstream hydropower operations and flow modulation. A wide array of field data was used to drive model development. The model also includes the hydrothermal impact of service and cooling water discharges from PBAPS. Like the water column, the sediment bed was represented in a three-dimensional manner. Bed properties (grain size distributions, bulk densities, erosion characteristics) were varied with depth through the sediment column based on geostatistical evaluation of field data collected over the past 20 years. Extensive bathymetric data were used to inform the sediment transport model and evaluations of bed elevation changes over time. The model also incorporates information from the USEPA HSPF (P6B2) watershed model as well as the more detailed HEC-RAS simulations of upstream reservoirs performed by WEST (2016).

The hydrodynamic components of the model were judged to appropriately simulate the most important aspects of water surface elevation changes over time. Differences in the timing and magnitude of water surface elevation fluctuations are typically small. With one exception, the model closely follows the trends and magnitudes of measured values at Muddy Run, Peach Bottom, and Conowingo Dam. The exception is a transient elevation decrease of approximately 3-6 feet (1-2 meters) at Conowingo that occurs in the model during Tropical Storm Lee (see Figures 12 and 19). This decrease occurs when flow is simultaneously withdrawn from the top two layers of the water column in grid cells representing crest gate spills. Flow withdrawals at the model downstream boundary are specified to match measured outflows at Conowingo. In this situation, the rate of water withdrawal at the Dam is faster than the rate at which the model transports water from upstream. Given the large velocity gradients between layers, the likely cause of this model behavior is the relatively coarse (five layer) representation of the water column and its affect on flow resistance (drag coefficients). The consequence of this behavior is that simulated flow velocities and shear stresses in an area near Conowingo Dam are larger than would otherwise be expected. Thus, during this transient, sediment deposition near the Dam would decrease and the potential for erosion (bed scour) would increase. From the perspective of model use as a tool to estimate sediment loads passing Conowingo Dam, model results are expected to be conservative (i.e., estimate larger loads than would otherwise be expected).

Similarly, hydrothermal components of the model were also judged to appropriately simulate the most important aspects of water temperature changes over time. Differences in measured and simulated water temperatures are likely to be driven by uncertainties in the temperature of inflows at Holtwood, particularly given the frequent availability of site-specific meteorological and solar radiation data, detailed characterization of temperature rises for the Peach Bottom thermal discharge, and short residence times of flows. The largest differences occur immediately adjacent to the Peach Bottom thermal discharge. However, differences between simulated and measured temperatures do not affect sediment transport results and are small enough to support unbiased development of nutrient transport simulations.

Sediment transport components of the model were also judged to appropriately simulate the most important aspects of suspended sediment loads and concentrations as well as bed elevation changes over time. However, loads and elevation changes are influenced by flows, the concentration and size distribution of sediments in the water column, and the erosion resistance of the bed through the depth of the sediment column. Consequently, this assessment of model performance is necessarily more nuanced given uncertainties in estimated sediment loads and interpolated bed elevation measurements.

Direct measurements of inflows at Holtwood, which are the largest source of flow to the Pond, were not available for this study. Relative to measurements at Marietta, flows at Holtwood are expected to be influenced by upstream hydropower operations. Although estimated by other means, uncertainties in flows at Holtwood contribute to uncertainties in sediment load estimates. Similarly, suspended sediment concentrations at Holtwood, which is the largest source of sediment to the Pond, have not been routinely measured and are also influenced by upstream hydropower operations. Uncertainties in SSC estimates contribute to uncertainties in sediment load estimates. Moreover, the grain size distribution of sediment loads entering Conowingo Pond are expected to be altered relative to conditions at Marietta as water moves through Lakes Clarke and Aldred.

Models used to estimate SSC at Holtwood exhibit different grain size distributions. The sediment load calculated by HEC-RAS (WEST, 2016) is predominantly comprised of silt-sized particles while the load from HSPF (P6B2) is largely clay-sized. The difference is important because settling velocities and corresponding deposition fluxes for silt-sized particles are more than two orders of magnitude larger than those for clay-sized particles at the same concentration. Thus, simulations that use HSPF loads will generate less sediment accumulation and switching from HSPF to HEC-RAS loads (WEST, 2016) necessarily alters patterns and magnitude of sediment accumulation in the sediment transport model for Conowingo Pond.

Given the influence that upstream conditions have on Conowingo Pond, it is important to consider how HSPF (P6B2) and HEC-RAS represent sediment transport processes through Lake Clarke and Lake Aldred reservoirs (WEST, 2016). HSPF is configured to provide

estimates of flows, transport for three sediment classes, and nutrient concentrations for the entire Susquehanna River watershed. As configured for P6B2, Lake Clarke and Lake Aldred are each a single compartment in HSPF. Each compartment is necessarily a spatial average, where processes are represented by a constant (within cell) parameterization. Consequently, HSPF does not account for within reservoir spatial variation of sediment properties and erosion characteristics. Moreover, HSPF (P6B2) does not account for the effect of hydropower operations at Safe Harbor, Holtwood, or Conowingo Dams.

In contrast, the WEST (2016) HEC-RAS efforts were designed to evaluate unsteady, one-dimensional sediment transport for the upper two reservoirs. The effect of hydropower operations is incorporated into the WEST HEC-RAS simulations through rating curves to account for powerhouse and gate capacity. The WEST HEC-RAS simulations also account for spatial variation of sediment composition (grain sizes) and erosion characteristics, including cohesive sediment behavior along the length of each reservoir, with particle-specific deposition and erosion occurring by 12 size classes that are summed into clay, silt, and sand. In this context, and relative to HSPF (P6B2) watershed model outputs, the WEST HEC-RAS (2016) simulations and sediment load estimates at Holtwood (and elsewhere in Lakes Clarke and Aldred) advance the state of the science regarding the behavior of the upstream reservoirs and provide the best available basis to drive Conowingo Pond sediment transport simulations.

Although the present study results enhance the body of information to evaluate sediment transport responses that occur in Conowingo Pond, water quality managers will also need to be cognizant of study limitations. In particular, the erosion characteristics of Pond sediments remain uncertain. The processes by which sediments deposited within the Pond transition over time from the more easily erodible state inferred from SEDFLUME study results (USACE, 2014) to a more erosion resistant state are not well-defined. Sediment cores from the Pond do not show consistent patterns of increasing bulk density or grain size coarsening with depth or other factors such as sediment consolidation that typically explain increased erosion resistance with depth.

Further, bed elevation measurements and interpolated elevation differences may be more uncertain than recognized. At face value, differences in interpolated elevations between surveys suggest that large deposition fluxes in any one cell are offset by erosion fluxes of nearly equal magnitude in adjacent cells to yield a small pond-wide average elevation difference. However, such inferences conflict with the deposition potential of relatively fine-grained sediment loads at Holtwood, particularly as estimated by HSPF. Given their magnitude and grain size distribution, those loads generate Pond-wide deposition fluxes of roughly 1 cm/year (0.03 feet/year) or less and are insufficient to reproduce the large cell-to-cell elevation differences (both gains and losses) inferred from bathymetric surveys. These inconsistencies suggest that inferred differences between survey years likely reflect measurement error and interpolation uncertainties rather than demonstrable differences in the net accumulation or loss of sediment from Conowingo Pond over time.

# 6. SUMMARY AND CONCLUSIONS

A coupled three-dimensional hydrodynamic and sediment transport model was developed as part of an overall project designed to simulate sediment and nutrient transport in Conowingo Pond. Hydrodynamic and sediment transport simulations were developed to evaluate Pond conditions and were used to drive nutrient transport simulations to evaluate nutrient loads and reactivity. The purpose of these simulations is to generate load estimates and system responses for sediments (and nutrients) to help inform the Phase 6 HSPF watershed model (or other tools) that USEPA uses for the 2017 mid-point assessment.

The hydrodynamic model and component hydrothermal model were constructed using a wide array of site-specific information. The influence of hydropower operations at Conowingo Dam was explicitly included in the model by accounting for the time-variable withdrawal of water from different depths in the water column to represent flow through the power-intake as well as spill over crest gates. Outflows at Conowingo Dam were measured. However, inflows at Holtwood were not available and had to be estimated from other data. The model nevertheless successfully reproduced water surface elevations and temperatures over time. These evaluations were based on comparisons to conditions defined from more than two million water surface elevation measurements and numerous water temperature measurements.

The sediment transport model was also constructed using a wide array of site-specific information. However, assessment of sediment transport model performance was more nuanced as a consequence of wide uncertainties in estimated sediment loads, grain size distributions, and bed elevation measurements. Sediment loads at Holtwood are uncertain in terms of their magnitude and grain size distribution. These factors influence the sediment accumulation in the model. Load estimates from both HSPF and HEC-RAS were evaluated. HSPF loads were primarily comprised of clay-sized particles and HEC-RAS loads (WEST, 2016) were more often comprised of silts. Differences in loads and grain size distributions lead to appreciable differences in simulated patterns and magnitudes of sediment accumulation in the model because of the underlying difference in settling velocities for clays and silts. Interpolated sediment properties (grain size distribution and wet bulk density) and bed elevations are also highly uncertain and have a direct impact on sediment transport model performance. Evaluations of bed elevation data indicate that uncertainties driven by locational accuracy and data density are nearly as large as differences between survey years.

Hydrodynamic and sediment transport simulation results at Conowingo are strongly influenced by flow and sediment inputs at Holtwood. Those inputs were derived from WEST (2016) HEC-RAS simulations for the upstream reservoirs. Thus, in as much as the three reservoirs collectively influence sediment transport between Marietta and Conowingo, the models for the three reservoirs should be considered as a system. The primary constraints on model performance were flow and SSC measurements at Marietta

and Conowingo Dam. The models were informed by bathymetric surveys and sediment core data to define bed properties and erosion characteristics at spatial scales that are not resolved by HSPF. Notwithstanding data limitations, the system of models was able to reproduce approximate average net sediment accumulation over time in the two upstream reservoirs (see Figures 3-9 and 3-10 in West, 2016) and Conowingo Pond as well as the time series of measured SSC at Conowingo Dam. Moreover, long-term simulations for Conowingo Pond driven by the HEC-RAS solids rating curve at Holtwood (WEST, 2016) were also able to reproduce average net sediment accumulation based on bathymetric surveys of the reservoir as well as the time series of measured SSC at Conowingo Dam.

In conjunction with the HEC-RAS hydraulic and sediment transport model for Lakes Clarke and Aldred (WEST, 2016), the hydrodynamic and sediment transport model for Conowingo Pond builds upon and extends prior modeling efforts. Short-term and long-term simulations were successfully performed. Although uncertainties remain, simulated sediment loads passing Conowingo Dam estimated using these models are expected to be the most reliable characterization of sediment transport performed to date for Conowingo Pond and the two upstream reservoirs.

# 7. REFERENCES

AECOM. 2016. Personal communication from Dr. Marjorie Zeff summarizing methods and results from the Conowingo Pond 2015 bed sediment coring event.

Ahsan, A. K. M. Q., and Blumberg, A. F. 1999. A three-dimensional hydrothermal model of Onondaga Lake, New York. Journal of Hydraulic Engineering, 125(9):912-923.

Baird. 2000a. Technical Memorandum 5b: ECOM-siz-SEDZL Model Application: Lower Fox River Downstream of the DePere Dam. W.F. Baird and Associates, Ltd., Madison, Wisconsin. 41 pp. plus figures and appendices.

Baird. 2000b. ECOMSED Model Application: Upstream Lower Fox River from Lake Winnebago to DePere Dam. W.F. Baird and Associates, Ltd., Madison, Wisconsin.

Blumberg, A. F. and Mellor, G. L. 1983. Diagnostic and prognostic numerical circulation studies of the South Atlantic Bight. Journal of Geophysical Research, 88:4579-4592.

Blumberg, A. F. and Mellor, G. L. 1985. A simulation of the circulation in the Gulf of Mexico. Israel Journal of Earth Sciences, 34:122-144.

Blumberg, A. F., and Mellor, G. L. 1987. A description of a three-dimensional coastal ocean circulation model. In: Three-Dimensional Coastal Ocean Models. N.S. Heaps (ed.) American Geophysical Union, Washington DC. pp. 1-16.

Blumberg, A. F., and Goodrich, D. M. 1990. Modeling of wind-induced destratification in Chesapeake Bay. Estuaries, 13:1236-1249.

Blumberg, A. F., Signell, R. P., and Jenter, H. L. 1993. Modeling transport processes in the coastal ocean. Journal of Marine Environmental Engineering, 1:3-52.

Blumberg, A. F., Khan, L. A., and St. John, J. P. 1999. Three-dimensional hydrodynamic model of New York Harbor Region. Journal of Hydraulic Engineering, 125:799-816.

Blumberg, A. F., and Kim, B. N. 2000. Flow balances in St. Andrew Bay revealed through hydrodynamic simulations. Estuaries, 23:21-33.

Cheng, N. S. 1997. Simplified settling velocity formula for sediment particle. Journal of Hydraulic Engineering, 123(2):149-152.

Clarke, T. L., Swift, D. J. P., and Young, R. A. 1982. A numerical model of fine sediment transport on the continental shelf. Environmental Geology, 4(2):117-129.

Clarke, T. L., Swift, D. J. P., and Young, R. A. 1983. A stochastic modeling approach to the fine sediment budget of the New York Bight. Journal of Geophysical Research, 88(C14):9653-9660.

Dingman, S.L. 2002. Physical Hydrology (Second Edition). Prentice Hall, Inc., Upper Saddle River, New Jersey. 646 p.

ESRI. 2014. ArcGIS Release 10.3. Environmental Systems Research Institute, Redlands, California.

Exelon. 2012a. Application for New License for Major Water Power Project-Existing Dam: Conowingo Hydroelectric Project, FERC Project No. 405, Volume 1: Initial Statement; Exhibit A – Project Description. Exelon Generation Company, LLC. 15 pp.

Exelon. 2012b. Application for New License for Major Water Power Project-Existing Dam: Conowingo Hydroelectric Project, FERC Project No. 405, Volume 1: Initial Statement; Exhibit B –Project Operation and Resource Utilization. Exelon Generation Company, LLC. 27 pp.

Exelon. 2012c. Appendix F, Final Study Report 3.15 (Sediment Introduction and Transport Study). Final License Application for Conowingo Power Project, FERC Project Number 405. Exelon Generation Company, LLC. 25 pp.

Galerpin, G., Kantha, L. H., Hassid, S., and Rosati, A. 1988. A quasi-equilibrium turbulent energy model for geophysical flows. Journal of Atmospheric Science, 45:55-62.

Galperin, B., and Mellor, G. L. 1990a. A time-dependent, three-dimensional model of the Delaware Bay and River System, part 1: description of the model and tidal analysis. Estuarine and Coastal Shelf Science, 31:231-253.

Galperin, B., and Mellor, G. L. 1990b. A time-dependent, three-dimensional model of the Delaware Bay and River System, part 2: three-dimensional flow fields and residual circulations. Estuarine and Coastal Shelf Science, 31:255-281.

Galperin, B., and Mellor, G. L. 1990c. Salinity intrusion and residual circulation in Delaware Bay during the drought of 1984. In: Residual Currents and Long-Term Transport (Coastal and Estuarine Studies, Volume 38). Cheng, R. T., ed. Springer-Verlag, Inc., New York. p. 469-480.

Gessler, J. 1965. The Beginning of Bedload Movement of Mixtures Investigated as Natural Armouring in Channels. Technical report No. 69, The Laboratory of Hydraulic Research and Soil Mechanics, Swiss Federal Institute of Technology, Zurich (translation by W. M.

Keck Laboratory of Hydraulics and Water Resources, California Institute of Technology, Pasadena, California).

Gessler, J. 1967. The beginning of bedload movement of mixtures investigated as natural armoring in channels. California Institute of Technology, Pasadena, California. 89pp.

Gessler, J. 1971. Beginning and ceasing of sediment motion. In: River Mechanics, Shen, H.W., ed. Fort Collins, Colorado. pp. 7:1–7:22.

Guo, J. 2002. Hunter Rouse and Shields diagram. Proceedings of the 13th International Association of Hydraulic Research Asian and Pacific Division Congress, Singapore, Malaysia, August 6-8.

HQI. 1999a. Newton Creek Water Pollution Control Project East River Water Quality Plan, Report to NYCDEP. Task 10.0 System-Wide Eutrophication Model (SWEM) Sub-task 10.1 Construct SWEM. Prepared under subcontract to Greeley and Hansen, New York, NY. HydroQual, Inc., Mahwah, New Jersey.

HQI. 1999b. Newton Creek Water Pollution Control Project East River Water Quality Plan, Report to NYCDEP. Task 10.0 System-Wide Eutrophication Model (SWEM) Sub-task 10.2 Obtain and Reduce Loading/Water Quality Data. Prepared under subcontract to Greeley and Hansen, New York, NY. HydroQual, Inc., Mahwah, New Jersey.

HQI. 1999c. Newton Creek Water Pollution Control Project East River Water Quality Plan, Report to NYCDEP. Task 10.0 System-Wide Eutrophication Model (SWEM) Sub-task 10.4 Calibrate SWEM Water Quality. Prepared under subcontract to Greeley and Hansen, New York, NY. HydroQual, Inc., Mahwah, New Jersey.

HQI. 1999d. Newton Creek Water Pollution Control Project East River Water Quality Plan, Report to NYCDEP. Task 10.0 System-Wide Eutrophication Model (SWEM) Sub-task 10.5 Apply SWEM for Preliminary Facility Design. Prepared under subcontract to Greeley and Hansen, New York, NY. HydroQual, Inc., Mahwah, New Jersey.

HQI. 1999e. Newton Creek Water Pollution Control Project East River Water Quality Plan, Report to NYCDEP. Task 10.0 System-Wide Eutrophication Model (SWEM) Sub-task 10.6 Validate SWEM Hydrodynamics. Prepared under subcontract to Greeley and Hansen, New York, NY. HydroQual, Inc., Mahwah, New Jersey.

HQI. 1999f. Newton Creek Water Pollution Control Project East River Water Quality Plan, Report to NYCDEP. Task 10.0 System-Wide Eutrophication Model (SWEM) Sub-task 10.7 Final Facility Design. Prepared under subcontract to Greeley and Hansen, New York, NY. HydroQual, Inc., Mahwah, New Jersey.

HQI. 1999g. Hydrodynamics, Sediment Transport, and Sorbent Dynamics in Green Bay. Prepared for Remediation Technologies, Inc. and the Wisconsin Department of Natural Resources. HydroQual, Inc., Mahwah, NJ. Project Number: RTCH0010.

HQI. 2000. Technical Memorandum 5c: Evaluation of the Hydrodynamics in the Lower Fox River Between Lake Winnebago and DePere, WI. Hydroqual, Inc., Mahwah, New Jersey.

HQI. 2001. Enhancement and application of a PCB fate and transport model for Green Bay. HydroQual, Inc., Mahwah, New Jersey. 100 p.

HQI. 2002. Calibration Enhancement of the System-Wide Eutrophication Model (SWEM) in the New Jersey Tributaries, Report to NJDEP. Final Technical Report April 23, 2001 through July 31, 2002. Prepared under subcontract to Passaic Valley Sewerage Commissioners, Newark, NJ. HydroQual, Inc., Mahwah, New Jersey.

HQI. 2005. Near field and far field study for the R.E. Ginna Nuclear Power Plant, Constellation Energy. HydroQual, Inc., Mahwah, New Jersey.

HQI. 2007. A model for the evaluation and management of contaminants of concern in water, sediment and biota in the NY/NJ Harbor Estuary: Contaminant fate & transport & bioaccumulation sub-models. Prepared for the Contamination Assessment and Reduction Project (CARP) Management Committee. HydroQual, Inc., Mahwah, New Jersey.

HQI. 2008. Near Field and Far Field Thermal Modeling Study for the Nine Mile Point Nuclear Power Plant, Constellation Energy. HydroQual, Inc., Mahwah, New Jersey.

HQI. 2010. A Primer for ECOMSED (Version 1.4-LPR): Users Manual. HydroQual, Inc., Mahwah, New Jersey. 218 p. (Release Date: March 5, 2010.)

Jacobs, W., Le Hir, P., Van Kesteren, W., and Cann, P. 2011. Erosion threshold of sand–mud mixtures. Continental Shelf Research, 31(10, Suppl. 1):S14-S25.

James, S. C., Jones, C. A., Grace M. D., and Roberts, J. D. 2010. Advanced in sediment transport modeling. Journal of Hydraulic Research, 48(6):754-763.

Jepsen, R., Roberts, J., and Lick, W. 1997. Effects of bulk density on sediment erosion rates. Water, Air, and Soil Pollution, 99(1-4): 21-31.

Jepsen, R., McNeil, J., and Lick, W. 2000. Effects of gas generation on the density and erosion of sediments from the Grand River. Journal of Great Lakes Research, 26(2):209-219.

Jones, C. A., and Lick, W. 2001. Contaminant flux due to sediment erosion. Proceedings of the 7th International Conference: Estuarine and Coastal Modeling, 280–293.

Julien, P. Y. 1998. Erosion and Sedimentation (First Paperback Edition). Cambridge University Press, Cambridge, UK. 280 p.

Krone, R. B. 1962. Flume Studies of the Transport of Sediment in Estuarial Shoaling Processes, Final Report. Hydraulic Engineering Laboratory and Sanitary Engineering Research Laboratory, Berkeley, CA. Prepared for U.S. Army Engineer District, San Francisco, San Francisco, CA, under US Army Contract No. DA-04-203 CIVENG-59-2.

Langland, M. J., and Koerkle, E. H. 2014. Calibration of a One-Dimensional Hydraulic Model (HEC-RAS) for Simulating Sediment Transport through Three Reservoirs, Lower Susquehanna River Basin, 2008-2011. Lower Susquehanna River Watershed Assessment, Phase 1, Appendix A with 3 Attachments, Washington, D.C.: U.S. Department of the Interior, U.S. Geological Survey.

McNeil, J., Taylor, C., and Lick, W. 1996. Measurement of erosion of undisturbed bottom sediments with depth. Journal of Hydraulic Engineering, 122(6): 316-324.

Mellor, G. L., and Yamada, T. 1982. Development of a turbulence closure model for geophysical fluid problems. Reviews of Geophysics and Space Physics. 20:851-875.

Middleton, G. V. 1984. Mechanics of Sediment Movement. Second Edition. Society of Economic Paleontologists and Mineralogists, Tulsa, OK. 401 pp.

Normandeau and ERM. 2014. Final Report for the Thermal Study to Support A §316(A) Demonstration: Peach Bottom Atomic Power Station. Prepared for: Exelon Generation, LLC. Prepared by: Normandeau Associates, Inc. and ERM, Inc. 417 p.

Normandeau and GSE. 2011. Seasonal and Diurnal Water Quality in Conowingo Pond and Below Conowingo Dam, RSP 3.1, Conowingo Hydroelectric Project, FERC Project Number 405. Prepared for: Exelon. Prepared by: Normandeau Associates, Inc. and Gomez and Sullivan Engineers, P.C. 148 p.

Oey, L. Y., Mellor, G. L., and Hires, R. I. 1985a. A three dimensional simulation of the Hudson-Raritan Estuary, part I: description of the model and model simulations, Journal of Physical Oceanography, 15:1676-1692.

Oey, L. Y., Mellor, G. L., and Hires, R. I. 1985b. A three dimensional simulation of the Hudson-Raritan Estuary, part II: comparison with observations. Journal of Physical Oceanography, 15:1693-1709.

Roberts, J. D., Jepsen, R., Gotthard, D., and Lick, W. 1998. Effect of particle size and bulk density on erosion of quartz particles. Journal of Hydraulic Engineering, 124(12):1261-1267.

Roberts, J.; Jepsen, R., and James, S. 2003. Measurement of sediment erosion and transport with the Adjustable Shear Stress Erosion and Transport flume. Journal of Hydraulic Engineering. 129(11): 862-871.

Sanford, L., Barletta, S., Hinkle, D., Fitzgerald, C., and Fisher, A. 2016. Particle transport processes. University of Maryland, Center for Environmental Studies, Horn Point Laboratory, Cambridge, MD. Presentation to the Chesapeake Bay Program (CBP) Scientific and Technical Advisory Committee (STAC). January 13-14.

Shields, A. 1936. Anwendung der aenlichkeitsmechanik und der turbulenzforschung auf die geschiebebewegung. Mitteilungen der Preussischen Versuchsanstalt fur Wasserbau und Schiffbau, Berlin, Germany (translation by W. P. Ott and J. C. van Uchelen, California Institute of Technology, Pasadena, California).

Signell, R., and List, J. 1997. Modeling waves and circulation in Lake Pontchartrain. Gulf Coast Association of Geological Societies Transactions, 47:529-532.

Soulsby, R. 1997. Dynamics of Marine Sands. Thomas Telford Publications, London, UK. 249 pp.

SRBC. 2006. Comprehensive Analysis of the Sediments Retained Behind Hydroelectric Dams of the Lower Susquehanna River. Publication 239. Prepared by: Robert E. Edwards, Special Projects Manager, Watershed Assessment and Protection Program, Susquehanna River Basin Commission. Dated: February 28. 154 p.

USACE. 2014. Sediment Transport Characteristics of Conowingo Reservoir. Appendix B, Lower Susquehanna River Watershed Assessment. Prepared by S. H. Scott and J. A. Sharp. U.S. Army Corps of Engineers, Engineer Research and Development Center, Vicksburg, MS. 264 p.

USEPA. 2014. Hydrodynamic and Sediment Transport Evaluation: Capping/Armoring Analyses. Appendix B: Remedial Investigation Report for the Focused Feasibility Study of the Lower Eight Miles of the Lower Passaic River. Prepared by The Louis Berger Group, Inc. in conjunction with Battelle and HDR|HydroQual. Prepared for U.S. Environmental Protection Agency Region II and U.S. Army Corps of Engineers Kansas City District. February, 2014. 3834 pp.

USEPA. 2016. Updated Mechanistic Model. Attachment E: Record of Decision, Lower 8.3 Miles of the Lower Passaic River, Part of the Diamond Alkali Superfund Site, Essex and

Hudson Counties, New Jersey. U.S. Environmental Protection Agency Region II, New York, New York. March 3, 2016. 532 pp.

USGS. 1992. Water Resources Data, Pennsylvania, Water Year 1991: Volume 2. Susquehanna and Potomac River Basins (by R. R. Durlin and W. P. Schaffstall). Water Data Report PA-91-2. U.S. Geological Survey, Pennsylvania Water Science Center, New Cumberland, PA.

USGS. 1997a. Changes in Bottom-Surface Elevations in Three Reservoirs On the Lower Susquehanna River, Pennsylvania and Maryland, Following the January 1996 Flood — Implications for Nutrient and Sediment Loads to Chesapeake Bay (by M. J. Langland and R. A. Hainly). Water-Resources Investigations Report 97-4138. U.S. Geological Survey, Pennsylvania Water Science Center, New Cumberland, PA. 39 pp.

USGS. 1997b. Water Resources Data, Pennsylvania, Water Year 1996: Volume 2. Susquehanna and Potomac River Basins (by R. R. Durlin and W. P. Schaffstall). Water Data Report PA-96-2. U.S. Geological Survey, Pennsylvania Water Science Center, New Cumberland, PA.

van Rijn, L. C. 1984a. Sediment transport, part I: bed load transport. Journal of Hydraulic Engineering, 110(10):1431-1456.

van Rijn, L. C. 1984b. Sediment transport, part II: suspended load transport. Journal of Hydraulic Engineering, 110(11):1612-1638.

van Rijn, L. C. 1984c. Sediment transport, part III: bed forms and alluvial roughness. Journal of Hydraulic Engineering, 110(12):1733-1754.

van Rijn, L. C. 1993. Principles of sediment transport in rivers, estuaries and coastal seas. Aqua Publications, Amsterdam, Netherlands.

WEST. 2016. Lake Clarke and Lake Aldred Sediment Transport Modeling, Draft Report (In Progress). Prepared by: WEST Consultants, Inc., San Diego, CA. Prepared for: Exelon Energy Corporation, Kennett Square, PA. July 2016. 64 p.

Winterwerp, J. C., and Van Kesteren, W. G. M. 2004. Introduction to the Physics of Cohesive Sediment in the Marine Environment. Elsevier B.V., Amsterdam, Netherlands. 466 p.

# TABLES

Table 1. Summary of measured suspended sediment concentration (SSC), flow, and loads at Conowingo: 1996-2014.

| *Sample Date* | *Sample Time* | *Instantaneous Flow (cfs)* | *Instantaneous Flow (cms)* | *Measured SSC (mg/L)* | *Estimated Sediment Load (tons/day)* | *Estimated Sediment Load (MT/day)* |
|---|---|---|---|---|---|---|
| 1/17/1996 | 15:45 | 4,120 | 117 | 3 | 33 | 30 |
| 1/20/1996 | 14:15 | 404,000 | 11,440 | 194 | 211,407 | 191,753 |
| 1/21/1996 | 13:15 | 623,000 | 17,641 | 1,200 | 2,016,539 | 1,829,060 |
| 1/21/1996 | 16:15 | 610,000 | 17,273 | 1,000 | 1,645,383 | 1,492,411 |
| 1/21/1996 | 19:00 | 587,000 | 16,622 | 863 | 1,366,426 | 1,239,389 |
| 1/22/1996 | 10:45 | 470,000 | 13,309 | 533 | 675,713 | 612,892 |
| 1/22/1996 | 15:00 | 394,000 | 11,157 | 462 | 490,993 | 445,345 |
| 1/22/1996 | 19:30 | 411,000 | 11,638 | 451 | 499,983 | 453,500 |
| 1/23/1996 | 14:15 | 274,000 | 7,759 | 315 | 232,808 | 211,164 |
| 1/23/1996 | 20:30 | 255,000 | 7,221 | 254 | 174,707 | 158,465 |
| 1/24/1996 | 16:00 | 209,000 | 5,918 | 104 | 58,630 | 53,179 |
| 1/24/1996 | 17:45 | 222,000 | 6,286 | 118 | 70,660 | 64,090 |
| 1/25/1996 | 12:30 | 198,000 | 5,607 | 111 | 59,282 | 53,771 |
| 1/25/1996 | 13:45 | 180,000 | 5,097 | 87 | 42,240 | 38,313 |
| 1/26/1996 | 11:15 | 180,000 | 5,097 | 96 | 46,610 | 42,277 |
| 1/29/1996 | 14:00 | 268,000 | 7,589 | 130 | 93,976 | 85,239 |
| 1/31/1996 | 14:00 | 142,000 | 4,021 | 63 | 24,130 | 21,887 |
| 2/9/1996 | 12:30 | 27,400 | 776 | 6 | 443 | 402 |
| 2/23/1996 | 16:00 | 91,800 | 2,599 | 11 | 2,724 | 2,471 |
| 2/23/1996 | 19:30 | 142,000 | 4,021 | 17 | 6,511 | 5,906 |
| 2/27/1996 | 12:15 | 175,000 | 4,955 | 41 | 19,353 | 17,554 |
| 3/12/1996 | 12:15 | 63,400 | 1,795 | 5 | 855 | 776 |
| 3/29/1996 | 15:00 | 74,500 | 2,110 | 13 | 2,612 | 2,370 |

Table 1. Summary of measured suspended sediment concentration (SSC), flow, and loads at Conowingo: 1996-2014 (continued).

| *Sample Date* | *Sample Time* | *Instantaneous Flow (cfs)* | *Instantaneous Flow (cms)* | *Measured SSC (mg/L)* | *Estimated Sediment Load (tons/day)* | *Estimated Sediment Load (MT/day)* |
|---|---|---|---|---|---|---|
| 4/9/1996 | 10:00 | 69,100 | 1,957 | 8 | 1,491 | 1,352 |
| 4/17/1996 | 10:00 | 181,000 | 5,125 | 30 | 14,647 | 13,285 |
| 4/18/1996 | 14:15 | 137,000 | 3,879 | 74 | 27,346 | 24,803 |
| 5/2/1996 | 12:00 | 135,000 | 3,823 | 13 | 4,734 | 4,294 |
| 5/3/1996 | 11:30 | 185,000 | 5,239 | 26 | 12,974 | 11,768 |
| 5/15/1996 | 11:30 | 186,000 | 5,267 | 91 | 45,655 | 41,411 |
| 6/11/1996 | 12:00 | 23,700 | 671 | 11 | 703 | 638 |
| 7/25/1996 | 12:30 | 61,400 | 1,739 | 12 | 1,987 | 1,803 |
| 8/19/1996 | 11:00 | 17,900 | 507 | 6 | 290 | 263 |
| 9/16/1996 | 13:30 | 64,900 | 1,838 | 27 | 4,727 | 4,287 |
| 10/22/1996 | 11:00 | 214,000 | 6,060 | 61 | 35,211 | 31,938 |
| 10/23/1996 | 10:30 | 164,000 | 4,644 | 34 | 15,040 | 13,642 |
| 11/11/1996 | 13:00 | 281,000 | 7,957 | 126 | 95,502 | 86,623 |
| 11/13/1996 | 13:00 | 164,000 | 4,644 | 100 | 44,237 | 40,124 |
| 12/3/1996 | 13:45 | 262,000 | 7,419 | 88 | 62,190 | 56,408 |
| 12/4/1996 | 14:30 | 255,000 | 7,221 | 123 | 84,602 | 76,737 |
| 12/6/1996 | 12:30 | 160,000 | 4,531 | 105 | 45,315 | 41,102 |
| 12/15/1996 | 18:30 | 231,000 | 6,541 | 73 | 45,485 | 41,257 |
| 1/22/1997 | 11:30 | 6,960 | 197 | 2 | 38 | 34 |
| 2/25/1997 | 14:15 | 100,000 | 2,832 | 16 | 4,316 | 3,915 |
| 3/18/1997 | 11:45 | 74,200 | 2,101 | 6 | 1,201 | 1,089 |
| 4/1/1997 | 12:00 | 74,200 | 2,101 | 23 | 4,603 | 4,175 |
| 4/30/1997 | 12:30 | 11,800 | 334 | 10 | 318 | 289 |

Table 1. Summary of measured suspended sediment concentration (SSC), flow, and loads at Conowingo: 1996-2014 (continued).

| *Sample Date* | *Sample Time* | *Instantaneous Flow (cfs)* | *Instantaneous Flow (cms)* | *Measured SSC (mg/L)* | *Estimated Sediment Load (tons/day)* | *Estimated Sediment Load (MT/day)* |
|---|---|---|---|---|---|---|
| 5/20/1997 | 13:00 | 58,400 | 1,654 | 4 | 630 | 572 |
| 6/10/1997 | 12:45 | 50,500 | 1,430 | 9 | 1,226 | 1,112 |
| 7/11/1997 | 8:15 | 5,290 | 150 | 8 | 114 | 104 |
| 8/6/1997 | 10:15 | 4,910 | 139 | 58 | 768 | 697 |
| 9/10/1997 | 11:00 | 5,830 | 165 | 6 | 94 | 86 |
| 10/7/1997 | 12:00 | 6,060 | 172 | 5 | 82 | 74 |
| 11/24/1997 | 13:15 | 42,800 | 1,212 | 8 | 924 | 838 |
| 12/29/1997 | 13:15 | 51,200 | 1,450 | 3 | 414 | 376 |
| 1/10/1998 | 9:45 | 345,000 | 9,769 | 123 | 114,462 | 103,820 |
| 1/12/1998 | 10:45 | 239,000 | 6,768 | 82 | 52,863 | 47,948 |
| 2/11/1998 | 11:30 | 62,600 | 1,773 | 9 | 1,520 | 1,378 |
| 3/11/1998 | 12:45 | 150,000 | 4,248 | 32 | 12,947 | 11,744 |
| 3/24/1998 | 11:45 | 119,000 | 3,370 | 39 | 12,518 | 11,355 |
| 4/13/1998 | 10:00 | 119,000 | 3,370 | 25 | 8,025 | 7,279 |
| 4/28/1998 | 12:45 | 68,100 | 1,928 | 17 | 3,123 | 2,832 |
| 5/14/1998 | 13:45 | 185,000 | 5,239 | 25 | 12,475 | 11,315 |
| 5/28/1998 | 13:15 | 46,400 | 1,314 | 9 | 1,126 | 1,022 |
| 6/10/1998 | 8:30 | 5,730 | 162 | 16 | 247 | 224 |
| 6/24/1998 | 8:30 | 6,300 | 178 | 17 | 289 | 262 |
| 7/9/1998 | 9:30 | 52,800 | 1,495 | 14 | 1,994 | 1,809 |
| 8/6/1998 | 7:30 | 6,500 | 184 | 7 | 123 | 111 |
| 9/10/1998 | 7:30 | 4,910 | 139 | 5 | 66 | 60 |
| 10/6/1998 | 10:15 | 3,510 | 99 | 10 | 95 | 86 |

Table 1. Summary of measured suspended sediment concentration (SSC), flow, and loads at Conowingo: 1996-2014 (continued).

| *Sample Date* | *Sample Time* | *Instantaneous Flow (cfs)* | *Instantaneous Flow (cms)* | *Measured SSC (mg/L)* | *Estimated Sediment Load (tons/day)* | *Estimated Sediment Load (MT/day)* |
|---|---|---|---|---|---|---|
| 11/4/1998 | 10:15 | 4,810 | 136 | 7 | 91 | 82 |
| 12/16/1998 | 12:15 | 3,470 | 98 | 5 | 47 | 42 |
| 1/7/1999 | 11:00 | 6,550 | 185 | 5 | 88 | 80 |
| 1/25/1999 | 10:30 | 206,000 | 5,833 | 58 | 32,228 | 29,232 |
| 1/26/1999 | 14:00 | 231,000 | 6,541 | 137 | 85,363 | 77,427 |
| 1/29/1999 | 11:15 | 130,000 | 3,681 | 50 | 17,533 | 15,903 |
| 2/9/1999 | 12:00 | 70,600 | 1,999 | 8 | 1,523 | 1,382 |
| 3/4/1999 | 12:00 | 31,500 | 892 | 5 | 425 | 385 |
| 4/8/1999 | 10:45 | 69,200 | 1,960 | 10 | 1,867 | 1,693 |
| 5/5/1999 | 11:15 | 11,000 | 311 | 7 | 208 | 188 |
| 6/9/1999 | 8:00 | 6,850 | 194 | 6 | 111 | 101 |
| 7/8/1999 | 8:30 | 4,910 | 139 | 7 | 93 | 84 |
| 8/5/1999 | 10:30 | 2,830 | 80 | 3 | 23 | 21 |
| 9/8/1999 | 10:15 | 54,300 | 1,538 | 6 | 879 | 797 |
| 9/21/1999 | 13:15 | 57,900 | 1,640 | 11 | 1,718 | 1,558 |
| 10/6/1999 | 7:15 | 35,300 | 1,000 | 11 | 1,047 | 950 |
| 11/2/1999 | 10:15 | 4,450 | 126 | 5 | 60 | 54 |
| 12/1/1999 | 11:15 | 71,400 | 2,022 | 11 | 2,118 | 1,922 |
| 1/6/2000 | 12:15 | 7,120 | 202 | 3 | 58 | 52 |
| 2/2/2000 | 12:15 | 14,500 | 411 | 1 | 39 | 35 |
| 2/28/2000 | 15:00 | 165,000 | 4,672 | 23 | 10,236 | 9,285 |
| 2/29/2000 | 13:00 | 180,000 | 5,097 | 53 | 25,733 | 23,340 |
| 3/1/2000 | 11:45 | 209,000 | 5,918 | 73 | 41,153 | 37,327 |

Table 1. Summary of measured suspended sediment concentration (SSC), flow, and loads at Conowingo: 1996-2014 (continued).

| *Sample Date* | *Sample Time* | *Instantaneous Flow (cfs)* | *Instantaneous Flow (cms)* | *Measured SSC (mg/L)* | *Estimated Sediment Load (tons/day)* | *Estimated Sediment Load (MT/day)* |
|---|---|---|---|---|---|---|
| 3/2/2000 | 10:45 | 194,000 | 5,493 | 65 | 34,014 | 30,851 |
| 3/23/2000 | 11:45 | 137,000 | 3,879 | 102 | 37,693 | 34,188 |
| 4/6/2000 | 12:15 | 76,700 | 2,172 | 17 | 3,517 | 3,190 |
| 4/11/2000 | 12:15 | 122,000 | 3,455 | 42 | 13,821 | 12,536 |
| 5/2/2000 | 12:15 | 54,300 | 1,538 | 13 | 1,904 | 1,727 |
| 5/24/2000 | 9:30 | 48,400 | 1,371 | 22 | 2,872 | 2,605 |
| 6/7/2000 | 10:30 | 43,200 | 1,223 | 12 | 1,398 | 1,268 |
| 6/20/2000 | 9:30 | 64,700 | 1,832 | 10 | 1,745 | 1,583 |
| 7/7/2000 | 11:00 | 26,800 | 759 | 4 | 289 | 262 |
| 7/18/2000 | 11:30 | 33,800 | 957 | 4 | 365 | 331 |
| 8/4/2000 | 13:00 | 54,700 | 1,549 | 6 | 885 | 803 |
| 8/21/2000 | 13:15 | 6,400 | 181 | 4 | 69 | 63 |
| 9/7/2000 | 12:00 | 6,800 | 193 | 5 | 92 | 83 |
| 9/21/2000 | 8:45 | 3,730 | 106 | 9 | 91 | 82 |
| 10/3/2000 | 10:30 | 18,500 | 524 | 4 | 200 | 181 |
| 10/18/2000 | 10:15 | 4,720 | 134 | 6 | 76 | 69 |
| 11/2/2000 | 11:45 | 5,500 | 156 | 5 | 74 | 67 |
| 11/20/2000 | 11:30 | 5,150 | 146 | 5 | 69 | 63 |
| 12/6/2000 | 12:30 | 4,910 | 139 | 2 | 26 | 24 |
| 12/18/2000 | 12:15 | 65,900 | 1,866 | 16 | 2,844 | 2,580 |
| 1/3/2001 | 11:45 | 18,500 | 524 | 6 | 299 | 272 |
| 1/24/2001 | 11:15 | 17,600 | 498 | 3 | 142 | 129 |
| 2/6/2001 | 11:30 | 51,400 | 1,455 | 3 | 416 | 377 |

Table 1. Summary of measured suspended sediment concentration (SSC), flow, and loads at Conowingo: 1996-2014 (continued).

| *Sample Date* | *Sample Time* | *Instantaneous Flow (cfs)* | *Instantaneous Flow (cms)* | *Measured SSC (mg/L)* | *Estimated Sediment Load (tons/day)* | *Estimated Sediment Load (MT/day)* |
|---|---|---|---|---|---|---|
| 2/21/2001 | 11:00 | 65,200 | 1,846 | 6 | 1,055 | 957 |
| 3/6/2001 | 10:15 | 65,500 | 1,855 | 5 | 883 | 801 |
| 3/17/2001 | 10:00 | 65,600 | 1,858 | 6 | 1,062 | 963 |
| 3/21/2001 | 11:00 | 59,800 | 1,693 | 8 | 1,290 | 1,170 |
| 3/23/2001 | 11:45 | 65,600 | 1,858 | 10 | 1,769 | 1,605 |
| 3/24/2001 | 9:15 | 79,400 | 2,248 | 12 | 2,570 | 2,331 |
| 3/26/2001 | 12:45 | 110,000 | 3,115 | 16 | 4,747 | 4,306 |
| 3/27/2001 | 12:15 | 94,300 | 2,670 | 12 | 3,052 | 2,769 |
| 3/28/2001 | 11:15 | 66,700 | 1,889 | 11 | 1,979 | 1,795 |
| 4/3/2001 | 9:45 | 108,000 | 3,058 | 21 | 6,118 | 5,549 |
| 4/11/2001 | 9:45 | 138,000 | 3,908 | 28 | 10,423 | 9,454 |
| 4/13/2001 | 10:00 | 121,000 | 3,426 | 41 | 13,382 | 12,137 |
| 4/18/2001 | 11:10 | 135,000 | 3,823 | 35 | 12,745 | 11,560 |
| 5/1/2001 | 11:30 | 9,960 | 282 | 11 | 296 | 268 |
| 5/16/2001 | 8:45 | 11,800 | 334 | 10 | 318 | 289 |
| 6/12/2001 | 9:00 | 11,300 | 320 | 5 | 152 | 138 |
| 6/27/2001 | 9:20 | 68,800 | 1,948 | 11 | 2,041 | 1,852 |
| 7/18/2001 | 8:30 | 7,610 | 215 | 12 | 246 | 223 |
| 8/7/2001 | 10:45 | 5,390 | 153 | 3 | 44 | 40 |
| 8/22/2001 | 9:50 | 5,390 | 153 | 4 | 58 | 53 |
| 9/10/2001 | 10:45 | 5,050 | 143 | 7 | 95 | 86 |
| 9/19/2001 | 11:20 | 4,630 | 131 | 9 | 112 | 102 |
| 10/4/2001 | 11:45 | 4,370 | 124 | 9 | 106 | 96 |

Table 1. Summary of measured suspended sediment concentration (SSC), flow, and loads at Conowingo: 1996-2014 (continued).

| *Sample Date* | *Sample Time* | *Instantaneous Flow (cfs)* | *Instantaneous Flow (cms)* | *Measured SSC (mg/L)* | *Estimated Sediment Load (tons/day)* | *Estimated Sediment Load (MT/day)* |
|---|---|---|---|---|---|---|
| 11/7/2001 | 11:15 | 4,370 | 124 | 7 | 83 | 75 |
| 11/20/2001 | 9:20 | 4,410 | 125 | 6 | 71 | 65 |
| 12/11/2001 | 9:45 | 23,300 | 660 | 9 | 566 | 513 |
| 12/18/2001 | 9:40 | 21,800 | 617 | 12 | 706 | 640 |
| 1/10/2002 | 11:00 | 4,720 | 134 | 4 | 51 | 46 |
| 1/24/2002 | 10:00 | 24,100 | 682 | 7 | 455 | 413 |
| 2/7/2002 | 11:45 | 63,800 | 1,807 | 5 | 860 | 780 |
| 2/14/2002 | 11:00 | 63,500 | 1,798 | 12 | 2,055 | 1,864 |
| 2/20/2002 | 9:20 | 57,900 | 1,640 | 9 | 1,406 | 1,275 |
| 3/8/2002 | 12:00 | 23,600 | 668 | 4 | 255 | 231 |
| 3/22/2002 | 9:00 | 46,400 | 1,314 | 10 | 1,252 | 1,135 |
| 3/28/2002 | 10:45 | 66,600 | 1,886 | 10 | 1,796 | 1,629 |
| 3/29/2002 | 10:30 | 156,000 | 4,417 | 22 | 9,257 | 8,397 |
| 4/3/2002 | 11:00 | 65,900 | 1,866 | 19 | 3,377 | 3,063 |
| 4/19/2002 | 10:10 | 65,200 | 1,846 | 11 | 1,935 | 1,755 |
| 5/2/2002 | 9:45 | 71,900 | 2,036 | 12 | 2,327 | 2,111 |
| 5/9/2002 | 10:45 | 56,000 | 1,586 | 6 | 906 | 822 |
| 5/16/2002 | 11:45 | 197,000 | 5,578 | 51 | 27,100 | 24,581 |
| 6/4/2002 | 10:00 | 23,800 | 674 | 5 | 321 | 291 |
| 6/10/2002 | 11:15 | 87,300 | 2,472 | 14 | 3,297 | 2,990 |
| 6/13/2002 | 10:10 | 66,100 | 1,872 | 12 | 2,140 | 1,941 |
| 7/11/2002 | 11:00 | 9,530 | 270 | 8 | 206 | 187 |
| 7/25/2002 | 10:00 | 5,870 | 166 | 7 | 111 | 101 |

Table 1. Summary of measured suspended sediment concentration (SSC), flow, and loads at Conowingo: 1996-2014 (continued).

| *Sample Date* | *Sample Time* | *Instantaneous Flow (cfs)* | *Instantaneous Flow (cms)* | *Measured SSC (mg/L)* | *Estimated Sediment Load (tons/day)* | *Estimated Sediment Load (MT/day)* |
|---|---|---|---|---|---|---|
| 8/2/2002 | 10:30 | 5,780 | 164 | 6 | 94 | 85 |
| 9/4/2002 | 9:45 | 4,080 | 116 | 6 | 66 | 60 |
| 9/18/2002 | 10:15 | 2,750 | 78 | 4 | 30 | 27 |
| 10/3/2002 | 9:00 | 17,600 | 498 | 6 | 285 | 258 |
| 11/8/2002 | 11:00 | 45,100 | 1,277 | 5 | 608 | 552 |
| 12/10/2002 | 10:00 | 45,600 | 1,291 | 1 | 123 | 112 |
| 12/16/2002 | 11:30 | 98,000 | 2,775 | 8 | 2,115 | 1,918 |
| 1/3/2003 | 11:15 | 104,000 | 2,945 | 11 | 3,086 | 2,799 |
| 1/9/2003 | 10:45 | 56,000 | 1,586 | 9 | 1,359 | 1,233 |
| 2/4/2003 | 12:00 | 24,100 | 682 | 1 | 65 | 59 |
| 2/25/2003 | 9:45 | 75,100 | 2,127 | 13 | 2,633 | 2,389 |
| 3/5/2003 | 10:00 | 73,500 | 2,081 | 6 | 1,190 | 1,079 |
| 3/17/2003 | 12:00 | 71,900 | 2,036 | 24 | 4,655 | 4,222 |
| 3/20/2003 | 12:00 | 254,000 | 7,192 | 54 | 36,997 | 33,557 |
| 4/2/2003 | 10:15 | 81,300 | 2,302 | 14 | 3,070 | 2,785 |
| 5/7/2003 | 12:00 | 63,300 | 1,792 | 7 | 1,195 | 1,084 |
| 6/4/2003 | 9:00 | 147,000 | 4,163 | 22 | 8,723 | 7,912 |
| 6/20/2003 | 9:30 | 24,600 | 697 | 8 | 531 | 481 |
| 7/1/2003 | 11:00 | 46,200 | 1,308 | 7 | 872 | 791 |
| 8/6/2003 | 8:45 | 59,100 | 1,674 | 14 | 2,232 | 2,024 |
| 9/4/2003 | 8:30 | 33,900 | 960 | 11 | 1,006 | 912 |
| 9/10/2003 | 8:00 | 48,200 | 1,365 | 14 | 1,820 | 1,651 |
| 9/24/2003 | 10:30 | 136,000 | 3,851 | 29 | 10,638 | 9,649 |

Table 1. Summary of measured suspended sediment concentration (SSC), flow, and loads at Conowingo: 1996-2014 (continued).

| *Sample Date* | *Sample Time* | *Instantaneous Flow (cfs)* | *Instantaneous Flow (cms)* | *Measured SSC (mg/L)* | *Estimated Sediment Load (tons/day)* | *Estimated Sediment Load (MT/day)* |
|---|---|---|---|---|---|---|
| 10/14/2003 | 9:00 | 45,200 | 1,280 | 7 | 853 | 774 |
| 10/30/2003 | 10:00 | 95,700 | 2,710 | 16 | 4,130 | 3,746 |
| 11/13/2003 | 9:30 | 79,600 | 2,254 | 8 | 1,718 | 1,558 |
| 11/21/2003 | 9:45 | 82,700 | 2,342 | 16 | 3,569 | 3,237 |
| 12/3/2003 | 10:30 | 79,800 | 2,260 | 17 | 3,659 | 3,319 |
| 12/17/2003 | 9:45 | 79,800 | 2,260 | 31 | 6,673 | 6,052 |
| 1/22/2004 | 10:30 | 51,400 | 1,455 | 2 | 277 | 252 |
| 2/10/2004 | 10:30 | 87,200 | 2,469 | 16 | 3,763 | 3,413 |
| 3/5/2004 | 10:00 | 82,500 | 2,336 | 8 | 1,780 | 1,615 |
| 3/16/2004 | 9:30 | 87,200 | 2,469 | 11 | 2,587 | 2,347 |
| 4/6/2004 | 9:00 | 90,500 | 2,563 | 18 | 4,394 | 3,985 |
| 4/15/2004 | 8:45 | 88,600 | 2,509 | 15 | 3,585 | 3,251 |
| 5/5/2004 | 10:30 | 87,200 | 2,469 | 16 | 3,763 | 3,413 |
| 6/16/2004 | 8:45 | 13,900 | 394 | 19 | 712 | 646 |
| 7/6/2004 | 10:15 | 5,450 | 154 | 6 | 88 | 80 |
| 8/5/2004 | 9:00 | 54,400 | 1,540 | 17 | 2,495 | 2,263 |
| 9/20/2004 | 9:00 | 597,000 | 16,905 | 3,680 | 5,925,969 | 5,375,029 |
| 9/22/2004 | 9:15 | 205,000 | 5,805 | 110 | 60,825 | 55,170 |
| 10/13/2004 | 8:45 | 66,700 | 1,889 | 7 | 1,259 | 1,142 |
| 11/16/2004 | 10:00 | 33,100 | 937 | 3 | 268 | 243 |
| 11/29/2004 | 10:15 | 103,000 | 2,917 | 9 | 2,500 | 2,268 |
| 12/14/2004 | 10:45 | 212,000 | 6,003 | 23 | 13,152 | 11,930 |
| 1/10/2005 | 11:30 | 180,000 | 5,097 | 30 | 14,566 | 13,212 |

Table 1. Summary of measured suspended sediment concentration (SSC), flow, and loads at Conowingo: 1996-2014 (continued).

| *Sample Date* | *Sample Time* | *Instantaneous Flow (cfs)* | *Instantaneous Flow (cms)* | *Measured SSC (mg/L)* | *Estimated Sediment Load (tons/day)* | *Estimated Sediment Load (MT/day)* |
|---|---|---|---|---|---|---|
| 1/26/2005 | 11:00 | 55,100 | 1,560 | 9 | 1,338 | 1,213 |
| 2/16/2005 | 10:30 | 78,400 | 2,220 | 17 | 3,595 | 3,261 |
| 3/7/2005 | 11:30 | 26,200 | 742 | 3 | 212 | 192 |
| 3/29/2005 | 11:00 | 211,000 | 5,975 | 22 | 12,521 | 11,357 |
| 3/31/2005 | 10:00 | 305,000 | 8,637 | 173 | 142,326 | 129,094 |
| 4/21/2005 | 9:15 | 84,800 | 2,401 | 10 | 2,287 | 2,075 |
| 5/12/2005 | 9:45 | 25,400 | 719 | 4 | 274 | 249 |
| 6/2/2005 | 10:15 | 6,220 | 176 | 14 | 235 | 213 |
| 7/20/2005 | 9:45 | 5,930 | 168 | 12 | 192 | 174 |
| 8/16/2005 | 8:00 | 4,780 | 135 | 4 | 52 | 47 |
| 9/14/2005 | 8:15 | 5,880 | 167 | 6 | 95 | 86 |
| 10/27/2005 | 13:00 | 87,200 | 2,469 | 14 | 3,293 | 2,987 |
| 11/9/2005 | 12:15 | 19,600 | 555 | 8 | 423 | 384 |
| 12/2/2005 | 9:00 | 265,000 | 7,504 | 115 | 82,202 | 74,559 |
| 12/14/2005 | 15:00 | 33,700 | 954 | 5 | 455 | 412 |
| 1/4/2006 | 10:30 | 80,200 | 2,271 | 7 | 1,514 | 1,374 |
| 1/10/2006 | 10:45 | 80,500 | 2,280 | 7 | 1,520 | 1,379 |
| 2/6/2006 | 12:15 | 113,000 | 3,200 | 20 | 6,096 | 5,529 |
| 3/7/2006 | 14:45 | 4,870 | 138 | 2 | 26 | 24 |
| 4/19/2006 | 9:30 | 48,700 | 1,379 | 6 | 788 | 715 |
| 5/2/2006 | 10:00 | 66,900 | 1,894 | 8 | 1,444 | 1,309 |
| 6/6/2006 | 10:15 | 82,700 | 2,342 | 7 | 1,561 | 1,416 |
| 6/30/2006 | 8:15 | 318,000 | 9,005 | 342 | 293,353 | 266,080 |

Table 1. Summary of measured suspended sediment concentration (SSC), flow, and loads at Conowingo: 1996-2014 (continued).

| *Sample Date* | *Sample Time* | *Instantaneous Flow (cfs)* | *Instantaneous Flow (cms)* | *Measured SSC (mg/L)* | *Estimated Sediment Load (tons/day)* | *Estimated Sediment Load (MT/day)* |
|---|---|---|---|---|---|---|
| 7/3/2006 | 10:15 | 142,000 | 4,021 | 163 | 62,433 | 56,628 |
| 7/13/2006 | 9:00 | 7,300 | 207 | 22 | 433 | 393 |
| 8/8/2006 | 9:45 | 6,510 | 184 | 11 | 193 | 175 |
| 9/7/2006 | 9:15 | 70,700 | 2,002 | 24 | 4,577 | 4,151 |
| 10/4/2006 | 9:00 | 4,460 | 126 | 8 | 96 | 87 |
| 10/24/2006 | 13:15 | 98,100 | 2,778 | 16 | 4,234 | 3,840 |
| 11/9/2006 | 14:15 | 58,000 | 1,642 | 8 | 1,252 | 1,135 |
| 11/17/2006 | 13:45 | 154,000 | 4,361 | 68 | 28,247 | 25,621 |
| 11/21/2006 | 14:45 | 131,000 | 3,710 | 156 | 55,123 | 49,998 |
| 12/6/2006 | 14:00 | 14,200 | 402 | 9 | 345 | 313 |
| 1/10/2007 | 9:45 | 152,000 | 4,304 | 18 | 7,380 | 6,694 |
| 2/13/2007 | 10:00 | 11,100 | 314 | 2 | 60 | 54 |
| 3/5/2007 | 14:00 | 82,700 | 2,342 | 38 | 8,477 | 7,689 |
| 3/17/2007 | 8:15 | 272,000 | 7,702 | 64 | 46,955 | 42,590 |
| 3/19/2007 | 13:45 | 142,000 | 4,021 | 156 | 59,752 | 54,197 |
| 3/26/2007 | 13:45 | 181,000 | 5,125 | 60 | 29,293 | 26,570 |
| 4/10/2007 | 12:45 | 26,600 | 753 | 11 | 789 | 716 |
| 4/16/2007 | 10:15 | 99,800 | 2,826 | 47 | 12,652 | 11,476 |
| 5/16/2007 | 11:00 | 65,900 | 1,866 | 8 | 1,422 | 1,290 |
| 6/5/2007 | 8:00 | 5,830 | 165 | 10 | 157 | 143 |
| 7/6/2007 | 9:45 | 5,830 | 165 | 9 | 142 | 128 |
| 8/1/2007 | 9:00 | 5,930 | 168 | 8 | 128 | 116 |
| 9/4/2007 | 9:15 | 4,600 | 130 | 21 | 261 | 236 |

Table 1. Summary of measured suspended sediment concentration (SSC), flow, and loads at Conowingo: 1996-2014 (continued).

| *Sample Date* | *Sample Time* | *Instantaneous Flow (cfs)* | *Instantaneous Flow (cms)* | *Measured SSC (mg/L)* | *Estimated Sediment Load (tons/day)* | *Estimated Sediment Load (MT/day)* |
|---|---|---|---|---|---|---|
| 10/4/2007 | 10:30 | 3,730 | 106 | 9 | 91 | 82 |
| 11/5/2007 | 12:15 | 19,400 | 549 | 9 | 471 | 427 |
| 12/5/2007 | 10:15 | 80,000 | 2,265 | 10 | 2,158 | 1,957 |
| 1/4/2008 | 11:45 | 52,300 | 1,481 | 11 | 1,552 | 1,408 |
| 1/14/2008 | 10:45 | 142,000 | 4,021 | 24 | 9,193 | 8,338 |
| 1/16/2008 | 10:30 | 80,500 | 2,280 | 14 | 3,040 | 2,757 |
| 2/6/2008 | 13:00 | 80,200 | 2,271 | 20 | 4,327 | 3,924 |
| 2/9/2008 | 10:45 | 243,000 | 6,881 | 86 | 56,369 | 51,129 |
| 2/21/2008 | 10:00 | 124,000 | 3,511 | 11 | 3,679 | 3,337 |
| 3/6/2008 | 10:45 | 337,000 | 9,543 | 326 | 296,336 | 268,786 |
| 3/9/2008 | 10:00 | 223,000 | 6,315 | 114 | 68,572 | 62,197 |
| 3/13/2008 | 13:30 | 142,000 | 4,021 | 52 | 19,917 | 18,066 |
| 3/19/2008 | 9:45 | 130,000 | 3,681 | 13 | 4,559 | 4,135 |
| 3/24/2008 | 11:00 | 129,000 | 3,653 | 78 | 27,141 | 24,617 |
| 4/3/2008 | 10:15 | 78,600 | 2,226 | 14 | 2,968 | 2,692 |
| 5/6/2008 | 8:30 | 80,000 | 2,265 | 9 | 1,942 | 1,762 |
| 6/2/2008 | 9:00 | 5,930 | 168 | 6 | 96 | 87 |
| 7/1/2008 | 8:45 | 5,600 | 159 | 7 | 106 | 96 |
| 8/5/2008 | 10:30 | 5,600 | 159 | 5 | 76 | 69 |
| 9/10/2008 | 10:45 | 5,650 | 160 | 11 | 168 | 152 |
| 10/8/2008 | 9:45 | 5,250 | 149 | 6 | 85 | 77 |
| 11/13/2008 | 10:45 | 13,900 | 394 | 5 | 187 | 170 |
| 12/2/2008 | 11:00 | 37,800 | 1,070 | 5 | 510 | 462 |

Table 1. Summary of measured suspended sediment concentration (SSC), flow, and loads at Conowingo: 1996-2014 (continued).

| *Sample Date* | *Sample Time* | *Instantaneous Flow (cfs)* | *Instantaneous Flow (cms)* | *Measured SSC (mg/L)* | *Estimated Sediment Load (tons/day)* | *Estimated Sediment Load (MT/day)* |
|---|---|---|---|---|---|---|
| 12/13/2008 | 10:00 | 80,000 | 2,265 | 13 | 2,805 | 2,544 |
| 1/8/2009 | 10:15 | 76,800 | 2,175 | 5 | 1,036 | 939 |
| 1/22/2009 | 10:00 | 37,100 | 1,051 | 3 | 300 | 272 |
| 2/5/2009 | 8:45 | 74,200 | 2,101 | 3 | 600 | 545 |
| 2/17/2009 | 10:00 | 81,500 | 2,308 | 16 | 3,517 | 3,190 |
| 3/4/2009 | 9:00 | 76,900 | 2,178 | 5 | 1,037 | 941 |
| 3/12/2009 | 9:30 | 143,000 | 4,049 | 14 | 5,400 | 4,898 |
| 3/18/2009 | 10:15 | 77,900 | 2,206 | 17 | 3,572 | 3,240 |
| 4/6/2009 | 8:00 | 77,500 | 2,195 | 10 | 2,090 | 1,896 |
| 4/9/2009 | 8:00 | 76,400 | 2,163 | 10 | 2,061 | 1,869 |
| 5/15/2009 | 8:15 | 44,200 | 1,252 | 7 | 835 | 757 |
| 6/3/2009 | 8:00 | 6,310 | 179 | 14 | 238 | 216 |
| 7/8/2009 | 8:15 | 5,790 | 164 | 6 | 94 | 85 |
| 8/5/2009 | 7:30 | 12,700 | 360 | 8 | 274 | 249 |
| 10/7/2009 | 8:15 | 26,500 | 750 | 6 | 429 | 389 |
| 10/27/2009 | 10:30 | 85,600 | 2,424 | 16 | 3,694 | 3,351 |
| 11/4/2009 | 10:30 | 62,300 | 1,764 | 11 | 1,848 | 1,677 |
| 12/2/2009 | 11:15 | 3,280 | 93 | 9 | 80 | 72 |
| 12/28/2009 | 9:45 | 79,800 | 2,260 | 7 | 1,507 | 1,367 |
| 1/7/2010 | 11:00 | 37,700 | 1,068 | 8 | 814 | 738 |
| 1/22/2010 | 9:45 | 78,100 | 2,212 | 8 | 1,685 | 1,529 |
| 1/26/2010 | 13:45 | 212,000 | 6,003 | 28 | 16,011 | 14,523 |
| 1/27/2010 | 15:45 | 310,000 | 8,778 | 263 | 219,915 | 199,469 |

Table 1. Summary of measured suspended sediment concentration (SSC), flow, and loads at Conowingo: 1996-2014 (continued).

| *Sample Date* | *Sample Time* | *Instantaneous Flow (cfs)* | *Instantaneous Flow (cms)* | *Measured SSC (mg/L)* | *Estimated Sediment Load (tons/day)* | *Estimated Sediment Load (MT/day)* |
|---|---|---|---|---|---|---|
| 2/4/2010 | 12:45 | 29,600 | 838 | 28 | 2,236 | 2,028 |
| 3/3/2010 | 10:45 | 32,900 | 932 | 12 | 1,065 | 966 |
| 3/15/2010 | 8:45 | 247,000 | 6,994 | 96 | 63,960 | 58,013 |
| 3/17/2010 | 8:30 | 202,000 | 5,720 | 91 | 49,583 | 44,973 |
| 4/7/2010 | 8:15 | 65,200 | 1,846 | 13 | 2,286 | 2,074 |
| 5/5/2010 | 8:15 | 9,490 | 269 | 6 | 154 | 139 |
| 6/3/2010 | 7:30 | 7,080 | 200 | 6 | 115 | 104 |
| 7/6/2010 | 8:15 | 5,930 | 168 | 7 | 112 | 102 |
| 7/15/2010 | 7:45 | 15,000 | 425 | 9 | 364 | 330 |
| 8/3/2010 | 8:15 | 5,930 | 168 | 6 | 96 | 87 |
| 9/1/2010 | 8:00 | 6,020 | 170 | 6 | 97 | 88 |
| 10/3/2010 | 9:15 | 83,300 | 2,359 | 20 | 4,494 | 4,076 |
| 10/6/2010 | 8:15 | 44,600 | 1,263 | 20 | 2,406 | 2,182 |
| 11/3/2010 | 9:00 | 6,310 | 179 | 7 | 119 | 108 |
| 12/3/2010 | 10:30 | 276,000 | 7,815 | 141 | 104,970 | 95,211 |
| 12/7/2010 | 10:00 | 108,000 | 3,058 | 41 | 11,944 | 10,833 |
| 1/6/2011 | 9:45 | 33,400 | 946 | 2 | 180 | 163 |
| 1/19/2011 | 10:30 | 7,350 | 208 | 6 | 119 | 108 |
| 2/3/2011 | 12:30 | 8,560 | 242 | 4 | 92 | 84 |
| 2/17/2011 | 12:45 | 4,290 | 121 | 5 | 58 | 52 |
| 3/2/2011 | 10:30 | 82,300 | 2,330 | 12 | 2,664 | 2,416 |
| 3/8/2011 | 10:00 | 274,000 | 7,759 | 129 | 95,341 | 86,477 |
| 3/12/2011 | 12:15 | 453,000 | 12,828 | 937 | 1,144,920 | 1,038,476 |

Table 1. Summary of measured suspended sediment concentration (SSC), flow, and loads at Conowingo: 1996-2014 (continued).

| *Sample Date* | *Sample Time* | *Instantaneous Flow (cfs)* | *Instantaneous Flow (cms)* | *Measured SSC (mg/L)* | *Estimated Sediment Load (tons/day)* | *Estimated Sediment Load (MT/day)* |
|---|---|---|---|---|---|---|
| 3/16/2011 | 8:30 | 194,000 | 5,493 | 63 | 32,967 | 29,902 |
| 4/6/2011 | 11:00 | 78,600 | 2,226 | 11 | 2,332 | 2,115 |
| 4/18/2011 | 9:45 | 255,000 | 7,221 | 206 | 141,692 | 128,519 |
| 4/30/2011 | 11:45 | 316,000 | 8,948 | 184 | 156,835 | 142,254 |
| 5/3/2011 | 8:00 | 140,000 | 3,964 | 52 | 19,637 | 17,811 |
| 5/20/2011 | 8:15 | 77,500 | 2,195 | 20 | 4,181 | 3,792 |
| 6/2/2011 | 8:15 | 78,800 | 2,231 | 19 | 4,038 | 3,663 |
| 7/6/2011 | 7:45 | 5,970 | 169 | 10 | 161 | 146 |
| 8/3/2011 | 7:30 | 6,070 | 172 | 7 | 115 | 104 |
| 8/30/2011 | 9:45 | 82,500 | 2,336 | 17 | 3,783 | 3,431 |
| 8/31/2011 | 8:30 | 81,700 | 2,313 | 17 | 3,746 | 3,398 |
| 9/8/2011 | 11:00 | 617,000 | 17,471 | 2,980 | 4,959,509 | 4,498,421 |
| 9/10/2011 | 9:30 | 481,000 | 13,620 | 741 | 961,392 | 872,011 |
| 9/11/2011 | 9:30 | 380,000 | 10,760 | 1,150 | 1,178,742 | 1,069,154 |
| 9/12/2011 | 9:00 | 232,000 | 6,570 | 332 | 207,761 | 188,445 |
| 9/14/2011 | 8:15 | 114,000 | 3,228 | 64 | 19,680 | 17,850 |
| 9/21/2011 | 8:45 | 37,900 | 1,073 | 15 | 1,533 | 1,391 |
| 9/29/2011 | 10:45 | 199,000 | 5,635 | 48 | 25,765 | 23,370 |
| 10/4/2011 | 8:00 | 140,000 | 3,964 | 41 | 15,483 | 14,043 |
| 11/2/2011 | 9:00 | 80,700 | 2,285 | 8 | 1,741 | 1,580 |
| 12/6/2011 | 9:15 | 79,400 | 2,248 | 9 | 1,928 | 1,748 |
| 12/9/2011 | 10:15 | 138,000 | 3,908 | 22 | 8,189 | 7,428 |
| 1/5/2012 | 9:15 | 79,800 | 2,260 | 6 | 1,291 | 1,171 |

Table 1. Summary of measured suspended sediment concentration (SSC), flow, and loads at Conowingo: 1996-2014 (continued).

| *Sample Date* | *Sample Time* | *Instantaneous Flow (cfs)* | *Instantaneous Flow (cms)* | *Measured SSC (mg/L)* | *Estimated Sediment Load (tons/day)* | *Estimated Sediment Load (MT/day)* |
|---|---|---|---|---|---|---|
| 1/18/2012 | 12:00 | 60,000 | 1,699 | 9 | 1,457 | 1,321 |
| 2/1/2012 | 8:45 | 81,100 | 2,296 | 18 | 3,938 | 3,572 |
| 2/22/2012 | 8:45 | 79,800 | 2,260 | 5 | 1,076 | 976 |
| 3/7/2012 | 9:15 | 80,300 | 2,274 | 7 | 1,516 | 1,375 |
| 3/21/2012 | 8:15 | 79,200 | 2,243 | 7 | 1,495 | 1,356 |
| 4/3/2012 | 10:45 | 14,200 | 402 | 12 | 460 | 417 |
| 5/9/2012 | 8:45 | 74,000 | 2,095 | 10 | 1,996 | 1,810 |
| 5/18/2012 | 8:45 | 81,100 | 2,296 | 19 | 4,156 | 3,770 |
| 6/5/2012 | 8:00 | 58,600 | 1,659 | 21 | 3,319 | 3,011 |
| 7/2/2012 | 7:30 | 5,740 | 163 | 11 | 170 | 154 |
| 8/7/2012 | 8:15 | 6,070 | 172 | 5 | 82 | 74 |
| 9/6/2012 | 7:15 | 6,020 | 170 | 7 | 114 | 103 |
| 9/20/2012 | 9:00 | 3,920 | 111 | 9 | 95 | 86 |
| 10/2/2012 | 9:15 | 26,400 | 748 | 12 | 855 | 775 |
| 10/31/2012 | 12:15 | 94,900 | 2,687 | 43 | 11,007 | 9,984 |
| 11/1/2012 | 9:45 | 109,000 | 3,087 | 40 | 11,760 | 10,667 |
| 11/2/2012 | 8:30 | 95,500 | 2,704 | 29 | 7,470 | 6,776 |
| 12/6/2012 | 10:45 | 21,700 | 614 | 6 | 351 | 319 |
| 1/3/2013 | 10:30 | 78,800 | 2,231 | 5 | 1,063 | 964 |
| 1/15/2013 | 10:45 | 79,000 | 2,237 | 4 | 852 | 773 |
| 1/17/2013 | 14:30 | 112,000 | 3,171 | 19 | 5,740 | 5,206 |
| 2/1/2013 | 16:00 | 181,000 | 5,125 | 74 | 36,128 | 32,769 |
| 2/5/2013 | 10:15 | 83,100 | 2,353 | 50 | 11,207 | 10,166 |

Table 1. Summary of measured suspended sediment concentration (SSC), flow, and loads at Conowingo: 1996-2014 (continued).

| *Sample Date* | *Sample Time* | *Instantaneous Flow (cfs)* | *Instantaneous Flow (cms)* | *Measured SSC (mg/L)* | *Estimated Sediment Load (tons/day)* | *Estimated Sediment Load (MT/day)* |
|---|---|---|---|---|---|---|
| 2/20/2013 | 10:00 | 62,200 | 1,761 | 6 | 1,007 | 913 |
| 3/5/2013 | 11:30 | 33,200 | 940 | 10 | 896 | 812 |
| 3/14/2013 | 14:45 | 71,600 | 2,027 | 12 | 2,318 | 2,102 |
| 3/19/2013 | 9:45 | 46,200 | 1,308 | 20 | 2,492 | 2,261 |
| 4/2/2013 | 12:00 | 66,200 | 1,875 | 9 | 1,607 | 1,458 |
| 4/15/2013 | 11:00 | 95,300 | 2,699 | 13 | 3,342 | 3,031 |
| 4/17/2013 | 10:00 | 78,800 | 2,231 | 15 | 3,188 | 2,892 |
| 5/1/2013 | 11:15 | 39,900 | 1,130 | 6 | 646 | 586 |
| 5/13/2013 | 10:15 | 78,600 | 2,226 | 7 | 1,484 | 1,346 |
| 5/15/2013 | 10:30 | 50,800 | 1,438 | 7 | 959 | 870 |
| 6/6/2013 | 11:00 | 6,310 | 179 | 6 | 102 | 93 |
| 7/2/2013 | 10:00 | 78,800 | 2,231 | 16 | 3,401 | 3,085 |
| 8/1/2013 | 9:15 | 5,880 | 167 | 9 | 143 | 129 |
| 9/5/2013 | 8:45 | 5,550 | 157 | 5 | 75 | 68 |
| 10/23/2013 | 9:30 | 15,900 | 450 | 7 | 300 | 272 |
| 11/6/2013 | 10:15 | 26,700 | 756 | 7 | 504 | 457 |
| 12/2/2013 | 10:00 | 79,200 | 2,243 | 5 | 1,068 | 969 |
| 12/4/2013 | 10:15 | 44,700 | 1,266 | 6 | 723 | 656 |
| 12/12/2013 | 14:00 | 71,300 | 2,019 | 7 | 1,346 | 1,221 |
| 1/6/2014 | 11:45 | 48,000 | 1,359 | 12 | 1,554 | 1,409 |
| 1/13/2014 | 9:45 | 65,300 | 1,849 | 17 | 2,994 | 2,716 |
| 1/23/2014 | 11:15 | 20,500 | 580 | 13 | 719 | 652 |
| 2/6/2014 | 12:15 | 71,600 | 2,027 | 4 | 773 | 701 |

Table 1. Summary of measured suspended sediment concentration (SSC), flow, and loads at Conowingo: 1996-2014 (continued).

| *Sample Date* | *Sample Time* | *Instantaneous Flow (cfs)* | *Instantaneous Flow (cms)* | *Measured SSC (mg/L)* | *Estimated Sediment Load (tons/day)* | *Estimated Sediment Load (MT/day)* |
|---|---|---|---|---|---|---|
| 2/19/2014 | 11:45 | 4,690 | 133 | 2 | 25 | 23 |
| 2/25/2014 | 8:15 | 79,000 | 2,237 | 4 | 852 | 773 |
| 3/5/2014 | 14:30 | 49,200 | 1,393 | 2 | 265 | 241 |
| 3/19/2014 | 9:15 | 79,000 | 2,237 | 19 | 4,049 | 3,672 |
| 4/1/2014 | 9:15 | 167,000 | 4,729 | 88 | 39,640 | 35,955 |
| 4/2/2014 | 11:00 | 139,000 | 3,936 | 52 | 19,496 | 17,684 |
| 4/17/2014 | 11:00 | 140,000 | 3,964 | 19 | 7,175 | 6,508 |
| 5/1/2014 | 10:00 | 85,000 | 2,407 | 39 | 8,942 | 8,110 |
| 5/7/2014 | 12:30 | 78,400 | 2,220 | 14 | 2,961 | 2,685 |
| 5/18/2014 | 11:15 | 179,000 | 5,069 | 70 | 33,798 | 30,656 |
| 5/19/2014 | 8:30 | 168,000 | 4,757 | 65 | 29,455 | 26,717 |
| 5/20/2014 | 9:00 | 158,000 | 4,474 | 29 | 12,359 | 11,210 |
| 5/21/2014 | 8:45 | 565 | 16 | 46 | 70 | 64 |
| 6/3/2014 | 10:45 | 59,900 | 1,696 | 8 | 1,293 | 1,172 |
| 7/1/2014 | 9:00 | 6,070 | 172 | 9 | 147 | 134 |
| 8/5/2014 | 12:15 | 37,000 | 1,048 | 5 | 499 | 453 |
| 9/3/2014 | 7:15 | 5,830 | 165 | 5 | 79 | 71 |
| 10/9/2014 | 10:30 | 3,800 | 108 | 6 | 61 | 56 |
| 11/4/2014 | 8:15 | 25,600 | 725 | 7 | 483 | 438 |

Table 2. Characteristics of Conowingo Pond bathymetric surveys: 1996-2015.

| *Survey* | *Conducted by* | *Number of Reported Soundings* | *Number of Transects* | *Upstream Limit* | *Downstream Limit* | *Equivalent Data Density* | *Vertical Error (±)* | *Interpolation RMS Error (±)* | *Notes* |
|---|---|---|---|---|---|---|---|---|---|
| 1996 | USGS | 4,138 | 23 cross-channel | 6,900 feet (2,100 meters) downstream of Muddy Creek | Boat barrier above Dam | 1.86 acres/point (7,520 $m^2$/point) | 1 foot (25 cm) | 1.13 feet (34 cm) | Frequency of raw soundings not reported. |
| 2008 | USGS | 513,368 | 26 cross-channel | Muddy Creek | Boat barrier above Dam | 0.15 acres/point (606 $m^2$/point) as averaged to a 1 Hz reporting frequency | 0.5 feet (15 cm) | 0.29 feet (7.4 cm) | Soundings at frequency of survey instrumentation (~10 Hz). Comparable to an equivalent of 51,337 points when averaged to a reporting frequency of one per second (1 Hz). |
| 2011 | Gomez and Sullivan | 89,389 | 59 cross-channel and 5 longitudinal | Muddy Creek | Conowingo Dam | 0.09 acres/point (360 $m^2$/point) | 0.2 feet (6 cm) | 0.39 feet (12 cm) | Soundings sampled at a frequency of 10-30 Hz using an ADCP. Averaged by instrument to a frequency of one per second (1 Hz). |
| 2013 | | 84,015 | | | | | | 0.35 feet (11 cm) | |
| 2014 | | 83,032 | | | | | | 0.43 feet (13 cm) | |
| 2015 | | 89,409 | | | | | | 0.33 feet (10 cm) | |

Notes: ADCP = Acoustic Doppler Current Profiler; Hz = Hertz (number of measurements per second); Surveyed area of Conowingo Pond (Muddy Creek to Conowingo Dam) was approximately 7,520 acres (31,120,120 $m^2$); Equivalent data density calculated as surface area of surveyed portion of Pond divided by the number of survey points; Interpolation RMS Error = root mean square error for interpolation of raw soundings.

Table 3. Conowingo Pond average bed elevation differences between bathymetric surveys.

| *Year End* | *Year Start* | *Type* | *Basis* | *Average Bed Elevation Difference [unweighted]* | | *Average Bed Elevation Difference [area weighted]* | | *Inferred Average Net Sedimentation Rate* | |
|---|---|---|---|---|---|---|---|---|---|
| | | | | *cm* | *feet* | *cm* | *feet* | *cm/year* | *feet/year* |
| 2008 | 1996 | grid-snapped (normalized) | 2008 USGS norm minus 1996 USGS norm | 42.10 | 1.38 | 29.60 | 0.97 | +2.47 | +0.08 |
| 2011 | 2008 | grid-snapped (normalized) | 2011 USGS norm minus 2008 USGS norm | 2.83 | 0.09 | -0.49 | -0.02 | -0.16 | -0.01 |
| 2011 | 2008 | grid-snapped (normalized) | 2011 GSE norm minus 2008 USGS norm | -21.79 | -0.71 | -17.89 | -0.59 | -5.96 | -0.20 |
| 2011 | 2011 | grid-snapped (normalized) | 2011 GSE norm minus 2011 USGS norm | 24.62 | 0.81 | 17.40 | 0.57 | | |
| 2013 | 2008 | grid-snapped (normalized) | 2011 GSE norm minus 2008 USGS norm | 4.37 | 0.14 | 1.50 | 0.05 | +0.30 | +0.01 |
| 2013 | 2011 | grid-snapped (normalized) | 2013 GSE norm minus 2011 GSE norm | 1.53 | 0.05 | 1.99 | 0.07 | +1.00 | +0.04 |
| 2014 | 2008 | grid-snapped (normalized) | 2014 GSE norm minus 2008 USGS norm | 2.91 | 0.10 | 0.53 | 0.02 | +0.09 | +0.001 |
| 2014 | 2011 | grid-snapped (normalized) | 2014 GSE norm minus 2011 GSE norm | 0.08 | 0.003 | 1.03 | 0.03 | +0.34 | +0.01 |

See notes and synopsis at end of table.

Table 3. Conowingo Pond average bed elevation differences between bathymetric surveys (continued).

| *Year End* | *Year Start* | *Type* | *Basis* | *Average Bed Elevation Difference [unweighted]* | | *Average Bed Elevation Difference [area weighted]* | | *Inferred Average Net Sedimentation Rate* | |
|---|---|---|---|---|---|---|---|---|---|
| | | | | *cm* | *feet* | *cm* | *feet* | *cm/year* | *feet/year* |
| 2014 | 2013 | grid-snapped (normalized) | 2014 GSE norm minus 2013 GSE norm | -1.45 | -0.05 | -0.96 | -0.03 | -0.96 | -0.03 |
| 2015 | 1996 | grid-snapped (normalized) | 2015 GSE norm minus 1996 USGS norm | 46.66 | 1.53 | 31.79 | 1.04 | +1.67 | +0.05 |
| 2015 | 2008 | grid-snapped (normalized) | 2015 GSE norm minus 2008 USGS norm | 4.55 | 0.15 | 2.20 | 0.07 | +0.31 | +0.01 |
| 2015 | 2008 | grid-snapped (normalized) | 2015 USGS norm minus 2008 USGS norm | 1.72 | 0.06 | 2.69 | 0.09 | +0.38 | +0.01 |
| 2015 | 2011 | grid-snapped (normalized) | 2015 GSE norm minus 2011 GSE norm | 0.18 | 0.006 | 0.70 | 0.02 | +0.18 | +0.01 |
| 2015 | 2013 | grid-snapped (normalized) | 2015 GSE norm minus 2013 GSE norm | 1.64 | 0.05 | 1.67 | 0.05 | +0.84 | +0.03 |
| 2015 | 2014 | grid-snapped (normalized) | 2015 GSE norm minus 2014 GSE norm | -19.82 | -0.65 | -16.21 | -0.53 | -16.21 | -0.53 |
| 2015 | 2015 | grid-snapped (normalized) | 2015 GSE norm minus 2015 USGS norm | 24.38 | 0.80 | 18.41 | 0.60 | | |

See notes and synopsis at end of table.

Table 3. Conowingo Pond average bed elevation differences between bathymetric surveys (continued).

| *Year End* | *Year Start* | *Type* | *Basis* | *Average Bed Elevation Difference [unweighted]* | | *Average Bed Elevation Difference [area weighted]* | | *Inferred Average Net Sedimentation Rate* | |
|---|---|---|---|---|---|---|---|---|---|
| | | | | *cm* | *feet* | *cm* | *feet* | *cm/year* | *feet/year* |
| 2008 | 1996 | raw | 2008 minus 1996 | 72.46 | 2.38 | 52.43 | 1.72 | +4.37 | +0.14 |
| 2011 | 1996 | raw | 2011 minus 2008 | 78.69 | 2.58 | 54.39 | 1.78 | +3.63 | +0.12 |
| 2011 | 2008 | raw | 2011 minus 2008 | 6.22 | 0.20 | 1.96 | 0.06 | +0.65 | +0.02 |
| 2013 | 2008 | raw | 2013 minus 2008 | 3.89 | 0.13 | 0.93 | 0.03 | +0.19 | +0.01 |
| 2013 | 2011 | raw | 2013 minus 2011 | -2.34 | -0.08 | -1.03 | -0.03 | -0.52 | -0.02 |
| 2014 | 2008 | raw | 2014 minus 2008 | 2.49 | 0.08 | 0.13 | 0.004 | +0.02 | +0.001 |
| 2014 | 2011 | raw | 2014 minus 2011 | -3.73 | -0.12 | -1.84 | -0.06 | -0.61 | -0.02 |
| 2014 | 2013 | raw | 2014 minus 2013 | -1.40 | -0.05 | -0.80 | -0.03 | -0.80 | -0.03 |
| 2015 | 1996 | raw | 2015 minus 1996 | 82.14 | 2.69 | 58.82 | 1.93 | +3.10 | +0.10 |

See notes and synopsis at end of table.

Table 3. Conowingo Pond average bed elevation differences between bathymetric surveys (continued).

| *Year End* | *Year Start* | *Type* | *Basis* | *Average Bed Elevation Difference [unweighted]* | | *Average Bed Elevation Difference [area weighted]* | | *Inferred Average Net Sedimentation Rate* | |
|---|---|---|---|---|---|---|---|---|---|
| | | | | *cm* | *feet* | *cm* | *feet* | *cm/year* | *feet/year* |
| 2015 | 2008 | raw | 2015 minus 2008 | 9.68 | 0.32 | 6.39 | 0.21 | +0.91 | +0.03 |
| 2015 | 2011 | raw | 2015 minus 2011 | 3.45 | 0.11 | 4.43 | 0.15 | +1.11 | +0.04 |
| 2015 | 2013 | raw | 2015 minus 2013 | 5.79 | 0.19 | 5.46 | 0.18 | +2.73 | +0.09 |
| 2015 | 2014 | raw | 2015 minus 2014 | 7.18 | 0.24 | 6.26 | 0.21 | +6.26 | +0.21 |

Notes: Spatially continuous representations of sediment bed elevations for each survey year were constructed from discrete measurements by geostatistical interpolation methods (Ordinary Kriging); Estimated root mean square (RMS) errors for interpolated surfaces ranged from 0.67 – 1.30 feet (20 – 40 cm); Unweighted average bed elevation differences represent an arithmetic average of values for individual model grid cells within the surveyed portion of the Pond, independent of the different surface areas associated with each cell; Weighted average bed elevation differences represent an arithmetic average of area-weighted values for individual model grid cells within the surveyed portion of the Pond; Inferred average net sedimentation rates based on area-weighted bed elevation differences between survey years.

Synopsis: Survey data were provided in grid-snapped ("normalized") and "raw" formats. Grid-snapped data were processed before interpolation to equalize numbers of points and align locations along transects. Raw data were interpolated without processing to adjust locations of points. To facilitate comparisons, Gomez and Sullivan ("GSE") 2011, 2013-2015 survey data were normalized to locations along transects from the USGS 2008 survey and also normalized to consistent locations along transects from all Gomez and Sullivan surveys. USGS 2008 data were also normalized to facilitate comparison with Gomez and Sullivan data. Interpolations using grid-snapped data attempt to minimize survey-to-survey differences caused by the number of measurements and their locations along transects. Spatial interpolations based on "raw" elevations were used for model development because they provided a larger number of points to inform interpolations. Elevation differences calculated using grid-snapped and raw data for the same survey year can be as large (or larger) than differences between surveys with different numbers of points.

Table 4. Summary of sediment transport model parameter values.

| ***Sediment Transport Model*** | | | | | | |
|---|---|---|---|---|---|---|
| *Parameter* | *Size Class* | | | | | *Source/Notes* |
| | *1 Clay* | *2 Silt* | *3 Sand* | *4 Gravel* | *5 Coal* | |
| $d_p$ (mm) | 3 | 35 | 500 | 4000 | 354 | Clay, silt, and sand values based on Sanford et al. (2016). Gravel was estimated from bed grain data. Coal is assigned as an equivalent diameter at a specific gravity of 2.65 assuming a 1 mm physical diameter and a specific gravity of 1.5 as inferred from SRBC (2006). |
| $d_*$ (dimensionless) | 0.08 | 0.88 | 12.6 | 101 | 8.95 | Equation (2-17) |
| $\tau_{ce}$ (Pa) [Particles] | 0.2 | 0.2 | 0.28 | 3.2 | 0.22 | Guo (2002), Equation (2-16), erosion threshold for transport as discrete particles. |
| $\tau_{cs}$ (Pa) [$\tau_{cd}$ (Pa)] | 0.2 | 0.2 | 0.4 | 12 | 0.35 | Equation (2-20) |
| $w_{s,q}$ (cm/s) | 0.0004 | 0.06 | 5 | 27.3 | 4.2 | Clay and sand values based on Sanford et al. (2016). Silt and gravel were estimated from literature. Coal inferred from value for sand after adjusting from particle density differences. During simulation effective settling speeds depend on the probability of deposition |
| $\tau_{ce}$ (Pa) [Bed Layers] | | | | | | Erosion thresholds for initial bed layers were determined as part of calibration in consideration of constraints imposed by net bed elevation changes over time and nutrient fluxes.<br><br>Erosion thresholds for bed layers that deposit during simulations were estimated from Equations (3-1) and (3-2). |

Notes: $d_p$ = particle diameter; $d_*$ = dimensionless diameter; $\tau_{ce}$ = critical shear stress for erosion (applied to particle class when erosion is in non-cohesive mode); $\tau_{cs}$ = critical shear stress for suspension (determines when particle class moves in suspended or bedload transport modes); in the SEDZLJS framework, $\tau_{cd}$ (critical shear stress for deposition) equals $\tau_{cs}$; $w_{s,q}$ = settling speed under quiescent conditions (when the probability of deposition equals 1.0)

Table 5. Summary of sediment influx and outflux by hydrologic year for management scenarios (metric units).

| *Year* | *Scenario 0 (100% of Loads)* | | | *Scenario 1 (Loads -35%)* | | | *Scenario 2 (Loads -10.5%)* | | | *Scenario 3 (Loads +14%)* | | |
|---|---|---|---|---|---|---|---|---|---|---|---|---|
| | *Influx (MT)* | *Outflux (MT)* | *Trapped (%)* | *Influx (MT)* | *Outflux (MT)* | *Trapped (%)* | *Influx (MT)* | *Outflux (MT)* | *Trapped (%)* | *Influx (MT)* | *Outflux (MT)* | *Trapped (%)* |
| 1997 | 4.51E+05 | 2.17E+05 | 51.9 | 2.94E+05 | 1.42E+05 | 51.7 | 4.04E+05 | 1.94E+05 | 52.0 | 5.14E+05 | 2.47E+05 | 51.9 |
| 1998 | 2.07E+06 | 1.48E+06 | 28.5 | 1.35E+06 | 9.80E+05 | 27.4 | 1.85E+06 | 1.33E+06 | 28.1 | 2.36E+06 | 1.68E+06 | 28.8 |
| 1999 | 5.52E+05 | 3.61E+05 | 34.6 | 3.59E+05 | 2.35E+05 | 34.5 | 4.94E+05 | 3.23E+05 | 34.6 | 6.29E+05 | 4.11E+05 | 34.7 |
| 2000 | 8.20E+05 | 4.94E+05 | 39.8 | 5.33E+05 | 3.22E+05 | 39.6 | 7.34E+05 | 4.43E+05 | 39.6 | 9.34E+05 | 5.64E+05 | 39.6 |
| 2001 | 3.80E+05 | 1.92E+05 | 49.5 | 2.47E+05 | 1.26E+05 | 49.0 | 3.40E+05 | 1.73E+05 | 49.1 | 4.33E+05 | 2.19E+05 | 49.4 |
| 2002 | 6.95E+05 | 4.03E+05 | 42.0 | 4.52E+05 | 2.62E+05 | 42.0 | 6.22E+05 | 3.60E+05 | 42.1 | 7.93E+05 | 4.60E+05 | 42.0 |
| 2003 | 2.47E+06 | 1.65E+06 | 33.2 | 1.60E+06 | 1.07E+06 | 33.1 | 2.21E+06 | 1.48E+06 | 33.0 | 2.81E+06 | 1.88E+06 | 33.1 |
| 2004 | 4.64E+06 | 3.58E+06 | 22.8 | 3.02E+06 | 2.32E+06 | 23.2 | 4.16E+06 | 3.17E+06 | 23.8 | 5.29E+06 | 3.99E+06 | 24.6 |
| 2005 | 3.70E+06 | 3.94E+06 | -6.5 | 2.41E+06 | 2.64E+06 | -9.5 | 3.31E+06 | 3.61E+06 | -9.1 | 4.22E+06 | 4.53E+06 | -7.3 |
| 2006 | 2.16E+06 | 1.50E+06 | 30.6 | 1.40E+06 | 9.89E+05 | 29.4 | 1.93E+06 | 1.35E+06 | 30.1 | 2.46E+06 | 1.71E+06 | 30.5 |
| 2007 | 1.21E+06 | 7.21E+05 | 40.4 | 7.84E+05 | 4.71E+05 | 39.9 | 1.08E+06 | 6.44E+05 | 40.4 | 1.38E+06 | 8.19E+05 | 40.7 |
| 2008 | 2.19E+06 | 1.49E+06 | 32.0 | 1.42E+06 | 9.67E+05 | 31.9 | 1.96E+06 | 1.34E+06 | 31.6 | 2.49E+06 | 1.70E+06 | 31.7 |
| 2009 | 5.25E+05 | 2.49E+05 | 52.6 | 3.42E+05 | 1.63E+05 | 52.3 | 4.07E+05 | 2.23E+05 | 45.2 | 5.99E+05 | 2.84E+05 | 52.6 |
| 2010 | 2.19E+06 | 1.66E+06 | 24.2 | 1.42E+06 | 1.07E+06 | 24.6 | 1.96E+06 | 1.48E+06 | 24.5 | 2.49E+06 | 1.87E+06 | 24.9 |
| 2011 | 1.02E+07 | 1.18E+07 | -15.7 | 6.62E+06 | 9.99E+06 | -50.9 | 9.11E+06 | 1.12E+07 | -22.9 | 1.16E+07 | 1.25E+07 | -7.8 |
| 2012 | 6.23E+05 | 2.88E+05 | 53.8 | 4.05E+05 | 1.90E+05 | 53.1 | 5.58E+05 | 2.59E+05 | 53.6 | 7.11E+05 | 3.27E+05 | 54.0 |
| 2013 | 7.85E+05 | 4.53E+05 | 42.3 | 5.11E+05 | 2.96E+05 | 42.1 | 7.03E+05 | 4.06E+05 | 42.2 | 8.96E+05 | 5.14E+05 | 42.6 |
| 2014 | 9.69E+05 | 5.23E+05 | 46.0 | 6.30E+05 | 3.44E+05 | 45.4 | 8.67E+05 | 4.69E+05 | 45.9 | 1.10E+06 | 5.94E+05 | 46.0 |

Notes: Year = hydrologic year; Influx = sum of loads into Pond; Outflux = load passing Conowingo Dam; Trapped = [Influx – Outflux]/influx × 100.

Table 6. Summary of sediment influx and outflux by hydrologic year for management scenarios (English units).

| *Year* | *Scenario 0 (100% of Loads)* | | | *Scenario 1 (Loads -35%)* | | | *Scenario 2 (Loads -10.5%)* | | | *Scenario 3 (Loads +14%)* | | |
|---|---|---|---|---|---|---|---|---|---|---|---|---|
| | *Influx (tons)* | *Outflux (tons)* | *Trapped (%)* | *Influx (tons)* | *Outflux (tons)* | *Trapped (%)* | *Influx (tons)* | *Outflux (tons)* | *Trapped (%)* | *Influx (tons)* | *Outflux (tons)* | *Trapped (%)* |
| 1997 | 4.97E+05 | 2.39E+05 | 51.9 | 3.24E+05 | 1.57E+05 | 51.7 | 4.45E+05 | 2.14E+05 | 52.0 | 5.67E+05 | 2.72E+05 | 51.9 |
| 1998 | 2.28E+06 | 1.63E+06 | 28.5 | 1.49E+06 | 1.08E+06 | 27.4 | 2.04E+06 | 1.47E+06 | 28.1 | 2.60E+06 | 1.85E+06 | 28.8 |
| 1999 | 6.09E+05 | 3.98E+05 | 34.6 | 3.96E+05 | 2.59E+05 | 34.5 | 5.45E+05 | 3.56E+05 | 34.6 | 6.93E+05 | 4.53E+05 | 34.7 |
| 2000 | 9.04E+05 | 5.45E+05 | 39.8 | 5.88E+05 | 3.55E+05 | 39.6 | 8.09E+05 | 4.88E+05 | 39.6 | 1.03E+06 | 6.22E+05 | 39.6 |
| 2001 | 4.19E+05 | 2.12E+05 | 49.5 | 2.72E+05 | 1.39E+05 | 49.0 | 3.75E+05 | 1.91E+05 | 49.1 | 4.77E+05 | 2.41E+05 | 49.4 |
| 2002 | 7.66E+05 | 4.44E+05 | 42.0 | 4.98E+05 | 2.89E+05 | 42.0 | 6.86E+05 | 3.97E+05 | 42.1 | 8.74E+05 | 5.07E+05 | 42.0 |
| 2003 | 2.72E+06 | 1.82E+06 | 33.2 | 1.76E+06 | 1.18E+06 | 33.1 | 2.44E+06 | 1.63E+06 | 33.0 | 3.10E+06 | 2.07E+06 | 33.1 |
| 2004 | 5.12E+06 | 3.95E+06 | 22.8 | 3.33E+06 | 2.56E+06 | 23.2 | 4.59E+06 | 3.49E+06 | 23.8 | 5.83E+06 | 4.40E+06 | 24.6 |
| 2005 | 4.08E+06 | 4.34E+06 | -6.5 | 2.66E+06 | 2.91E+06 | -9.5 | 3.65E+06 | 3.98E+06 | -9.1 | 4.65E+06 | 4.99E+06 | -7.3 |
| 2006 | 2.38E+06 | 1.65E+06 | 30.6 | 1.54E+06 | 1.09E+06 | 29.4 | 2.13E+06 | 1.49E+06 | 30.1 | 2.71E+06 | 1.89E+06 | 30.5 |
| 2007 | 1.33E+06 | 7.95E+05 | 40.4 | 8.64E+05 | 5.19E+05 | 39.9 | 1.19E+06 | 7.10E+05 | 40.4 | 1.52E+06 | 9.03E+05 | 40.7 |
| 2008 | 2.41E+06 | 1.64E+06 | 32.0 | 1.57E+06 | 1.07E+06 | 31.9 | 2.16E+06 | 1.48E+06 | 31.6 | 2.75E+06 | 1.87E+06 | 31.7 |
| 2009 | 5.79E+05 | 2.75E+05 | 52.6 | 3.77E+05 | 1.80E+05 | 52.3 | 4.49E+05 | 2.46E+05 | 45.2 | 6.60E+05 | 3.13E+05 | 52.6 |
| 2010 | 2.41E+06 | 1.83E+06 | 24.2 | 1.57E+06 | 1.18E+06 | 24.6 | 2.16E+06 | 1.63E+06 | 24.5 | 2.75E+06 | 2.06E+06 | 24.9 |
| 2011 | 1.12E+07 | 1.30E+07 | -15.7 | 7.30E+06 | 1.10E+07 | -50.9 | 1.00E+07 | 1.23E+07 | -22.9 | 1.28E+07 | 1.38E+07 | -7.8 |
| 2012 | 6.87E+05 | 3.18E+05 | 53.8 | 4.47E+05 | 2.09E+05 | 53.1 | 6.15E+05 | 2.86E+05 | 53.6 | 7.84E+05 | 3.61E+05 | 54.0 |
| 2013 | 8.65E+05 | 4.99E+05 | 42.3 | 5.63E+05 | 3.26E+05 | 42.1 | 7.75E+05 | 4.48E+05 | 42.2 | 9.88E+05 | 5.67E+05 | 42.6 |
| 2014 | 1.07E+06 | 5.77E+05 | 46.0 | 6.95E+05 | 3.79E+05 | 45.4 | 9.56E+05 | 5.17E+05 | 45.9 | 1.21E+06 | 6.55E+05 | 46.0 |

Notes: Year = hydrologic year; Influx = sum of loads into Pond; Outflux = load passing Conowingo Dam; Trapped = [Influx – Outflux]/influx × 100.

Table 7. Summary of cumulative sediment influx, outflux, net bed elevation change, and average net sediment accumulations rates.

| *Metric* | *Simulation* | | | | |
|---|---|---|---|---|---|
| | *Long-Term* | *Scenario 0 (100% of Loads)* | *Scenario 1 (Loads -35%)* | *Scenario 2 (Loads -10.5%)* | *Scenario 3 (Loads +14%)* |
| | 1997-2014 Hydrology | Repeated (Second Cycle) of 1997-2014 Hydrology | | | |
| Cumulative Influx | 3.66E+07 (MT)<br>4.04E+07 (tons) | 3.66E+07 (MT)<br>4.04E+07 (tons) | 2.38E+07 (MT)<br>2.62E+07 (tons) | 3.27E+07 (MT)<br>3.61E+07 (tons) | 4.17E+07 (MT)<br>4.60E+07 (tons) |
| Cumulative Outflux | 3.07E+07 (MT)<br>3.39E+07 (tons) | 3.10E+07 (MT)<br>3.42E+07 (tons) | 2.26E+07 (MT)<br>2.49E+07 (tons) | 2.85E+07 (MT)<br>3.14E+07 (tons) | 3.43E+07 (MT)<br>3.78E+07 (tons) |
| Cumulative Net Bed Elevation Change (18 years) | 10.65 (cm)<br>0.35 (feet) | 9.86 (cm)<br>0.32 (feet) | 2.19 (cm)<br>0.07 (feet) | 7.75 (cm)<br>0.25 (feet) | 13.16 (cm)<br>0.43 (feet) |
| Average Net Sediment Accumulation Rate | 0.59 (cm/year)<br>0.019 (feet/year) | 0.55 (cm/year)<br>0.018 (feet/year) | 0.12 (cm/year)<br>0.004 (feet/year) | 0.43 (cm/year)<br>0.014 (feet/year) | 0.73 (cm/year)<br>0.024 (feet/year) |

# FIGURES

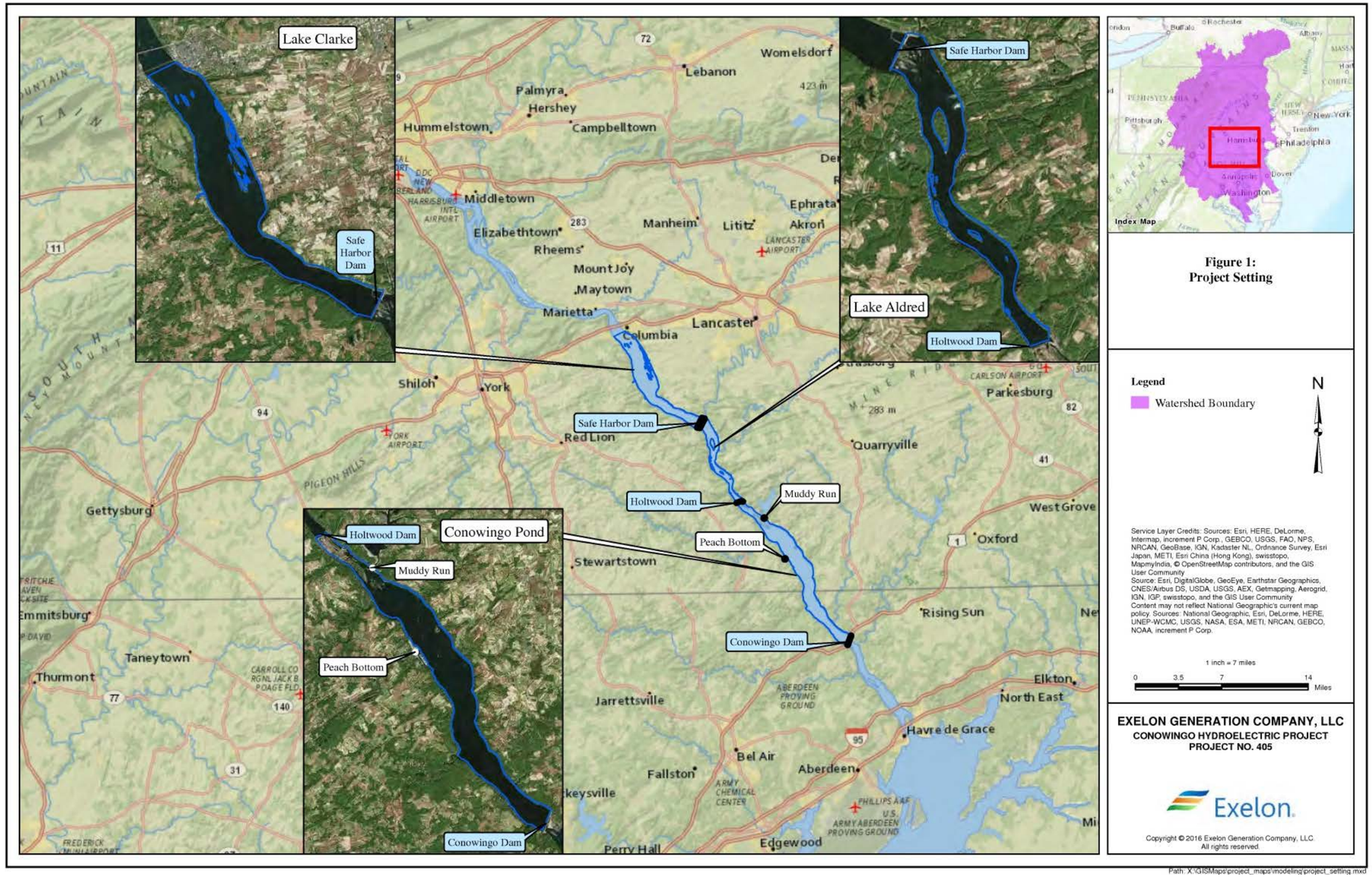


Notes: Project setting shown in context of the Susquehanna River watershed (uppermost right inset) and system of three impoundments formed by Safe Harbor Dam (Lake Clarke). Holtwood Dam (Lake Aldred), and Conowingo Dam (Conowingo Pond). Figure provided courtesy of Gomez and Sullivan Engineers.

Figure 1. Project setting: Susquehanna River watershed and Conowingo Pond.

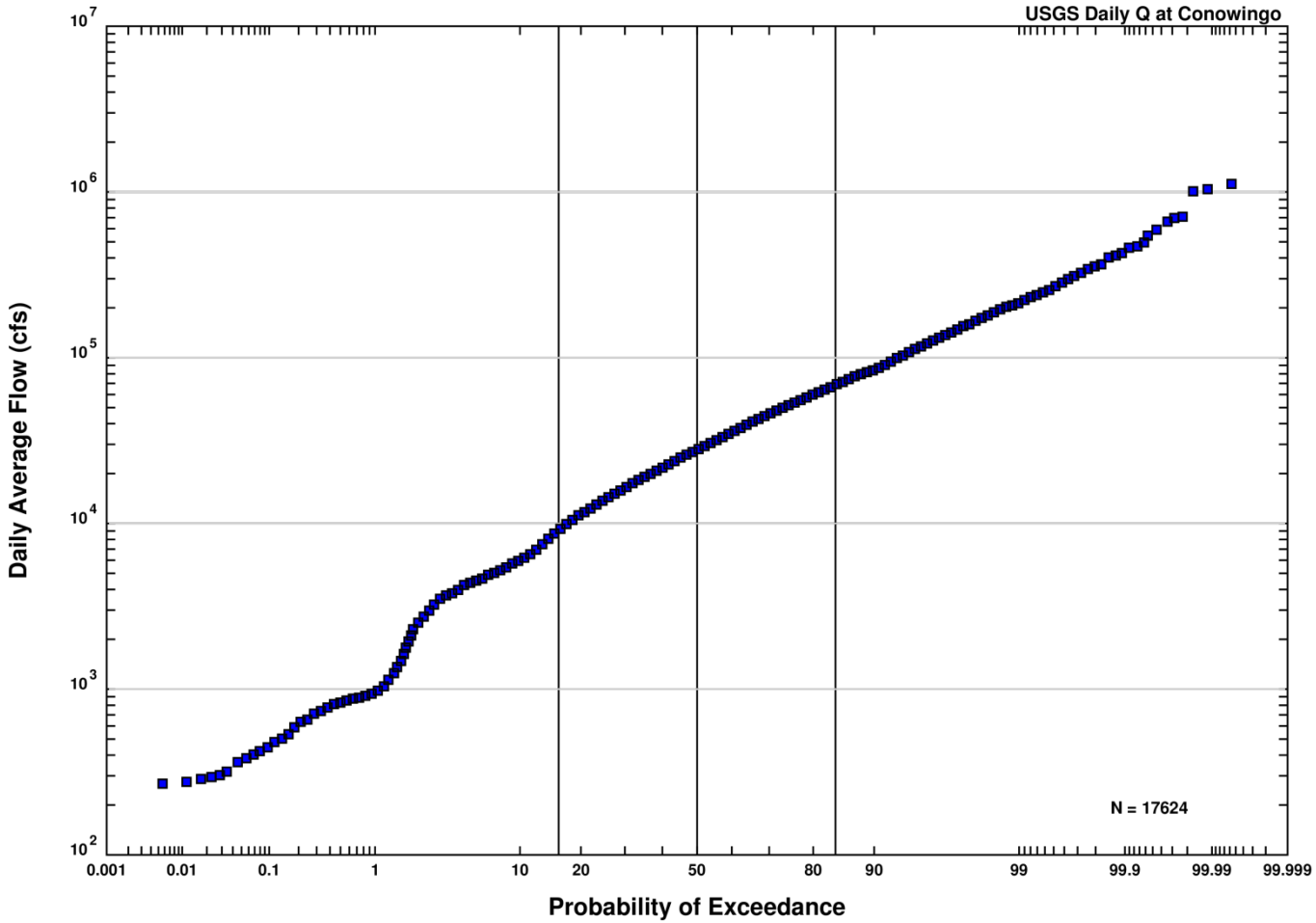


Note: spill over crest gates occurs when flow exceeds 86,000 cfs (2,435 cms).

Figure 2. Probability distribution of daily average flows reported at the USGS Conowingo gaging station: October 1, 1967 – December 31, 2015.

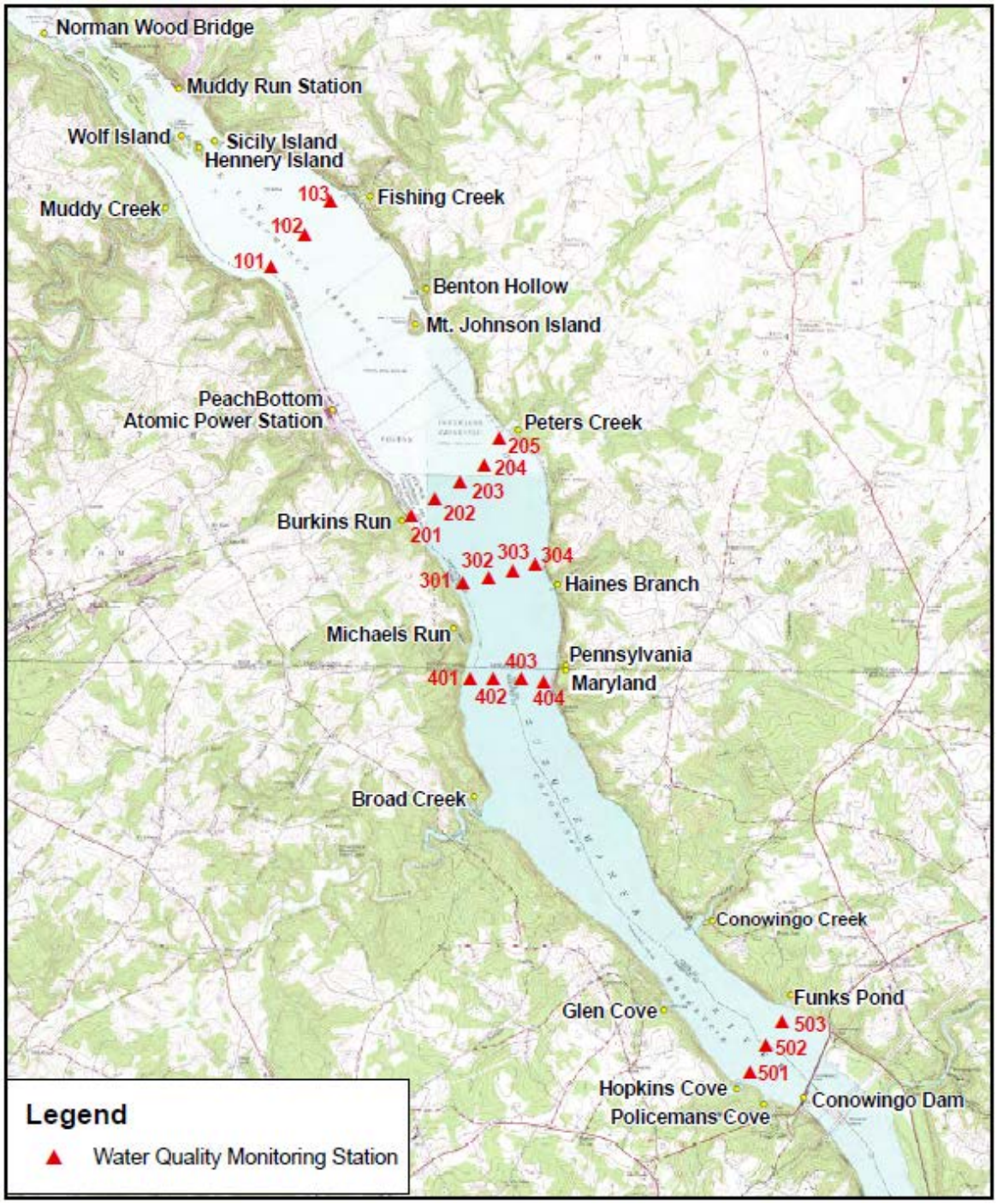


Figure 3. Conowingo Pond temperature (and water quality) at 19 monitoring stations: 2010 (from Normandeau and Gomez and Sullivan, 2011).

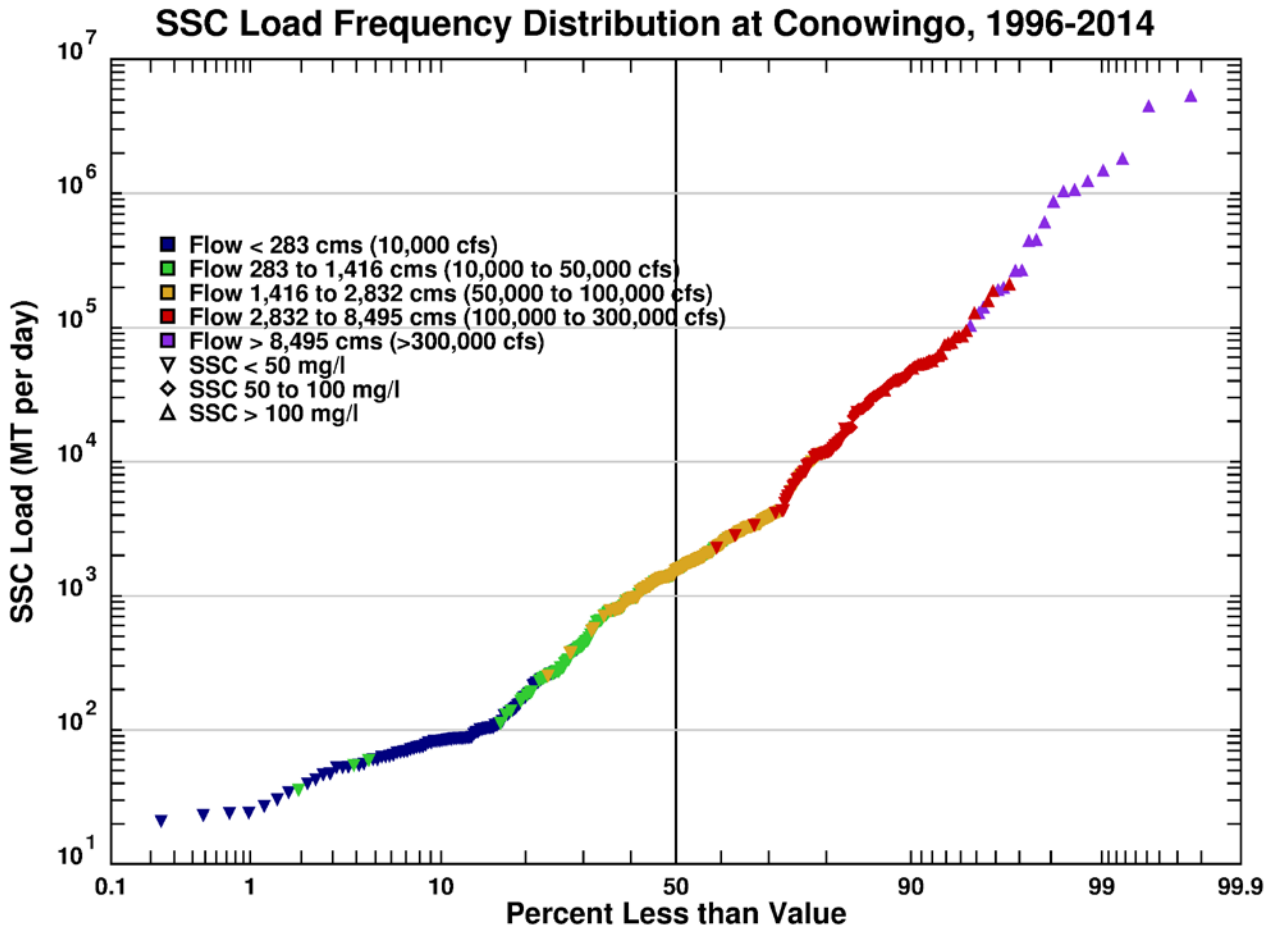


Notes: SSC = suspended sediment concentration; MT = metric tons (1 MT = 1,000 kilograms = 1.1 English short tons); short ton = 2,000 pound; loads represent the product of measured SSC and the associated instantaneous flow value reported at the time of measurement; all values from USGS Conowingo station.

Figure 4. Probability distribution suspended sediment concentration (SSC) loads at Conowingo.

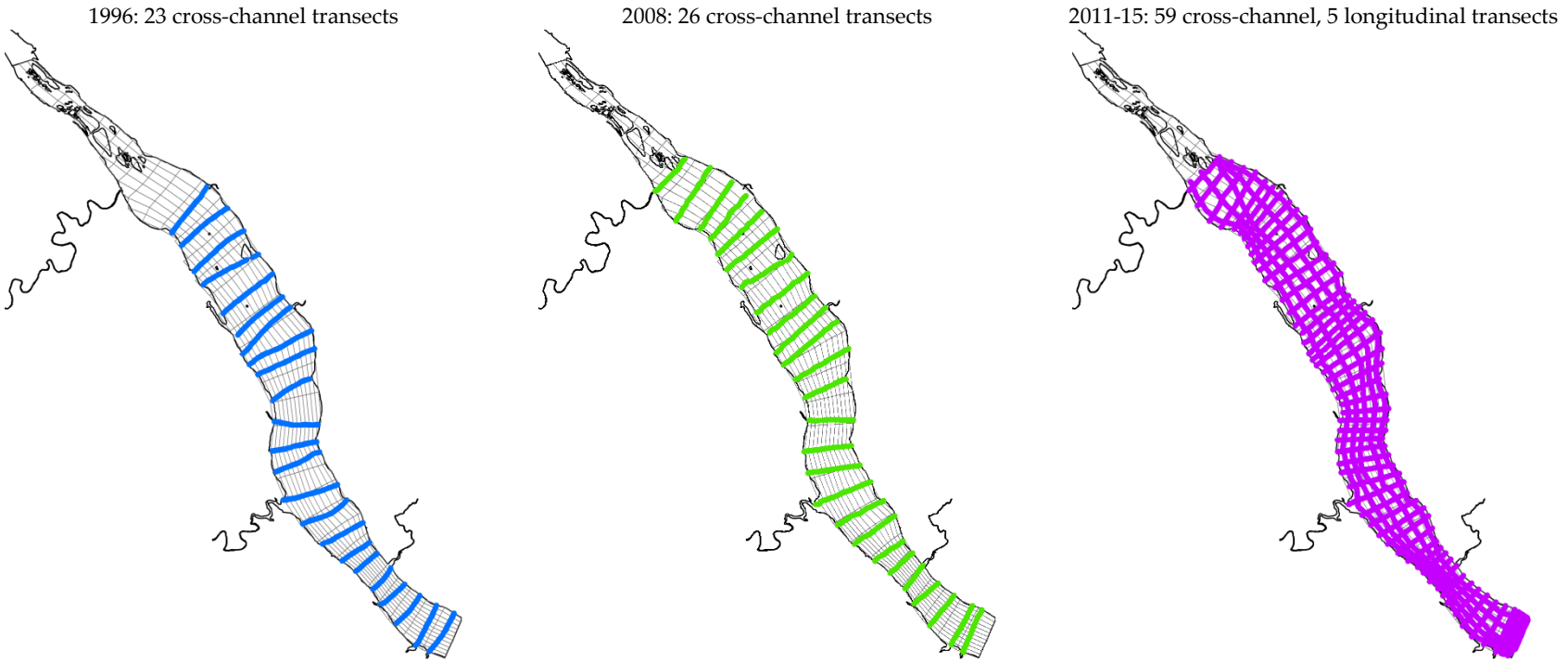


Note: surveys were conducted in 1996, 2008, 2011, 2013, 2014, and 2015. The upstream limit of the 1996 survey was approximately 6,900 ft (2,100 m) downstream of Muddy Creek. The upstream limit of surveys for other years was at the approximate location of Muddy Creek. The downstream limit of the 1996 and 2008 surveys was approximately 1,000 – 1,600 ft (300 – 500 m) upstream of Conowingo Dam. The 2011, 2013, 2014, and 2015 surveys included transects extending nearly to the face of the dam.

Figure 5. Locations of transect lines for Conowingo Pond sediment bed elevation surveys: 1996 (USGS), 2008 (USGS), and 2011 – 2015 (Gomez and Sullivan).

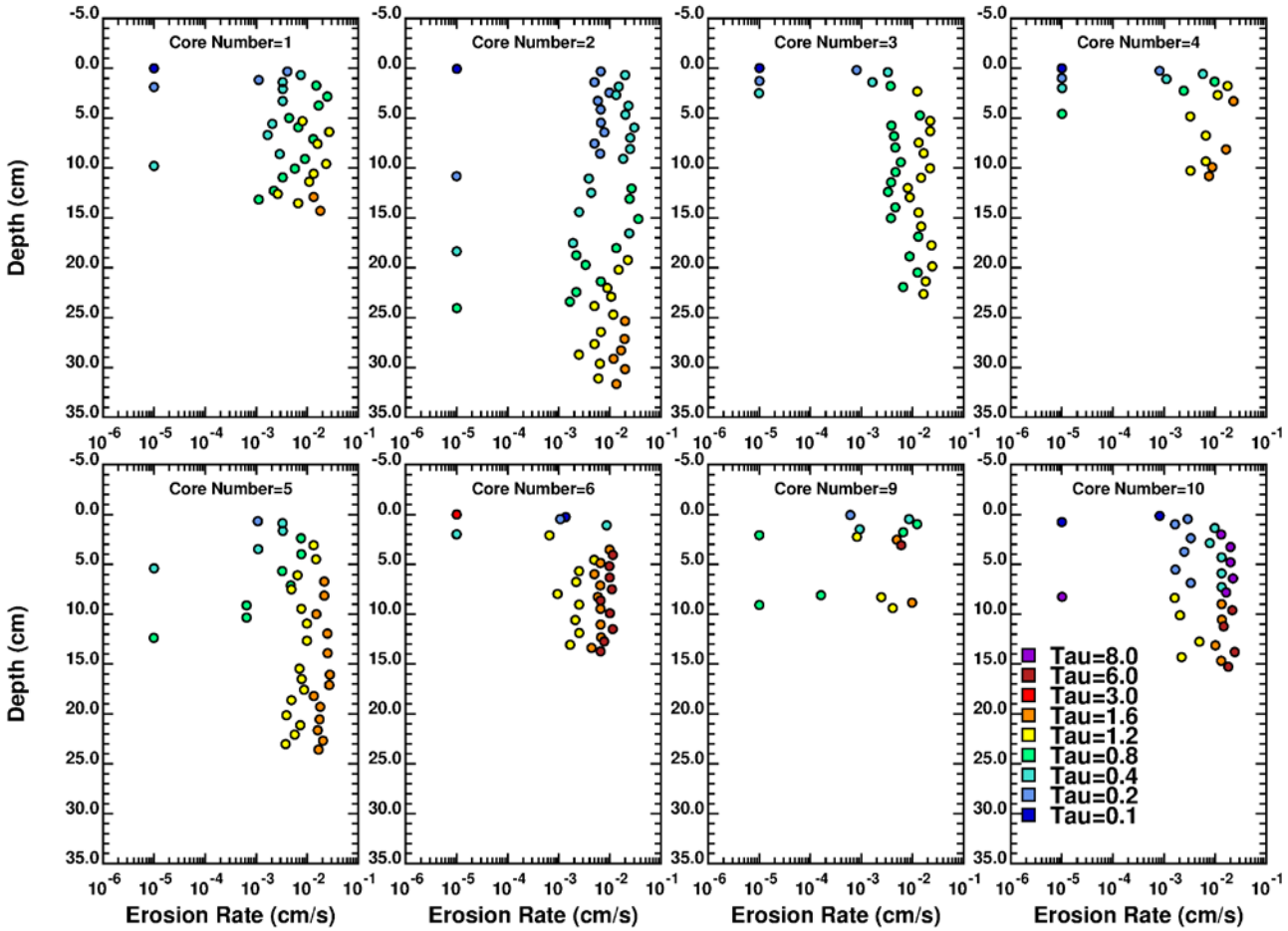


Notes: erosion rates were estimated using the SEDFLUME device as described by USACE (2014); values plotted at $10^{-5}$ cm/s represent no erosion recorded; Tau = estimated shear stress at which cores were tested (dynes/cm$^2$); 1 dyne/cm$^2$ = 0.1 Pa; erosion rate variations were generally similar across depths and shear stresses.

Figure 6. Erosion rates of Conowingo Pond sediment cores determined using the SEDFLUME device.

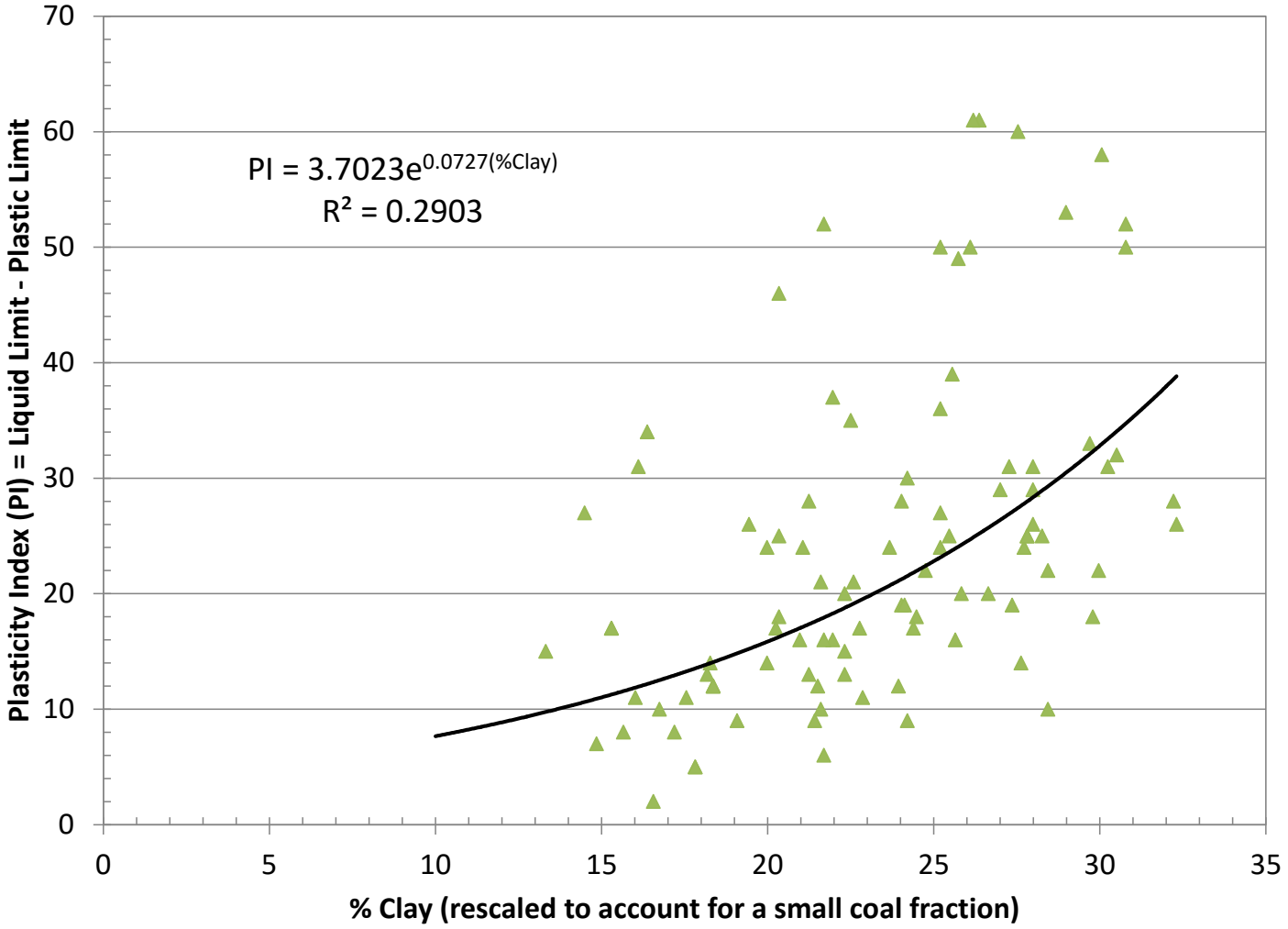


Figure 7. Relationship between measured Plasticity Index and clay content of Conowingo Pond sediment (measurements from AECOM, 2016).

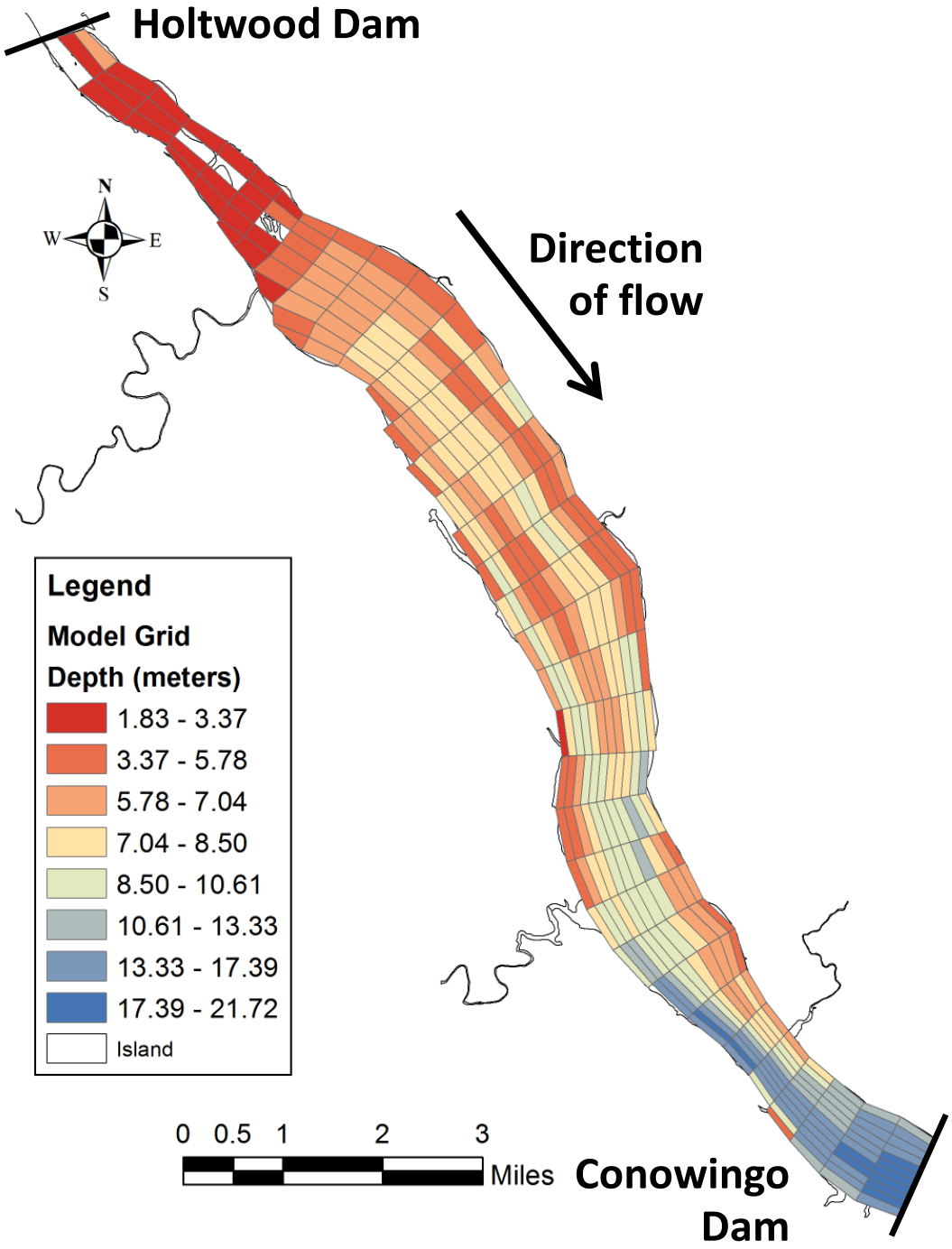


Notes: Depths are relative to a water surface elevation of 109.2 feet using the National Geodetic Vertical Datum of 1929 (NGVD29). There are 11 grid cells along the face of the dam, numbered from right to left (facing the dam from upstream) as Cells 36, 3 – 36, 13, with Cells 36, 5 – 36, 6 representing the power-intake and Cells 36, 7 – 36, 11 representing crest gates.

Figure 8. Overview of model grid used for Conowingo Pond hydrodynamic and sediment transport simulations.

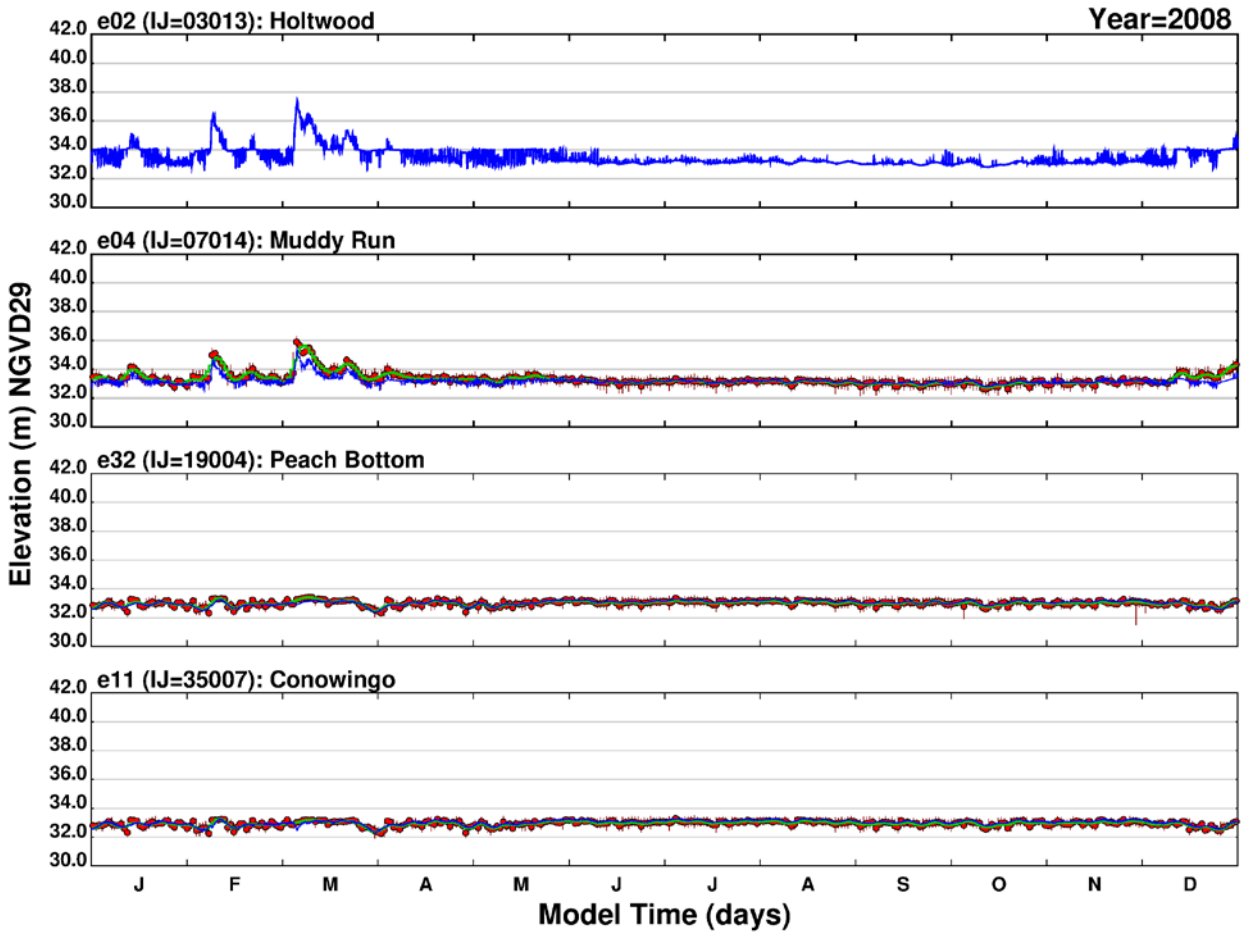


Note: Blue = simulated (hourly); Red = measured daily average and range (measurements begin in 2004); Green = 168-hour lowpass filtered measurements (hourly); IJ indicates the model grid cell from which outputs were retrieved; x-axis divisions indicate a one-character abbreviation for month of year in sequence from January through December; y-axis maximum indicates the approximate maximum water level that occurs during Tropical Storm Lee in 2011.

Figure 9. Simulated and measured water surface elevations over time at Holtwood, Muddy Run, Peach Bottom, and Conowingo: 2008.

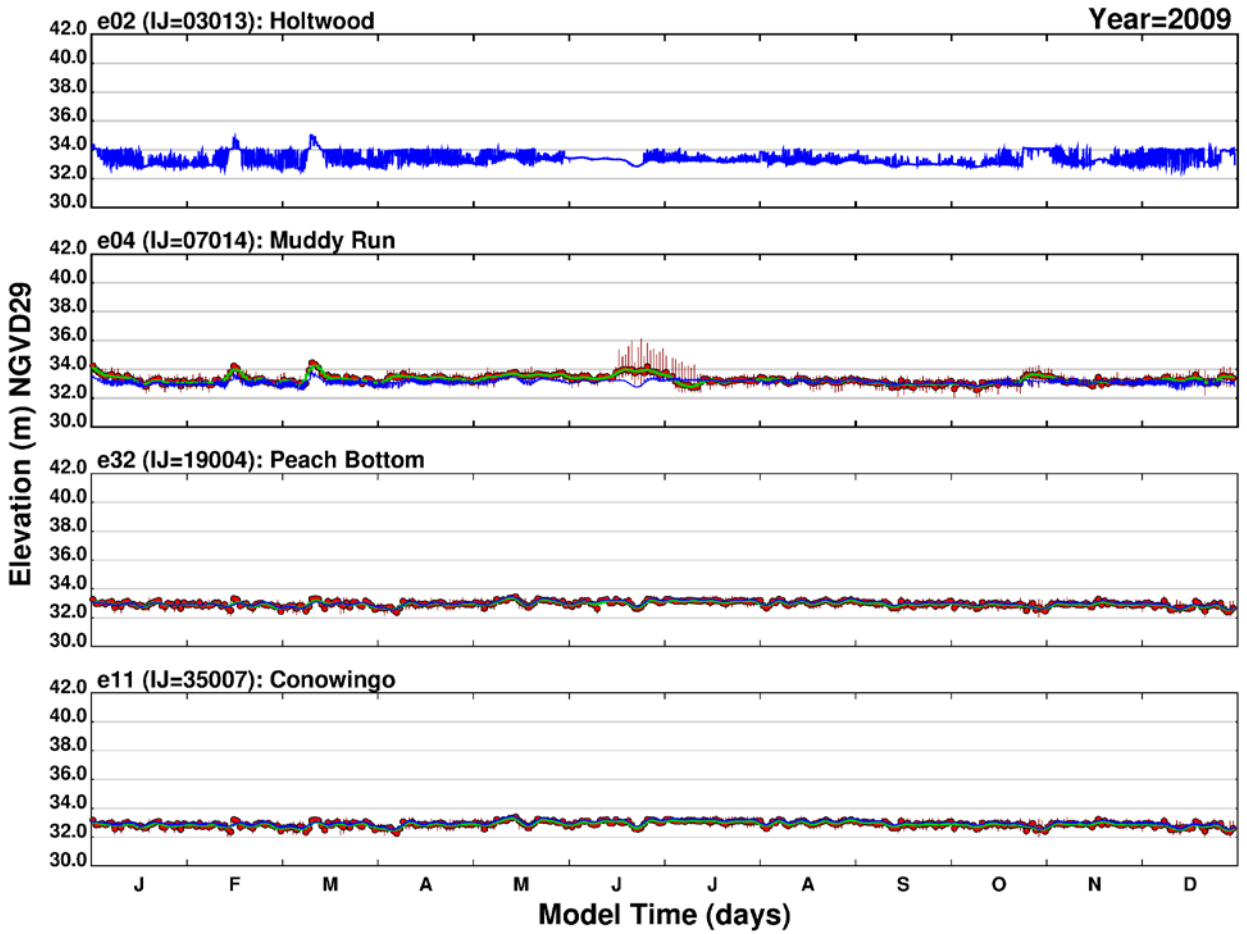


Note: Blue = simulated (hourly); Red = measured daily average and range (measurements begin in 2004); Green = 168-hour lowpass filtered measurements (hourly); IJ indicates the model grid cell from which outputs were retrieved; x-axis divisions indicate a one-character abbreviation for month of year in sequence from January through December; y-axis maximum indicates the approximate maximum water level that occurs during Tropical Storm Lee in 2011.

Figure 10. Simulated and measured water surface elevations over time at Holtwood, Muddy Run, Peach Bottom, and Conowingo: 2009.

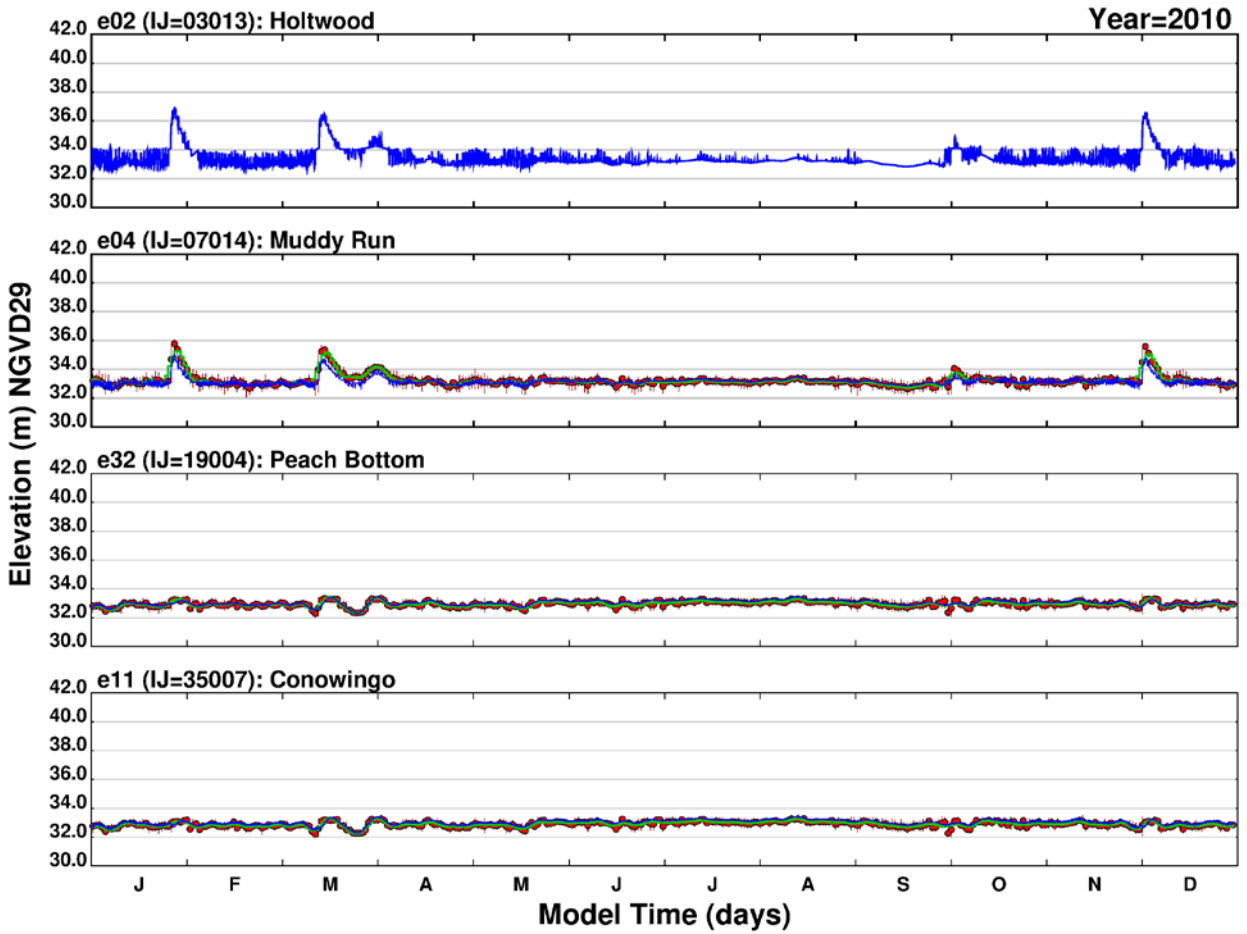


Note: Blue = simulated (hourly); Red = measured daily average and range (measurements begin in 2004); Green = 168-hour lowpass filtered measurements (hourly); IJ indicates the model grid cell from which outputs were retrieved; x-axis divisions indicate a one-character abbreviation for month of year in sequence from January through December; y-axis maximum indicates the approximate maximum water level that occurs during Tropical Storm Lee in 2011.

Figure 11. Simulated and measured water surface elevations over time at Holtwood, Muddy Run, Peach Bottom, and Conowingo: 2010.

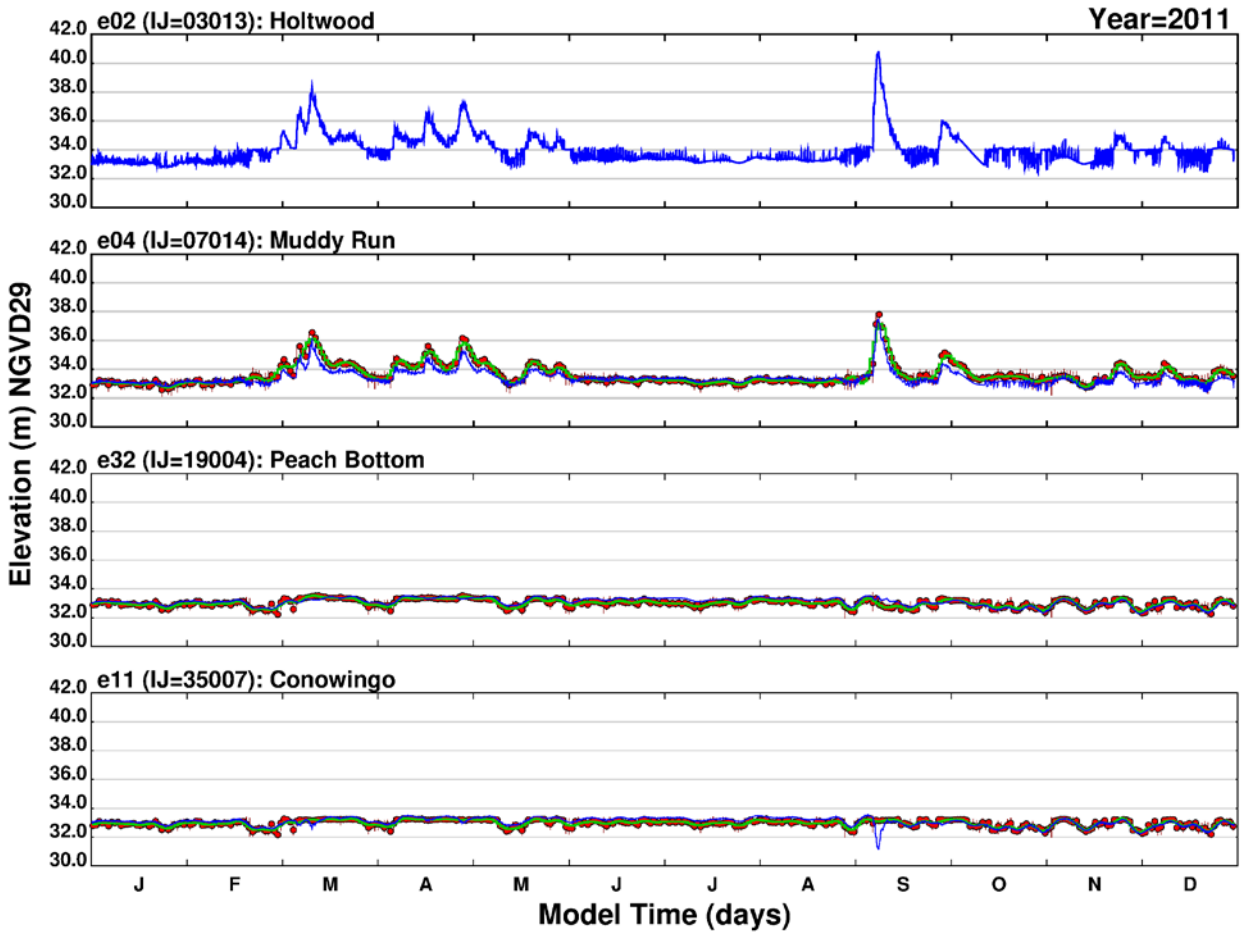


Note: Blue = simulated (hourly); Red = measured daily average and range (measurements begin in 2004); Green = 168-hour lowpass filtered measurements (hourly); IJ indicates the model grid cell from which outputs were retrieved; x-axis divisions indicate a one-character abbreviation for month of year in sequence from January through December; y-axis maximum indicates the approximate maximum water level that occurs during Tropical Storm Lee in 2011.

Figure 12. Simulated and measured water surface elevations over time at Holtwood, Muddy Run, Peach Bottom, and Conowingo: 2011.

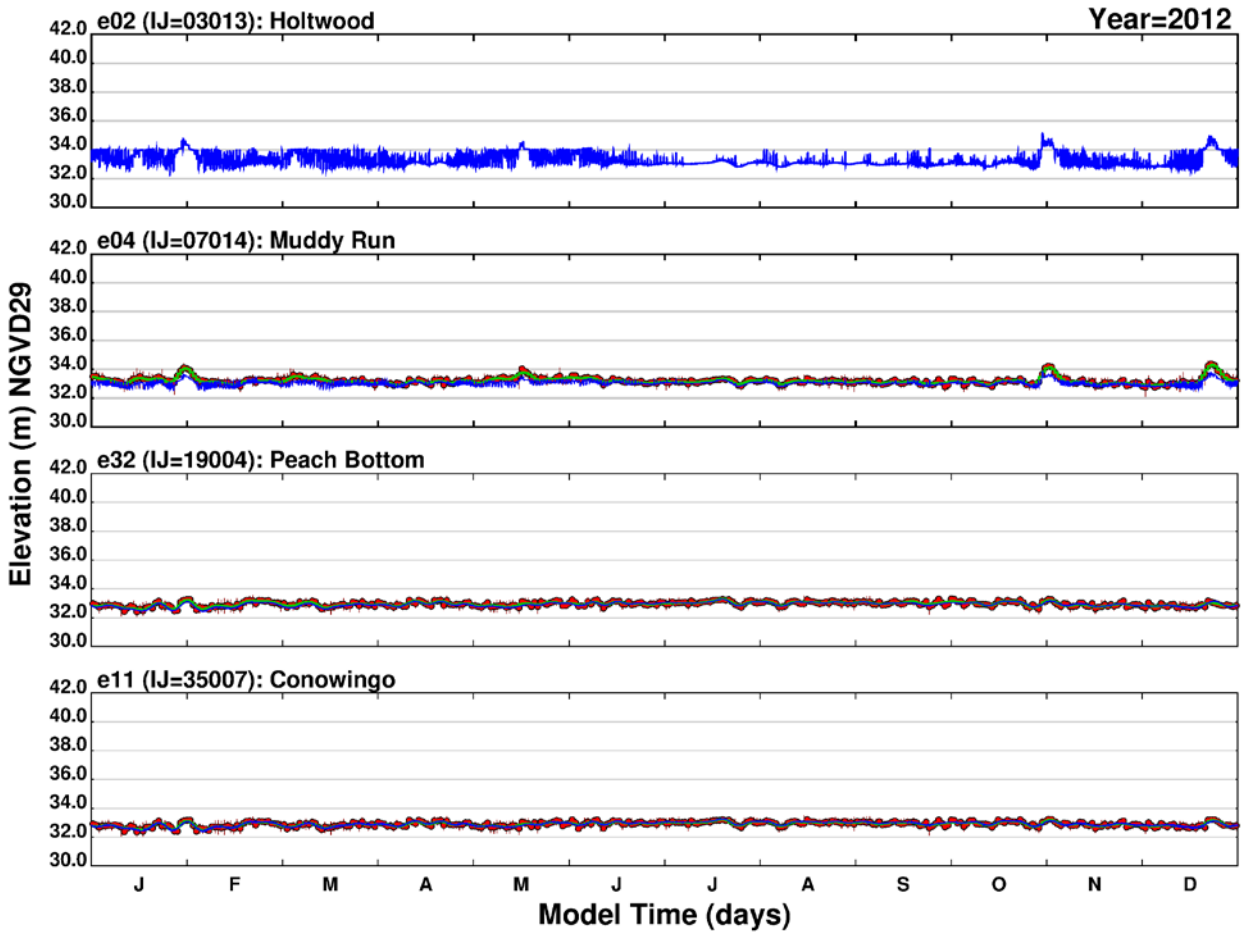


Note: Blue = simulated (hourly); Red = measured daily average and range (measurements begin in 2004); Green = 168-hour lowpass filtered measurements (hourly); IJ indicates the model grid cell from which outputs were retrieved; x-axis divisions indicate a one-character abbreviation for month of year in sequence from January through December; y-axis maximum indicates the approximate maximum water level that occurs during Tropical Storm Lee in 2011.

Figure 13. Simulated and measured water surface elevations over time at Holtwood, Muddy Run, Peach Bottom, and Conowingo: 2012.

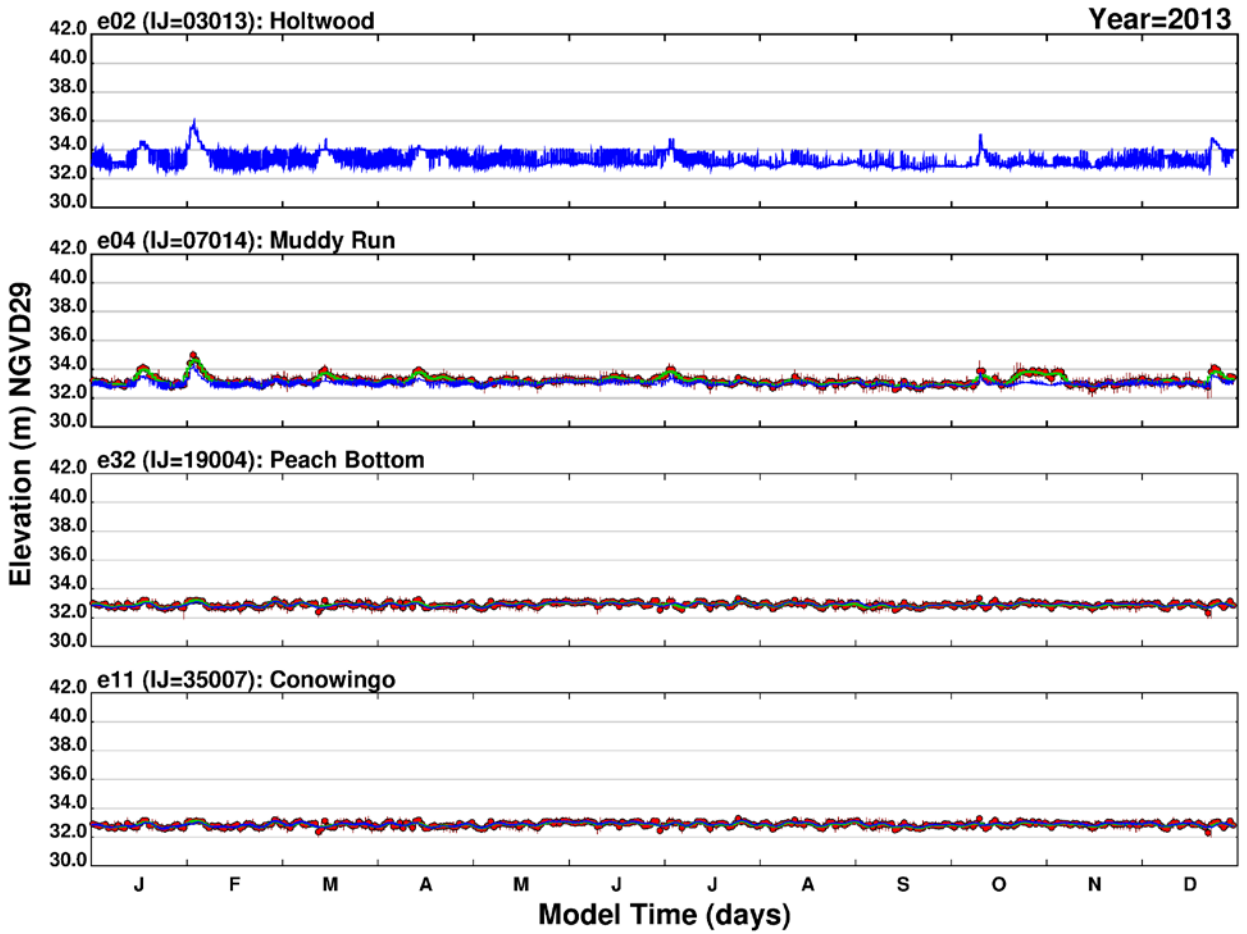


Note: Blue = simulated (hourly); Red = measured daily average and range (measurements begin in 2004); Green = 168-hour lowpass filtered measurements (hourly); IJ indicates the model grid cell from which outputs were retrieved; x-axis divisions indicate a one-character abbreviation for month of year in sequence from January through December; y-axis maximum indicates the approximate maximum water level that occurs during Tropical Storm Lee in 2011.

Figure 14. Simulated and measured water surface elevations over time at Holtwood, Muddy Run, Peach Bottom, and Conowingo: 2013.

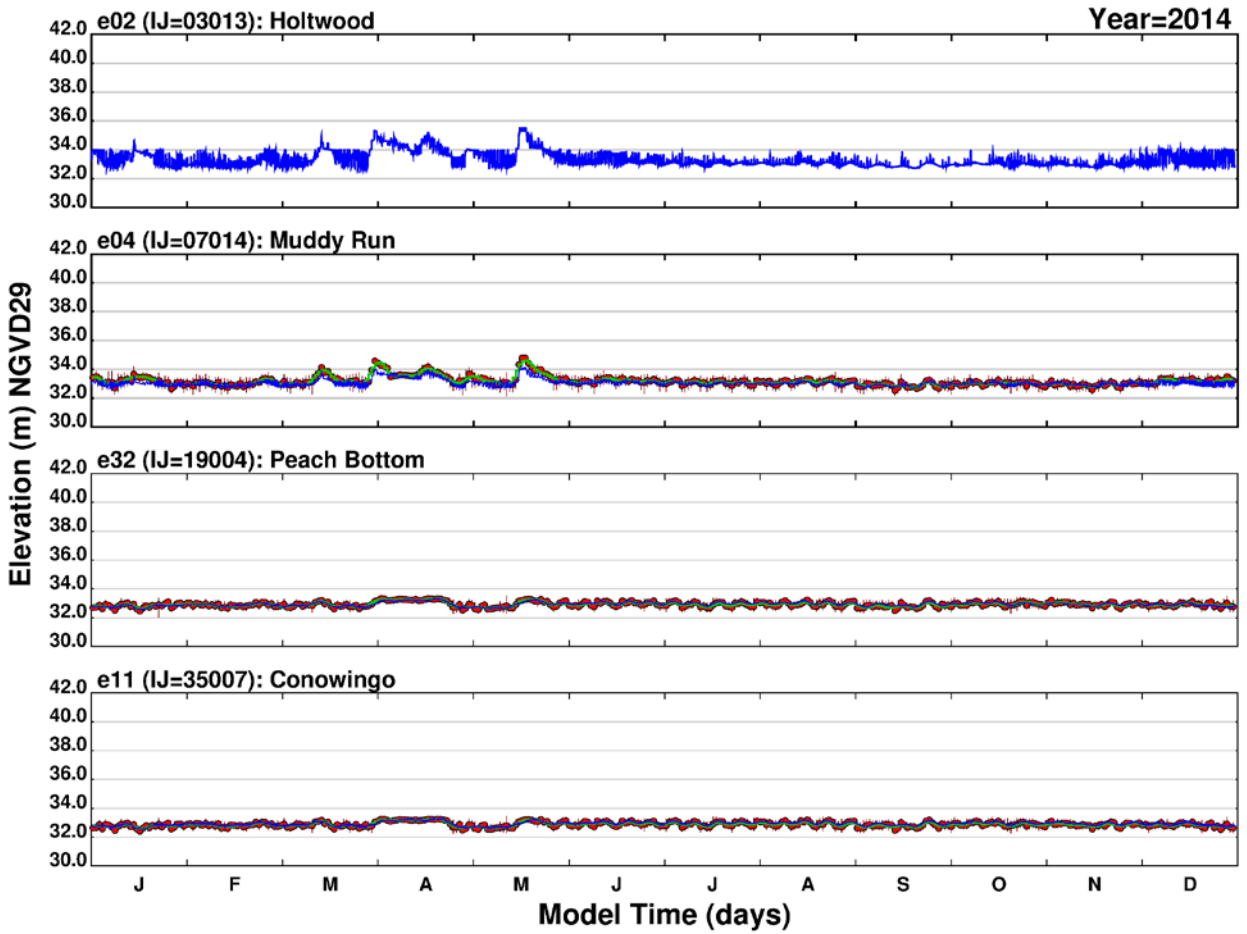


Note: Blue = simulated (hourly); Red = measured daily average and range (measurements begin in 2004); Green = 168-hour lowpass filtered measurements (hourly); IJ indicates the model grid cell from which outputs were retrieved; x-axis divisions indicate a one-character abbreviation for month of year in sequence from January through December; y-axis maximum indicates the approximate maximum water level that occurs during Tropical Storm Lee in 2011.

Figure 15. Simulated and measured water surface elevations over time at Holtwood, Muddy Run, Peach Bottom, and Conowingo: 2014.

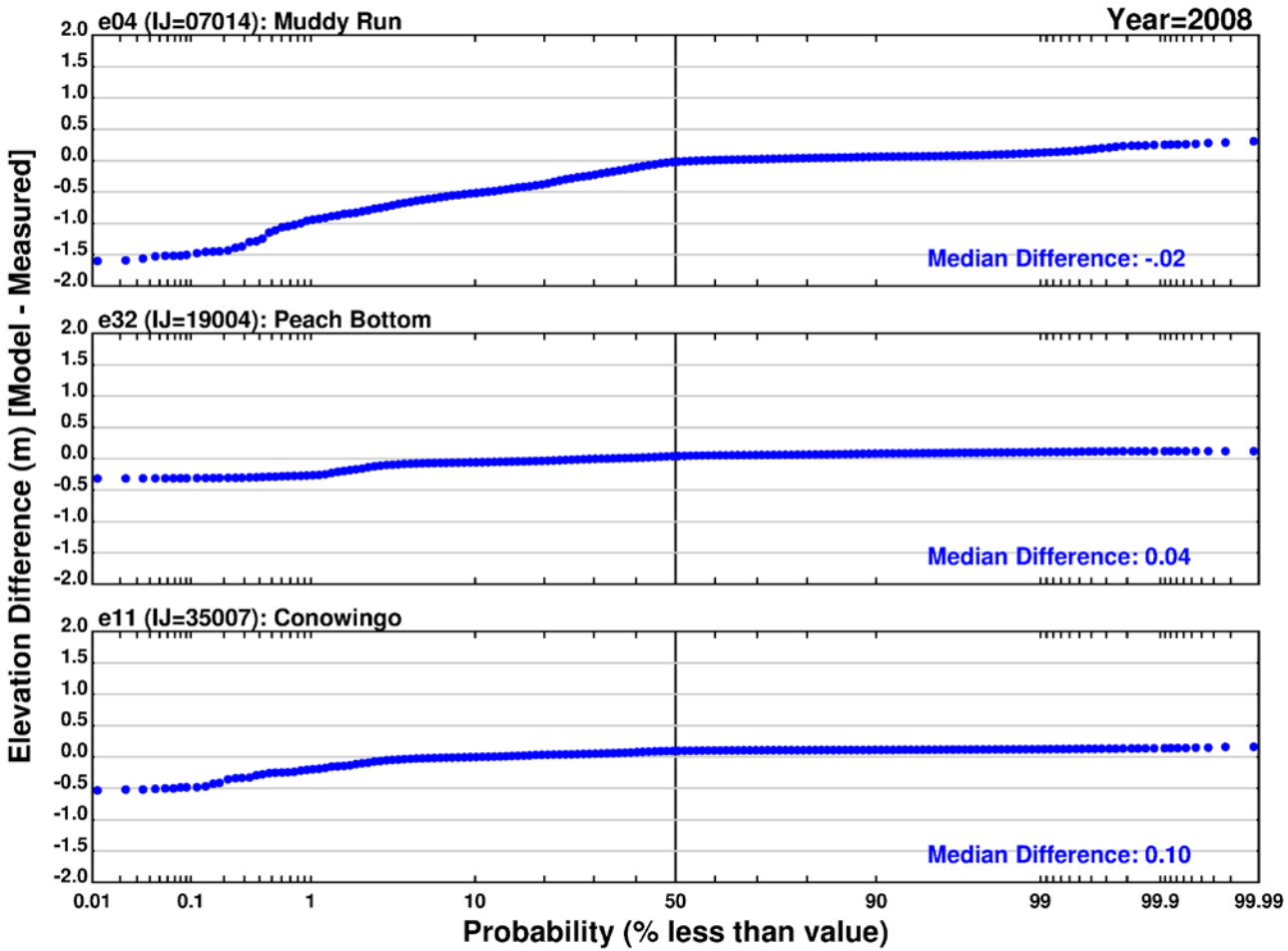


Note: Differences computed as simulated value minus measured value; IJ indicates the model grid cell from which outputs were retrieved.

Figure 16. Probability distributions of paired differences between simulated and measured water surface elevations over time at Holtwood, Peach Bottom, and Conowingo: 2008.

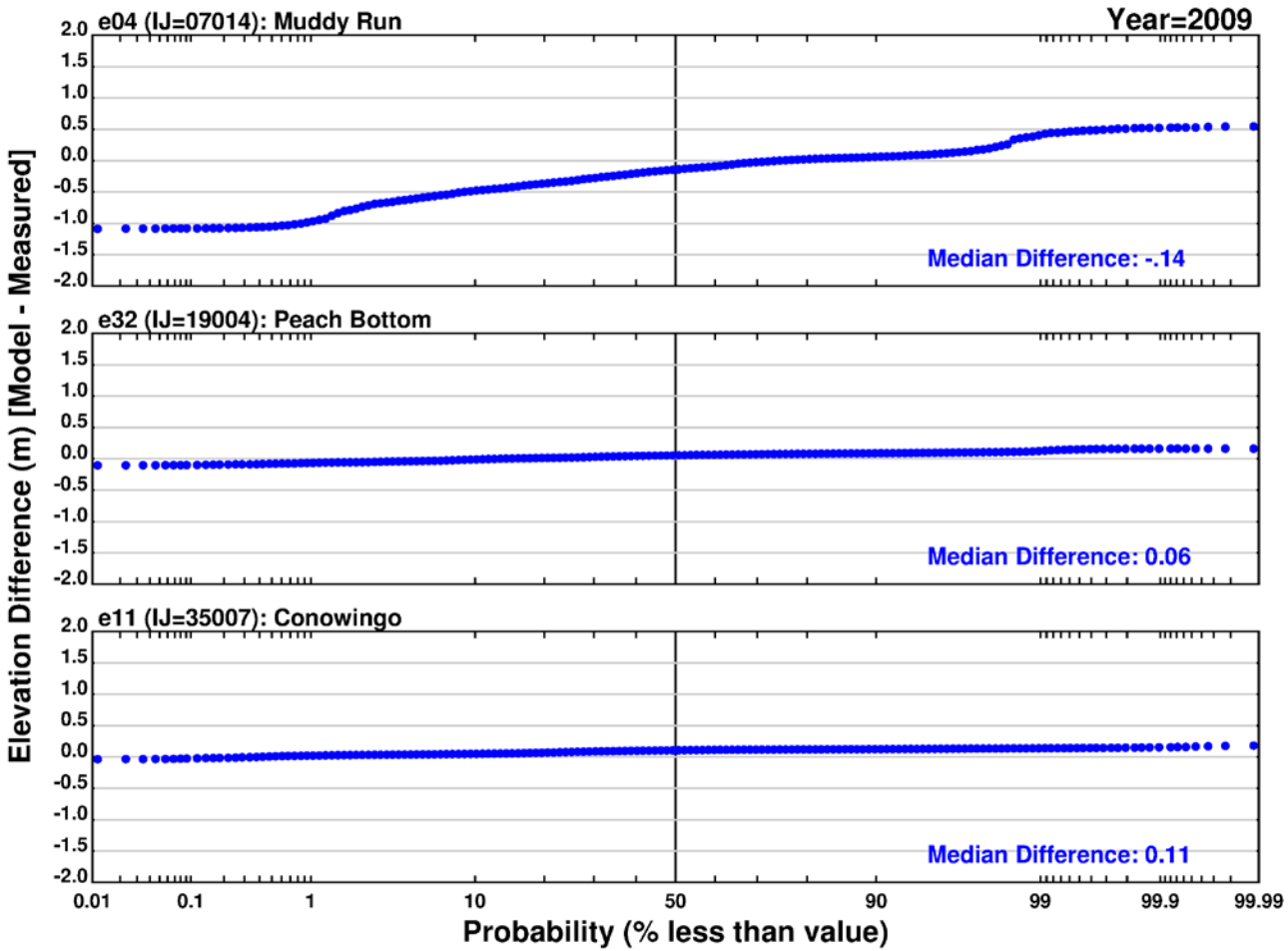


Note: Differences computed as simulated value minus measured value; IJ indicates the model grid cell from which outputs were retrieved.

Figure 17. Probability distributions of paired differences between simulated and measured water surface elevations over time at Holtwood, Peach Bottom, and Conowingo: 2009.

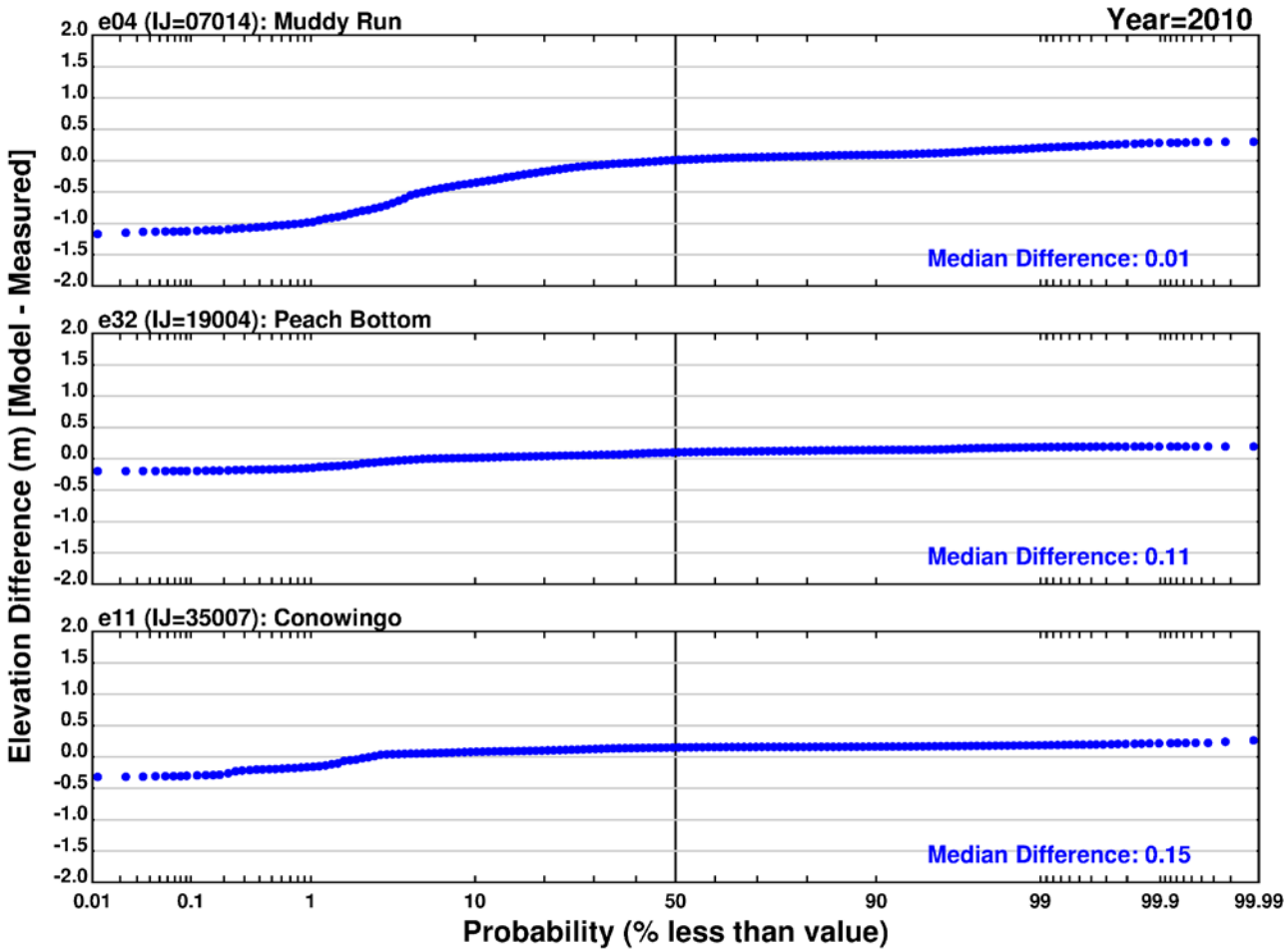


Note: Differences computed as simulated value minus measured value; IJ indicates the model grid cell from which outputs were retrieved.

Figure 18. Probability distributions of paired differences between simulated and measured water surface elevations over time at Holtwood, Peach Bottom, and Conowingo: 2010.

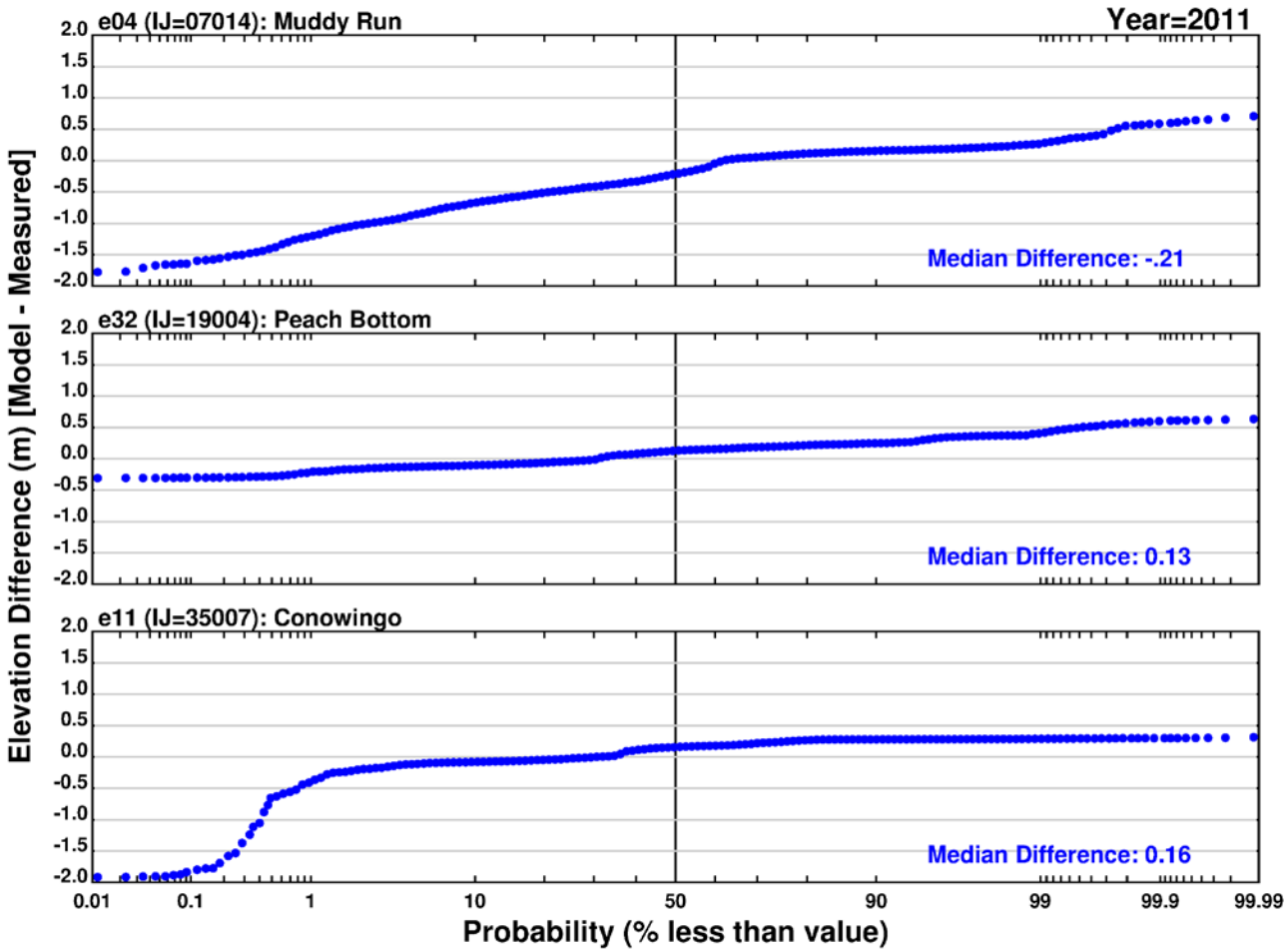


Note: Differences computed as simulated value minus measured value; IJ indicates the model grid cell from which outputs were retrieved.

Figure 19. Probability distributions of paired differences between simulated and measured water surface elevations over time at Holtwood, Peach Bottom, and Conowingo: 2011.

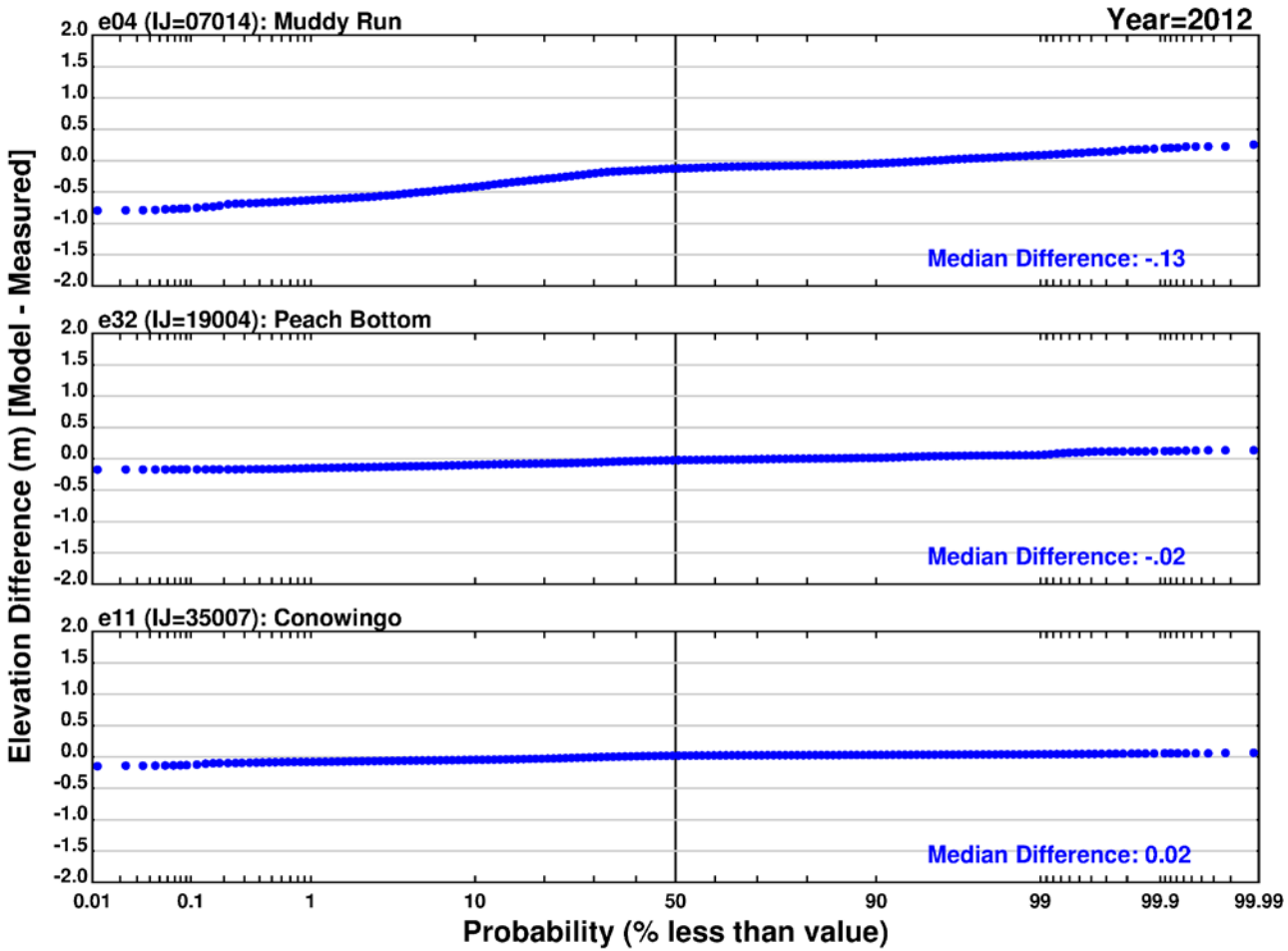


Note: Differences computed as simulated value minus measured value; IJ indicates the model grid cell from which outputs were retrieved.

Figure 20. Probability distributions of paired differences between simulated and measured water surface elevations over time at Holtwood, Peach Bottom, and Conowingo: 2012.

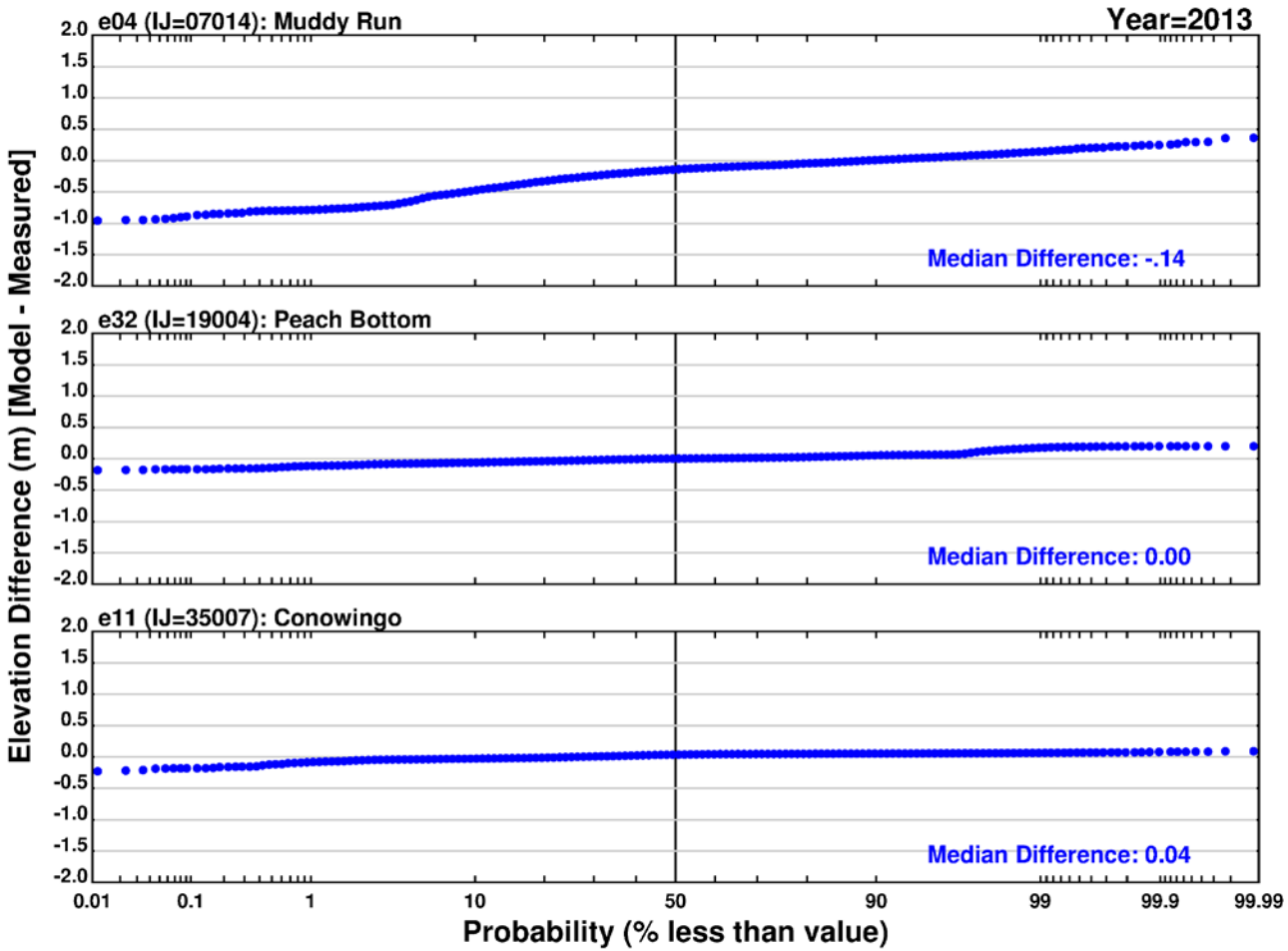


Note: Differences computed as simulated value minus measured value; IJ indicates the model grid cell from which outputs were retrieved.

Figure 21. Probability distributions of paired differences between simulated and measured water surface elevations over time at Holtwood, Peach Bottom, and Conowingo: 2013.

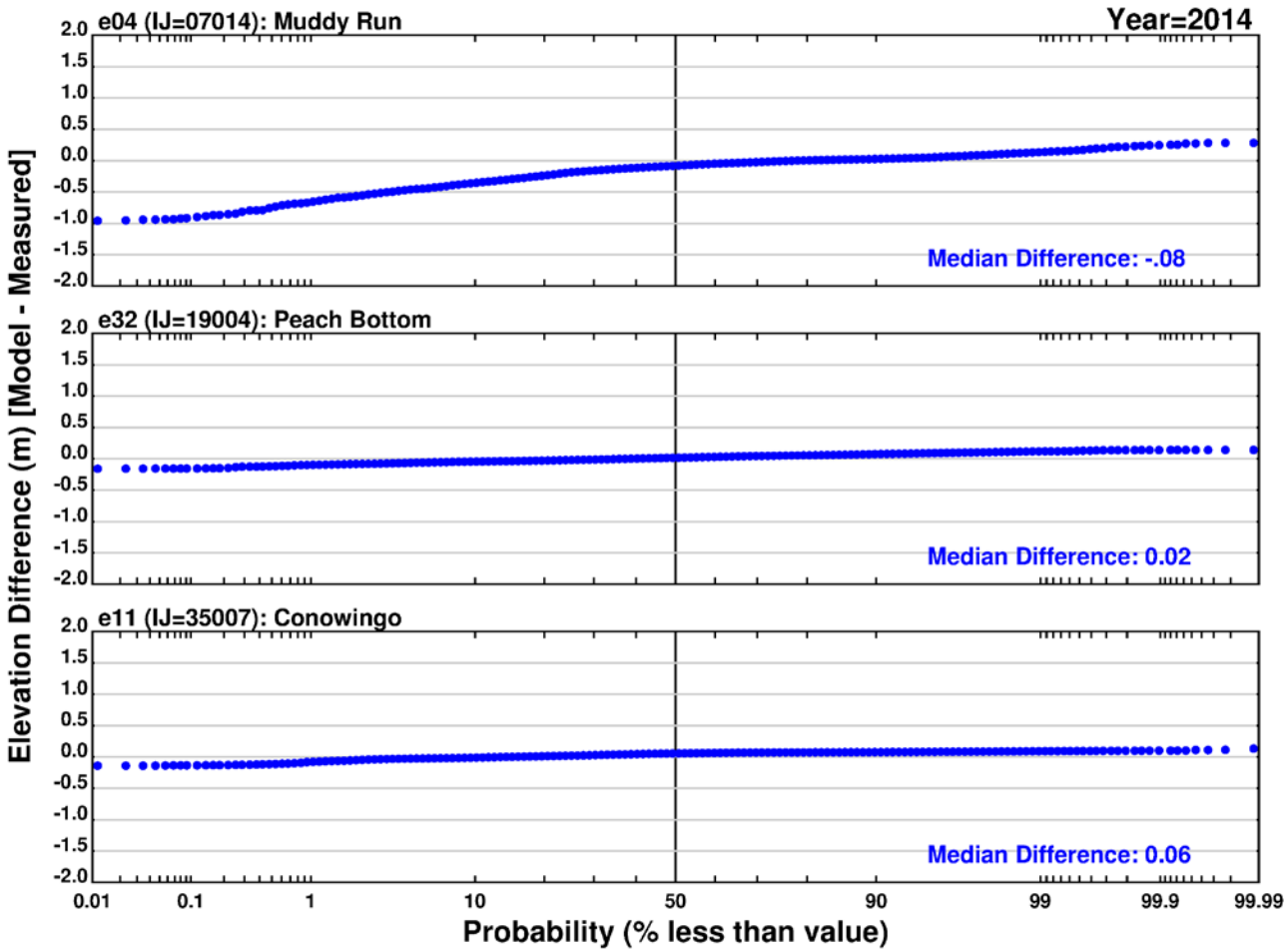


Note: Differences computed as simulated value minus measured value; IJ indicates the model grid cell from which outputs were retrieved.

Figure 22. Probability distributions of paired differences between simulated and measured water surface elevations over time at Holtwood, Peach Bottom, and Conowingo: 2014.

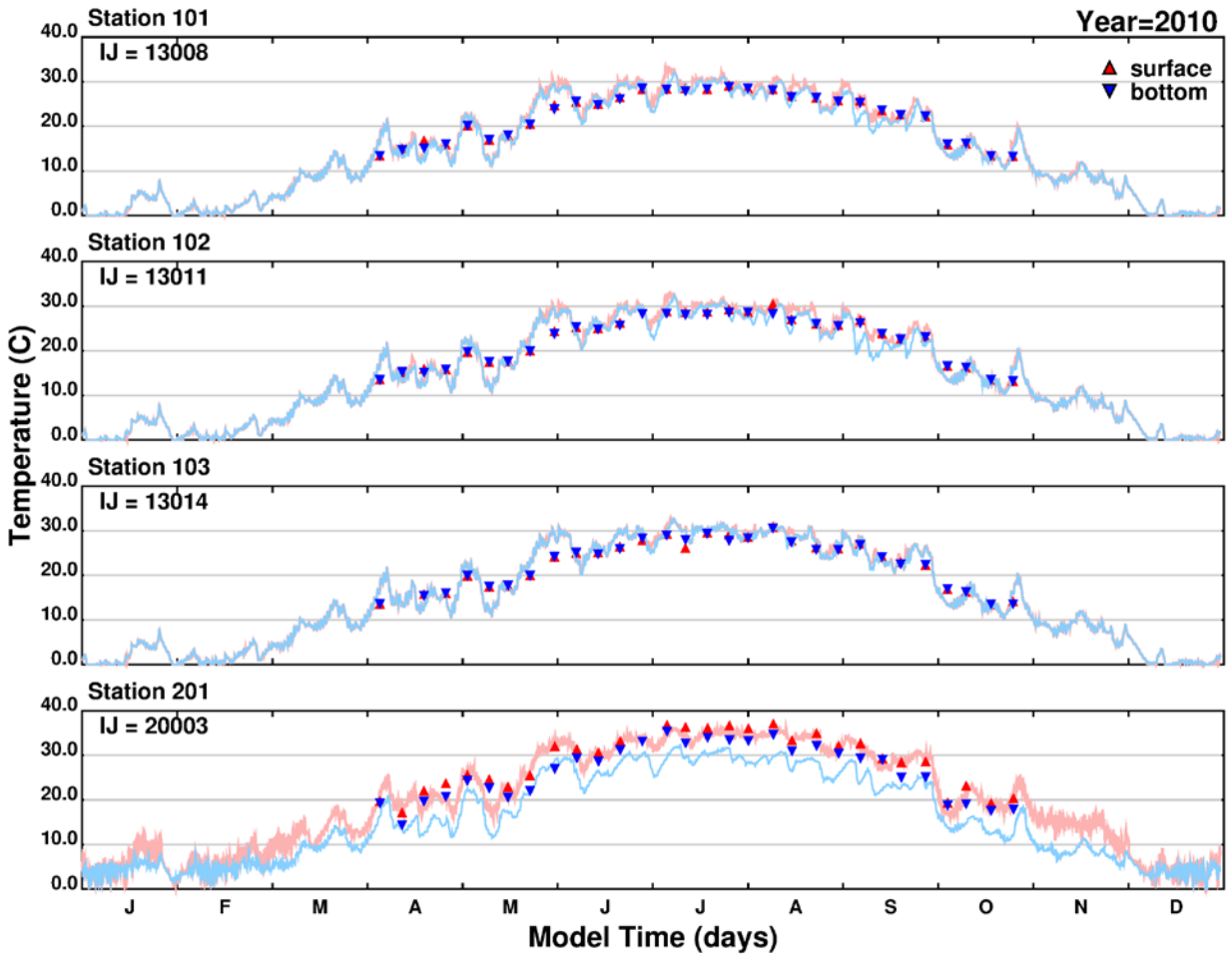


Note: Blue line = simulated near-bottom water temperature; Red line = simulated surface water temperature; Blue inverted triangle = measured near-bottom water temperature; Red triangle = measured surface water temperature; IJ indicates the model grid cell from which outputs were retrieved; x-axis divisions indicate a one character abbreviation for month of year in sequence from January through December; y-axis maximum indicates the approximate maximum temperature.

Figure 23. Simulated and measured water temperatures over time during 2010: Stations 101, 102, 103, and 201.

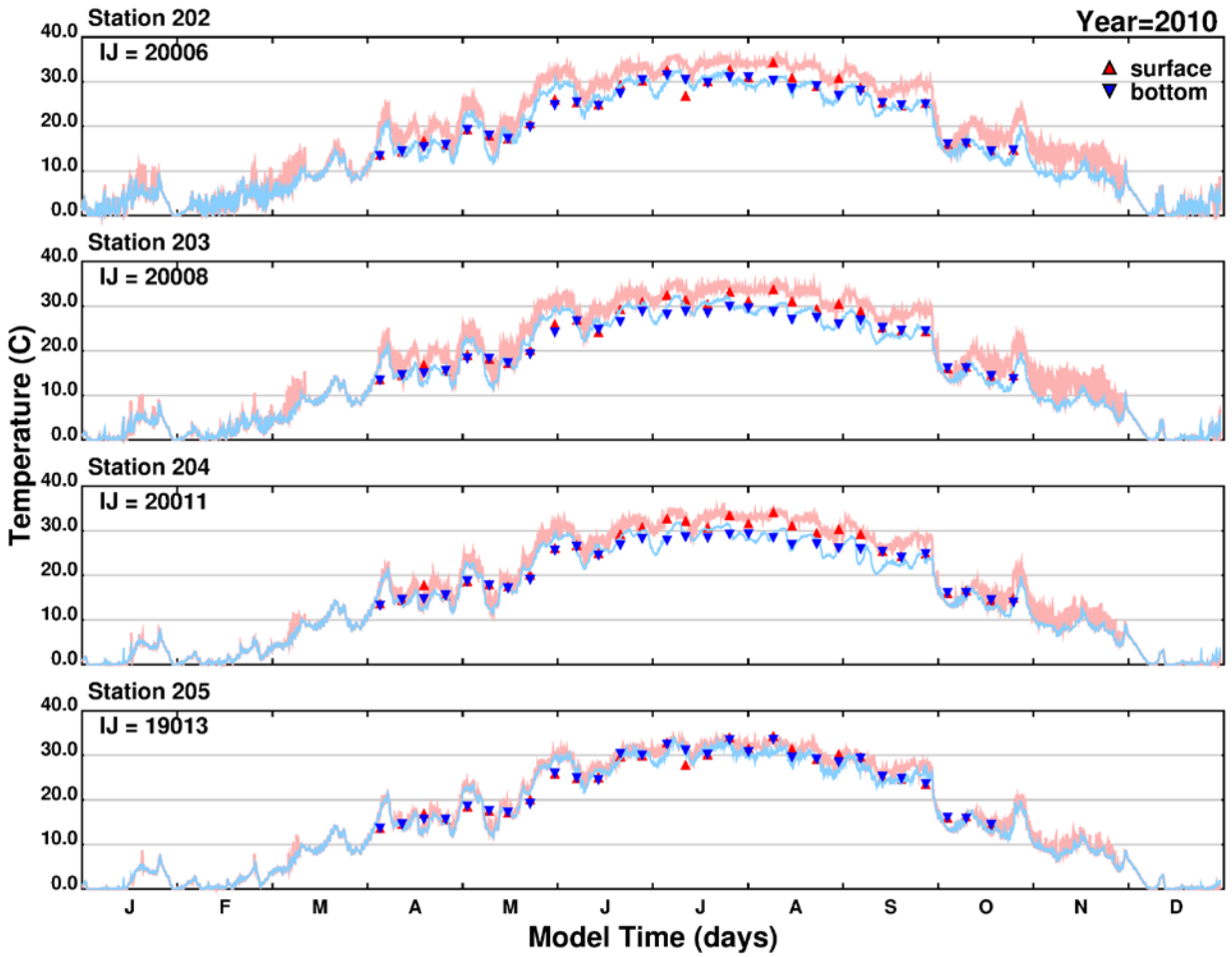


Note: Blue line = simulated near-bottom water temperature; Red line = simulated surface water temperature; Blue inverted triangle = measured near-bottom water temperature; Red triangle = measured surface water temperature; IJ indicates the model grid cell from which outputs were retrieved; x-axis divisions indicate a one character abbreviation for month of year in sequence from January through December; y-axis maximum indicates the approximate maximum temperature.

Figure 24. Simulated and measured water temperatures over time during 2010: Stations 202, 203, 204, and 205.

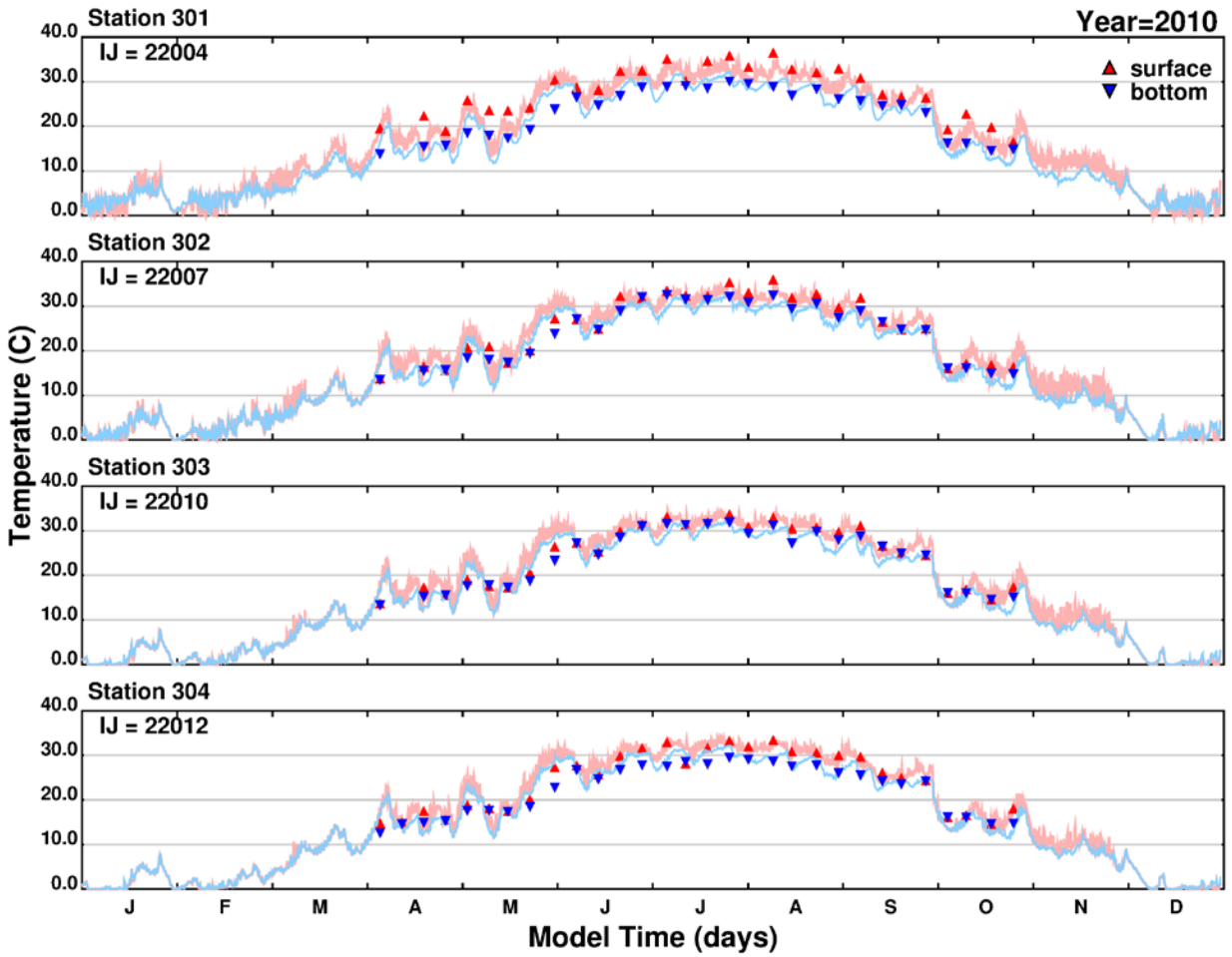


Note: Blue line = simulated near-bottom water temperature; Red line = simulated surface water temperature; Blue inverted triangle = measured near-bottom water temperature; Red triangle = measured surface water temperature; IJ indicates the model grid cell from which outputs were retrieved; x-axis divisions indicate a one character abbreviation for month of year in sequence from January through December; y-axis maximum indicates the approximate maximum temperature.

Figure 25. Simulated and measured water temperatures over time during 2010: Stations 301, 302, 303, and 304.

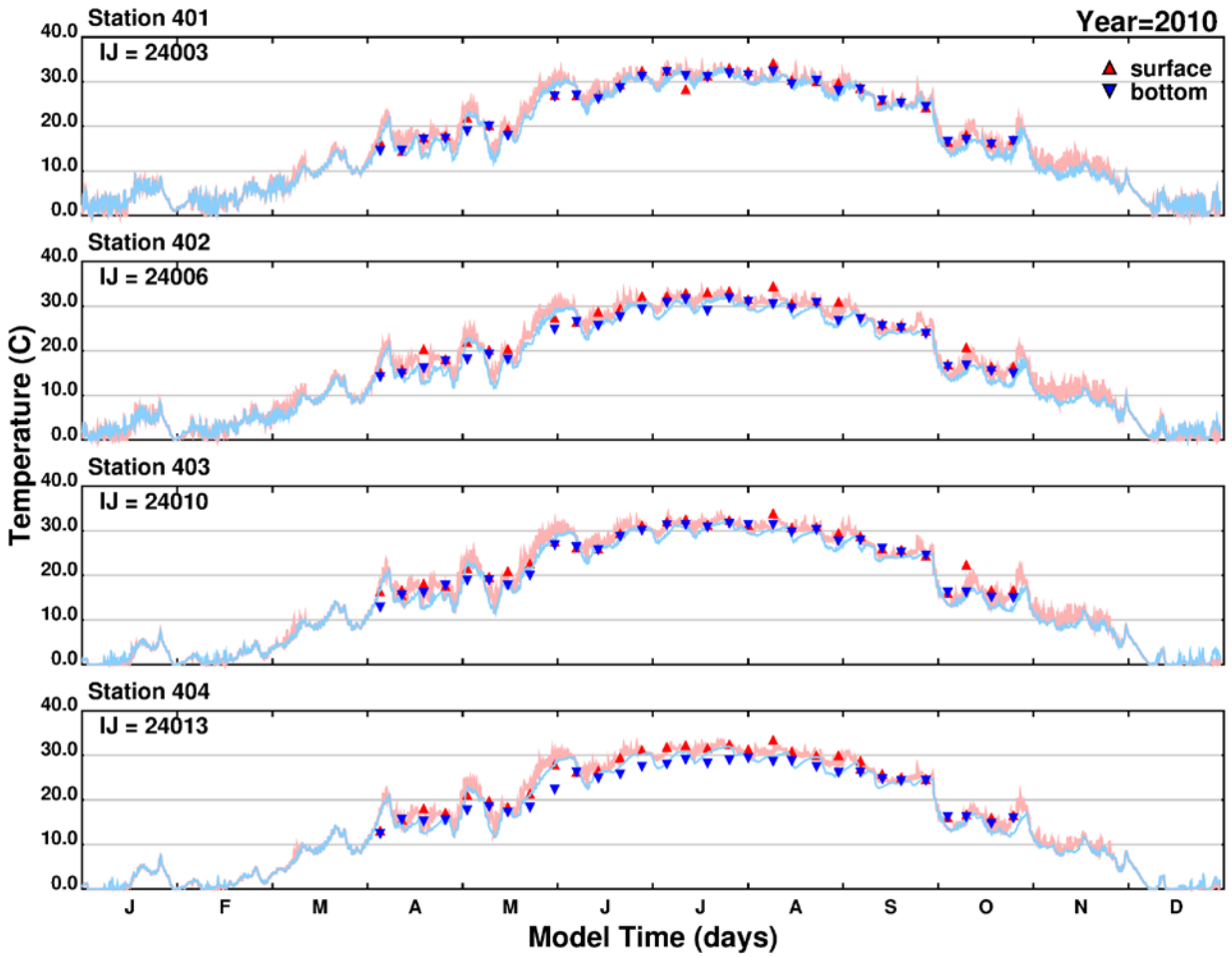


Note: Blue line = simulated near-bottom water temperature; Red line = simulated surface water temperature; Blue inverted triangle = measured near-bottom water temperature; Red triangle = measured surface water temperature; IJ indicates the model grid cell from which outputs were retrieved; x-axis divisions indicate a one character abbreviation for month of year in sequence from January through December; y-axis maximum indicates the approximate maximum temperature.

Figure 26. Simulated and measured water temperatures over time during 2010: Stations 401, 402, 403, and 404.

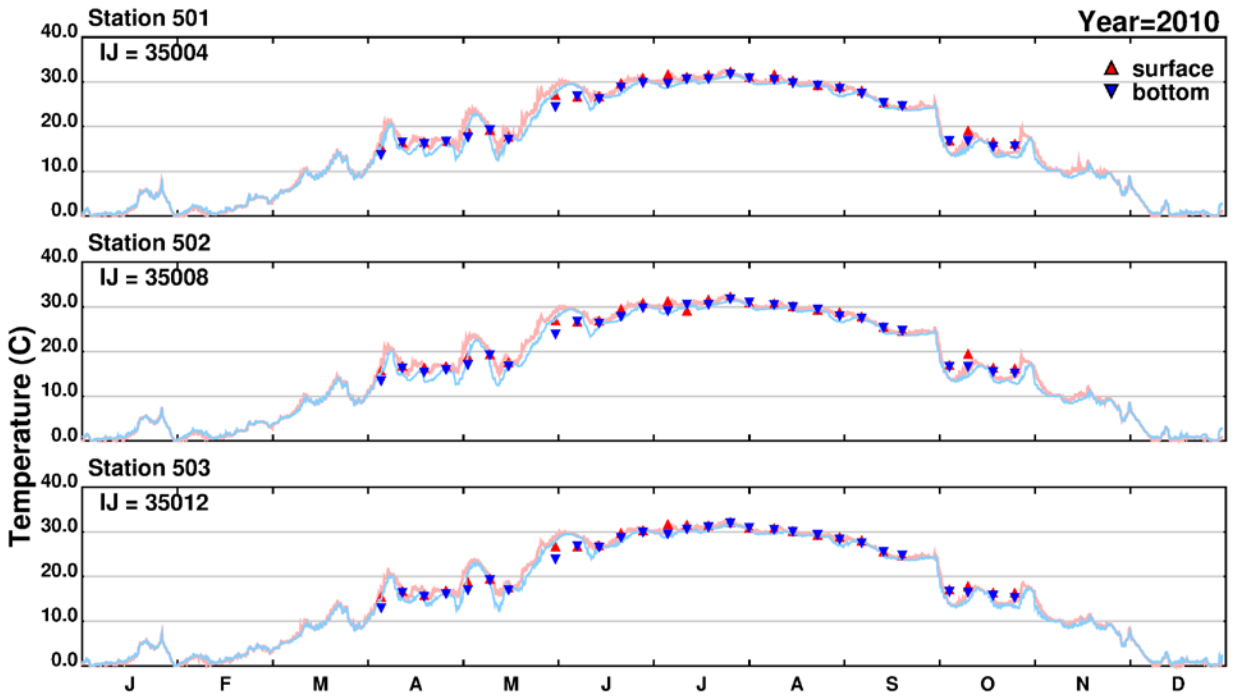


Note: Blue line = simulated near-bottom water temperature; Red line = simulated surface water temperature; Blue inverted triangle = measured near-bottom water temperature; Red triangle = measured surface water temperature; IJ indicates the model grid cell from which outputs were retrieved; x-axis divisions indicate a one character abbreviation for month of year in sequence from January through December; y-axis maximum indicates the approximate maximum temperature.

Figure 27. Simulated and measured water temperatures over time during 2010: Stations 501, 502, and 503.

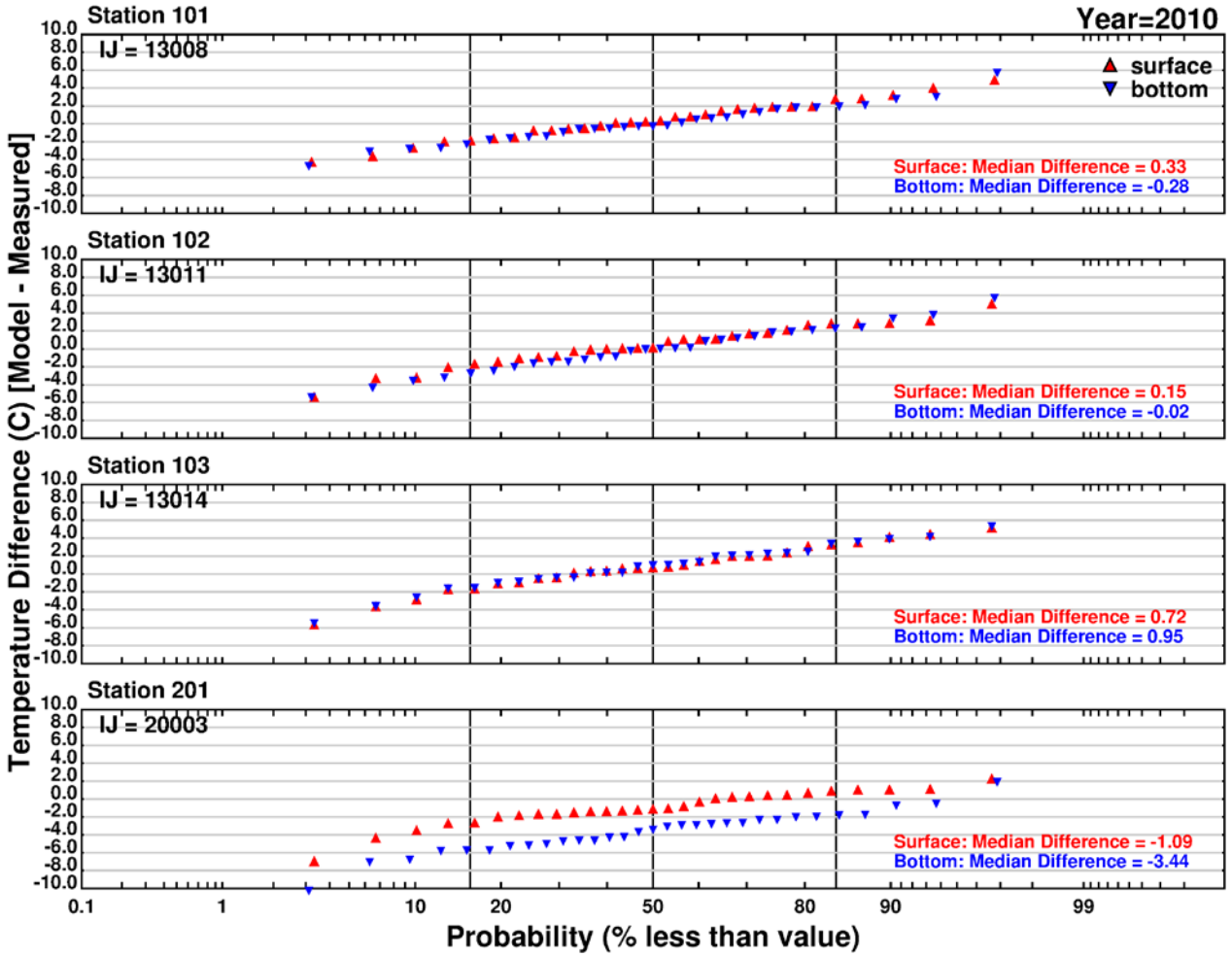


Note: Differences computed as simulated value minus measured value; IJ indicates the model grid cell from which outputs were retrieved.

Figure 28. Probability distributions of paired differences between simulated and measured water temperatures over time during 2010: Stations 101, 102, 103, and 201.

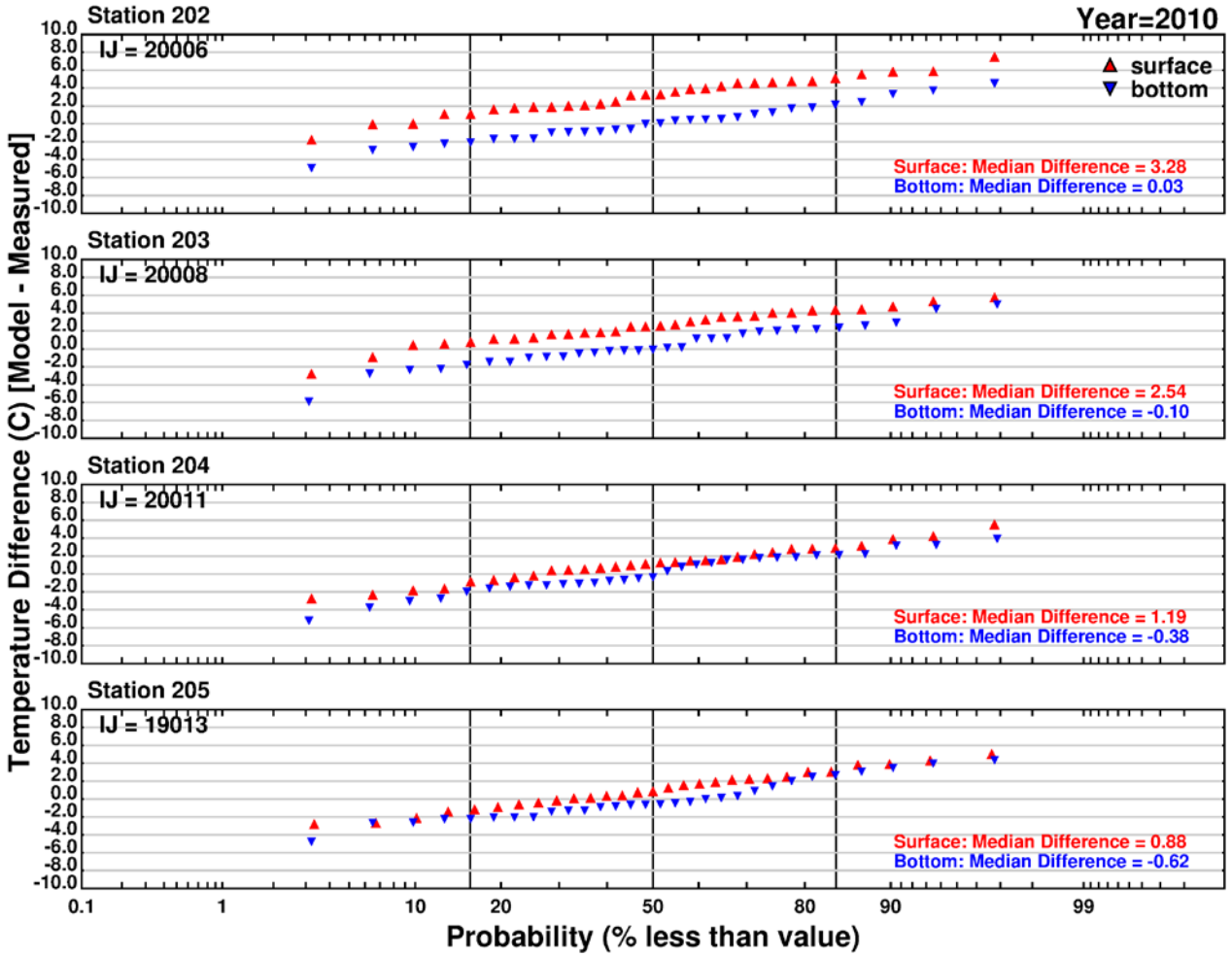


Note: Differences computed as simulated value minus measured value; IJ indicates the model grid cell from which outputs were retrieved.

Figure 29. Probability distributions of paired differences between simulated and measured water temperatures over time during 2010: Stations 202, 203, 204, and 205.

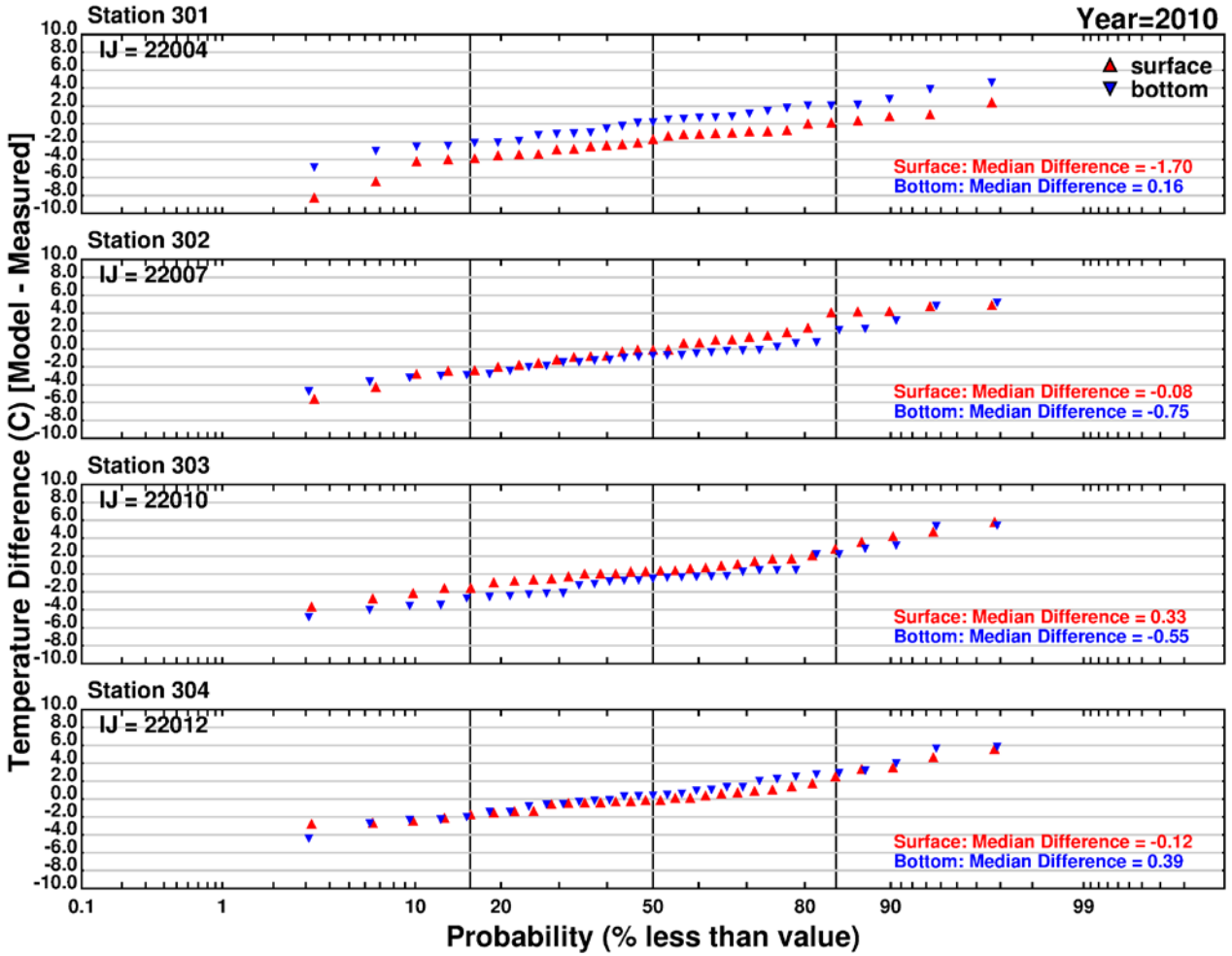


Note: Differences computed as simulated value minus measured value; IJ indicates the model grid cell from which outputs were retrieved.

Figure 30. Probability distributions of paired differences between simulated and measured water temperatures over time during 2010: Stations 301, 302, 303, and 304.

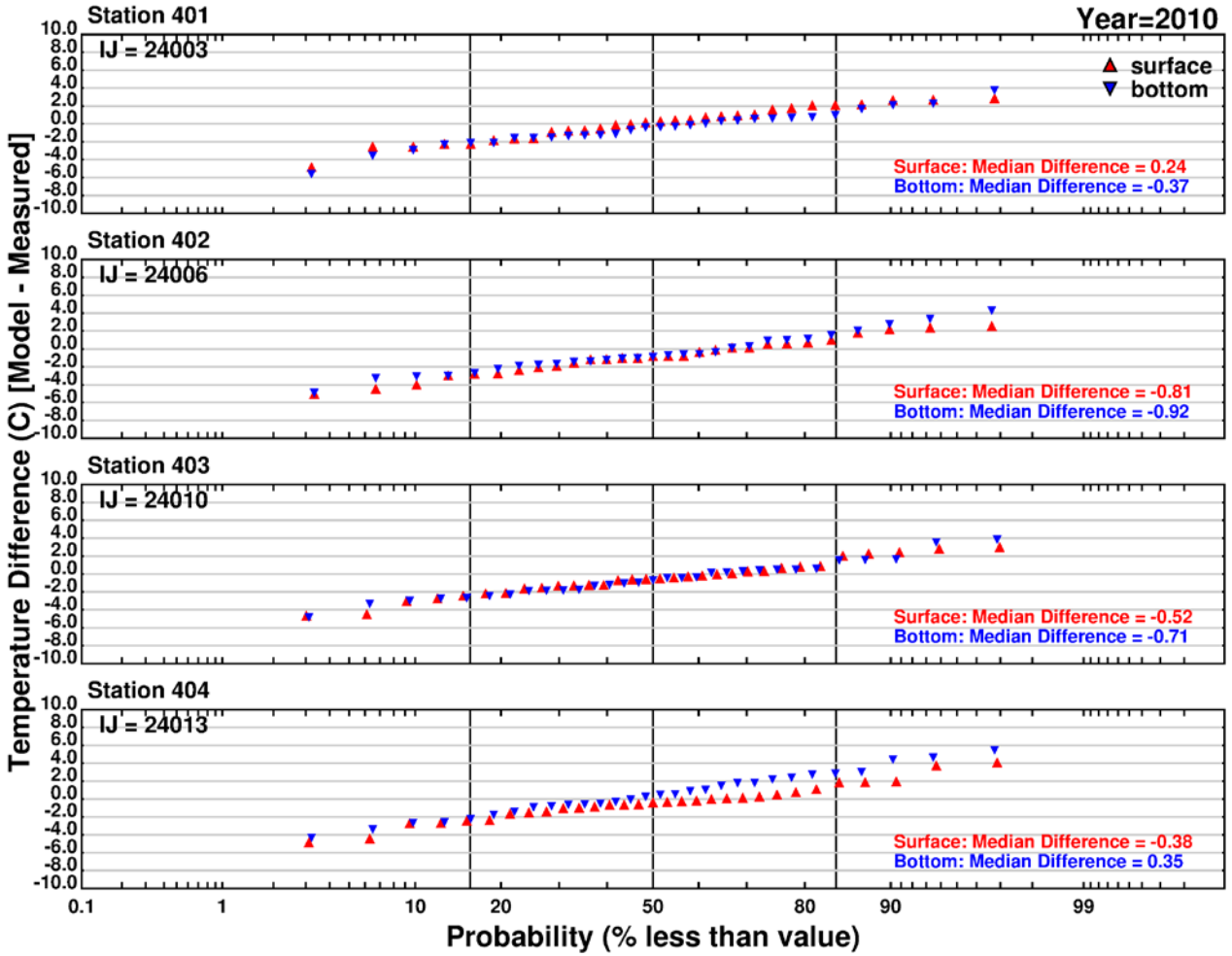


Note: Differences computed as simulated value minus measured value; IJ indicates the model grid cell from which outputs were retrieved.

Figure 31. Probability distributions of paired differences between simulated and measured water temperatures over time during 2010: Stations 401, 402, 403, and 404.

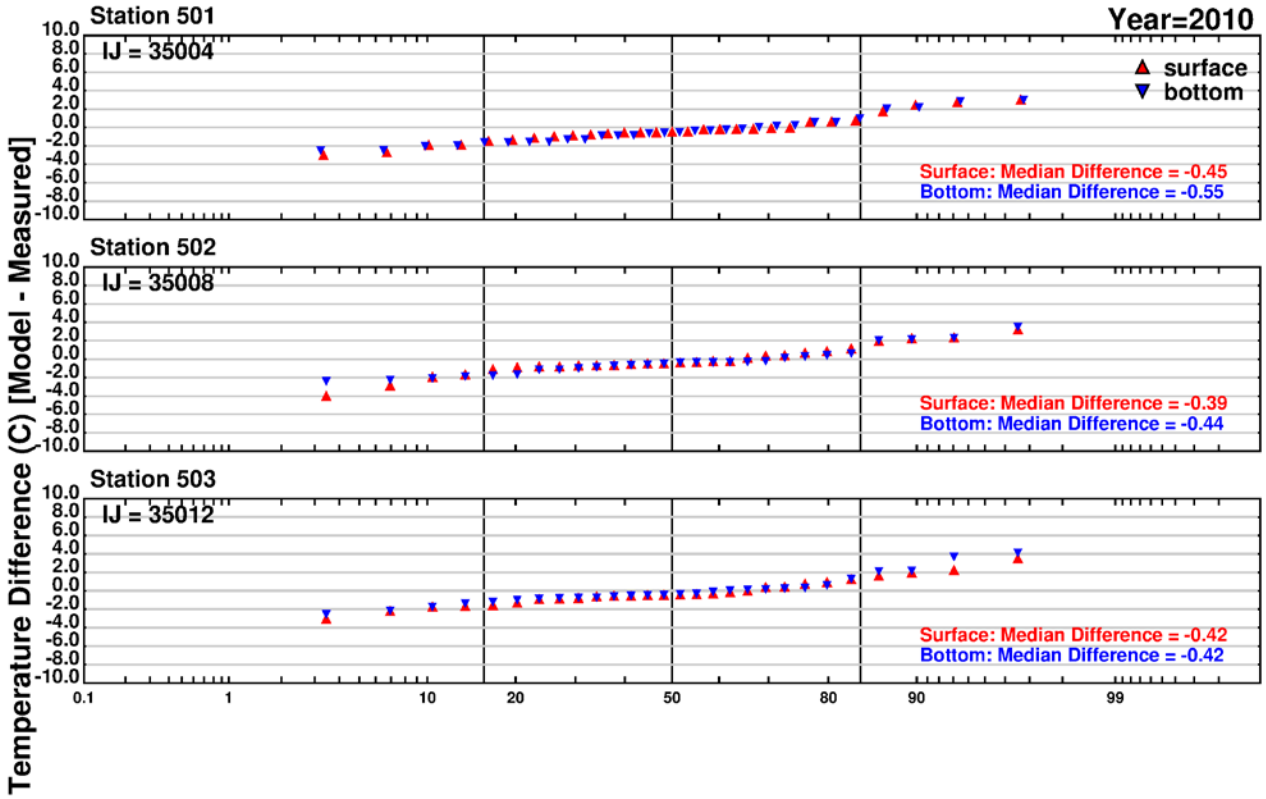


Note: Differences computed as simulated value minus measured value; IJ indicates the model grid cell from which outputs were retrieved.

Figure 32. Probability distributions of paired differences between simulated and measured water temperatures over time during 2010: Stations 501, 502, and 503.

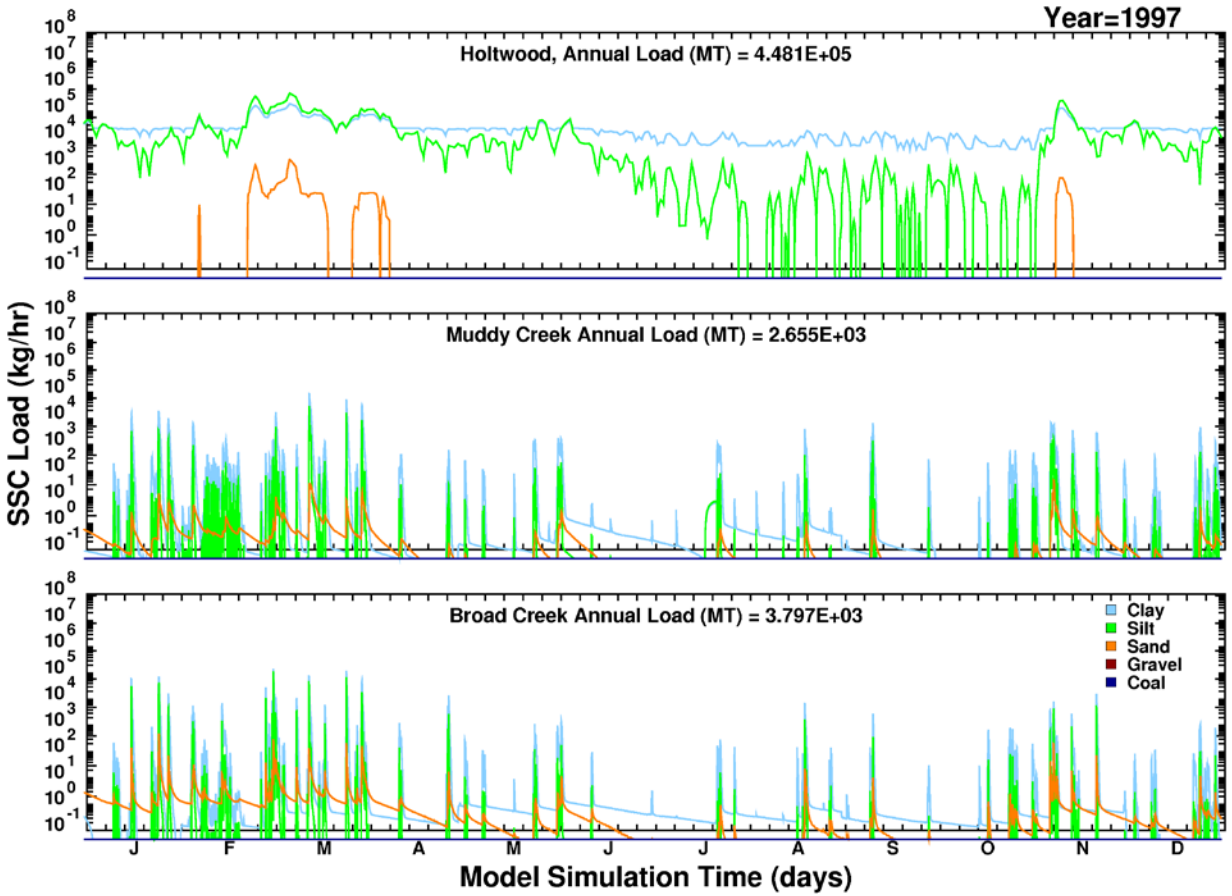


Note: Loads presented by solids class: clay, silt, sand, gravel, and coal; Clay concentrations (and loads) at Holtwood were adjusted so that the minimum SSC value would be 10 mg/L; Loads at Holtwood derived from WEST (2016) HEC-RAS results; Loads for Muddy Creek and Broad Creek specified from HSPF (P6B2) results; x-axis divisions indicate a one character abbreviation for month of year in sequence from January through December. Modulation that appears in loads beginning in October, 2007 reflects high frequency flow fluctuations that occur in in the USGS 15-minute flow measurements; Prior to October, 2007 flows used to calculate loads were daily average values linearly interpolated to hourly values.

Figure 33. Time series of solids loads entering Conowingo Pond at Holtwood, Muddy Creek, and Broad Creek: 1997.

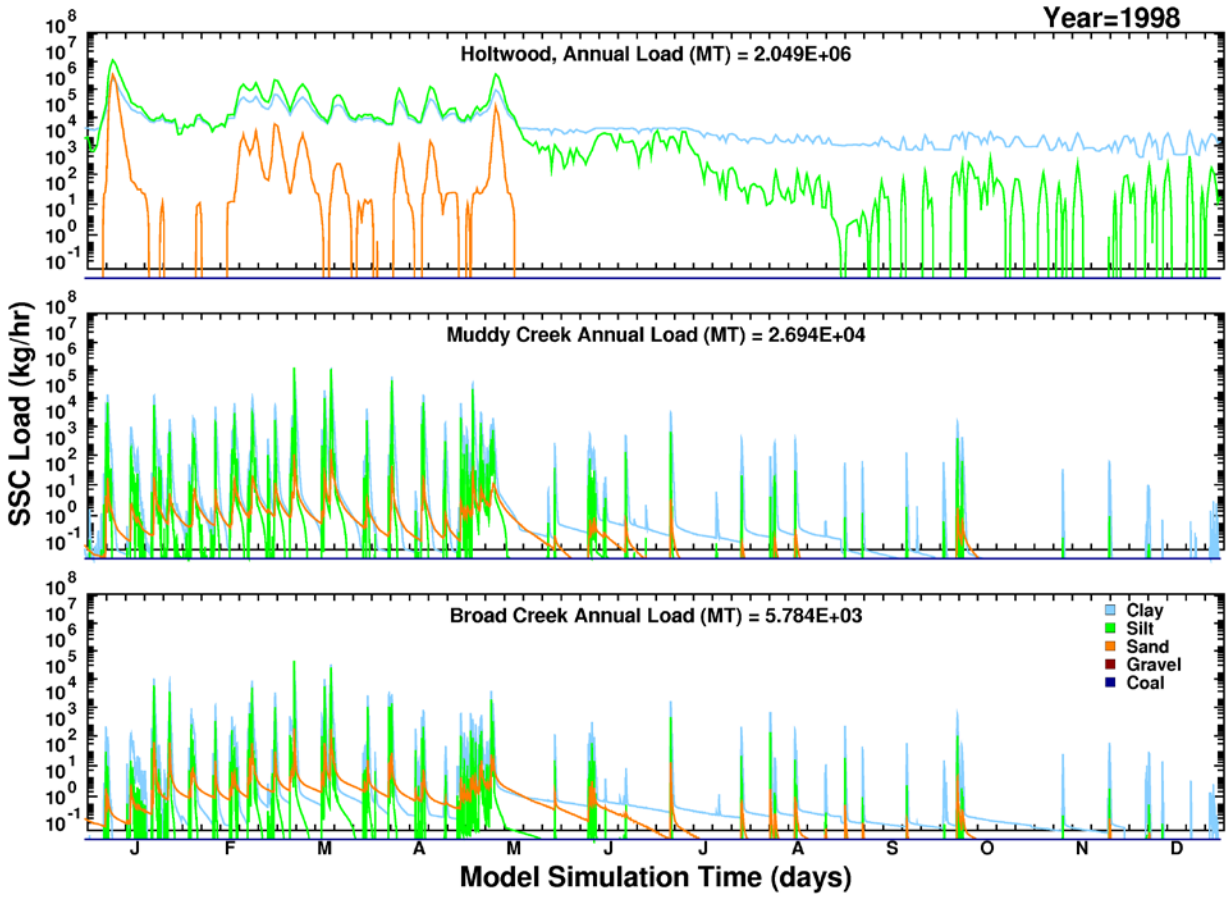


Note: Loads presented by solids class: clay, silt, sand, gravel, and coal; Clay concentrations (and loads) at Holtwood were adjusted so that the minimum SSC value would be 10 mg/L; Loads at Holtwood derived from WEST (2016) HEC-RAS results; Loads for Muddy Creek and Broad Creek specified from HSPF (P6B2) results; x-axis divisions indicate a one character abbreviation for month of year in sequence from January through December. Modulation that appears in loads beginning in October, 2007 reflects high frequency flow fluctuations that occur in in the USGS 15-minute flow measurements; Prior to October, 2007 flows used to calculate loads were daily average values linearly interpolated to hourly values.

Figure 34. Time series of solids loads entering Conowingo Pond at Holtwood, Muddy Creek, and Broad Creek: 1998.

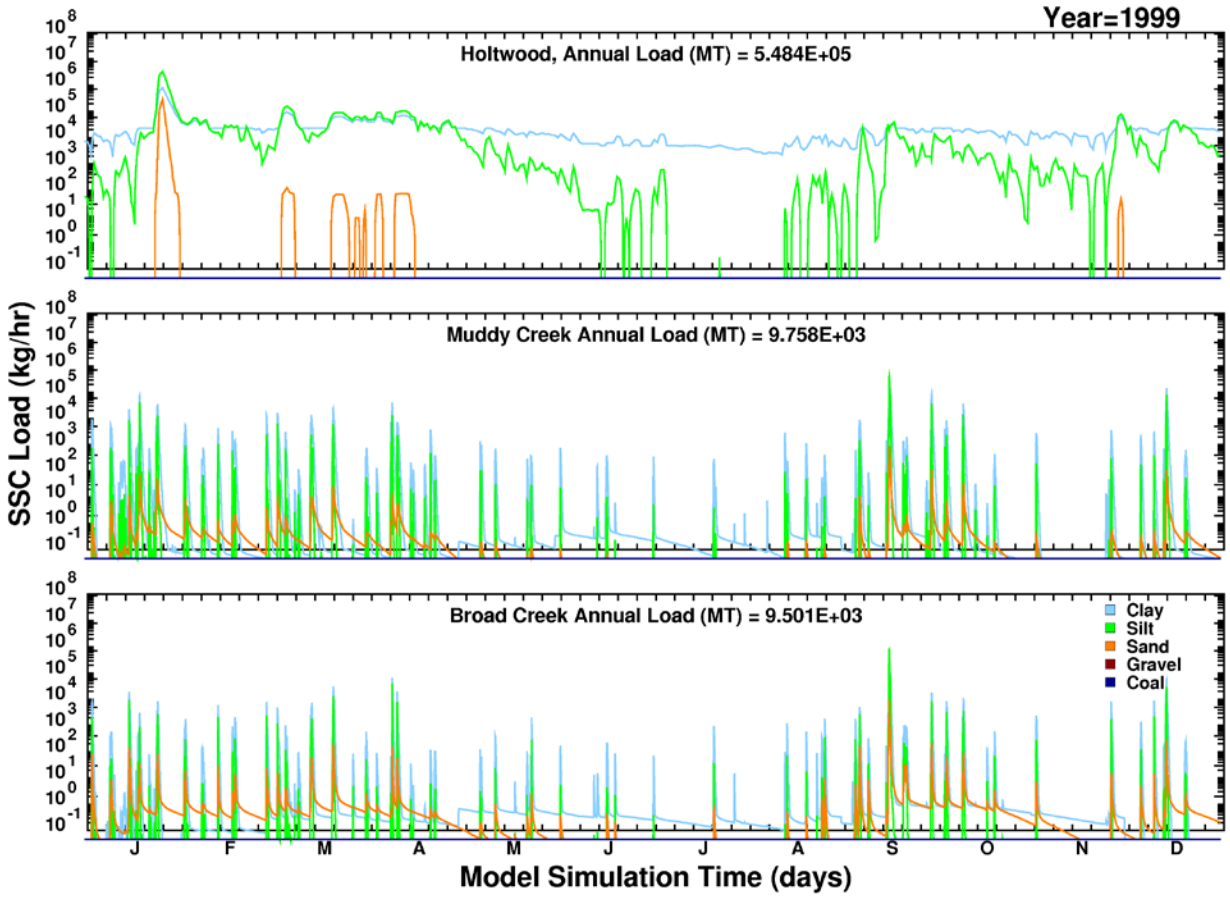


Note: Loads presented by solids class: clay, silt, sand, gravel, and coal; Clay concentrations (and loads) at Holtwood were adjusted so that the minimum SSC value would be 10 mg/L; Loads at Holtwood derived from WEST (2016) HEC-RAS results; Loads for Muddy Creek and Broad Creek specified from HSPF (P6B2) results; x-axis divisions indicate a one character abbreviation for month of year in sequence from January through December. Modulation that appears in loads beginning in October, 2007 reflects high frequency flow fluctuations that occur in in the USGS 15-minute flow measurements; Prior to October, 2007 flows used to calculate loads were daily average values linearly interpolated to hourly values.

Figure 35. Time series of solids loads entering Conowingo Pond at Holtwood, Muddy Creek, and Broad Creek: 1999.

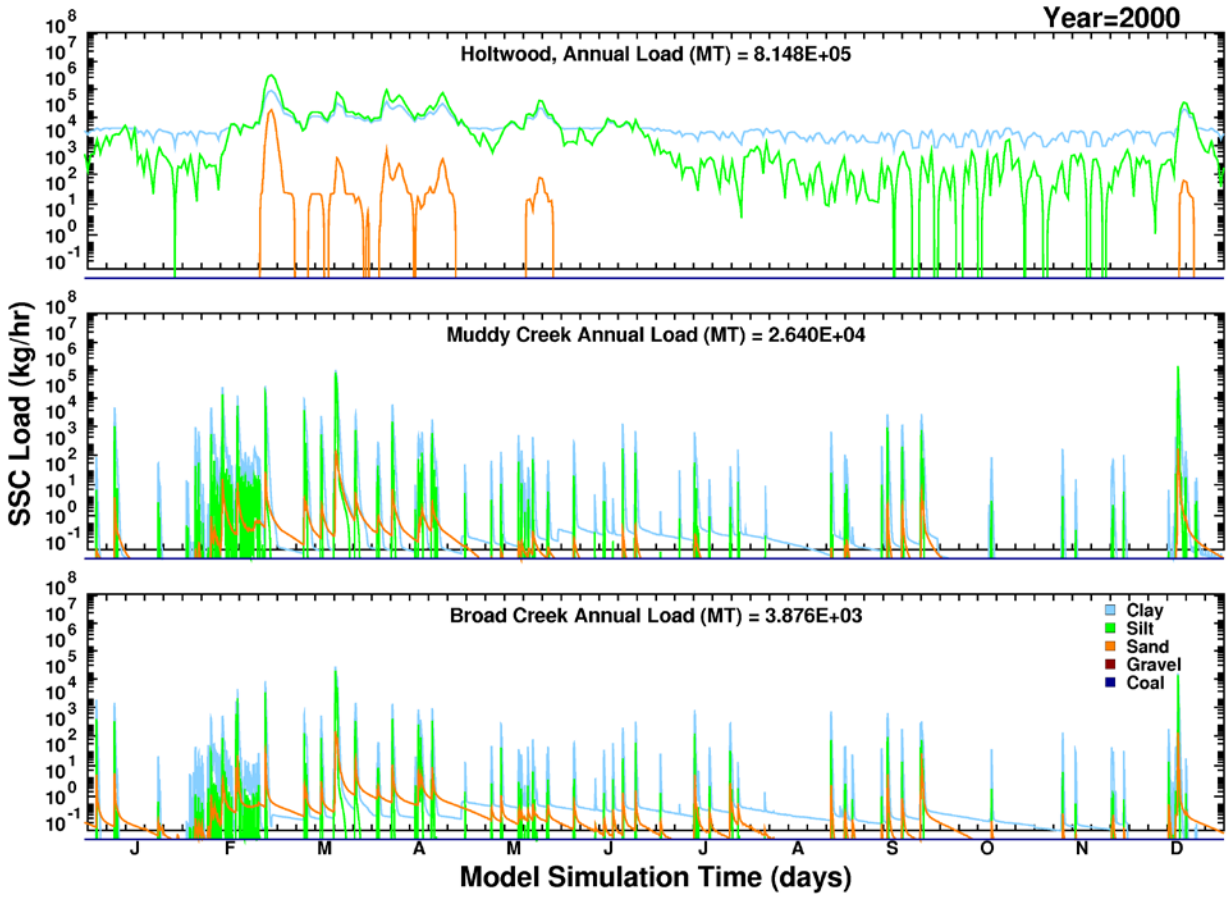


Note: Loads presented by solids class: clay, silt, sand, gravel, and coal; Clay concentrations (and loads) at Holtwood were adjusted so that the minimum SSC value would be 10 mg/L; Loads at Holtwood derived from WEST (2016) HEC-RAS results; Loads for Muddy Creek and Broad Creek specified from HSPF (P6B2) results; x-axis divisions indicate a one character abbreviation for month of year in sequence from January through December. Modulation that appears in loads beginning in October, 2007 reflects high frequency flow fluctuations that occur in in the USGS 15-minute flow measurements; Prior to October, 2007 flows used to calculate loads were daily average values linearly interpolated to hourly values.

Figure 36. Time series of solids loads entering Conowingo Pond at Holtwood, Muddy Creek, and Broad Creek: 2000.

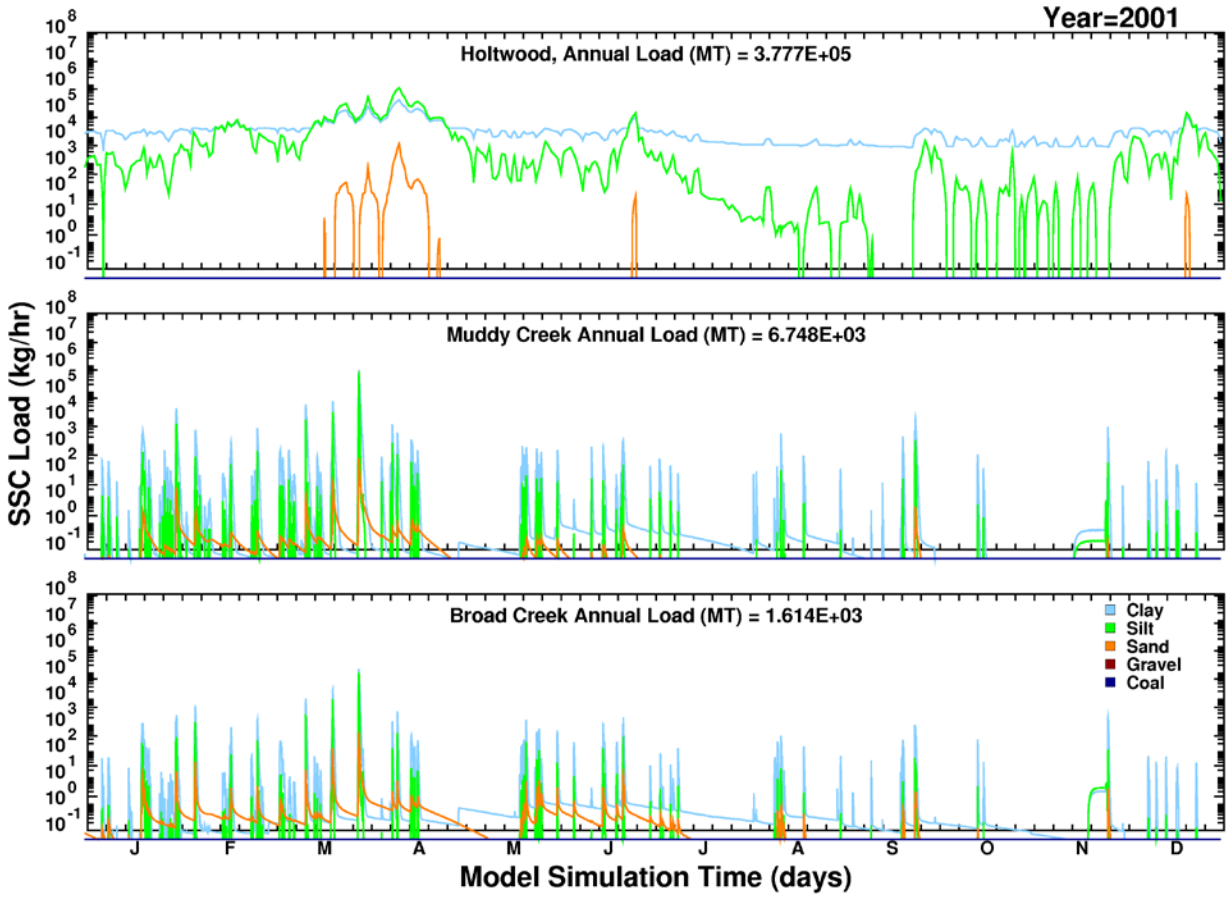


Note: Loads presented by solids class: clay, silt, sand, gravel, and coal; Clay concentrations (and loads) at Holtwood were adjusted so that the minimum SSC value would be 10 mg/L; Loads at Holtwood derived from WEST (2016) HEC-RAS results; Loads for Muddy Creek and Broad Creek specified from HSPF (P6B2) results; x-axis divisions indicate a one character abbreviation for month of year in sequence from January through December. Modulation that appears in loads beginning in October, 2007 reflects high frequency flow fluctuations that occur in in the USGS 15-minute flow measurements; Prior to October, 2007 flows used to calculate loads were daily average values linearly interpolated to hourly values.

Figure 37. Time series of solids loads entering Conowingo Pond at Holtwood, Muddy Creek, and Broad Creek: 2001.

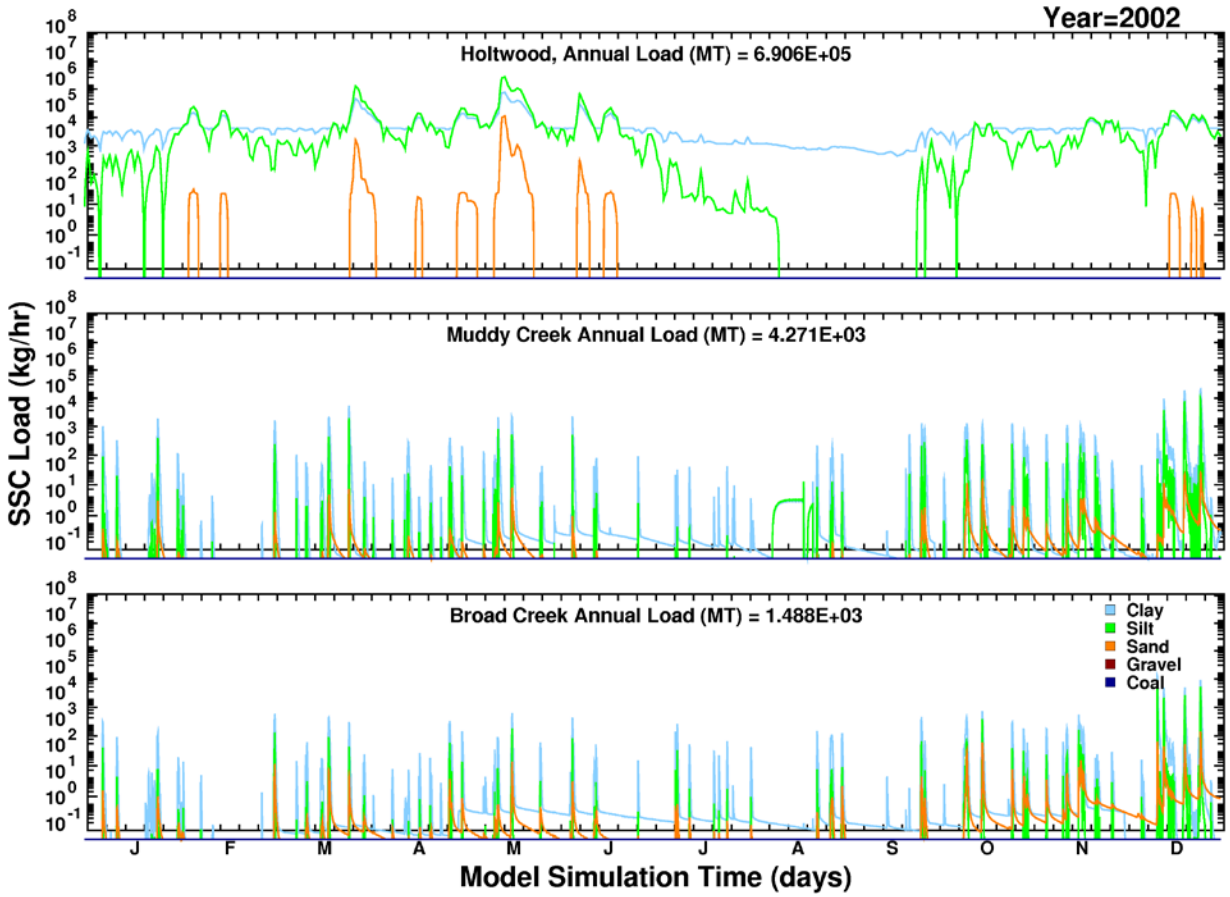


Note: Loads presented by solids class: clay, silt, sand, gravel, and coal; Clay concentrations (and loads) at Holtwood were adjusted so that the minimum SSC value would be 10 mg/L; Loads at Holtwood derived from WEST (2016) HEC-RAS results; Loads for Muddy Creek and Broad Creek specified from HSPF (P6B2) results; x-axis divisions indicate a one character abbreviation for month of year in sequence from January through December. Modulation that appears in loads beginning in October, 2007 reflects high frequency flow fluctuations that occur in in the USGS 15-minute flow measurements; Prior to October, 2007 flows used to calculate loads were daily average values linearly interpolated to hourly values.

Figure 38. Time series of solids loads entering Conowingo Pond at Holtwood, Muddy Creek, and Broad Creek: 2002.

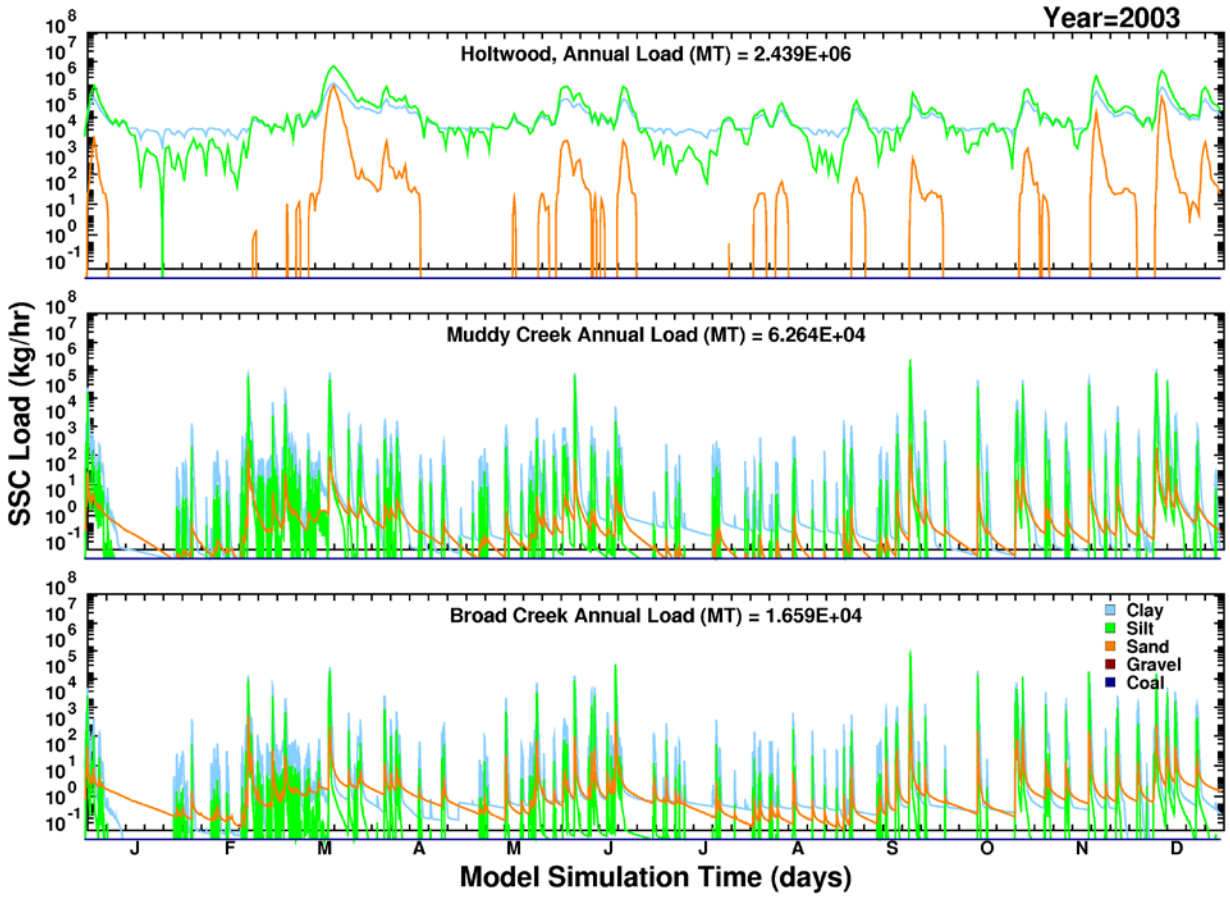


Note: Loads presented by solids class: clay, silt, sand, gravel, and coal; Clay concentrations (and loads) at Holtwood were adjusted so that the minimum SSC value would be 10 mg/L; Loads at Holtwood derived from WEST (2016) HEC-RAS results; Loads for Muddy Creek and Broad Creek specified from HSPF (P6B2) results; x-axis divisions indicate a one character abbreviation for month of year in sequence from January through December. Modulation that appears in loads beginning in October, 2007 reflects high frequency flow fluctuations that occur in in the USGS 15-minute flow measurements; Prior to October, 2007 flows used to calculate loads were daily average values linearly interpolated to hourly values.

Figure 39. Time series of solids loads entering Conowingo Pond at Holtwood, Muddy Creek, and Broad Creek: 2003.

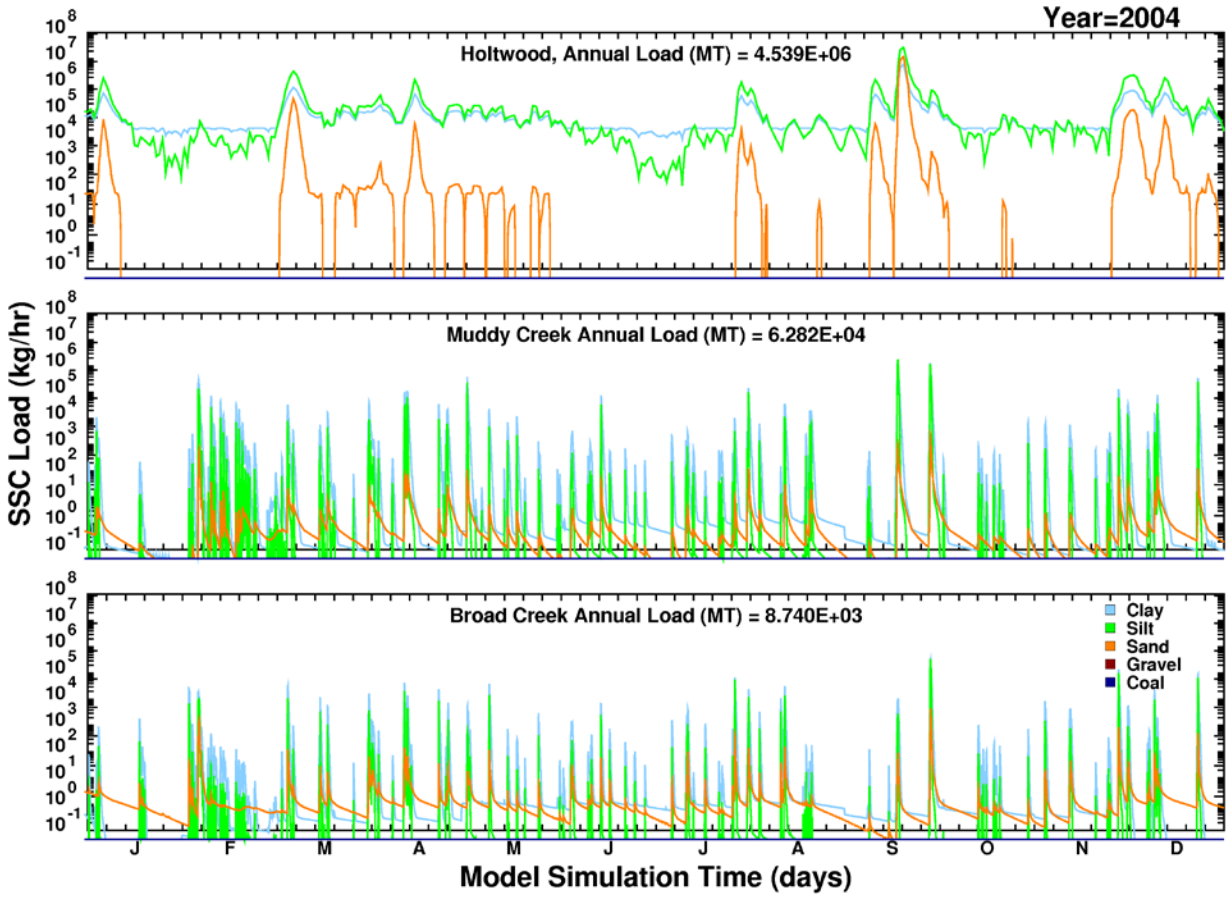


Note: Loads presented by solids class: clay, silt, sand, gravel, and coal; Clay concentrations (and loads) at Holtwood were adjusted so that the minimum SSC value would be 10 mg/L; Loads at Holtwood derived from WEST (2016) HEC-RAS results; Loads for Muddy Creek and Broad Creek specified from HSPF (P6B2) results; x-axis divisions indicate a one character abbreviation for month of year in sequence from January through December. Modulation that appears in loads beginning in October, 2007 reflects high frequency flow fluctuations that occur in in the USGS 15-minute flow measurements; Prior to October, 2007 flows used to calculate loads were daily average values linearly interpolated to hourly values.

Figure 40. Time series of solids loads entering Conowingo Pond at Holtwood, Muddy Creek, and Broad Creek: 2004.

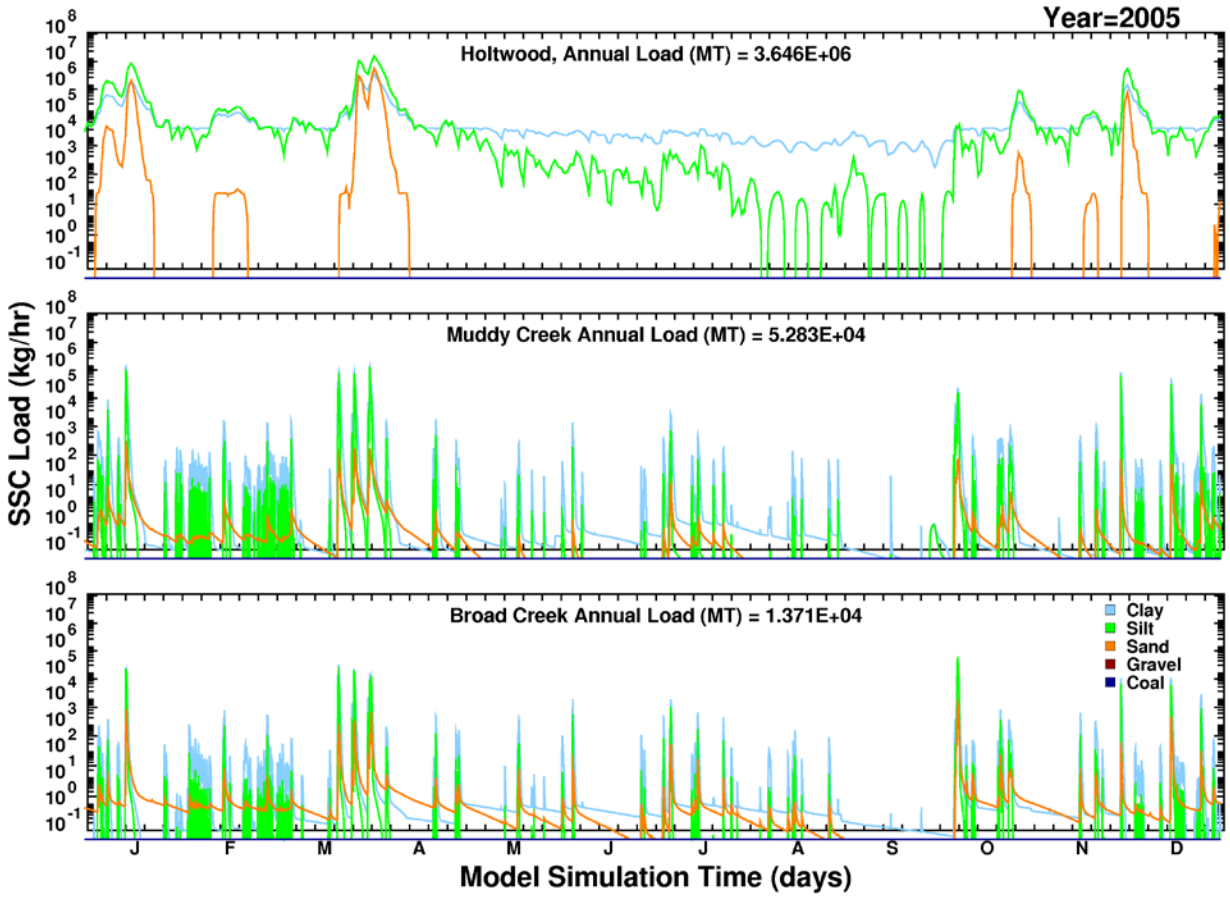


Note: Loads presented by solids class: clay, silt, sand, gravel, and coal; Clay concentrations (and loads) at Holtwood were adjusted so that the minimum SSC value would be 10 mg/L; Loads at Holtwood derived from WEST (2016) HEC-RAS results; Loads for Muddy Creek and Broad Creek specified from HSPF (P6B2) results; x-axis divisions indicate a one character abbreviation for month of year in sequence from January through December. Modulation that appears in loads beginning in October, 2007 reflects high frequency flow fluctuations that occur in in the USGS 15-minute flow measurements; Prior to October, 2007 flows used to calculate loads were daily average values linearly interpolated to hourly values.

Figure 41. Time series of solids loads entering Conowingo Pond at Holtwood, Muddy Creek, and Broad Creek: 2005.

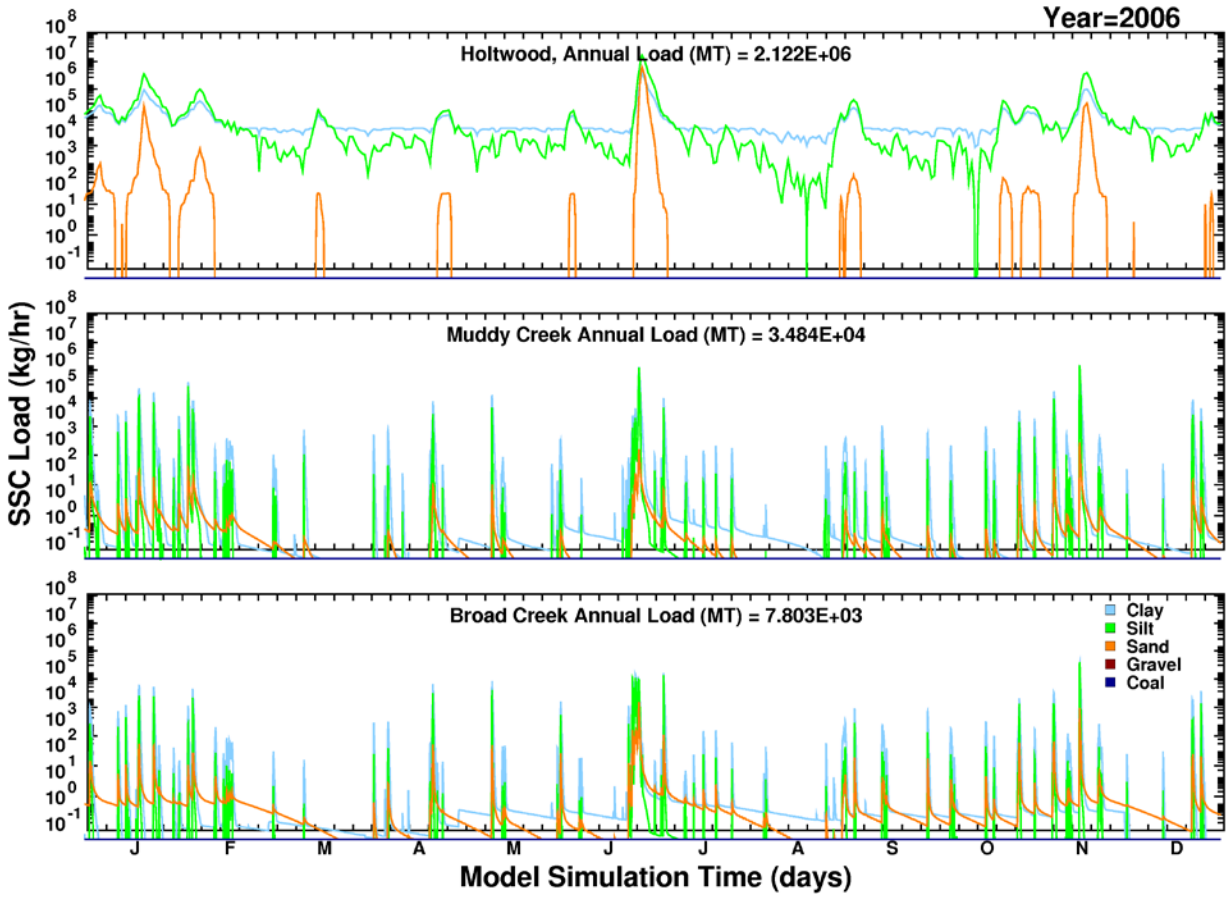


Note: Loads presented by solids class: clay, silt, sand, gravel, and coal; Clay concentrations (and loads) at Holtwood were adjusted so that the minimum SSC value would be 10 mg/L; Loads at Holtwood derived from WEST (2016) HEC-RAS results; Loads for Muddy Creek and Broad Creek specified from HSPF (P6B2) results; x-axis divisions indicate a one character abbreviation for month of year in sequence from January through December. Modulation that appears in loads beginning in October, 2007 reflects high frequency flow fluctuations that occur in in the USGS 15-minute flow measurements; Prior to October, 2007 flows used to calculate loads were daily average values linearly interpolated to hourly values.

Figure 42. Time series of solids loads entering Conowingo Pond at Holtwood, Muddy Creek, and Broad Creek: 2006.

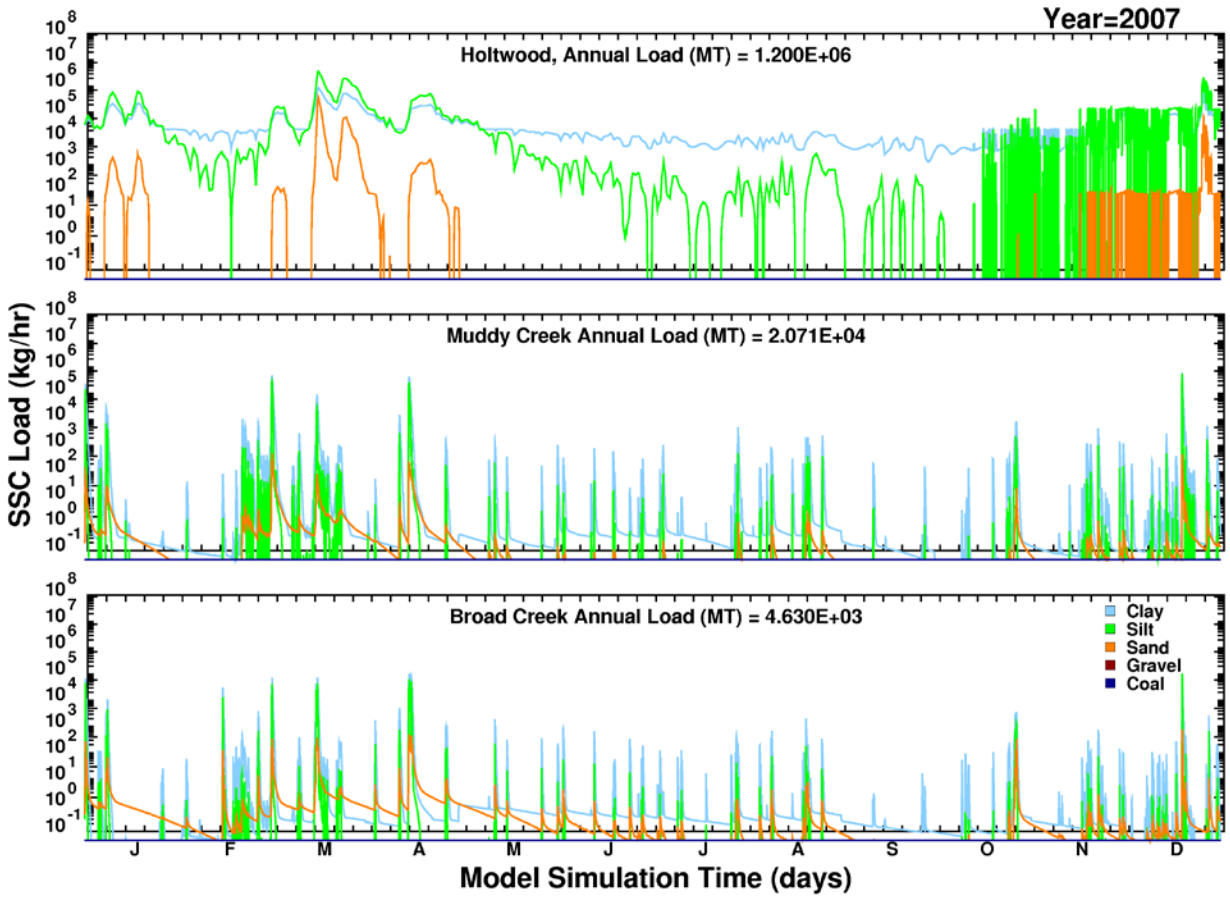


Note: Loads presented by solids class: clay, silt, sand, gravel, and coal; Clay concentrations (and loads) at Holtwood were adjusted so that the minimum SSC value would be 10 mg/L; Loads at Holtwood derived from WEST (2016) HEC-RAS results; Loads for Muddy Creek and Broad Creek specified from HSPF (P6B2) results; x-axis divisions indicate a one character abbreviation for month of year in sequence from January through December. Modulation that appears in loads beginning in October, 2007 reflects high frequency flow fluctuations that occur in in the USGS 15-minute flow measurements; Prior to October, 2007 flows used to calculate loads were daily average values linearly interpolated to hourly values.

Figure 43. Time series of solids loads entering Conowingo Pond at Holtwood, Muddy Creek, and Broad Creek: 2007.

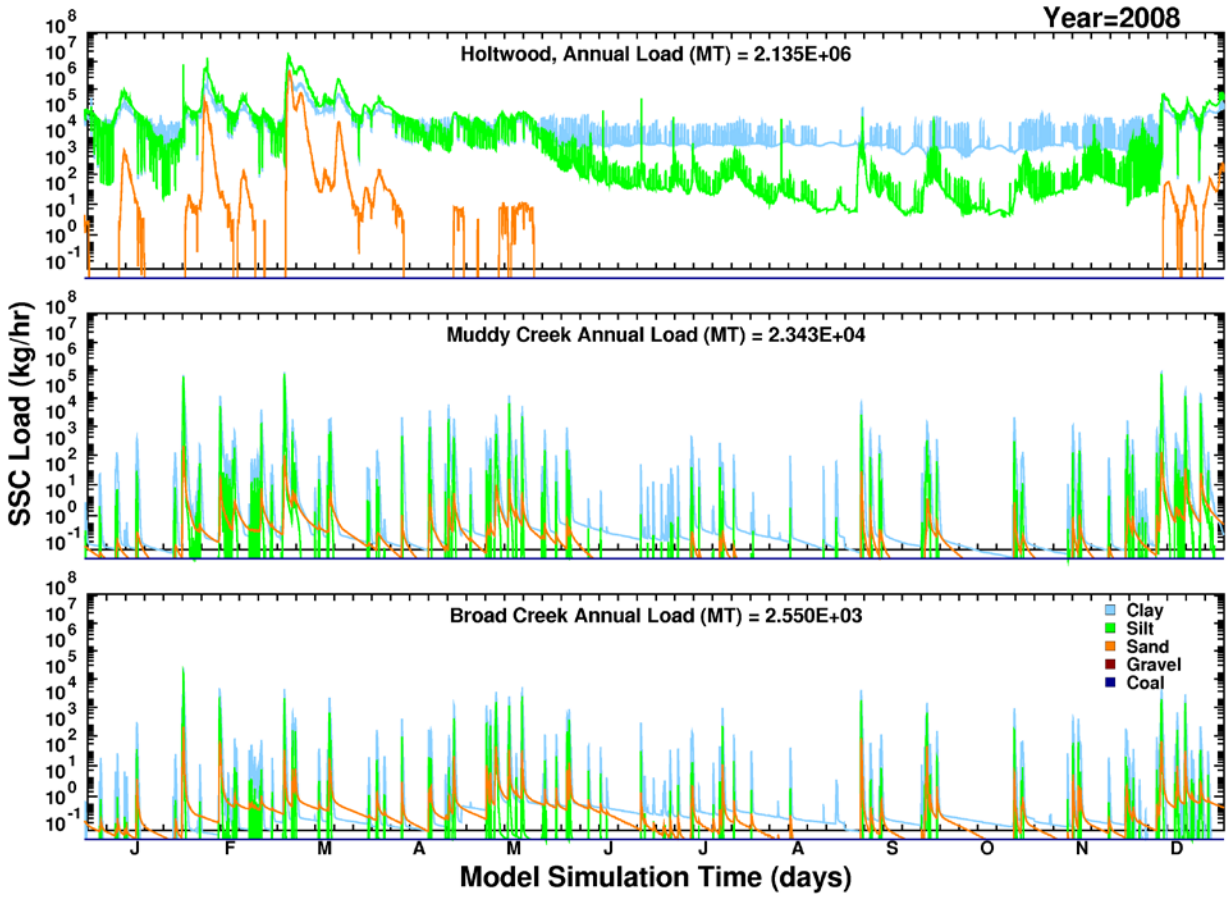


Note: Loads presented by solids class: clay, silt, sand, gravel, and coal; Clay concentrations (and loads) at Holtwood were adjusted so that the minimum SSC value would be 10 mg/L; Loads at Holtwood derived from WEST (2016) HEC-RAS results; Loads for Muddy Creek and Broad Creek specified from HSPF (P6B2) results; x-axis divisions indicate a one character abbreviation for month of year in sequence from January through December. Modulation that appears in loads beginning in October, 2007 reflects high frequency flow fluctuations that occur in in the USGS 15-minute flow measurements; Prior to October, 2007 flows used to calculate loads were daily average values linearly interpolated to hourly values.

Figure 44. Time series of solids loads entering Conowingo Pond at Holtwood, Muddy Creek, and Broad Creek: 2008.

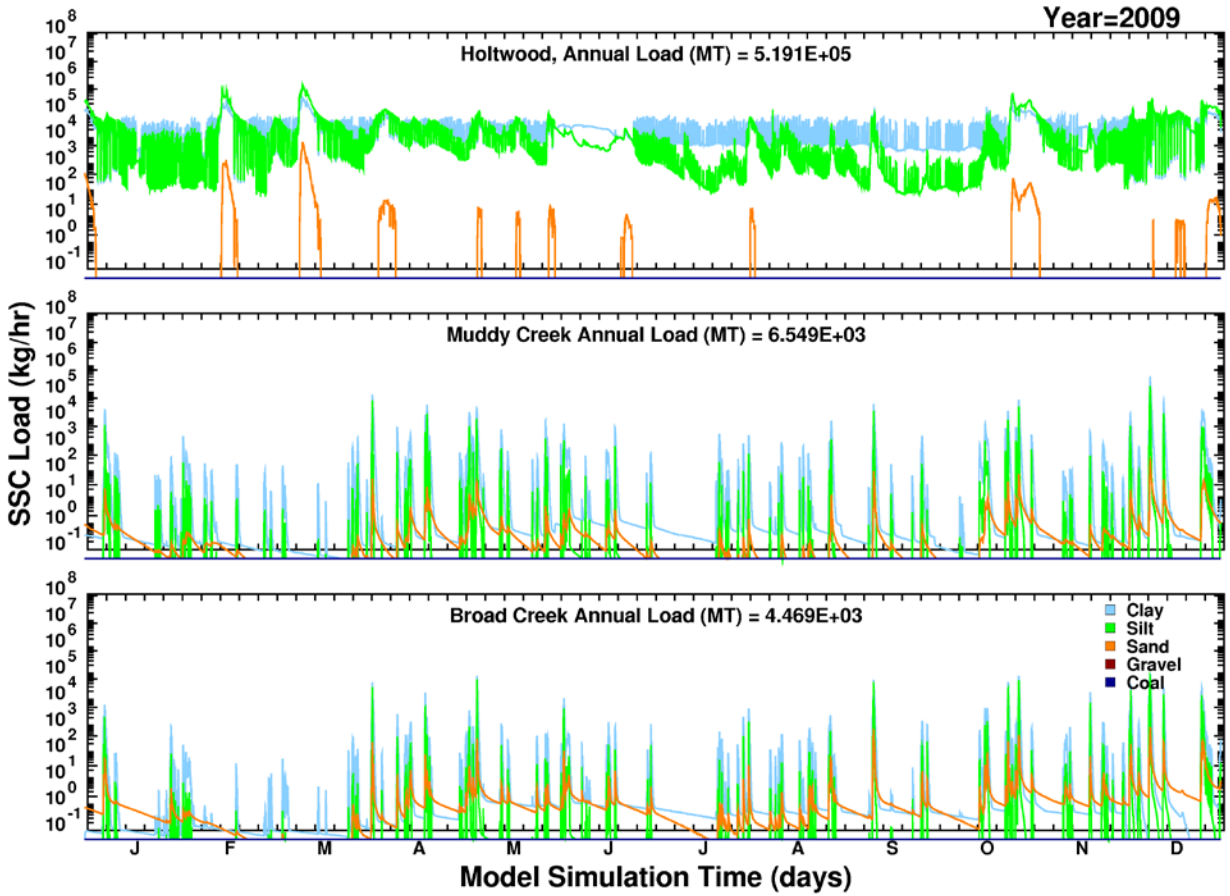


Note: Loads presented by solids class: clay, silt, sand, gravel, and coal; Clay concentrations (and loads) at Holtwood were adjusted so that the minimum SSC value would be 10 mg/L; Loads at Holtwood derived from WEST (2016) HEC-RAS results; Loads for Muddy Creek and Broad Creek specified from HSPF (P6B2) results; x-axis divisions indicate a one character abbreviation for month of year in sequence from January through December. Modulation that appears in loads beginning in October, 2007 reflects high frequency flow fluctuations that occur in in the USGS 15-minute flow measurements; Prior to October, 2007 flows used to calculate loads were daily average values linearly interpolated to hourly values.

Figure 45. Time series of solids loads entering Conowingo Pond at Holtwood, Muddy Creek, and Broad Creek: 2009.

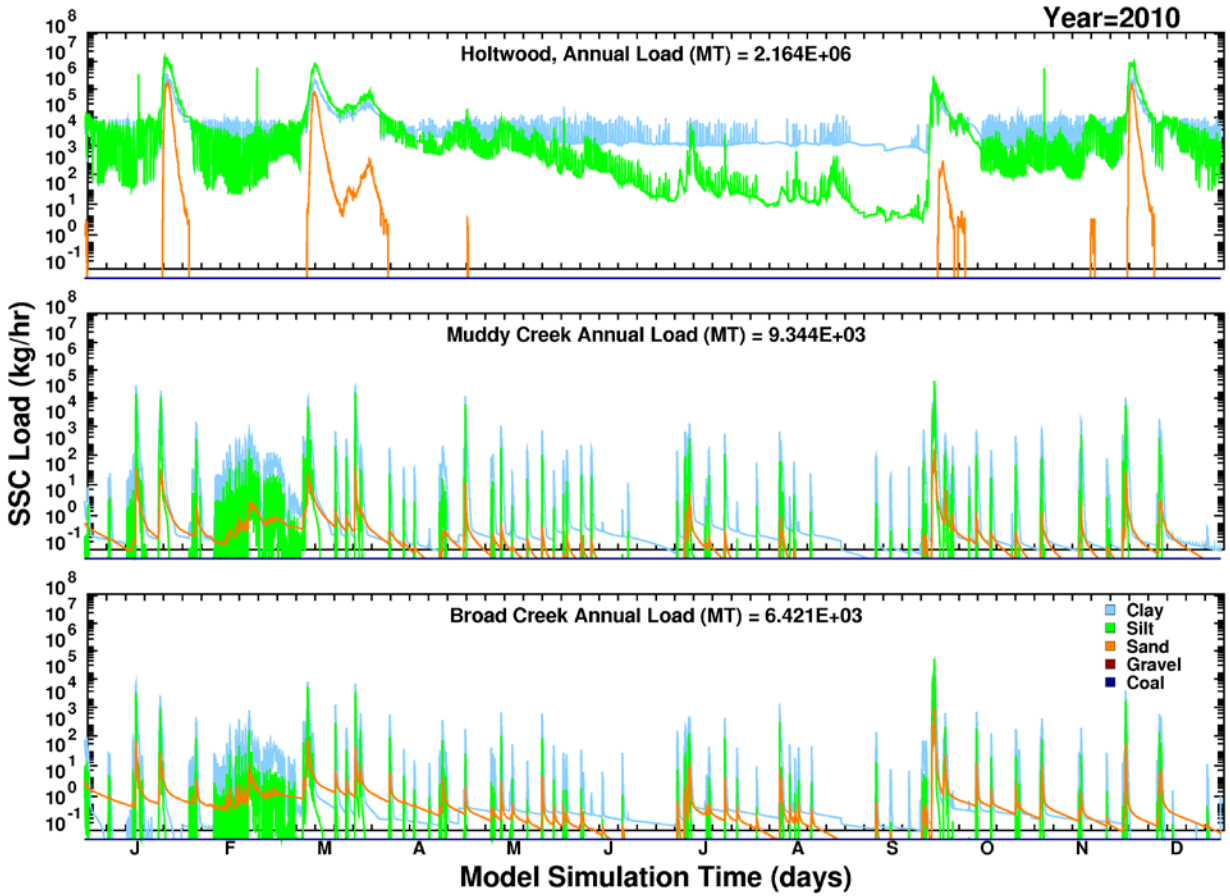


Note: Loads presented by solids class: clay, silt, sand, gravel, and coal; Clay concentrations (and loads) at Holtwood were adjusted so that the minimum SSC value would be 10 mg/L; Loads at Holtwood derived from WEST (2016) HEC-RAS results; Loads for Muddy Creek and Broad Creek specified from HSPF (P6B2) results; x-axis divisions indicate a one character abbreviation for month of year in sequence from January through December. Modulation that appears in loads beginning in October, 2007 reflects high frequency flow fluctuations that occur in in the USGS 15-minute flow measurements; Prior to October, 2007 flows used to calculate loads were daily average values linearly interpolated to hourly values.

Figure 46. Time series of solids loads entering Conowingo Pond at Holtwood, Muddy Creek, and Broad Creek: 2010.

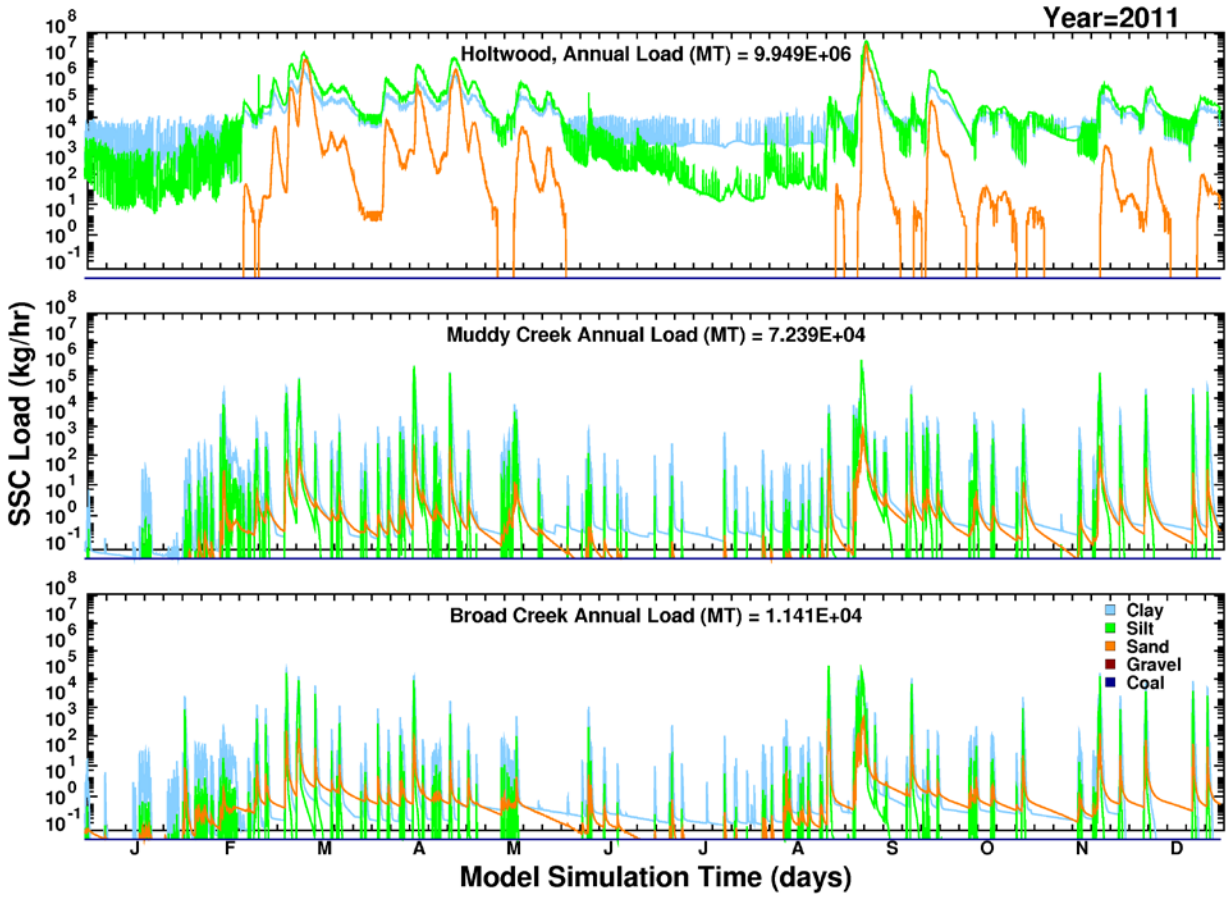


Note: Loads presented by solids class: clay, silt, sand, gravel, and coal; Clay concentrations (and loads) at Holtwood were adjusted so that the minimum SSC value would be 10 mg/L; Loads at Holtwood derived from WEST (2016) HEC-RAS results; Loads for Muddy Creek and Broad Creek specified from HSPF (P6B2) results; x-axis divisions indicate a one character abbreviation for month of year in sequence from January through December. Modulation that appears in loads beginning in October, 2007 reflects high frequency flow fluctuations that occur in in the USGS 15-minute flow measurements; Prior to October, 2007 flows used to calculate loads were daily average values linearly interpolated to hourly values.

Figure 47. Time series of solids loads entering Conowingo Pond at Holtwood, Muddy Creek, and Broad Creek: 2011.

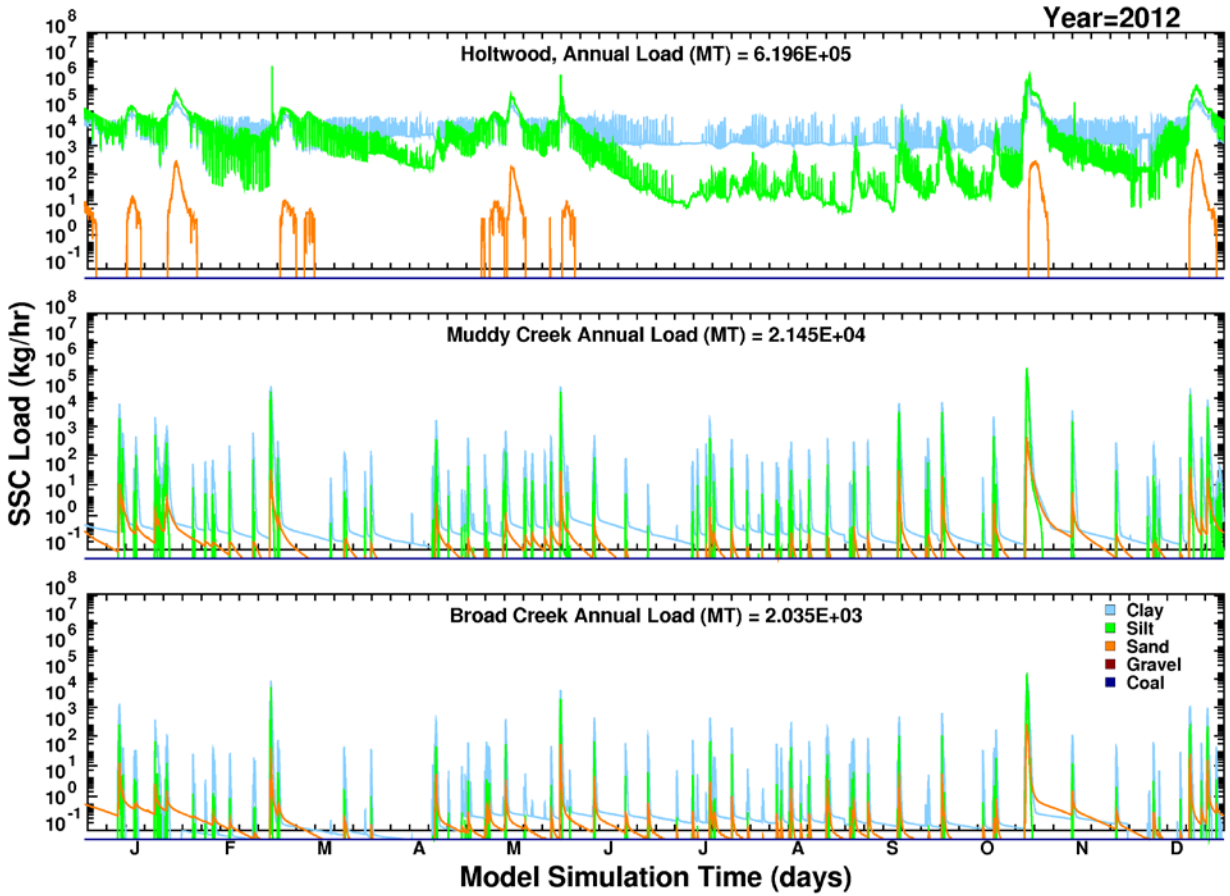


Note: Loads presented by solids class: clay, silt, sand, gravel, and coal; Clay concentrations (and loads) at Holtwood were adjusted so that the minimum SSC value would be 10 mg/L; Loads at Holtwood derived from WEST (2016) HEC-RAS results; Loads for Muddy Creek and Broad Creek specified from HSPF (P6B2) results; x-axis divisions indicate a one character abbreviation for month of year in sequence from January through December. Modulation that appears in loads beginning in October, 2007 reflects high frequency flow fluctuations that occur in in the USGS 15-minute flow measurements; Prior to October, 2007 flows used to calculate loads were daily average values linearly interpolated to hourly values.

Figure 48. Time series of solids loads entering Conowingo Pond at Holtwood, Muddy Creek, and Broad Creek: 2012.

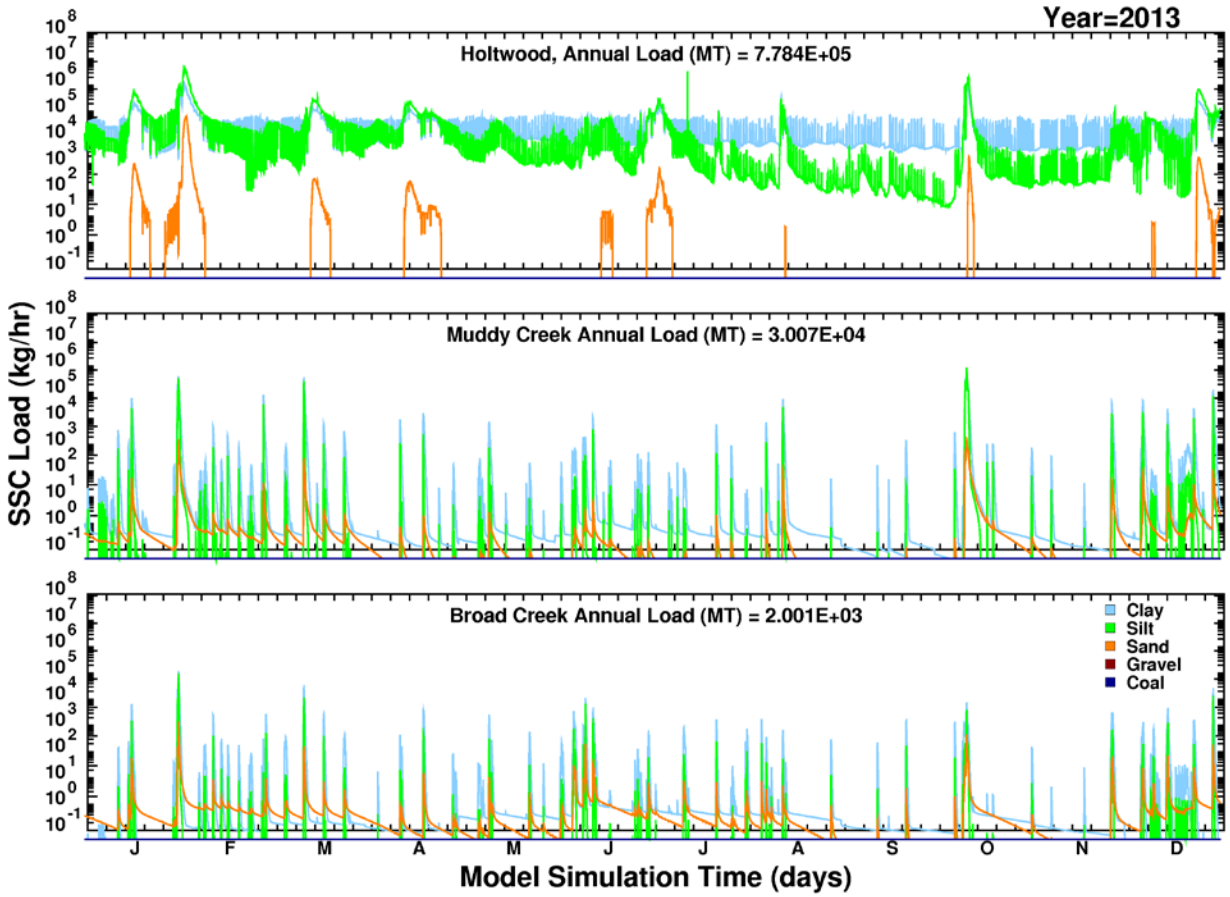


Note: Loads presented by solids class: clay, silt, sand, gravel, and coal; Clay concentrations (and loads) at Holtwood were adjusted so that the minimum SSC value would be 10 mg/L; Loads at Holtwood derived from WEST (2016) HEC-RAS results; Loads for Muddy Creek and Broad Creek specified from HSPF (P6B2) results; x-axis divisions indicate a one character abbreviation for month of year in sequence from January through December. Modulation that appears in loads beginning in October, 2007 reflects high frequency flow fluctuations that occur in in the USGS 15-minute flow measurements; Prior to October, 2007 flows used to calculate loads were daily average values linearly interpolated to hourly values.

Figure 49. Time series of solids loads entering Conowingo Pond at Holtwood, Muddy Creek, and Broad Creek: 2013.

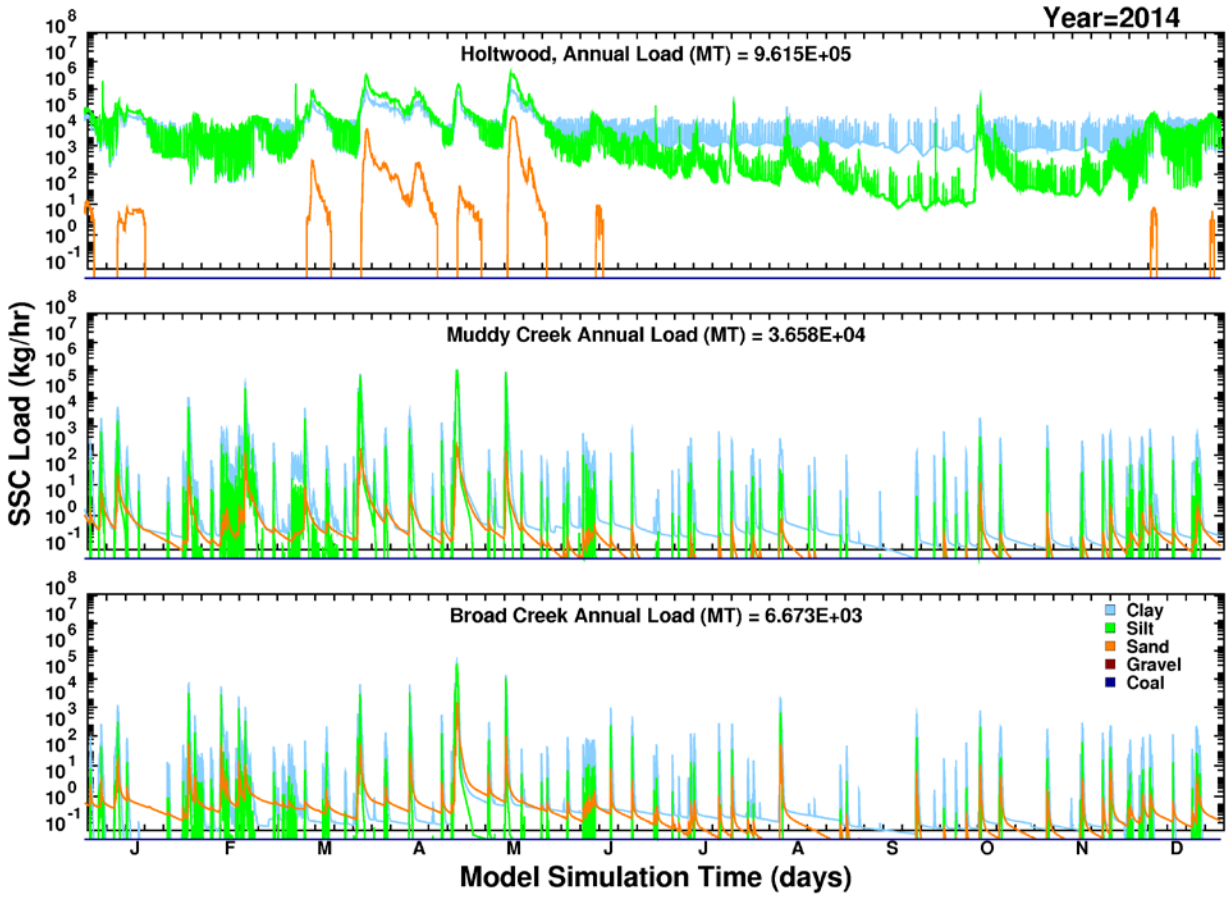


Note: Loads presented by solids class: clay, silt, sand, gravel, and coal; Clay concentrations (and loads) at Holtwood were adjusted so that the minimum SSC value would be 10 mg/L; Loads at Holtwood derived from WEST (2016) HEC-RAS results; Loads for Muddy Creek and Broad Creek specified from HSPF (P6B2) results; x-axis divisions indicate a one character abbreviation for month of year in sequence from January through December. Modulation that appears in loads beginning in October, 2007 reflects high frequency flow fluctuations that occur in in the USGS 15-minute flow measurements; Prior to October, 2007 flows used to calculate loads were daily average values linearly interpolated to hourly values.

Figure 50. Time series of solids loads entering Conowingo Pond at Holtwood, Muddy Creek, and Broad Creek: 2014.

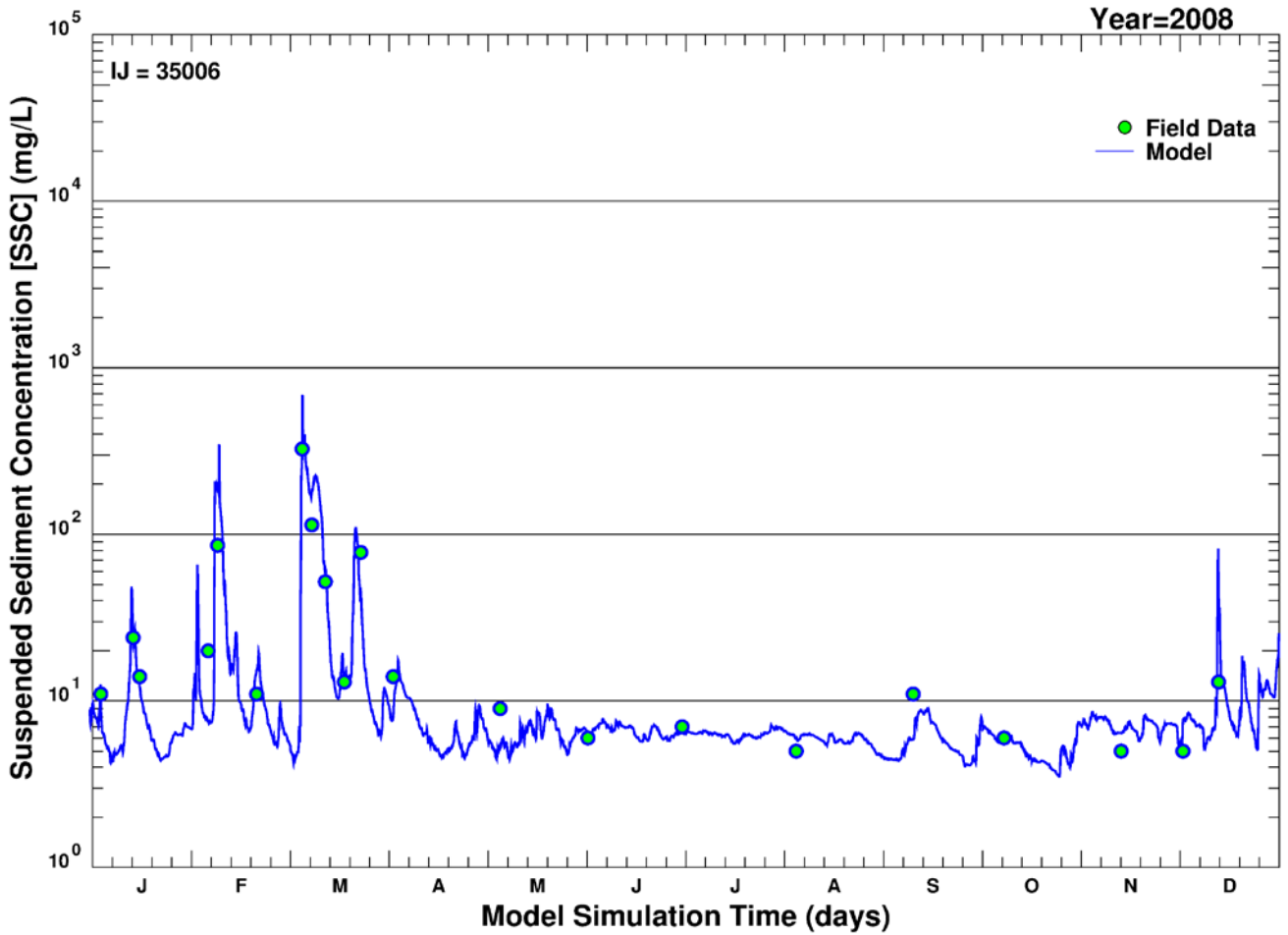


Note: Blue line = simulated SSC (depth-averaged sum of all size classes); Green circle = measured SSC; IJ indicates the model grid cell from which outputs were retrieved; x-axis divisions indicate a one character abbreviation for month of year in sequence from January through December; y-axis maximum indicates the log cycle closest to but not less than the maximum concentration simulated (which occurred during Tropical Storm Lee in 2011).

Figure 51. Simulated (hourly) and measured (instantaneous) suspended sediment concentration (SSC) over time at Conowingo: 2008.

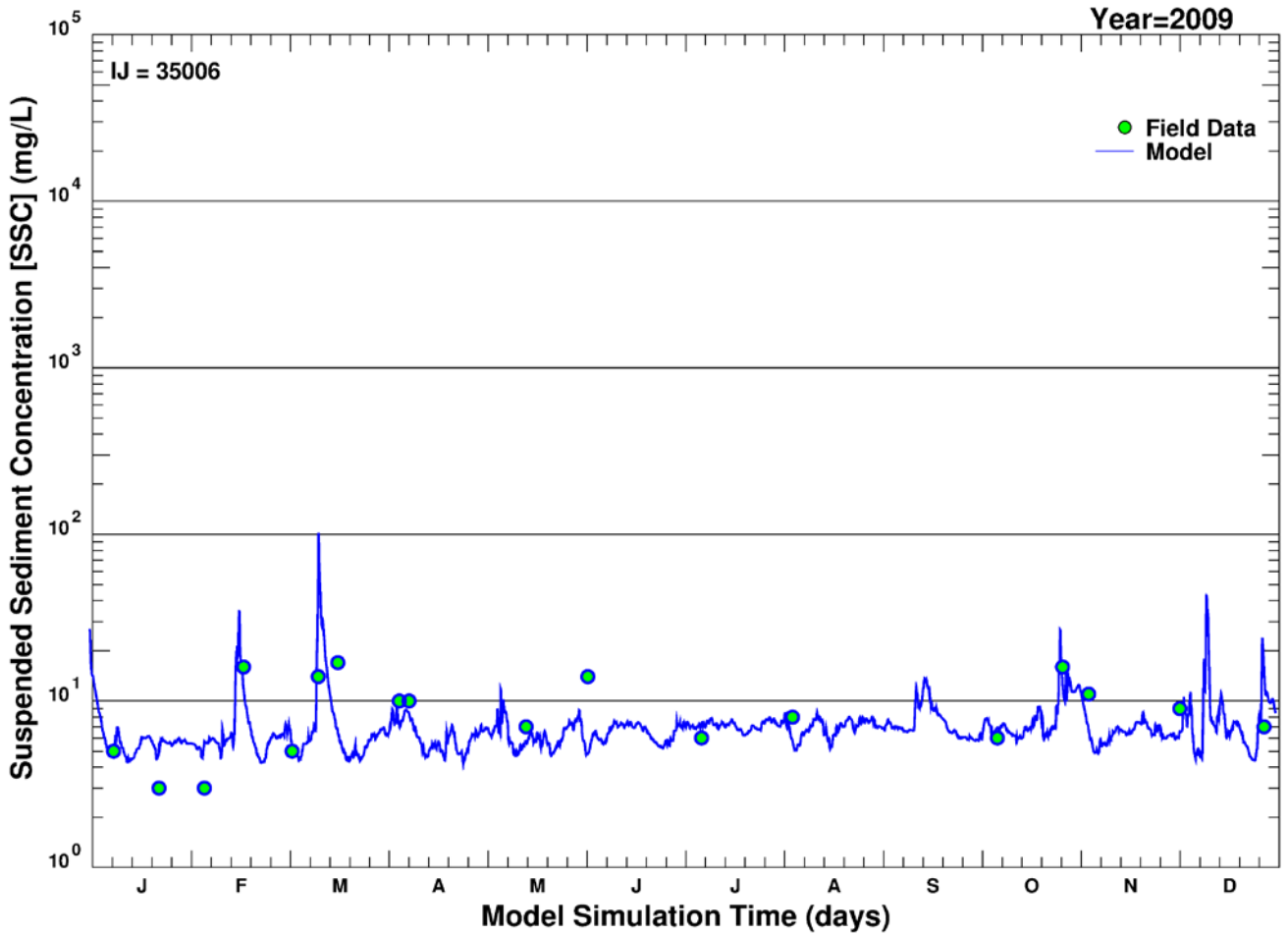


Note: Blue line = simulated SSC (depth-averaged sum of all size classes); Green circle = measured SSC; IJ indicates the model grid cell from which outputs were retrieved; x-axis divisions indicate a one character abbreviation for month of year in sequence from January through December; y-axis maximum indicates the log cycle closest to but not less than the maximum concentration simulated (which occurred during Tropical Storm Lee in 2011).

Figure 52. Simulated (hourly) and measured (instantaneous) suspended sediment concentration (SSC) over time at Conowingo: 2009.

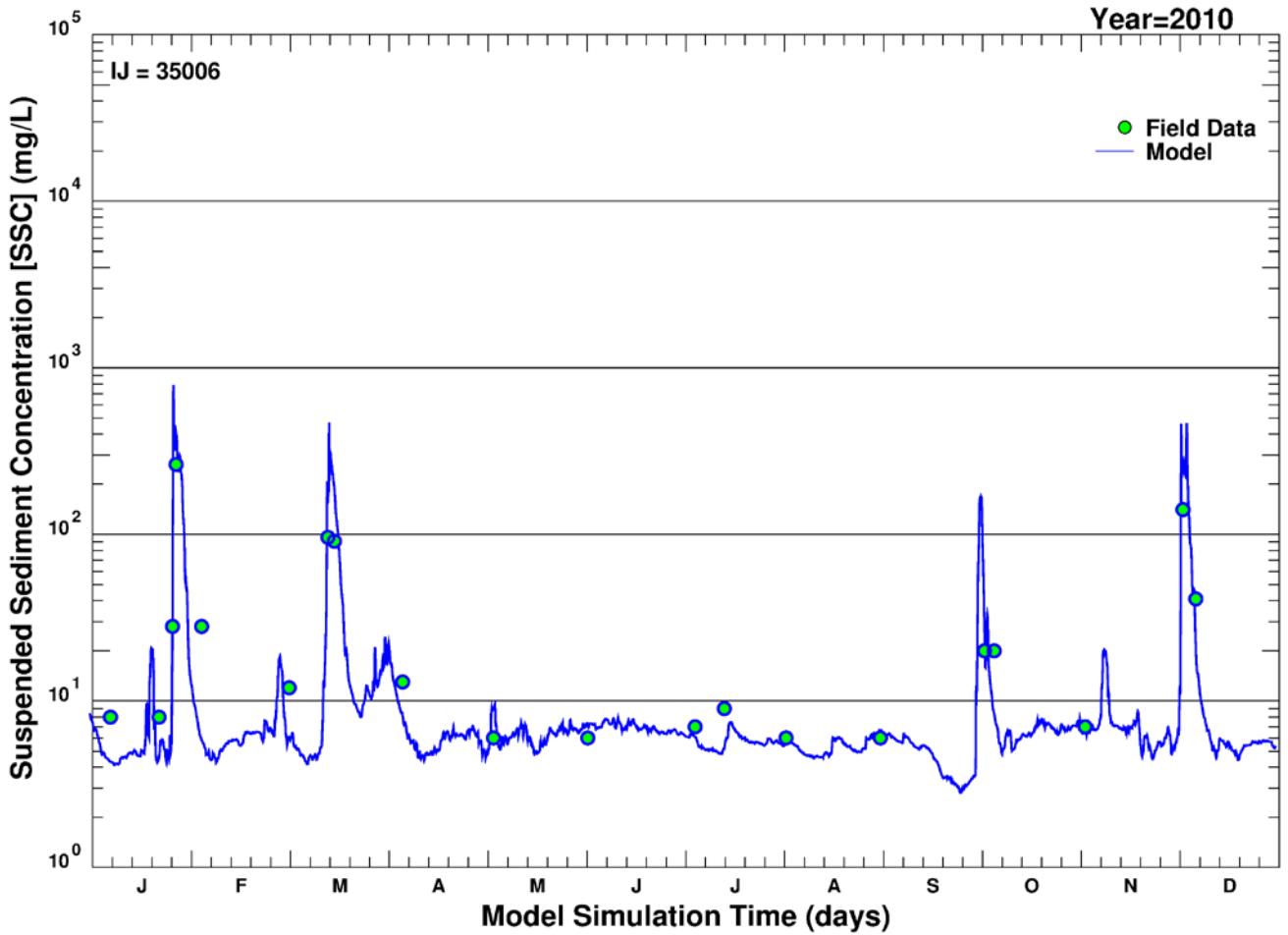


Note: Blue line = simulated SSC (depth-averaged sum of all size classes); Green circle = measured SSC; IJ indicates the model grid cell from which outputs were retrieved; x-axis divisions indicate a one character abbreviation for month of year in sequence from January through December; y-axis maximum indicates the log cycle closest to but not less than the maximum concentration simulated (which occurred during Tropical Storm Lee in 2011).

Figure 53. Simulated (hourly) and measured (instantaneous) suspended sediment concentration (SSC) over time at Conowingo: 2010.

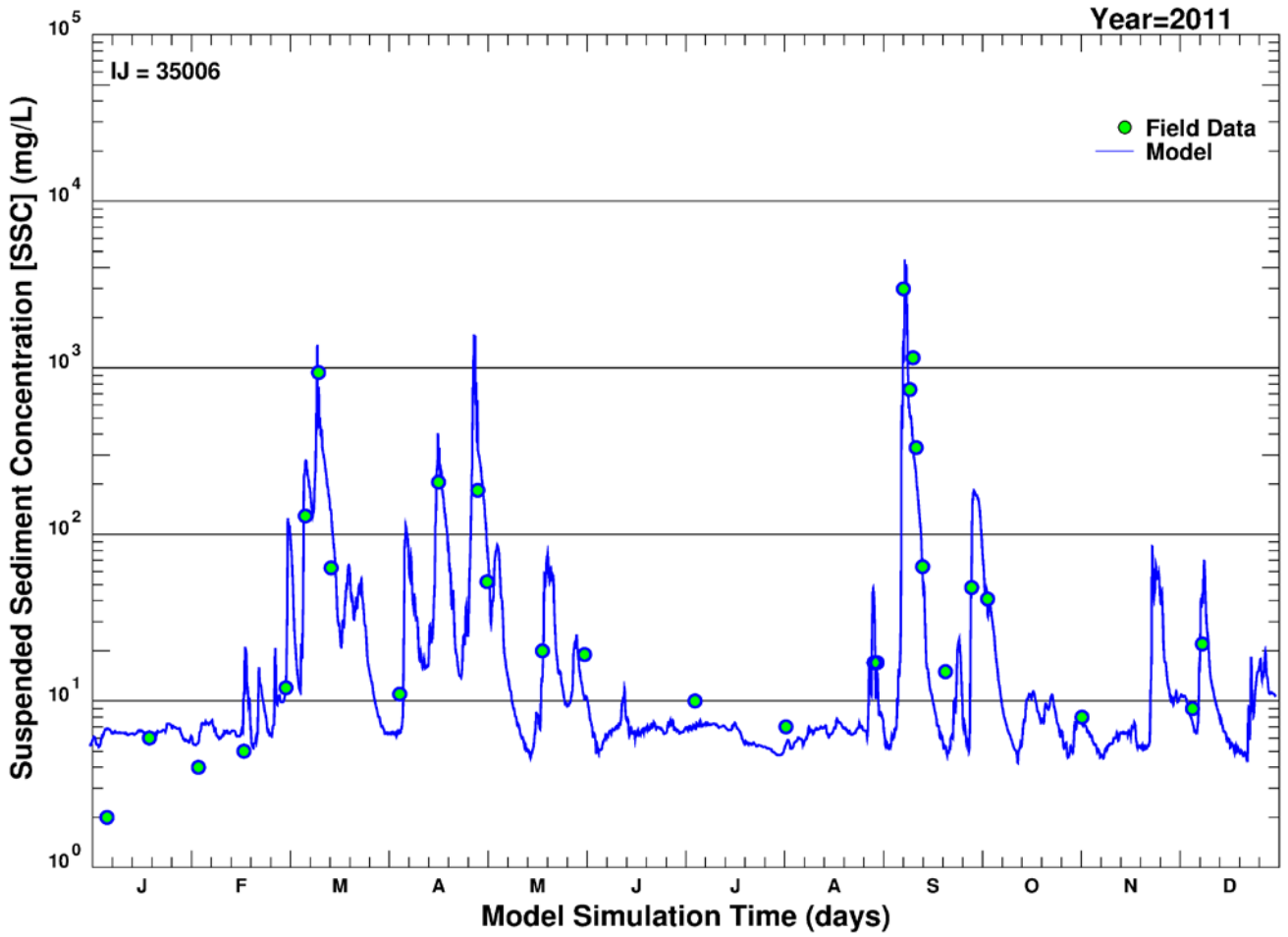


Note: Blue line = simulated SSC (depth-averaged sum of all size classes); Green circle = measured SSC; IJ indicates the model grid cell from which outputs were retrieved; x-axis divisions indicate a one character abbreviation for month of year in sequence from January through December; y-axis maximum indicates the log cycle closest to but not less than the maximum concentration simulated (which occurred during Tropical Storm Lee in 2011).

Figure 54. Simulated (hourly) and measured (instantaneous) suspended sediment concentration (SSC) over time at Conowingo: 2011.

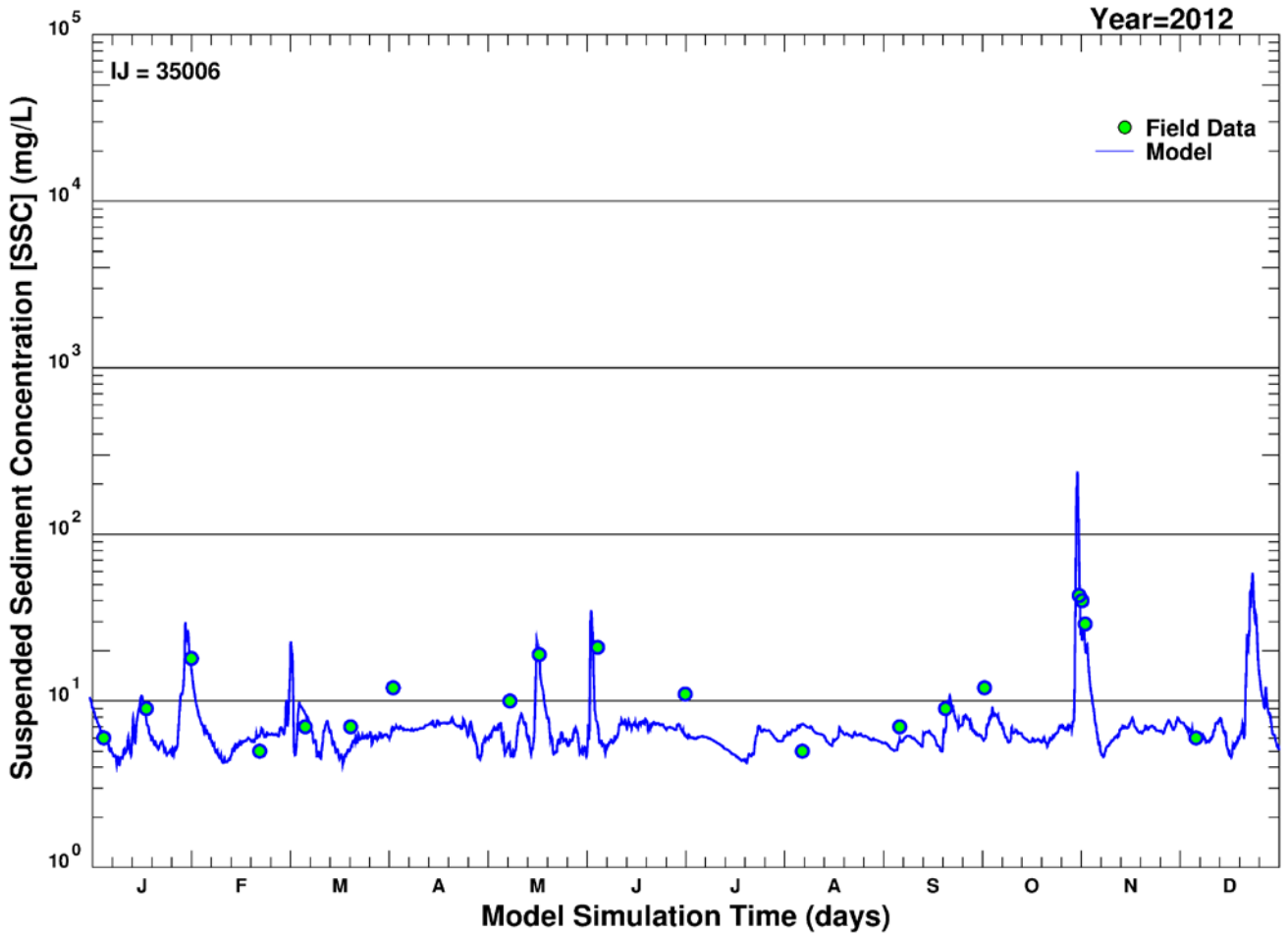


Note: Blue line = simulated SSC (depth-averaged sum of all size classes); Green circle = measured SSC; IJ indicates the model grid cell from which outputs were retrieved; x-axis divisions indicate a one character abbreviation for month of year in sequence from January through December; y-axis maximum indicates the log cycle closest to but not less than the maximum concentration simulated (which occurred during Tropical Storm Lee in 2011).

Figure 55. Simulated (hourly) and measured (instantaneous) suspended sediment concentration (SSC) over time at Conowingo: 2012.

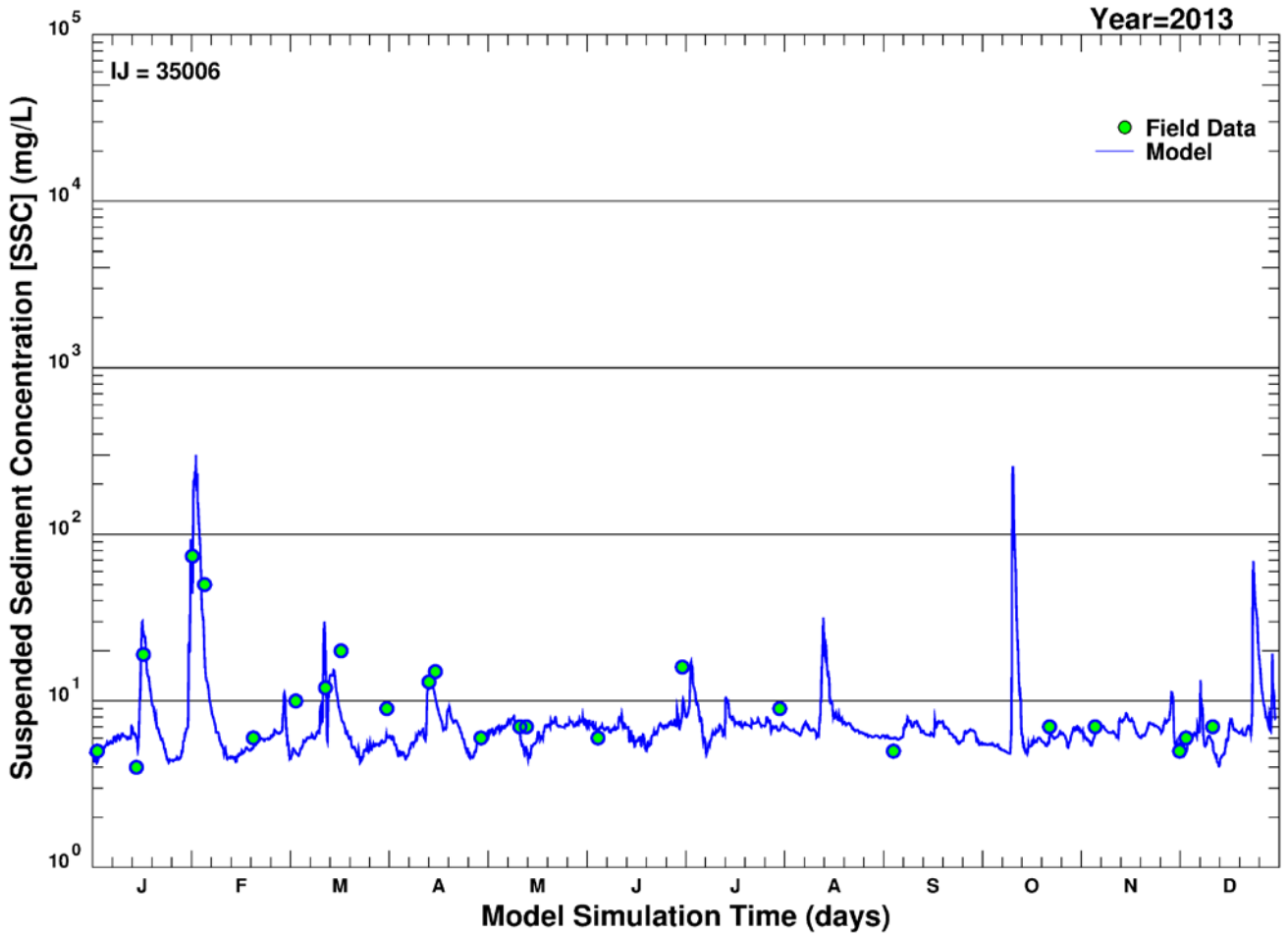


Note: Blue line = simulated SSC (depth-averaged sum of all size classes); Green circle = measured SSC; IJ indicates the model grid cell from which outputs were retrieved; x-axis divisions indicate a one character abbreviation for month of year in sequence from January through December; y-axis maximum indicates the log cycle closest to but not less than the maximum concentration simulated (which occurred during Tropical Storm Lee in 2011).

Figure 56. Simulated (hourly) and measured (instantaneous) suspended sediment concentration (SSC) over time at Conowingo: 2013.

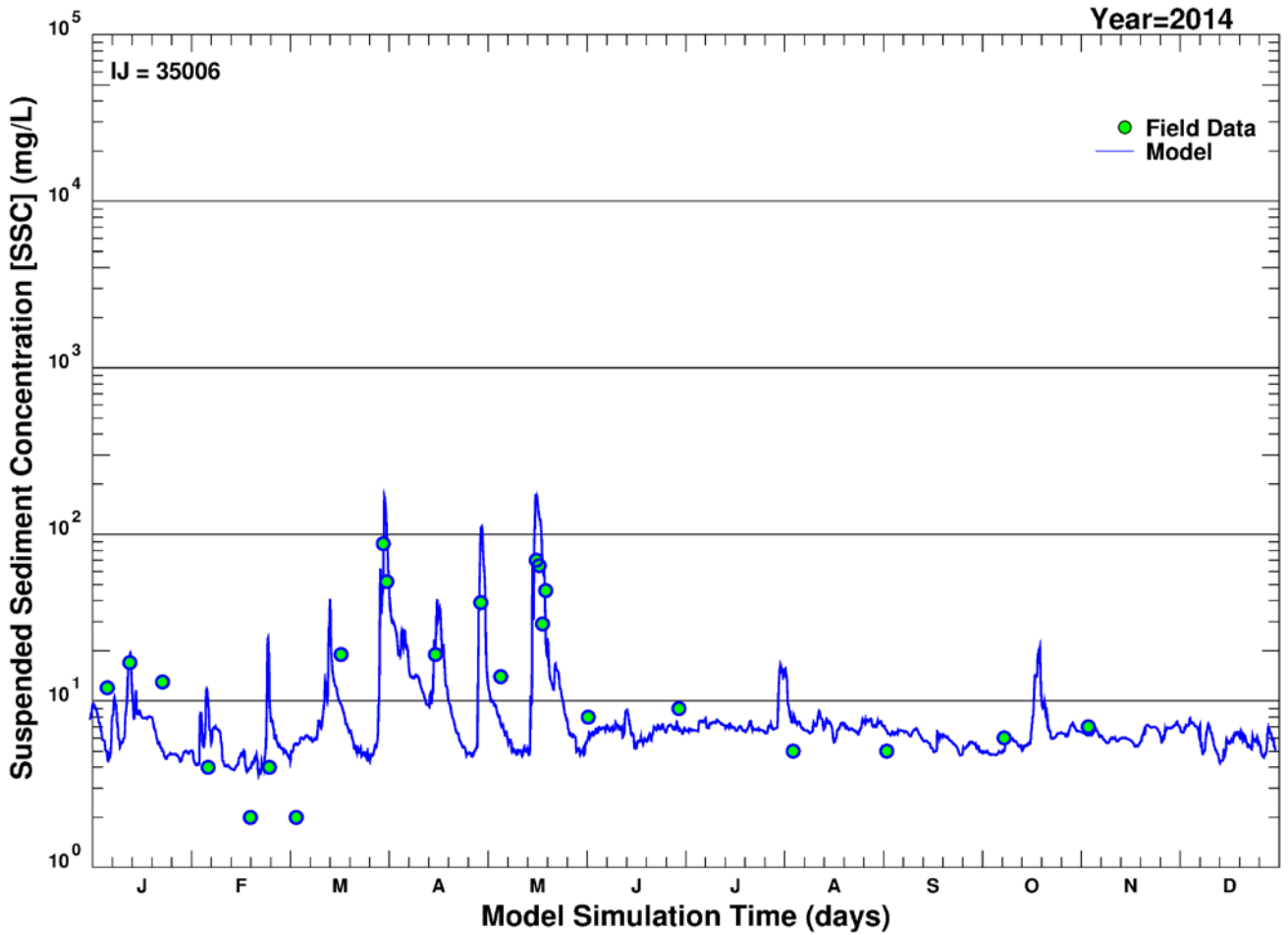


Note: Blue line = simulated SSC (depth-averaged sum of all size classes); Green circle = measured SSC; IJ indicates the model grid cell from which outputs were retrieved; x-axis divisions indicate a one character abbreviation for month of year in sequence from January through December; y-axis maximum indicates the log cycle closest to but not less than the maximum concentration simulated (which occurred during Tropical Storm Lee in 2011).

Figure 57. Simulated (hourly) and measured (instantaneous) suspended sediment concentration (SSC) over time at Conowingo: 2014.

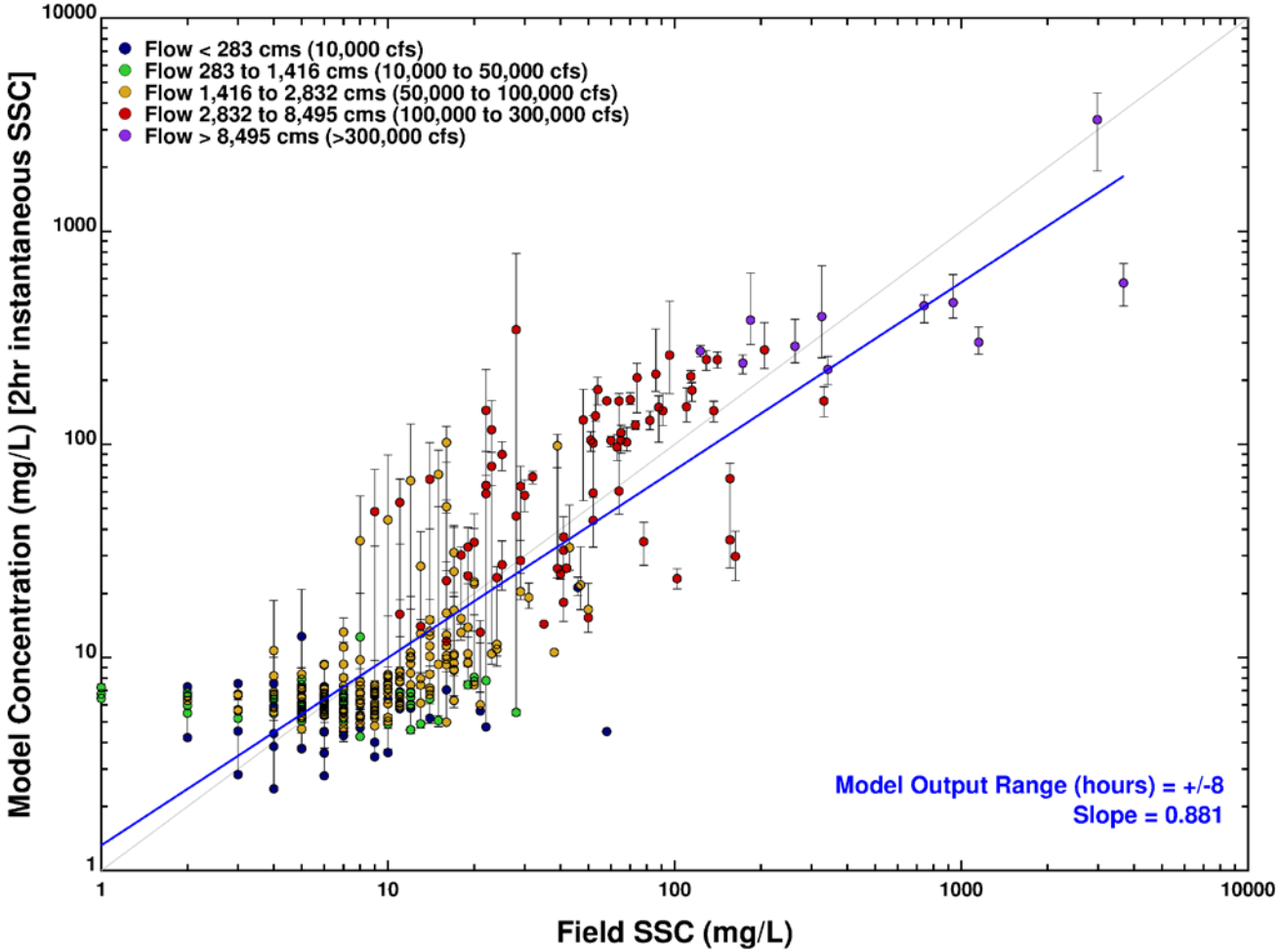


Note: Black bars = range of model results within ±8 hour interval of sampling times; Blue line = linear regression result (model result vs. field value at times of measurement); Slope = slope of linear regression result; simulated = model instantaneous value reported to nearest 2 hour interval; measured = field value.

Figure 58. Comparison of simulated and measured suspended sediment concentration (SSC) at Conowingo.

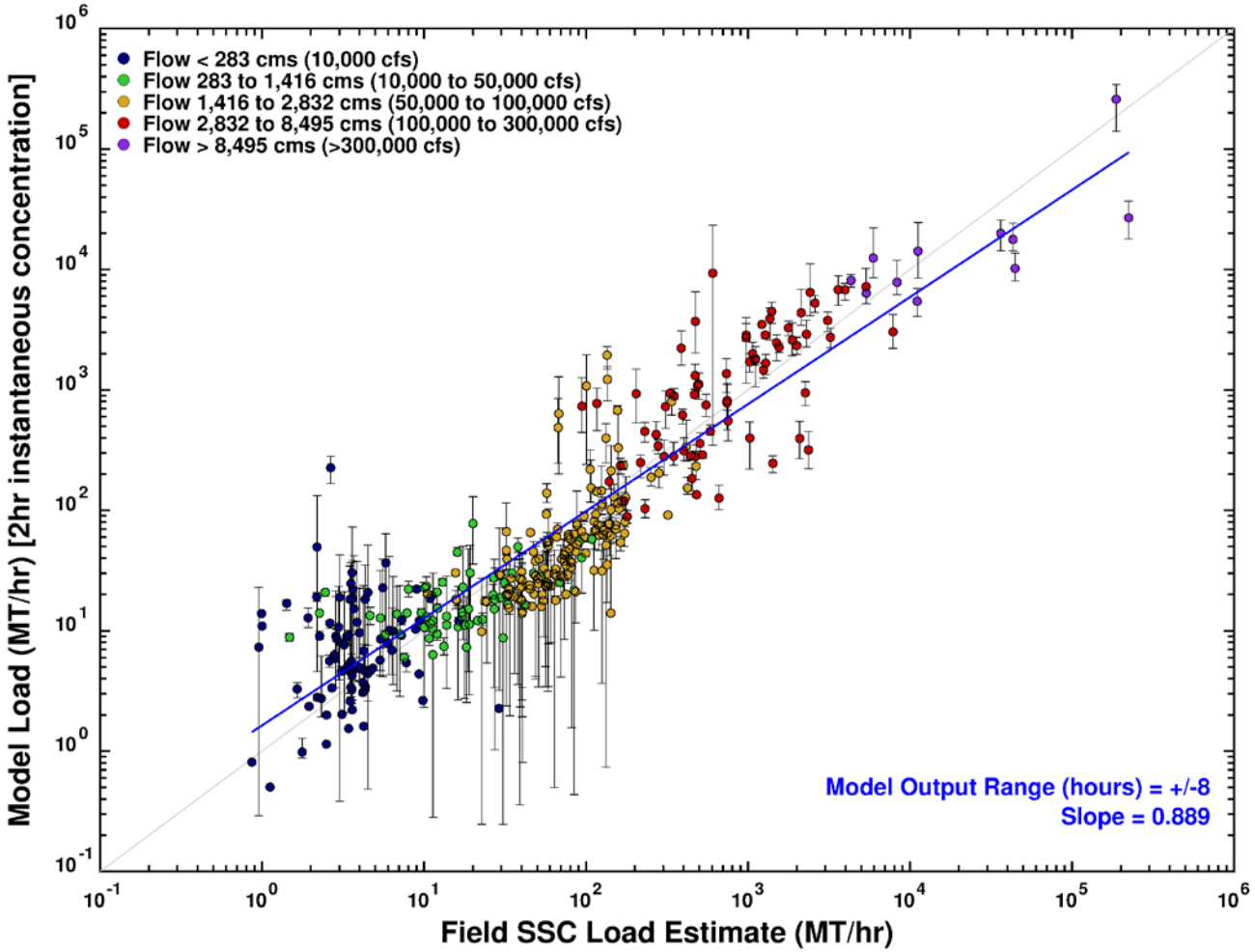


Note: Black bars = range of model results within ±8 hour interval of sampling times; Blue line = linear regression result (model result vs. field value at times of measurement); Slope = slope of linear regression result; simulated = model instantaneous flow and SSC; measured = field instantaneous flow and SSC.

Figure 59. Comparison of simulated and measured suspended sediment concentration (SSC) loads at Conowingo.

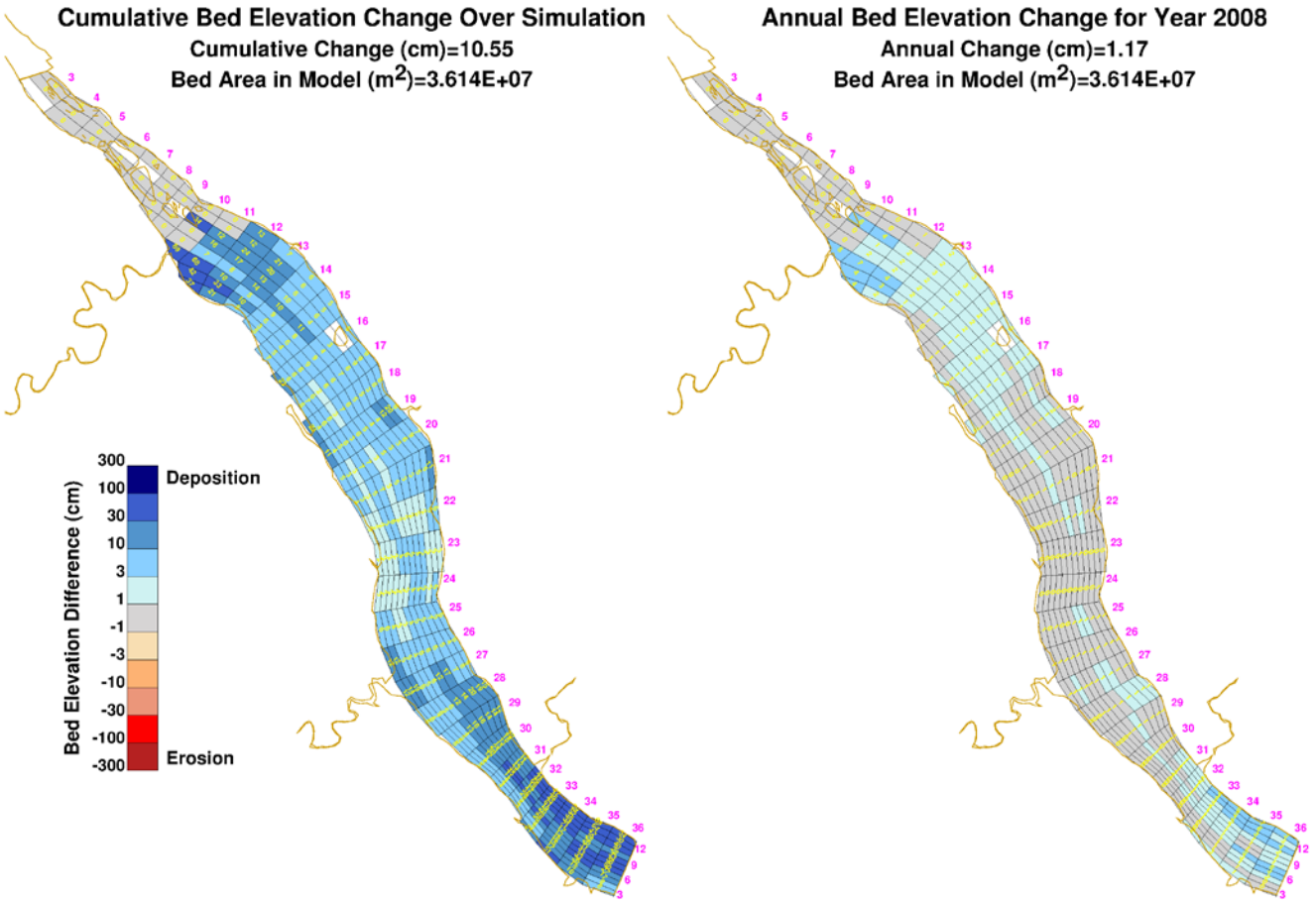


Note: Panel on the Left = simulated cumulative bed elevation change since simulation start; Panel on the Right = simulated annual bed elevation change for year indicated; values shown for all model grid cells; pink numbers listed along sides of images indicate "row" and "column" references for the model grid.

Figure 60. Simulated cumulative (since 1997) and annual bed elevation change for Conowingo Pond: 2008.

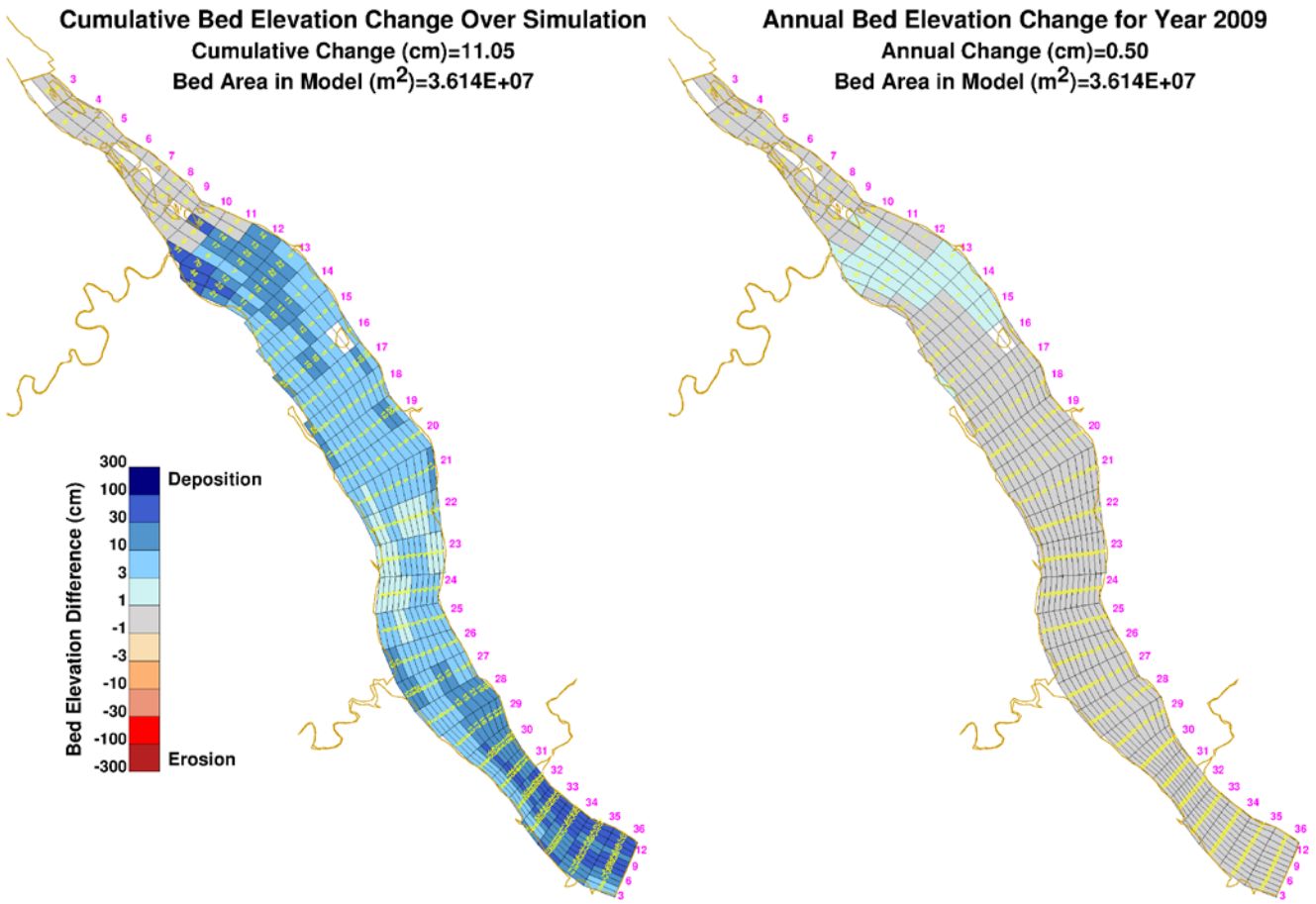


Note: Panel on the Left = simulated cumulative bed elevation change since simulation start; Panel on the Right = simulated annual bed elevation change for year indicated; values shown for all model grid cells; pink numbers listed along sides of images indicate "row" and "column" references for the model grid.

Figure 61. Simulated cumulative (since 1997) and annual bed elevation change for Conowingo Pond: 2009.

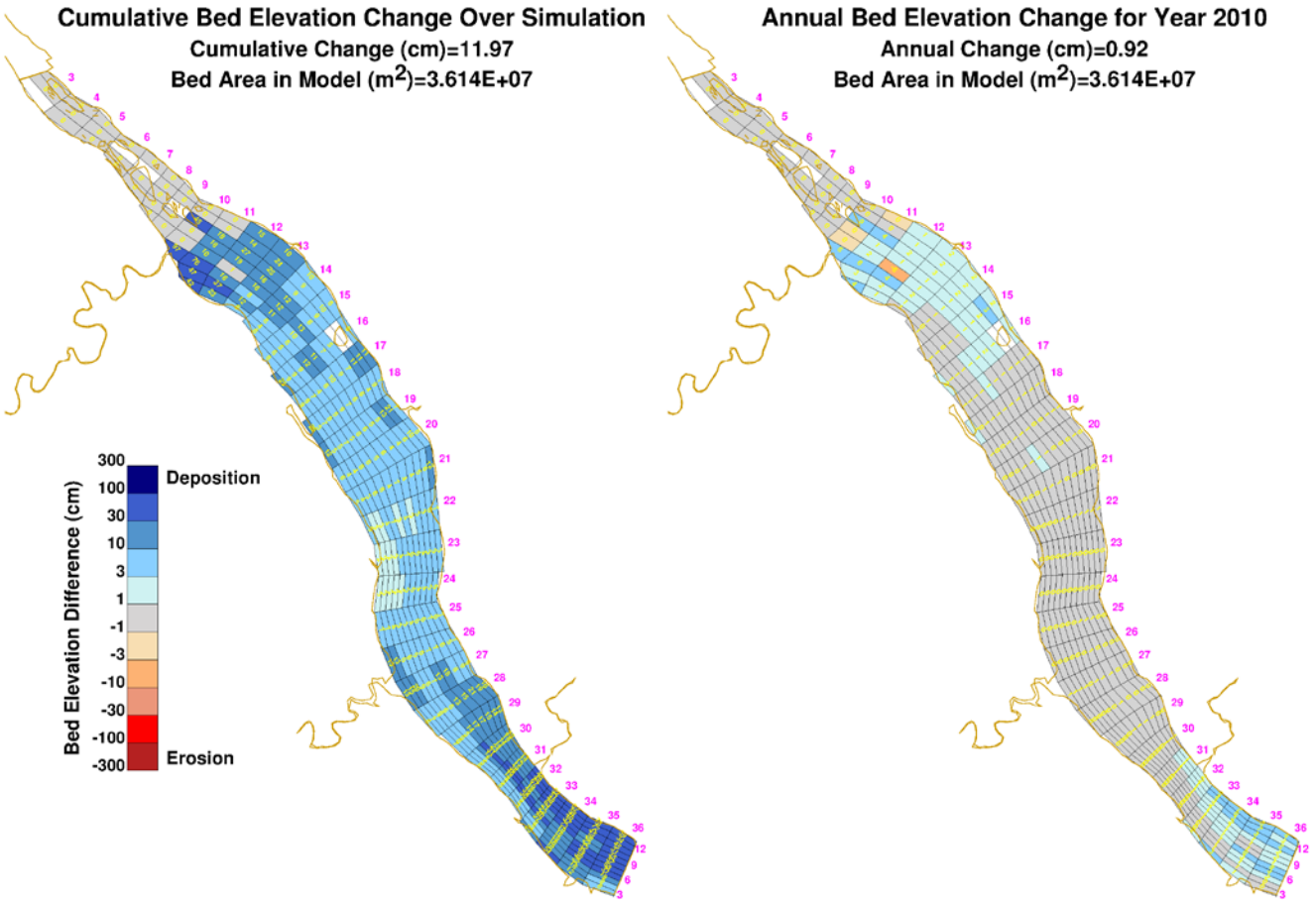


Note: Panel on the Left = simulated cumulative bed elevation change since simulation start; Panel on the Right = simulated annual bed elevation change for year indicated; values shown for all model grid cells; pink numbers listed along sides of images indicate "row" and "column" references for the model grid.

Figure 62. Simulated cumulative (since 1997) and annual bed elevation change for Conowingo Pond: 2010.

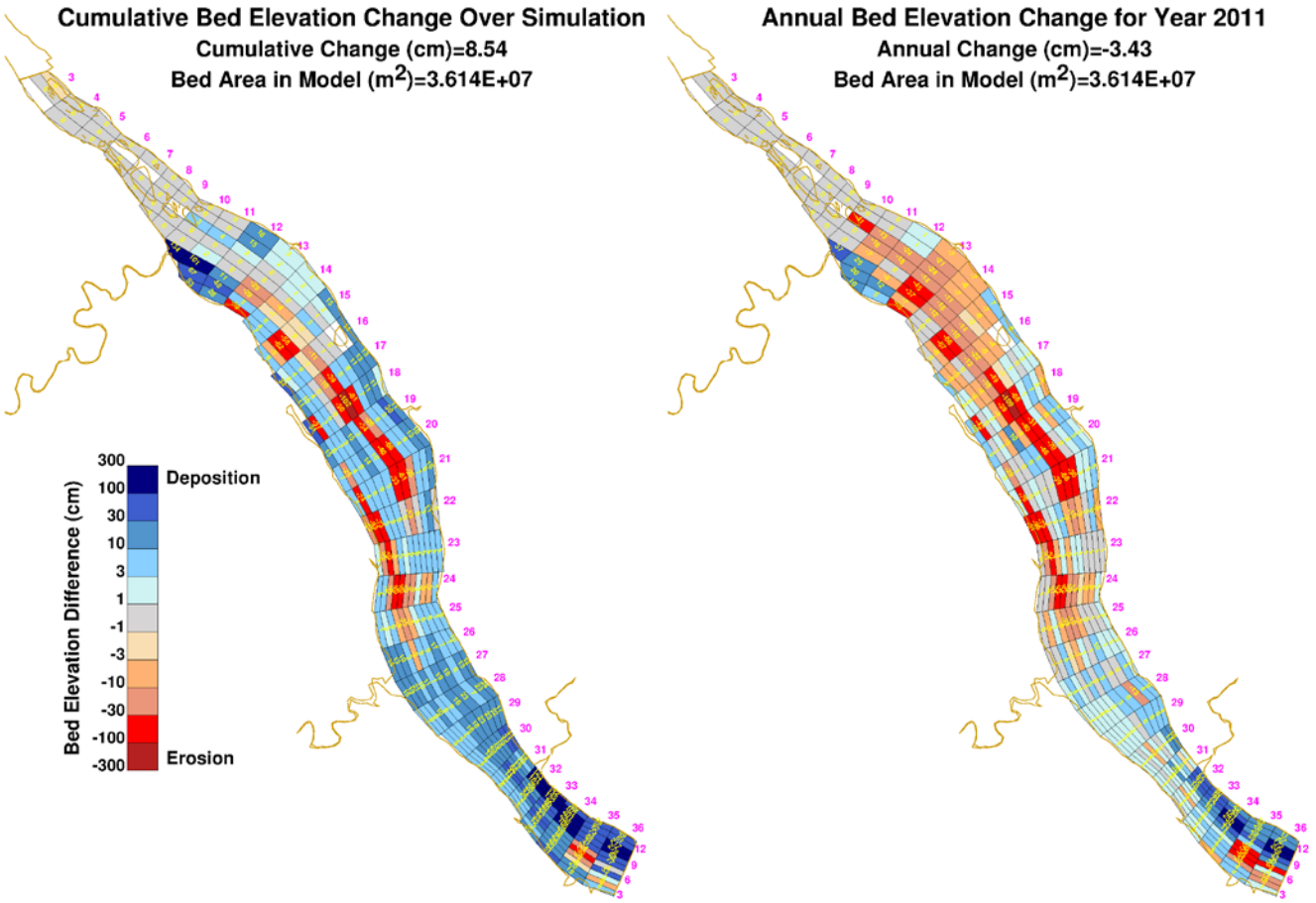


Note: Panel on the Left = simulated cumulative bed elevation change since simulation start; Panel on the Right = simulated annual bed elevation change for year indicated; values shown for all model grid cells; pink numbers listed along sides of images indicate "row" and "column" references for the model grid.

Figure 63. Simulated cumulative (since 1997) and annual bed elevation change for Conowingo Pond: 2011.

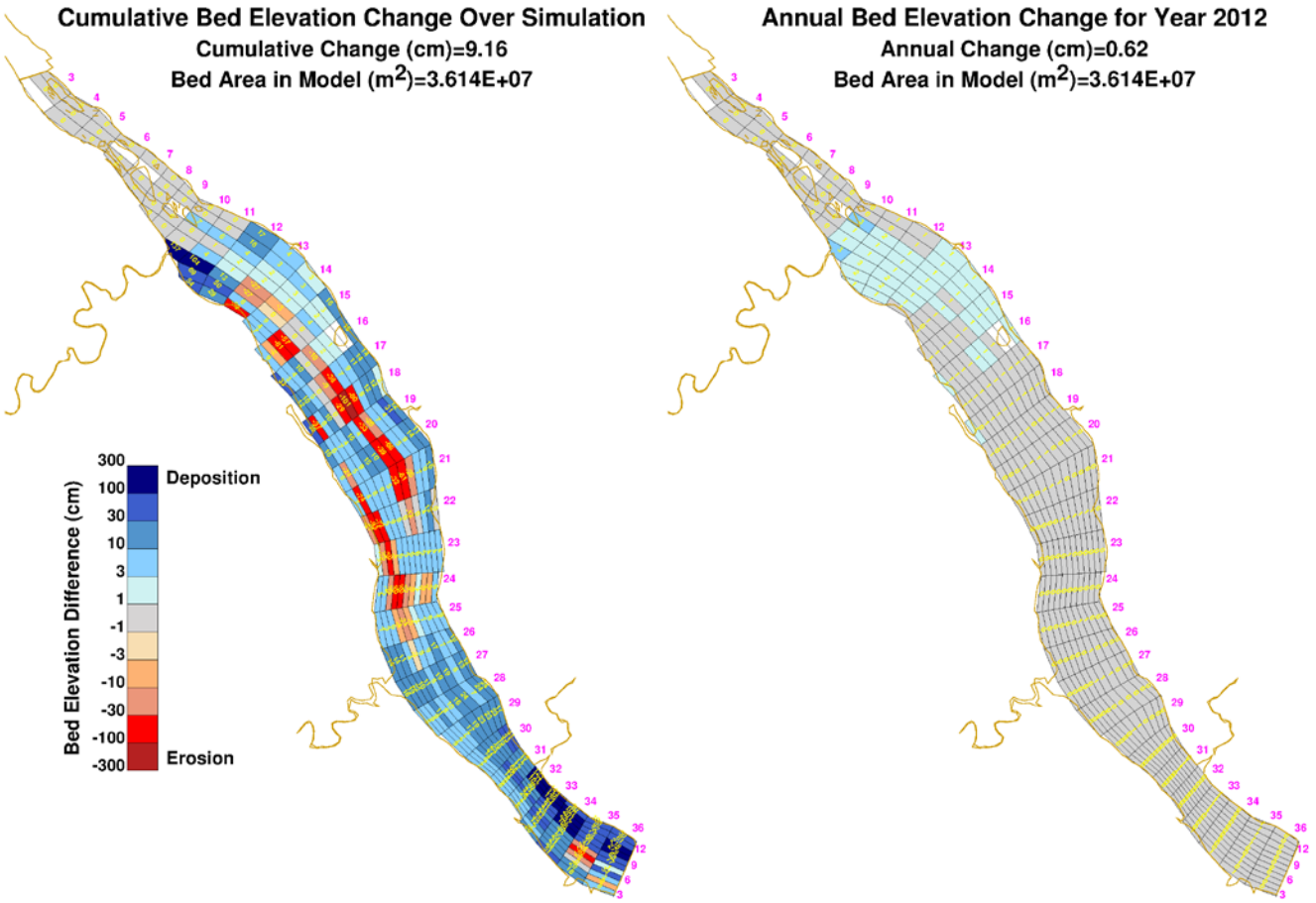


Note: Panel on the Left = simulated cumulative bed elevation change since simulation start; Panel on the Right = simulated annual bed elevation change for year indicated; values shown for all model grid cells; pink numbers listed along sides of images indicate "row" and "column" references for the model grid.

Figure 64. Simulated cumulative (since 1997) and annual bed elevation change for Conowingo Pond: 2012.

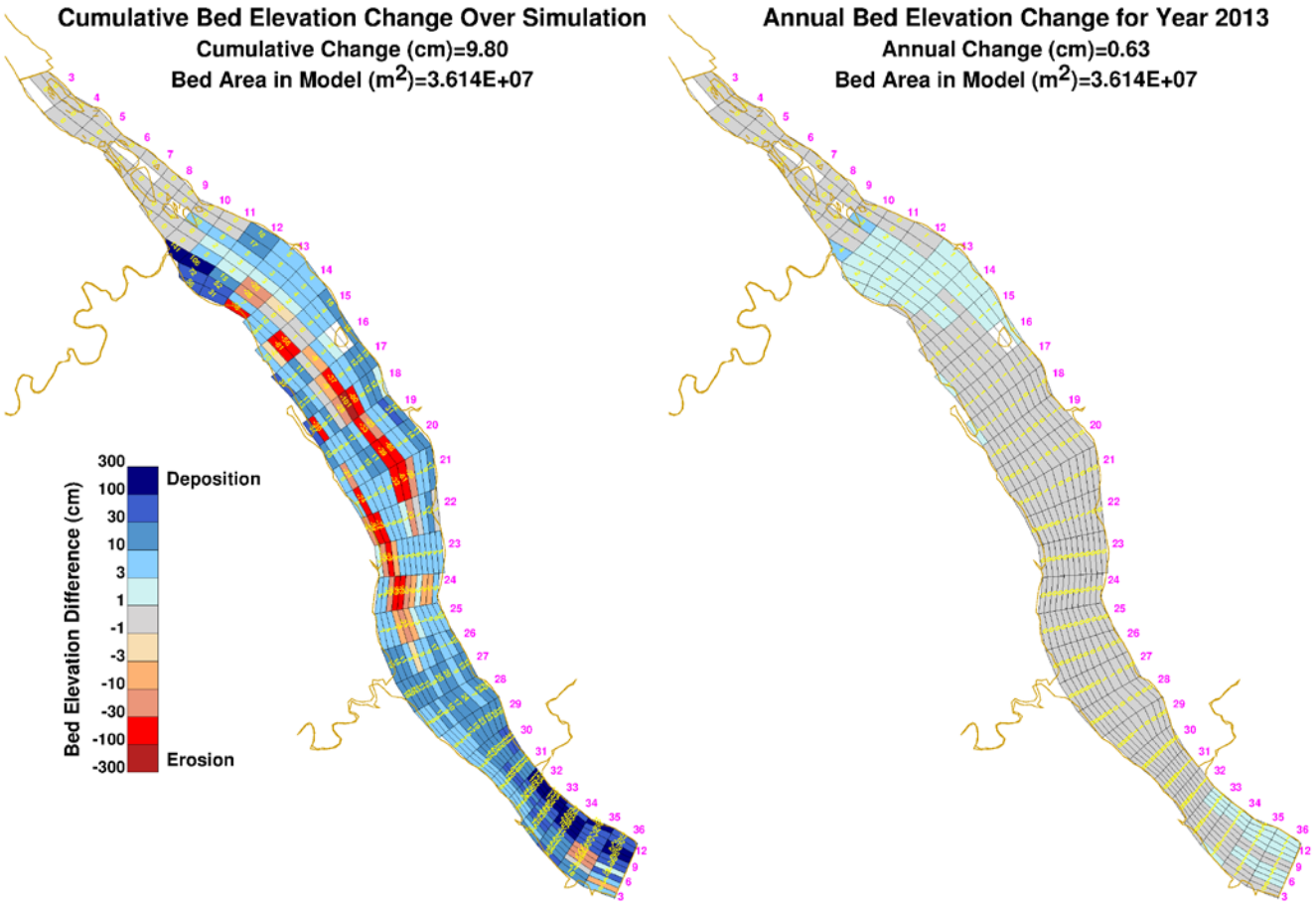


Note: Panel on the Left = simulated cumulative bed elevation change since simulation start; Panel on the Right = simulated annual bed elevation change for year indicated; values shown for all model grid cells; pink numbers listed along sides of images indicate "row" and "column" references for the model grid.

Figure 65. Simulated cumulative (since 1997) and annual bed elevation change for Conowingo Pond: 2013.

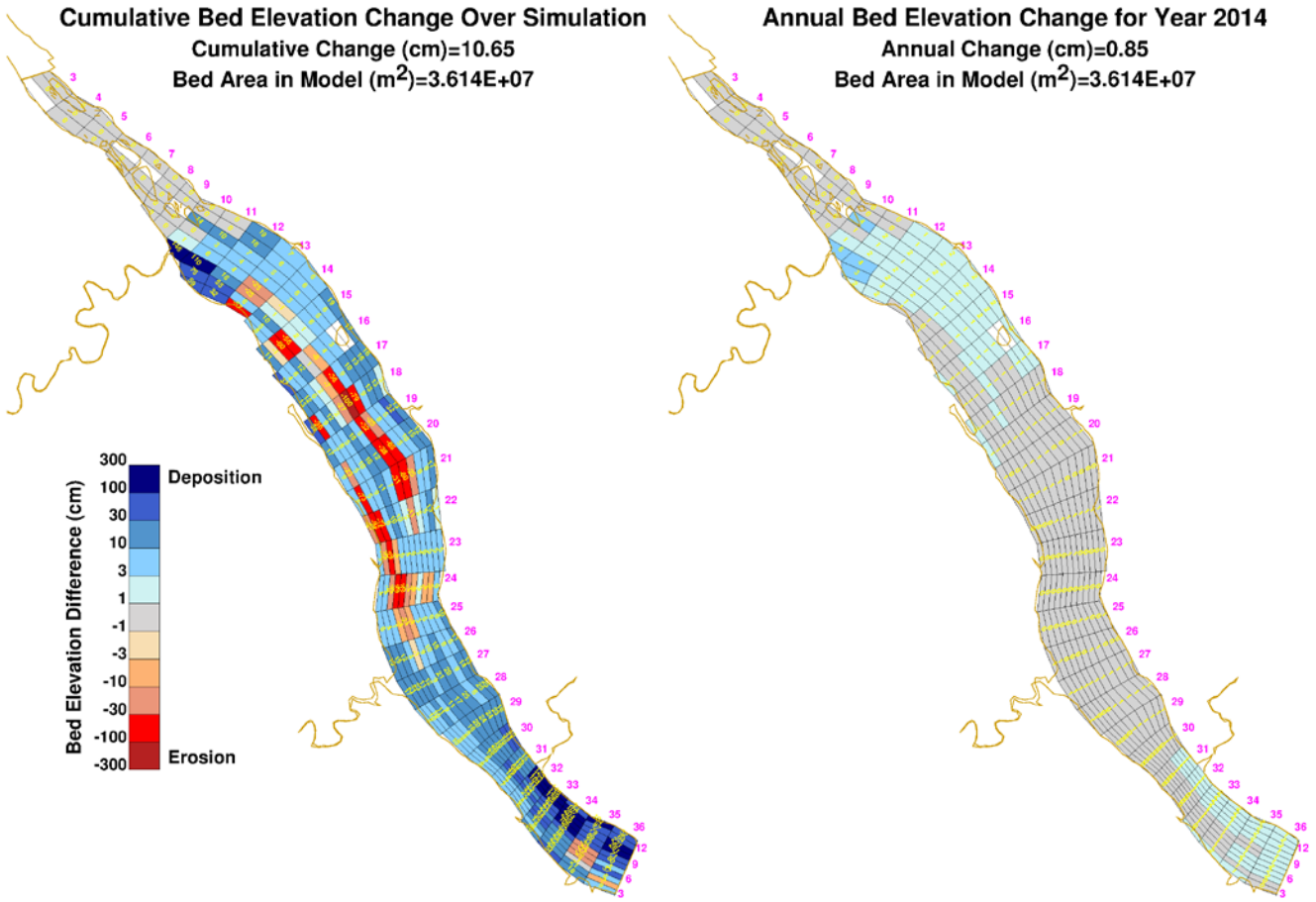


Note: Panel on the Left = simulated cumulative bed elevation change since simulation start; Panel on the Right = simulated annual bed elevation change for year indicated; values shown for all model grid cells; pink numbers listed along sides of images indicate "row" and "column" references for the model grid.

Figure 66. Simulated cumulative (since 1997) and annual bed elevation change for Conowingo Pond: 2014.

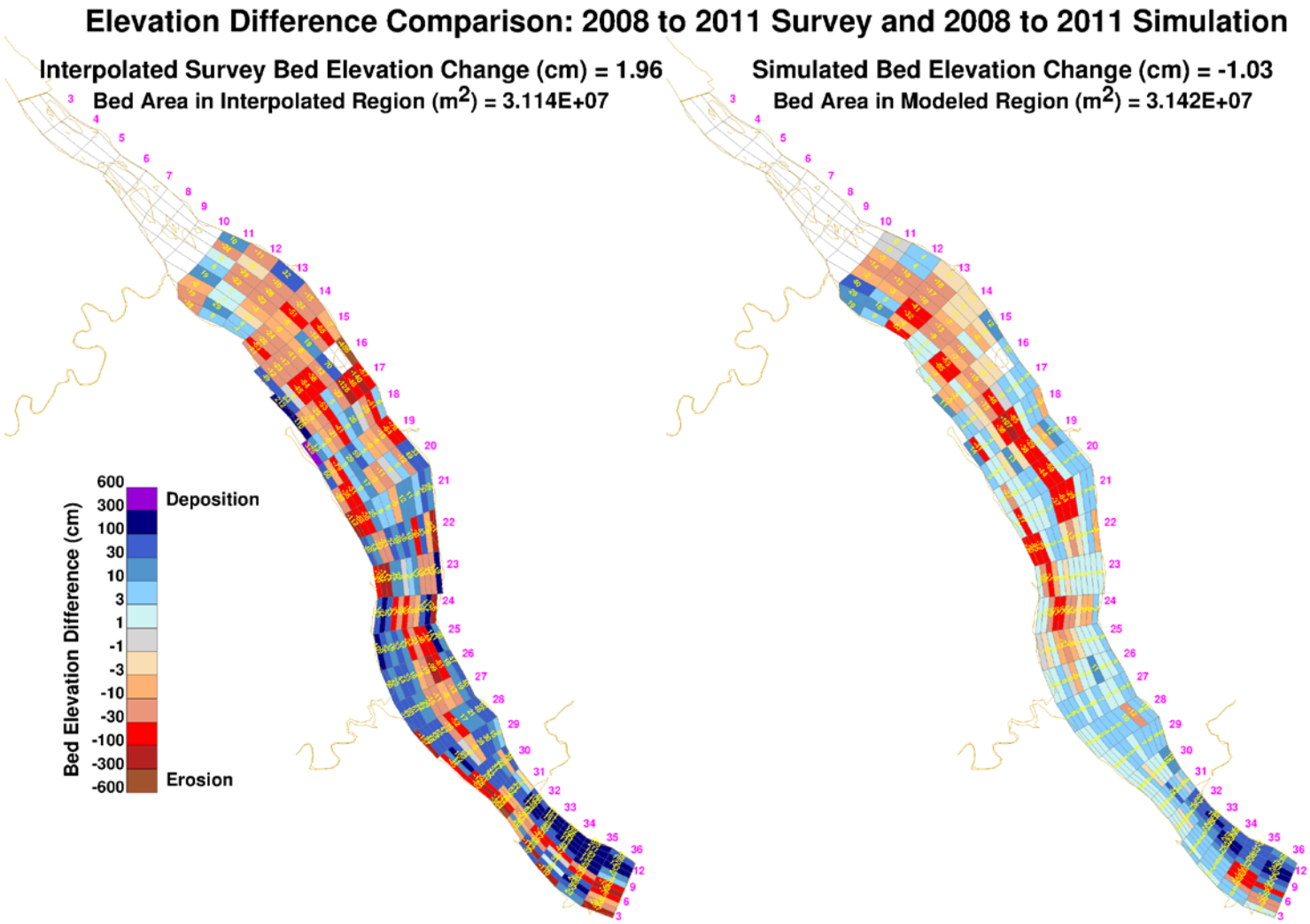


Figure 67. Comparison of bed elevation changes estimated from difference between interpolated (kriged) bathymetric survey results and simulated cumulative bed elevation change for Conowingo Pond (long-term model): 2008-2011.

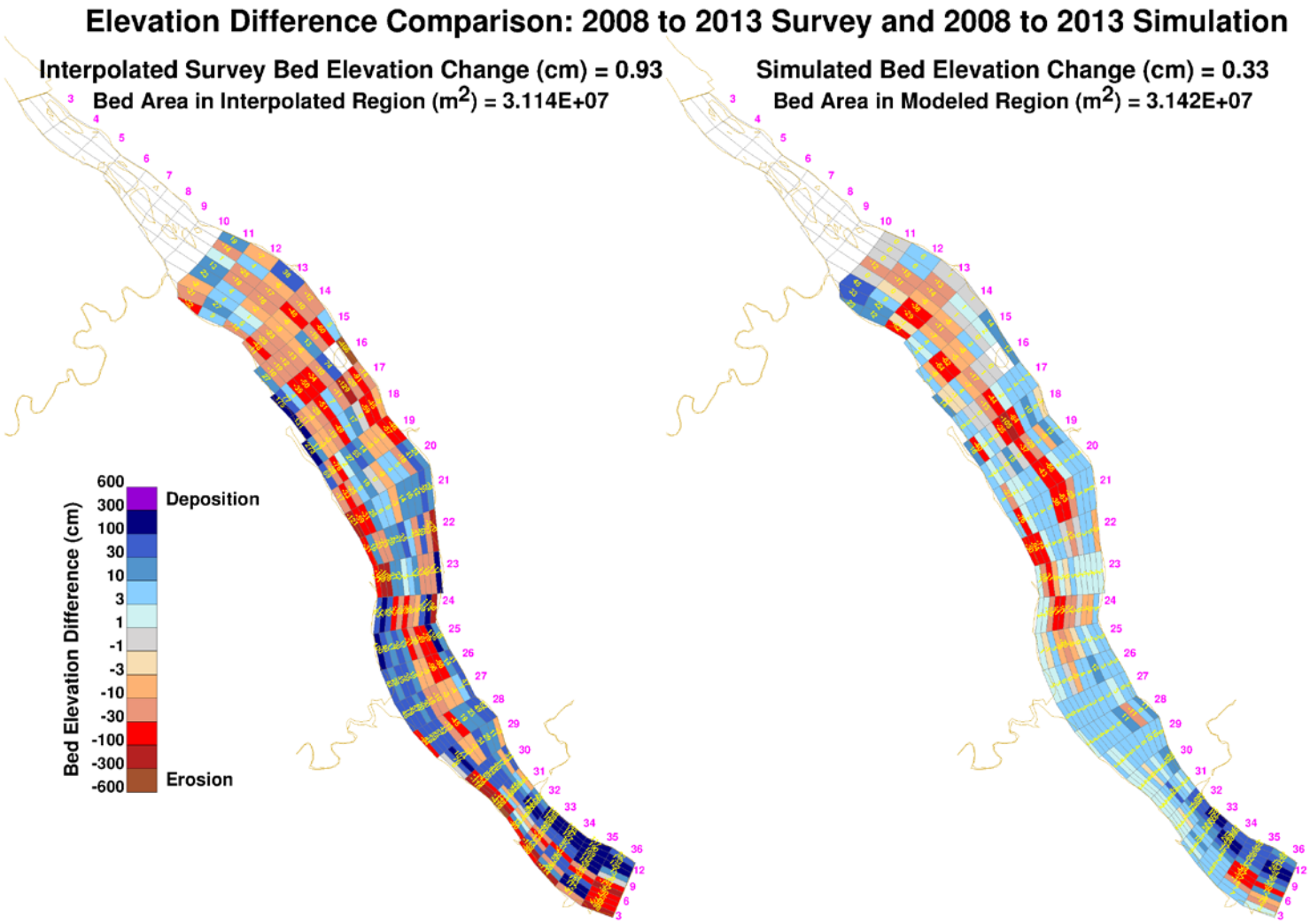


Figure 68. Comparison of bed elevation changes estimated from difference between interpolated (kriged) bathymetric survey results and simulated cumulative bed elevation change for Conowingo Pond: 2008-2013.

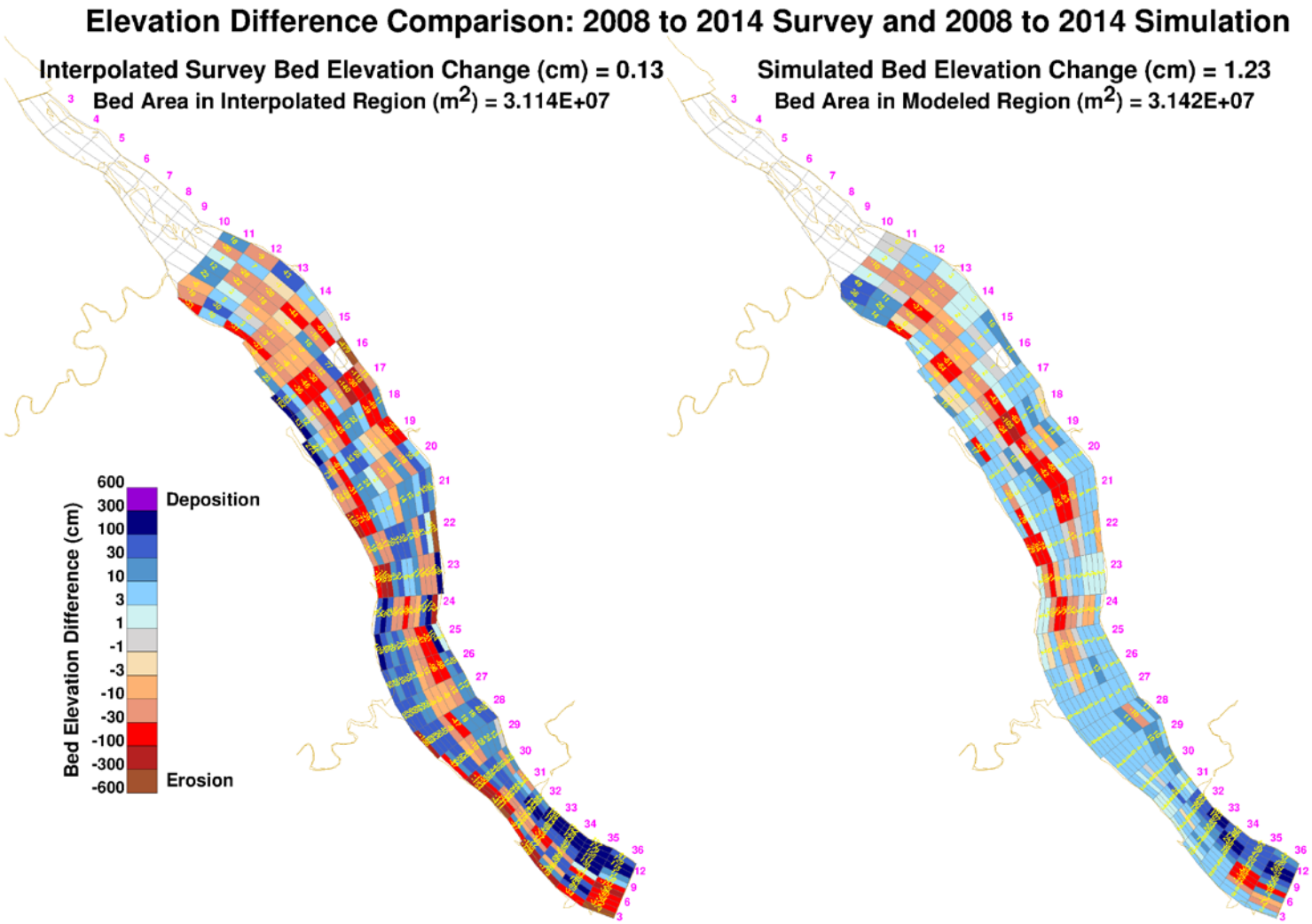


Figure 69. Comparison of bed elevation changes estimated from difference between interpolated (kriged) bathymetric survey results and simulated cumulative bed elevation change for Conowingo Pond: 2008-2014.

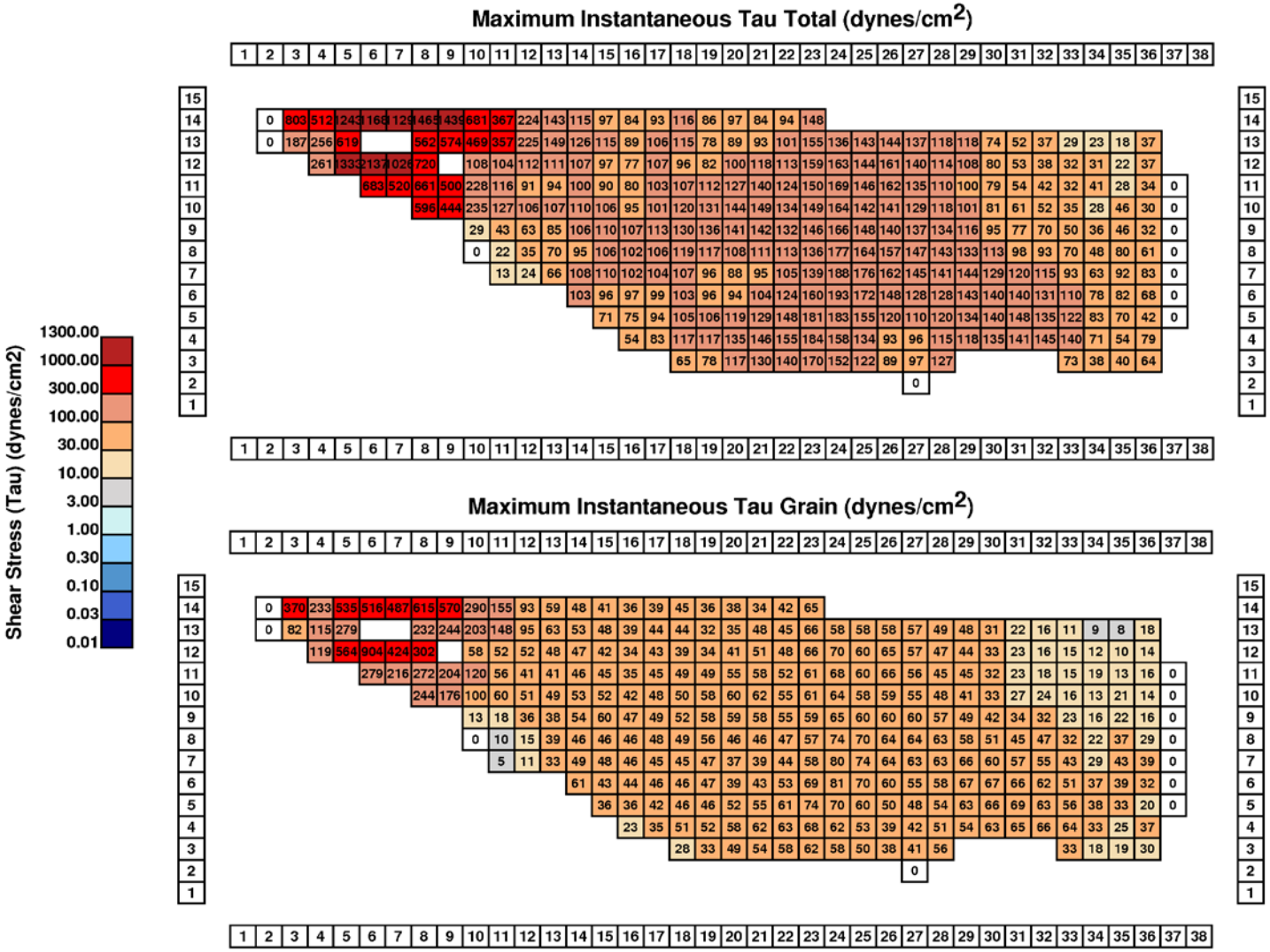


Figure 70. Maximum total bed (Tau Total) and grain (Tau Grain) shear stresses occurring during 2011: long-term model.

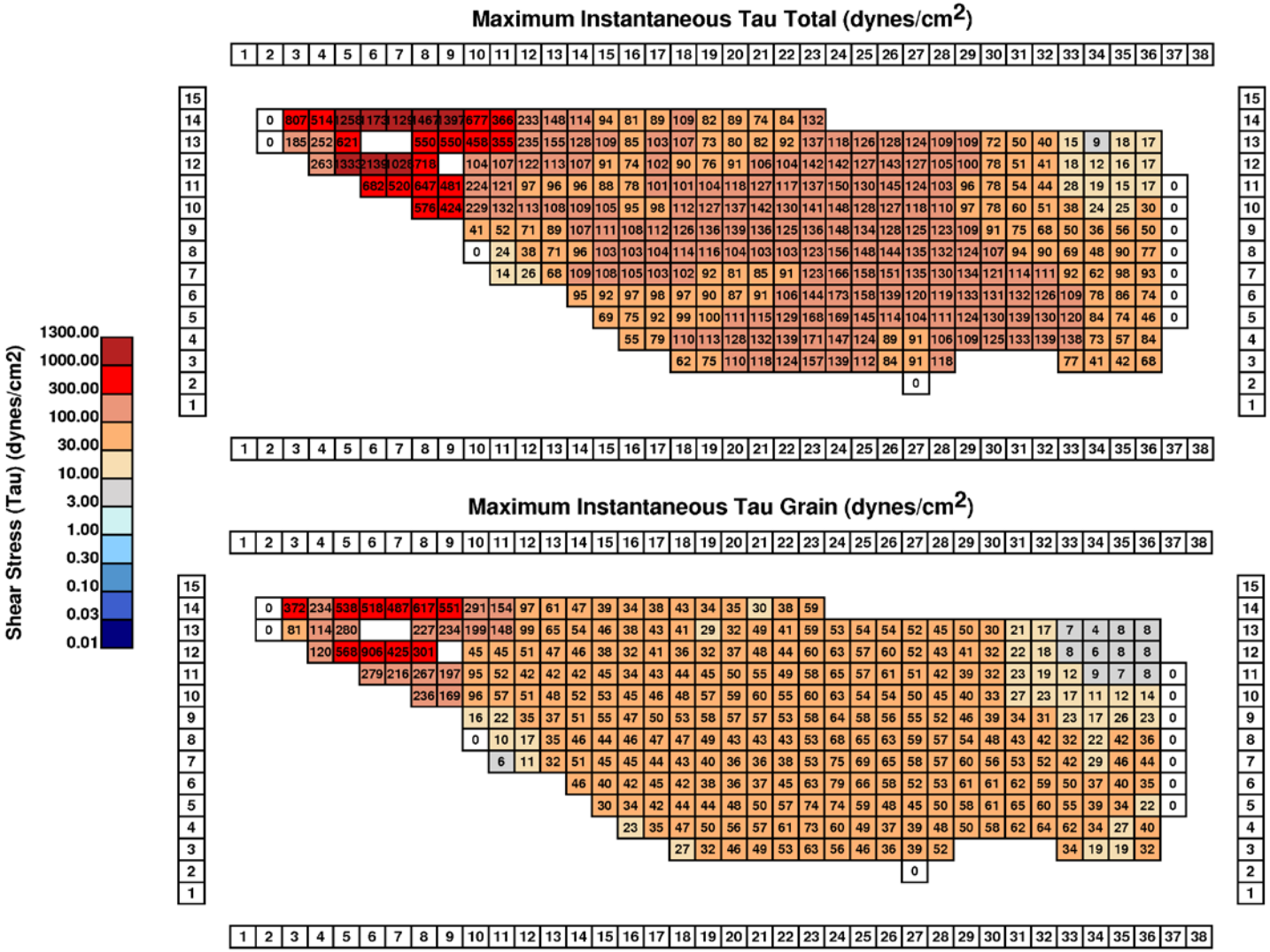


Figure 71. Maximum total bed (Tau Total) and grain (Tau Grain) shear stresses occurring during hydrologic year 2011: Scenario 0.

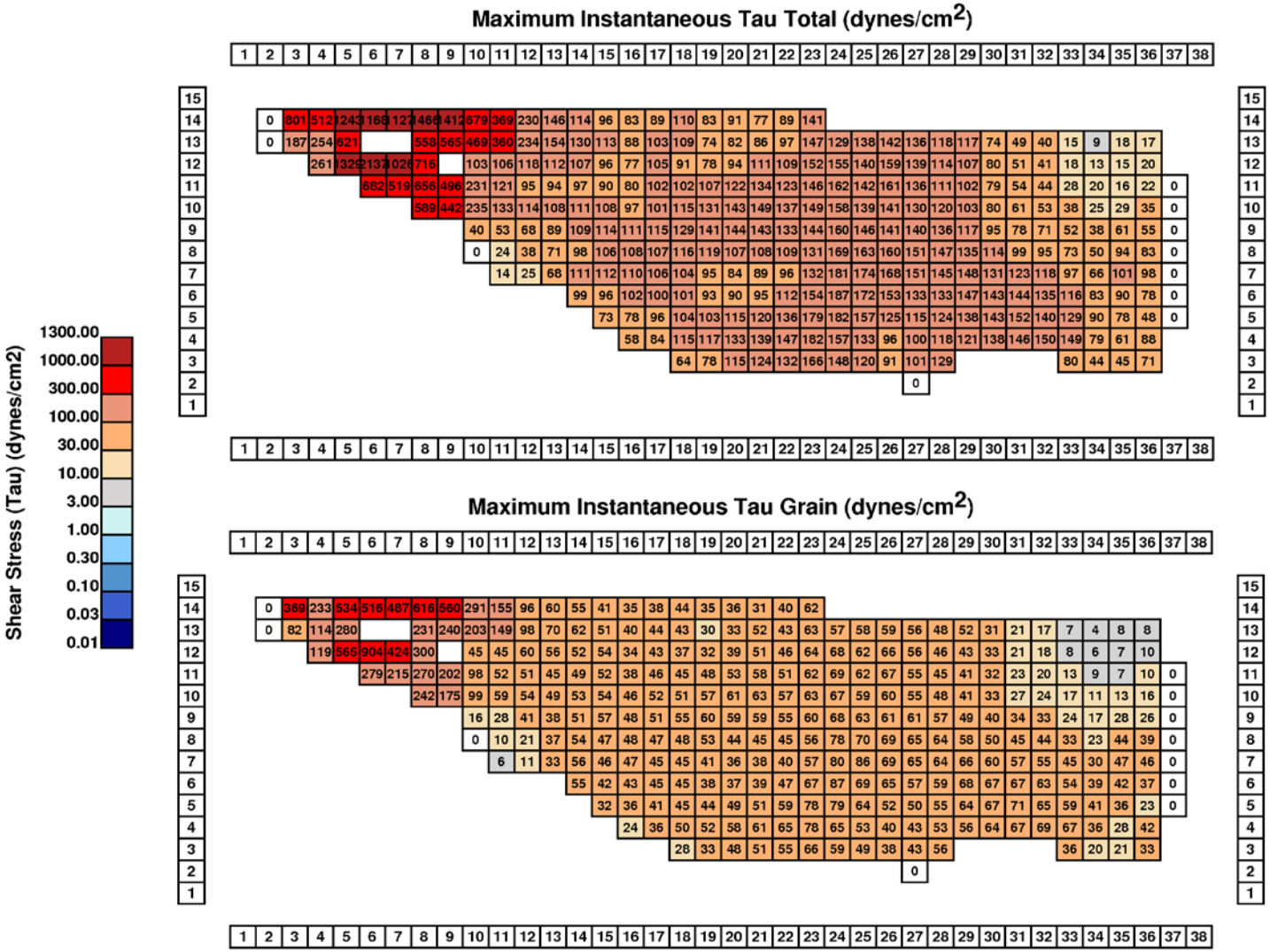


Figure 72. Maximum total bed (Tau Total) and grain (Tau Grain) shear stresses occurring during hydrologic year 2011: Scenario 1.

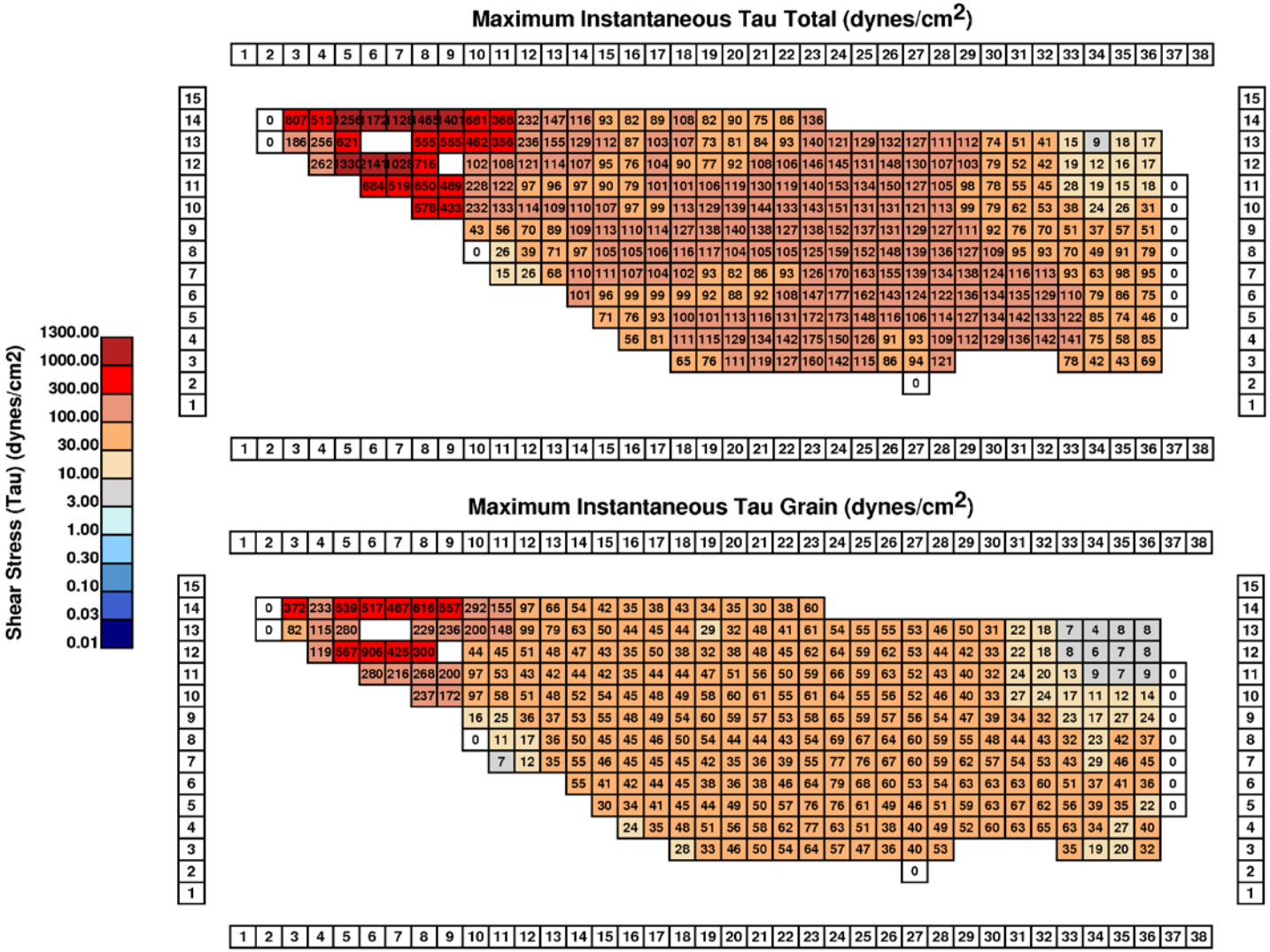


Figure 73. Maximum total bed (Tau Total) and grain (Tau Grain) shear stresses occurring during hydrologic year 2011: Scenario 2.

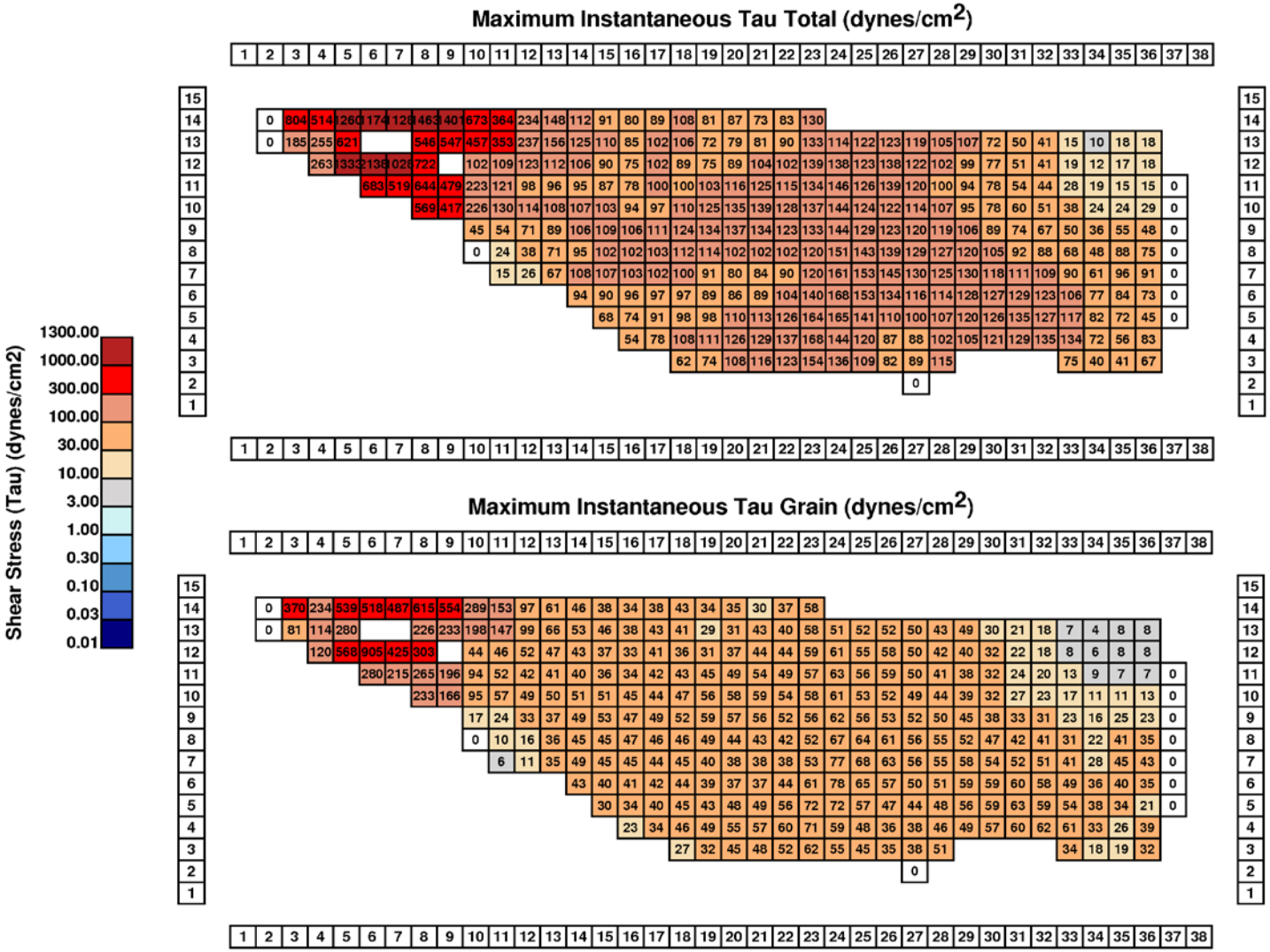


Figure 74. Maximum total bed (Tau Total) and grain (Tau Grain) shear stresses occurring during hydrologic year 2011: Scenario 3.

# APPENDIX A. SHEAR STRESS PARTITIONING

To perform sediment transport calculations, hydrodynamic (total) shear stresses acting at the bottom of the water column need to be separated into surface drag and form drag components because individual grains on the bed surface are only subject to the surface drag component of the total shear stress.

Total hydrodynamic shear stresses are related to eddy viscosity, velocity gradients, drag and velocities near the sediment bed:

$$\rho_w K_M \frac{\partial U}{\partial z} = \tau_b \tag{A-1}$$

$$\tau_b = \rho_w u_*^{\,2} = \rho_w C_D \left[u(z_b)\right]^2 \tag{A-2}$$

where:

| | | |
|---|---|---|
| $\rho_w$ | = | density of water [M $L^{-3}$] |
| $K_M$ | = | vertical eddy viscosity [$L^2$ $T^{-1}$] |
| $\frac{\partial U}{\partial z}$ | = | vertical velocity gradient [$T^{-1}$] |
| $\tau_b$ | = | total (hydrodynamic) bed shear stress [M $L^{-1}$ $T^{-2}$] |
| $u_*$ | = | shear (friction) velocity [L $T^{-1}$] |
| $u(z_b)$ | = | velocity at a height $z_b$ above the bed [L $T^{-1}$] |
| $C_D$ | = | coefficient of drag [dimensionless] |

Eddy viscosity and velocity gradients in the water column are calculated in the hydrodynamic model. A logarithmic velocity profile is used to relate hydrodynamic roughness to water velocities in the last sigma layer of the water column and also the drag coefficient:

$$\frac{u(z_b)}{u_*} = \frac{1}{\kappa} \ln\left(\frac{z_b}{z_0}\right) \tag{A-3}$$

$$C_D = \left[\frac{1}{\kappa} \ln\left(\frac{z}{z_0}\right)\right]^{-2} \tag{A-4}$$

where:

$\kappa$ = von Karman constant = 0.4 [dimensionless]

$z_b$ = height above the bed [L]

$z_o$ = hydrodynamic roughness height of the bed [L]

$C_D$ = coefficient of drag [dimensionless]

The height above the bed ($z_b$) is set equal to one half the thickness of the bottom sigma layer in the water column of the hydrodynamic model.

To perform sediment transport calculations, total hydrodynamic bed shear stress ($\tau_b$) is separated (partitioned) into surface and form drag components. The relationship between total bed shear stress and its components is:

$$\tau_b = \tau_g + \tau_f \quad \text{(A-5)}$$

where:

$\tau_b$ = total (hydrodynamic) bed shear stress [M $L^{-1}$ $T^{-2}$]

$\tau_g$ = surface drag ("grain") shear stress [M $L^{-1}$ $T^{-2}$]

$\tau_f$ = form drag shear stress [M $L^{-1}$ $T^{-2}$]

The surface drag (grain stress) component of the total shear stress acts on particle surfaces and is iteratively calculated from total hydrodynamic bed shear stress ($\tau_b$), total shear velocity ($u_*$), and an initial (first) estimate of grain roughness height (Kamphuis, 1974) assuming hydraulically smooth turbulent flow:[11, 12]

$$k_s = 2d_{50} \quad \text{(A-6)}$$

$$z_{0g}^{(1)} = \frac{k_s}{30} = \frac{d_{50}}{15} \quad \text{(A-7)}$$

[11] Boundary roughness heights are typically expressed in terms of the Nikuradse roughness height ($k_s$) and is approximated as $k_s = 2\ d_{50}$. For hydraulically rough turbulent flow, $z_{og} = k_s/30 = d_{50}/15$.

[12] As an expedient, the model calculates an initial estimate of grain shear stress ($\tau_g$) from total bed shear stress ($\tau_b$) and grain roughness height ($z_{0g}$) using the square of Equation (A-7). This is mathematically equivalent because $u_*^2 = \tau_b/\rho_w$ and $u_{*g}^2 = \tau_g/\rho_w$ [see Equation (A-2)].

$$u_{*g}^{(1)} = u_* \left( \frac{\ln \frac{z_b}{z_o}}{\ln \frac{z_b}{z_{og}^{(1)}}} \right) \quad \text{(A-8)}$$

where:

$u_{*g}^{(1)}$ = initial (first) estimate of grain stress shear velocity [L $T^{-1}$]

$z_{og}^{(1)}$ = initial (first) estimate for grain roughness height [L]

$d_{50}$ = median (i.e., 50th percentile) diameter of bulk sediment [L]

Equations (A-6) and (A-7) are applicable to hydraulically rough turbulent flow (i.e. where particles on the bed protrude beyond the boundary layer that exists in a thin layer next to the bed surface). A second estimate of grain roughness height is calculated using the approach of Winterwerp and van Kesteren (2004):

$$z_{0g}^{(2)} = \frac{0.11\nu}{u_{*g}^{(1)}} + z_{0g}^{(1)} \quad \text{(A-8)}$$

where:

$\nu$ = kinematic viscosity [$L^2$ $T^{-1}$]

$z_{og}^{(2)}$ = second estimate for grain roughness height [L]

Equation (A-8) is applicable to transitionally rough turbulent flow. Additional iterations could be performed to allow more resolved estimates of bed roughness height ($z_{0g}$) to be calculated. A boundary layer Reynolds number could also be calculated to further refine bed roughness height estimates over the spectrum of hydraulically smooth, transitionally rough, and hydraulically rough turbulent flow conditions. However, for simplicity and to avoid the added computational overhead associated with additional iterations, the second estimate of bed roughness height is used to calculate a second estimate of grain stress shear velocity and the surface drag component of the total shear stress as follows:

$$u_{*g}^{(2)} = u_* \left( \frac{\ln \frac{z_b}{z_o}}{\ln \frac{z_b}{z_{og}^{(2)}}} \right) \quad \text{(A-9)}$$

$$\tau_g = \rho_w u_{*g}{}^2 = \rho_w \left( u_{*g}{}^{(2)} \right)^2 \quad \text{(A-10)}$$

where:

$u_{*g}^{(2)}$ = second (refined) estimate of grain stress shear velocity [L $T^{-1}$]

$z_{og}^{(2)}$ = second (refined) estimate for grain roughness height [L]

$\tau_g$ = grain stress (surface drag) component of total shear stress [M $L^{-1}$ $T^{-2}$]

$u_{*g}$ = grain stress shear velocity [L $T^{-1}$]

Additional adjustments to the bed shear stress partitioning process are performed to account for the presence of bedforms. Bedform formation and decay over time alters bed roughness. Increasing bedform roughness causes greater form drag and reduces the surface drag component of the total shear stress. Decreasing bedform roughness results in less form drag and increases the surface drag component of total shear stress. Conversely, increasing bedform roughness results in additional form drag and decreases the surface drag component of total shear stress.

# References

Winterwerp, J. C., and van Kesteren, W. G. M. 2004. *Introduction to the Physics of Cohesive Sediment in the Marine Environment*. Elsevier B.V., Amsterdam, Netherlands. 466 p.

# APPENDIX B. SIMULATED AND MEASURED WATER SURFACE ELEVATIONS (LONG-TERM): 1997-2014

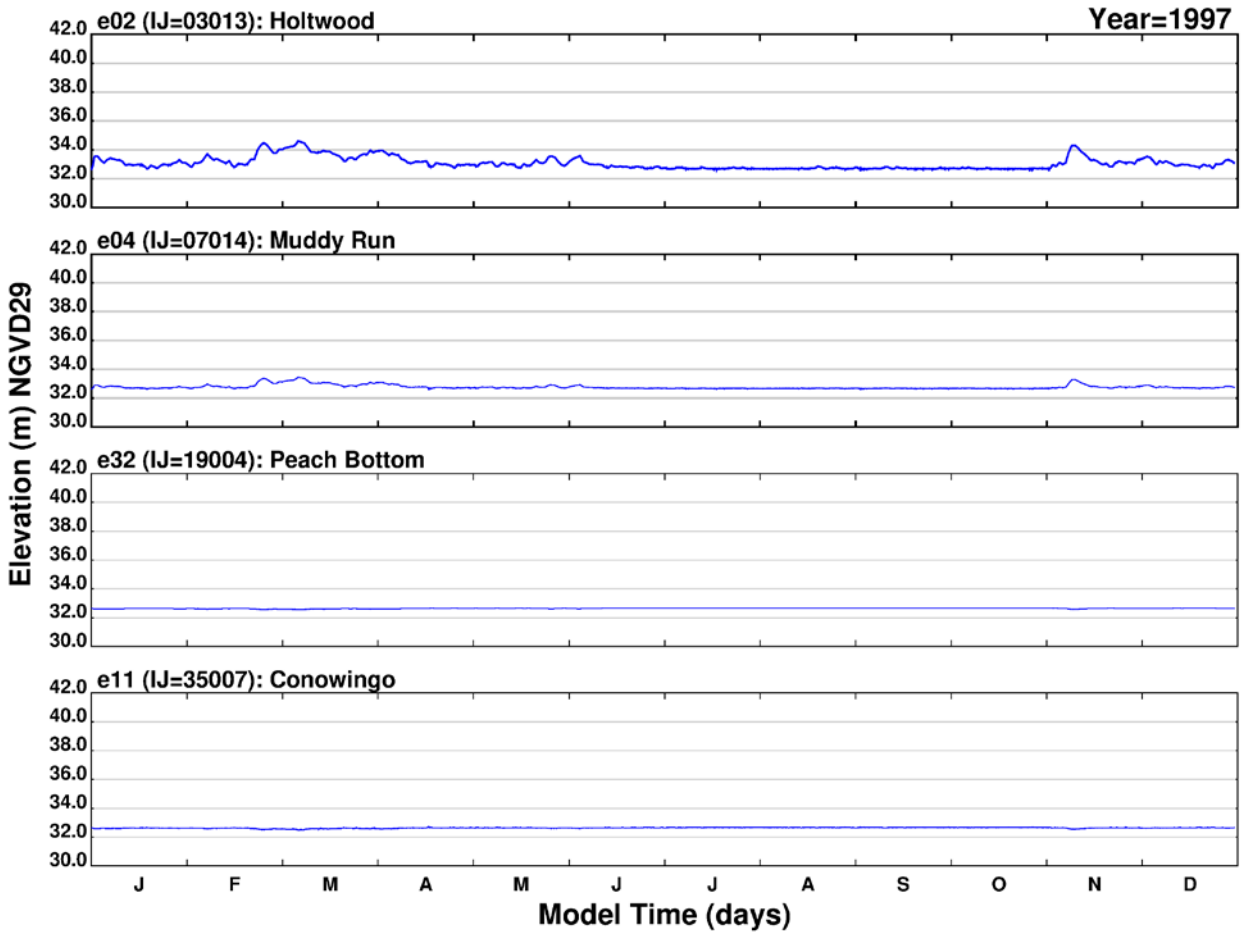


Note: Blue = simulated (hourly); Red = measured daily average and range (measurements begin in 2004); Green = 168-hour lowpass filtered measurements (hourly); IJ indicates the model grid cell from which outputs were retrieved; x-axis divisions indicate a one character abbreviation for month of year in sequence from January through December; y-axis maximum indicates the approximate maximum water level that occurs during Tropical Storm Lee in 2011.

Figure B-1. Simulated and measured water surface elevations over time at Holtwood, Muddy Run, Peach Bottom, and Conowingo: 1997 (long-term simulation).

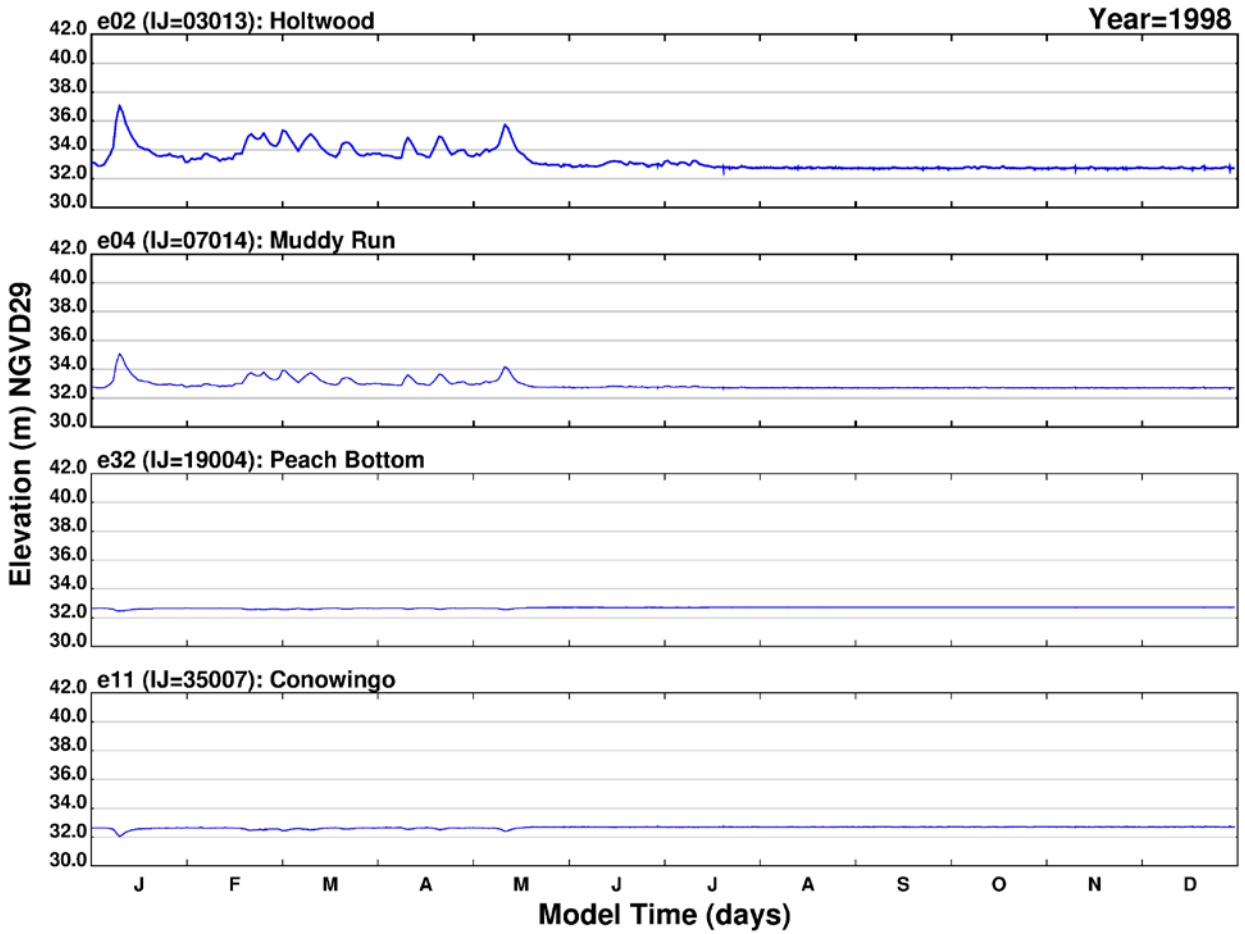


Note: Blue = simulated (hourly); Red = measured daily average and range (measurements begin in 2004); Green = 168-hour lowpass filtered measurements (hourly); IJ indicates the model grid cell from which outputs were retrieved; x-axis divisions indicate a one character abbreviation for month of year in sequence from January through December; y-axis maximum indicates the approximate maximum water level that occurs during Tropical Storm Lee in 2011.

Figure B-2. Simulated and measured water surface elevations over time at Holtwood, Muddy Run, Peach Bottom, and Conowingo: 1998 (long-term simulation).

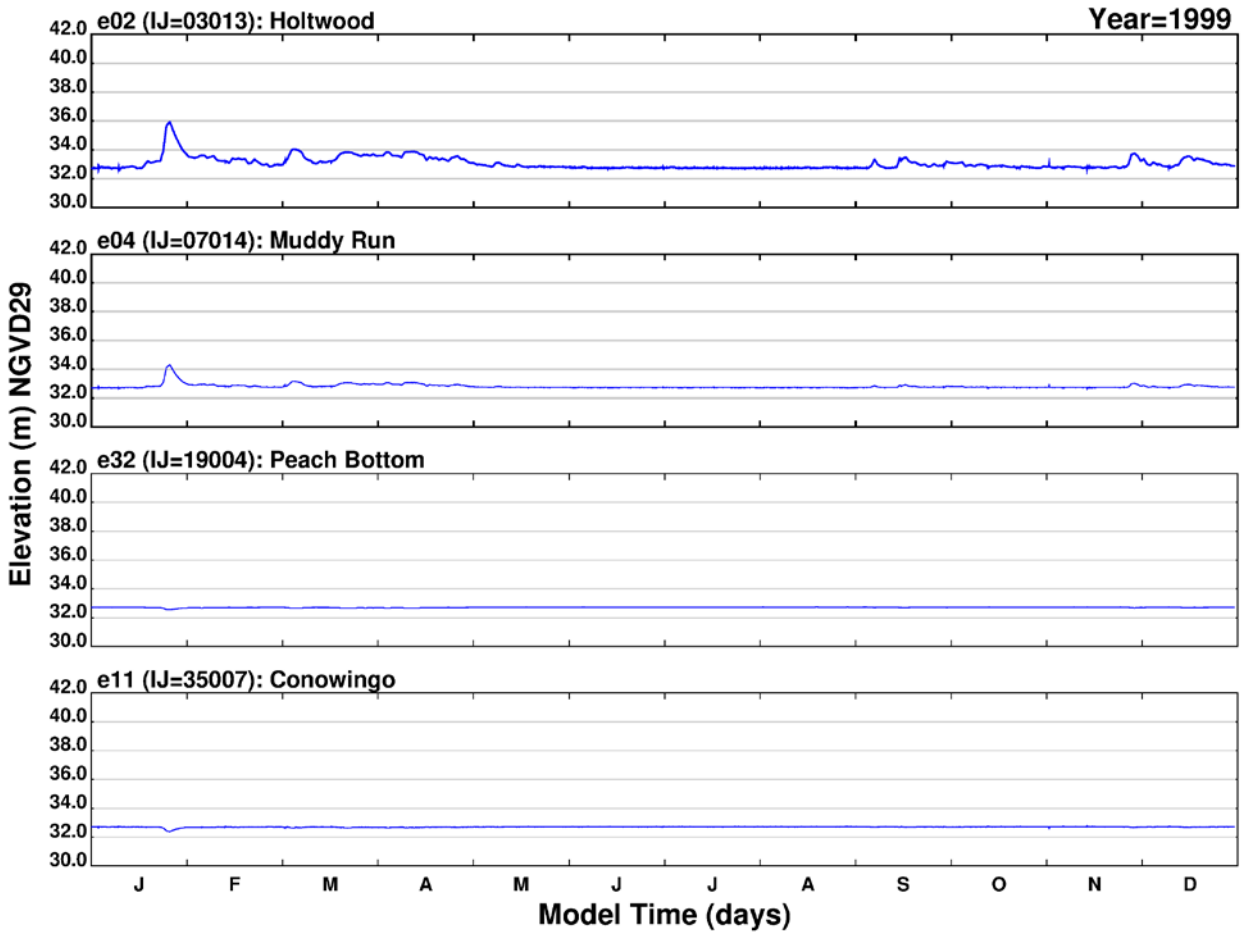


Note: Blue = simulated (hourly); Red = measured daily average and range (measurements begin in 2004); Green = 168-hour lowpass filtered measurements (hourly); IJ indicates the model grid cell from which outputs were retrieved; x-axis divisions indicate a one character abbreviation for month of year in sequence from January through December; y-axis maximum indicates the approximate maximum water level that occurs during Tropical Storm Lee in 2011.

Figure B-3. Simulated and measured water surface elevations over time at Holtwood, Muddy Run, Peach Bottom, and Conowingo: 1999 (long-term simulation).

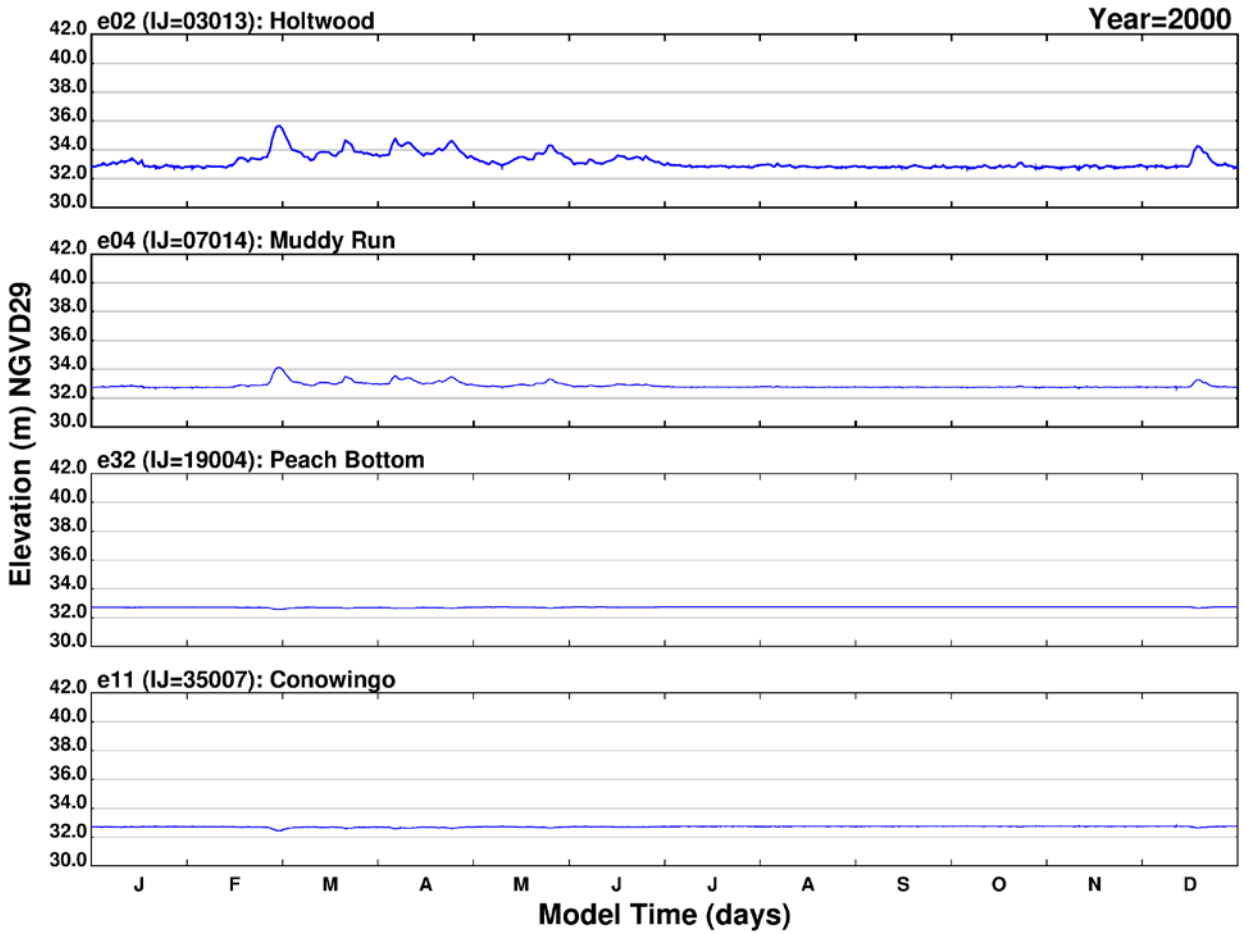


Note: Blue = simulated (hourly); Red = measured daily average and range (measurements begin in 2004); Green = 168-hour lowpass filtered measurements (hourly); IJ indicates the model grid cell from which outputs were retrieved; x-axis divisions indicate a one character abbreviation for month of year in sequence from January through December; y-axis maximum indicates the approximate maximum water level that occurs during Tropical Storm Lee in 2011.

Figure B-4. Simulated and measured water surface elevations over time at Holtwood, Muddy Run, Peach Bottom, and Conowingo: 2000 (long-term simulation).

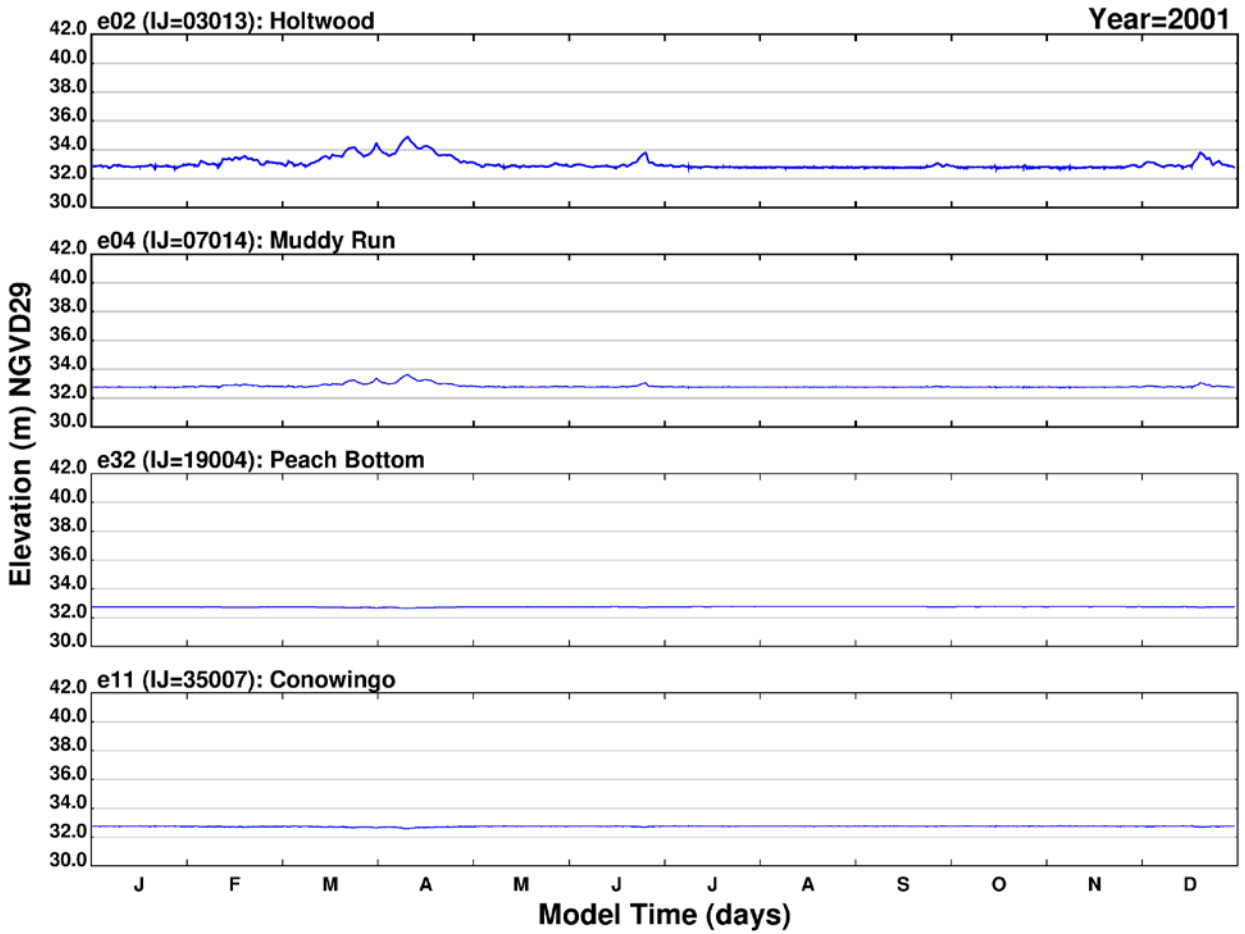


Note: Blue = simulated (hourly); Red = measured daily average and range (measurements begin in 2004); Green = 168-hour lowpass filtered measurements (hourly); IJ indicates the model grid cell from which outputs were retrieved; x-axis divisions indicate a one character abbreviation for month of year in sequence from January through December; y-axis maximum indicates the approximate maximum water level that occurs during Tropical Storm Lee in 2011.

Figure B-5. Simulated and measured water surface elevations over time at Holtwood, Muddy Run, Peach Bottom, and Conowingo: 2001 (long-term simulation).

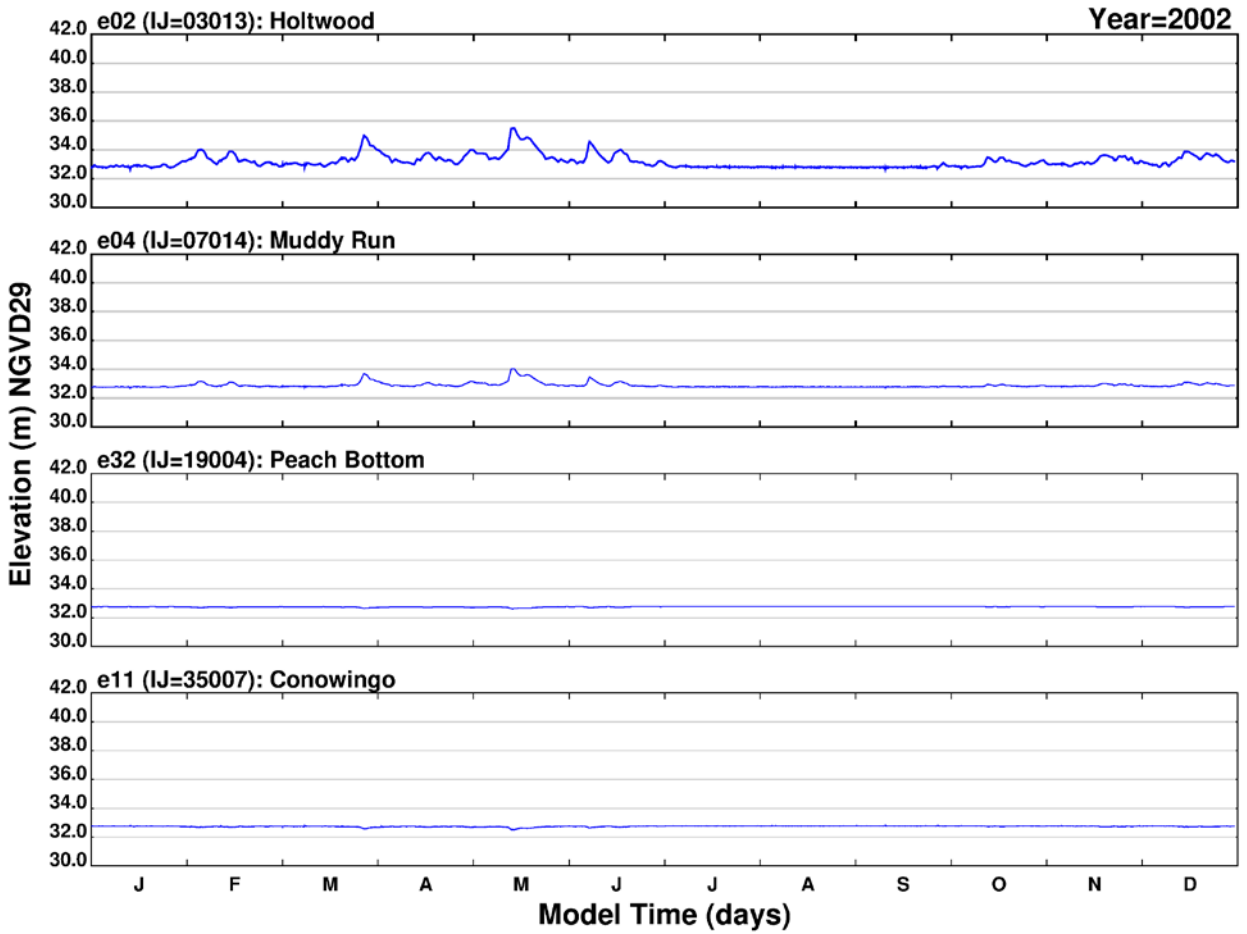


Note: Blue = simulated (hourly); Red = measured daily average and range (measurements begin in 2004); Green = 168-hour lowpass filtered measurements (hourly); IJ indicates the model grid cell from which outputs were retrieved; x-axis divisions indicate a one character abbreviation for month of year in sequence from January through December; y-axis maximum indicates the approximate maximum water level that occurs during Tropical Storm Lee in 2011.

Figure B-6. Simulated and measured water surface elevations over time at Holtwood, Muddy Run, Peach Bottom, and Conowingo: 2002 (long-term simulation).

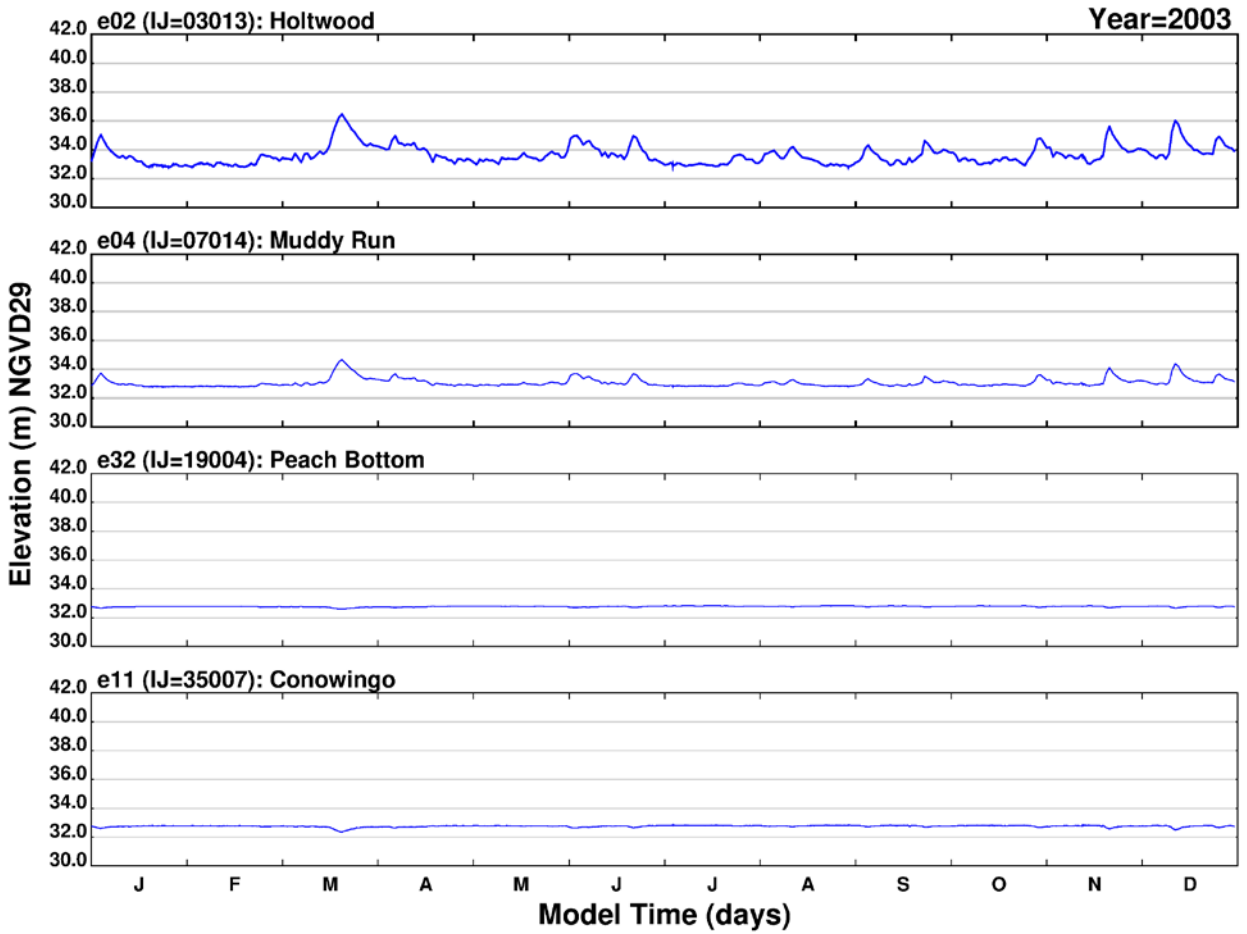


Note: Blue = simulated (hourly); Red = measured daily average and range (measurements begin in 2004); Green = 168-hour lowpass filtered measurements (hourly); IJ indicates the model grid cell from which outputs were retrieved; x-axis divisions indicate a one character abbreviation for month of year in sequence from January through December; y-axis maximum indicates the approximate maximum water level that occurs during Tropical Storm Lee in 2011.

Figure B-7. Simulated and measured water surface elevations over time at Holtwood, Muddy Run, Peach Bottom, and Conowingo: 2003 (long-term simulation).

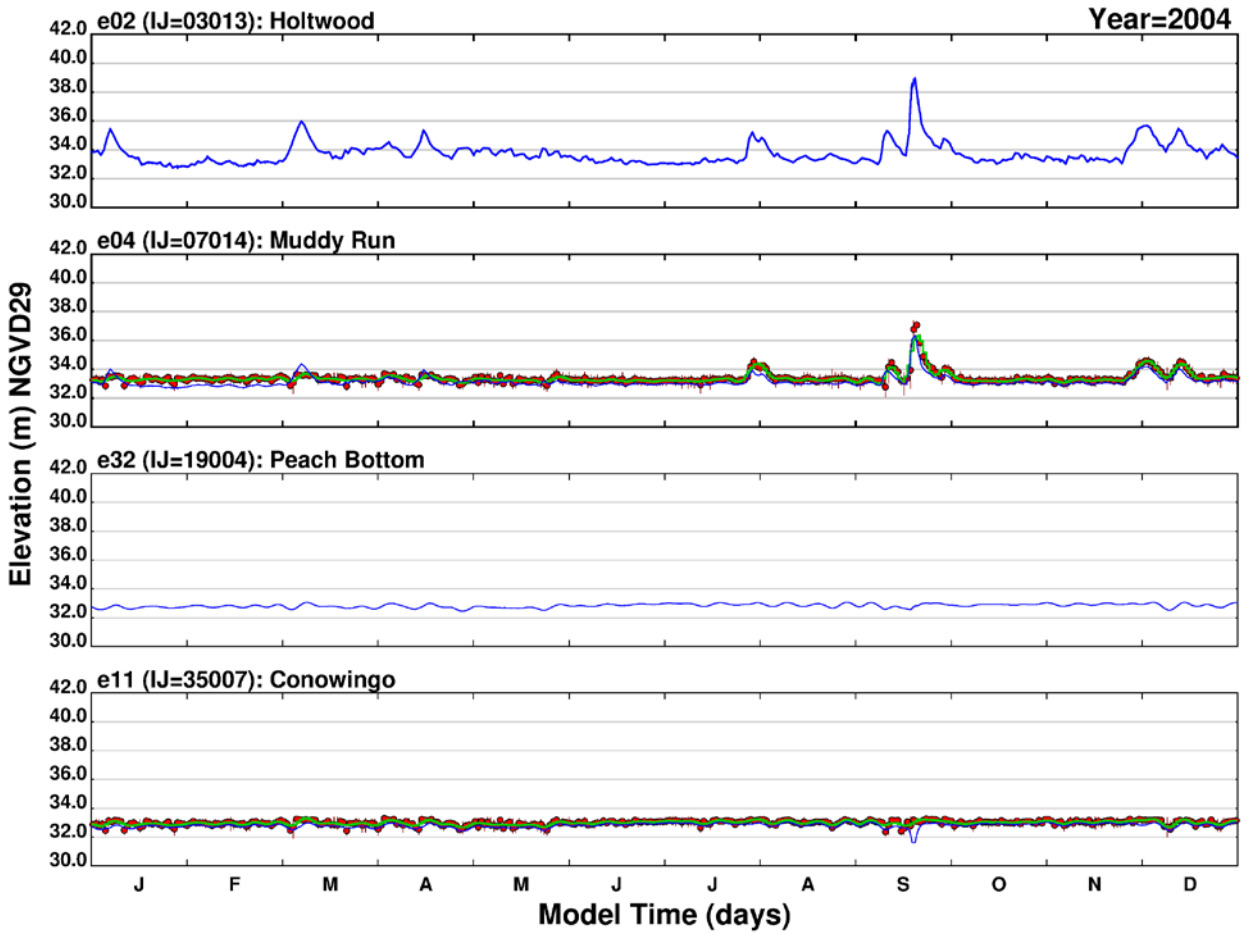


Note: Blue = simulated (hourly); Red = measured daily average and range (measurements begin in 2004); Green = 168-hour lowpass filtered measurements (hourly); IJ indicates the model grid cell from which outputs were retrieved; x-axis divisions indicate a one character abbreviation for month of year in sequence from January through December; y-axis maximum indicates the approximate maximum water level that occurs during Tropical Storm Lee in 2011.

Figure B-8. Simulated and measured water surface elevations over time at Holtwood, Muddy Run, Peach Bottom, and Conowingo: 2004 (long-term simulation).

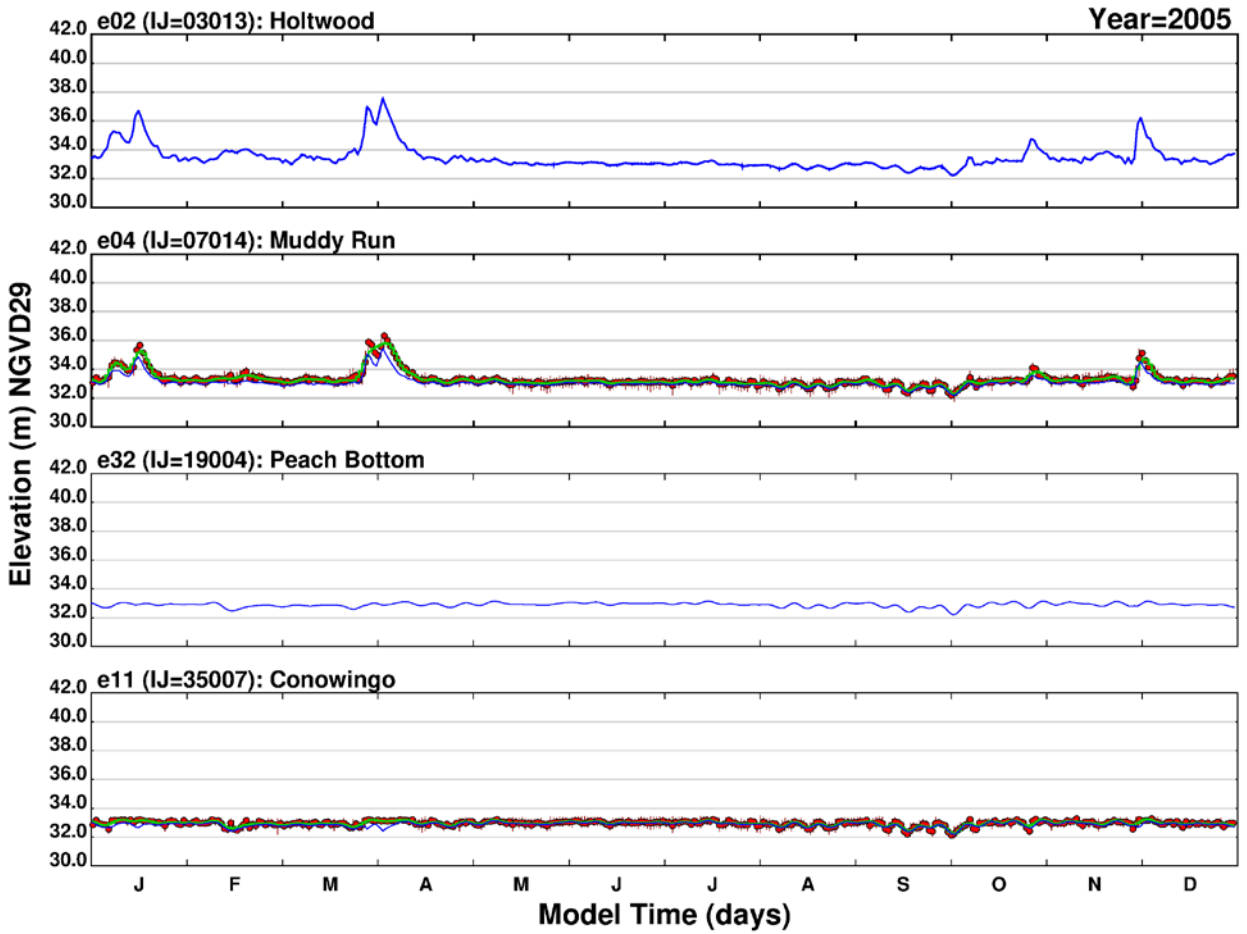


Note: Blue = simulated (hourly); Red = measured daily average and range (measurements begin in 2004); Green = 168-hour lowpass filtered measurements (hourly); IJ indicates the model grid cell from which outputs were retrieved; x-axis divisions indicate a one character abbreviation for month of year in sequence from January through December; y-axis maximum indicates the approximate maximum water level that occurs during Tropical Storm Lee in 2011.

Figure B-9. Simulated and measured water surface elevations over time at Holtwood, Muddy Run, Peach Bottom, and Conowingo: 2005 (long-term simulation).

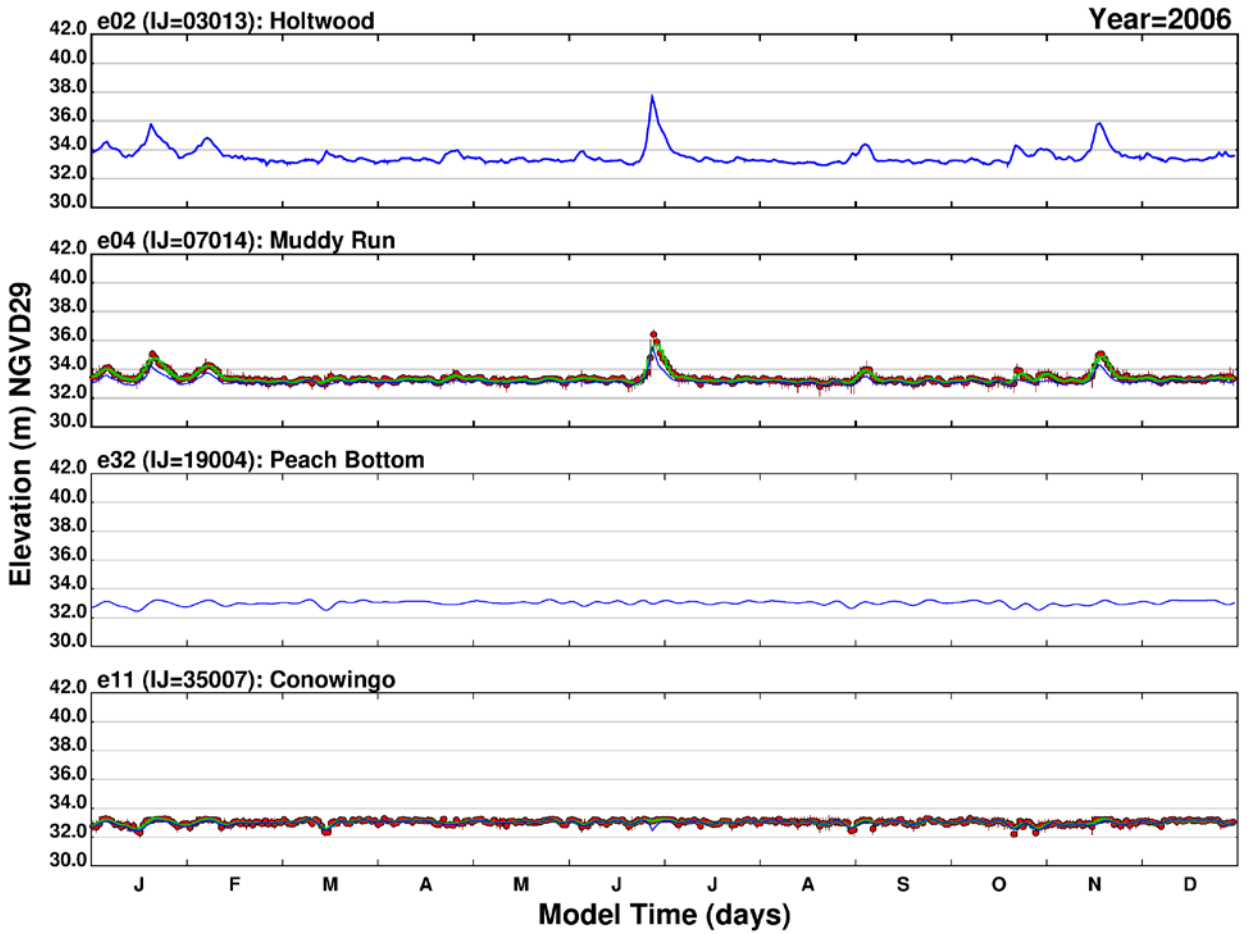


Note: Blue = simulated (hourly); Red = measured daily average and range (measurements begin in 2004); Green = 168-hour lowpass filtered measurements (hourly); IJ indicates the model grid cell from which outputs were retrieved; x-axis divisions indicate a one character abbreviation for month of year in sequence from January through December; y-axis maximum indicates the approximate maximum water level that occurs during Tropical Storm Lee in 2011.

Figure B-10. Simulated and measured water surface elevations over time at Holtwood, Muddy Run, Peach Bottom, and Conowingo: 2006 (long-term simulation).

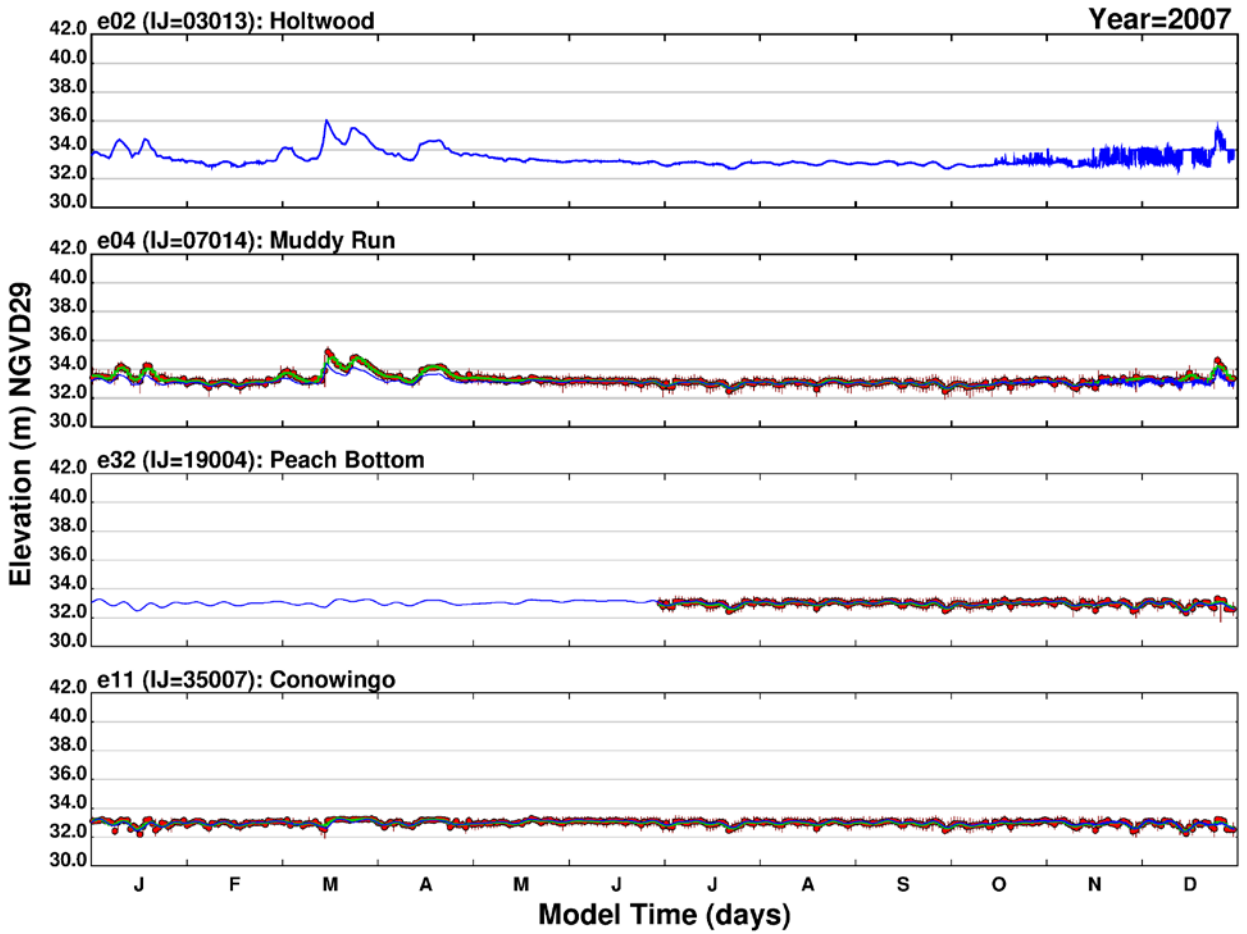


Note: Blue = simulated (hourly); Red = measured daily average and range (measurements begin in 2004); Green = 168-hour lowpass filtered measurements (hourly); IJ indicates the model grid cell from which outputs were retrieved; x-axis divisions indicate a one character abbreviation for month of year in sequence from January through December; y-axis maximum indicates the approximate maximum water level that occurs during Tropical Storm Lee in 2011.

Figure B-11. Simulated and measured water surface elevations over time at Holtwood, Muddy Run, Peach Bottom, and Conowingo: 2007 (long-term simulation).

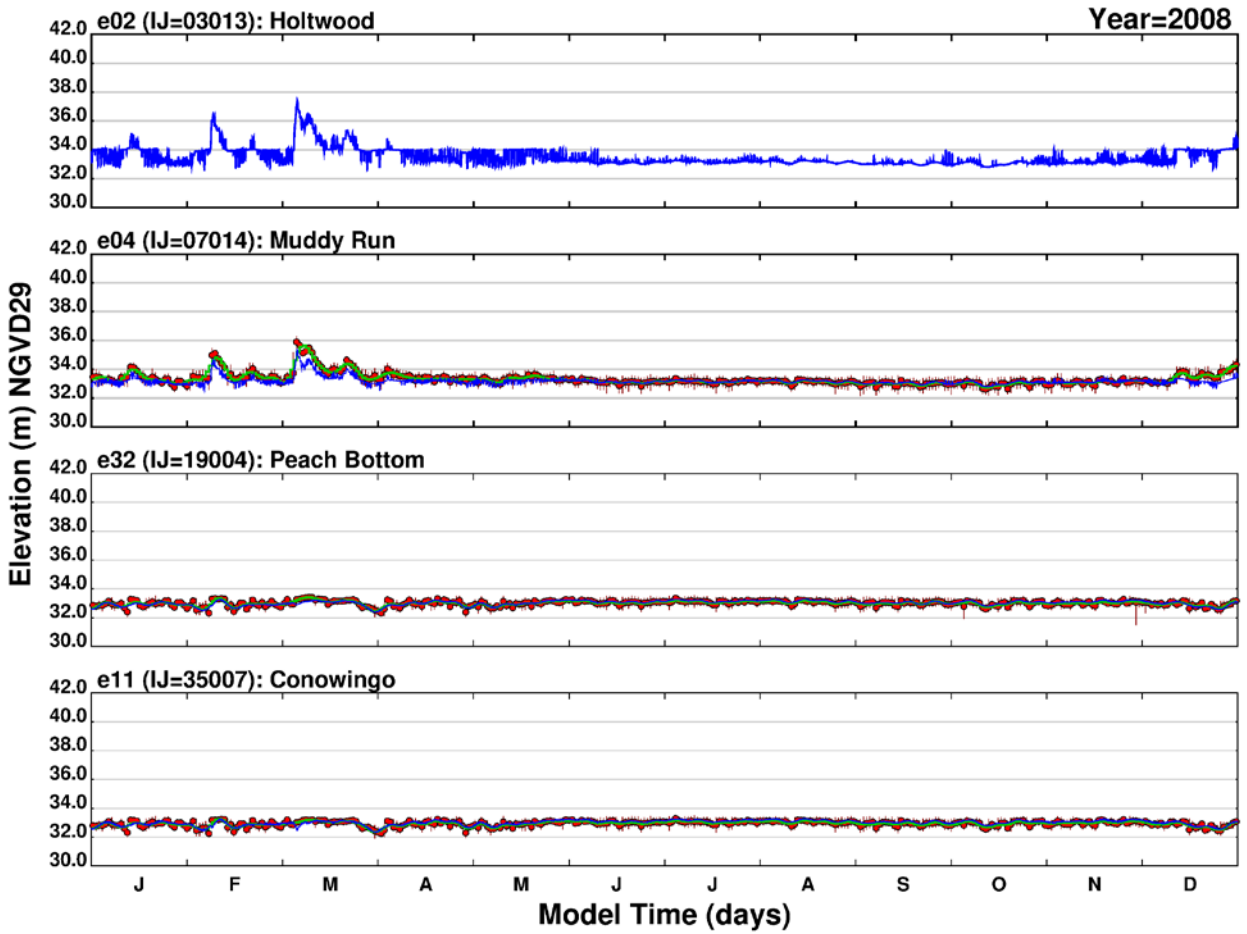


Note: Blue = simulated (hourly); Red = measured daily average and range (measurements begin in 2004); Green = 168-hour lowpass filtered measurements (hourly); IJ indicates the model grid cell from which outputs were retrieved; x-axis divisions indicate a one character abbreviation for month of year in sequence from January through December; y-axis maximum indicates the approximate maximum water level that occurs during Tropical Storm Lee in 2011.

Figure B-12. Simulated and measured water surface elevations over time at Holtwood, Muddy Run, Peach Bottom, and Conowingo: 2008 (long-term simulation).

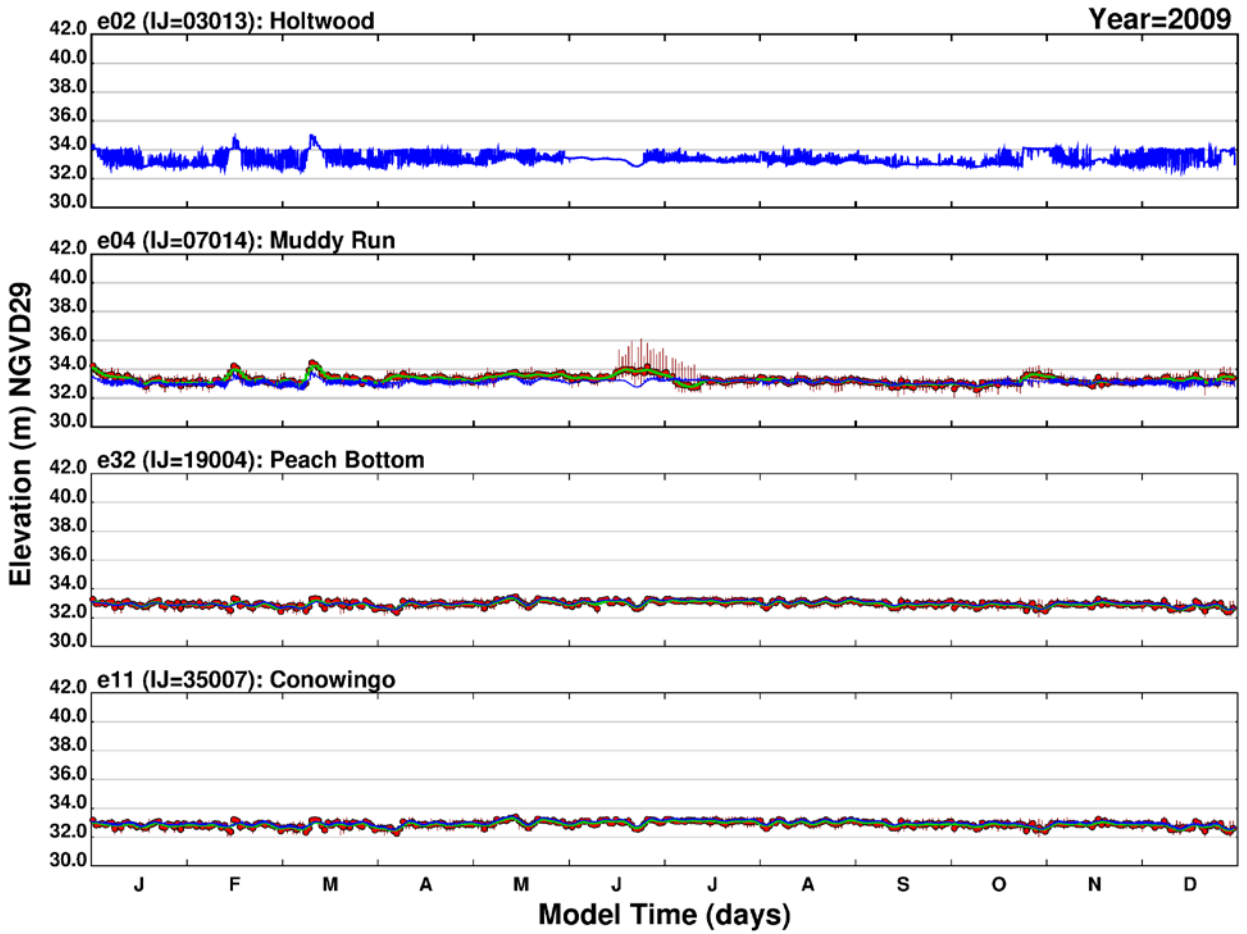


Note: Blue = simulated (hourly); Red = measured daily average and range (measurements begin in 2004); Green = 168-hour lowpass filtered measurements (hourly); IJ indicates the model grid cell from which outputs were retrieved; x-axis divisions indicate a one character abbreviation for month of year in sequence from January through December; y-axis maximum indicates the approximate maximum water level that occurs during Tropical Storm Lee in 2011.

Figure B-13. Simulated and measured water surface elevations over time at Holtwood, Muddy Run, Peach Bottom, and Conowingo: 2009 (long-term simulation).

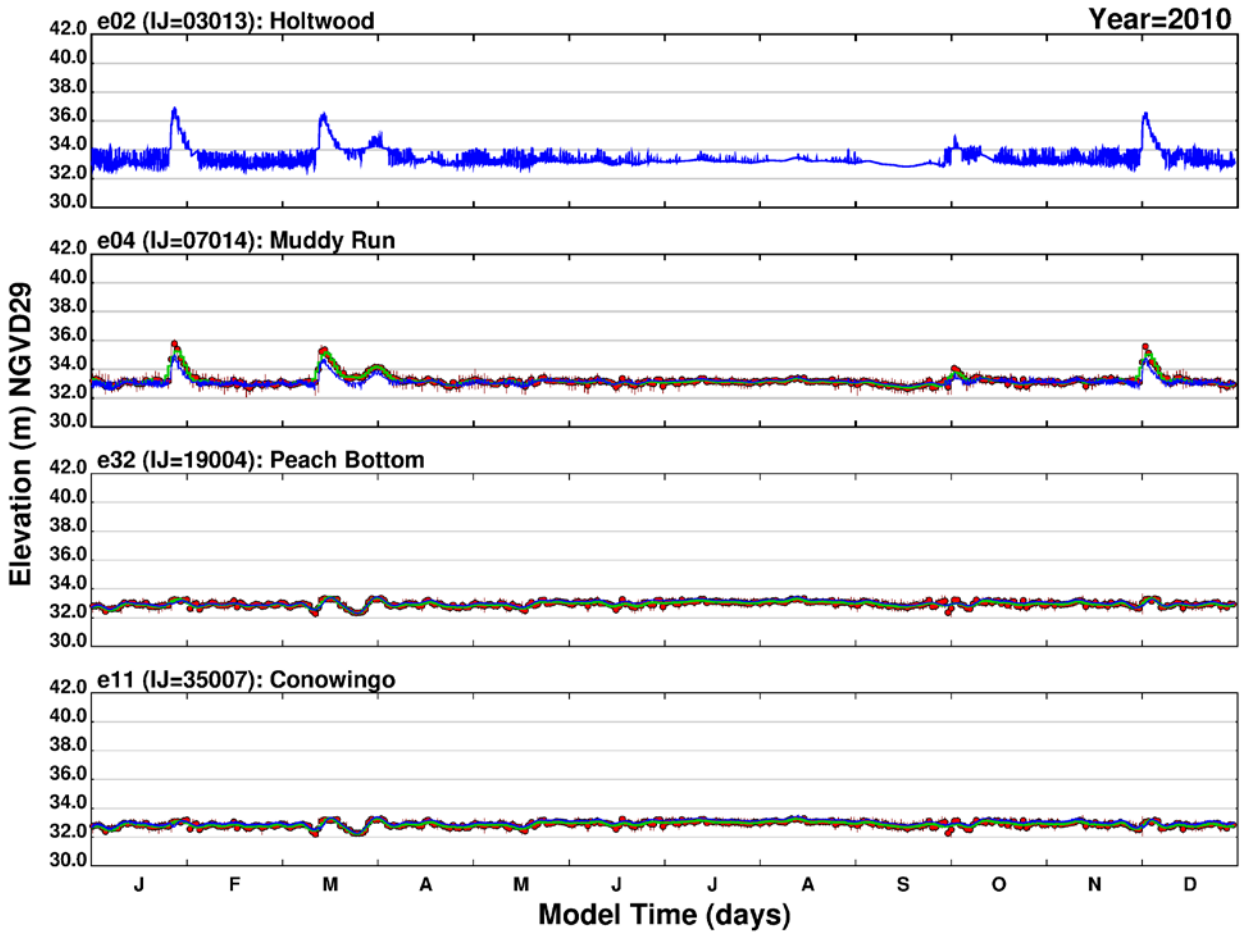


Note: Blue = simulated (hourly); Red = measured daily average and range (measurements begin in 2004); Green = 168-hour lowpass filtered measurements (hourly); IJ indicates the model grid cell from which outputs were retrieved; x-axis divisions indicate a one character abbreviation for month of year in sequence from January through December; y-axis maximum indicates the approximate maximum water level that occurs during Tropical Storm Lee in 2011.

Figure B-14. Simulated and measured water surface elevations over time at Holtwood, Muddy Run, Peach Bottom, and Conowingo: 2010 (long-term simulation).

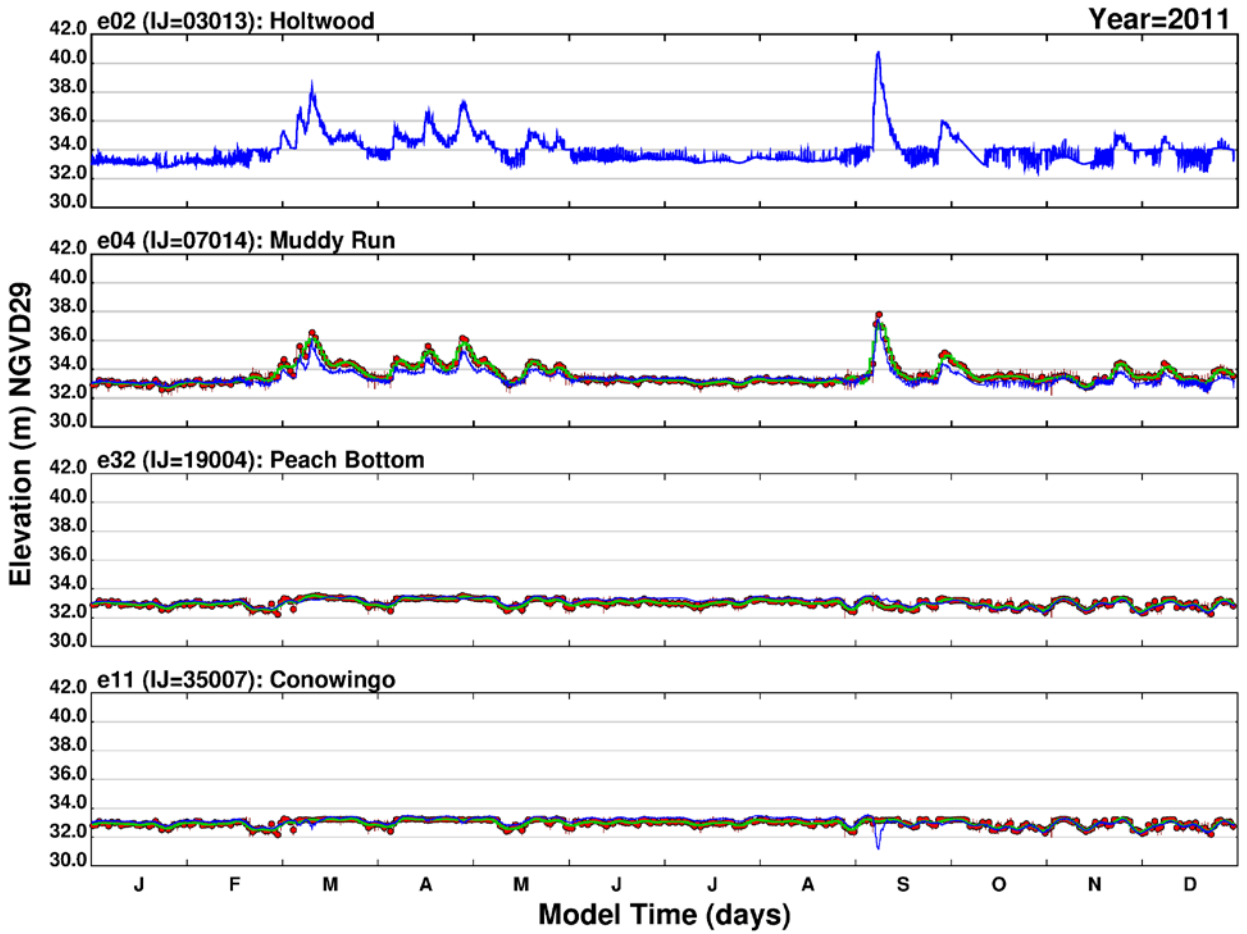


Note: Blue = simulated (hourly); Red = measured daily average and range (measurements begin in 2004); Green = 168-hour lowpass filtered measurements (hourly); IJ indicates the model grid cell from which outputs were retrieved; x-axis divisions indicate a one character abbreviation for month of year in sequence from January through December; y-axis maximum indicates the approximate maximum water level that occurs during Tropical Storm Lee in 2011.

Figure B-15. Simulated and measured water surface elevations over time at Holtwood, Muddy Run, Peach Bottom, and Conowingo: 2011 (long-term simulation).

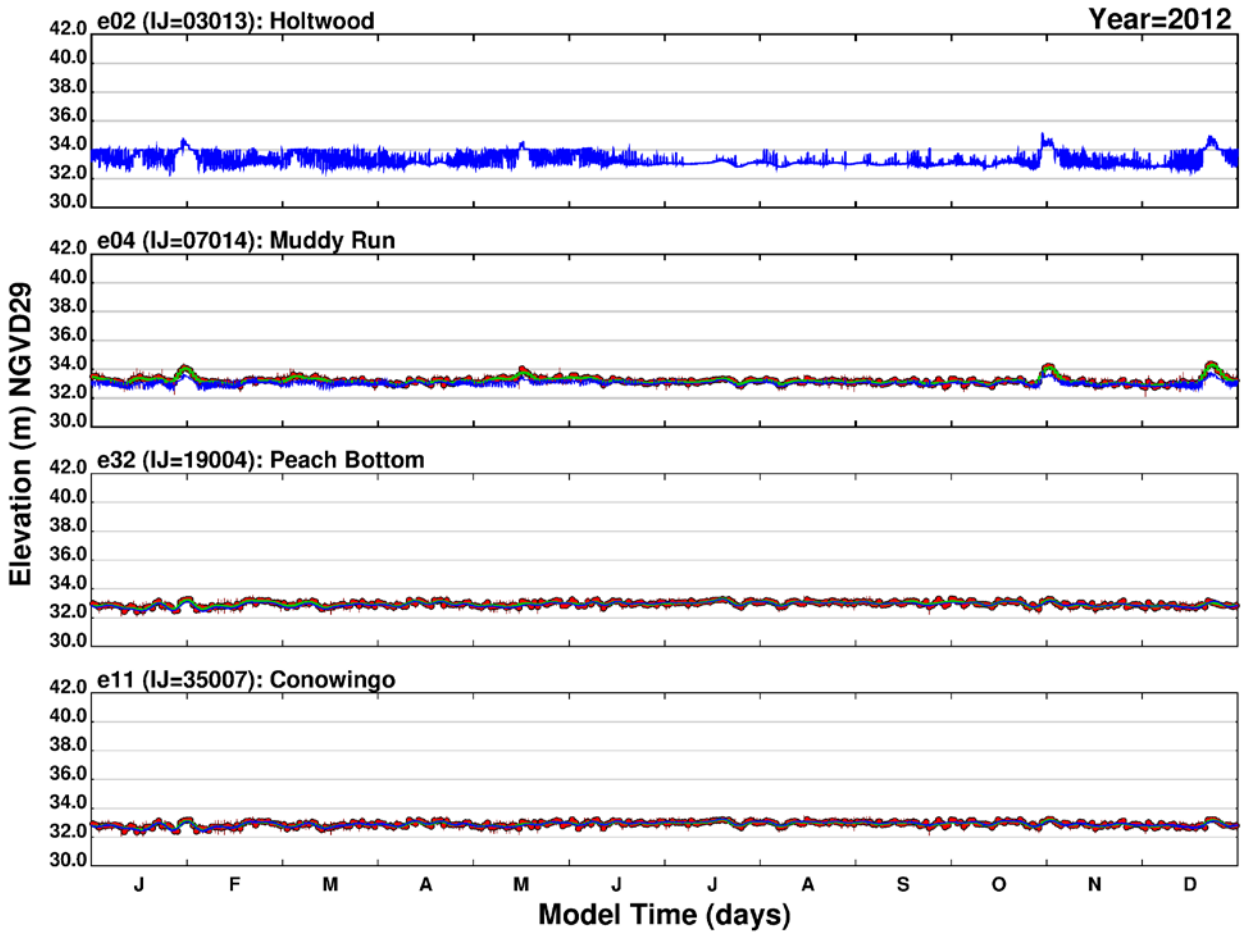


Note: Blue = simulated (hourly); Red = measured daily average and range (measurements begin in 2004); Green = 168-hour lowpass filtered measurements (hourly); IJ indicates the model grid cell from which outputs were retrieved; x-axis divisions indicate a one character abbreviation for month of year in sequence from January through December; y-axis maximum indicates the approximate maximum water level that occurs during Tropical Storm Lee in 2011.

Figure B-16. Simulated and measured water surface elevations over time at Holtwood, Muddy Run, Peach Bottom, and Conowingo: 2012 (long-term simulation).

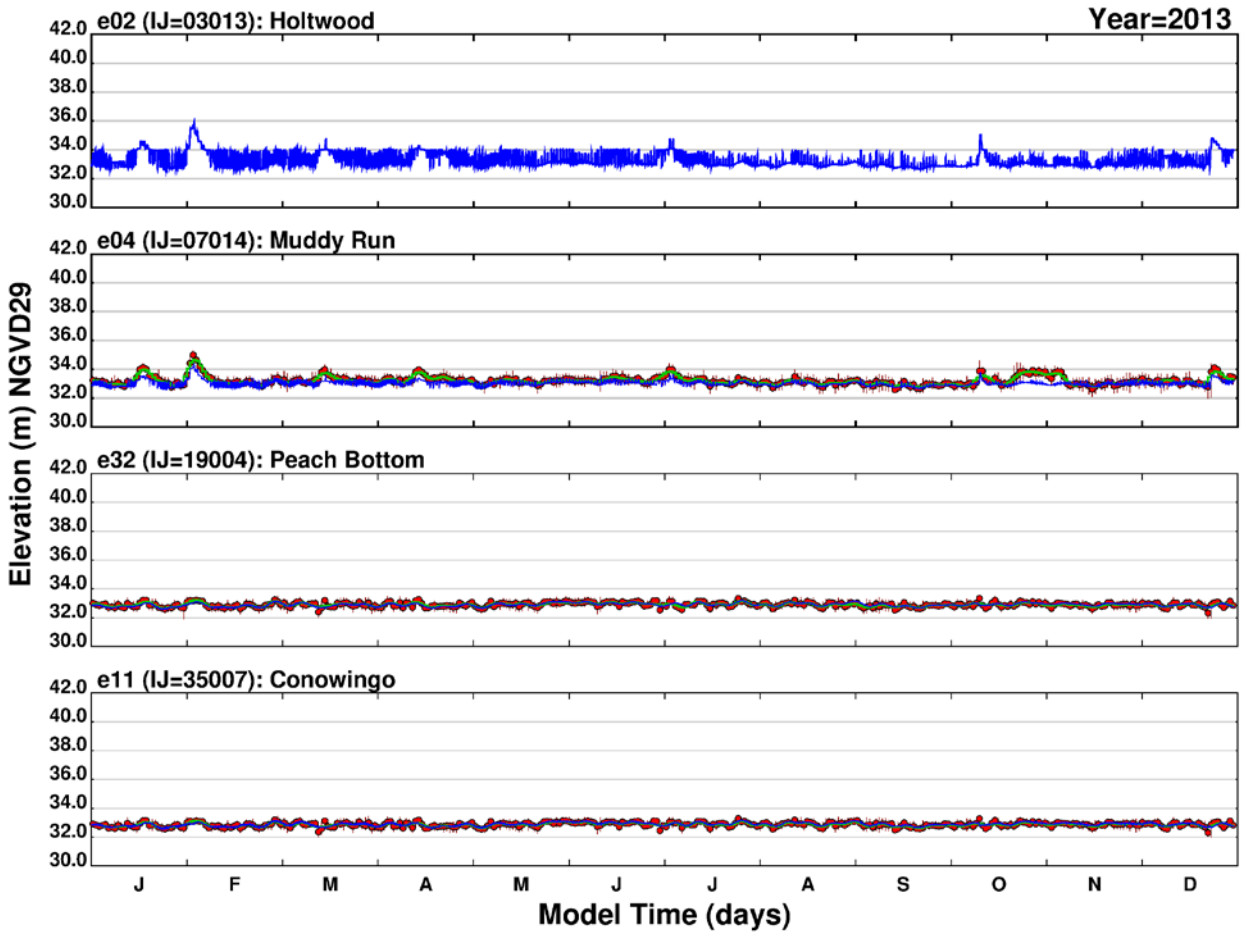


Note: Blue = simulated (hourly); Red = measured daily average and range (measurements begin in 2004); Green = 168-hour lowpass filtered measurements (hourly); IJ indicates the model grid cell from which outputs were retrieved; x-axis divisions indicate a one character abbreviation for month of year in sequence from January through December; y-axis maximum indicates the approximate maximum water level that occurs during Tropical Storm Lee in 2011.

Figure B-17. Simulated and measured water surface elevations over time at Holtwood, Muddy Run, Peach Bottom, and Conowingo: 2013 (long-term simulation).

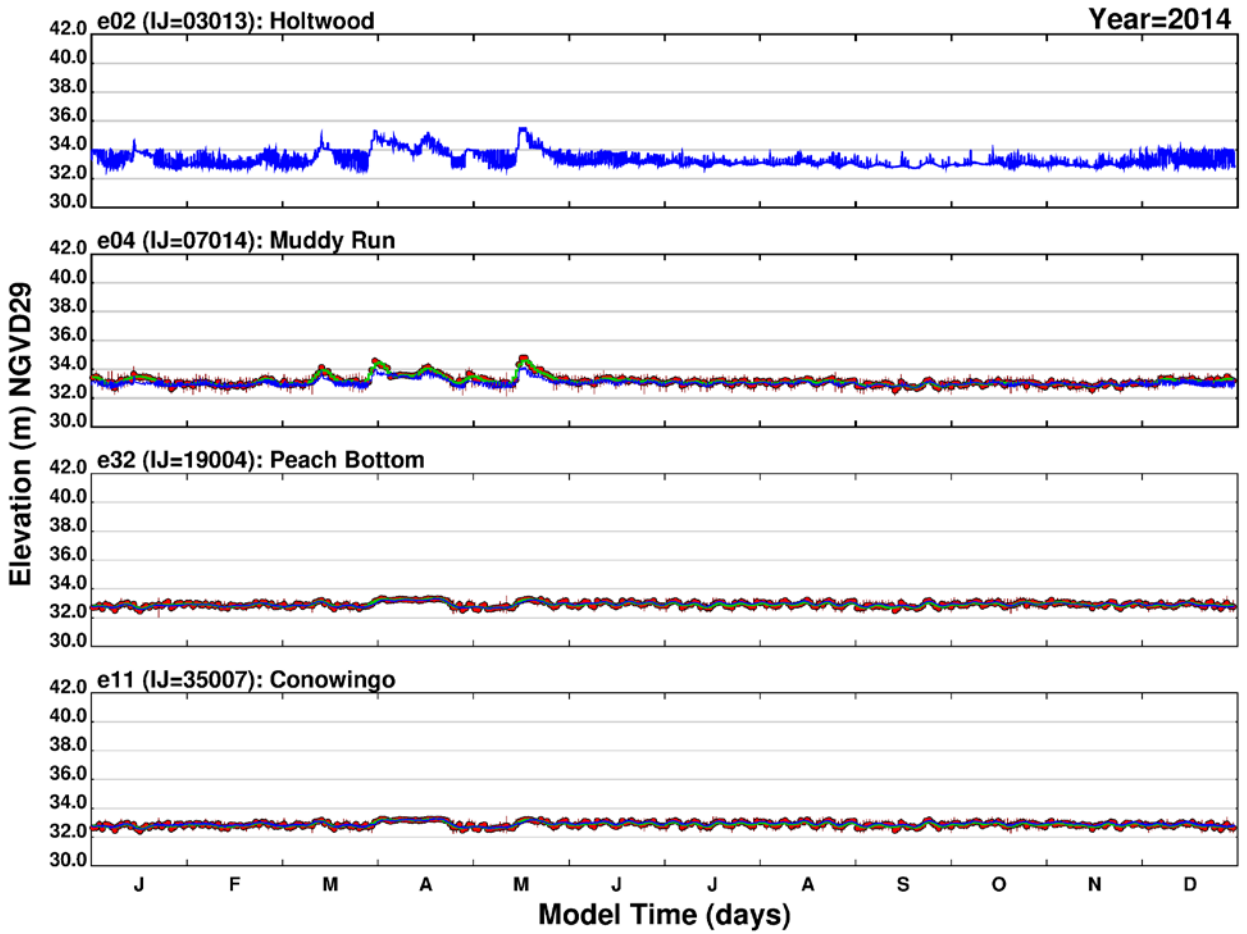


Note: Blue = simulated (hourly); Red = measured daily average and range (measurements begin in 2004); Green = 168-hour lowpass filtered measurements (hourly); IJ indicates the model grid cell from which outputs were retrieved; x-axis divisions indicate a one character abbreviation for month of year in sequence from January through December; y-axis maximum indicates the approximate maximum water level that occurs during Tropical Storm Lee in 2011.

Figure B-18. Simulated and measured water surface elevations over time at Holtwood, Muddy Run, Peach Bottom, and Conowingo: 2014 (long-term simulation).

# APPENDIX C. SIMULATED AND MEASURED WATER SURFACE ELEVATIONS (SHORT-TERM): 2008-2014

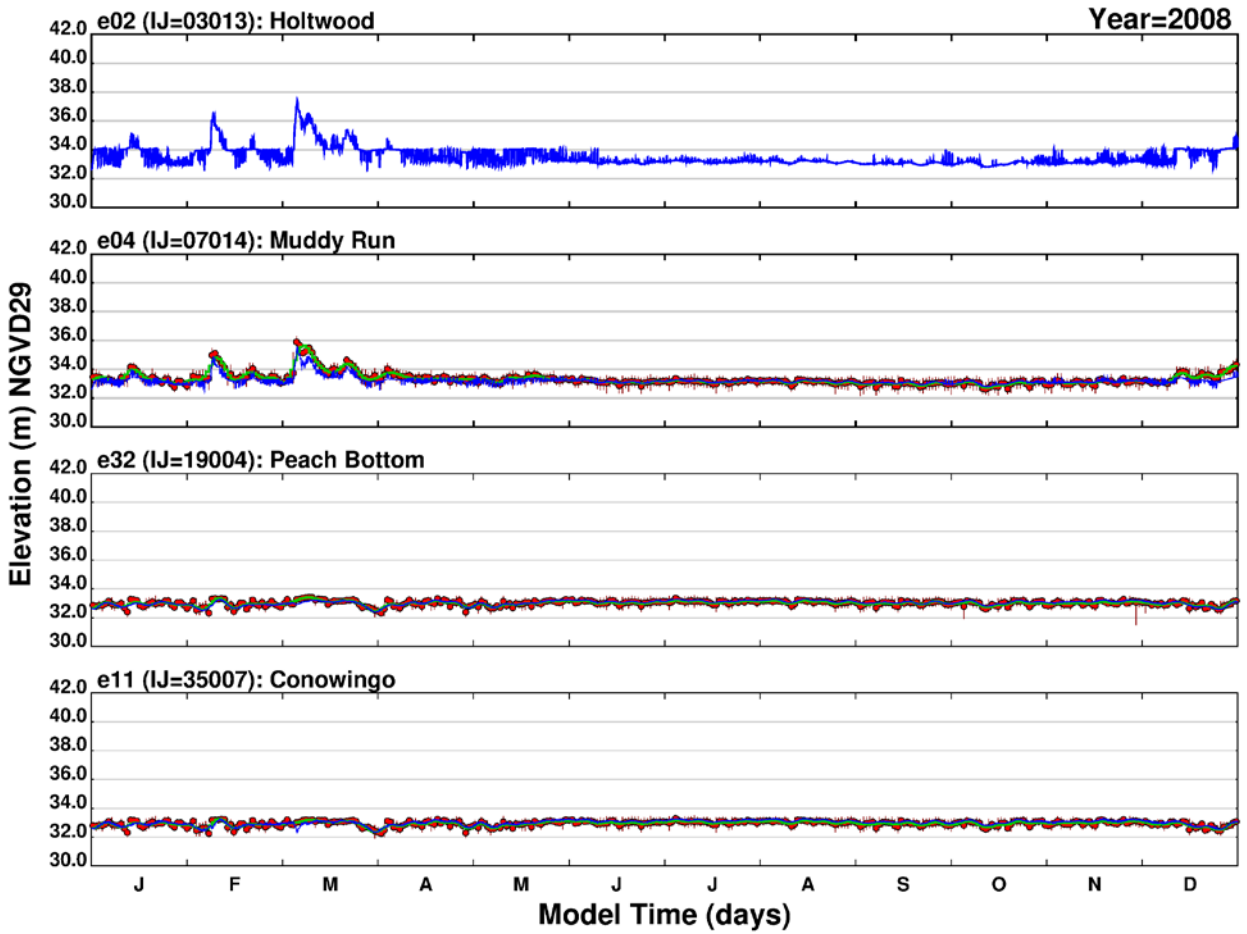


Note: Blue = simulated (hourly); Red = measured daily average and range (measurements begin in 2004); Green = 168-hour lowpass filtered measurements (hourly); IJ indicates the model grid cell from which outputs were retrieved; x-axis divisions indicate a one character abbreviation for month of year in sequence from January through December; y-axis maximum indicates the approximate maximum water level that occurs during Tropical Storm Lee in 2011.

Figure C-1. Simulated and measured water surface elevations over time at Holtwood, Muddy Run, Peach Bottom, and Conowingo: 2008 (short-term simulation).

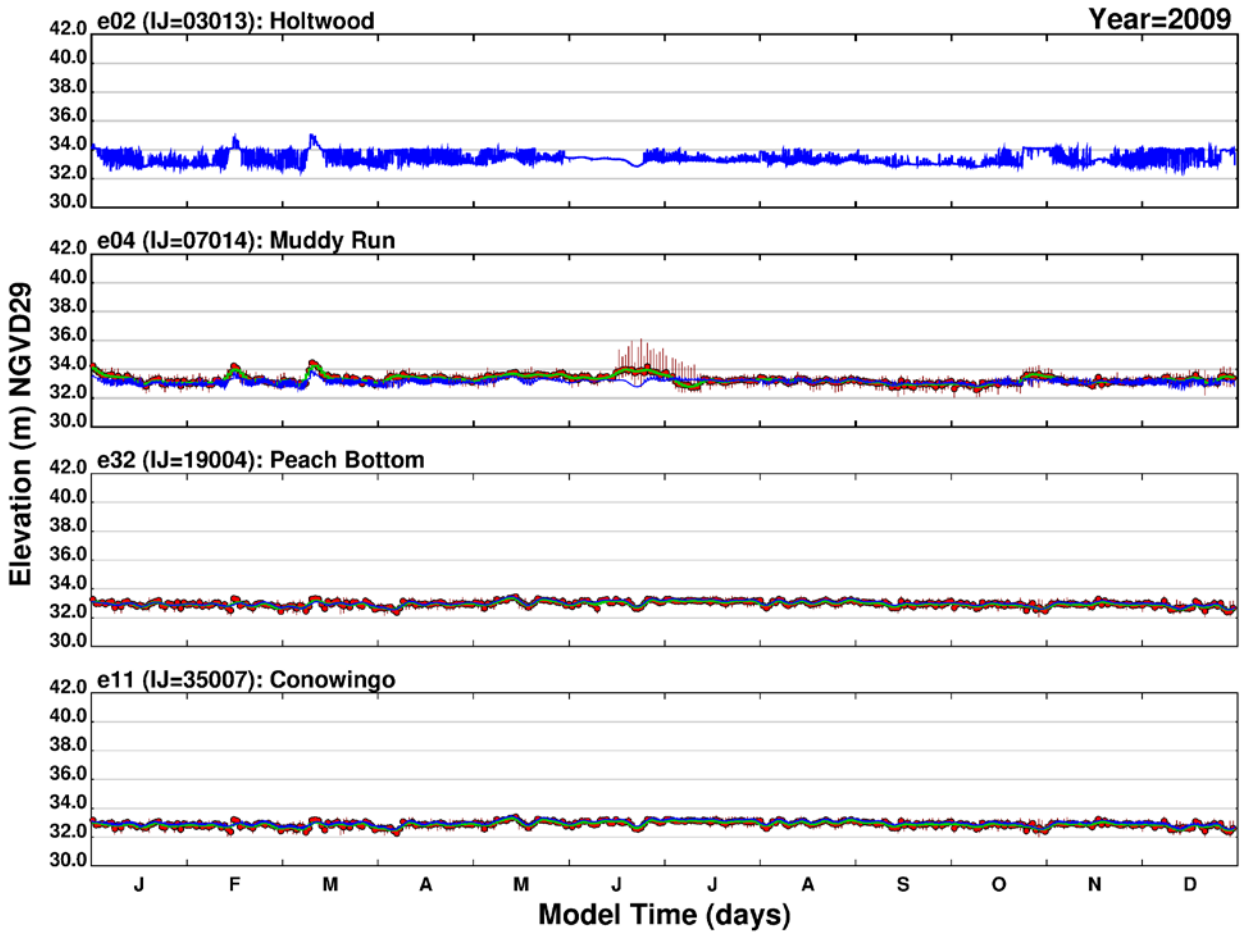


Note: Blue = simulated (hourly); Red = measured daily average and range (measurements begin in 2004); Green = 168-hour lowpass filtered measurements (hourly); IJ indicates the model grid cell from which outputs were retrieved; x-axis divisions indicate a one character abbreviation for month of year in sequence from January through December; y-axis maximum indicates the approximate maximum water level that occurs during Tropical Storm Lee in 2011.

Figure C-2. Simulated and measured water surface elevations over time at Holtwood, Muddy Run, Peach Bottom, and Conowingo: 2009 (short-term simulation).

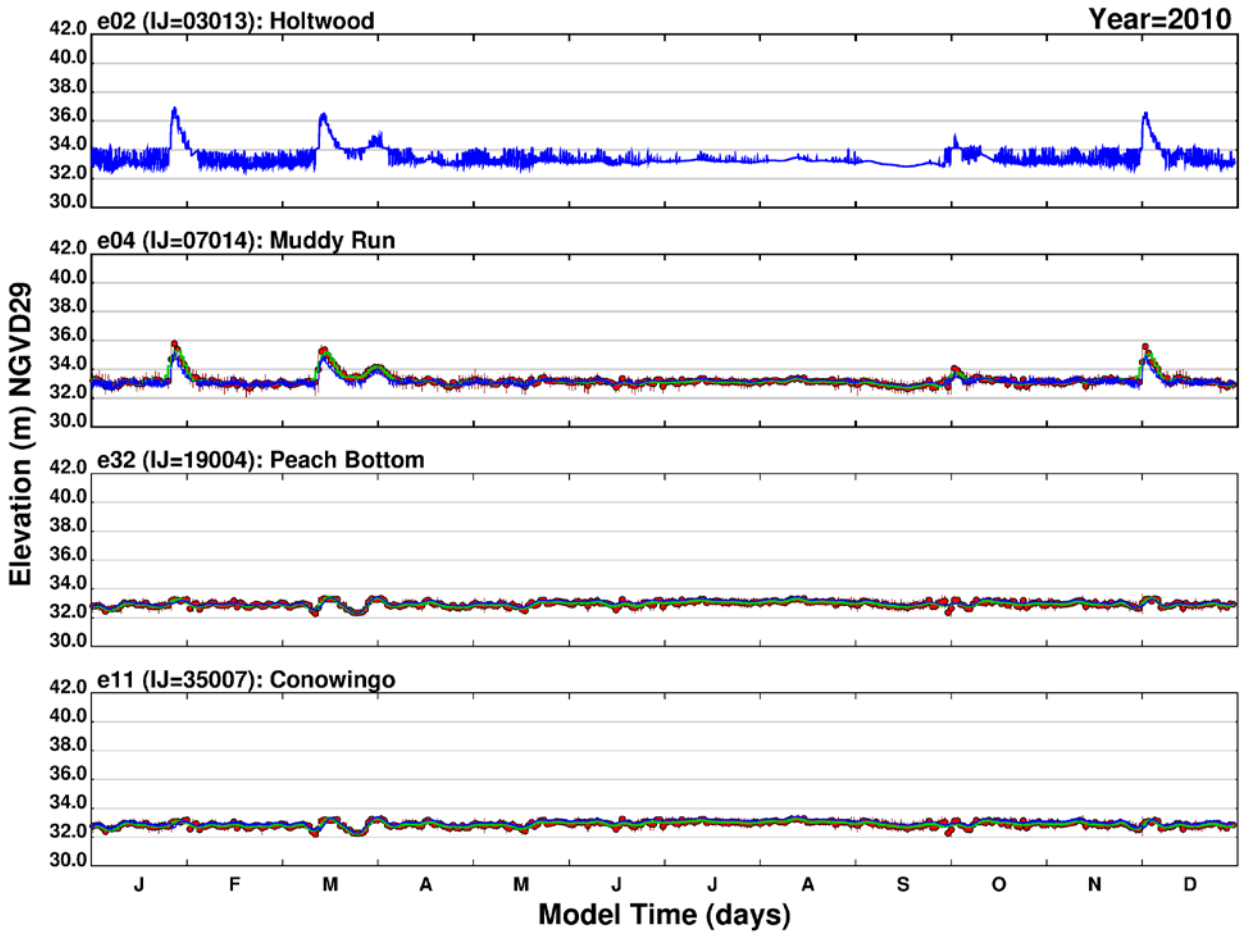


Note: Blue = simulated (hourly); Red = measured daily average and range (measurements begin in 2004); Green = 168-hour lowpass filtered measurements (hourly); IJ indicates the model grid cell from which outputs were retrieved; x-axis divisions indicate a one character abbreviation for month of year in sequence from January through December; y-axis maximum indicates the approximate maximum water level that occurs during Tropical Storm Lee in 2011.

Figure C-3. Simulated and measured water surface elevations over time at Holtwood, Muddy Run, Peach Bottom, and Conowingo: 2010 (short-term simulation).

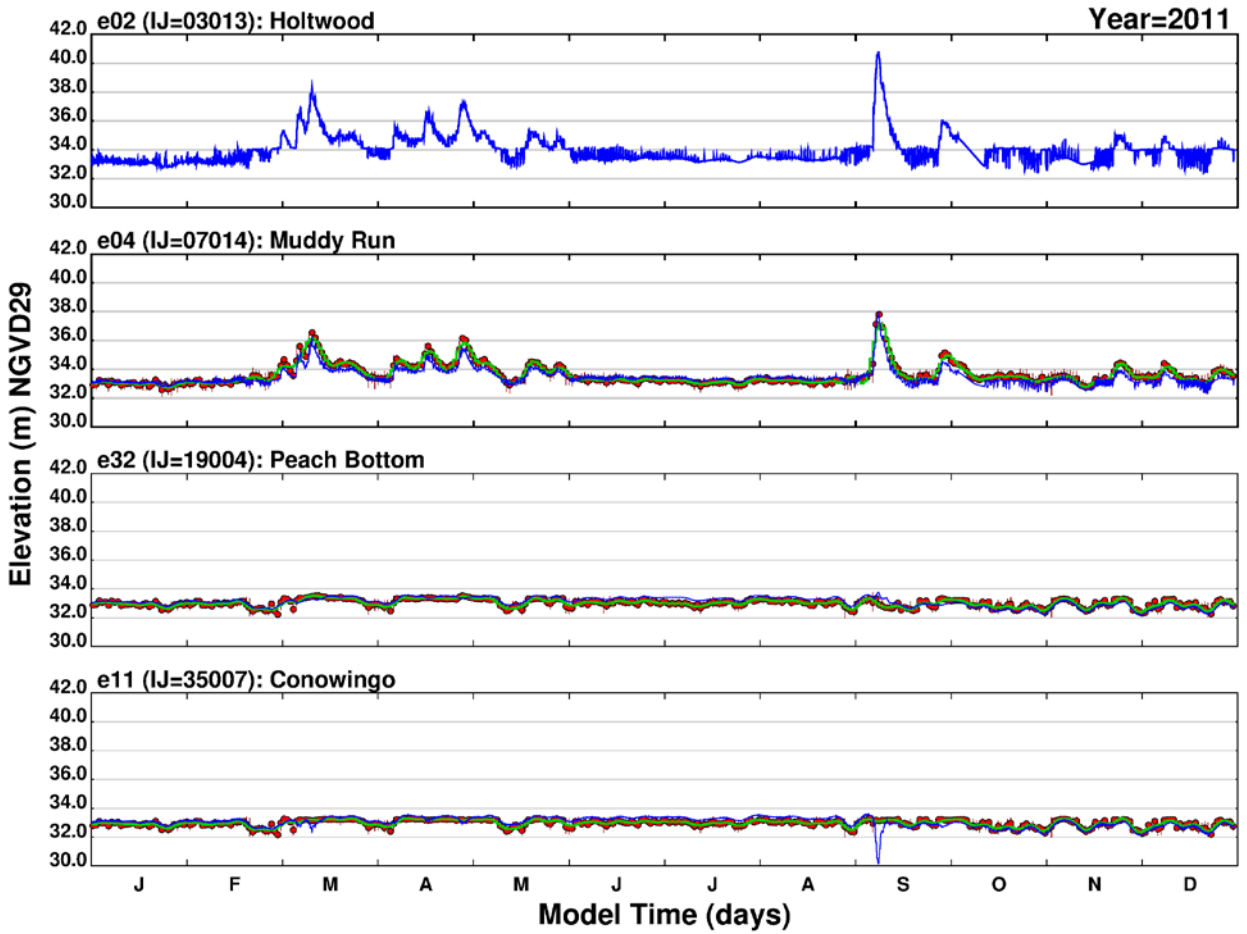


Note: Blue = simulated (hourly); Red = measured daily average and range (measurements begin in 2004); Green = 168-hour lowpass filtered measurements (hourly); IJ indicates the model grid cell from which outputs were retrieved; x-axis divisions indicate a one character abbreviation for month of year in sequence from January through December; y-axis maximum indicates the approximate maximum water level that occurs during Tropical Storm Lee in 2011.

Figure C-4. Simulated and measured water surface elevations over time at Holtwood, Muddy Run, Peach Bottom, and Conowingo: 2011 (short-term simulation).

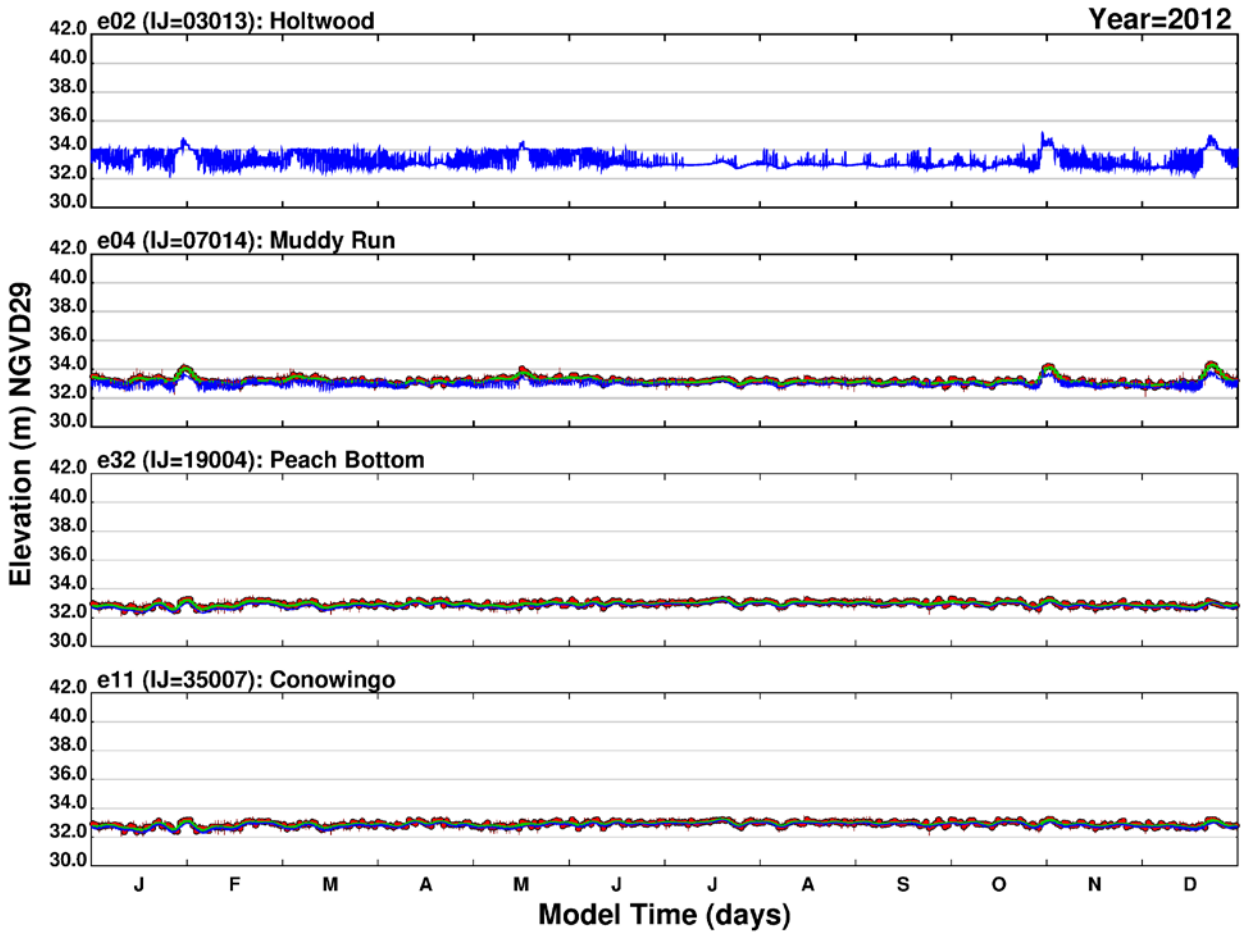


Note: Blue = simulated (hourly); Red = measured daily average and range (measurements begin in 2004); Green = 168-hour lowpass filtered measurements (hourly); IJ indicates the model grid cell from which outputs were retrieved; x-axis divisions indicate a one character abbreviation for month of year in sequence from January through December; y-axis maximum indicates the approximate maximum water level that occurs during Tropical Storm Lee in 2011.

Figure C-5. Simulated and measured water surface elevations over time at Holtwood, Muddy Run, Peach Bottom, and Conowingo: 2012 (short-term simulation).

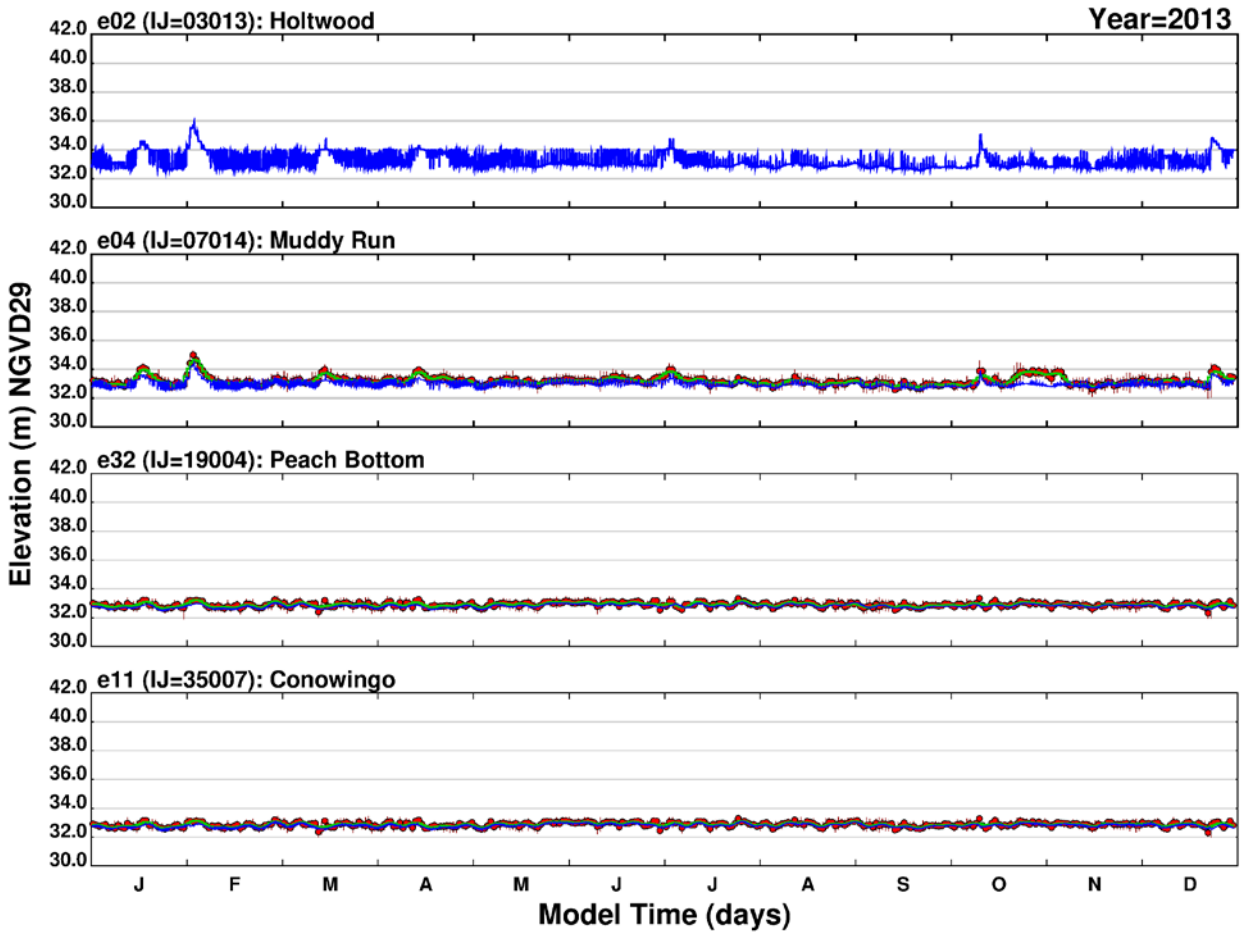


Note: Blue = simulated (hourly); Red = measured daily average and range (measurements begin in 2004); Green = 168-hour lowpass filtered measurements (hourly); IJ indicates the model grid cell from which outputs were retrieved; x-axis divisions indicate a one character abbreviation for month of year in sequence from January through December; y-axis maximum indicates the approximate maximum water level that occurs during Tropical Storm Lee in 2011.

Figure C-6. Simulated and measured water surface elevations over time at Holtwood, Muddy Run, Peach Bottom, and Conowingo: 2013 (short-term simulation).

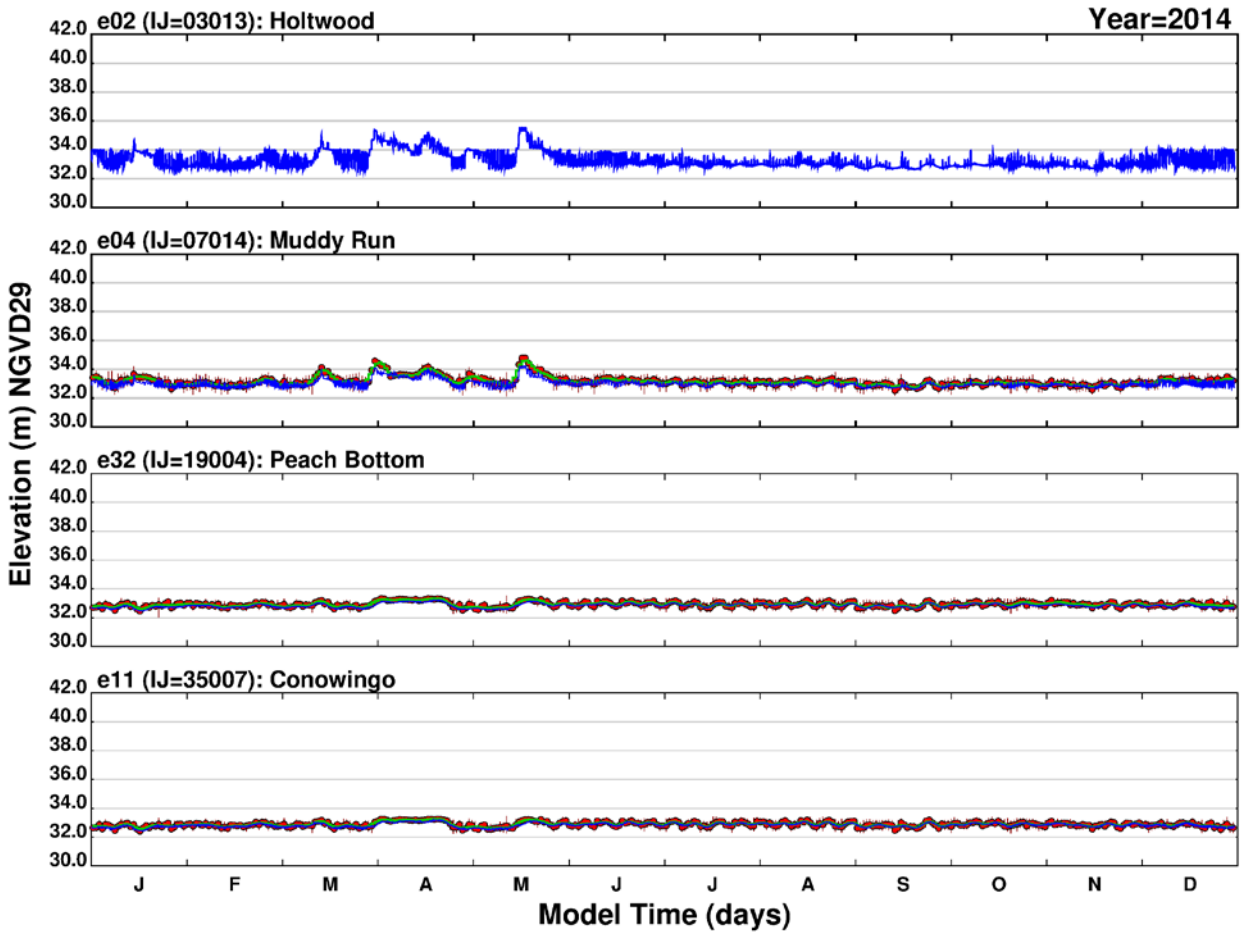


Note: Blue = simulated (hourly); Red = measured daily average and range (measurements begin in 2004); Green = 168-hour lowpass filtered measurements (hourly); IJ indicates the model grid cell from which outputs were retrieved; x-axis divisions indicate a one character abbreviation for month of year in sequence from January through December; y-axis maximum indicates the approximate maximum water level that occurs during Tropical Storm Lee in 2011.

Figure C-7. Simulated and measured water surface elevations over time at Holtwood, Muddy Run, Peach Bottom, and Conowingo: 2014 (short-term simulation).

# APPENDIX D. SIMULATED AND MEASURED WATER TEMPERATURES AT 19 STATIONS (SHORT-TERM): 2010

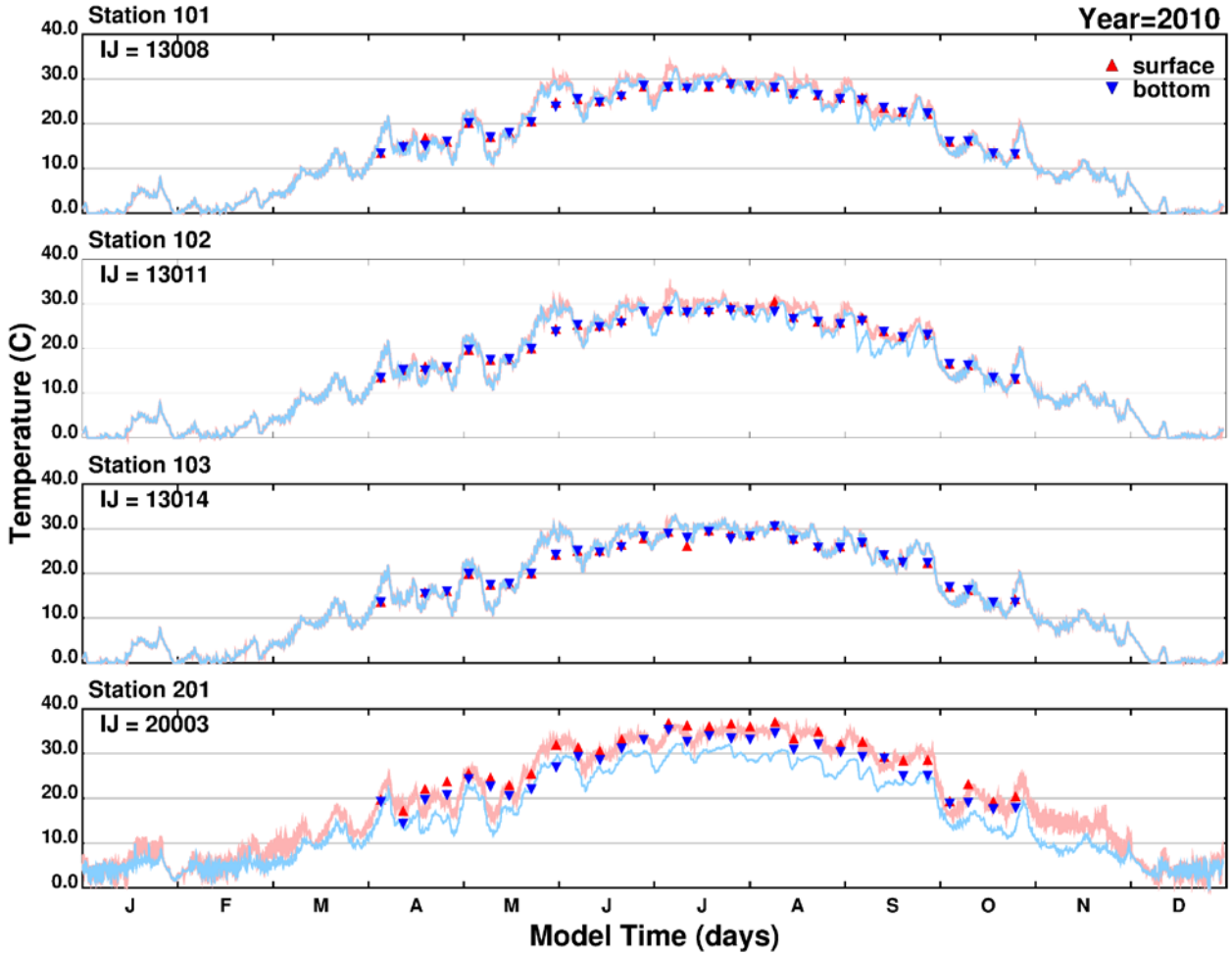


Note: Blue line = simulated near-bottom water temperature; Red line = simulated surface water temperature; Blue inverted triangle = measured near-bottom water temperature; Red triangle = measured surface water temperature; IJ indicates the model grid cell from which outputs were retrieved; x-axis divisions indicate a one character abbreviation for month of year in sequence from January through December; y-axis maximum indicates the approximate maximum temperature.

Figure D-1. Simulated and measured water temperatures during 2010: Stations 101, 102, 103, and 201 (short-term simulation).

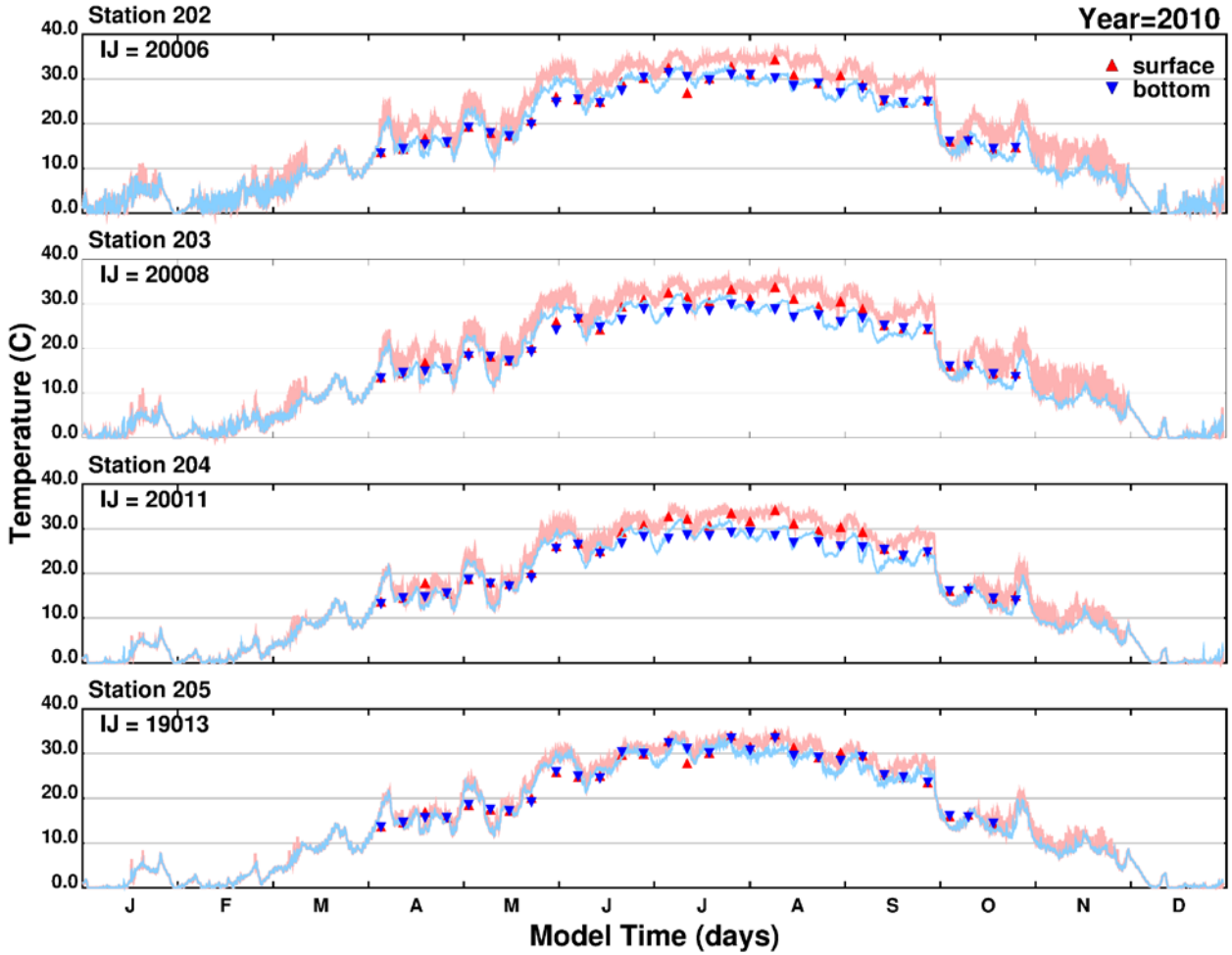


Note: Blue line = simulated near-bottom water temperature; Red line = simulated surface water temperature; Blue inverted triangle = measured near-bottom water temperature; Red triangle = measured surface water temperature; IJ indicates the model grid cell from which outputs were retrieved; x-axis divisions indicate a one character abbreviation for month of year in sequence from January through December; y-axis maximum indicates the approximate maximum temperature.

Figure D-2. Simulated and measured water temperatures during 2010: Stations 202, 203, 204, and 205 (short-term simulation).

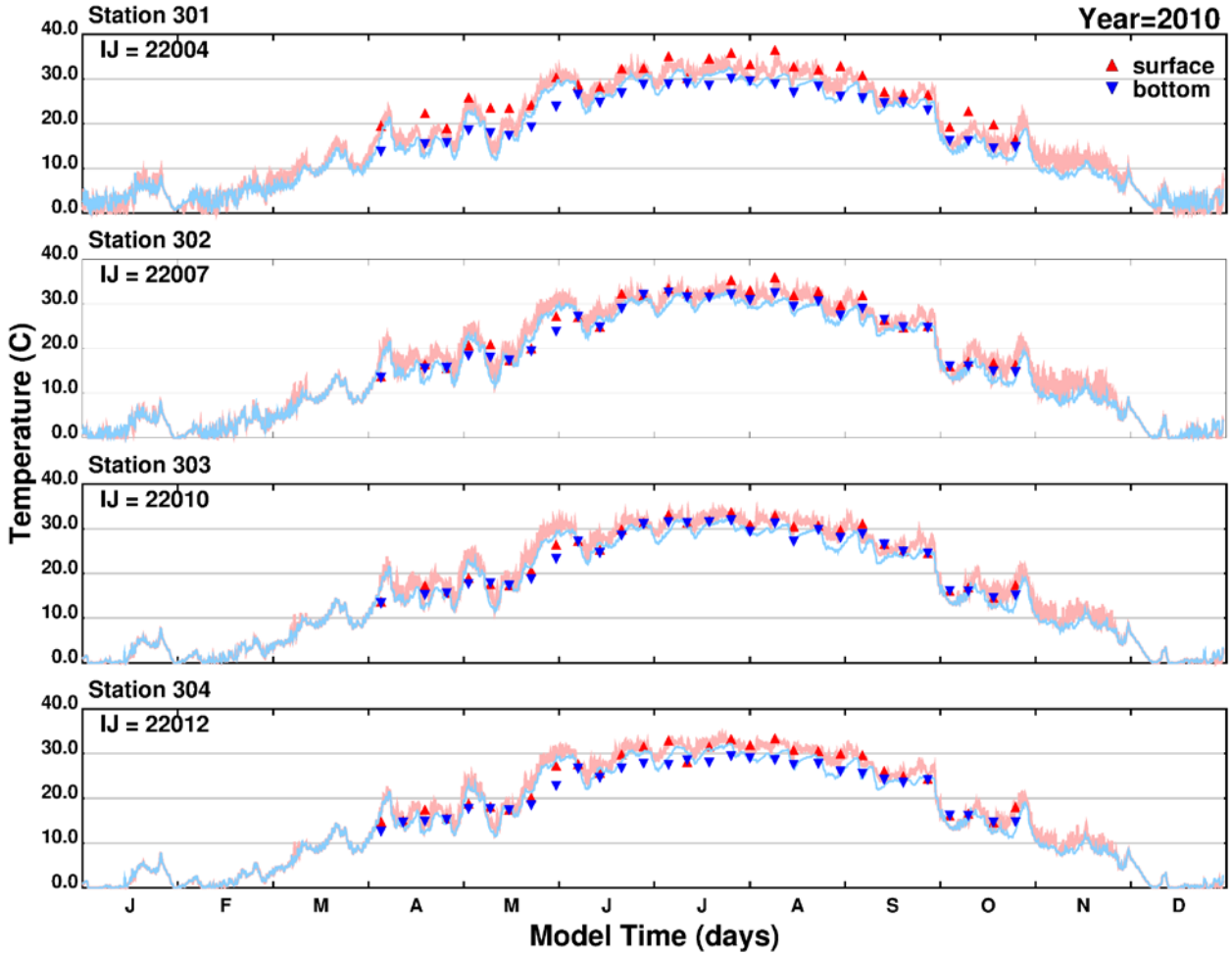


Note: Blue line = simulated near-bottom water temperature; Red line = simulated surface water temperature; Blue inverted triangle = measured near-bottom water temperature; Red triangle = measured surface water temperature; IJ indicates the model grid cell from which outputs were retrieved; x-axis divisions indicate a one character abbreviation for month of year in sequence from January through December; y-axis maximum indicates the approximate maximum temperature.

Figure D-3. Simulated and measured water temperatures during 2010: Stations 301, 302, 303, and 304 (short-term simulation).

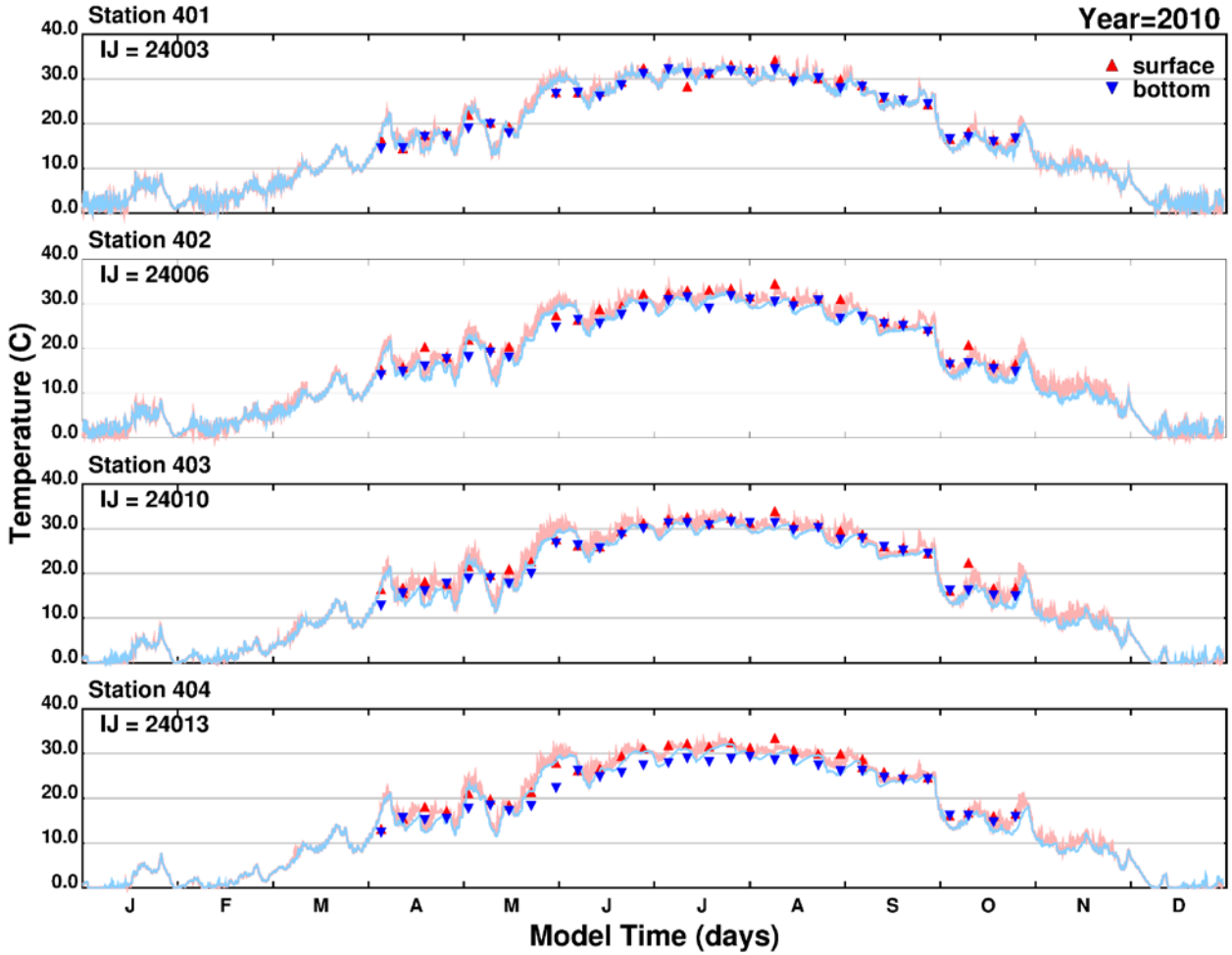


Note: Blue line = simulated near-bottom water temperature; Red line = simulated surface water temperature; Blue inverted triangle = measured near-bottom water temperature; Red triangle = measured surface water temperature; IJ indicates the model grid cell from which outputs were retrieved; x-axis divisions indicate a one character abbreviation for month of year in sequence from January through December; y-axis maximum indicates the approximate maximum temperature.

Figure D-4. Simulated and measured water temperatures during 2010: Stations 401, 402, 403, and 404 (short-term simulation).

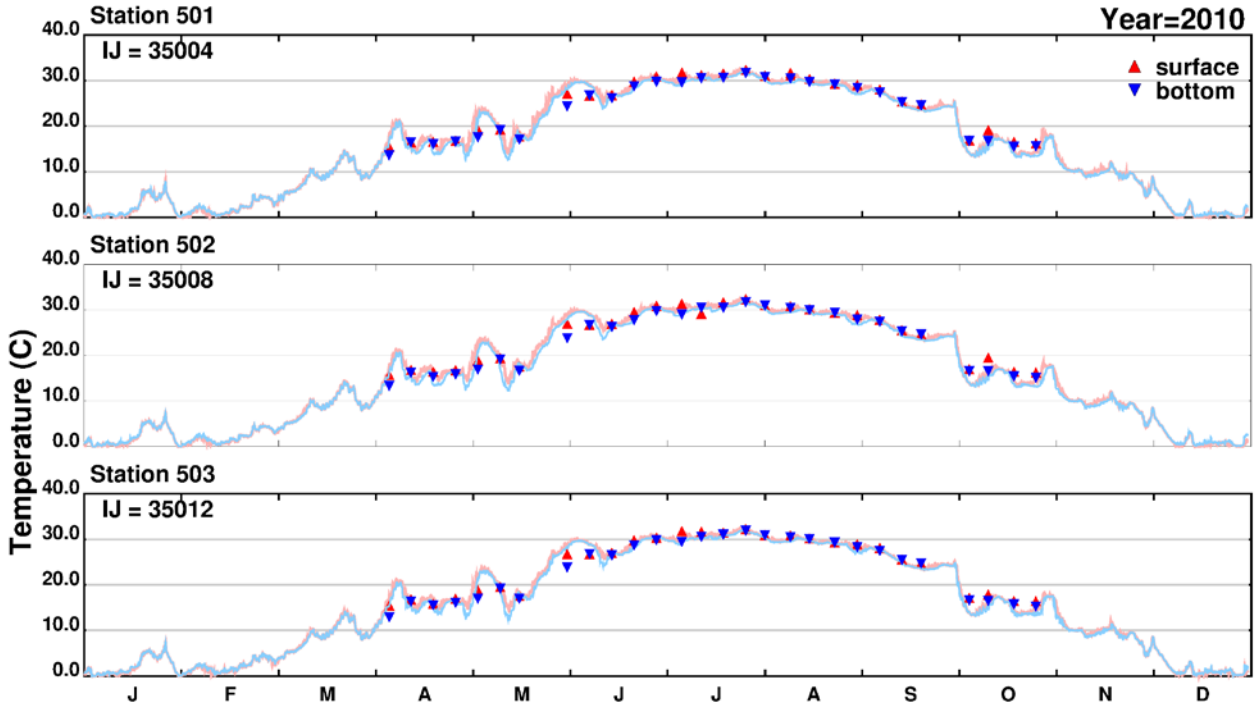


Note: Blue line = simulated near-bottom water temperature; Red line = simulated surface water temperature; Blue inverted triangle = measured near-bottom water temperature; Red triangle = measured surface water temperature; IJ indicates the model grid cell from which outputs were retrieved; x-axis divisions indicate a one character abbreviation for month of year in sequence from January through December; y-axis maximum indicates the approximate maximum temperature.

Figure D-5. Simulated and measured water temperatures during 2010: Stations 501, 502, and 503 (short-term simulation).

# APPENDIX E. SIMULATED AND MEASURED SUSPENDED SEDIMENT CONCENTRATIONS (LONG-TERM): 1997-2014

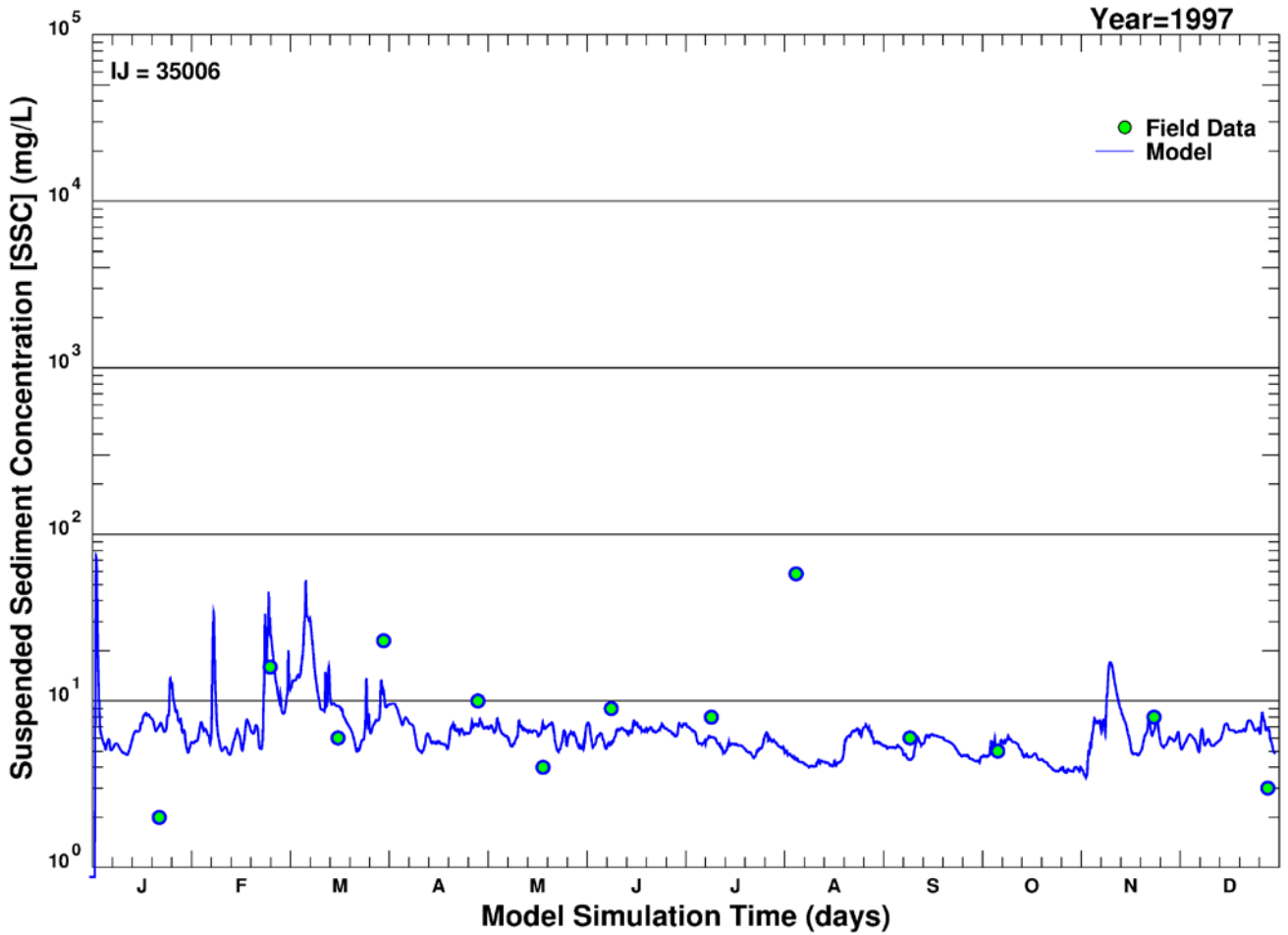


Note: Blue line = simulated suspended sediment concentration (depth-averaged sum of all size classes in the model); Green circle = measured suspended sediment concentration; IJ indicates the model grid cell from which outputs were retrieved; x-axis divisions indicate time in days; y-axis maximum indicates the log cycle closest to but not less than the maximum concentration simulated (which occurred during Tropical Storm Lee in 2011).

Figure E-1. Simulated and measured suspended sediment concentrations over time at Conowingo: 1997 (long-term simulation).

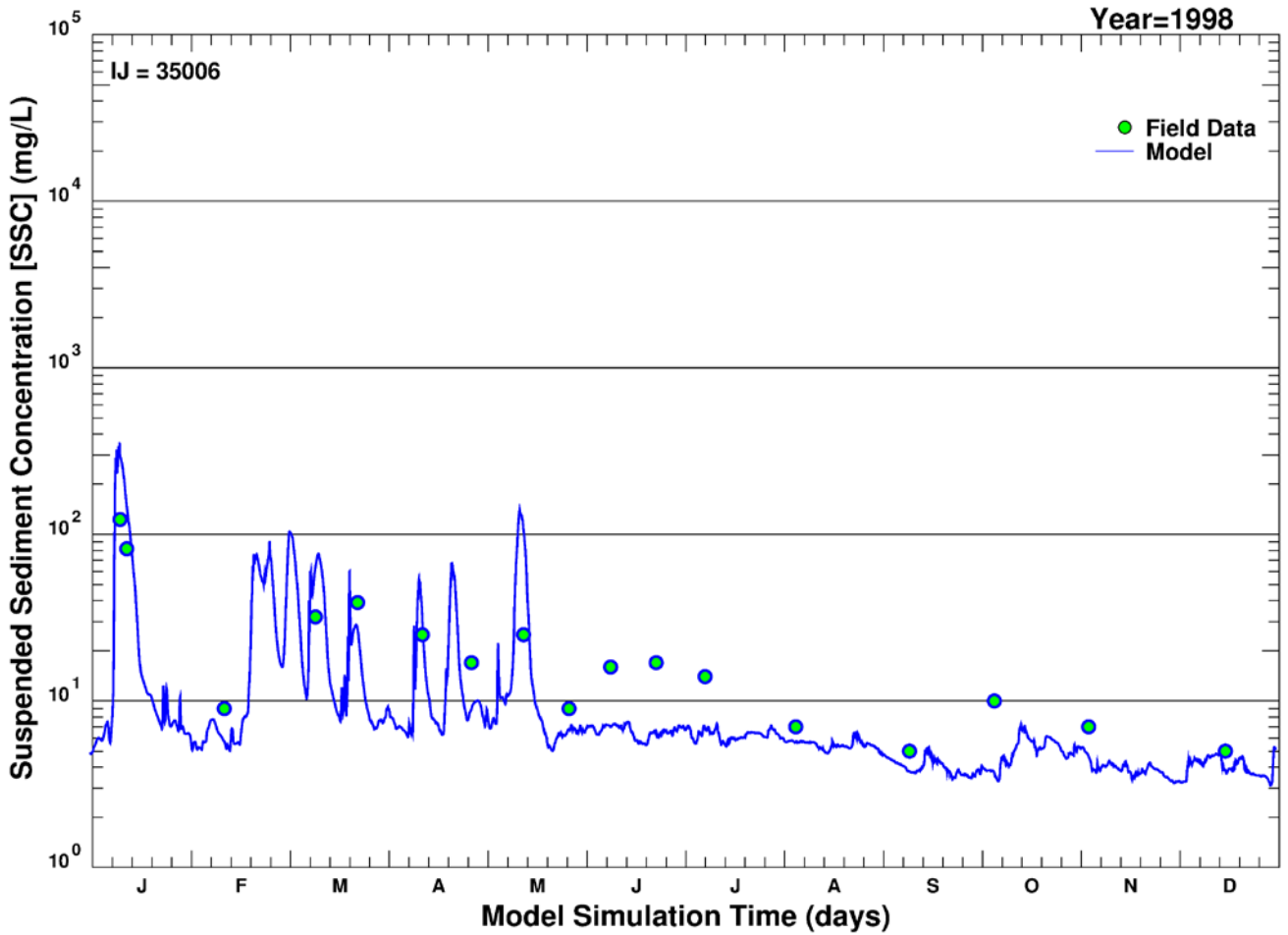


Note: Blue line = simulated suspended sediment concentration (depth-averaged sum of all size classes in the model); Green circle = measured suspended sediment concentration; IJ indicates the model grid cell from which outputs were retrieved; x-axis divisions indicate time in days; y-axis maximum indicates the log cycle closest to but not less than the maximum concentration simulated (which occurred during Tropical Storm Lee in 2011).

Figure E-2. Simulated and measured suspended sediment concentrations over time at Conowingo: 1998 (long-term simulation).

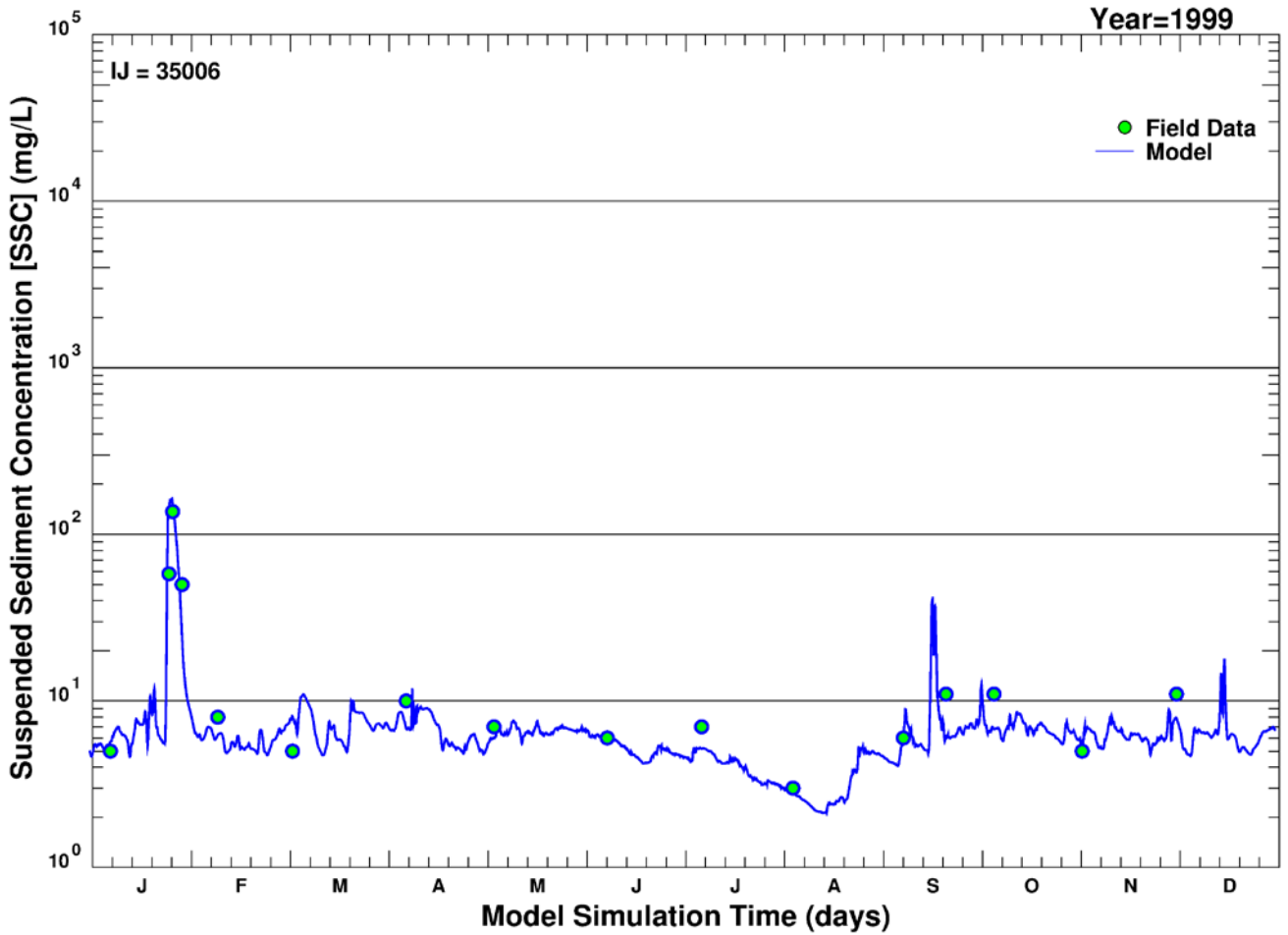


Note: Blue line = simulated suspended sediment concentration (depth-averaged sum of all size classes in the model); Green circle = measured suspended sediment concentration; IJ indicates the model grid cell from which outputs were retrieved; x-axis divisions indicate time in days; y-axis maximum indicates the log cycle closest to but not less than the maximum concentration simulated (which occurred during Tropical Storm Lee in 2011).

Figure E-3. Simulated and measured suspended sediment concentrations over time at Conowingo: 1999 (long-term simulation).

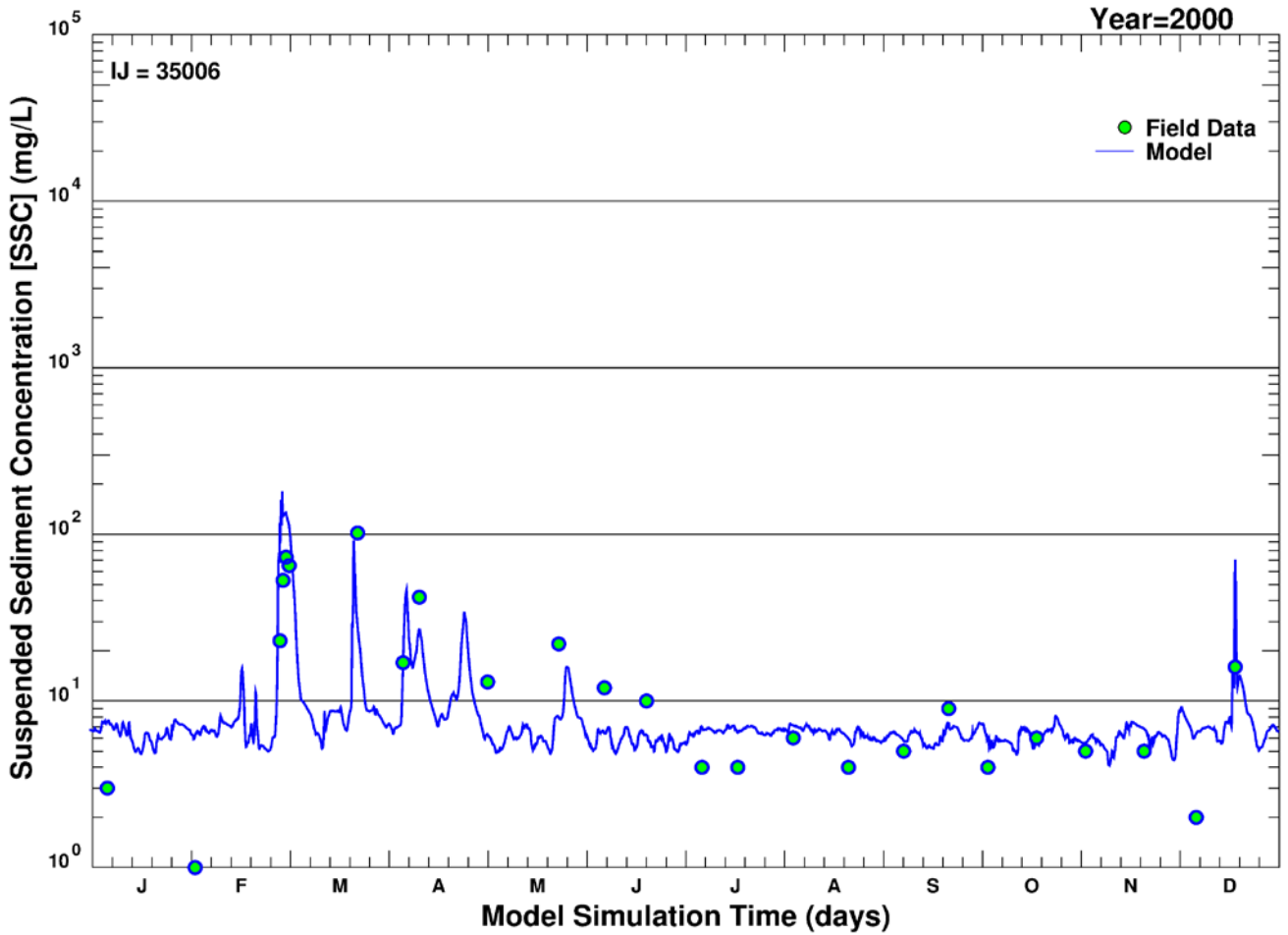


Note: Blue line = simulated suspended sediment concentration (depth-averaged sum of all size classes in the model); Green circle = measured suspended sediment concentration; IJ indicates the model grid cell from which outputs were retrieved; x-axis divisions indicate time in days; y-axis maximum indicates the log cycle closest to but not less than the maximum concentration simulated (which occurred during Tropical Storm Lee in 2011).

Figure E-4. Simulated and measured suspended sediment concentrations over time at Conowingo: 2000 (long-term simulation).

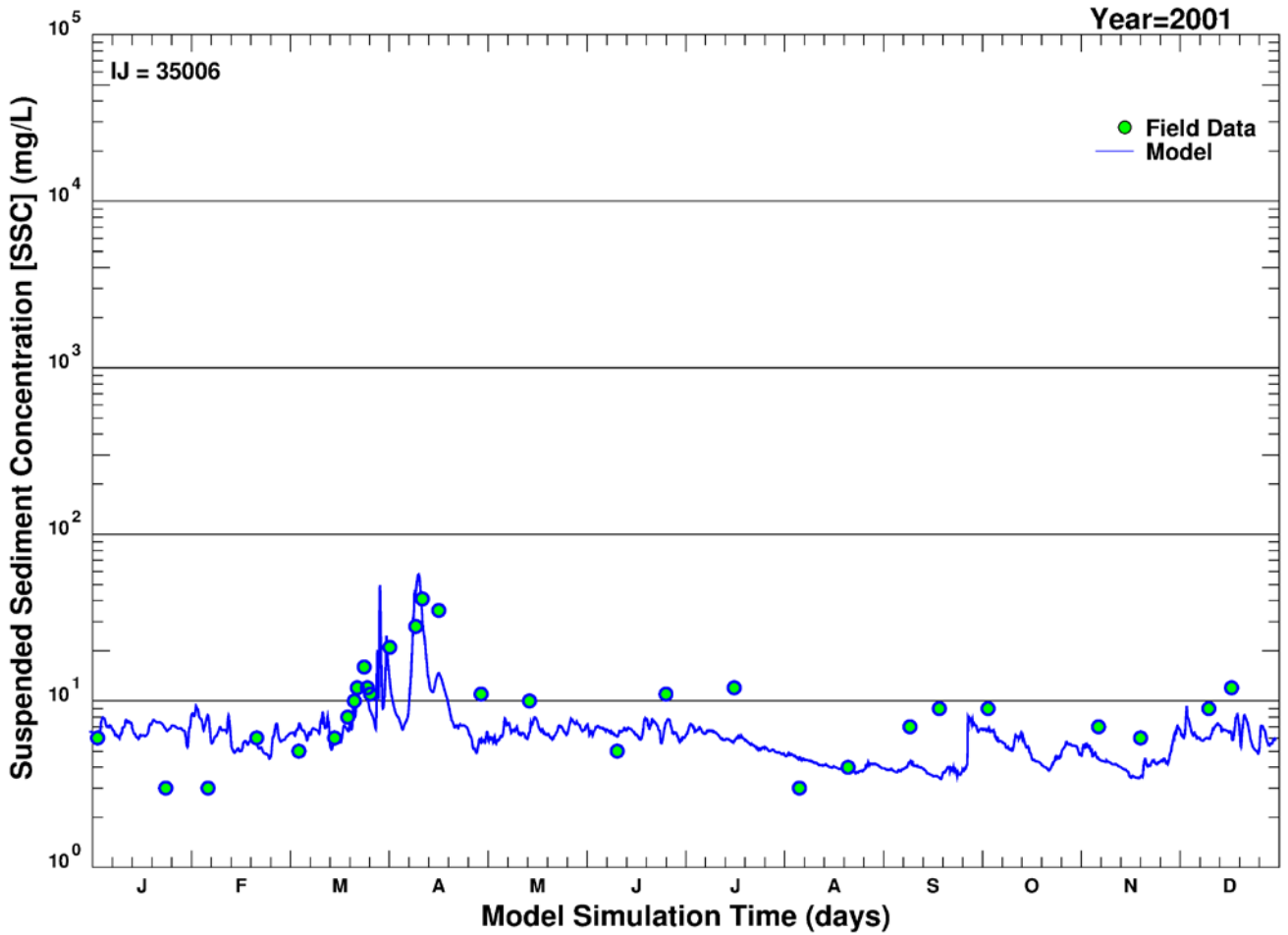


Note: Blue line = simulated suspended sediment concentration (depth-averaged sum of all size classes in the model); Green circle = measured suspended sediment concentration; IJ indicates the model grid cell from which outputs were retrieved; x-axis divisions indicate time in days; y-axis maximum indicates the log cycle closest to but not less than the maximum concentration simulated (which occurred during Tropical Storm Lee in 2011).

Figure E-5. Simulated and measured suspended sediment concentrations over time at Conowingo: 2001 (long-term simulation).

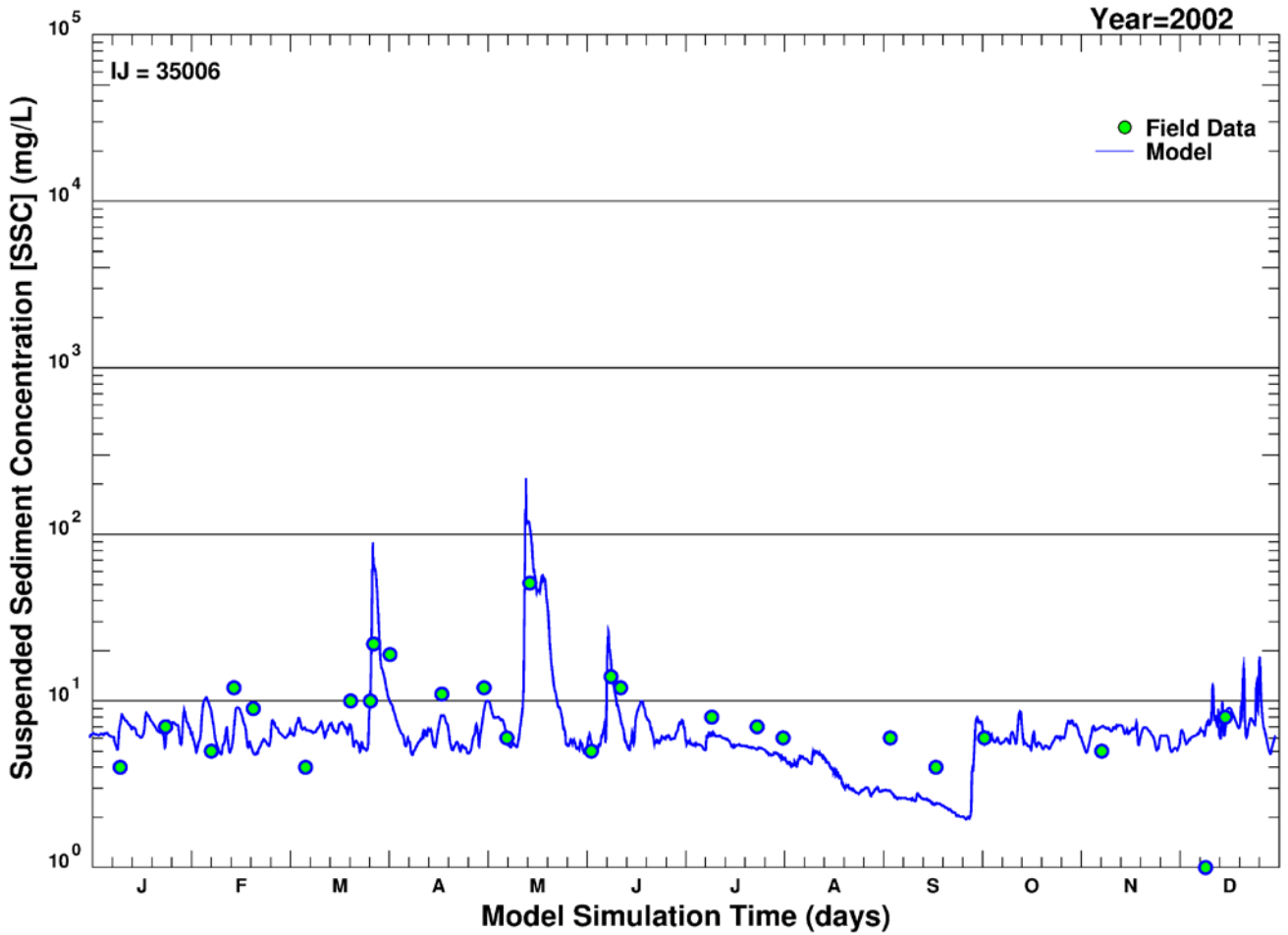


Note: Blue line = simulated suspended sediment concentration (depth-averaged sum of all size classes in the model); Green circle = measured suspended sediment concentration; IJ indicates the model grid cell from which outputs were retrieved; x-axis divisions indicate time in days; y-axis maximum indicates the log cycle closest to but not less than the maximum concentration simulated (which occurred during Tropical Storm Lee in 2011).

Figure E-6. Simulated and measured suspended sediment concentrations over time at Conowingo: 2002 (long-term simulation).

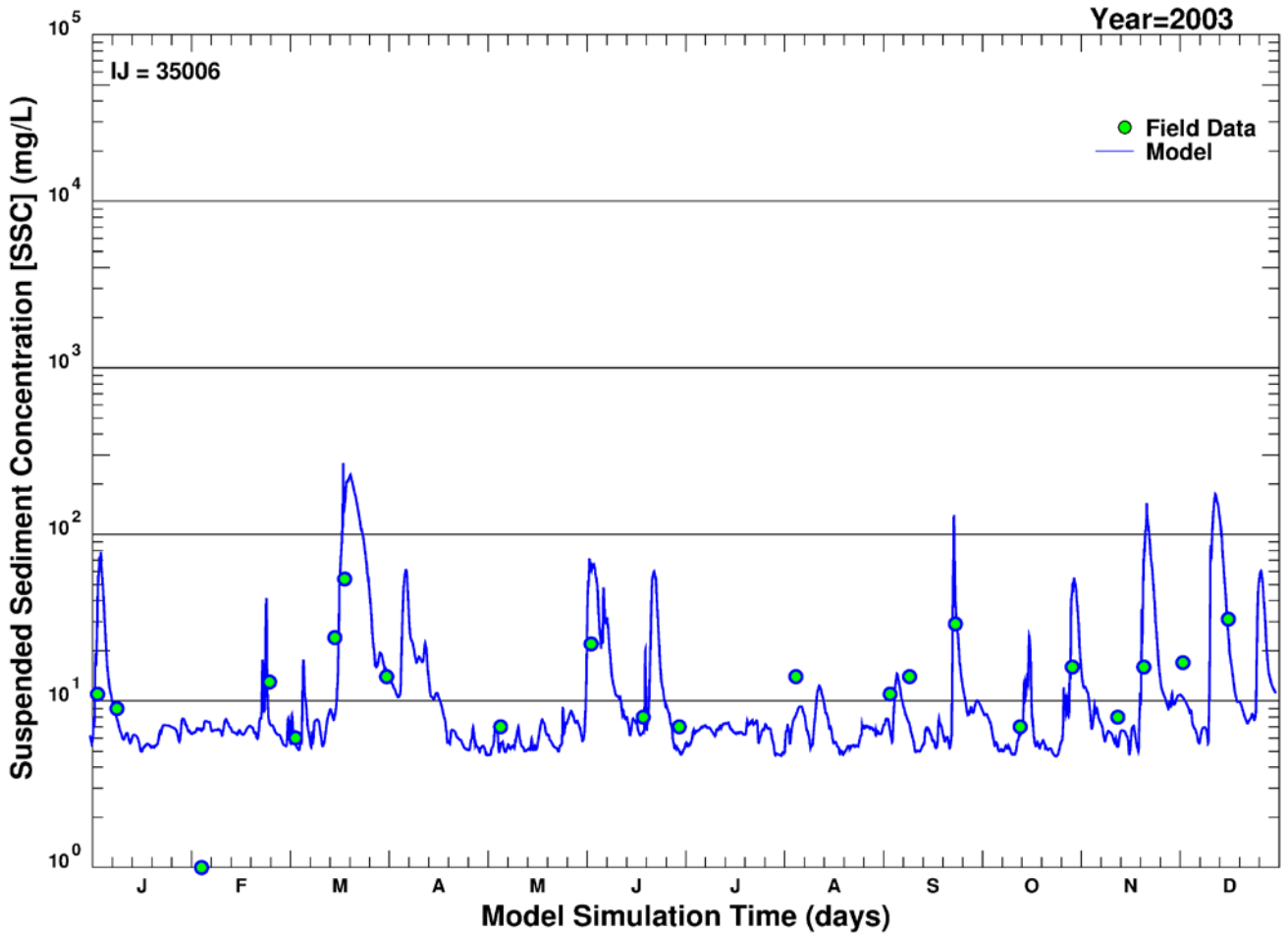


Note: Blue line = simulated suspended sediment concentration (depth-averaged sum of all size classes in the model); Green circle = measured suspended sediment concentration; IJ indicates the model grid cell from which outputs were retrieved; x-axis divisions indicate time in days; y-axis maximum indicates the log cycle closest to but not less than the maximum concentration simulated (which occurred during Tropical Storm Lee in 2011).

Figure E-7. Simulated and measured suspended sediment concentrations over time at Conowingo: 2003 (long-term simulation).

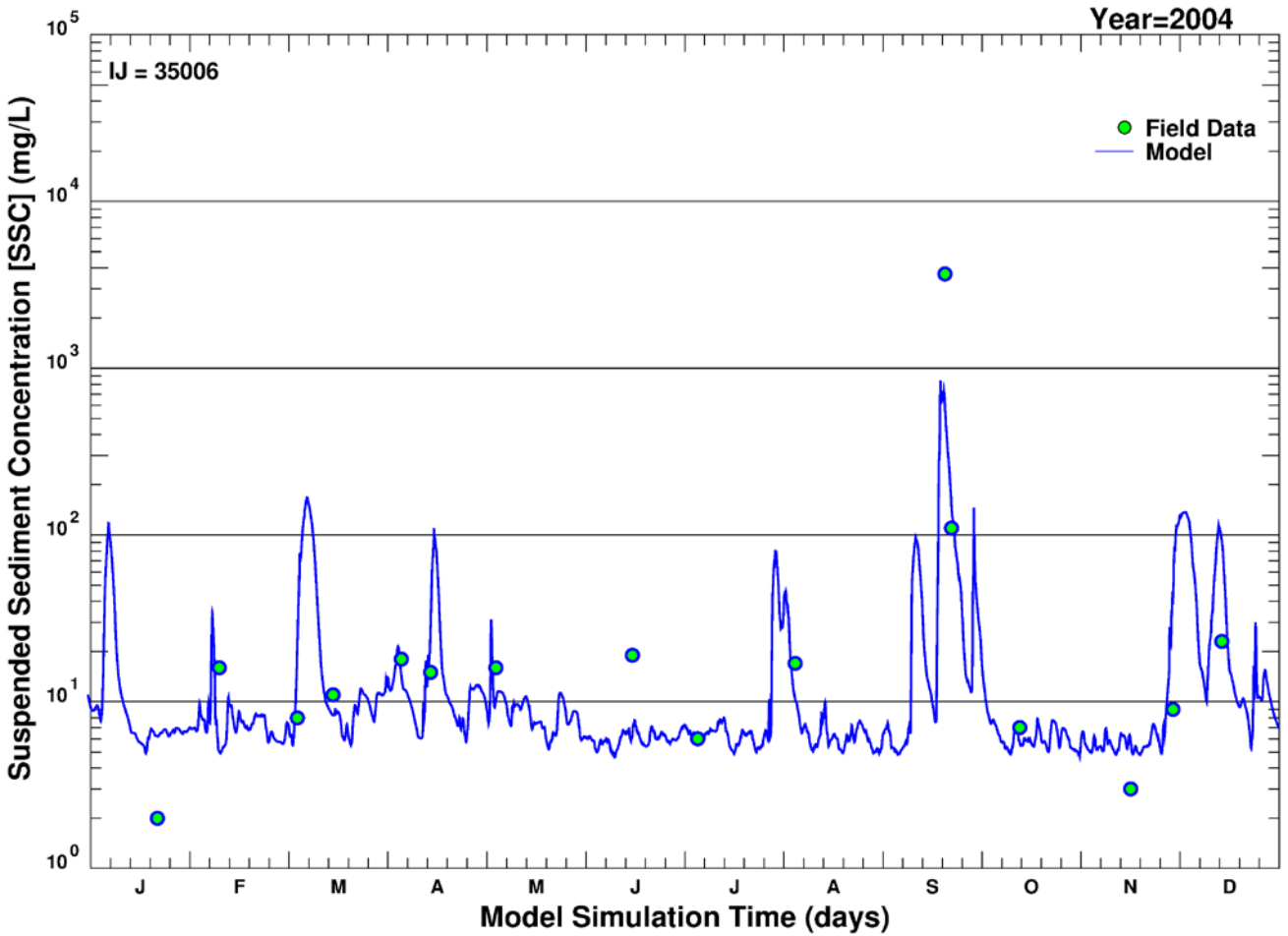


Note: Blue line = simulated suspended sediment concentration (depth-averaged sum of all size classes in the model); Green circle = measured suspended sediment concentration; IJ indicates the model grid cell from which outputs were retrieved; x-axis divisions indicate time in days; y-axis maximum indicates the log cycle closest to but not less than the maximum concentration simulated (which occurred during Tropical Storm Lee in 2011).

Figure E-8. Simulated and measured suspended sediment concentrations over time at Conowingo: 2004 (long-term simulation).

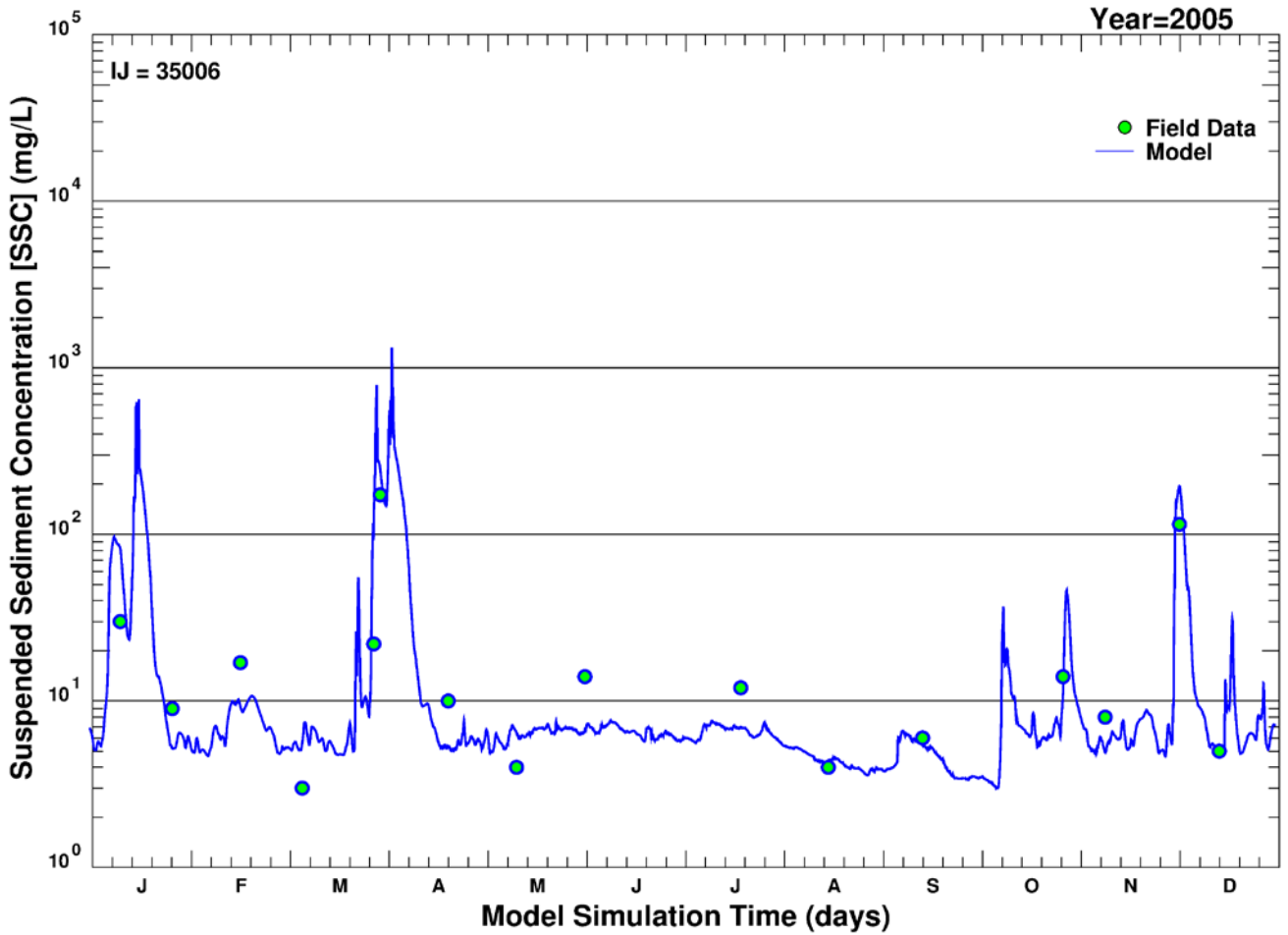


Note: Blue line = simulated suspended sediment concentration (depth-averaged sum of all size classes in the model); Green circle = measured suspended sediment concentration; IJ indicates the model grid cell from which outputs were retrieved; x-axis divisions indicate time in days; y-axis maximum indicates the log cycle closest to but not less than the maximum concentration simulated (which occurred during Tropical Storm Lee in 2011).

Figure E-9. Simulated and measured suspended sediment concentrations over time at Conowingo: 2005 (long-term simulation).

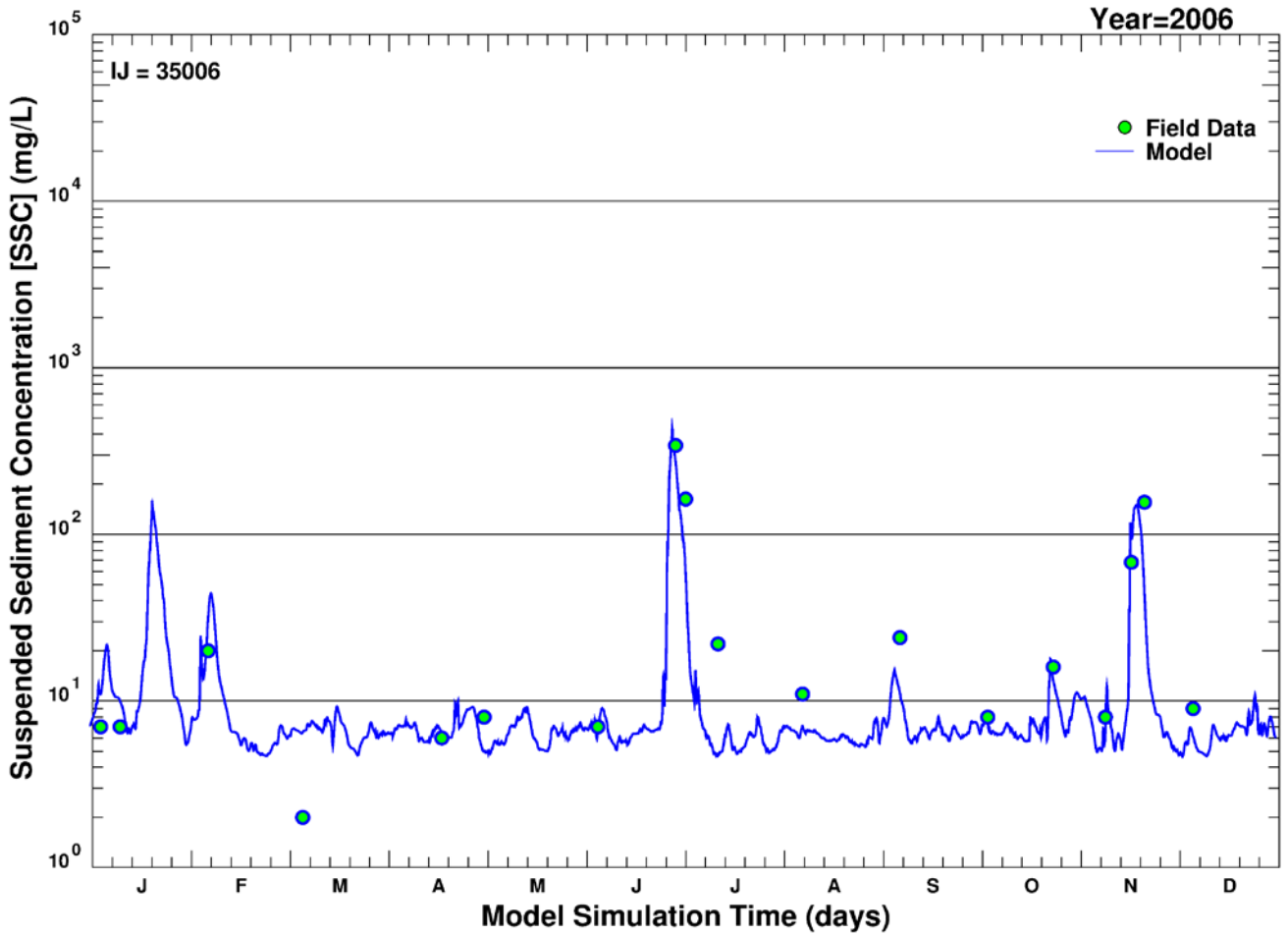


Note: Blue line = simulated suspended sediment concentration (depth-averaged sum of all size classes in the model); Green circle = measured suspended sediment concentration; IJ indicates the model grid cell from which outputs were retrieved; x-axis divisions indicate time in days; y-axis maximum indicates the log cycle closest to but not less than the maximum concentration simulated (which occurred during Tropical Storm Lee in 2011).

Figure E-10. Simulated and measured suspended sediment concentrations over time at Conowingo: 2006 (long-term simulation).

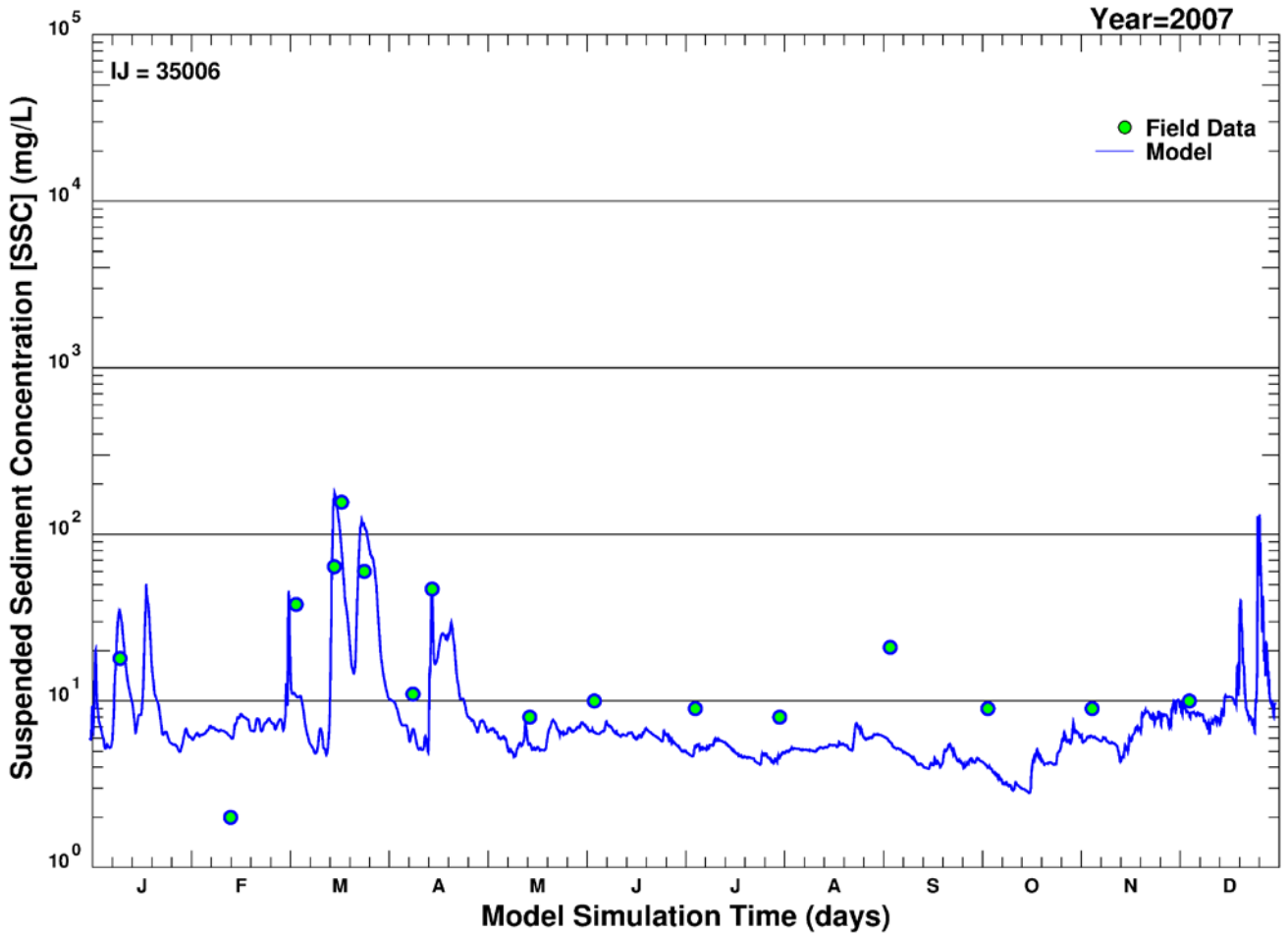


Note: Blue line = simulated suspended sediment concentration (depth-averaged sum of all size classes in the model); Green circle = measured suspended sediment concentration; IJ indicates the model grid cell from which outputs were retrieved; x-axis divisions indicate time in days; y-axis maximum indicates the log cycle closest to but not less than the maximum concentration simulated (which occurred during Tropical Storm Lee in 2011).

Figure E-11. Simulated and measured suspended sediment concentrations over time at Conowingo: 2007 (long-term simulation).

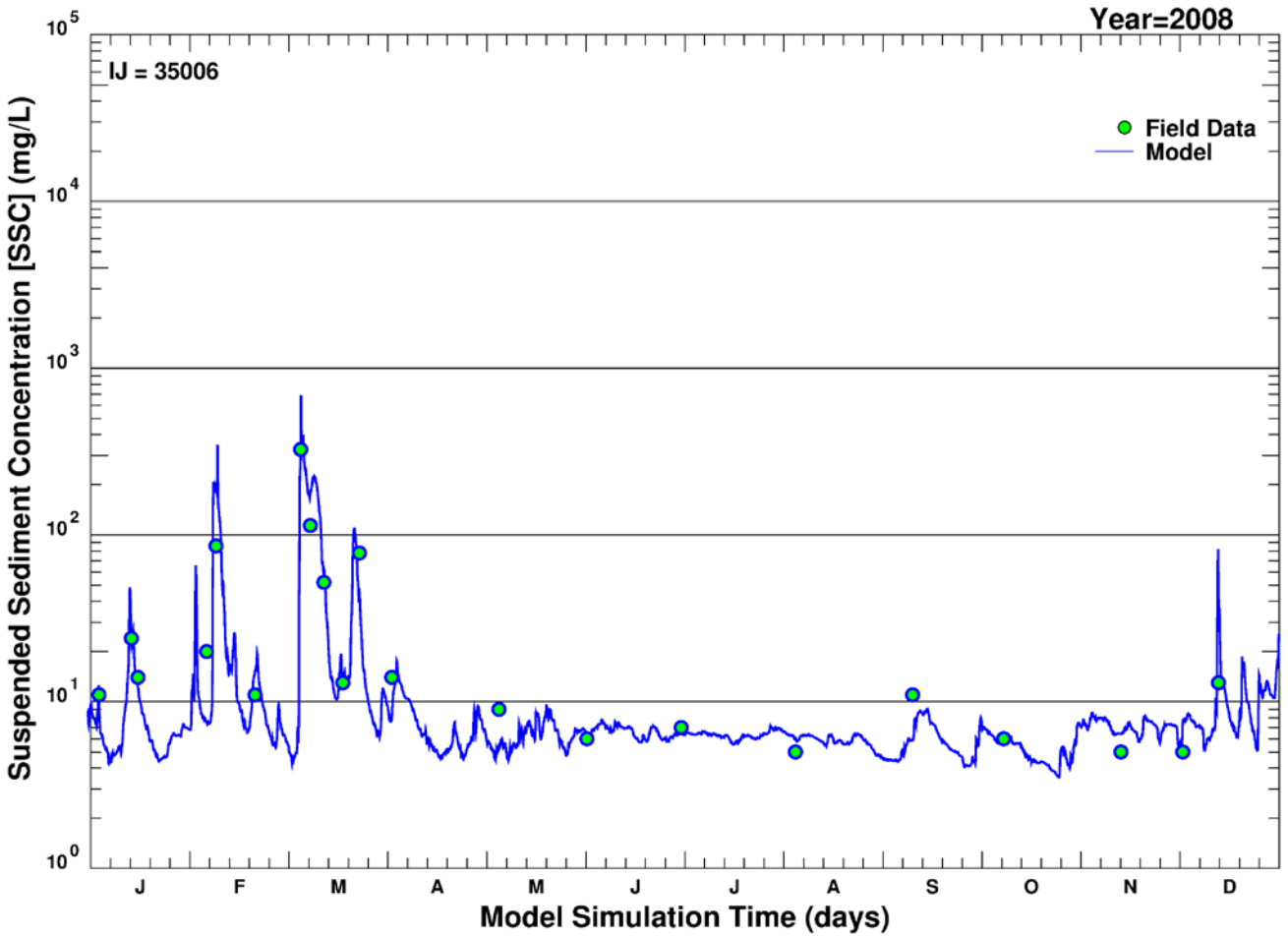


Note: Blue line = simulated suspended sediment concentration (depth-averaged sum of all size classes in the model); Green circle = measured suspended sediment concentration; IJ indicates the model grid cell from which outputs were retrieved; x-axis divisions indicate time in days; y-axis maximum indicates the log cycle closest to but not less than the maximum concentration simulated (which occurred during Tropical Storm Lee in 2011).

Figure E-12. Simulated and measured suspended sediment concentrations over time at Conowingo: 2008 (long-term simulation).

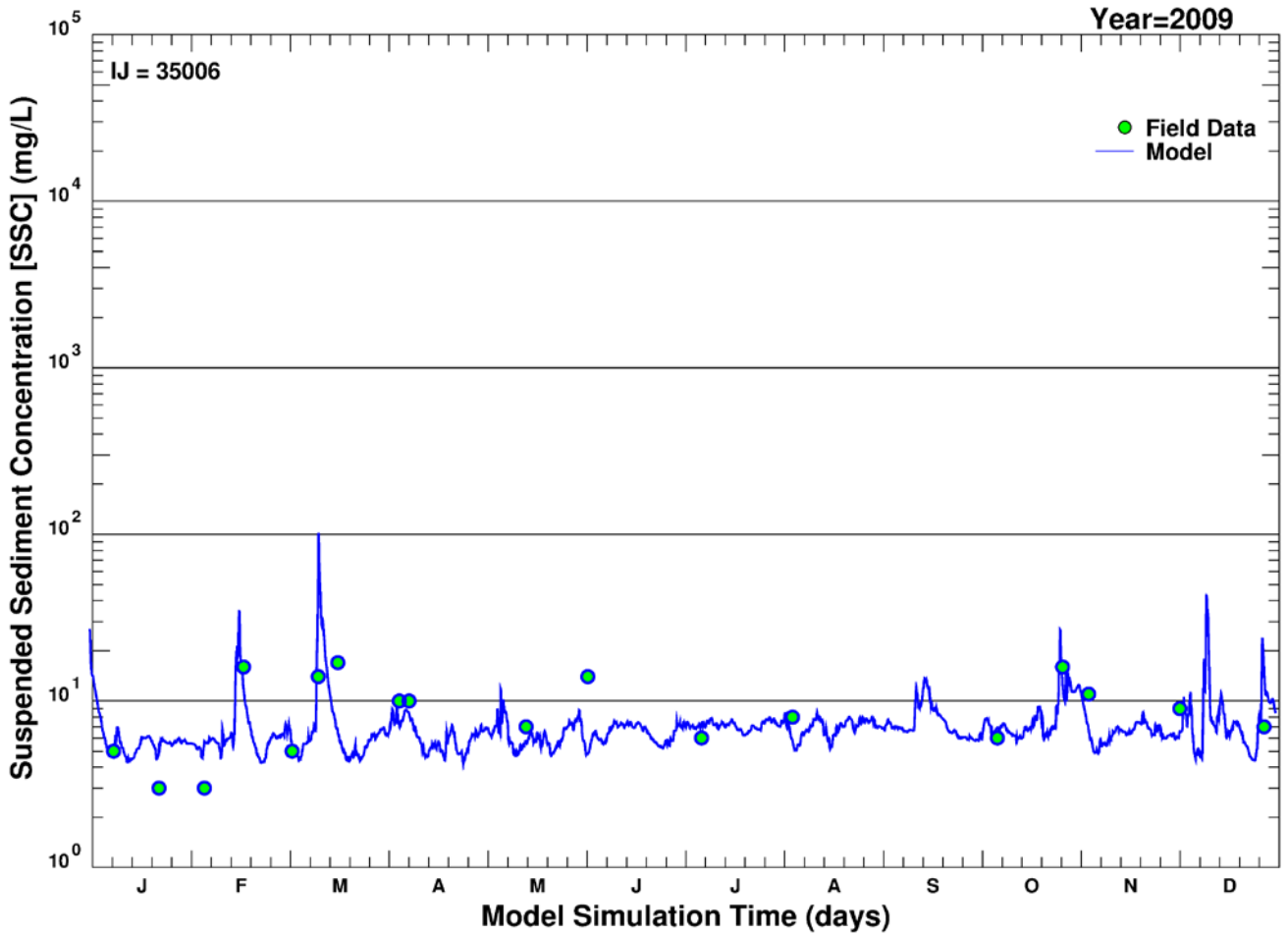


Note: Blue line = simulated suspended sediment concentration (depth-averaged sum of all size classes in the model); Green circle = measured suspended sediment concentration; IJ indicates the model grid cell from which outputs were retrieved; x-axis divisions indicate time in days; y-axis maximum indicates the log cycle closest to but not less than the maximum concentration simulated (which occurred during Tropical Storm Lee in 2011).

Figure E-13. Simulated and measured suspended sediment concentrations over time at Conowingo: 2009 (long-term simulation).

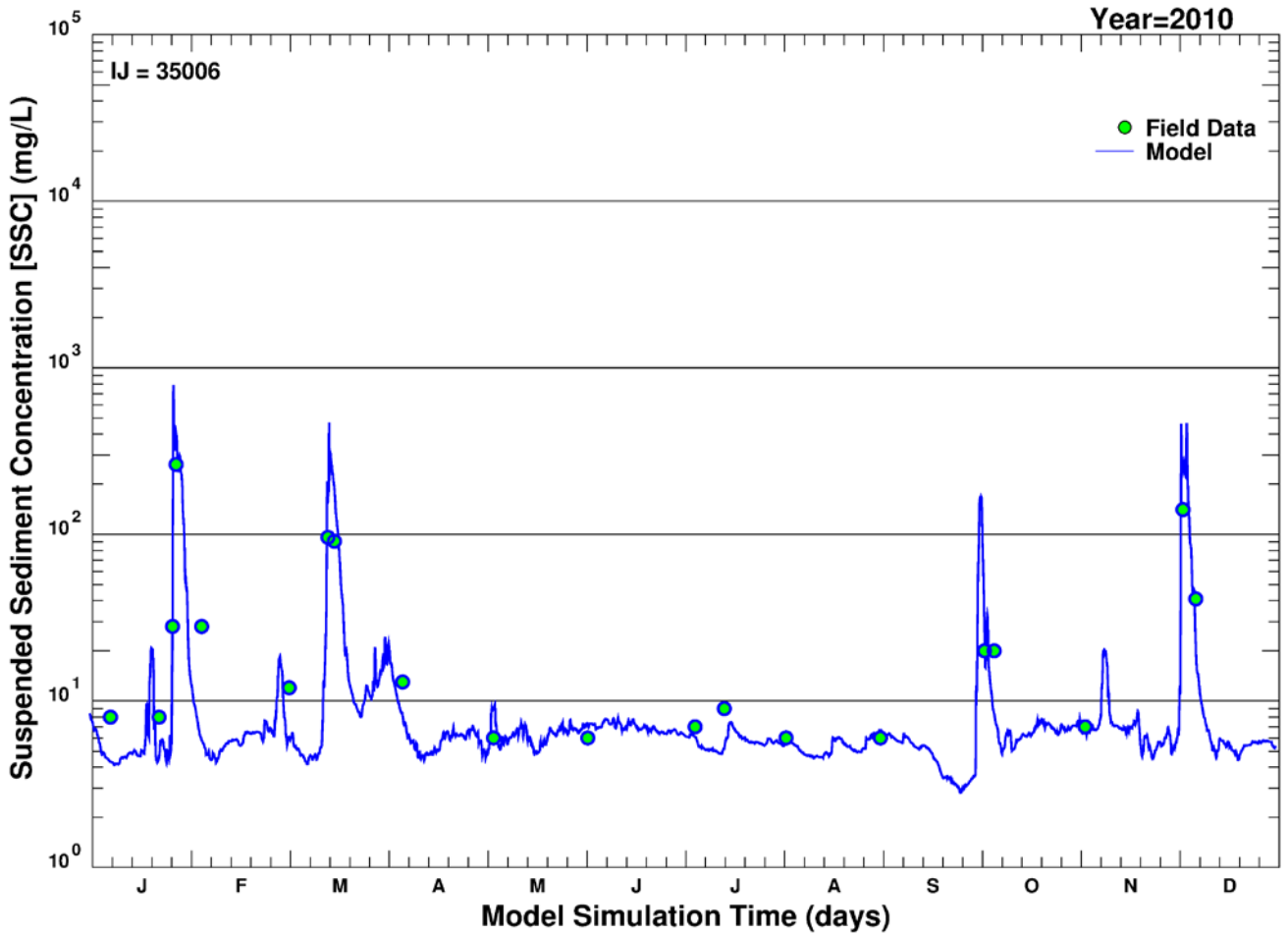


Note: Blue line = simulated suspended sediment concentration (depth-averaged sum of all size classes in the model); Green circle = measured suspended sediment concentration; IJ indicates the model grid cell from which outputs were retrieved; x-axis divisions indicate time in days; y-axis maximum indicates the log cycle closest to but not less than the maximum concentration simulated (which occurred during Tropical Storm Lee in 2011).

Figure E-14. Simulated and measured suspended sediment concentrations over time at Conowingo: 2010 (long-term simulation).

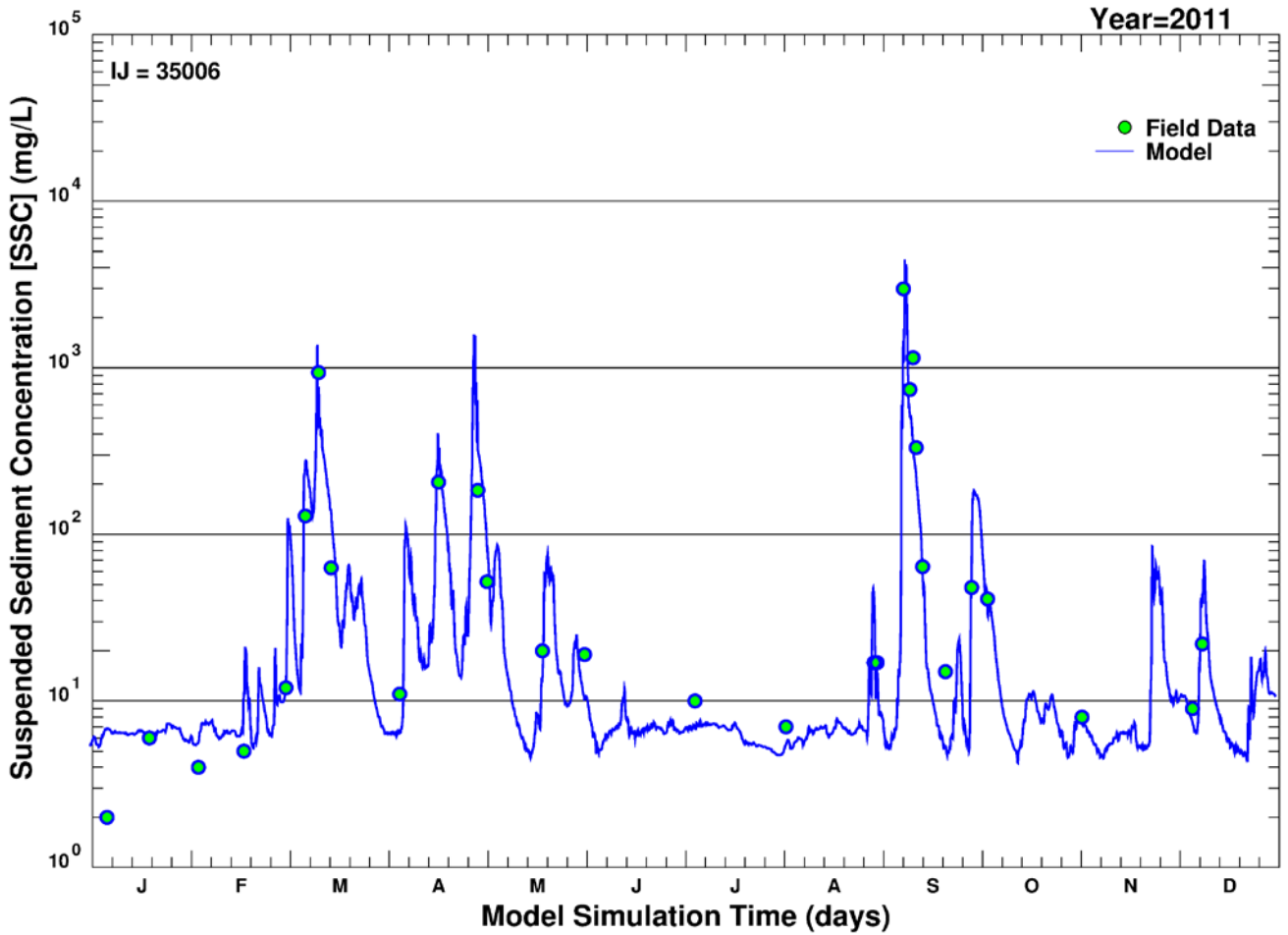


Note: Blue line = simulated suspended sediment concentration (depth-averaged sum of all size classes in the model); Green circle = measured suspended sediment concentration; IJ indicates the model grid cell from which outputs were retrieved; x-axis divisions indicate time in days; y-axis maximum indicates the log cycle closest to but not less than the maximum concentration simulated (which occurred during Tropical Storm Lee in 2011).

Figure E-15. Simulated and measured suspended sediment concentrations over time at Conowingo: 2011 (long-term simulation).

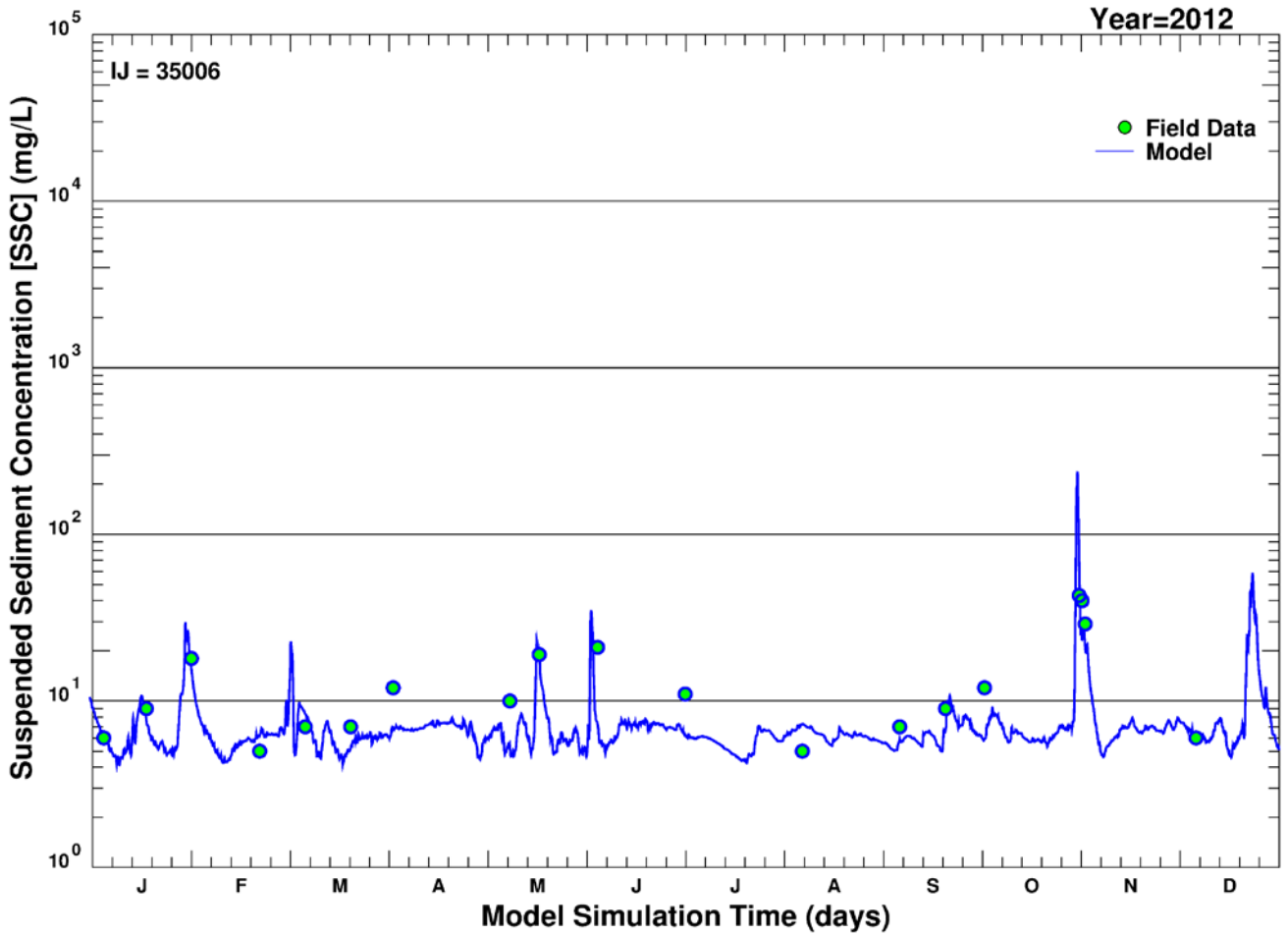


Note: Blue line = simulated suspended sediment concentration (depth-averaged sum of all size classes in the model); Green circle = measured suspended sediment concentration; IJ indicates the model grid cell from which outputs were retrieved; x-axis divisions indicate time in days; y-axis maximum indicates the log cycle closest to but not less than the maximum concentration simulated (which occurred during Tropical Storm Lee in 2011).

Figure E-16. Simulated and measured suspended sediment concentrations over time at Conowingo: 2012 (long-term simulation).

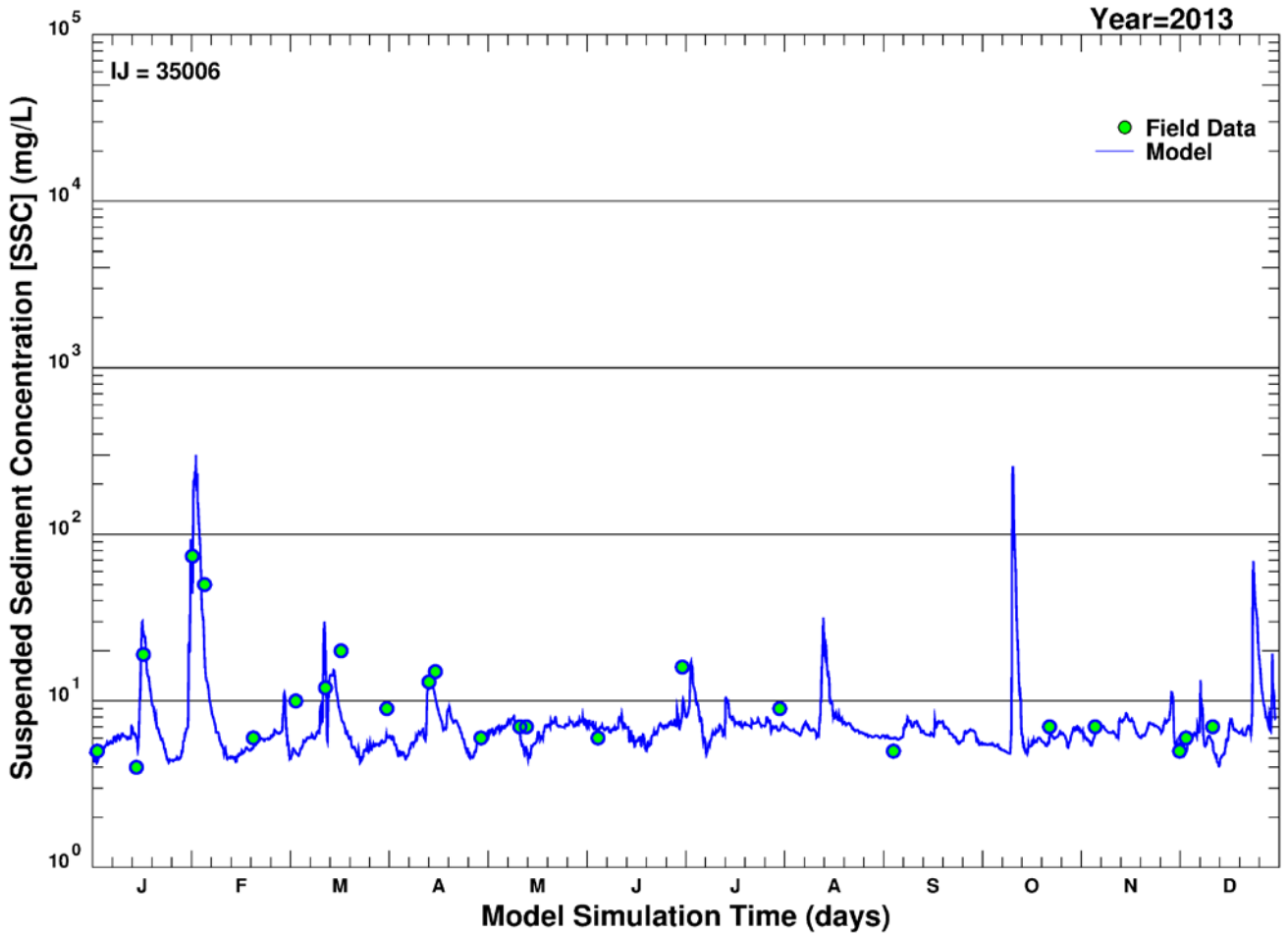


Note: Blue line = simulated suspended sediment concentration (depth-averaged sum of all size classes in the model); Green circle = measured suspended sediment concentration; IJ indicates the model grid cell from which outputs were retrieved; x-axis divisions indicate time in days; y-axis maximum indicates the log cycle closest to but not less than the maximum concentration simulated (which occurred during Tropical Storm Lee in 2011).

Figure E-17. Simulated and measured suspended sediment concentrations over time at Conowingo: 2013 (long-term simulation).

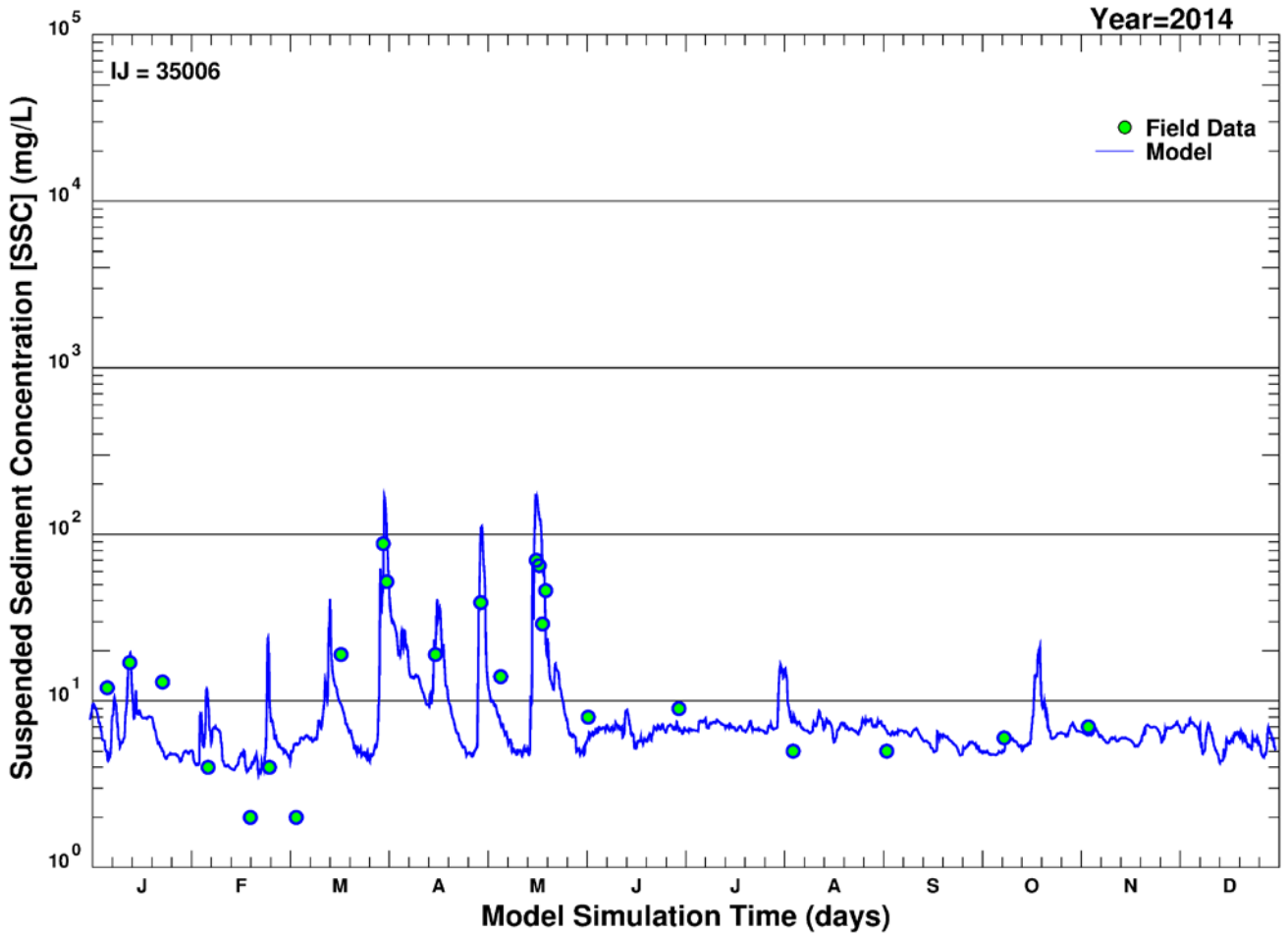


Note: Blue line = simulated suspended sediment concentration (depth-averaged sum of all size classes in the model); Green circle = measured suspended sediment concentration; IJ indicates the model grid cell from which outputs were retrieved; x-axis divisions indicate time in days; y-axis maximum indicates the log cycle closest to but not less than the maximum concentration simulated (which occurred during Tropical Storm Lee in 2011).

Figure E-18. Simulated and measured suspended sediment concentrations over time at Conowingo: 2014 (long-term simulation).

# APPENDIX F. SIMULATED AND MEASURED SUSPENDED SEDIMENT CONCENTRATIONS (SHORT-TERM): 2008-2014

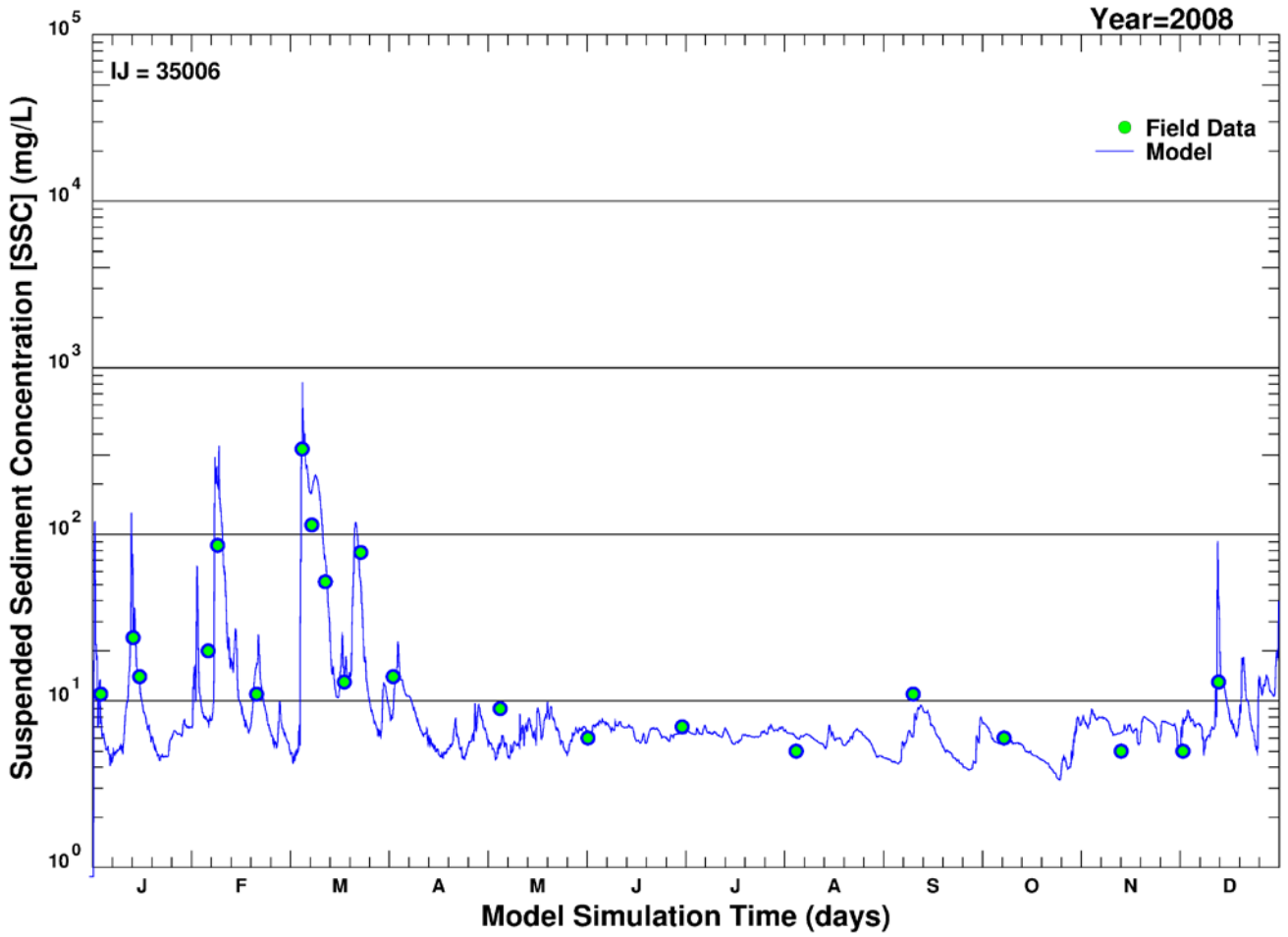


Note: Blue line = simulated suspended sediment concentration (depth-averaged sum of all size classes in the model); Green circle = measured suspended sediment concentration; IJ indicates the model grid cell from which outputs were retrieved; x-axis divisions indicate time in days; y-axis maximum indicates the log cycle closest to but not less than the maximum concentration simulated (which occurred during Tropical Storm Lee in 2011).

Figure F-1. Simulated and measured suspended sediment concentrations over time at Conowingo: 2008 (short-term simulation).

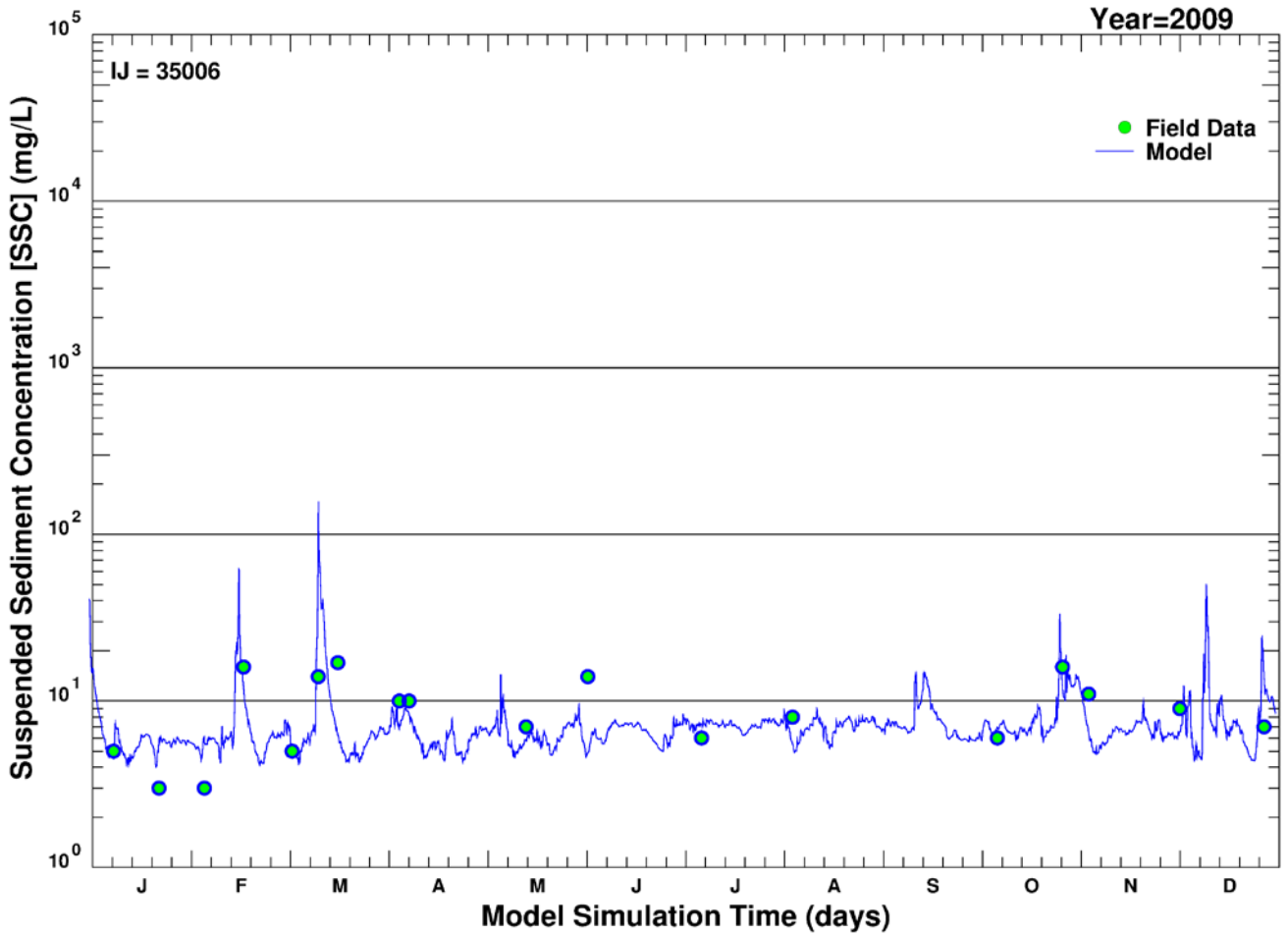


Note: Blue line = simulated suspended sediment concentration (depth-averaged sum of all size classes in the model); Green circle = measured suspended sediment concentration; IJ indicates the model grid cell from which outputs were retrieved; x-axis divisions indicate time in days; y-axis maximum indicates the log cycle closest to but not less than the maximum concentration simulated (which occurred during Tropical Storm Lee in 2011).

Figure F-2. Simulated and measured suspended sediment concentrations over time at Conowingo: 2009 (short-term simulation).

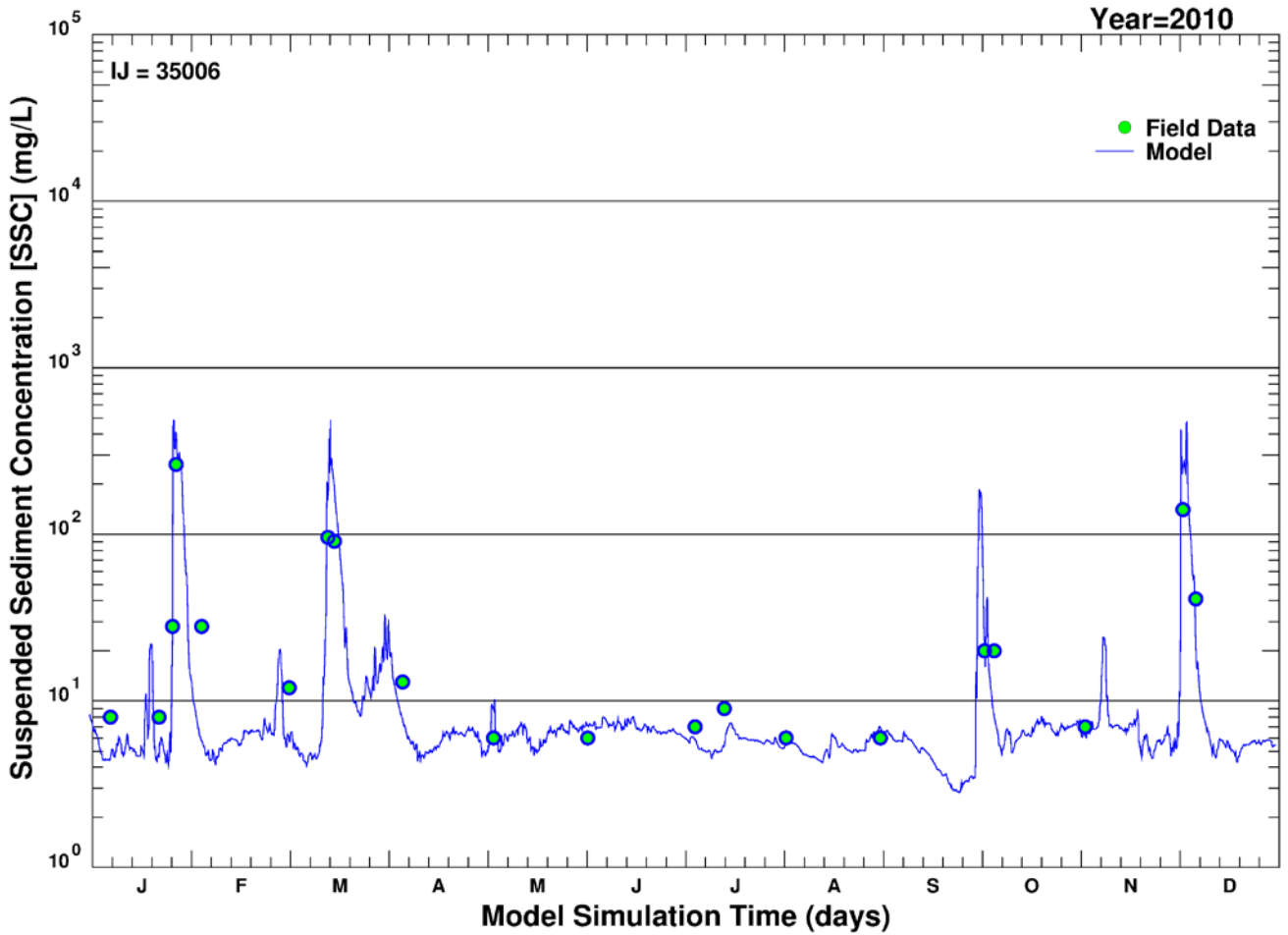


Note: Blue line = simulated suspended sediment concentration (depth-averaged sum of all size classes in the model); Green circle = measured suspended sediment concentration; IJ indicates the model grid cell from which outputs were retrieved; x-axis divisions indicate time in days; y-axis maximum indicates the log cycle closest to but not less than the maximum concentration simulated (which occurred during Tropical Storm Lee in 2011).

Figure F-3. Simulated and measured suspended sediment concentrations over time at Conowingo: 2010 (short-term simulation).

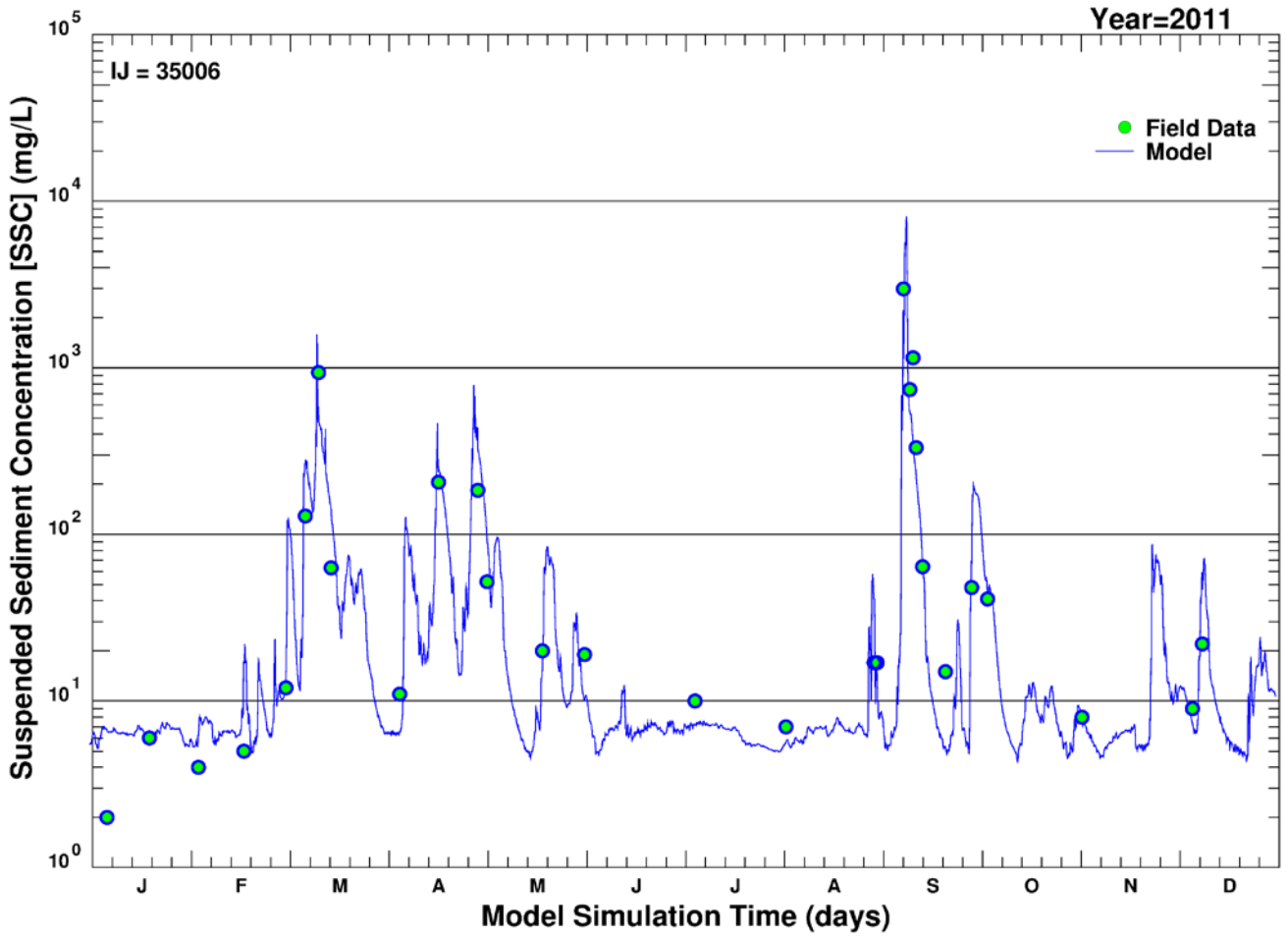


Note: Blue line = simulated suspended sediment concentration (depth-averaged sum of all size classes in the model); Green circle = measured suspended sediment concentration; IJ indicates the model grid cell from which outputs were retrieved; x-axis divisions indicate time in days; y-axis maximum indicates the log cycle closest to but not less than the maximum concentration simulated (which occurred during Tropical Storm Lee in 2011).

Figure F-4. Simulated and measured suspended sediment concentrations over time at Conowingo: 2011 (short-term simulation).

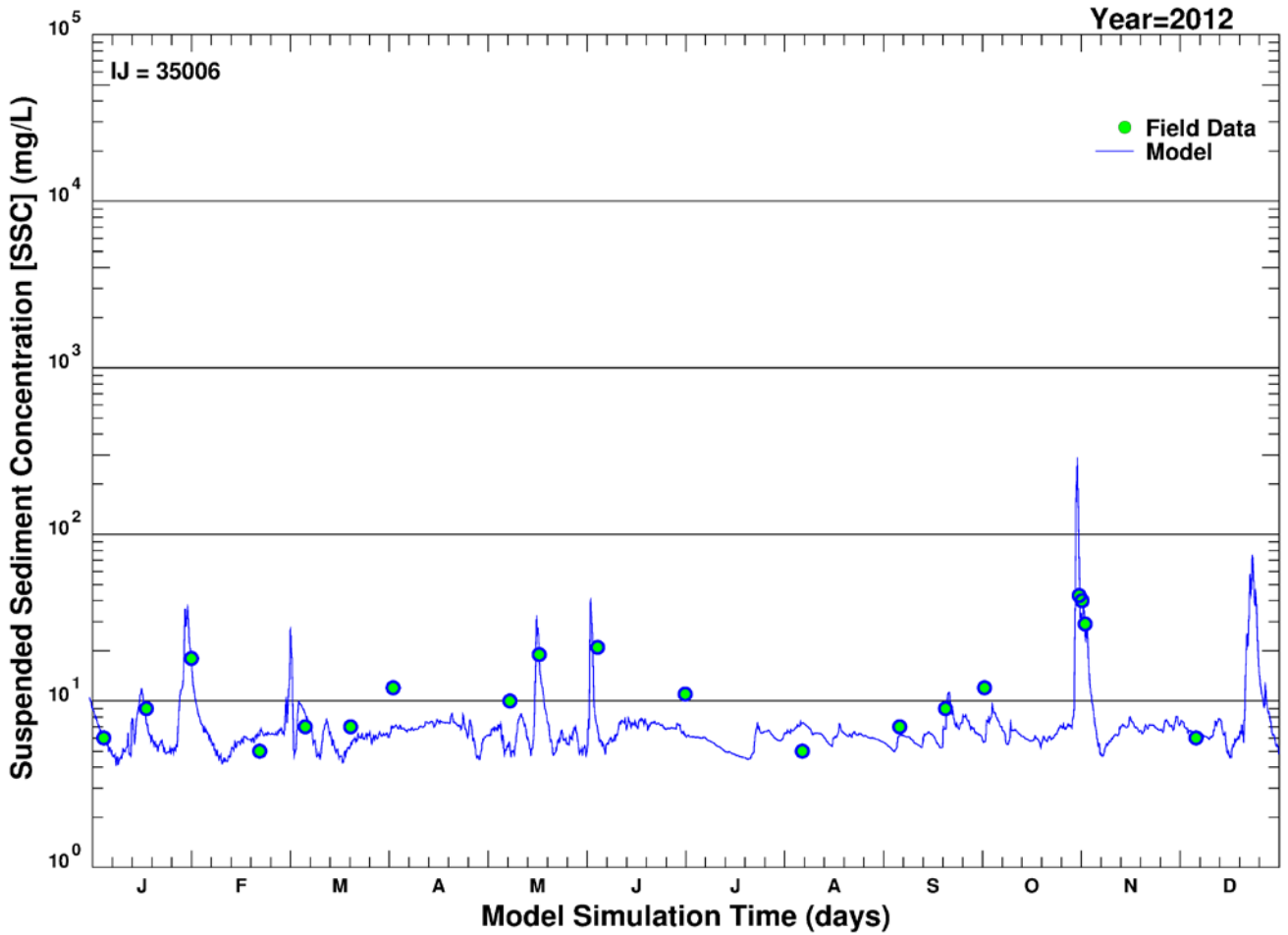


Note: Blue line = simulated suspended sediment concentration (depth-averaged sum of all size classes in the model); Green circle = measured suspended sediment concentration; IJ indicates the model grid cell from which outputs were retrieved; x-axis divisions indicate time in days; y-axis maximum indicates the log cycle closest to but not less than the maximum concentration simulated (which occurred during Tropical Storm Lee in 2011).

Figure F-5. Simulated and measured suspended sediment concentrations over time at Conowingo: 2012 (short-term simulation).

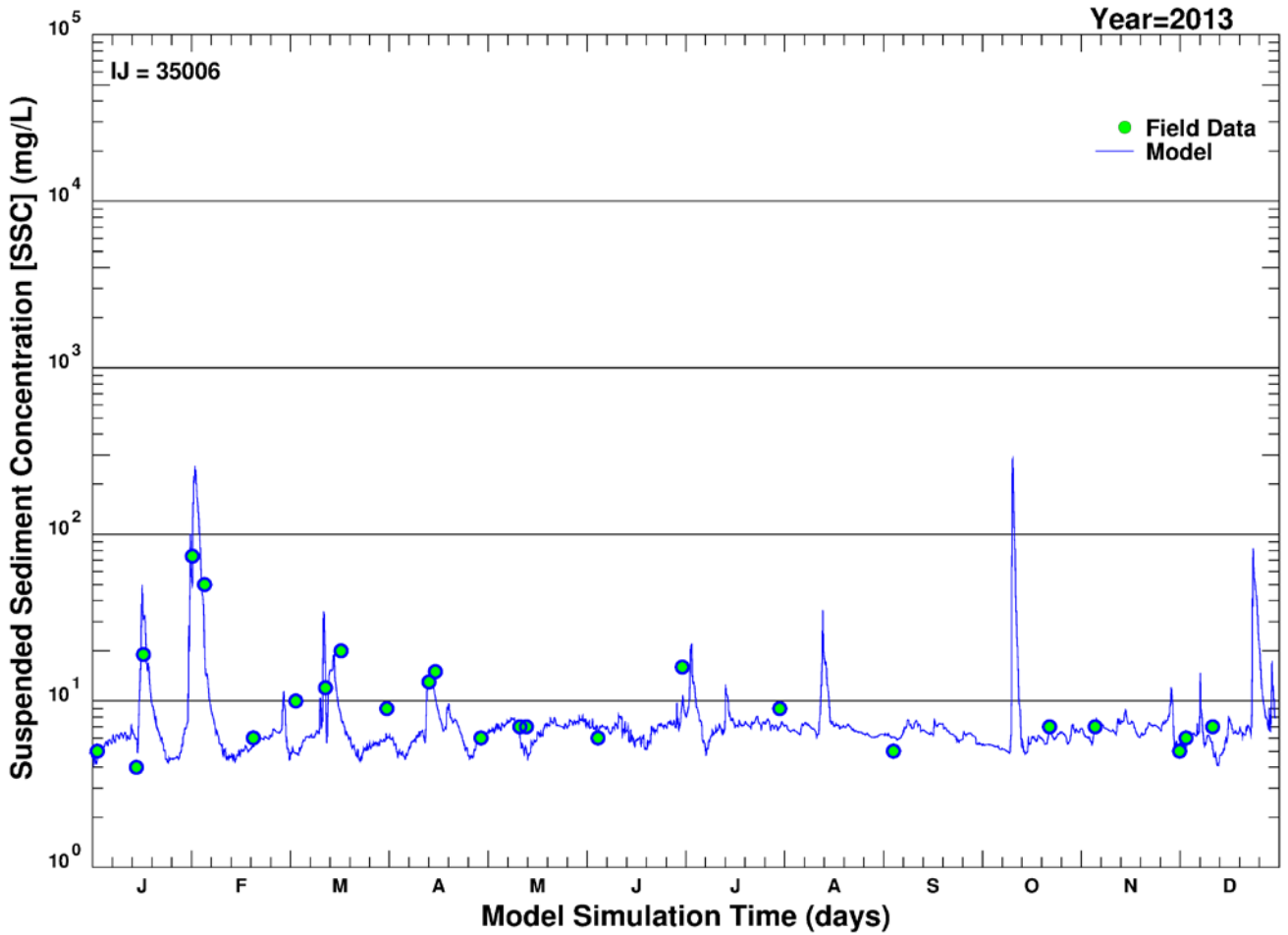


Note: Blue line = simulated suspended sediment concentration (depth-averaged sum of all size classes in the model); Green circle = measured suspended sediment concentration; IJ indicates the model grid cell from which outputs were retrieved; x-axis divisions indicate time in days; y-axis maximum indicates the log cycle closest to but not less than the maximum concentration simulated (which occurred during Tropical Storm Lee in 2011).

Figure F-6. Simulated and measured suspended sediment concentrations over time at Conowingo: 2013 (short-term simulation).

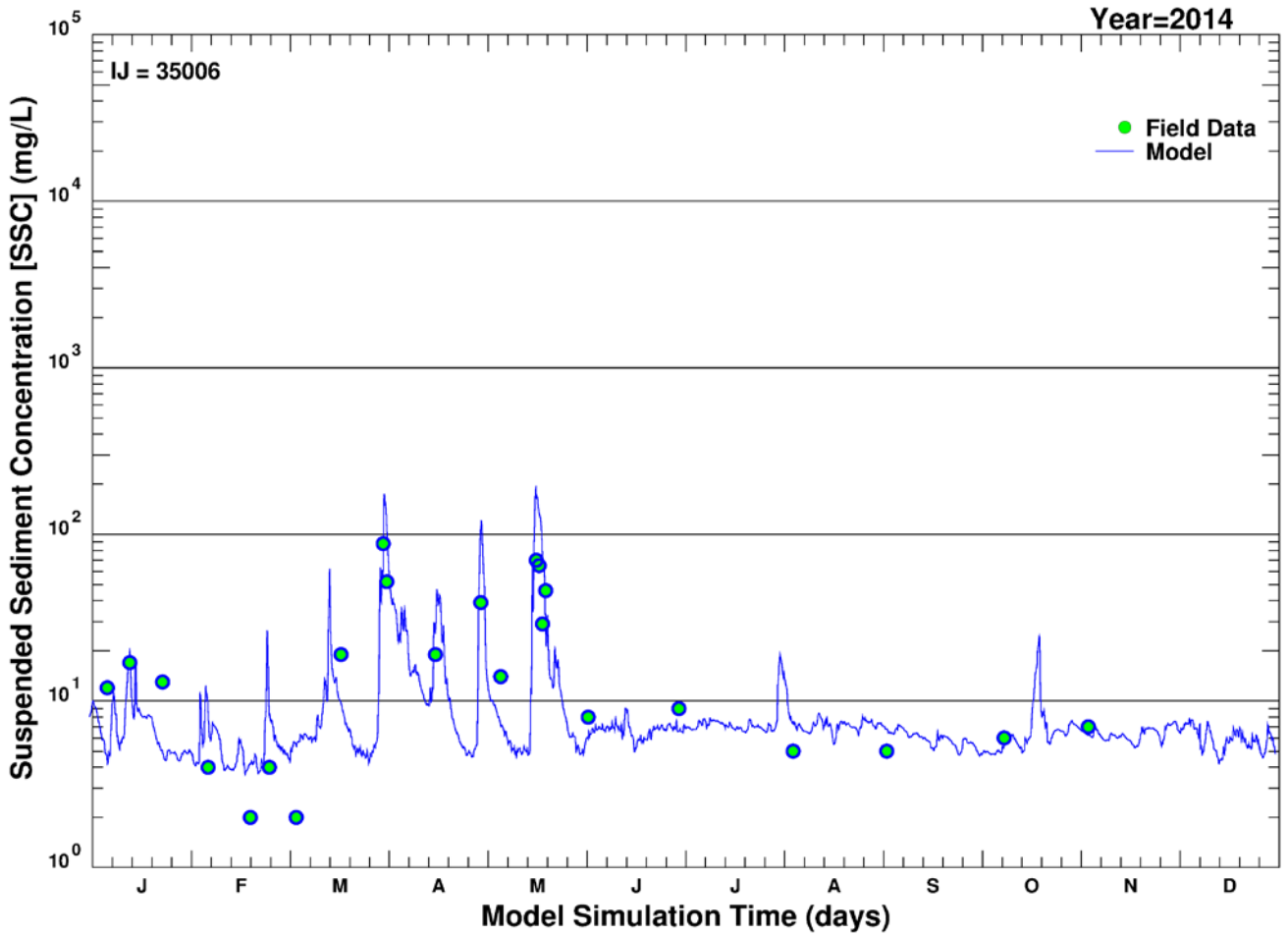


Note: Blue line = simulated suspended sediment concentration (depth-averaged sum of all size classes in the model); Green circle = measured suspended sediment concentration; IJ indicates the model grid cell from which outputs were retrieved; x-axis divisions indicate time in days; y-axis maximum indicates the log cycle closest to but not less than the maximum concentration simulated (which occurred during Tropical Storm Lee in 2011).

Figure F-7. Simulated and measured suspended sediment concentrations over time at Conowingo: 2014 (short-term simulation).

# APPENDIX G. SIMULATED SEDIMENT BED ELEVATION CHANGES (LONG-TERM): 1997-2014

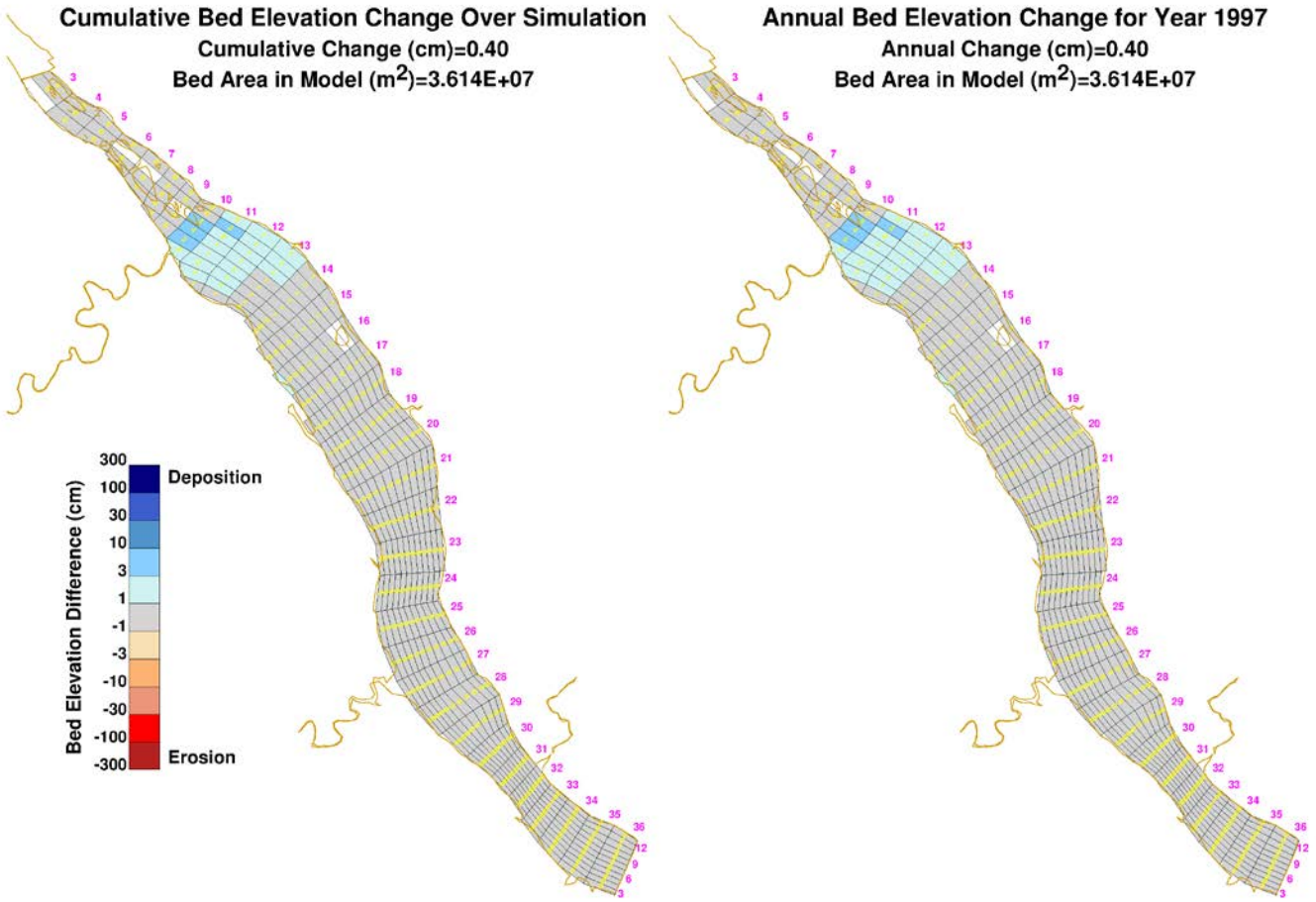


Note: Panel on the Left = simulated cumulative bed elevation change since simulation start; Panel on the Right = simulated annual bed elevation change for year indicated; values shown for all model grid cells; pink numbers along sides of images indicate "row" and "column" references for the model grid.

Figure G-1. Simulated cumulative (since 1997) and annual bed elevation change for Conowingo Pond: 1997 (long-term).

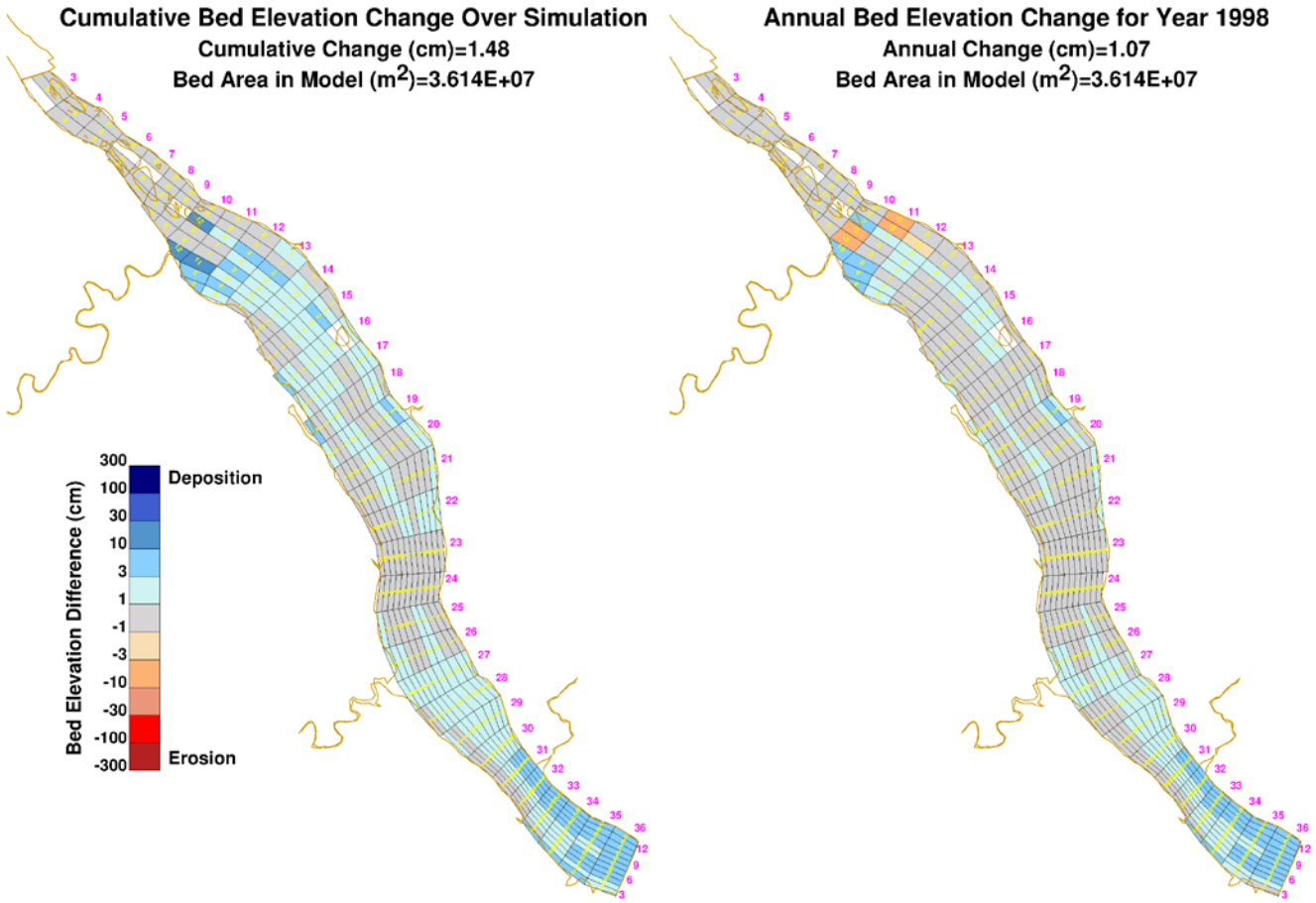


Note: Panel on the Left = simulated cumulative bed elevation change since simulation start; Panel on the Right = simulated annual bed elevation change for year indicated; values shown for all model grid cells; pink numbers along sides of images indicate "row" and "column" references for the model grid.

Figure G-2. Simulated cumulative (since 1997) and annual bed elevation change for Conowingo Pond: 1998 (long-term).

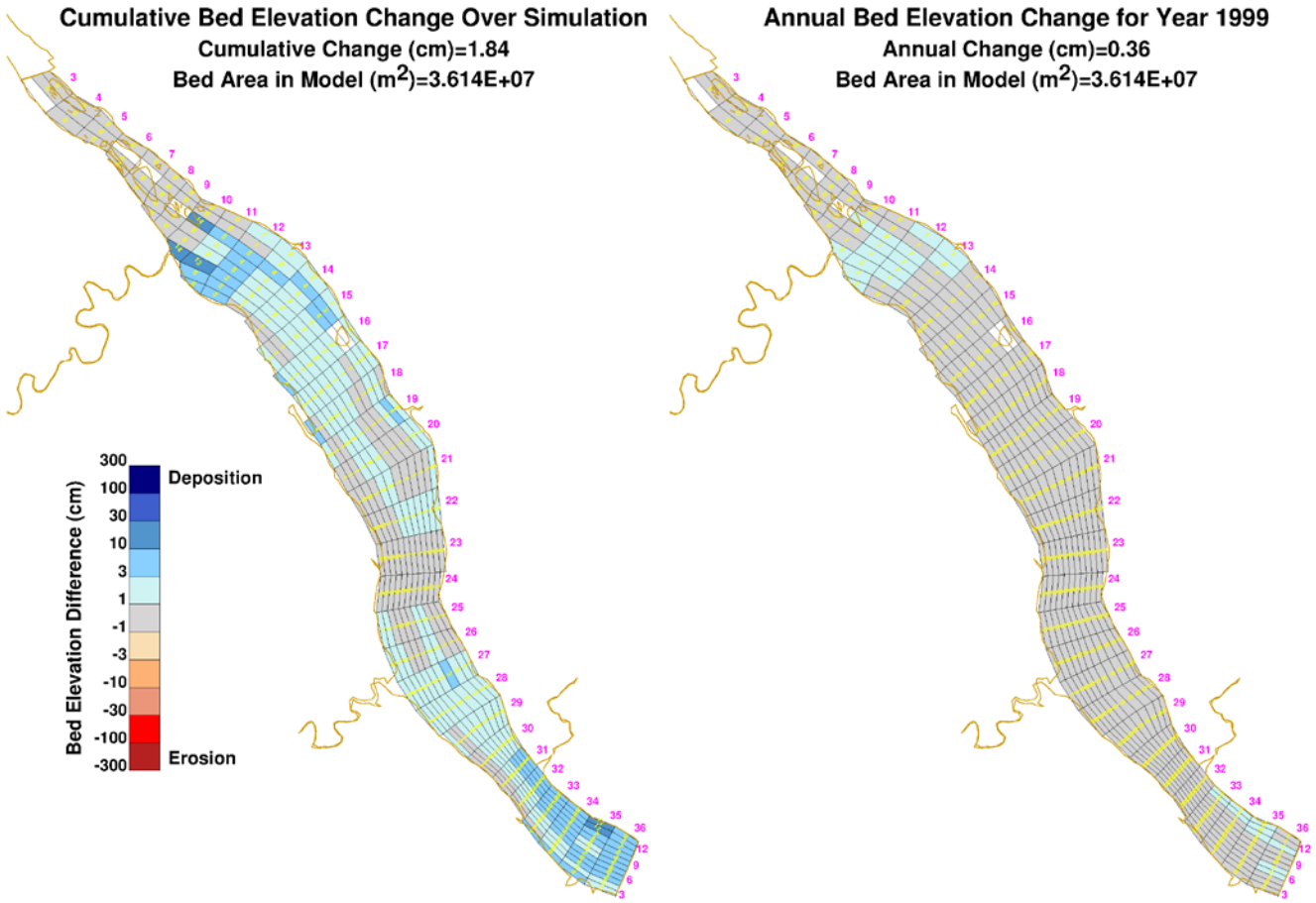


Note: Panel on the Left = simulated cumulative bed elevation change since simulation start; Panel on the Right = simulated annual bed elevation change for year indicated; values shown for all model grid cells; pink numbers along sides of images indicate "row" and "column" references for the model grid.

Figure G-3. Simulated cumulative (since 1997) and annual bed elevation change for Conowingo Pond: 1999 (long-term).

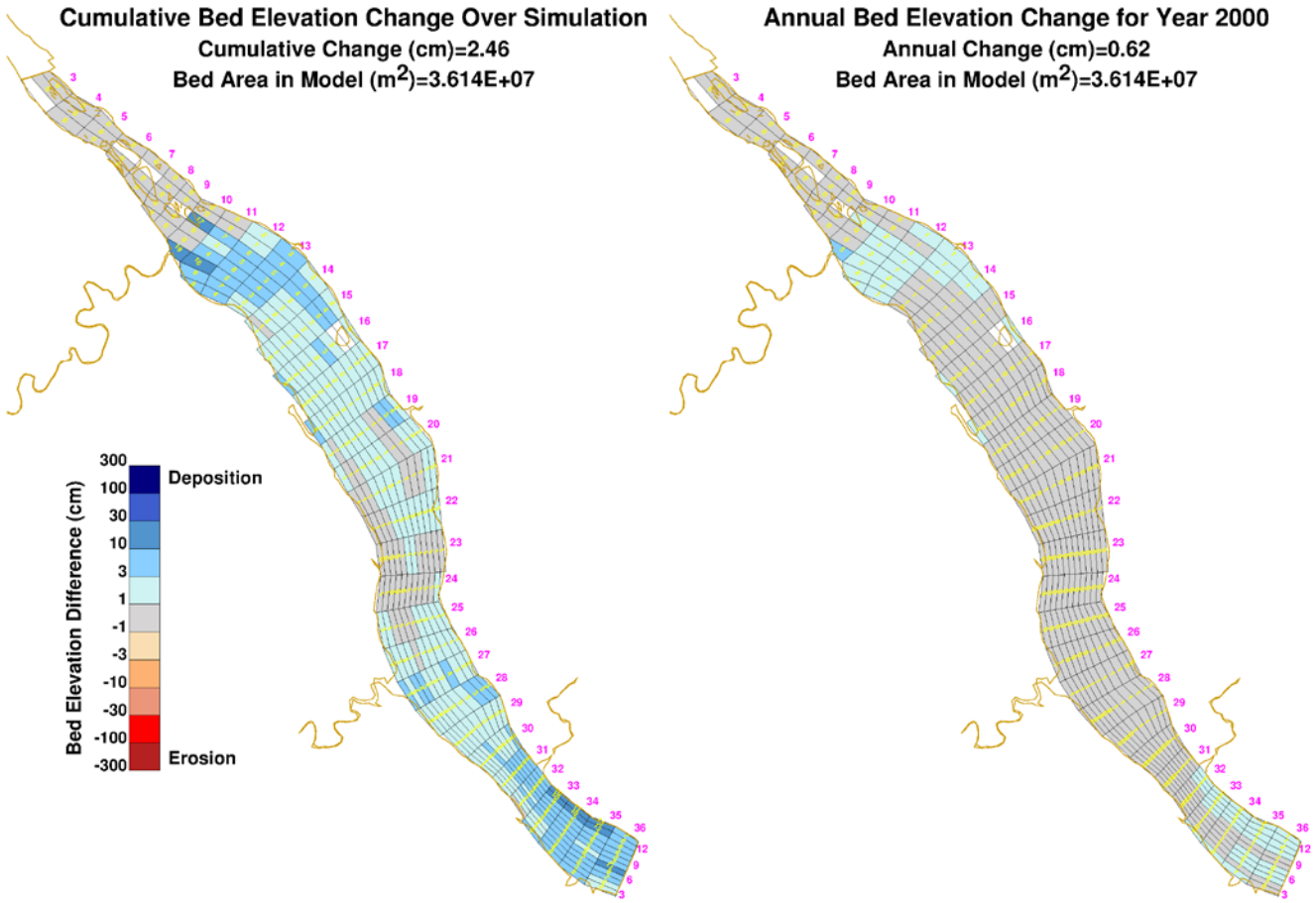


Note: Panel on the Left = simulated cumulative bed elevation change since simulation start; Panel on the Right = simulated annual bed elevation change for year indicated; values shown for all model grid cells; pink numbers along sides of images indicate "row" and "column" references for the model grid.

Figure G-4. Simulated cumulative (since 1997) and annual bed elevation change for Conowingo Pond: 2000 (long-term).

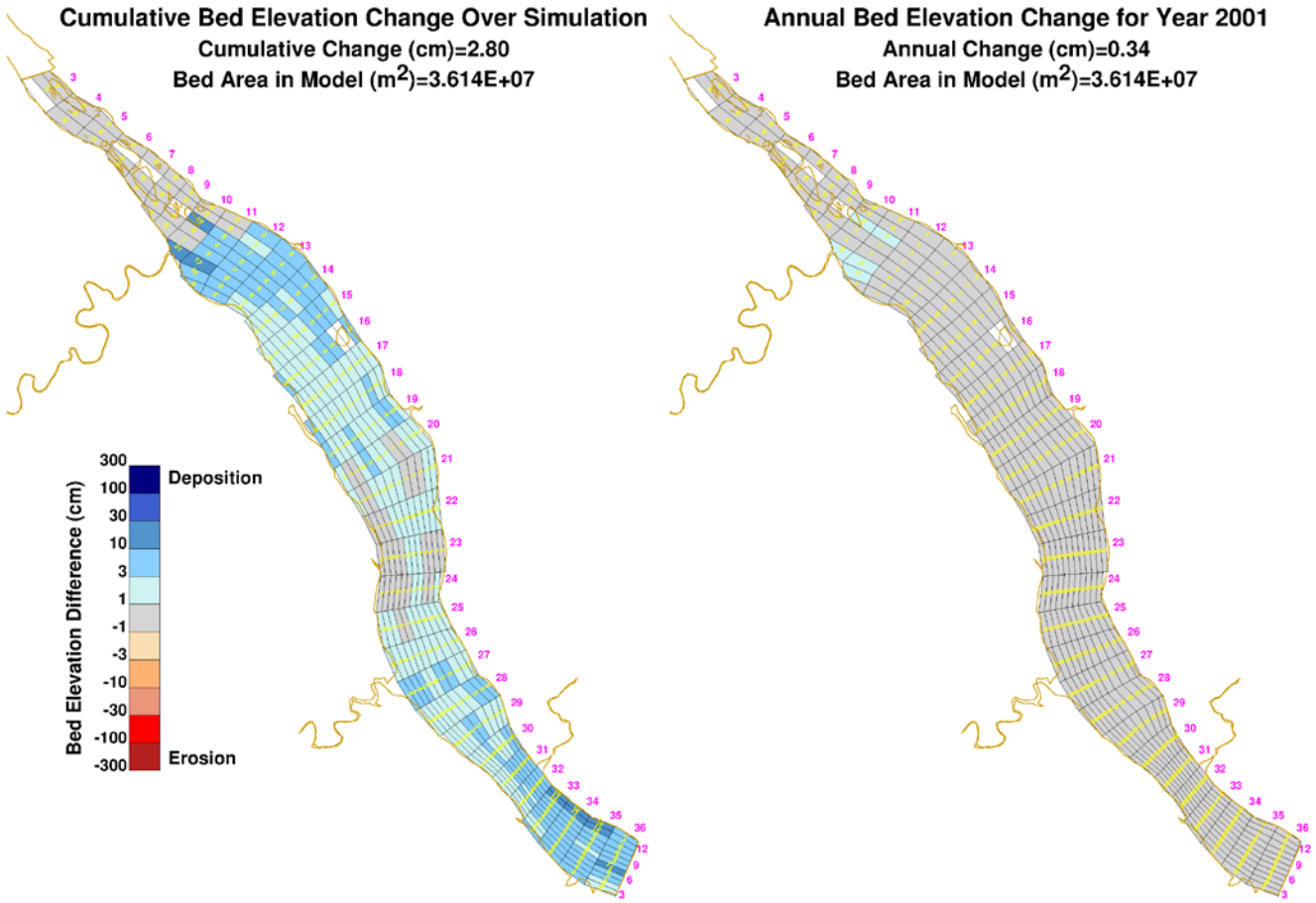


Note: Panel on the Left = simulated cumulative bed elevation change since simulation start; Panel on the Right = simulated annual bed elevation change for year indicated; values shown for all model grid cells; pink numbers along sides of images indicate "row" and "column" references for the model grid.

Figure G-5. Simulated cumulative (since 1997) and annual bed elevation change for Conowingo Pond: 2001 (long-term).

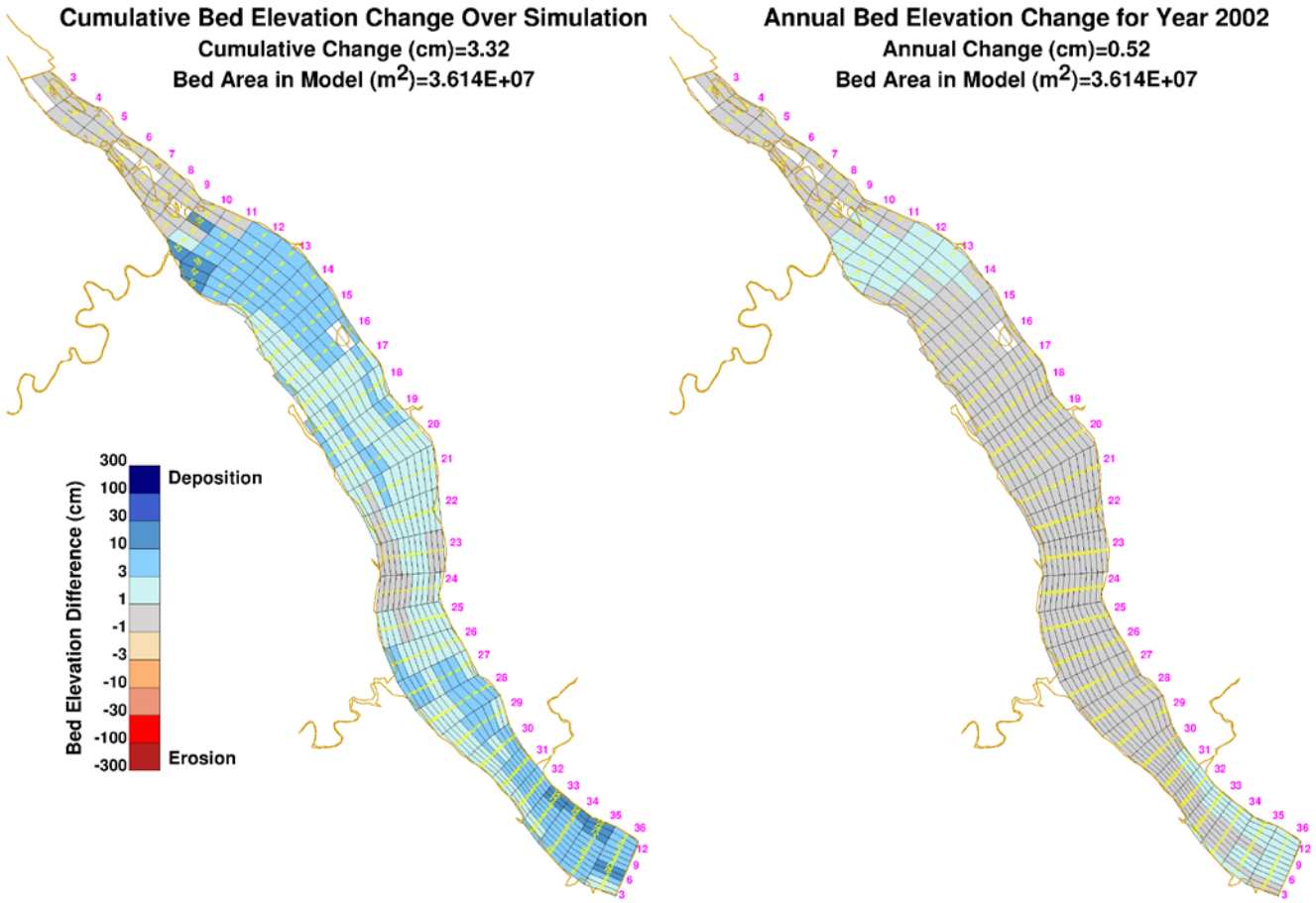


Note: Panel on the Left = simulated cumulative bed elevation change since simulation start; Panel on the Right = simulated annual bed elevation change for year indicated; values shown for all model grid cells; pink numbers along sides of images indicate "row" and "column" references for the model grid.

Figure G-6. Simulated cumulative (since 1997) and annual bed elevation change for Conowingo Pond: 2002 (long-term).

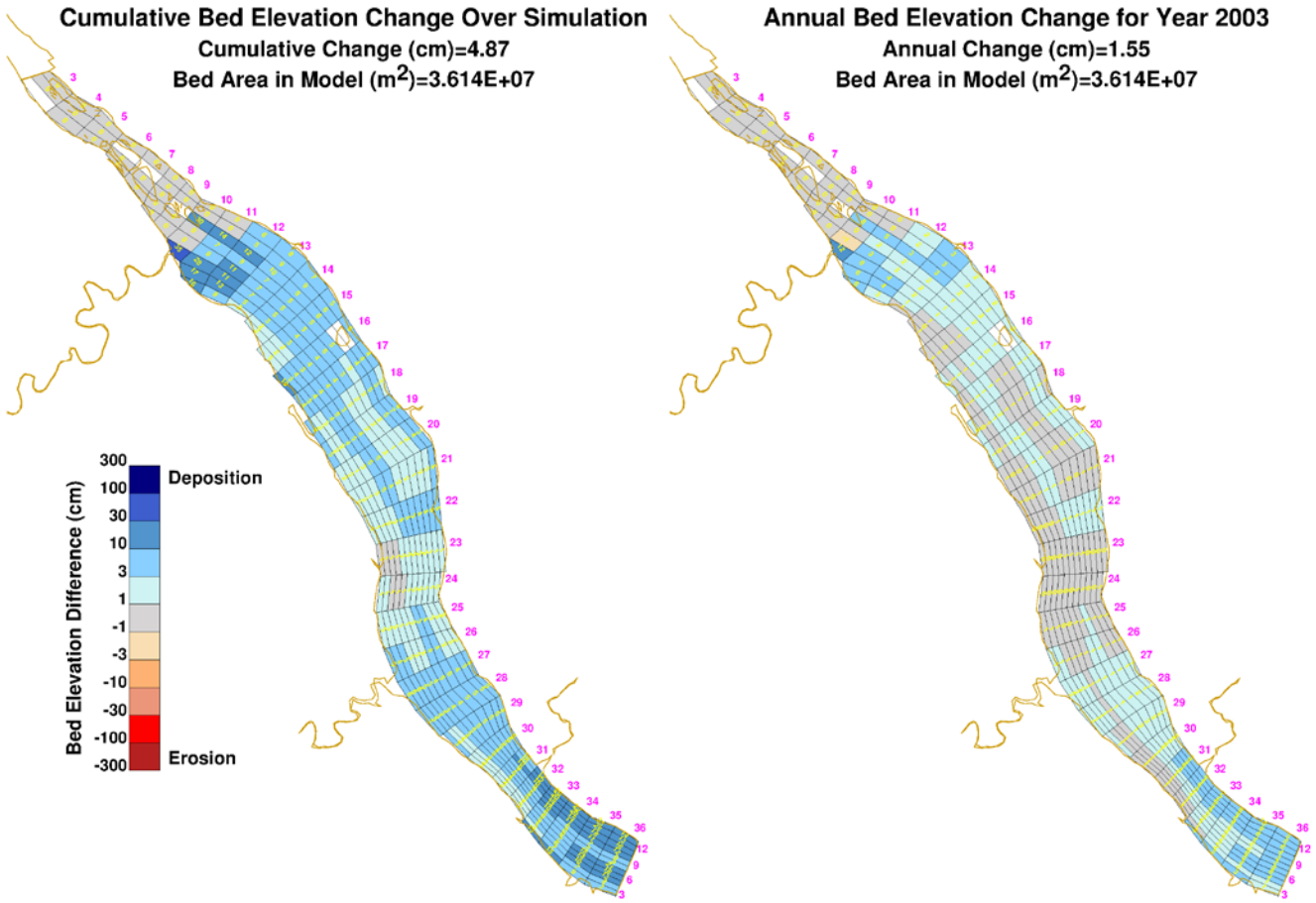


Note: Panel on the Left = simulated cumulative bed elevation change since simulation start; Panel on the Right = simulated annual bed elevation change for year indicated; values shown for all model grid cells; pink numbers along sides of images indicate "row" and "column" references for the model grid.

Figure G-7. Simulated cumulative (since 1997) and annual bed elevation change for Conowingo Pond: 2003 (long-term).

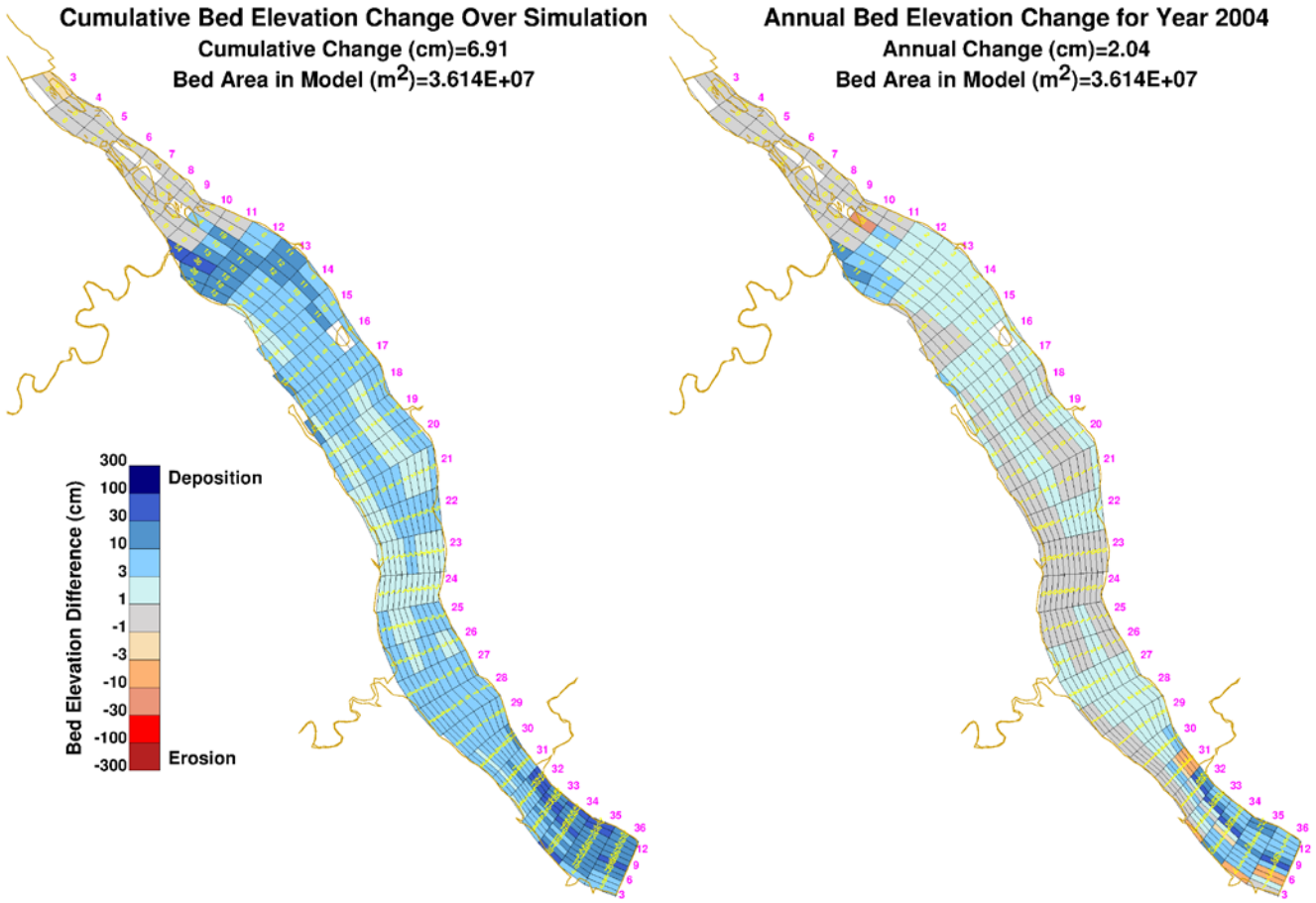


Note: Panel on the Left = simulated cumulative bed elevation change since simulation start; Panel on the Right = simulated annual bed elevation change for year indicated; values shown for all model grid cells; pink numbers along sides of images indicate "row" and "column" references for the model grid.

Figure G-8. Simulated cumulative (since 1997) and annual bed elevation change for Conowingo Pond: 2004 (long-term).

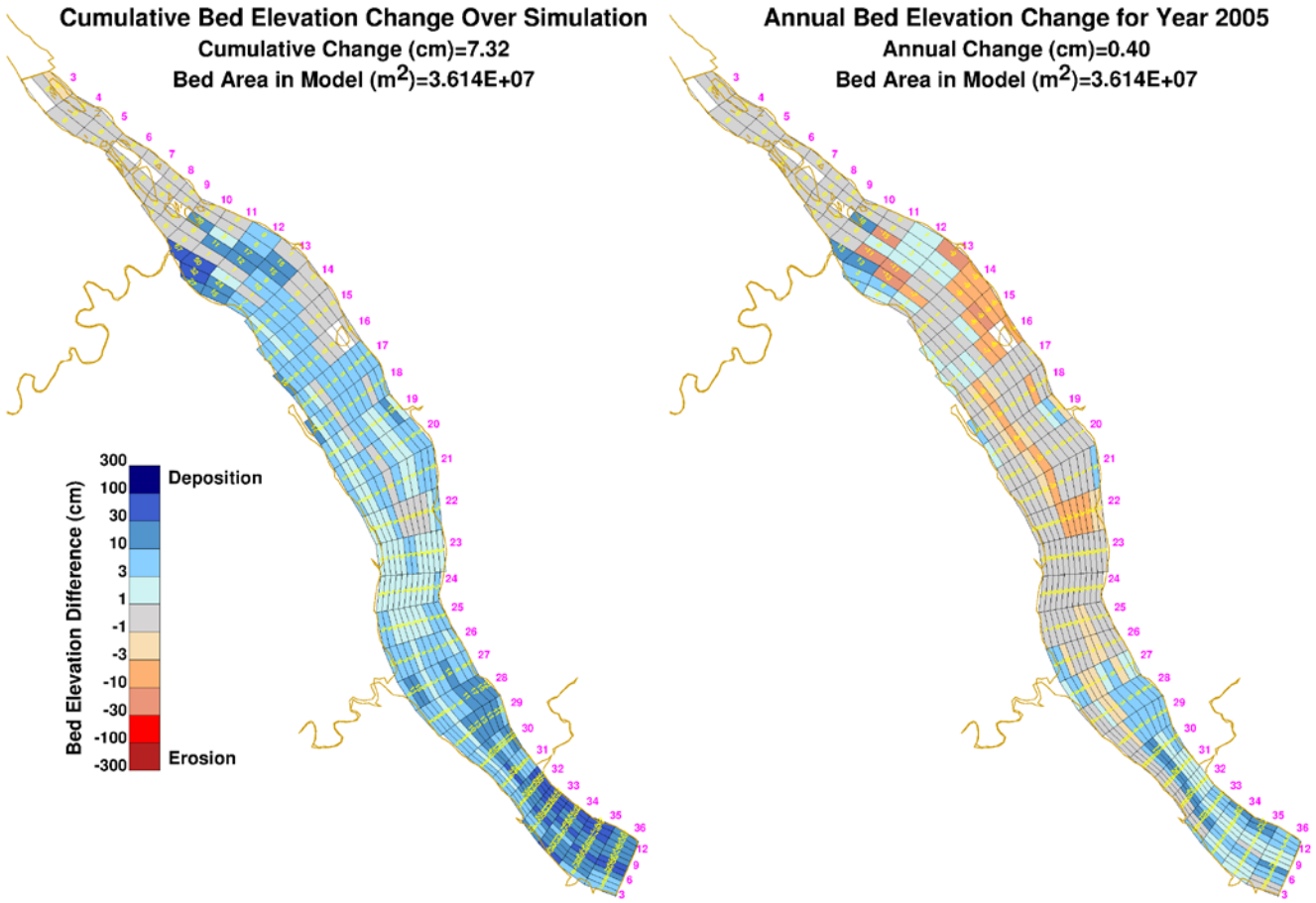


Note: Panel on the Left = simulated cumulative bed elevation change since simulation start; Panel on the Right = simulated annual bed elevation change for year indicated; values shown for all model grid cells; pink numbers along sides of images indicate "row" and "column" references for the model grid.

Figure G-9. Simulated cumulative (since 1997) and annual bed elevation change for Conowingo Pond: 2005 (long-term).

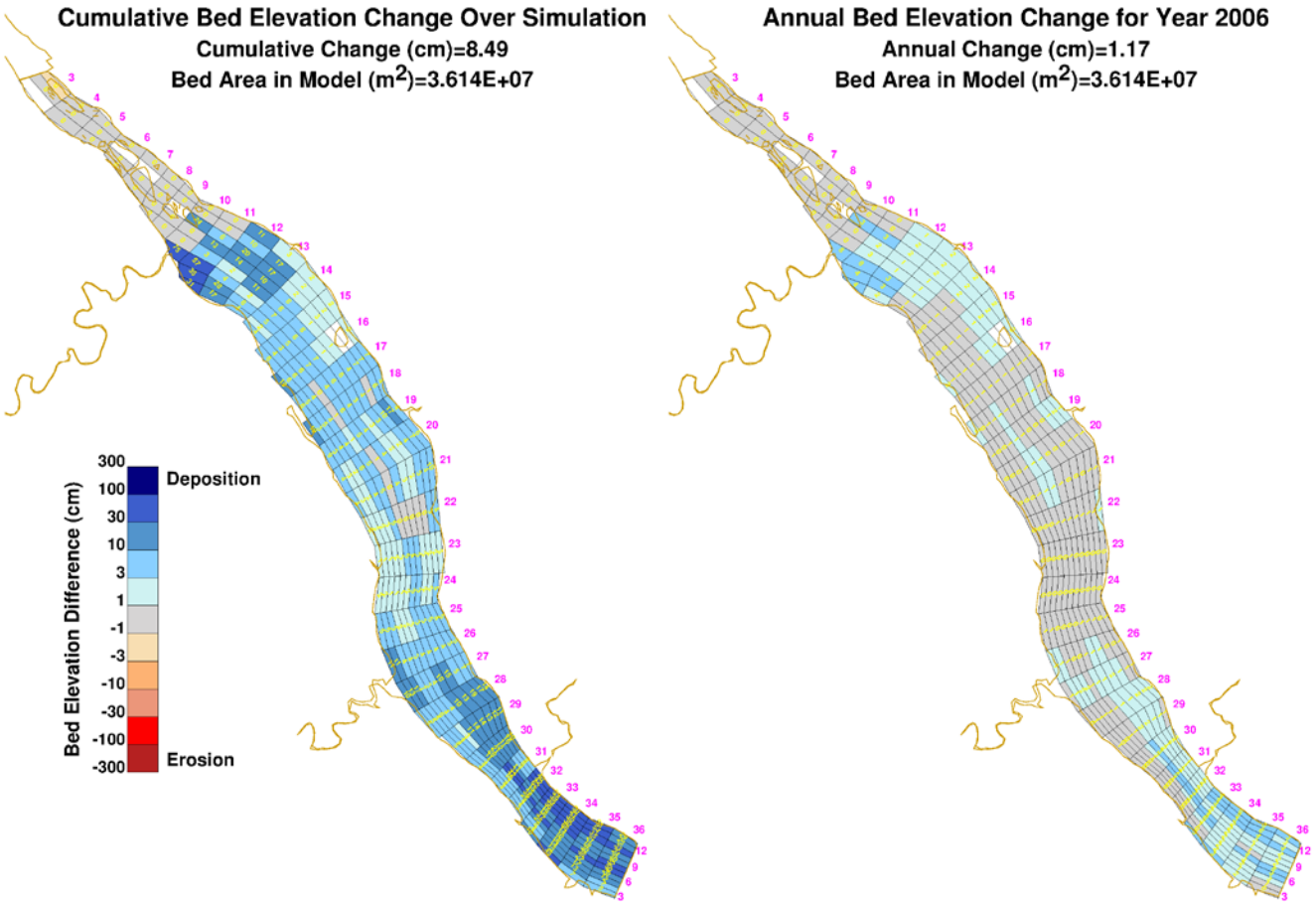


Note: Panel on the Left = simulated cumulative bed elevation change since simulation start; Panel on the Right = simulated annual bed elevation change for year indicated; values shown for all model grid cells; pink numbers along sides of images indicate "row" and "column" references for the model grid.

Figure G-10. Simulated cumulative (since 1997) and annual bed elevation change for Conowingo Pond: 2006 (long-term).

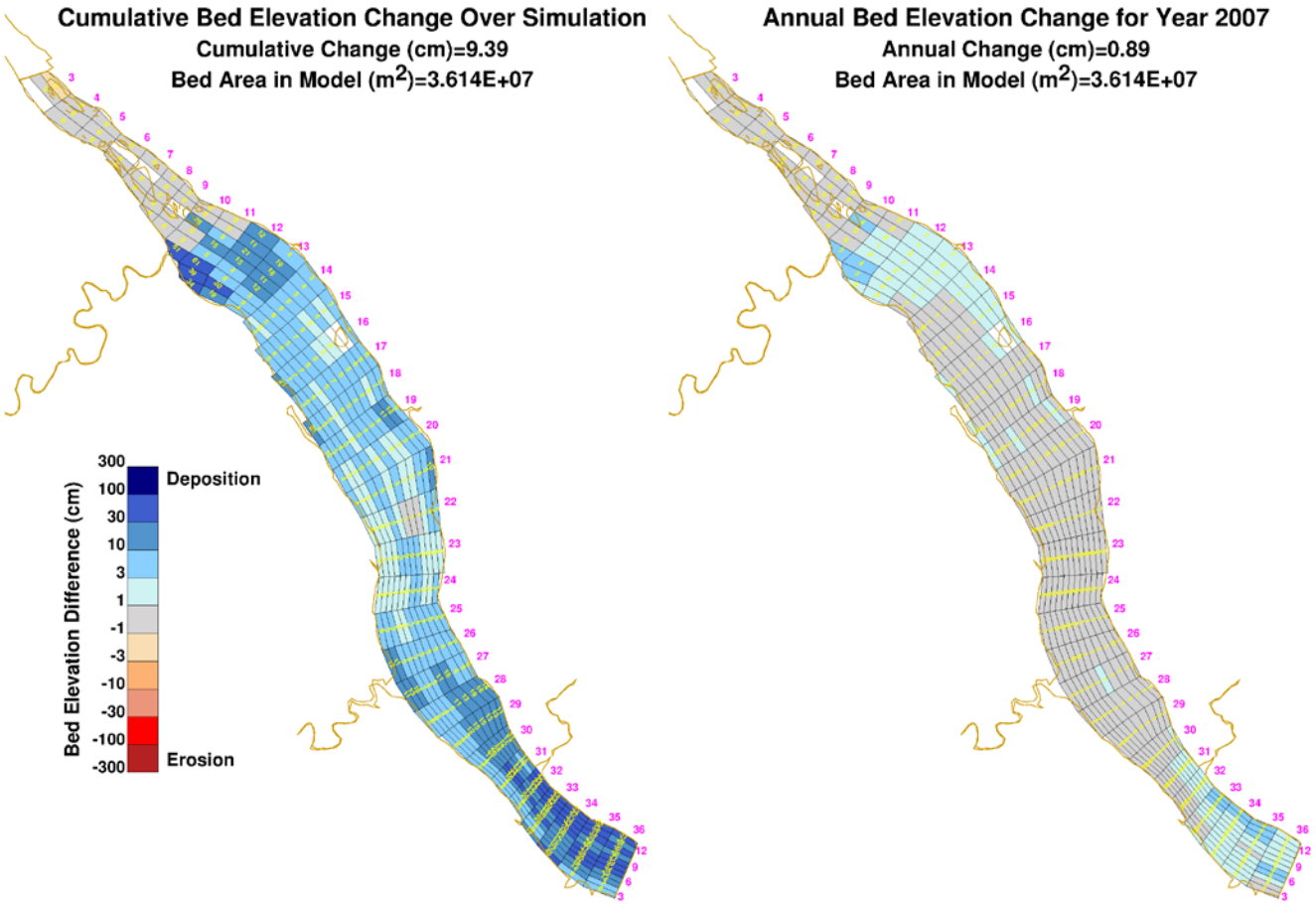


Note: Panel on the Left = simulated cumulative bed elevation change since simulation start; Panel on the Right = simulated annual bed elevation change for year indicated; values shown for all model grid cells; pink numbers along sides of images indicate "row" and "column" references for the model grid.

Figure G-11. Simulated cumulative (since 1997) and annual bed elevation change for Conowingo Pond: 2007 (long-term).

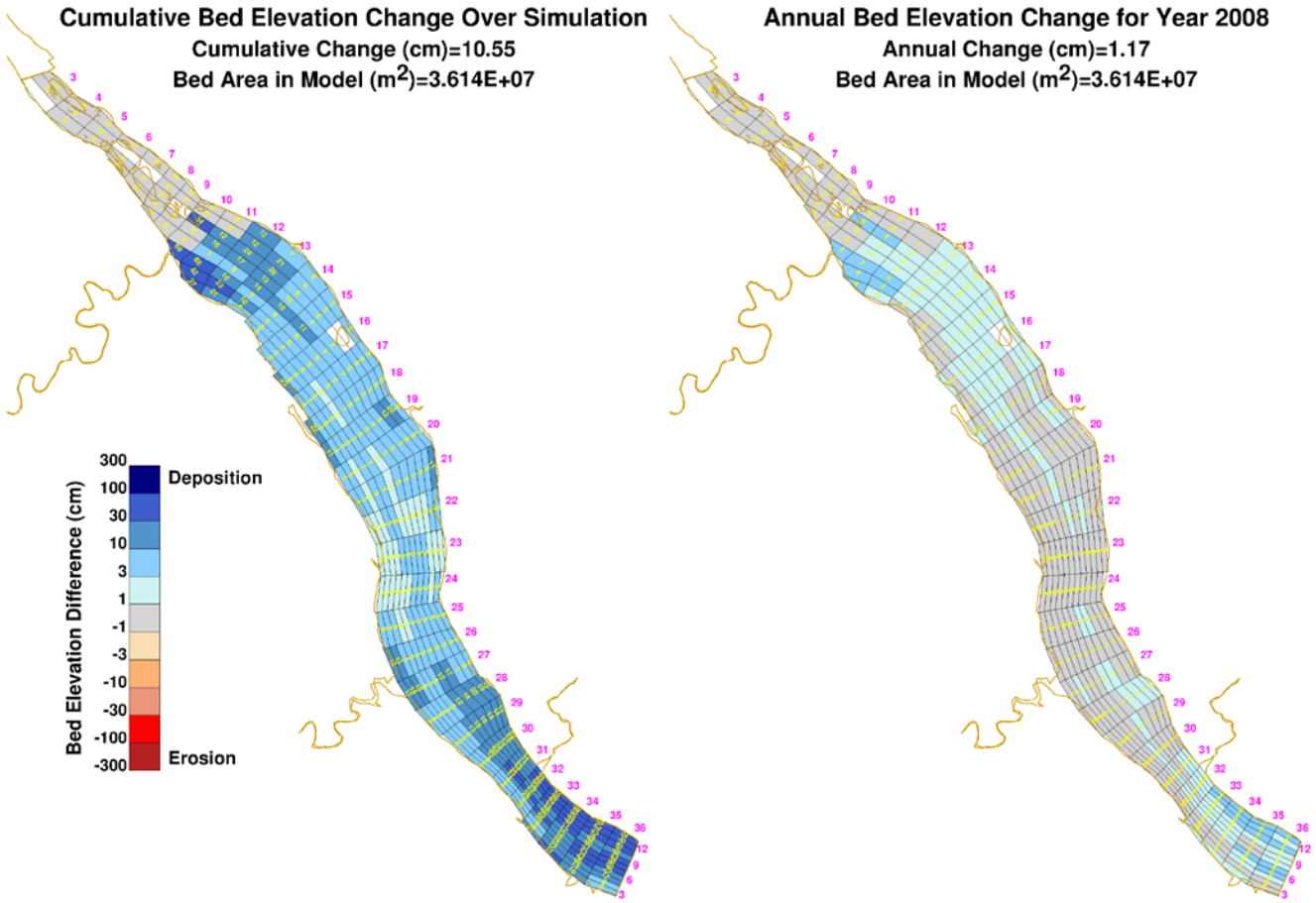


Note: Panel on the Left = simulated cumulative bed elevation change since simulation start; Panel on the Right = simulated annual bed elevation change for year indicated; values shown for all model grid cells; pink numbers along sides of images indicate "row" and "column" references for the model grid.

Figure G-12. Simulated cumulative (since 1997) and annual bed elevation change for Conowingo Pond: 2008 (long-term).

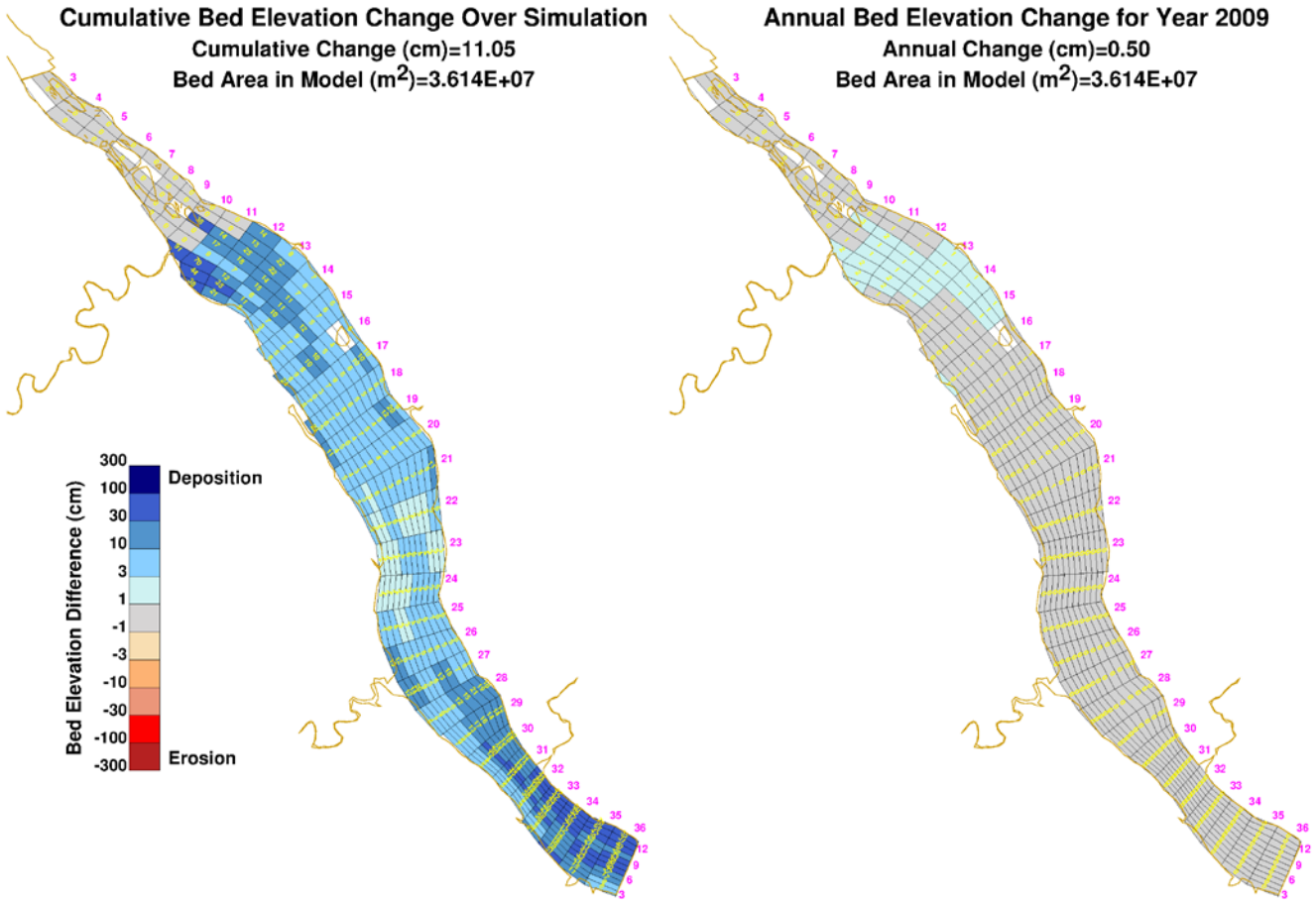


Note: Panel on the Left = simulated cumulative bed elevation change since simulation start; Panel on the Right = simulated annual bed elevation change for year indicated; values shown for all model grid cells; pink numbers along sides of images indicate "row" and "column" references for the model grid.

Figure G-13. Simulated cumulative (since 1997) and annual bed elevation change for Conowingo Pond: 2009 (long-term).

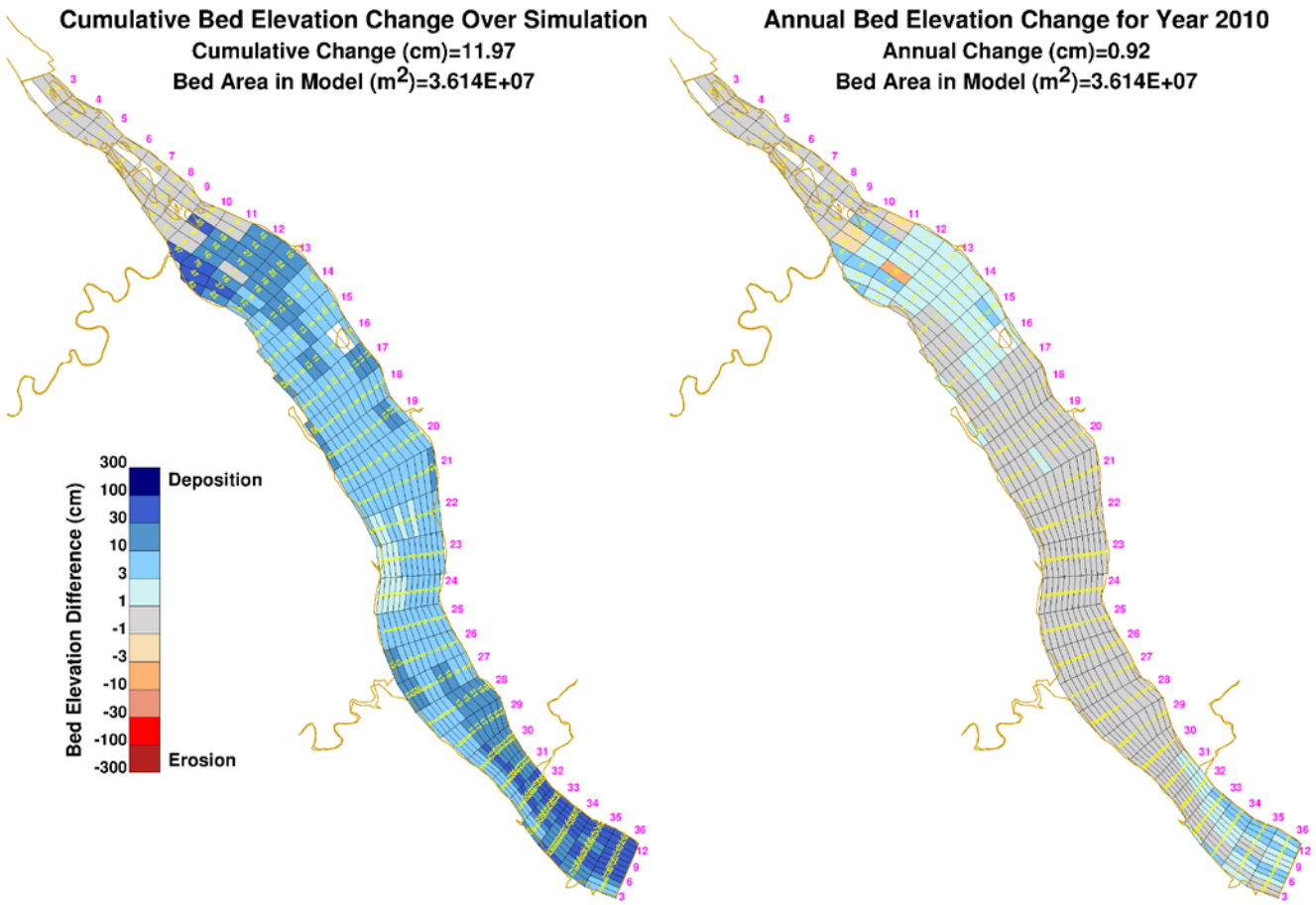


Note: Panel on the Left = simulated cumulative bed elevation change since simulation start; Panel on the Right = simulated annual bed elevation change for year indicated; values shown for all model grid cells; pink numbers along sides of images indicate "row" and "column" references for the model grid.

Figure G-14. Simulated cumulative (since 1997) and annual bed elevation change for Conowingo Pond: 2010 (long-term).

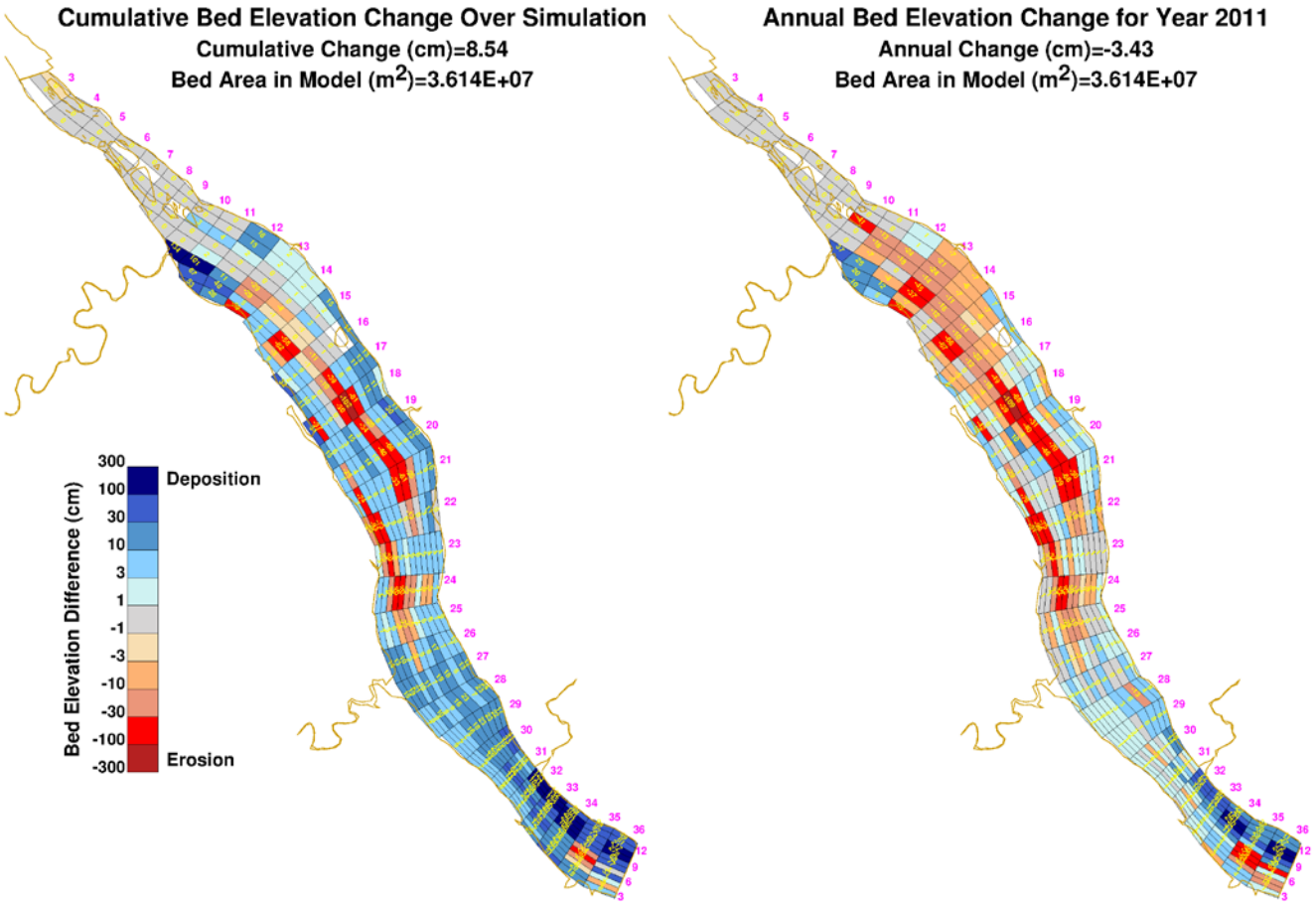


Note: Panel on the Left = simulated cumulative bed elevation change since simulation start; Panel on the Right = simulated annual bed elevation change for year indicated; values shown for all model grid cells; pink numbers along sides of images indicate "row" and "column" references for the model grid.

Figure G-15. Simulated cumulative (since 1997) and annual bed elevation change for Conowingo Pond: 2011 (long-term).

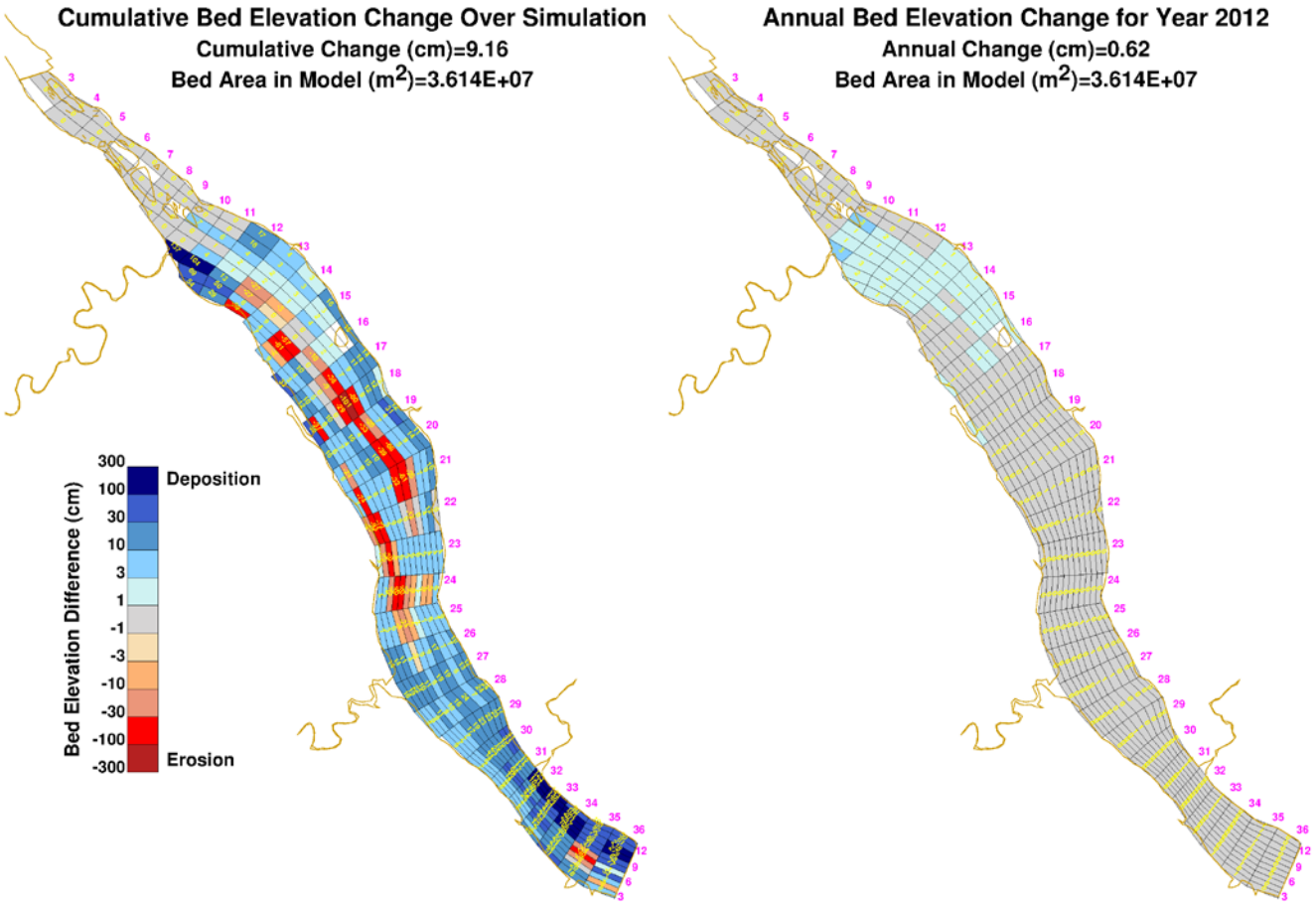


Note: Panel on the Left = simulated cumulative bed elevation change since simulation start; Panel on the Right = simulated annual bed elevation change for year indicated; values shown for all model grid cells; pink numbers along sides of images indicate "row" and "column" references for the model grid.

Figure G-16. Simulated cumulative (since 1997) and annual bed elevation change for Conowingo Pond: 2012 (long-term).

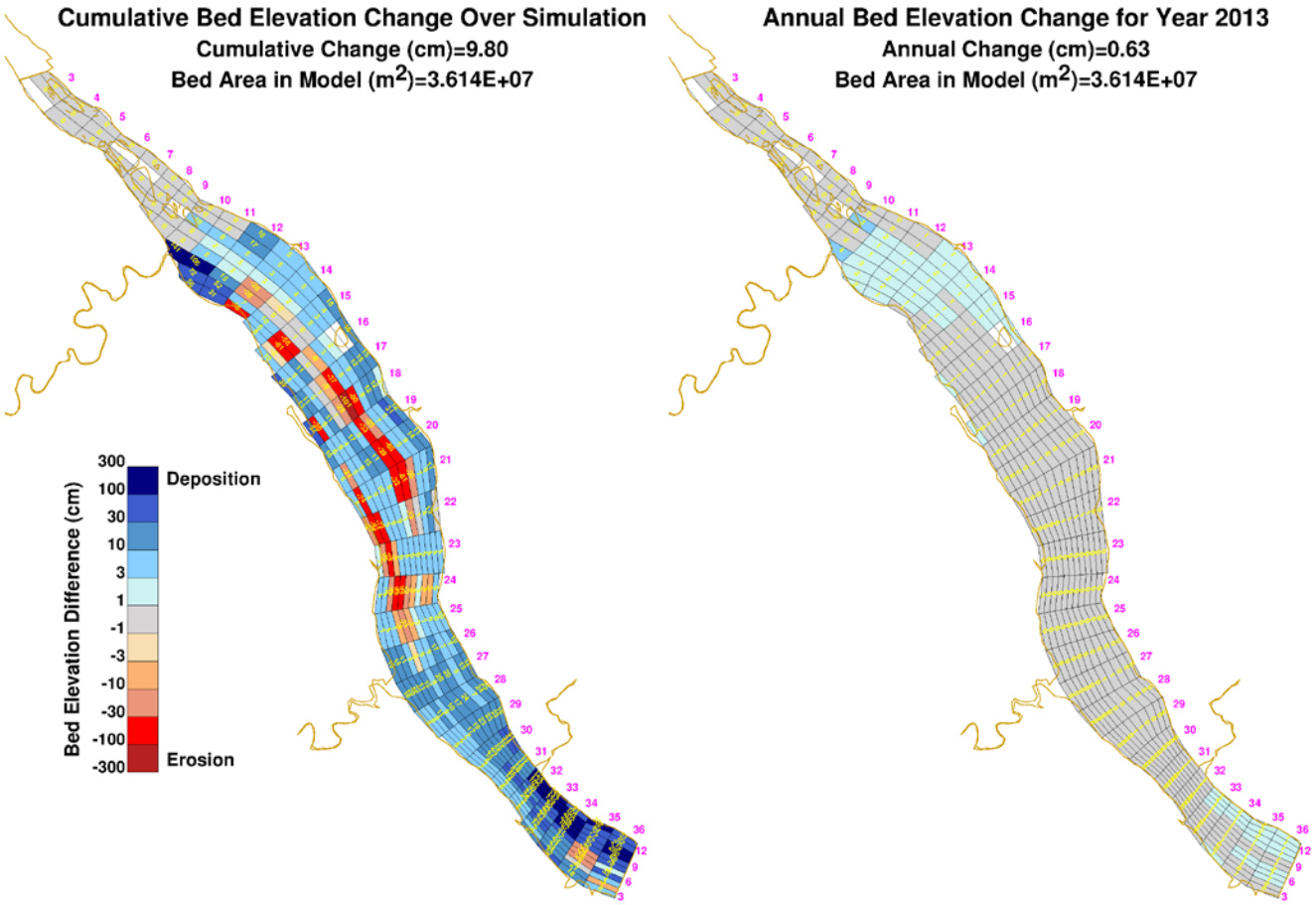


Note: Panel on the Left = simulated cumulative bed elevation change since simulation start; Panel on the Right = simulated annual bed elevation change for year indicated; values shown for all model grid cells; pink numbers along sides of images indicate "row" and "column" references for the model grid.

Figure G-17. Simulated cumulative (since 1997) and annual bed elevation change for Conowingo Pond: 2013 (long-term).

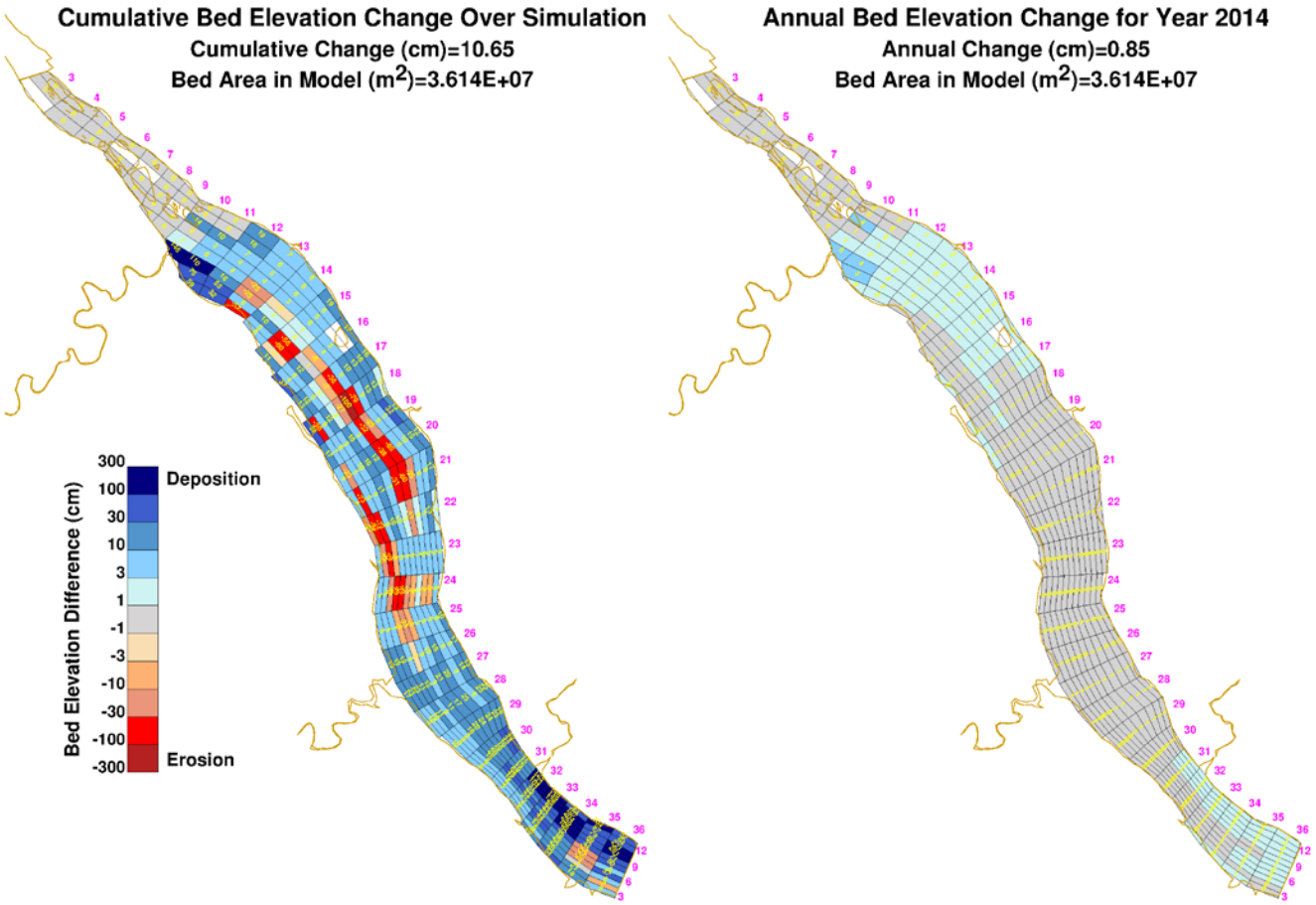


Note: Panel on the Left = simulated cumulative bed elevation change since simulation start; Panel on the Right = simulated annual bed elevation change for year indicated; values shown for all model grid cells; pink numbers along sides of images indicate "row" and "column" references for the model grid.

Figure G-18. Simulated cumulative (since 1997) and annual bed elevation change for Conowingo Pond: 2014 (long-term).

# APPENDIX H. SIMULATED SEDIMENT BED ELEVATION CHANGES (SHORT-TERM): 2008-2014

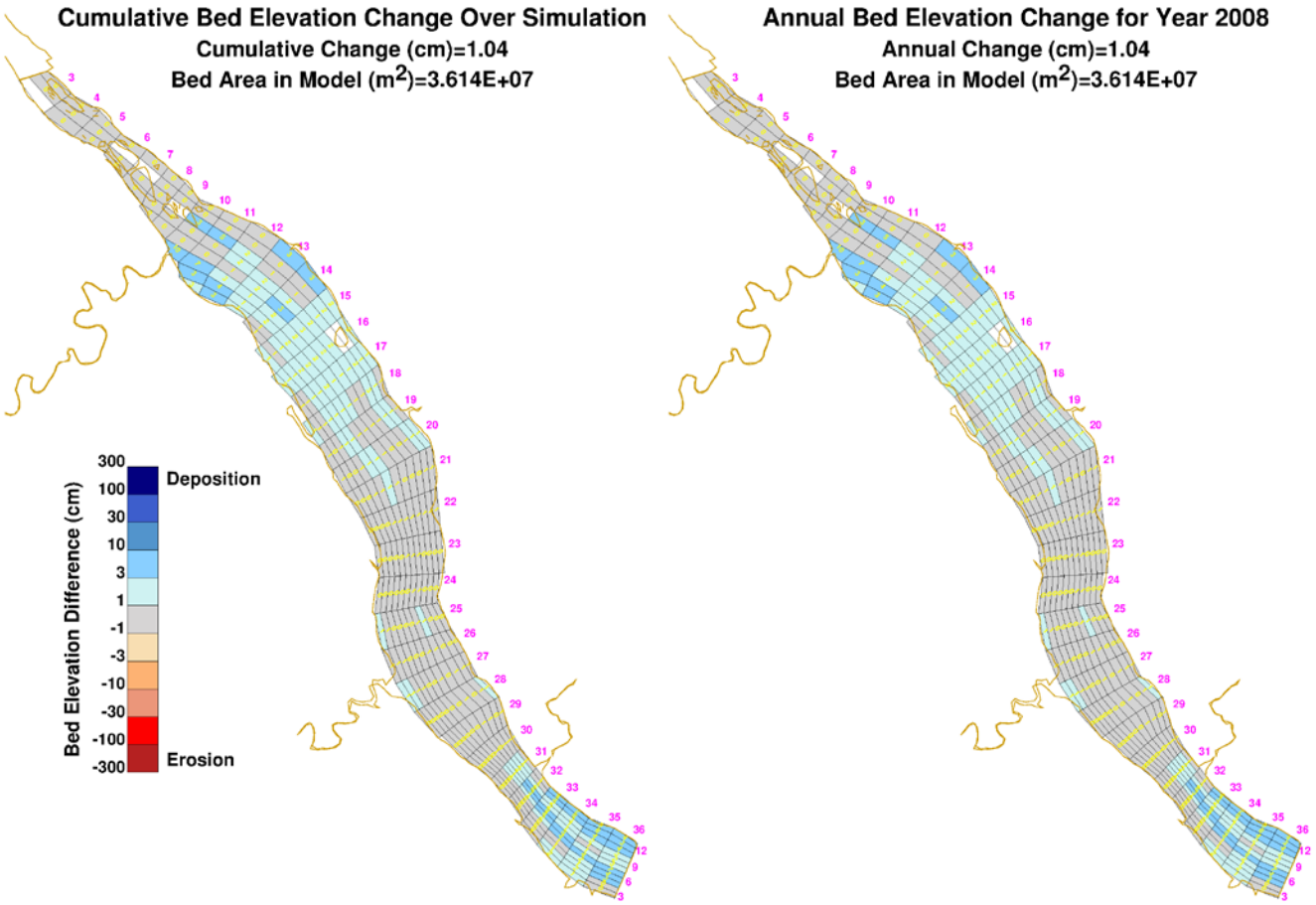


Note: Panel on the Left = simulated cumulative bed elevation change since simulation start; Panel on the Right = simulated annual bed elevation change for year indicated; values shown for all model grid cells; pink numbers along sides of images indicate "row" and "column" references for the model grid.

Figure H-1. Simulated cumulative (since 2008) and annual bed elevation change for Conowingo Pond: 2008 (short-term).

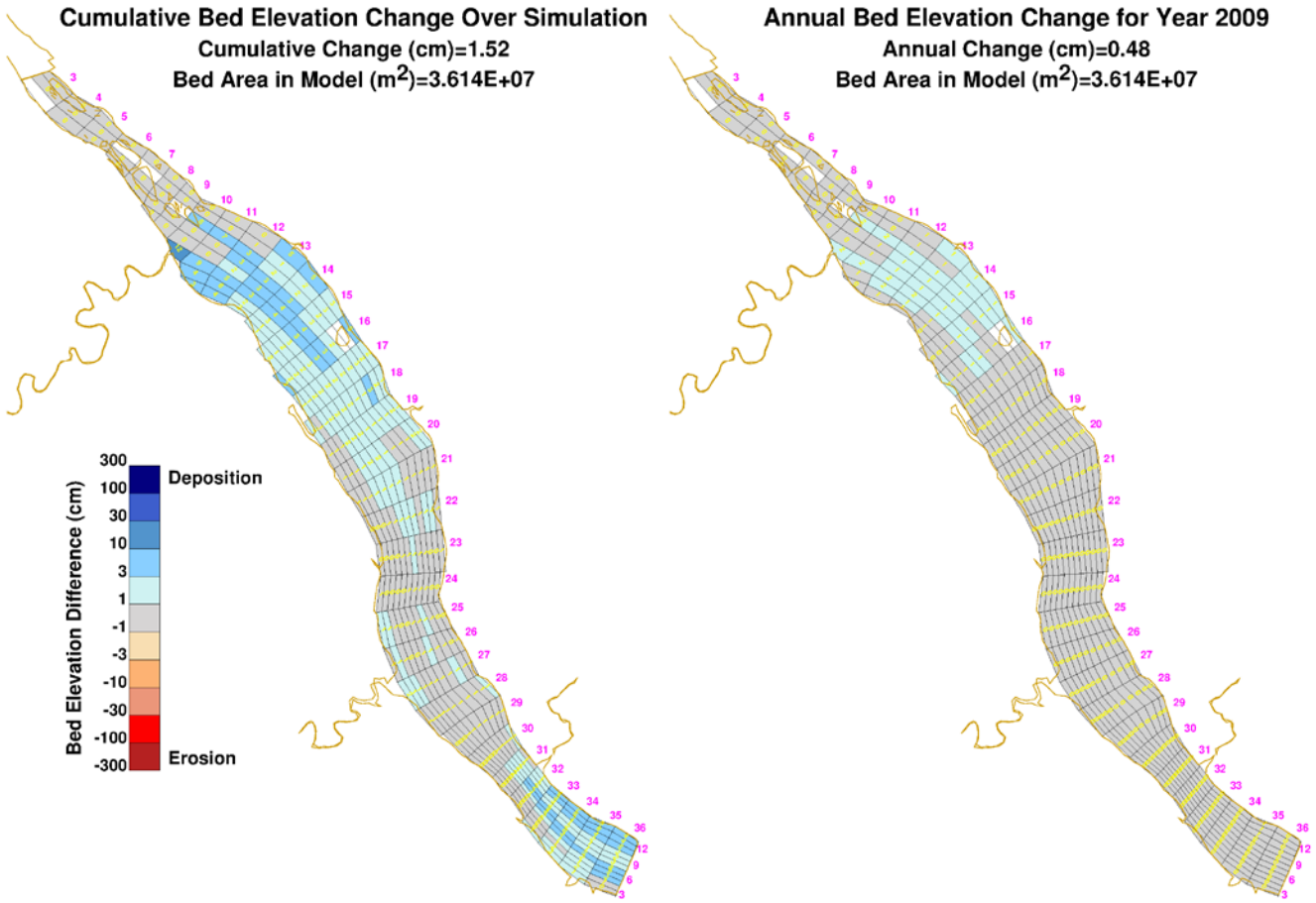


Note: Panel on the Left = simulated cumulative bed elevation change since simulation start; Panel on the Right = simulated annual bed elevation change for year indicated; values shown for all model grid cells; pink numbers along sides of images indicate "row" and "column" references for the model grid.

Figure H-2. Simulated cumulative (since 2008) and annual bed elevation change for Conowingo Pond: 2009 (short-term).

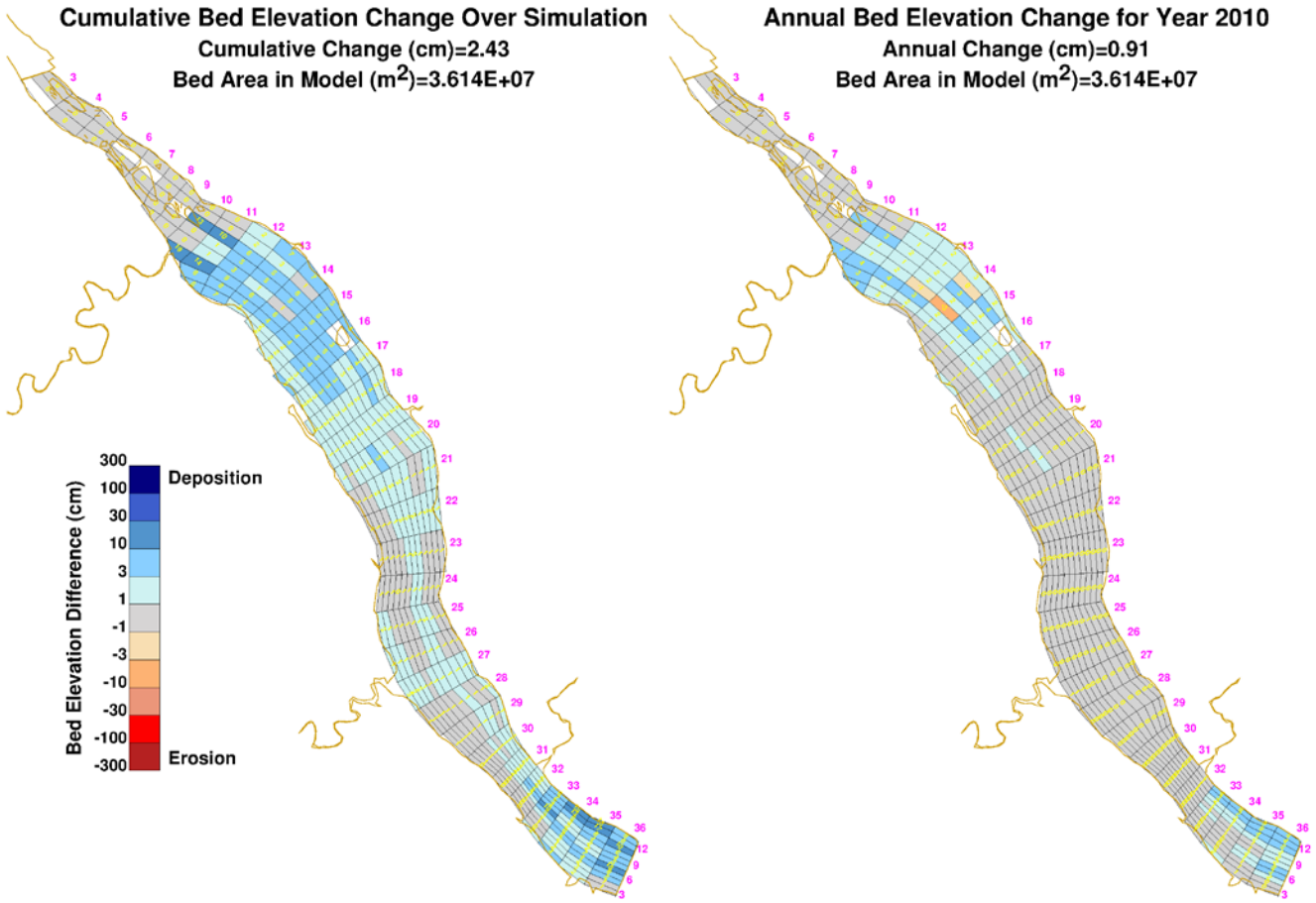


Note: Panel on the Left = simulated cumulative bed elevation change since simulation start; Panel on the Right = simulated annual bed elevation change for year indicated; values shown for all model grid cells; pink numbers along sides of images indicate "row" and "column" references for the model grid.

Figure H-3. Simulated cumulative (since 2008) and annual bed elevation change for Conowingo Pond: 2010 (short-term).

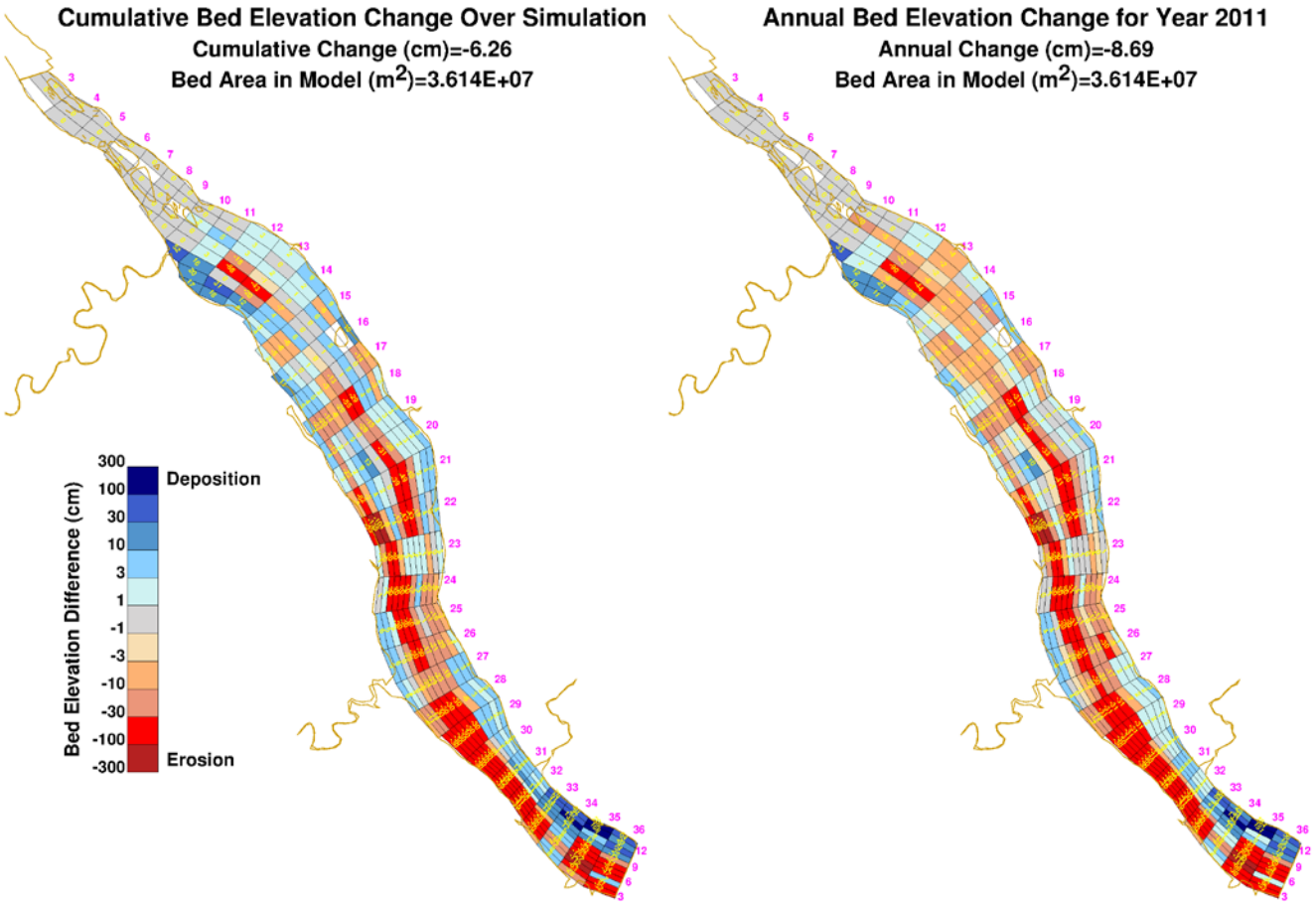


Note: Panel on the Left = simulated cumulative bed elevation change since simulation start; Panel on the Right = simulated annual bed elevation change for year indicated; values shown for all model grid cells; pink numbers along sides of images indicate "row" and "column" references for the model grid.

Figure H-4. Simulated cumulative (since 2008) and annual bed elevation change for Conowingo Pond: 2011 (short-term).

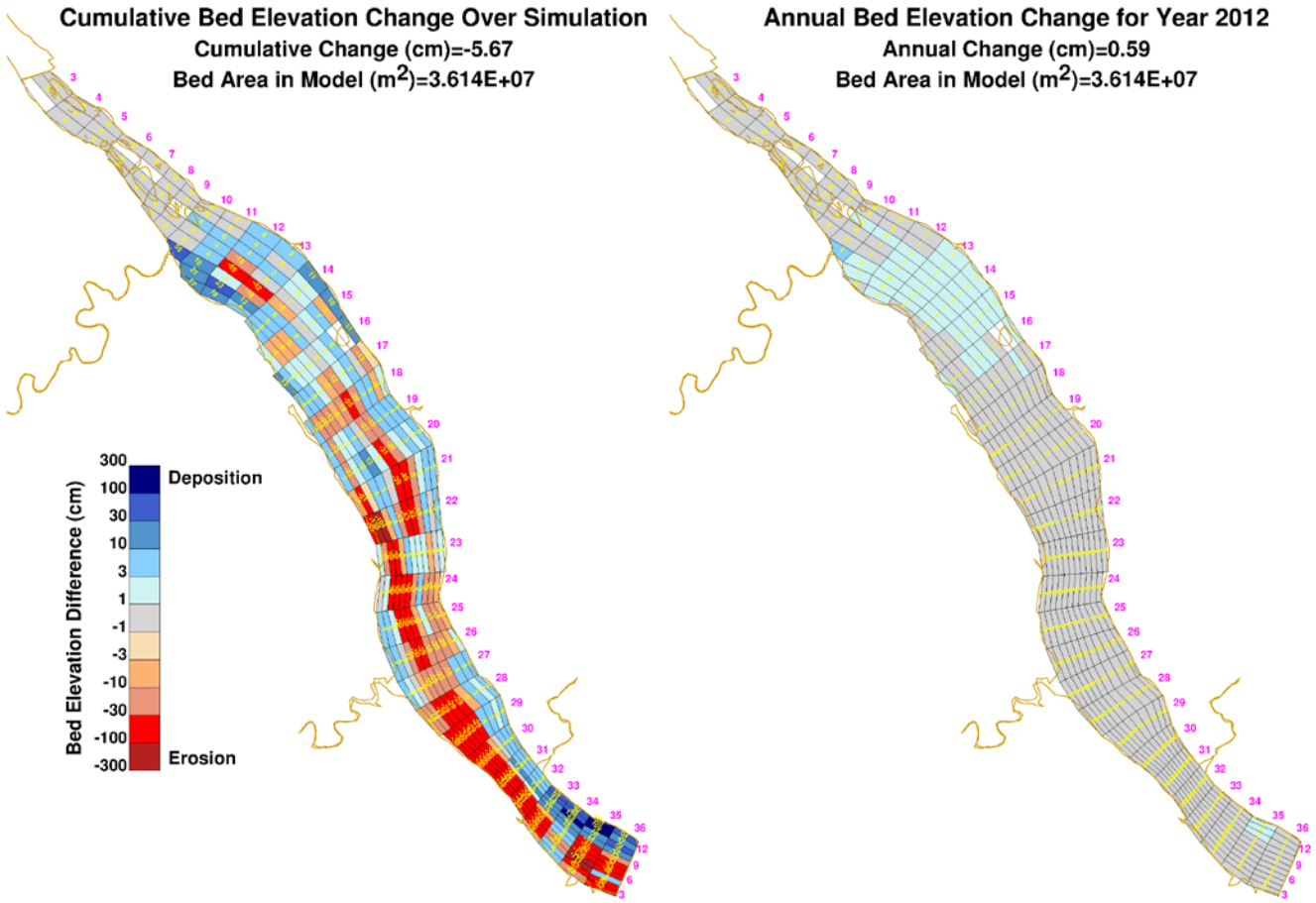


Note: Panel on the Left = simulated cumulative bed elevation change since simulation start; Panel on the Right = simulated annual bed elevation change for year indicated; values shown for all model grid cells; pink numbers along sides of images indicate "row" and "column" references for the model grid.

Figure H-5. Simulated cumulative (since 2008) and annual bed elevation change for Conowingo Pond: 2012 (short-term).

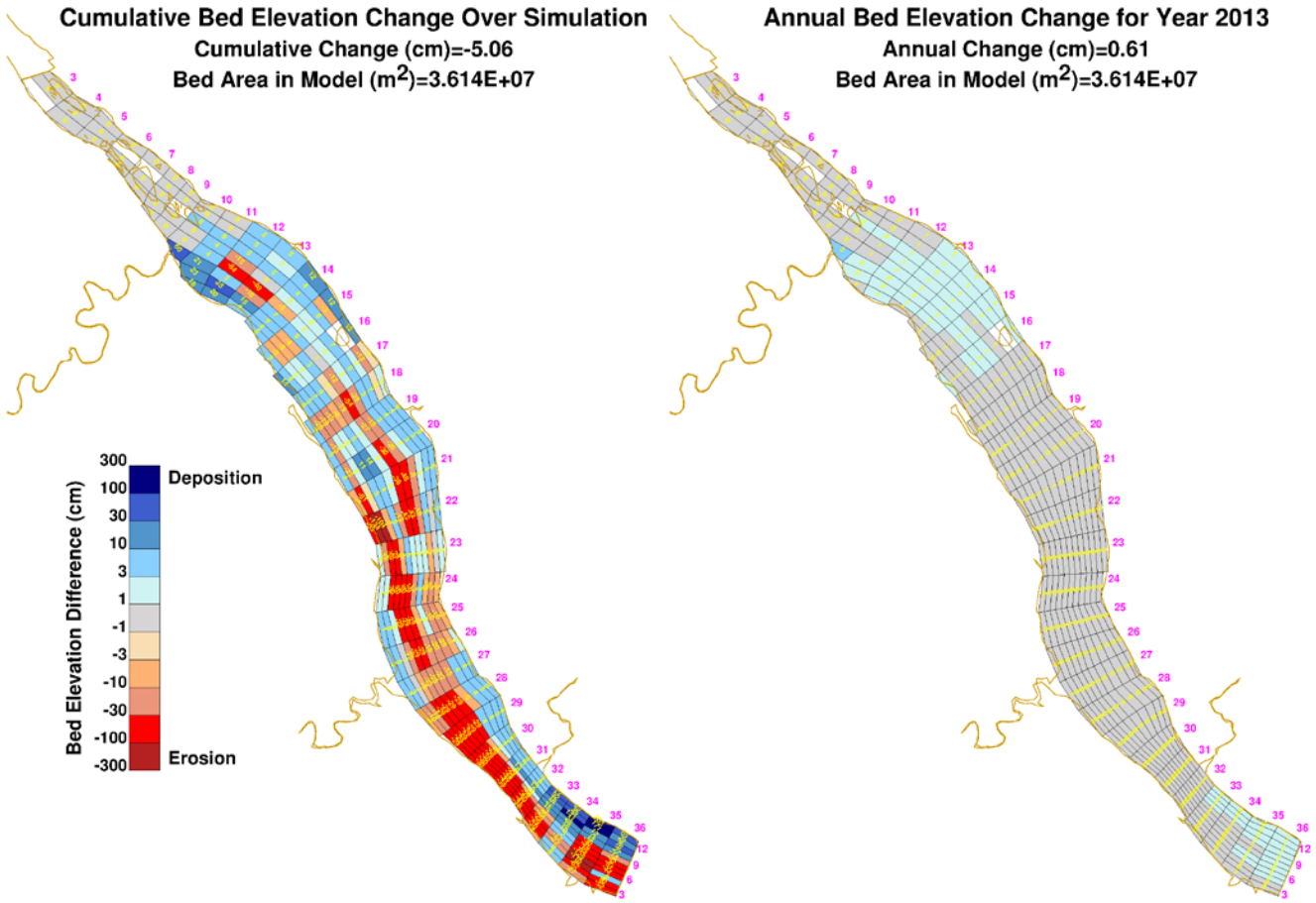


Note: Panel on the Left = simulated cumulative bed elevation change since simulation start; Panel on the Right = simulated annual bed elevation change for year indicated; values shown for all model grid cells; pink numbers along sides of images indicate "row" and "column" references for the model grid.

Figure H-6. Simulated cumulative (since 2008) and annual bed elevation change for Conowingo Pond: 2013 (short-term).

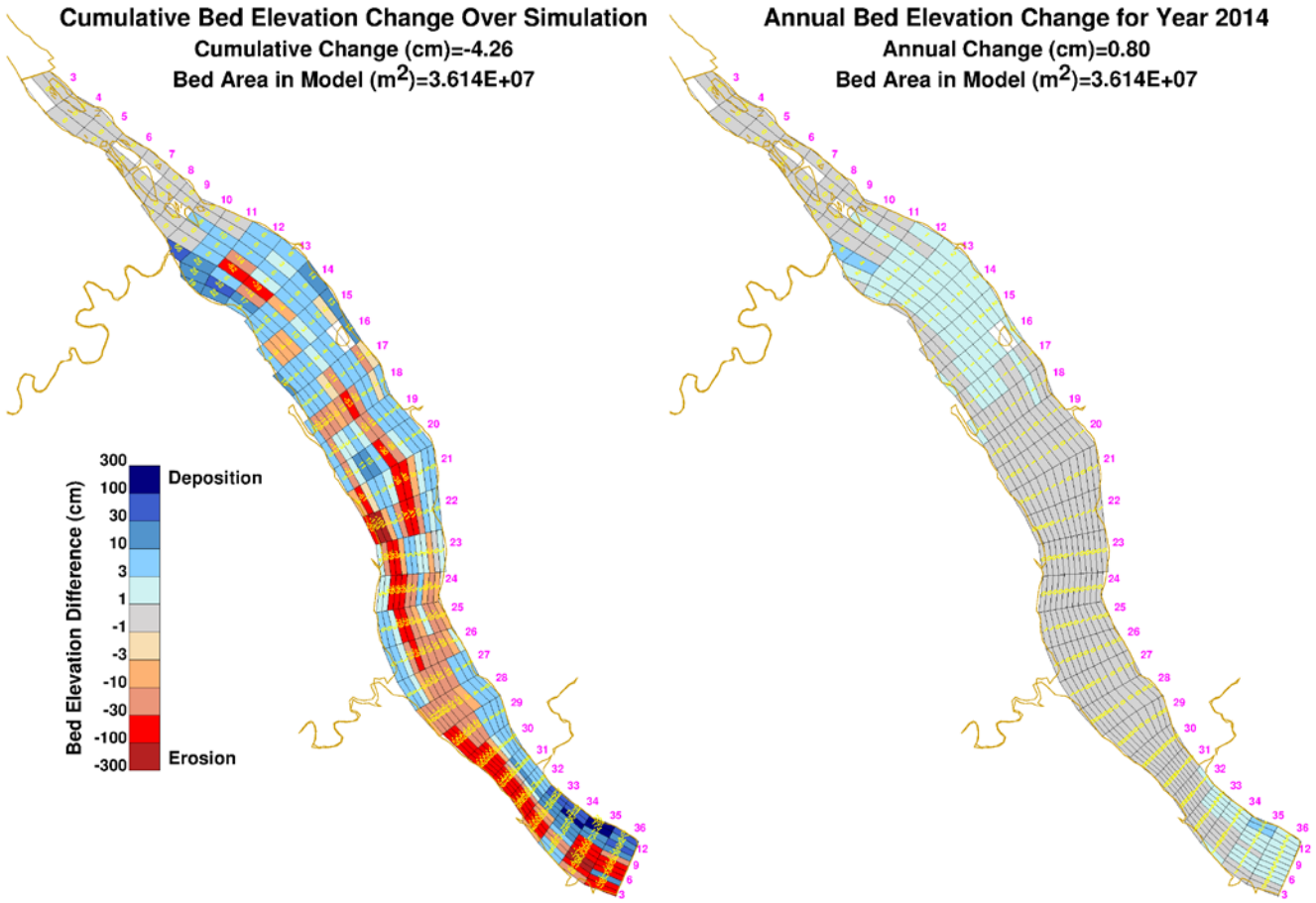


Note: Panel on the Left = simulated cumulative bed elevation change since simulation start; Panel on the Right = simulated annual bed elevation change for year indicated; values shown for all model grid cells; pink numbers along sides of images indicate "row" and "column" references for the model grid.

Figure H-7. Simulated cumulative (since 2008) and annual bed elevation change for Conowingo Pond: 2014 (short-term).

# APPENDIX I. SIMULATED SEDIMENT BED ELEVATION CHANGES (LONG-TERM): 1996-2015

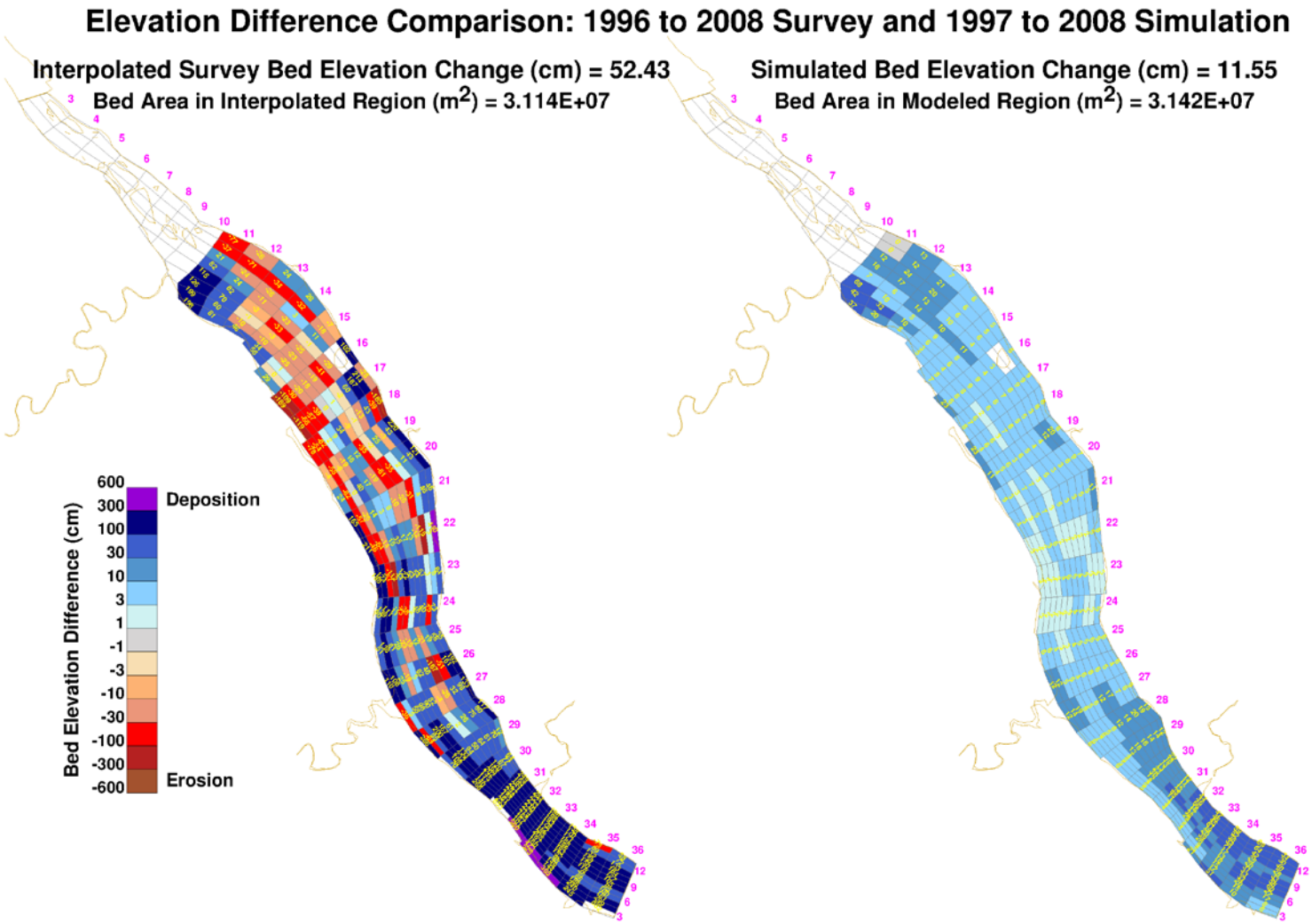


Figure I-1. Comparison of bed elevation changes estimated from differences between interpolated bathymetric surveys and simulated cumulative bed elevation change for Conowingo Pond: 1996-2008 (long-term).

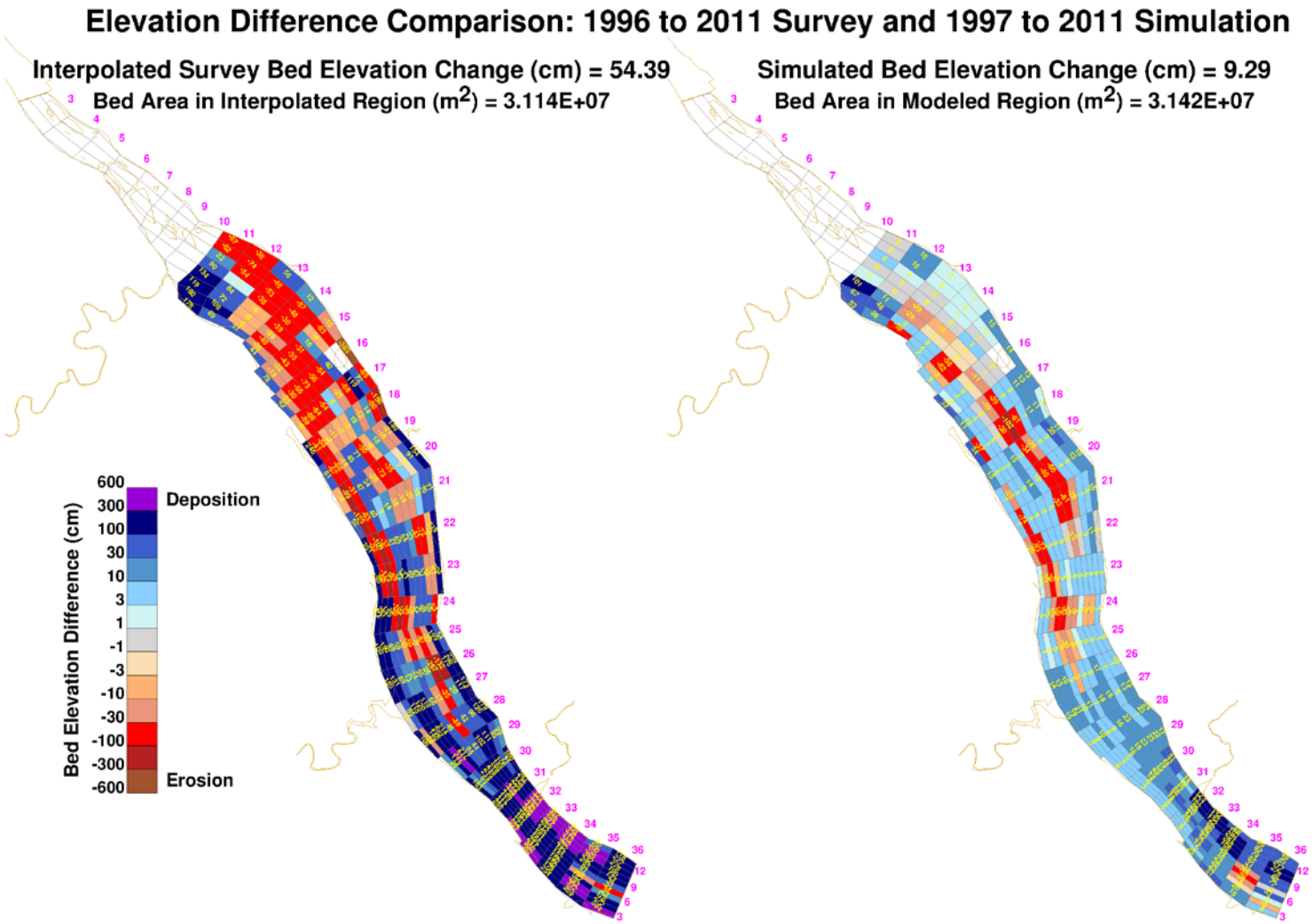


Figure I-2. Comparison of bed elevation changes estimated from differences between interpolated bathymetric surveys and simulated cumulative bed elevation change for Conowingo Pond: 1996-2011 (long-term).

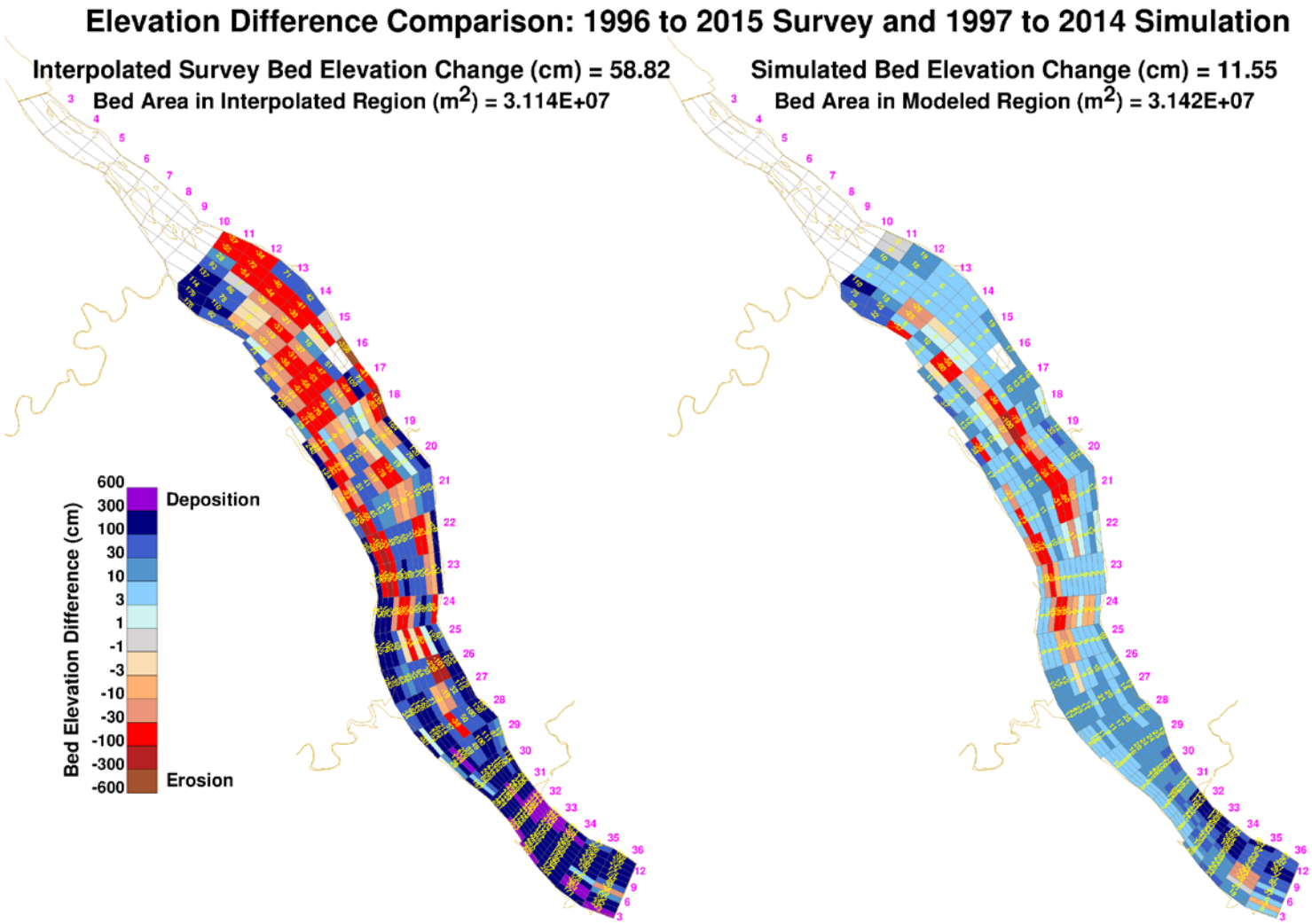


Figure I-3. Comparison of bed elevation changes estimated from differences between interpolated bathymetric surveys and simulated cumulative bed elevation change for Conowingo Pond: 1996-2015 (long-term).

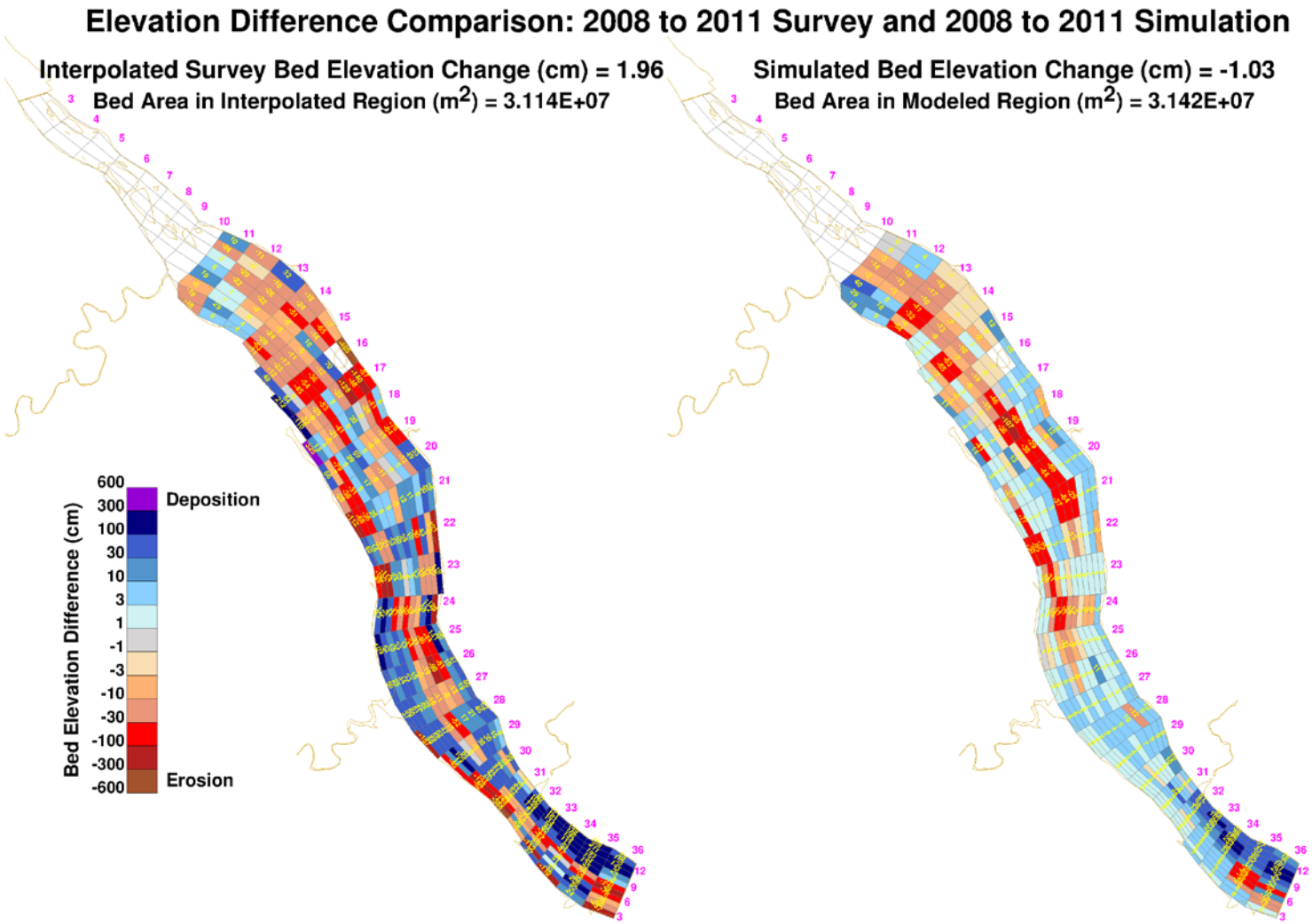


Figure I-4. Comparison of bed elevation changes estimated from differences between interpolated bathymetric surveys and simulated cumulative bed elevation change for Conowingo Pond: 2008-2011 (long-term).

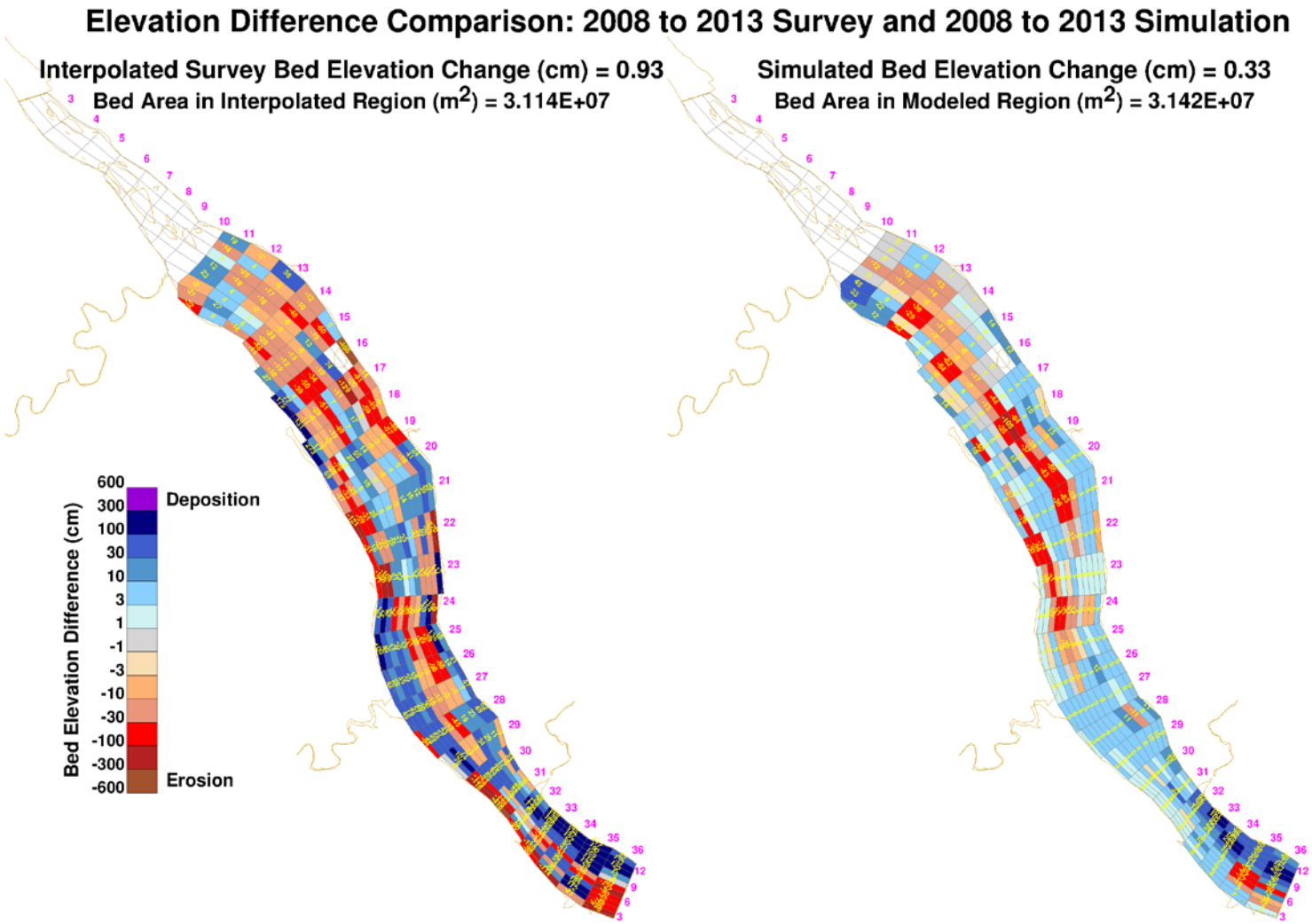


Figure I-5. Comparison of bed elevation changes estimated from differences between interpolated bathymetric surveys and simulated cumulative bed elevation change for Conowingo Pond: 2008-2013 (long-term).

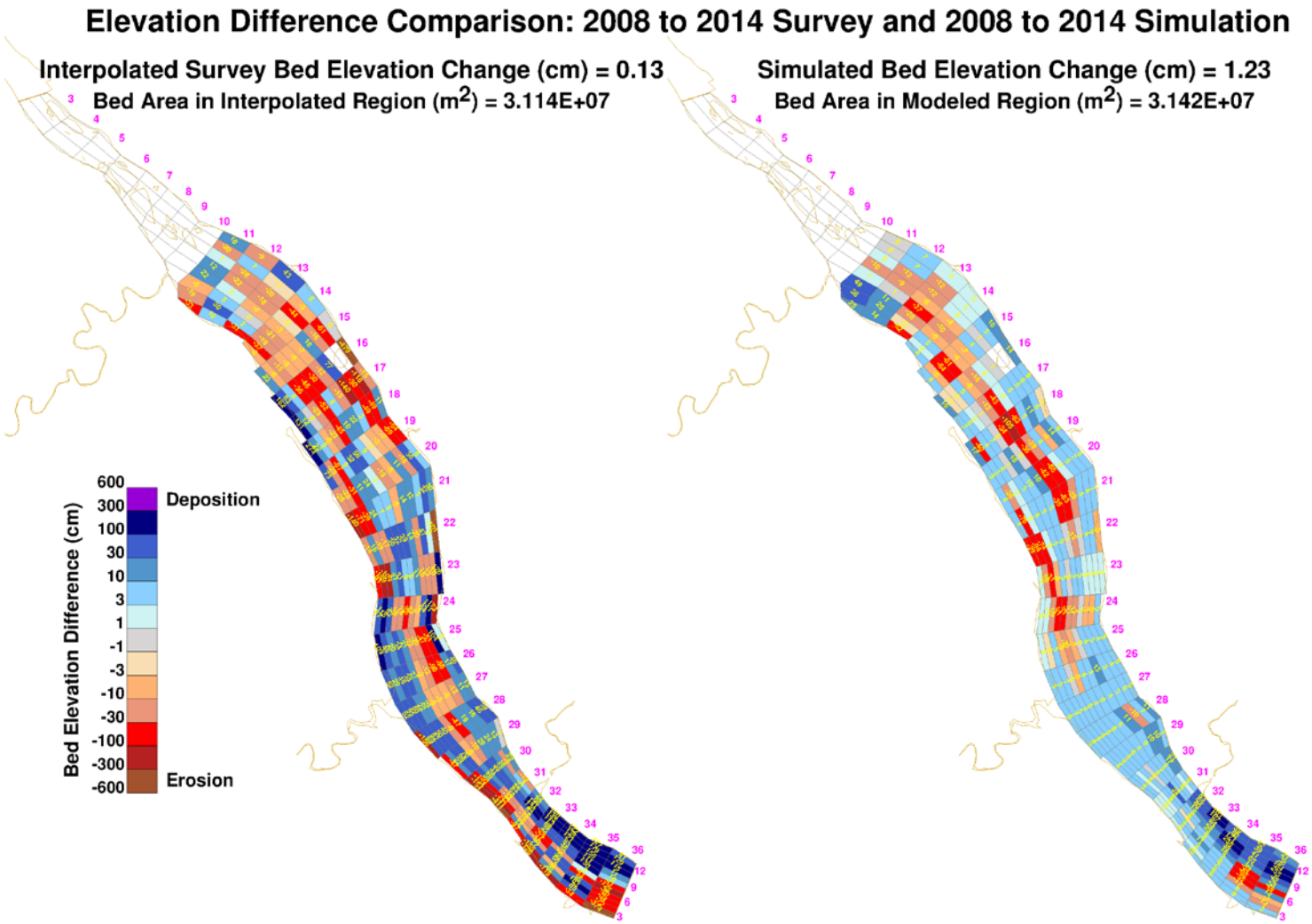


Figure I-6. Comparison of bed elevation changes estimated from differences between interpolated bathymetric surveys and simulated cumulative bed elevation change for Conowingo Pond: 2008-2014 (long-term).

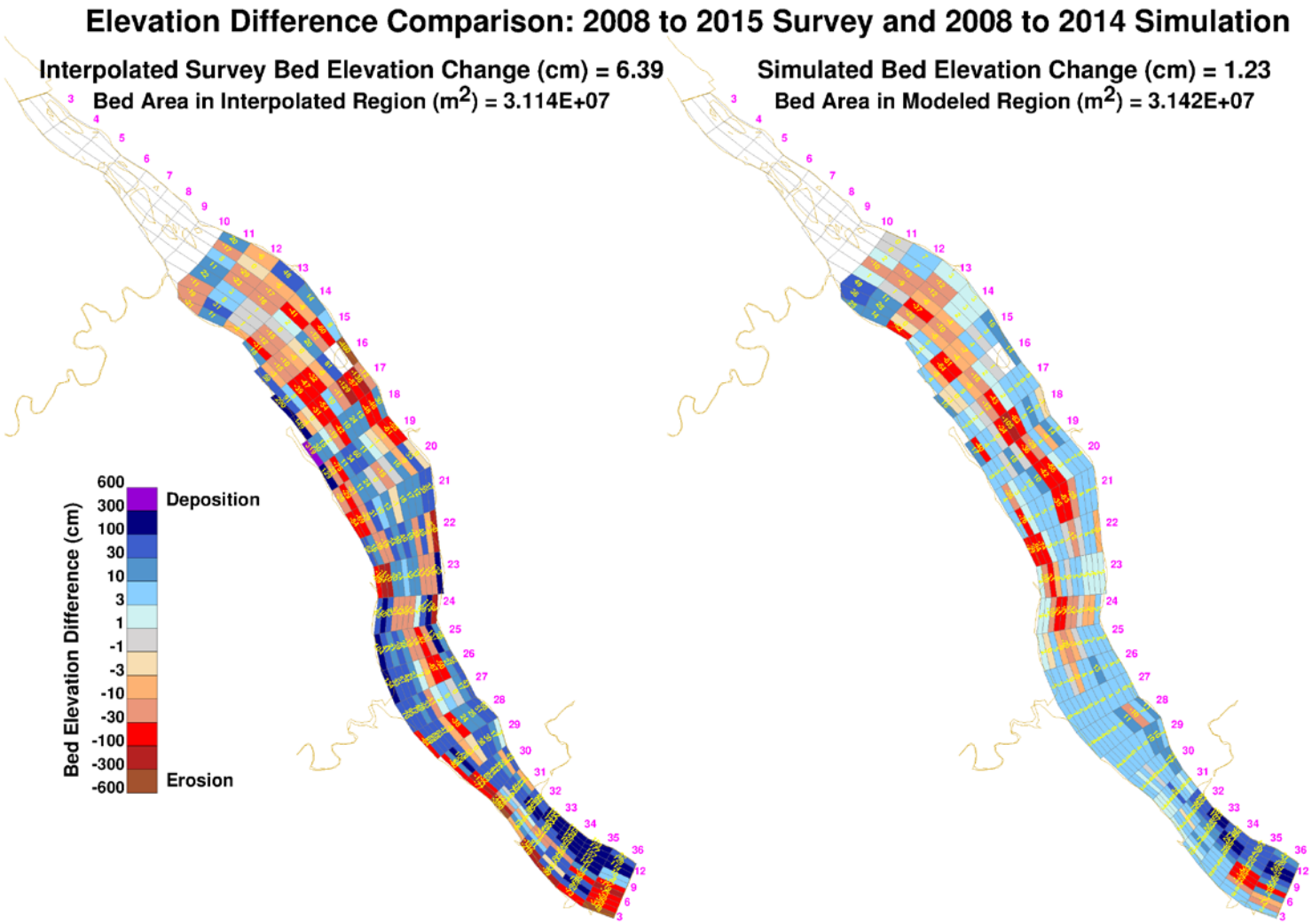


Figure I-7. Comparison of bed elevation changes estimated from differences between interpolated bathymetric surveys and simulated cumulative bed elevation change for Conowingo Pond: 2008-2015 (long-term).

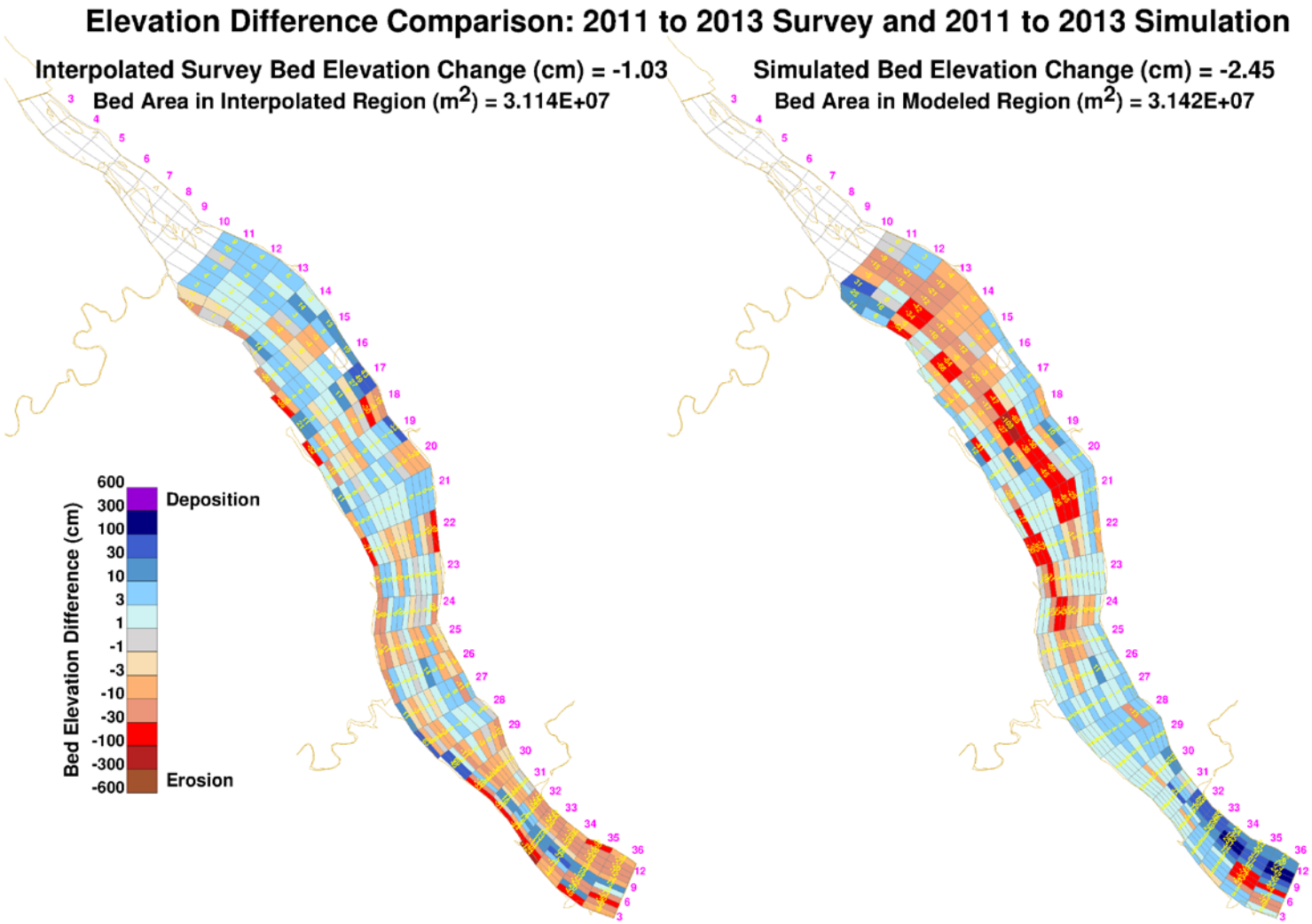


Figure I-8. Comparison of bed elevation changes estimated from differences between interpolated bathymetric surveys and simulated cumulative bed elevation change for Conowingo Pond: 2011-2013 (long-term).

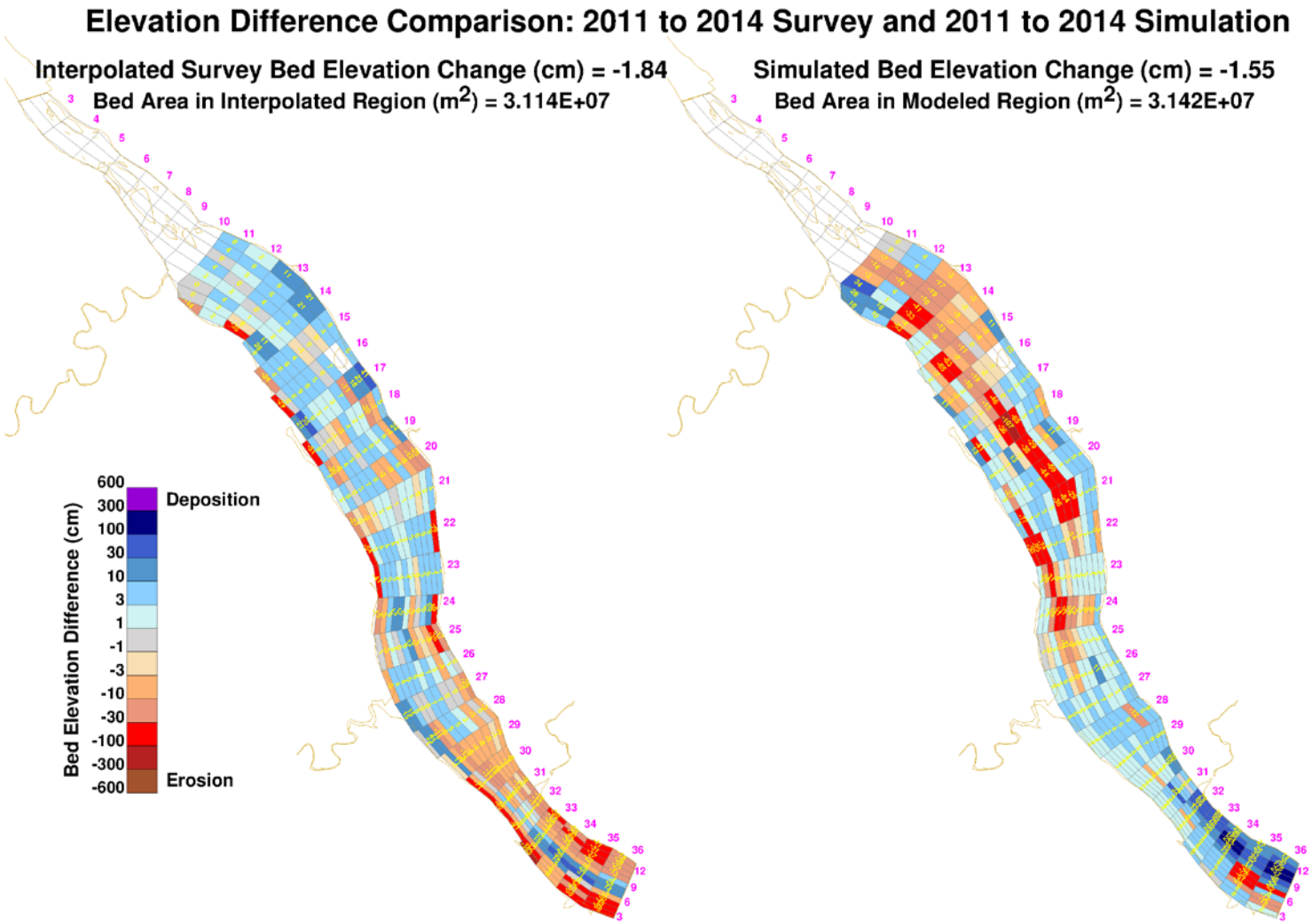


Figure I-9. Comparison of bed elevation changes estimated from differences between interpolated bathymetric surveys and simulated cumulative bed elevation change for Conowingo Pond: 2011-2014 (long-term).

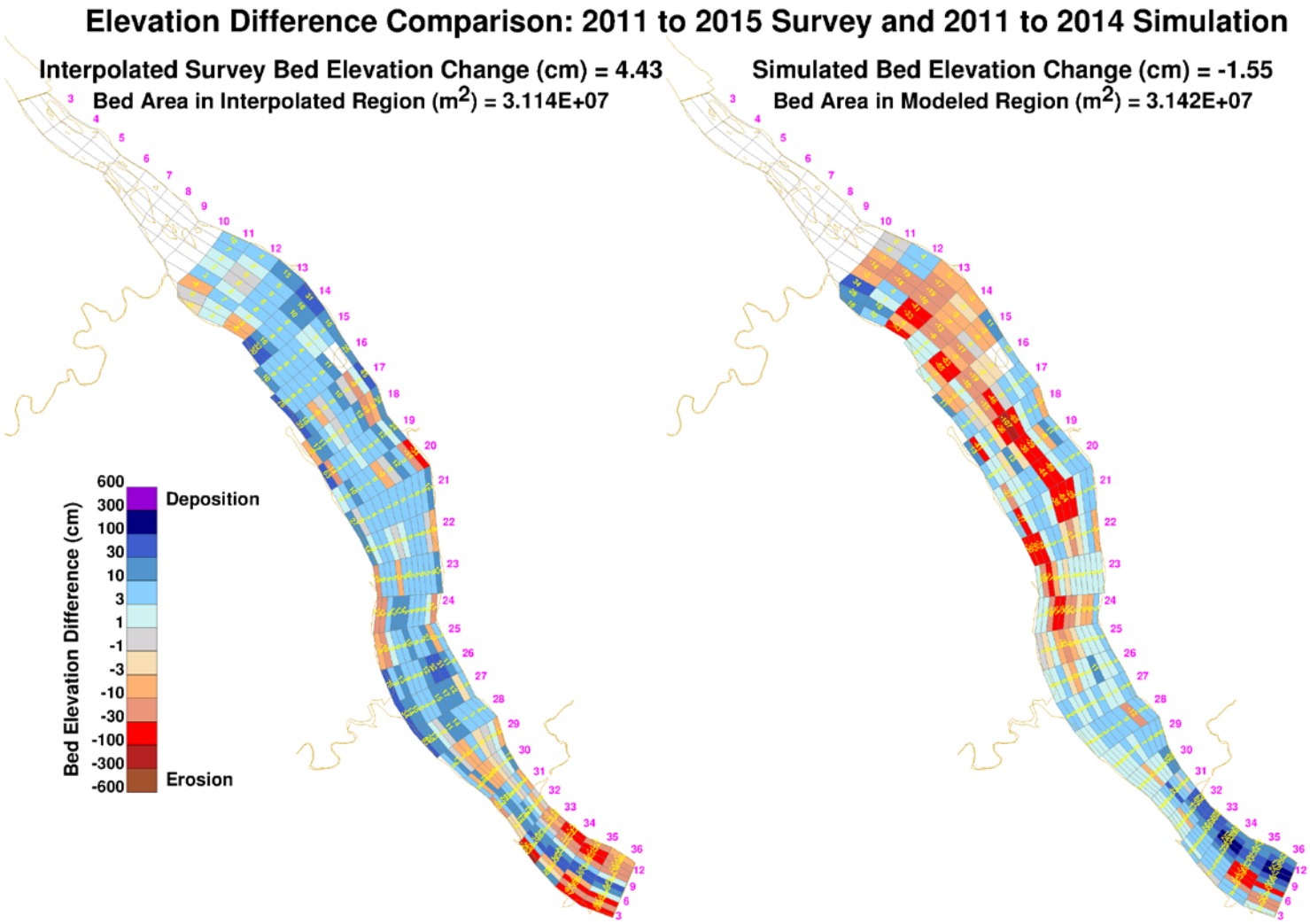


Figure I-10. Comparison of bed elevation changes estimated from differences between interpolated bathymetric surveys and simulated cumulative bed elevation change for Conowingo Pond: 2011-2015 (long-term).

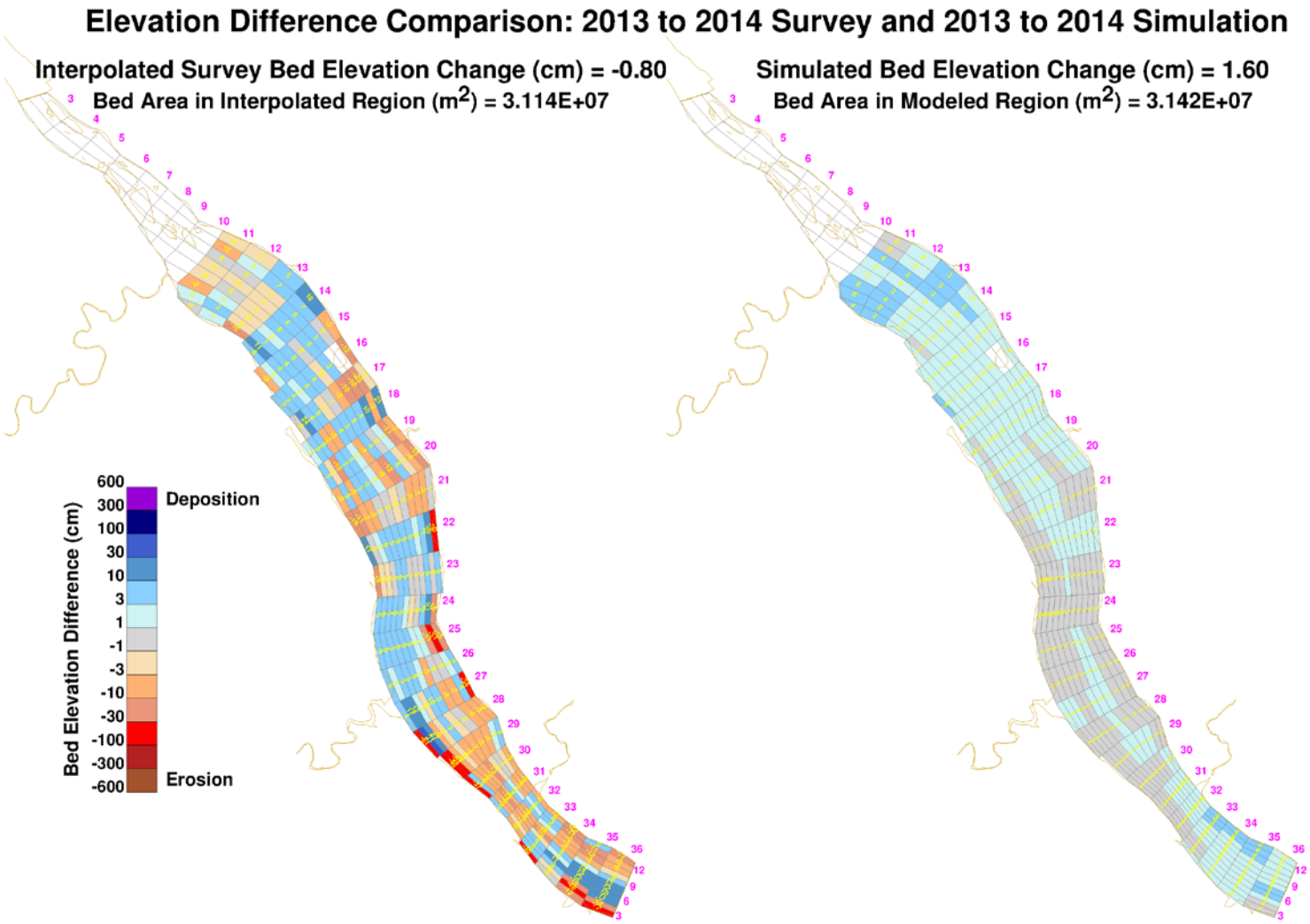


Figure I-11. Comparison of bed elevation changes estimated from differences between interpolated bathymetric surveys and simulated cumulative bed elevation change for Conowingo Pond: 2013-2014 (long-term).

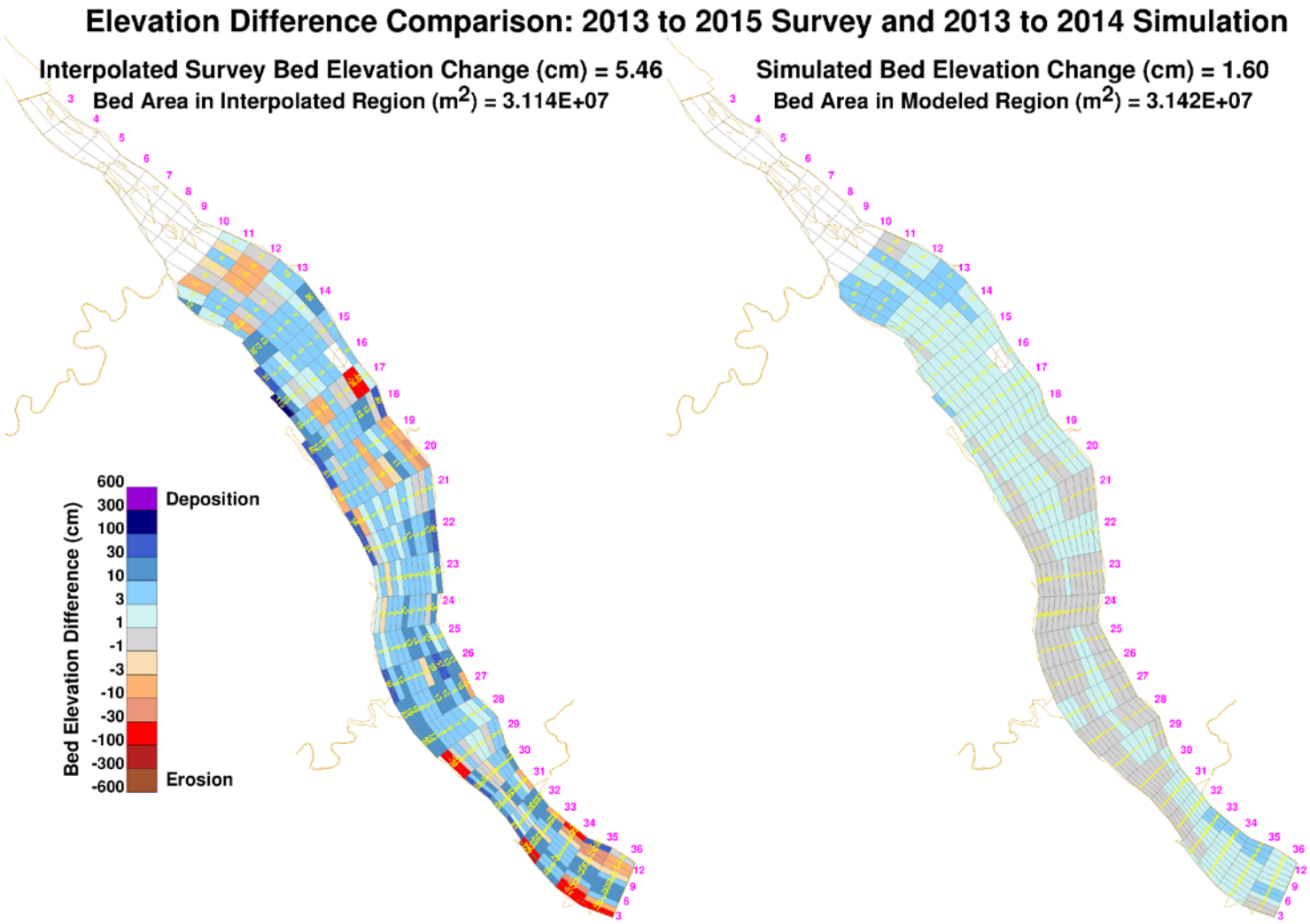


Figure I-12. Comparison of bed elevation changes estimated from differences between interpolated bathymetric surveys and simulated cumulative bed elevation change for Conowingo Pond: 2013-2015 (long-term).

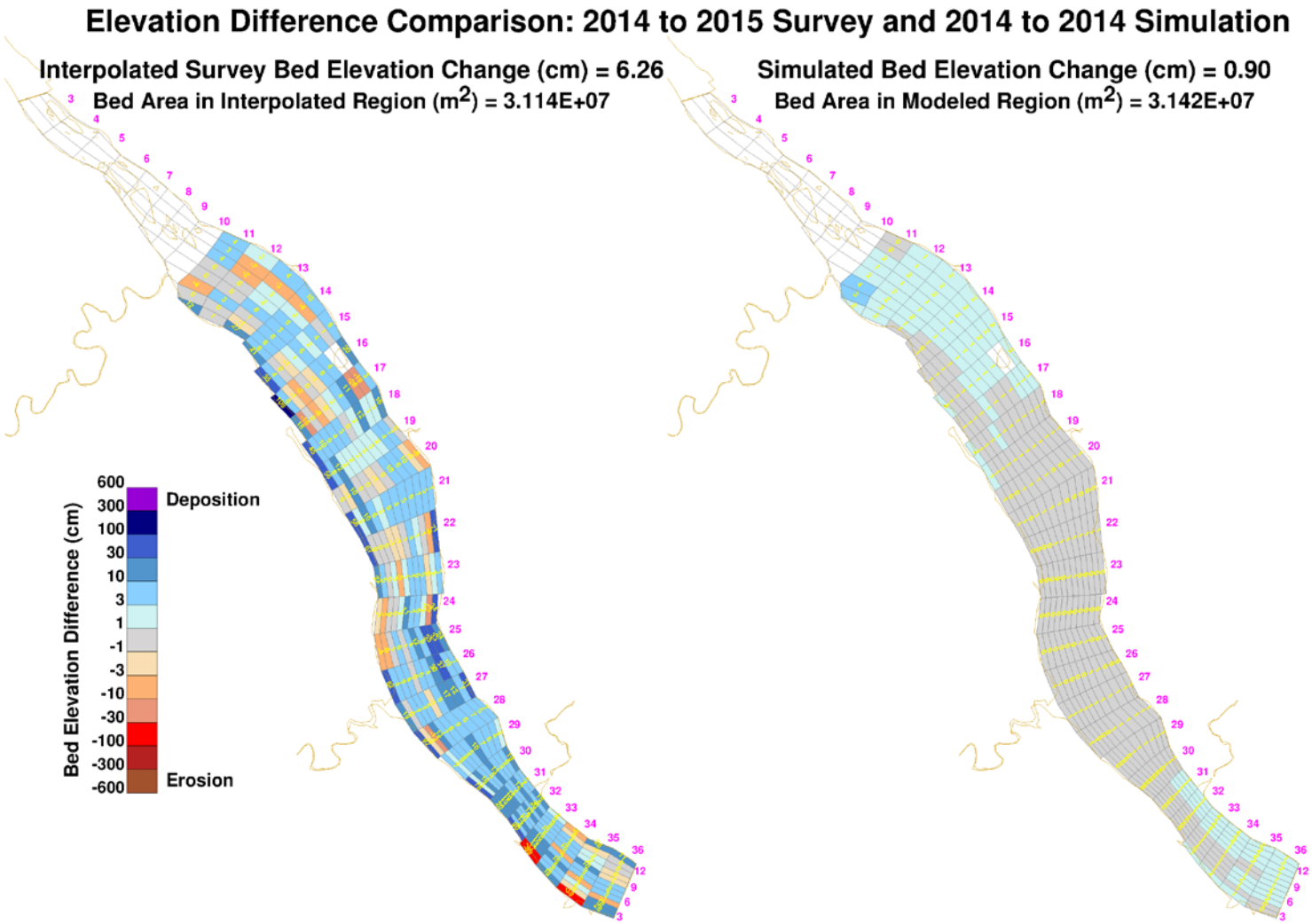


Figure I-13. Comparison of bed elevation changes estimated from differences between interpolated bathymetric surveys and simulated cumulative bed elevation change for Conowingo Pond: 2014-2015 (long-term).

# APPENDIX J. SIMULATED SEDIMENT BED ELEVATION CHANGES (SHORT-TERM): 2008-2015

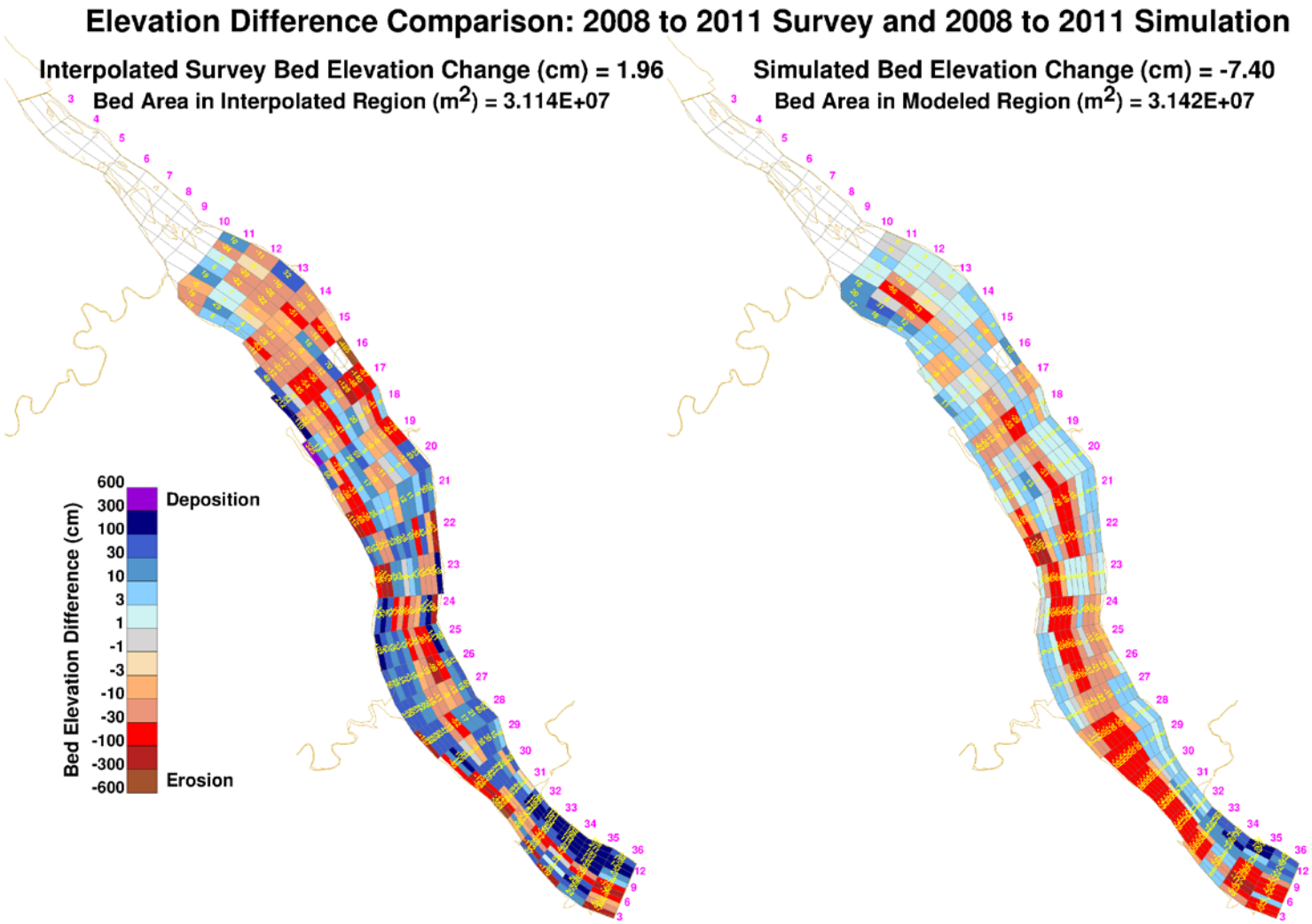


Figure J-1. Comparison of bed elevation changes estimated from differences between interpolated bathymetric surveys and simulated cumulative bed elevation change for Conowingo Pond: 2008-2011 (short-term).

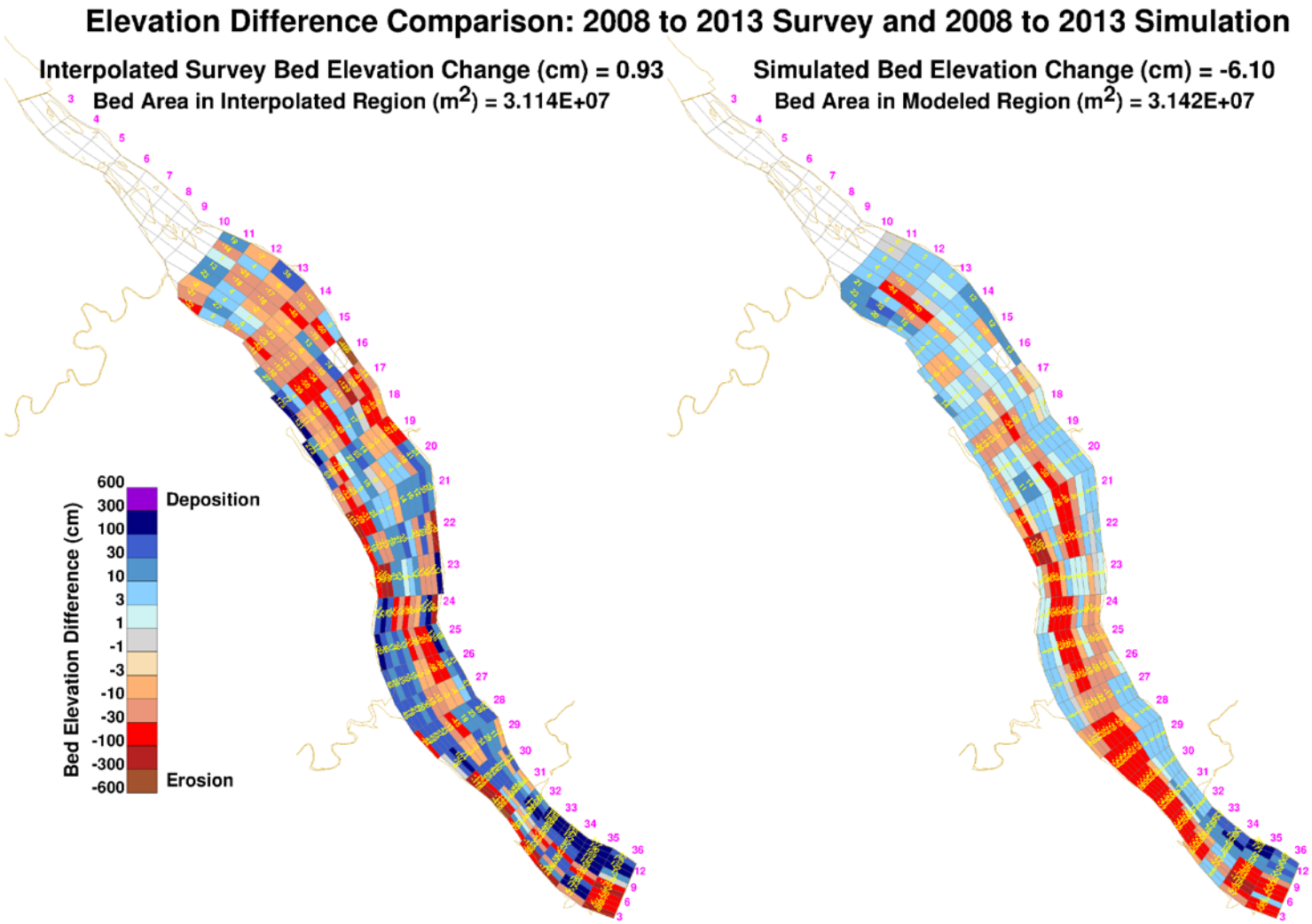


Figure J-2. Comparison of bed elevation changes estimated from differences between interpolated bathymetric surveys and simulated cumulative bed elevation change for Conowingo Pond: 2008-2013 (short-term).

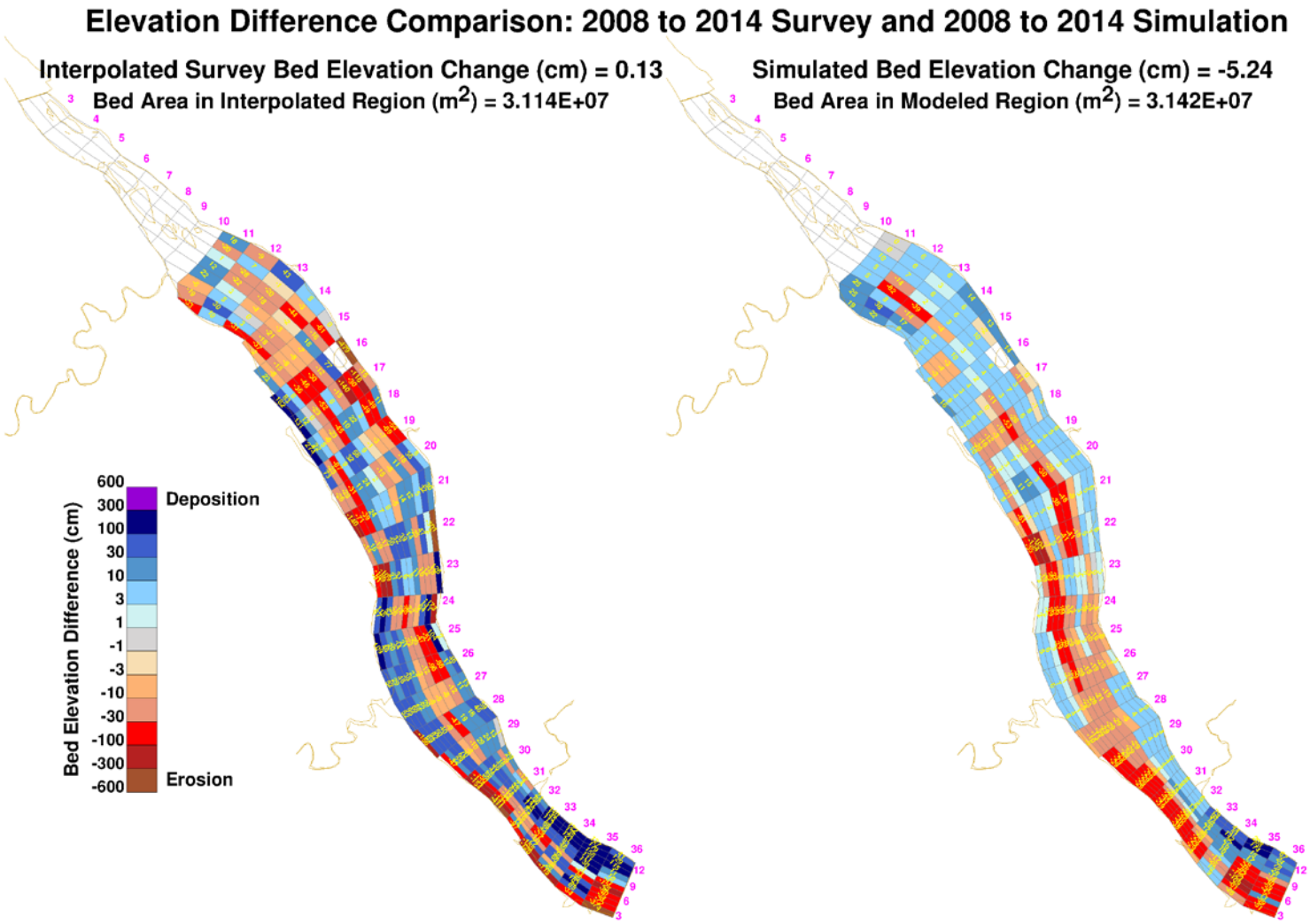


Figure J-3. Comparison of bed elevation changes estimated from differences between interpolated bathymetric surveys and simulated cumulative bed elevation change for Conowingo Pond: 2008-2014 (short-term).

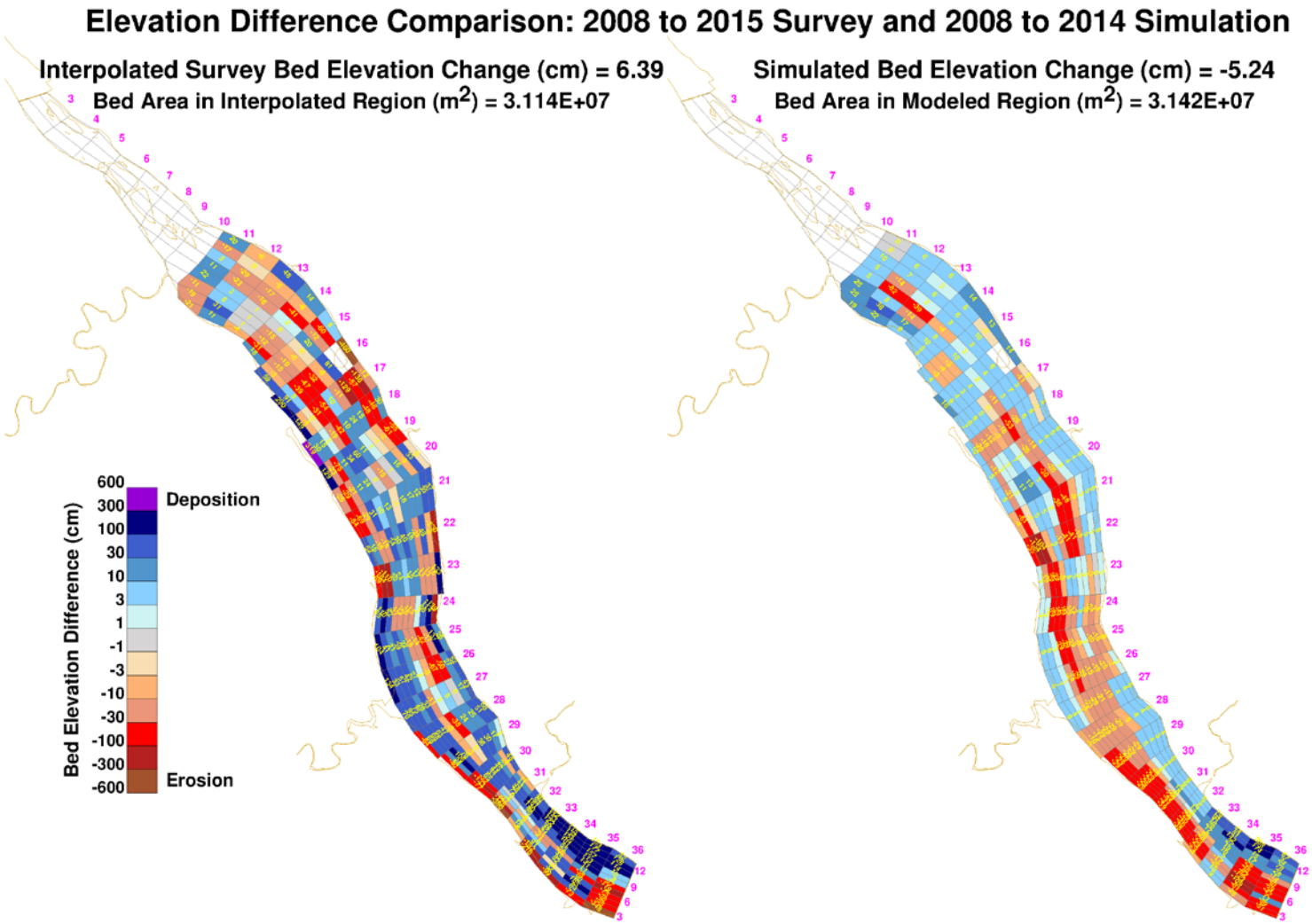


Figure J-4. Comparison of bed elevation changes estimated from differences between interpolated bathymetric surveys and simulated cumulative bed elevation change for Conowingo Pond: 2008-2015 (short-term).

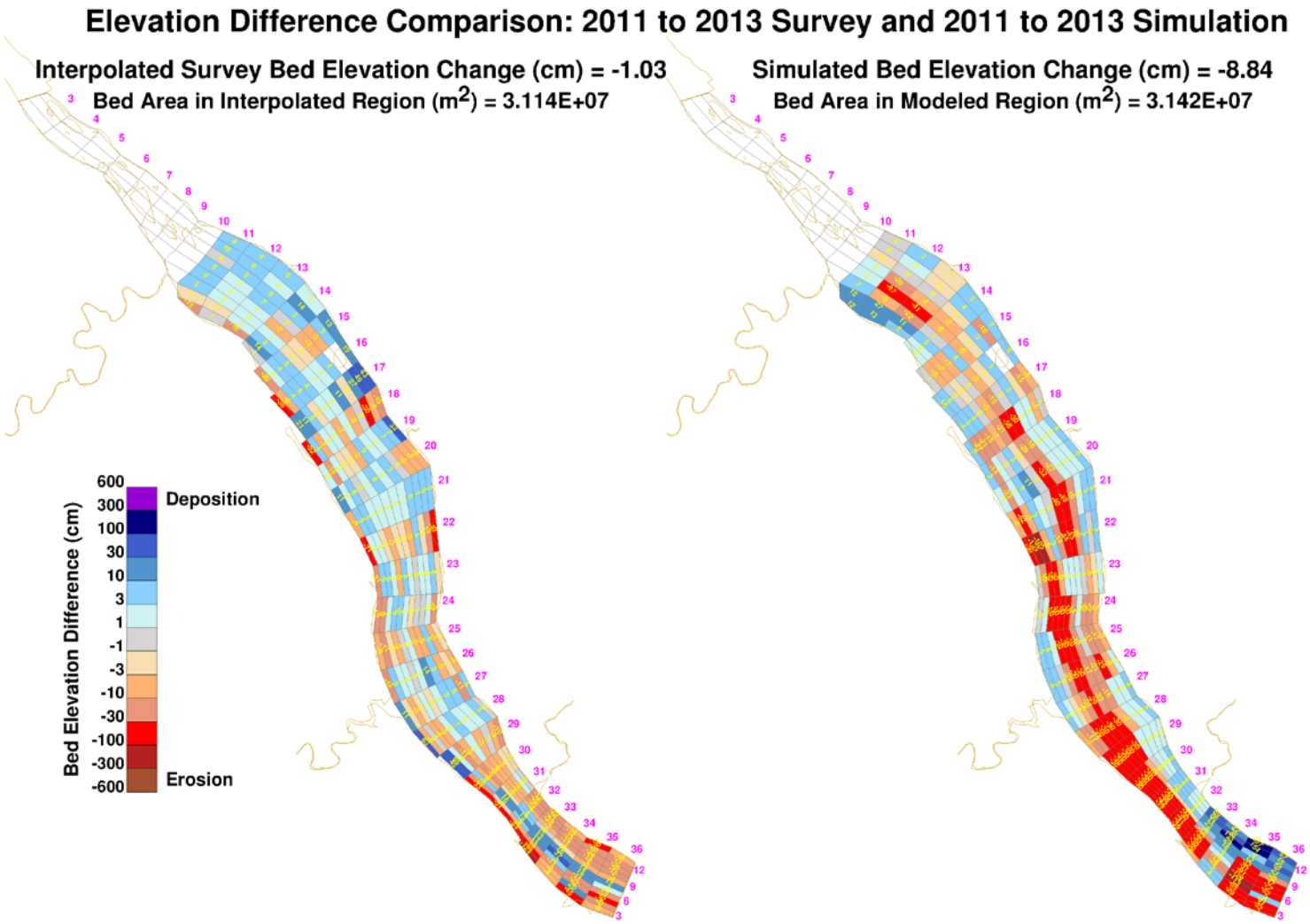


Figure J-5. Comparison of bed elevation changes estimated from differences between interpolated bathymetric surveys and simulated cumulative bed elevation change for Conowingo Pond: 2011-2013 (short-term).

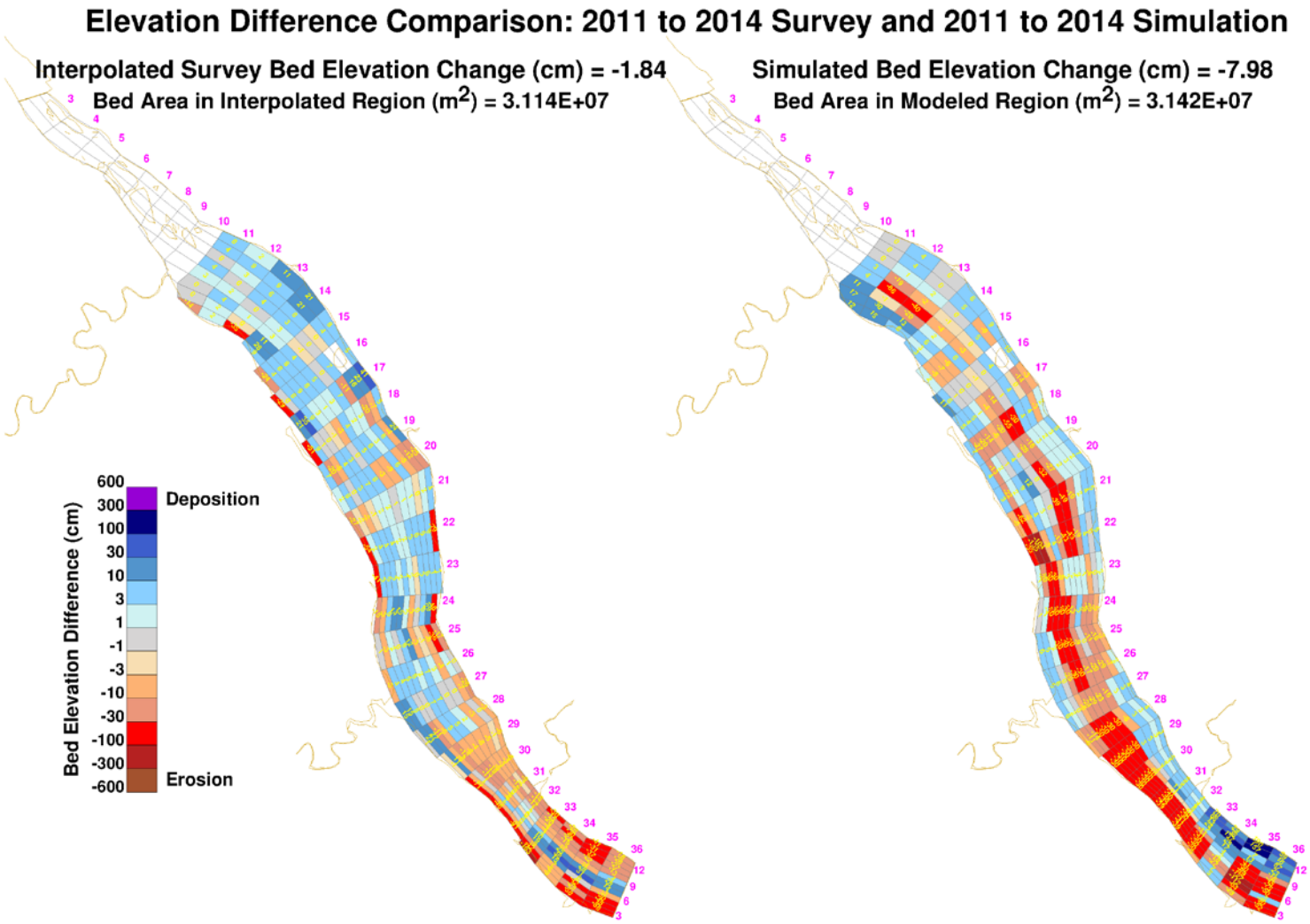


Figure J-6. Comparison of bed elevation changes estimated from differences between interpolated bathymetric surveys and simulated cumulative bed elevation change for Conowingo Pond: 2011-2014 (short-term).

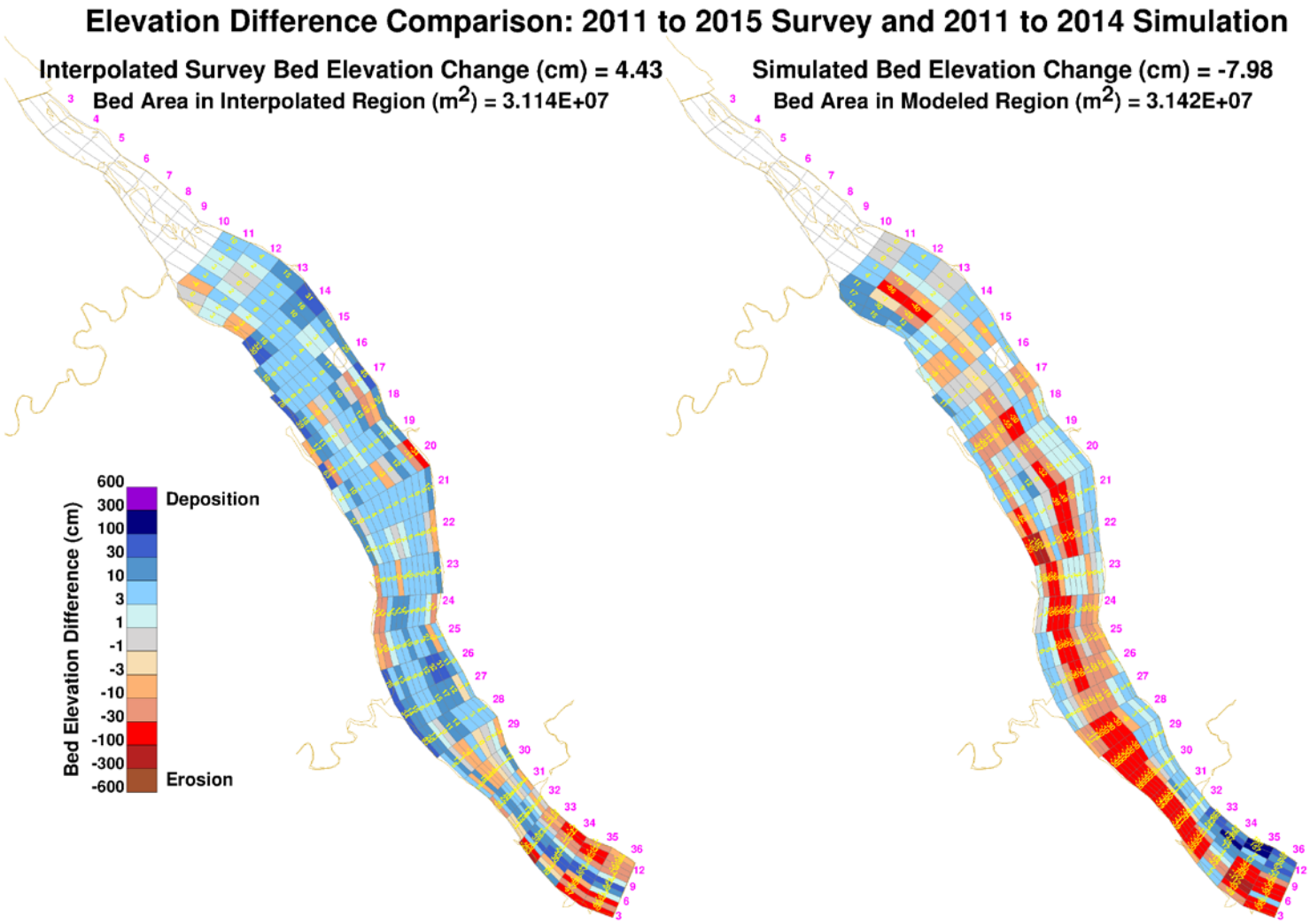


Figure J-7. Comparison of bed elevation changes estimated from differences between interpolated bathymetric surveys and simulated cumulative bed elevation change for Conowingo Pond: 2011-2015 (short-term).

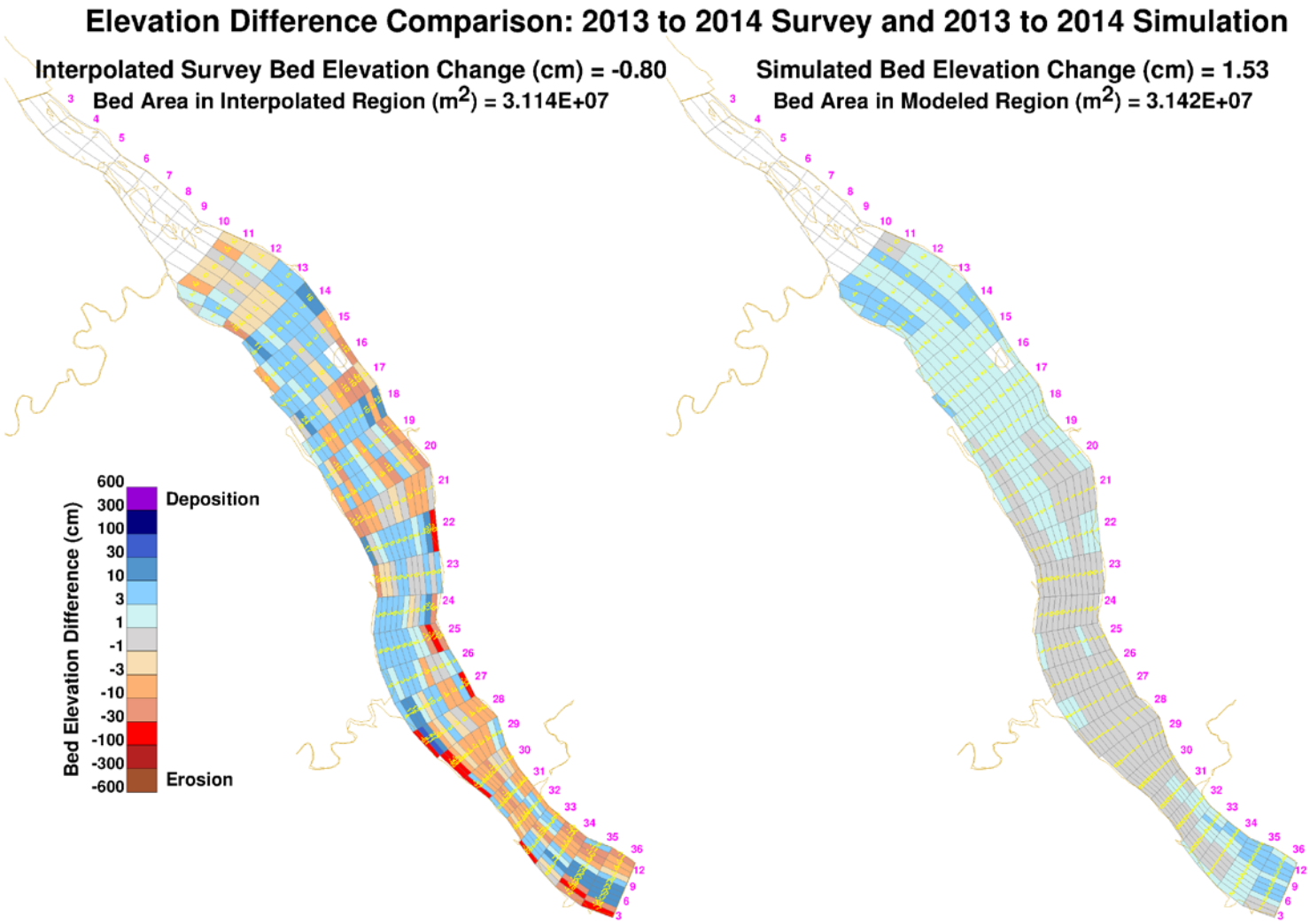


Figure J-8. Comparison of bed elevation changes estimated from differences between interpolated bathymetric surveys and simulated cumulative bed elevation change for Conowingo Pond: 2013-2014 (short-term).

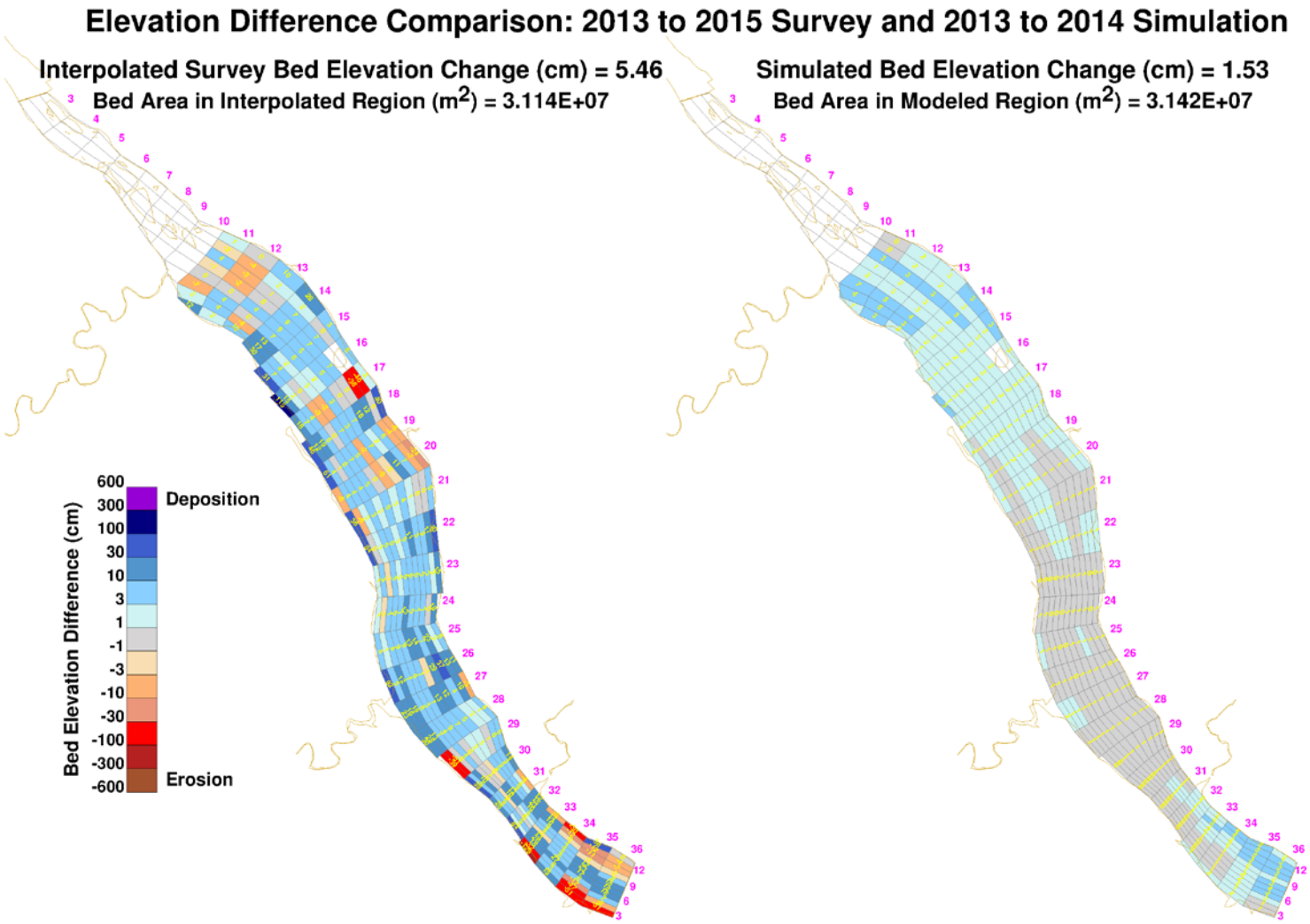


Figure J-9. Comparison of bed elevation changes estimated from differences between interpolated bathymetric surveys and simulated cumulative bed elevation change for Conowingo Pond: 2013-2015 (short-term).

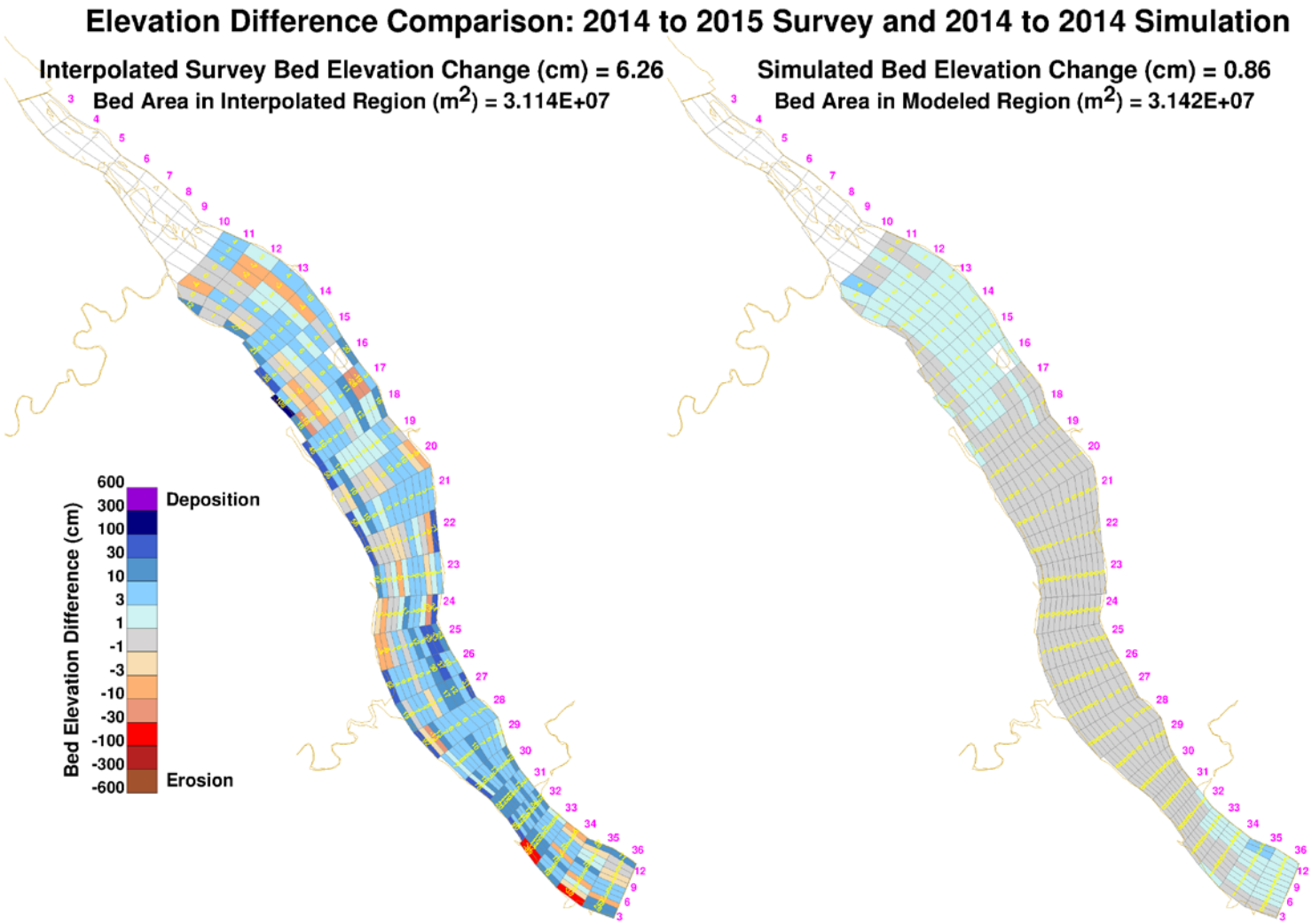


Figure J-10. Comparison of bed elevation changes estimated from differences between interpolated bathymetric surveys and simulated cumulative bed elevation change for Conowingo Pond: 2014-2015 (short-term).